Studies of Some Properties of Hydroxide-Catalysis Bonds

Valentina Mangano

Institute for Gravitational Research
School of Physics and Astronomy
University of Glasgow

Presented as a thesis for the degree of Doctor of Philosophy
in the University of Glasgow

June 2018

Ai miei genitori.
Grazie per avermi sempre ascoltato,
sostenuto e incoraggiato.

To my parents.
Thanks for always listening to me,
supporting me and encouraging me.

Summary

Jointing materials is an inevitable step in the fabrication of many high performance optical devices. Today there is an increasing demand, both from industry and academic research, for reliable techniques for jointing of optical components which can be performed simply and inexpensively, where the bonds possess high strength and precision with low mechanical loss.

Several methods of bonding have been defined and employed over time. Currently, the most common techniques of bonding are *optical contacting*, *diffusion*, *epoxy* and *glass frit*.

Each of these techniques has positive aspects which make them appropriate for a range of applications, but not ideal in cases where a thin optically transparent and mechanically strong joint between optical compounds is required.

Hydroxide-catalysis bonding is an interesting candidate in such cases: it has already been demonstrated to have excellent performance with respect to mechanical stability, precision and strength in numerous applications, such as in space systems, optics and gravitational wave detectors.

At present, there are not many papers that talk exhaustively about the optical properties of hydroxide-catalysis bonding. Most of the time, the published results are closely dependent on requirements imposed by the experiment that is being conducted.

Since there are a lot of interesting potential applications and increasing industrial interest in usage of hydroxide-catalysis bonding, it is important to develop techniques to characterise the optical properties of these bonds.

In this thesis, a non-destructive technique for measuring the optical properties of hydroxide-catalysis bonding is reported. More specifically, the bond refractive index and thickness are determined from reflectivity measurements. By applying this method, it will be possible to understand how the optical properties and chemistry of a hydroxide-catalysis bond vary when different bonding solutions and substrate materials are used and, consequently, to tailor better the bonds to various utilisations of interest.

Sodium silicate solution at different concentrations with water and potassium hydroxide solution are used to bond fused silica and sapphire substrates. Curing at room temperature and at 100 $^{\circ}C$ for eight hours is chosen to study the influence of temperature on the properties of a hydroxide-catalysis bond. It was found that the bond optical reflectivities are less than 1% for fused silica samples and less than 10% for sapphire samples and they decrease over time. Bond refractive indices start from a value close to the refractive index of water and approach the refractive index of fused silica as the cure proceeds. Bond thicknesses cured at room temperature decrease over time plateauing at a more or less constant value, different for each case studied (about a few hundred nanometres), whereas bond thicknesses cured at high temperature seem to increase over time (less than about 400 nanometres).

Acknowledgements

This thesis would not have been possible without the support and advice of all the people who I have had the pleasure to meet over the years. This is my attempt to thank all of them.

First of all, I would like to thank my supervisors *Prof. Sheila Rowan*, *Dr. Mariëlle van Veggel* and *Prof. James Hough* for their guidance, support and patience, without which I could not have completed this PhD. I am very grateful to have had the opportunity to work in the Institute for Gravitational Research, to attend conferences which have allowed me to learn more, meet new people and visit amazing places, and to feel the extraordinary experience to be part of the team who detected the first gravitational wave directly. Thank all of you for this.

I would also like to express my gratitude to the *Royal Society* for providing the funding required to carry out my PhD studies, and to the *Institute for Gravitational Research* and the *University of Glasgow* for the facilities available to allow me to do the research presented in this thesis.

A big thank you is due to *all members* of the Institute for Gravitational Research, *my colleagues* and *office mates* (past and present): thanks for helping me when I needed it, for all the good conversations and for making environment in which to work and study so friendly. I never felt alone.

I would also like to thank *Prof. Fulvio Ricci* and *Dr. Paola Puppo* who encouraged me to apply for this PhD.

Thanks to *all the people* I have met outside the University and *my old friends* for all the good times we have spent together and, above all, for all the trips to discover beautiful Scotland.

My most heartfelt thanks go to *my mum* and *my dad* for loving and supporting me. I will never be able to thank you enough for always being there for me.

And thanks *Glasgow*. I enjoyed my stay here. These four years have flown very quickly.

Preface

This thesis is an account of work carried out by the author with support from staff in the Institute for Gravitational Research (IGR) at the University of Glasgow between October 2013 and June 2018.

The aim of this thesis is to develop a non-destructive method of measuring reflectivity of hydroxide-catalysis bonds and then extract the information on their refractive indices and thicknesses. Using this method, fused silica and sapphire substrates were bonded using different bonding solutions and curing conditions. Their effects on the bond reflectivity, refractive index and thickness were studied giving valuable insight in the chemistry.

These investigations were carried out at the suggestion and supervision of Prof. S. Rowan (Director of the IGR), Dr. A. A. van Veggel (Research Fellow in the IGR) and Prof. J. Hough (Associate Director of the IGR).

This thesis is composed of six chapters and five appendices. The topics covered in each of them are briefly summarised below.

Chapter 1 introduces the four most common methods of bonding (optical contacting, diffusion, epoxy and glass frit) used in industry and academic research along with their pros and cons. However, these jointing techniques may not be ideal for applications in which a thin optically transparent and mechanically strong bond between optical components is required. Hydroxide-catalysis bonding is an interesting candidate in such cases: it demonstrated to have excellent performance with respect to mechanical stability, precision and strength in numerous applications, such as in space systems and gravitational wave detectors. The chemistry, the properties and advantages and some successful applications of this jointing technique are also introduced. This work has been derived from current literature.

In Chapter 2 the method to determine refractive index and thickness of hydroxide-catalysis bonds from optical reflectivity measurements is illustrated. It contains the description of the construction processes which led to the optical assembly used to collect reflectivity measurements. All of the fabrication was carried out by the author. Guidance and advice on the fabrication were given by Prof. S. Rowan, Prof. J. Hough and Dr. A. A. van Veggel. Mr.

A. Grant (Honorary Research Associate) designed and built the electronics of one of two photodiode circuit boxes (the other one was made by the author) used in this thesis. Mr. R. Jones (Research Fellow), Mr. S. Craig (Mechanical Technician) and Mr. C. Craig (Senior Research Technician) provided help with the design and manufacturing of some elements necessary to build the optical assembly. Mr. S. O'Shea (Electronics Technician) and Dr. J. Scott (IT Administrator) provided electronic and computer support.
In this chapter the theoretical optical model developed for describing the reflectivity of bonds between isotropic and anisotropic materials is also discussed along with the corresponding Bayesian likelihood analysis which allowed the experimental and theoretical data to be statistically compared. The models were developed by the author under the supervision of Prof. S. Rowan, Prof. J. Hough and Dr. A. A. van Veggel. Valuable advice on the corresponding Bayesian likelihood analysis was given by Dr. C. Messenger (Lecturer). The bonding procedure used to make all samples analysed in this thesis is reported. It was taught in the laboratory to the author by Dr. K. Haughian (Research Fellow in the IGR) and Dr. A. A. van Veggel.

Chapter 3 contains the measurements on fused silica samples bonded at room temperature with sodium silicate solution at different concentrations with de-ionised water (volumetric ratios of 1 : 3, 1 : 6 and 1 : 10). The focus of this research was to investigate the effect of different concentrations of sodium silicate on the reflectivity, refractive index and thickness of hydroxide-catalysis bonds. Also, one fused silica sample made with sodium silicate solution at a volumetric ratio of 1 : 6 and cured at elevated temperatures (100 $^{\circ}C$) for 8 hours only was reported. In this way, the comparison between sodium silicate bonds cured at different temperatures was possible. The experimental results and the corresponding analysis were carried out by the author with the help and supervision of Prof. S. Rowan, Prof. J. Hough and Dr. A. A. van Veggel. The SEM (scanning electron microscopy) measurements of bond thickness were taken by Dr. A. A. van Veggel, Dr. J. Scott and Dr. M. Phelps, which allowed the author to insert their measurements in this thesis. The group Materials and Condensed Matter Physics of the University of Glasgow kindly allowed Dr. A. A. van Veggel, Dr. J. Scott and Dr. M. Phelps to use their scanning electron microscope.

In Chapter 4 bonds between fused silica substrates made using potassium hydroxide solution are investigated. The results obtained curing hydroxide-catalysis bonds at both room temperature and elevated temperature (100 $^{\circ}C$) for 8 hours and thereafter at room temperature are reported. The aim of these measurements was to understand the difference between potassium hydroxide bonds cured at room or elevated temperatures. The experimental results

and the corresponding analysis were carried out by the author under the supervision of Prof. S. Rowan, Prof. J. Hough and Dr. A. A. van Veggel.

For Chapter 5 bonds between sapphire substrate materials are discussed. Two bonding solutions were used for making these bonds: sodium silicate solution diluted with de-ionised water (1 : 6) and potassium hydroxide solution (0.1 N). The aim of these measurements was to investigate how the properties of bonds could vary when different bonding solutions and substrate materials were used. The results were obtained by the author under supervision of Prof. S. Rowan, Prof. J. Hough and Dr. A. A. van Veggel.

In Chapter 6 the results of this thesis are summarised, and suggestions for future work are outlined.

Appendix A introduces the most important thermal noise sources which currently limit the sensitivity of the gravitational wave detectors.

Appendix B reports the description of the current to voltage converter circuit used in this thesis. This circuit gave the measure of the voltage produced by the laser light incident on and reflected off a hydroxide-catalysis bond. Two current to voltage converter circuits were built under the supervision of Mr. A. Grant.

In Appendix C the algebraic steps necessary to derive some equations used in this thesis are shown.

Appendix D contains the MATLAB codes used to carry out the Bayesian analysis on the reflectance data and obtain the refractive index and thickness of a hydroxide-catalysis bond, as described in Chapter 2. These codes were written by the author under the supervision of Prof. S. Rowan, Prof. J. Hough, Dr. A. A. van Veggel and Dr. C. Messenger.

Appendix E contains the MATLAB code for determining the relative separation between two bonding surfaces. This code, written by the author under the supervision of Prof. S. Rowan, Prof. J. Hough and Dr. A. A. van Veggel, included some Matlab files of the Simtools package (download from http://www.gwoptics.org/simtools/) used in gravitational wave field.

A paper was written by the author together with Dr. A. A. van Veggel, Dr. R. Douglas, Prof. J. Faller, Mr. A. Grant, Prof. J. Hough and Prof. S. Rowan. It contains the results obtained in the first years of research of the author and was published by Optics Express [1].

Table of contents

List of figures

List of tables

Chapter 1

Methods of bonding

Jointing optical components is a critical step in the fabrication of high performance instruments or devices. A variety of technologies for jointing materials exists. Generally, the various jointing techniques can be divided into two kinds: direct and indirect bonding. The former does not use any intermediate layers between materials to be bonded, whereas the latter uses an intermediate layer to make the bond.

The choice of one jointing technique over another depends on the type of application to be developed and the requirements which a bond has to meet, such as accuracy and precision in alignment of optical components, simplicity of the bonding process, optical, chemical and thermal properties of the joint and its mechanical strength.

The most common techniques of direct jointing are optical contacting [2–4] and diffusion bonding [5–7], whereas epoxy bonding [8–10] and glass frit bonding [11–13] are indirect processes. Each of these jointing techniques has strong points which make them appropriate for fulfilling a limited range of requirements only.

Requirements on jointing techniques are varied and hydroxide-catalysis bonding, which is an indirect bonding technique, is a candidate that has properties of particular interest for use in certain optical applications. This technique has already been used in a range of opto-mechanical applications for bonding silica and Zerodur^{TM}, like Gravity Probe B [14–17], and both ground and space based gravitational wave instrumentation, such as aLIGO [18–21] and LISA Pathfinder [22–26], as will be explained more in this chapter.

Hydroxide-catalysis bonding can form very strong and extremely thin joints [3, 4, 19], with only a small amount of resulting thermal noise [27, 28], and is vacuum and cryogenic temperature compatible [3, 4, 19]. It allows samples to be bonded easily and precisely. As the bonds are transparent in the optical spectrum [3, 4, 19], this jointing technique may be

an excellent candidate for optical applications as well. Exploring a few of the properties of these bonds is the topic of this thesis.

In the following sections, the five jointing techniques mentioned above are introduced and explained. Optical contact bonding (1.1), diffusion bonding (1.2), epoxy bonding (1.3) and glass frit bonding (1.4) are not discussed in detail, because they are not part of the current work: their detailed description is beyond the scope of this thesis. For this reason, only the principle mechanisms of the respective bonding processes and the most important advantages and drawbacks are considered.

The hydroxide-catalysis bonding technique (1.5) is illustrated thoroughly, highlighting the chemistry behind the bonding process (1.5.1) and the properties and advantages of its bonds (1.5.2) which make it the bonding technique of choice in a number of successful applications. The most important applications of this jointing technique are also reported (1.5.3). In the last part of this chapter, the properties with pros and cons of these five bonding techniques are summarised (1.6).

1.1 Optical contact bonding

Optical contacting is a direct bonding technique which joints the surfaces of two materials to be bonded together at room temperature and without the use of intermediate layers (like glues or binders) [2–4]. Two surfaces may form an optical contact when the distance between them is $10 - 100\ nm$ (less than a wavelength of visible light), which is of the order of the action range of the intermolecular force [29, 30]. To be optically contacted, these surfaces have to be extremely flat, highly polished and cleaned [2–4, 31].

The main attraction mechanism responsible for the formation of an optical contact bond between two surfaces is the intermolecular van der Waals attractive force [2, 14, 30, 31]. It is the sum of the three dipole-dipole interactions acting between atoms and molecules [32–34]:

- the Keesom force between permanent dipoles: polar molecules tend to orient themselves with the positive end of a dipole facing the negative ends of the surrounding dipoles and vice versa;

- the Debye force between a permanent dipole and a corresponding induced dipole: the originally symmetrical electron clouds of the non-polar molecules are deformed temporarily (induced dipole) because of the proximity of the permanent dipoles of polar molecules;

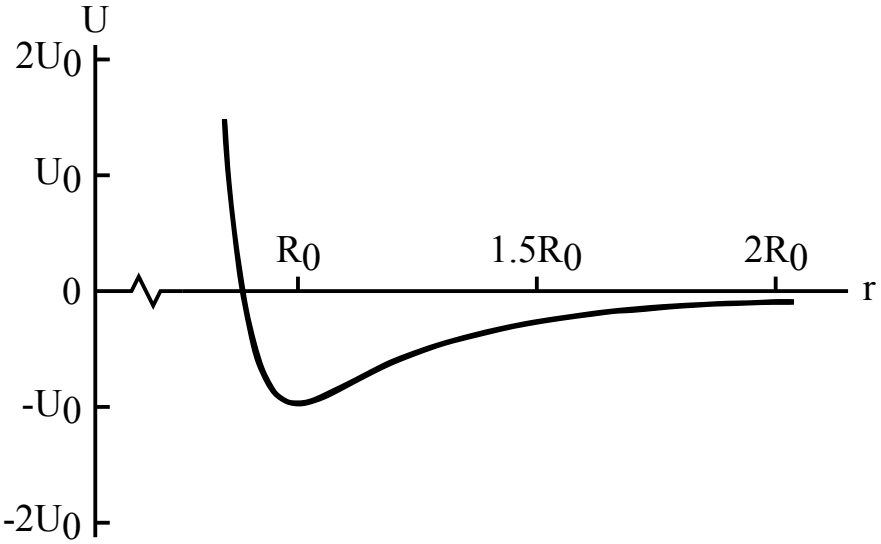

Fig. 1.1 Potential energy U of two atoms as a function of the distance r between centres of two atoms, where U is minimum at the equilibrium point $r = R_0$.

- the London force between an instantaneous dipole and an induced dipole: the continuous movement of the electrons around the atomic nuclei makes the electron cloud temporarily asymmetric, transforming each molecule into an instantaneous dipole which in turn generates induced dipoles in the adjacent molecule.

Given two atoms, whose centres are spaced apart by distance r, the potential energy $U(r)$ and the corresponding force $F(r)$ of this system are defined by the following relationships [34]:

$$U(r) = U_0\left[\left(\frac{R_0}{r}\right)^{12} - 2\left(\frac{R_0}{r}\right)^{6}\right] \tag{1.1}$$

$$F(r) = -\frac{dU(r)}{dr} = 12\frac{U_0}{R_0}\left[\left(\frac{R_0}{r}\right)^{13} - \left(\frac{R_0}{r}\right)^{7}\right] \tag{1.2}$$

with U_0 a positive constant expressed in J and R_0 the equilibrium point where $U(R_0) = -U_0$ and $F(R_0) = 0$.

When the distance between two atoms is greater than equilibrium point ($r > R_0$), the force is attractive but falls off quickly with distance; whereas if their distance is small ($r < R_0$), their electron shells overlap and the force becomes repulsive (Figure 1.1) [34].

Therefore, van der Waals potential energy can be considered as the sum of a repulsive (r^{-12}) and attractive (r^{-6}) component [34].

Using the microscopic approach of Hamaker, it is possible to determine the van der Waals force between surfaces of two substrates from the interaction between two molecules [32, 33]. For the sake of convenience, the potential energy $U_{\text{A-B}}$ between two molecules A and B, whose distance from each other is D, is rewritten here as the sum of contributions of all three dipole-dipole interactions which decrease with D^{-6} [2, 32, 33]:

$$U_{\text{A-B}}(D) = -\frac{C_{Keesom}}{D^6} - \frac{C_{Debye}}{D^6} - \frac{C_{London}}{D^6} = -\frac{C_{AB}}{D^6} \tag{1.3}$$

where the minus sign indicates that the force is attractive, and C_{AB} is the interaction constant $(J\ m^6)$ which encompasses all the three dipole-dipole interactions.
From this relationship, the potential energy $U_{\text{A-surface}}$ between the molecule A and the plane surface of the substrate, which are a distance D apart, is calculated [2, 32, 33]:

$$U_{\text{A-surface}}(D) = -\frac{\pi\rho_B C_{AB}}{6D^3} \tag{1.4}$$

where ρ_B is the constant volume number density of substrate B (m^{-3}).
In the last step, the potential energy per unit area $u(D)$ between two surfaces, which are a distance D apart, is defined as [2, 32, 33]:

$$u(D) = -\frac{\pi\rho_A\rho_B C_{AB}}{12D^2} = -\frac{A_H}{12\pi D^2} \tag{1.5}$$

where ρ_A and ρ_B are the constant volume number densities of the two substrates A and B, and $A_H = \pi^2\rho_A\rho_B C_{AB}$ is the Hamaker constant expressed in J.
Finally, the van der Waals attractive force per unit area $F_{vdW}(D)$ between the surfaces of two substrates is obtained from the negative derivative of equation 1.5 [2, 30, 32, 33]:

$$F_{vdW}(D) = -\frac{A_H}{6\pi D^3} \tag{1.6}$$

Even though the van der Waals force is weaker than other strong chemical bonds, in the case of interaction between the surfaces of two substrates, it can reach significant values if small distances D are achieved. The force per unit area between the surfaces of two substrates is proportional to D^{-3}, namely, it can act over slightly larger distances than originally expected from the D^{-6} dependence of the potential energy for single molecules [32, 33].

Once the surfaces to be contacted have been polished and cleaned, two substrates have to be bonded immediately to avoid any surface contamination. If the surfaces are very flat, parallel and clean, no interference fringes might be expected to form. Often there is some entrapped air between them, so a pattern of interference fringes will be created. A pressure can be applied to the top substrate in order to push air out and initiate the contacting process. Once the contacting process has initiated, it is not necessary to apply any further pressure: the process will continue until the entire interface has been covered [29].

One of the advantages of optical contact bonding is that a successful bond may be as strong as the substrates jointed [35, 36].
Also, the bonds produced by this jointing technique are optically transparent and, therefore, have a low reflectivity [14, 29].
An optical contacting bond can be made between any type of material (metal, semiconductor, carbide, fluoride, oxide, nitride, compound, composite, organic material) and state of the material (monocrystalline, polycrystalline, amorphous) [37].
The strength of an optical contact bond is influenced by environmental contamination of the bonding surfaces (for example, dust particle) and surface roughness. Therefore, areas that are not in contact can be present in the bonding interface, preventing or weakening the formation of a bond. This makes optical contacting an unreliable jointing technique [2–4, 14, 29].
If the surfaces to be bonded are clean, flat and smooth, a good bond will form immediately. However, this can be a big disadvantage in the case of failure, for example, if the two substrates are misaligned or in the presence of dust. Once two surfaces have bonded, it is not possible to adjust the alignment or de-bond them without degrading the surface quality. Therefore, this bonding technique has a low first-try success rate that lowers further with re-bonding [3, 4, 31].
Finally, the bonds neither tolerate thermal shocks nor survive in a cryogenic environment [3, 4, 14].

This bonding technique is used in optical instruments, like interferometers, in the production of short stable gas lasers, in contacting laser crystals, in silicon-on-insulator (SOI) technology and silicon wafer bonding in the field of electronics [2, 37].

1.2 Diffusion bonding

Another direct jointing process is diffusion bonding. It is a thermo-compression process based on the diffusion of atoms across the interfaces of substrates to be bonded under pressure and high temperature so making a monolithic joint [5–7].

To obtain the formation of this bond, the surfaces of two substrates have to be brought into contact within the range of interatomic forces so that the atomic diffusion may occur [5–7, 38, 39].

Even if these surfaces were very flat, smooth and clean, it would not be possible to reach this range on the whole bonding area by simple contact, because they would always show microscopic flaws and surface oxide layers. Because the surface roughness is inevitably greater than atomic scales, the contact between two substrates can only occur at their flaws. Also, the atoms of a surface tend to interact mainly with oxygen atoms from the surrounding environment forming oxide layers which block atomic diffusion. This effect can be mitigated by conducting diffusion bonding in vacuum or an inert gas environment [5–7, 38–40].

When applying a pressure within the range $0-100\ MPa$ on materials to be bonded, the asperities on each of the surfaces deform plastically and oxide layers fracture. This allows surfaces to contact each other within interatomic distances, avoiding macroscopic deformation. But the pressure only is not sufficient to create a strong bond between surfaces [5–7, 38, 39].

Diffusion is a process facilitated by high temperatures and the rate at which atoms diffuse is related to the diffusion coefficient D. This diffusion coefficient is given by an Arrhenius equation expressed as follows [5, 38, 41]:

$$\mathsf{D} = \mathsf{D}_0 \exp\left(\frac{-Q}{RT}\right) \tag{1.7}$$

where D_0 is the diffusion coefficient when $T = \infty$, Q is the activation energy in $J\ mol^{-1}$ required to move an atom from one lattice site to another (lower activation energy means easier diffusion), $R = 8.314\ J\ mol^{-1}\ K^{-1}$ is the universal gas constant, and T is the absolute temperature in K.

As the temperature increases (approximately $50-80\%$ of the absolute melting point of one of the objects), the diffusion coefficient increases exponentially and the atoms of both substrates start to migrate across the interface [5–7, 38, 39, 41].

Migration of atoms, facilitated by the proximity of two substrates by pressure, can occur by two main mechanisms referred to as vacancy diffusion and interstitial diffusion (Figure 1.2) [5, 41].

The difference between these two types of migration depends on the size of the diffusing atom.

In vacancy diffusion, an atom moves from its starting position to an adjacent vacant site in the lattice. This atom will create a vacancy at the original site that could be filled by another atom, and so on.

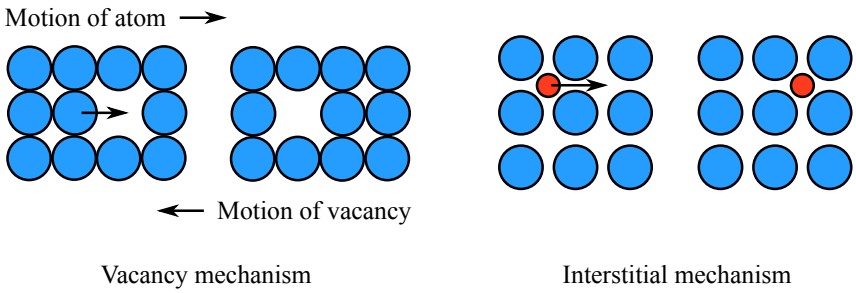

Fig. 1.2 (left) Schematic illustration of vacancy and (right) interstitial mechanism (image reproduced from [41]).

Interstitial diffusion is the displacement of very small atoms from one interstitial site to another without displacing any other atoms in the lattice [5, 41].

When atomic diffusion across the interface takes place, voids reduce and bonded areas increase. Through the formation of bonds at atomic level, after a sufficient dwell time related to chosen values of temperature and pressure, a strong bond between two substrates is formed along the entire interface (see Figure 1.3) [5–7, 38, 39].

With this jointing technique, high quality and high strength joints can be formed which have the same properties as the parent materials [5, 38, 40].
Materials of the same or different type and also with complicated shapes can be bonded together, making the development of new structures possible [5, 7, 38, 40].
A disadvantage of this jointing technique is the time that has to be spent for the preparation of surfaces to be bonded which have to be very flat and clean to obtain a successful bond [5]. Also, the dwell time has to be sufficient to let atoms diffuse and create bonds between two materials, but an excessive diffusion time can change the chemical composition of the material [5].
As diffusion bonding has to be conducted at high temperature, pressure and often in an inert environment, the equipment costs are high [5, 7, 38, 40].

This bonding technique is used in electronic and ceramic packaging, in wire bonding and flip chip assembly [7].

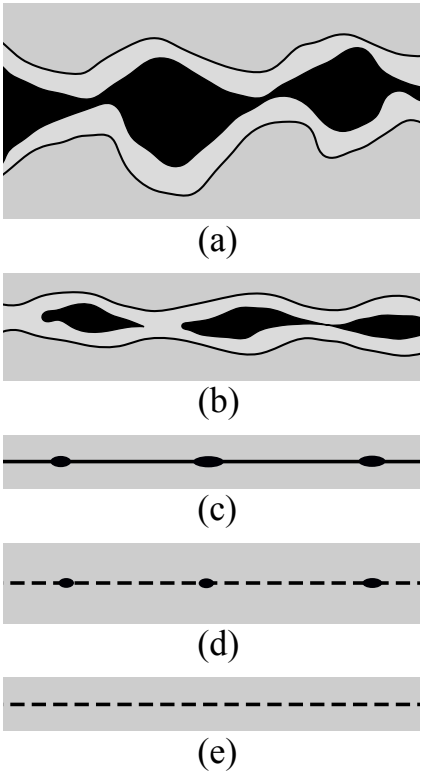

Fig. 1.3 Schematic illustration of diffusion bonding process (image reproduced from [7]): (a) initial contact between two materials where black areas are the voids and light grey bands are the oxide layers; (b) application of pressure and consequent plastic deformation of surface asperities; (c) diffusion process; (d) diffusion and reduction of voids; (e) final bond between two substrates.

1.3 Epoxy bonding

An epoxy bond is formed by jointing two substrates together by means of epoxy-based adhesives. These adhesives are generally composed of an epoxy resin and a curing agent known as hardener [8–10].

The epoxy resin is a thermosetting polymer which contains three-membered epoxide rings (two carbon atoms individually bonded to an oxygen atom) referred to as epoxy groups. When epoxy resin is mixed with the hardener, the epoxy resin starts to harden through thermally induced cross-linking reactions with the hardener. This thermally induced cross-linking process is known as curing. As the cure proceeds, the hardener, reacting with epoxy groups, forms larger and larger molecules, which give rise to branched molecules and successively branched structures. With the extension of these structures, the critical gel point is reached and the mixture becomes a weak gel. The cure will stop when the gel solidifies and the epoxy bond has then been created. The success of curing depends on the reactivity of the hardener with the epoxy group [8–10].

Components can be added to the epoxy resin and hardener to modify the properties and adapt them to various desirable application requirements [8, 9, 42, 43]. Here the most important additional components are introduced briefly:

- solvents or diluents regulate the viscosity of the mixture so that curing can be completed quickly [8, 9, 42];
- various types of fillers, such as silver or gold which make the epoxy electrically conductive [8, 9];
- elastomeric modifications improve the toughness of epoxies, mitigating its brittleness [9];
- coupling agents are small bifunctional molecules that provide a chemical bridge between epoxy, filler and attachment surface [8, 9];
- accelerators speed the reaction between the epoxy resin and hardener [8, 42].

The epoxy-based adhesives are available as single-part or two-part epoxy systems [43]. In single-part epoxies, the epoxy resin and hardener are already mixed together. They are not active at room temperature and need high temperatures, more than 100 $^{\circ}C$, to start the curing process. The higher the temperature is, the faster the curing is, with curing times sometimes less than ten minutes [43].

In two-part epoxies, the epoxy resin and hardener have to be mixed together by the user at precise mix ratios. Once they are mixed, the two-part epoxies can cure at either room temperature or elevated temperature. The curing time is strongly affected by temperature: as a general indication, as the temperature increases by 10 $^{\circ}C$, the curing time will be halved. At room temperature, the epoxies solidify in a few minutes to several days, whereas at temperatures below 10 $^{\circ}C$ chemical bonds may be compromised reducing their cohesive strength and resistance [43].

Summarising, the advantage of using a single-part epoxy is that no mixing takes place, but its disadvantage is that heat is necessary to cure the bond; whereas, the advantage of a two-part epoxy is that curing can already occur at room temperature, but the disadvantage is that a mixing of epoxy resin and hardener at accurate mix ratios is involved.
Another positive aspect of using epoxies is their low mechanical stiffness. This means that any stresses induced by the bonding process are absorbed by the epoxy itself and they are not transferred to the substrate [8].
Differently from the bonding techniques that require surfaces to be extremely flat and smooth, this indirect bonding method does not need special surface treatments. The epoxies fill any gaps between the bonding surfaces, reducing the problem of the surface roughness [42].
One of the drawbacks of these adhesives is the release of volatile materials and impurities over time. Material can escape from the bulk as a gaseous product or by diffusion along surfaces, meaning very few epoxies are suitable for high vacuum applications [8, 42].
Environmental effects, such as atmospheric moisture and radiation, can compromise the properties of epoxy-based adhesives [9]. Water molecules, present as atmospheric moisture, can be absorbed in epoxies and deteriorate the interfacial region between the substrate and adhesive dramatically. This can affect the reliability of the bond or even result in a de-bond. For this reason, it is advisable to control the environmental moisture during the whole process [9, 42, 44]. Adhesive bonds also cannot tolerate high intensity lasers or ultraviolet light because of the organic nature of epoxy [3, 4, 9].
As the epoxy-based adhesive is a complex mixture of materials, different chemical reactions can occur. This means that a well-defined, homogeneous and very thin bond cannot be formed [3, 4, 8].

Epoxies are commonly used in micro-electro-mechanical systems, civil infrastructures and aerospace industry [8, 9, 44].

1.4 Glass frit bonding

Glass frit bonding, also referred to as glass soldering, is another indirect technique which utilises a low-temperature melting point glass as an intermediate layer [11–13]. More precisely, the glass frit is a viscous paste obtained from milling low-temperature melting glass into a powder and mixing it with an organic binder. Solvents can be added to this paste to regulate its viscosity, and inorganic fillers can be added to influence its properties [13].

The procedure of this bonding technique consists of four main steps: deposition, thermal conditioning, bonding and cooling down [13].

Once the glass frit is ready, it can be deposited on the material to be bonded, hence the name of the first step. To place the bonding material only in areas where bonding is required and prevent the paste from flowing elsewhere, screen printing can be used [11, 13].

The paste that has been deposited on a substrate cannot be used as is. If it was used in the bonding step and it was heated at the wetting temperature (viscosity decreases to the point where it wets the surfaces to be bonded), the organic binder and solvent would cause voids inside the glass, lowering strength and reliability of bond. To avoid this, the paste is heated at different temperatures to transform it into a pre-melted glass. This thermal conditioning consists of four steps (Figure 1.4):

- at 120 $^{\circ}C$ the paste is dried to remove most of the solvents and the organic binder starts its polymerisation;
- at 360 $^{\circ}C$ the organic binder is burned out and the glass particles start to adhere to each other and to the surface of substrate where the paste was deposited;
- at 450 $^{\circ}C$ the glass is melted and does not have any voids, except for fillers which are trapped inside it;
- at room temperature, the substrate to be bonded is placed with high precision on top of the substrate baked with the glass frit and a light pressure is applied.

After this thermal conditioning phase, the glass frit and two substrates are ready to be bonded together and form the bond [11–13, 45].

The glass frit bonding is a thermo-compressive process. The glass frit, together with the two well-aligned substrates, is heated again to its wetting temperature ($440 - 450\ ^{\circ}C$) to reduce its viscosity. When it becomes soft and liquid to flow and wet the surfaces to be bonded, the two substrates are pressed together mechanically. The surfaces of substrates are

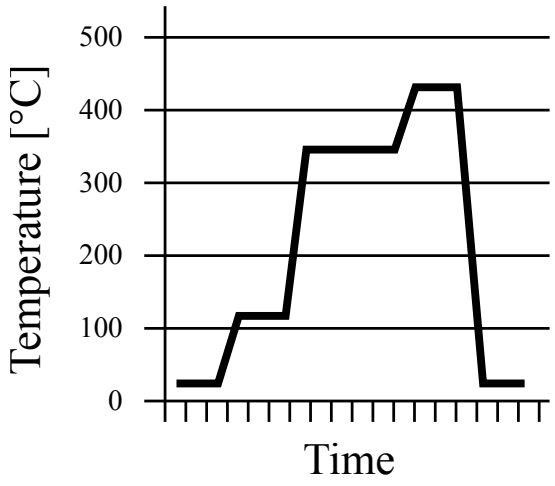

Fig. 1.4 Thermal conditioning of the glass frit paste (image reproduced from [12]).

fused into the glass at an atomic level and a bond starts to be formed between the glass frit and the surfaces of substrates [11–13].

When the bonding material has fully flowed and wetted the surfaces of both substrates, the bonded object can be cooled down. If the right temperature and pressure are used, the glass frit will solidify and form a mechanically strong bond between the glass frit and the substrates [11–13].

Throughout the entire bonding process, the surfaces to be bonded have to be horizontal to avoid sliding of bonding material because of gravitation-related effects [13].

The main advantages of using this bonding technique is that it produces mechanically strong and chemically resistant bonds [3, 4, 11, 13, 45] and very low mechanical stress applied to bonded components [11, 13, 45].
Just like for the epoxy-based adhesives, this technique does not requires bonding surfaces to be perfectly flat or smooth [11, 13, 45].
Also, the reliability is very good [11, 13] and the process is safe and reproducible [11, 13, 45].
One of the main disadvantages is that the bond is thick and opaque, making it not appropriate for precision applications and transmission optics [3, 4].
This bonding technique requires the use of high temperature which can damage bonds, make glass frit flow again or limit the choice of the materials to be used. Solutions to solve these problems increase the complexity of the process and, consequently, the expenses, in addition to the costs of glass frit material and processing [3, 4, 11, 13, 45, 46].

Glass frit bonding is mainly used in the hermetical encapsulation of microsensors [13, 45].

1.5 Hydroxide-catalysis bonding

Hydroxide-catalysis bonding is an indirect jointing technique which produces chemical bonds between oxide or oxidisable substrates, such as silica, sapphire and silicon, using hydroxide ions in an aqueous solution at room temperature [3, 4, 47]. It was further developed and patented by Gwo [3, 4] at Stanford University and first used in the construction of an all fused silica star tracking telescope for the Gravity Probe B satellite-based mission (see subsection 'Gravity Probe B' in section 1.5.3 for details) [3, 4].

After the description of the chemical process of hydroxide-catalysis bonding (1.5.1), its most important properties and advantages are summarised, dwelling in particular on the refractive index and thickness of a hydroxide-catalysis bond which are important parameters for those applications requiring low reflectivities and thin joints and their study represents the purpose of this thesis (1.5.2). At the end of this section, some applications of hydroxide-catalysis bonding in various fields of research, such as its contribution to the detection of the first gravitational wave, are discussed (1.5.3).

1.5.1 Chemistry

Hydroxide-catalysis bonding is based on hydroxide-catalysed hydration and dehydration reactions. Hydration is a chemical reaction in which a water molecule is added to a chemical element or structure, whereas dehydration is the loss of this water molecule from the chemical entity. The general formula which describes hydration (forward reaction) and dehydration (reverse reaction) is [3, 4]:

$$\mathrm{X{-}O{-}Y + H_2O \rightleftharpoons X{-}OH + Y{-}OH} \tag{1.8}$$

where X and Y represent the chemical elements of the substrate surface to be bonded.

The minimum energy required to activate the dehydration process depends on the chemical entities involved and varies from few to several eV. It is possible to lower the activation energy to less than a few k_BT (Boltzmann's constant $k_B = 8.617 \times 10^{-5}\ eV\ K^{-1}$ and temperature T in Kelvin) if the reactions of hydration and dehydration are catalysed by hydroxides (OH^-). This means that hydration and dehydration can occur at room temperature. The hydroxide ions are typically dissolved in water (hydroxide solution) and can be produced by ionic salts, such as potassium hydroxide KOH and sodium hydroxide NaOH [3, 4].

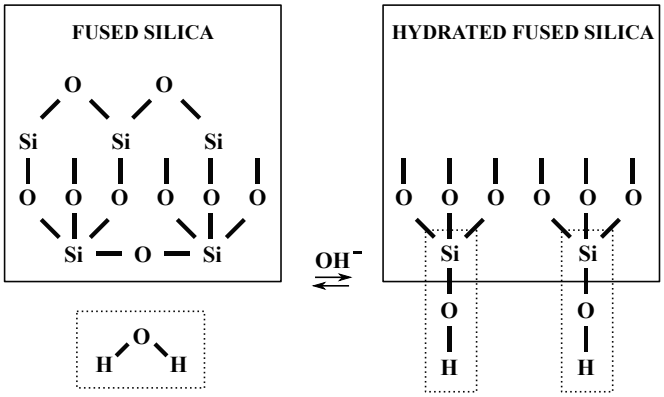

Fig. 1.5 Schematic illustration of hydration and dehydration process of a fused silica surface.

In the case of a fused silica substrate (silicon dioxide SiO_2), the general formula 1.8 becomes:

$$\mathrm{Si{-}O{-}Si + H_2O \rightleftharpoons[OH^-] Si{-}OH + Si{-}OH} \tag{1.9}$$

and these reactions of hydration and dehydration, catalysed by hydroxides, are shown in Figure 1.5 [3, 4].

The fused silica substrate (Figure 1.5, left) is a network of siloxane linkages (Si−O−Si) whose surface is exposed to water H_2O and hydroxide ions OH^-. In the forward process of hydration, atoms of silicon and oxygen at the surface are hydrated by a water molecule and form two Si−O−H structural groups. In the reverse process of dehydration, one oxygen atom and two hydrogen atoms are removed from two Si−O−H structural groups to form a water molecule [3, 4].

For silica-based materials (SiO_2), the chemical process which leads to the formation of a hydroxide-catalysis bond can be described in four steps: hydration, etching, polymerisation and dehydration [19, 28, 48].

In the hydration process, the surface to be bonded (if it is hydrophilic like clean silica) will attract hydroxide ions OH^- that are present in the bonding solution and fill any open bonds on the surface (Figure 1.6) [19, 28, 48].

After the surface is hydrated, the remaining hydroxide ions OH^- in the bonding solution will start etching of the silica surfaces. Free hydroxide ions OH^- create weak bonds with silicon atoms on the silica surface. This will cause the weakening of the lattice bonds Si−O−Si and the liberation of the silicate molecule $Si(OH)_4$ from the bulk substrate, producing silicate ions $Si(OH)_5^-$ in bonding solution, as described in the following chemical reaction

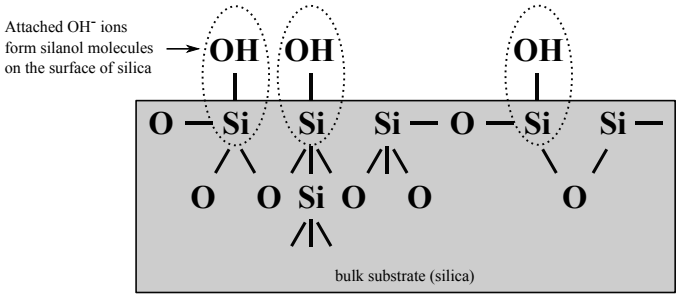

Fig. 1.6 Schematic illustration of hydration process of hydroxide-catalysis bonding, where OH^- ions form silanol molecules Si−O−H on the silica surface.

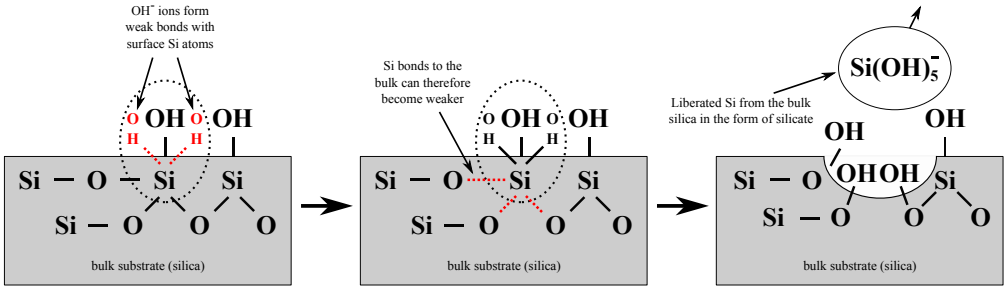

Fig. 1.7 Schematic illustration of etching process of hydroxide-catalysis bonding.

(Figure 1.7) [19, 28, 48]:

$$SiO_2 + 2\,H_2O + OH^- \longrightarrow Si(OH)_4 + OH^- \xrightarrow{\text{pH>11}} Si(OH)_5^- \tag{1.10}$$

During the etching process, the number of the silicate ions $Si(OH)_5^-$ increases, whereas the number of the free hydroxide ions OH^- reduces and the pH of the solution decreases. When the number of the hydroxide ions OH^- is low enough to have a pH below 11, the silicate ions $Si(OH)_5^-$ disassociate to form silicate molecules $Si(OH)_4$ and OH^-. When the concentration of silicate molecules $Si(OH)_4$ reaches $\sim 2\%$, they begin to combine and polymerise, creating siloxane chains (Si−O−Si) and water. This is the process of polymerisation (Figure 1.8) which is described by the following chemical reaction, where hydroxide-catalysis bond is $(HO)_3SiOSi(OH)_3$ [19, 28, 48]:

$$2\,Si(OH)_5^- \xrightarrow{\text{pH<11}} 2\,Si(OH)_4 + 2\,OH^- \longrightarrow (HO)_3SiOSi(OH)_3 + H_2O + 2\,OH^- \tag{1.11}$$

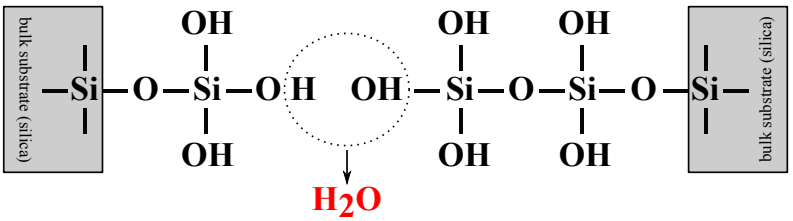

Fig. 1.8 Schematic illustration of polymerisation process of hydroxide-catalysis bonding.

In the final step of dehydration, the water created during the polymerisation starts to evaporate and/or enter the bulk of the bonded materials. During this time, the bond forms, reducing its thickness and increasing its strength [19, 28, 48].

It is not clear what exactly happens with the potassium or sodium atoms during this process (such as in potassium hydroxide KOH and sodium hydroxide NaOH solutions). It is possible that some of those are attached to the silicate chains, or that they act as interstitial atoms sitting in gaps (as sodium and potassium atoms are small), or that both the sodium and potassium migrate into the silica (as the sodium is smaller than potassium it will diffuse further in). Considering the scale of the bonds it is also hard to say of the sodium or potassium ions are preferably close to the substrate or if they are uniformly distributed.

Similar reactions can occur on an alumina surface, as shown in the following general formula [3, 4]:

$$\mathrm{Al{-}O{-}Al + H_2O \overset{OH^-}{\rightleftharpoons} Al{-}OH + Al{-}OH} \tag{1.12}$$

The main difference between fused silica and alumina is the extension of their hydrated surface (Figure 1.9). For fused silica, the hydrated surface is a relatively thick three dimensional layer, whereas for alumina it is a quasi-two-dimensional layer, where the dimension perpendicular to surface is smaller than its other two dimensions parallel to surface [3, 4].
In the case of a sapphire substrate (aluminium oxide Al_2O_3), it cannot form a silicate-like network on the surface of its own, but can attach to an existing one to form an aluminosilicate network, which consists of a mixture of aluminate and siloxane chains (Al−O−Si) [49].
A sodium silicate solution Na_2SiO_3, which is composed of sodium hydroxide NaOH and silicon dioxide SiO_2 dissolved in water, can be used to make it possible. It is not entirely clear what the reaction for sapphire looks like, however it is probable that the hydroxide ions OH^- of this solution interact with the alumina surface by one of the following chemical reactions (1.13 or 1.14) to form the aluminate ions [49]:

$$\mathrm{Al(OH)_{3(s)} + OH^-_{(aq)} \longrightarrow Al(OH)^-_{4\,(l)}} \tag{1.13}$$

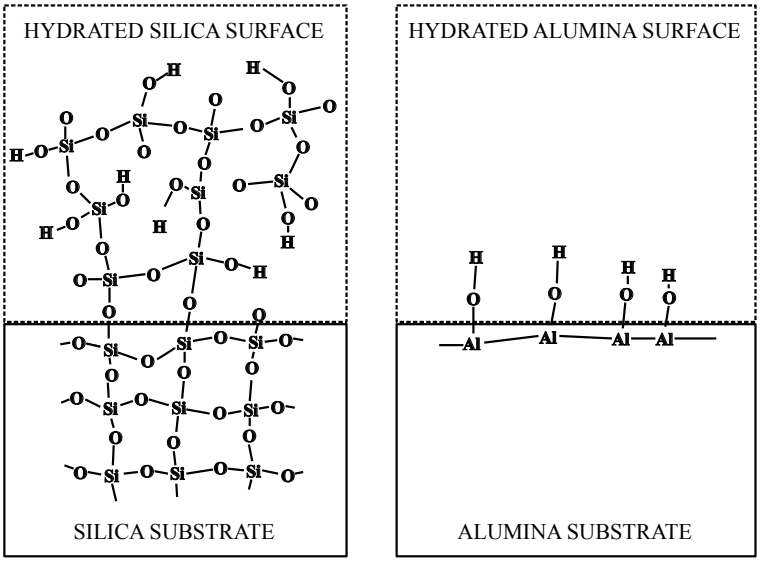

Fig. 1.9 (left) Schematic illustration of hydrated surfaces of a fused silica and (right) an alumina substrate.

$$Al(OH_2)_6^{3+}{}_{(s)} \longrightarrow Al(OH_2)_5OH^{2+}{}_{(l)} + H^+{}_{(aq)} \tag{1.14}$$

where the subscripts (s), (aq) and (l) indicate the physical state of each substance and stand for solid, aqueous solution (namely, dissolved in water) and liquid, respectively.
The aluminate ions $Al(OH)_4^-$ and $Al(OH_2)_5OH^{2+}$ can then start a dimerisation process, as described in the reaction 1.15 or 1.16 [49]:

$$2\,Al(OH)_4^- \longrightarrow (HO)_3AlOAl(OH)_3^{2-} + H_2O \tag{1.15}$$

$$2\,Al(OH_2)_5OH^{2+} \longrightarrow (H_2O)_4Al(OH)_2Al(OH_2)_4^{4+} + 2\,H_2O \tag{1.16}$$

The aluminate ions $Al(OH)_4^-$ and $Al(OH_2)_5OH^{2+}$ liberated from the hydrated alumina surfaces will chemically react with the silicate molecules $Si(OH)_4$ of silicate-like network contained in the bonding solution and form a three-dimensional aluminosilicate network, where some of the Si atoms of the silicate structure are replaced by Al atoms, as shown in the chemical reaction 1.17 or 1.18 [49]:

$$Si(OH)_4 + Al(OH)_4^- \xrightarrow{OH^-} (HO)_2AlOSi(OH)_3 + H_2O + OH^- \tag{1.17}$$

$$Si(OH)_4 + Al(OH_2)_5OH^{2+} \xrightarrow{OH^-} (HO)_2AlOSi(OH)_3 + 2\,H^+ \tag{1.18}$$

Summarising, if substrates have or can generate a silicate-like network, or they can be chemically linked to a silicate-like network produced by a silicate material added in bonding solution, it will be possible to bond their surfaces together by hydroxide-catalysis bonding. The same applies to an aluminate-like network [3, 4].

Of course the etching rate of sapphire using metal hydroxides (like potassium or sodium hydroxide) is likely to be extremely slow, but etching of alumina has been reported [50]. It is therefore likely that success of bonding using no additional silicates in the solution is highly dependent on the surface conditions of the sapphire substrates. Research using electron microscopy techniques to provide answers to these questions is ongoing.

Two cases were considered to explain the hydroxide-catalysed hydration and dehydration reactions: fused silica substrates with hydroxide ions in aqueous solution and sapphire substrates with sodium silicate solution. In both cases, silicon atoms are used to bond two substrates together (silicate or aluminosilicate network), which come from fused silica substrate and/or bonding solution.
In case no silicon atoms are available to form a silicate-like network and only hydroxide ions are used, the surfaces of the two substrates have to be very close together to achieve bonding (almost touching) [3, 4]. Of course this is difficult to achieve and so in that case, without a silicate filler, the bonds are found to be quite weak [51].

The amount of solution used to bond two substrates together can be approximated by a volume of which the base is equal to the area of the bonding surface and the height equals the starting thickness of the bond layer. During the dehydration phase, the bond thickness decreases because of the evaporation/absorption of the water molecules, and also the value of the bond refractive index varies, from the refractive index of wet to dry bonding solution. The values of the bond thickness and refractive index depend on the efficiency of the hydroxide-catalysed hydration and dehydration reactions which depend, in turn, on the bonding solution, substrate material and curing process chosen. Also, it is not possible to know the exact boundary position and this may be different when different methods of measurement are used (for example, in this thesis the optical thickness of bond is obtained from reflectivity measurements).

In preparation of bonding using a hydroxide solution, it is important to consider if the substrates to be bonded can or cannot generate a silicate-like network and the figure mismatch of their surfaces. In order to make a high-quality bond, the chemistry of the bonding solution has to be adjusted taking these two factors in consideration [3, 4].

If the surfaces of two substrates to be bonded can generate an adequate silicate-like network and their surface figure mismatch is small, then hydroxide solution (hydroxide ions in aqueous solution) is sufficient to make a bond between them. When the siloxane linkages are present along the entire surface, two substrates will be bonded together [3, 4].
If the surfaces to be bonded cannot generate an adequate silicate-like network or if they generate this silicate-like network but it is not sufficient to bond the surfaces between them because of a large surface figure mismatch, then it is possible to use solutions which contain both hydroxide ions and silicate. Silicate material consists of silicon dioxide or silicate salts (such as sodium silicate Na_2SiO_3) dissolved in a high pH (namely in a high concentration of hydroxide ions) aqueous solution to fill various gaps between bonding surfaces. In this case, siloxane linkages are not formed directly between two surfaces, but between the surfaces and the silicate material [3, 4].
Finally, in the case the surfaces have a significantly large surface figure mismatch, then a filling material, which contains surface hydroxyl groups, can be included in the bonding solution to facilitate the creation of a silicate-like network and corresponding linkages. This filling material can be powders, particulate materials, foams or liquids of various viscosity [3, 4].

Examples of substrate materials which can generate silicate-like networks through hydroxide-catalysed hydration and dehydration reactions are silica, fused silica, natural quartz, silicon with a surface oxide layer, Zerodur^{TM} (extremely low expansion glass ceramic from SCHOTT), ULE^{TM} (ultra low expansion titania silicate glass from Corning), borosilicate, opal, granite, and other silica-based or silica-containing materials. The substrate materials which cannot generate a silicate-like network but can be linked to a silicate-like network are copper, iron, titanium, their oxides, alumina-based materials (like sapphire), and calcite [3, 4].

In addition to the requirements of silicate-like network and surface figure mismatch, the success of a bond made by hydroxide-catalysis bonding also depends on the cleanliness of surfaces to be bonded. For this reason, it is convenient to prepare these bonds in clean environments and clean the surfaces making them hydrophilic and free of contamination so that the efficiency of the bonding mechanism is maximised [3, 4]. Operating procedures to prepare bonding solution, clean and bond the surfaces of substrates to be jointed will be described in detail in section 2.4.

Even though the principal bonding mechanism involved in hydroxide-catalysis jointing technique is the hydroxide-catalysed hydration and dehydration, other minor effects can be present, such as electrostatic forces due to the charges at the bonding interface, hydrogen

bonds formed among surface hydroxyl groups and water molecules trapped in the interface, and van der Waals forces if the surfaces are contaminated by hydrophobic organic material [4].

1.5.2 Properties and advantages

In this section, the most important properties and advantages of hydroxide-catalysis bonds are given.

Bonds can be made between many optical materials (mainly evidenced for silica, silicon, Zerodur^{TM}, borosilicate and sapphire). The bonds are very strong and can be made extremely thin (between 10 nm and 10 μm) depending on surface match and filler material used. This helps with minimising their contribution to thermal noise and allows high precision alignment and high positional stability to be obtained (see section 1.5.3) [3, 4, 19].

Also, the possibility to perform the bonding process at room temperature, the availability of inexpensive bonding materials and the extremely high first-try success rate make it an attractive low cost process [3, 4, 19].

This bonding technique can be also used in cryogenic systems down to 2.5 K, and in ultra-high vacuum where it has a negligibly small outgassing due to water molecules [3, 4, 19].

The bonds, when made between matching materials such as silica and silica, sapphire and sapphire, and silicon and silicon, can survive thermal shocks without being degraded when they are submerged into liquid nitrogen ($77K$) or liquid helium from a room temperature environment [3, 4, 19].

The time elapsed before the materials become attached and impossible to move without mechanical destruction of the bond is referred to as settling time [27, 28]. It can be adjusted by changing the concentration of hydroxide ions and silicate material in the bonding solution, or the temperature at which bonding occurs [3, 4, 27, 28]. The settling time increases as the concentration of hydroxide ions OH^- of the bonding solution grows. Even though a longer time can be useful in applications where high accuracy of alignment is required, an increase of hydroxide ions implies longer etching times and consequently thicker bonds. The thickness of a bond can affect the mechanical strength of the bond itself, and the thicker the bond the larger its contribution to thermal noise (see section 1.5.3 for details) [27, 28]. The settling time generally decreases as the concentration of silicate material in the bonding solution increases: the more silicate, the shorter the time needed for the bonds to become strong [3, 4]. The settling time increases as the temperature at which the bonding process takes place decreases [27, 28].

Below, three relevant properties of hydroxide-catalysis bonds are described, giving the status of research on mechanical strength, optical properties and thickness of this bond.

Mechanical strength

The strength of a hydroxide-catalysis bond depends on a number of factors, such as the type of bonding solution and its concentration, the materials to be bonded characterised by flatness and roughness, the procedure of cleaning and bonding, the type of strength test conducted, and so on [19].

This explains the large variation in average mechanical strengths found, from 1.19 ± 0.14 *MPa* (silica to silica bonds made using potassium hydroxide at a molecular ratio of $1:500$ with de-ionised water at room temperature) to 70^{+19}_{-32} *MPa* (sapphire to sapphire bonds made using sodium silicate at a molecular ratio of $1:6$ with de-ionised water at 77 *K*), that can be found in the literature. The low bond strength of 1.19 ± 0.14 *MPa* could have been caused by the introduction of strong peeling stresses in the measurements [19, 27, 52].

The mechanical strength tests performed on bonded silica substrates have showed that if the bond is of good optical quality, the substrate material fractures before the bond. This suggests that the mechanical strength of bond is close to or stronger than that of the substrate material [3, 4, 19, 27].

The strength of the bulk material influences the strength of bond, where the strongest to the weakest bond strengths are, respectively, for sapphire, silicon and silica [19].

The hydroxide chosen for making the bonding solution can determine the mechanical strength of the bond. For different substrate materials, bonds made with sodium silicate solution are stronger than bonds made with a pure NaOH or KOH solution [19, 27, 52].

As an example, Douglas et al. measured the strength of sapphire to sapphire bonds using four different bonding solutions, sodium aluminate (14^{+3}_{-7} *MPa* at room temperature), sodium hydroxide (12^{+4}_{-5} *MPa* at room temperature), potassium hydroxide (16^{+42}_{-9} *MPa* at room temperature) and sodium silicate (65^{+26}_{-27} *MPa* at room temperature and 70^{+19}_{-32} *MPa* at 77 *K*). They found that bonds produced with sodium silicate solution were stronger and their strength was not influenced by exposure to cryogenic temperatures down to 77 *K* [52].

Optical properties

Although hydroxide-catalysis bonding has been studied thoroughly with respect to its mechanical strength, very little optical characterisation of its bonds has been reported in the literature.

One of first immediate characteristics of the hydroxide-catalysis bonds is their transparency in the visible and near-infrared range, which makes these bonds particularly interesting for optical applications, potentially ones in which the transmission of a high power light through an interface, without damaging it and with low absorption, is required [3, 4, 19].

Sinha et al. conducted first studies on the optical properties of hydroxide-catalysis bonding. They measured the reflection of light at normal angle of incidence from bonded interfaces between silica substrates made using different solution concentrations, solution volumes and curing temperatures. They measured the reflectivity of a hydroxide-catalysis bond to be less than 7.08×10^{-4} [48].

Sinha et al. also demonstrated that the use of this bonding technique to join a fused silica flat to a fibre end improved the reliability of high power systems, reducing damage due to high intensity of light [48]. See subsection 'Other applications' in section 1.5.3 for more details on Sinha's work.

Thickness

Gwo stated that it is possible to make very thin bonds by adapting the bonding solution, namely modifying its chemistry, to the characteristics of the surfaces to be bonded [3, 4].

This is an important property of the hydroxide-catalysis bonding, above all for those applications which require to keep thermal noise as low as possible, such as in the gravitational wave detectors (see subsection 'Advanced LIGO detectors' in section 1.5.3 for details).

Very thin bonds are also important for minimising the tilt of bonded components and obtaining high precision alignment and high positional stability [3, 4, 19]. This is an important requirement for LISA (see subsection 'LISA Pathfinder' in section 1.5.3 for details).

For the Gravity Probe B mission, the thickness of bonds between fused silica substrates made using potassium hydroxide solution was found to be around 200 *nm* and was measured by scanning electron microscopy (SEM) which corresponded to the surface figure mismatch of the bonding fused silica surfaces [14].

Elliffe et al. measured the thickness of some bonds between silica substrates using atomic force microscopy (AFM). They found an average thickness of 26 ± 6 *nm* for bonds made using potassium hydroxide at a molecular ratio of $1 : 500$ with de-ionised water, 81 ± 3 *nm* and 100 ± 7 *nm* for sodium silicate at a molecular ratio of $1 : 6$ and $1 : 4$ with de-ionised water, respectively [27].

Cunningham et al. measured the thickness of the bond between fused silica substrates using sodium silicate solution. It was 61 ± 4 *nm* using scanning electron and atomic force microscopy [53].

It is important to highlight that AFM and SEM techniques are used to estimate the thickness of a bond between substrates. These are destructive methods as bonded samples are cut in slices to expose a cross-section of the bond and then polished to allow for AFM or SEM imaging [14, 27, 53, 54].

Refractive index and thickness from reflectivity

The purpose of this thesis is the study of some properties of a hydroxide-catalysis bond, more specifically the bond refractive index and thickness which can be determined from reflectivity measurements (see Chapter 2 for details).

For many applications, the knowledge of the refractive index and thickness of a bond is particularly helpful for improving the performance of the bonded components and their reliability.

The bond refractive index is an important property for those applications that require low reflectivities from their joints so that the reflection coefficients can be reduced, resulting in a corresponding reduction of the spurious signals. For instance, this is an important requirement for the fabrication of high power fibre lasers which can be designed to minimise or eliminate internal reflections increasing their efficiency (see subsection 'Other applications' in section 1.5.3 for details).

The bond thickness is crucial for those applications that need high positioning accuracy for minimising parallel, angular and axial misalignments between the bonded components (see subsection 'LISA Pathfinder' in section 1.5.3 for details). Also, it is becoming increasingly important to accurately know the thickness of the bonds between the ears and mirrors in gravitational wave detectors. The thermal noise contribution from the bonds is a component in the total thermal noise contribution in the mirror suspensions of gravitational wave detectors. The thermal noise depends on the mechanical loss of the bonds and on the amount of strain energy stored in the bonds during operation. The larger either of these is, the larger is the thermal noise. The strain energy has been shown through FE modelling to increase approximately linearly with the thickness of the bonds [53]. In aLIGO the thermal noise contribution from the bonds is less than 10% of the total thermal noise budget and measuring bond thickness directly, accurately and non-destructively is not necessary. However, for future detectors where coating noise is suppressed further, this will probably be necessary.

The strength of the study proposed here lies not only in the fact that it represents the first step towards a better understanding of the properties of these bonds and the parameters which can influence them, but also in the fact that it is a non-destructive approach which allows the determination of these properties without damaging the bonded optical components.

There are already methods for measuring the refractive index (like refractive index matching liquids sold by Cargille Laboratories) or the thickness (like scanning electron microscope and atomic force microscopy) of a bond, but these are destructive techniques: a bonded component has to be cut so that the part of bond of interest can be studied directly. Therefore, such methods are not ideal for those applications where the bonded component does not have to be destroyed or the properties of a bond and their temporal evolution (curing), together with quality and spatial homogeneity control, have to be studied in situ without changing the boundary conditions. On the contrary, the non-invasive technique based on reflectivity measurements reported in this thesis is.

1.5.3 Applications

Thanks to its reliability and versatility, hydroxide-catalysis bonding can be tailored to a wide range of possible applications. For this reason, it has been selected as the jointing technique of choice for the fabrication and assembly of opto-mechanical components with high performance in a number of applications [3, 4, 19]. As an example, it has been used in the NASA satellite mission Gravity Probe B [14], in the ESA LISA Pathfinder mission [25], in several ground-based gravitational wave detectors such as GEO600 [55] and advanced LIGO [20], and in other applications, from lightweight composite mirrors to high power fibre lasers. Below, an overview of these applications is given.

Gravity Probe B

The first successful application of hydroxide-catalysis bonding was the assembly of the science instrument of Gravity Probe B, which consisted of four gyroscopes and a star tracking telescope attached to a block (all made of fused quartz). Gwo himself stated that hydroxide-catalysis bonding was the only possible technique for making this assembly reliably with high accuracy and precision [14–17].

Gravity Probe B was a satellite-based mission developed by NASA and Stanford University, of which the aim was to test two fundamental predictions of Einstein's theory of General Relativity, the warping (geodetic effect) and twisting (frame-dragging effect) of space-time around the Earth [16, 17].

It was fundamental that both telescope and gyroscopes were connected with the fused quartz block as firmly as possible. Also, the optical components of the telescope had to be firmly mounted. The major difficulty was how to reliably assemble fused quartz components

together ensuring high mechanical strength and pointing stability, even when cooled to cryogenic temperatures [14–16].

For this reason, the hydroxide-catalysis bonding was developed and tested by Gwo [14]. Tests were made on fused quartz discs, which had 2.5 *cm* of diameter and 0.6 *cm* of thickness. The bonding surfaces were polished to $50 - 100$ *nm* peak-to-valley flatness, and the bonds were made using an aqueous solution of potassium hydroxide. The tests showed that bonds had shear strength of approximately 30 MPa, close to the bulk strength, and could tolerate thermal shocks and cryogenic cycling without losing their reliability [14].

After these promising results, the hydroxide-catalysis bonding was chosen as the jointing technique for the Gravity Probe B mission. The bonds were made using potassium hydroxide at a molecular ratio of $1 : 500$ with de-ionised water and their thickness was typically 200 *nm*, which corresponded to the surface figure mismatch of the two bonding surfaces [4, 14, 16, 19].

LISA Pathfinder

Another successful application of hydroxide-catalysis bonding is the construction of the interferometer optical bench for the LISA Pathfinder mission (LISA stands for Laser Interferometer Space Antenna).

Developed for ESA, LISA Pathfinder is a technology demonstrator for the eLISA (evolved LISA), an ESA space gravitational wave observatory, planned for the future, which will observe the gravitational waves between 0.1 mHz and 1 Hz directly from space. The first results demonstrated that it is possible to put two test masses in a near-perfect gravitational free fall, controlling and measuring their motion with unprecedented accuracy. LISA Pathfinder has performed the first high-precision laser interferometric tracking of orbiting bodies in space. The successful demonstration of the key technologies necessary to place two test masses in free fall was essential for eLISA to be approved as a mission [22–26].

To achieve the condition of free fall, any non-gravitational disturbances acting on test masses have to be minimised, such as solar radiation pressure and internal thermal, magnetic and electrical forces, by measuring the position and orientation of each mass. The interferometer optical bench located between the two masses measures the small differential acceleration produced by fluctuating forces on the test masses [23, 26, 56].

To be able to measure these distances with high accuracy and precision, it is required that the bonds between various optical components are mechanical strong and stable. They have to withstand significant vibration forces during launch and they should not generate spurious signals due to the movement of a component which can simulate the movement of a test mass. Also, any jointing technique for the optical components had to meet stringent outgassing

requirements and some components had to be precision aligned to within 10 μrad. For this reason, hydroxide-catalysis bonding was chosen and a quasi-monolithic hydroxide-catalysis bonded interferometer optical bench was made and flown successfully [19, 56, 57].

Advanced LIGO detectors

"Ladies and gentlemen, we... have detected... gravitational waves! We did it!".

With these words, on the 11th of February 2016 David Reitze, executive director of the Laser Interferometer Gravitational-Wave Observatory (LIGO), announced the first direct gravitational wave observation to the world. A century after Einstein predicted the existence of gravitational waves [58], the LIGO Scientific Collaboration and Virgo Collaboration detected the first gravitational wave signal (GW150914 matched the waveform predicted by General Relativity for the inspiral and merger of a pair of black holes) on the 14th of September 2015, using the two advanced LIGO detectors, one in Hanford (Washington, USA) and the other in Livingston (Louisiana, USA) [20, 21].
More detections have been made since including an event that was also observed by many other types of instruments and by Virgo [59–63].

The advanced LIGO detectors are modified Michelson laser interferometers which operate in the frequency range from 10 Hz to 1 kHz. Each of the two perpendicular arms of the interferometer has a pair of input and end mirrors, separated by 4 km. Each of these mirrors is suspended as the final stage of a quadruple pendulum system to attenuate the motion due to seismic noise and thus behave as freely falling test masses in the detector bandwidth above the pendulum resonance frequencies. Using laser interferometry, the passage of a gravitational wave is detected through the variation along the optical axis of the relative length of the interferometer arms formed by freely suspended test masses. To achieve sufficient sensitivity to detect gravitational waves, it is necessary to reduce noise sources as much as possible [19–21].

GEO600 was the first gravitational wave detector to test the hydroxide-catalysis bonding for lowering thermal noise of fused silica mirror suspensions (see Appendix A for details) [55, 64]. In initial LIGO detectors, the input and end test fused silica masses of 10.7 kg were suspended on steel wires, which could cause excess thermal noise due to friction effects in the contact points between the suspension wires and the mirrors [18]. The GEO600 detector uses sodium silicate solution at a molecular ratio of 1 : 6 with de-ionised water to joint interface pieces called ears to the sides of the mirrors to which fused silica fibres could be welded, making the first ultra-low loss, quasi-monolithic fused silica mirror suspensions [19].

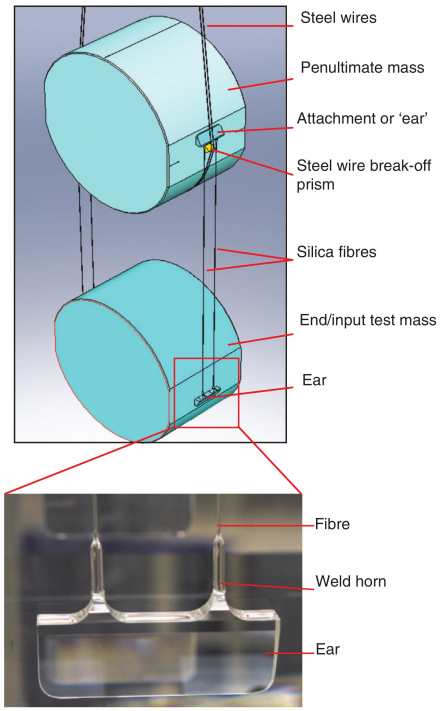

Fig. 1.10 Schematic illustration of an advanced LIGO quasi-monolithic fused silica mirror suspension and photo of an ear bonded to the side of a test mass where suspension fibres are welded to horns of the ear (courtesy of Dr. van Veggel [19]).

To keep the thermal noise as low as possible, in the advanced LIGO detectors, the input and end test fused silica masses of 40 *kg* were attached to their corresponding penultimate masses through fused silica ears and suspension fibres, making a GEO600-like quasi-monolithic fused silica mirror suspensions. The ears were bonded to the sides of the intermediate and test masses also using sodium silicate solution at a molecular ratio of 1 : 6 with de-ionised water, and the fused silica fibres were welded to the horns of ears using a CO_2 laser. The other stages still use steel wires (Figure 1.10) [18–21].

To reduce the thermal noise further in the next generation of gravitational wave detectors, the use of cryogenic temperatures with mirrors and suspension fibres made of sapphire or silicon has been proposed. The Japanese KAGRA detector will use sapphire optics with bonded quasi-monolithic sapphire ears and fibres [65]. The European Einstein Telescope detector and LIGO Voyager, and possibly Cosmic Explorer, propose to use silicon mirrors and suspension [66, 67]. Investigating if a quasi-monolithic mirror suspension made of sapphire and/or silicon is possible using hydroxide-catalysis bonding is currently an active area of research [51, 52, 68, 69].

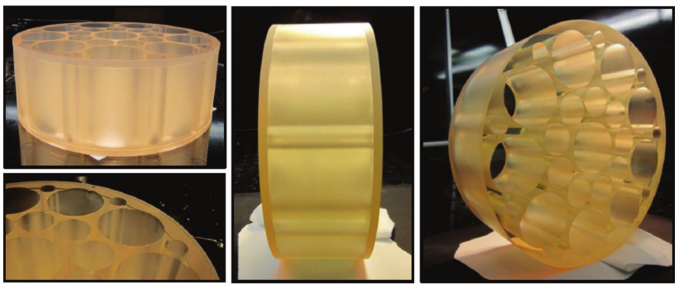

Fig. 1.11 Photos of an uncoated lightweight composite mirror composed of thin-walled cylinders bonded together (courtesy of Dr. van Veggel [19]).

Other applications

Mirrors are used in astronomical instruments for gathering light from distant objects and forming their images. Larger mirrors gather more light, and thus have better sensitivity and hence the demand for ever larger mirrors is always present. However, the fabrication of a very large mirror involves some drawbacks, such as the increase of its mass and reduction of its stability. One solution to this problem is the formation of large mirrors from smaller individual components bonded together by hydroxide-catalysis bonding. Gooch and Housego UK and Surrey Satellite Technology Limited, together with the Institute for Gravitational Research (University of Glasgow, UK), tested the hydroxide-catalysis bonding for making lightweight composite mirrors. Two thin slabs of low expansion material were bonded to a lighter middle section. The latter was a close packed array of thin-walled cylinders which were bonded between them and had varying hole sizes to optimise both lightweighting and manufacturability (Figure 1.11). After bonding, the mirror could be polished and coated as requested. The high mechanical strength of hydroxide-catalysis bonds made it possible to create a very large, but lightweighted mirror, reducing manufacturing risks and guaranteeing rigidity and stability at the same time [19, 70].

Hydroxide-catalysed bonding has been considered, as a reliable alternative to epoxy, in the construction of small and large deformable mirrors for adaptive telescopes. Normally the surface of a deformable mirror is bonded onto an actuator array using epoxy. This may cause difficulties, because an excess of epoxy between two surfaces to be bonded may alter the mechanical performance from actuator to actuator, introducing distortions or stresses in the mirror surface, and accumulate at the base of actuator. Instead, hydroxide-catalysis bonding produces very thin and strong bonds only at the bonding interface without dispersing material around. Strachan et al., in collaboration with the Institute for Gravitational Research

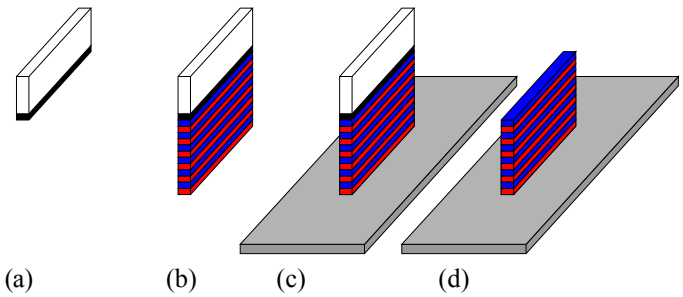

Fig. 1.12 Schematic illustration of coating transfer process (image reproduced from [73]): (a) deposition of the sacrificial layer; (b) deposition of the coating; (c) adhesion on the final substrate; (d) etching of the sacrificial layer.

at the University of Glasgow (UK), have tested this jointing technique by bonding PZT (lead zirconate titanate) actuators to silicon and silicon carbide (SiC) mirror substrates successfully [71, 72].

Another use of hydroxide-catalysis bonding is the transfer of a multilayer optical coating from the substrate where it is deposited to another one to create components having a high number of different filters known as array filters. This is an interesting solution for the cases where it is necessary to reduce the size and the weight of an optical instrument, particularly for space use. The main steps of a coating transfer process can be seen in Figure 1.12 and involve the deposition of the sacrificial layer onto the initial substrate (a), the deposition of a multilayer coating (in the reverse order) to be transferred (b), the hydroxide-catalysis bonding of the coating on the final substrate (c) and the chemical removal of the sacrificial layer from the initial substrate (d). Duchêne et al. have tested the resistance of these bonds to two etching solutions, ceric nitrate ammonium solution and potassium hydroxide solution. These solutions remove, respectively, a chromium or an aluminium sacrificial layer, which were chosen for these tests. The bonds were between silica substrates and a SiO_2/Ta_2O_5 coating, where the final coating layer was a silica layer to optimise the bonding process. In the case of the chromium sacrificial layer and using ceric nitrate ammonium etching solution to remove it, the coating was successfully transferred with no degradation of either the coating or the hydroxide-catalysis bond. In the case of the aluminium sacrificial layer and using potassium hydroxide etching solution, partial degradation of the bond and many defects on the coating were observed [73].

Sinha et al. have investigated the suitability of hydroxide-catalysis bonding for the construction of high power fibre lasers. They demonstrated that an optical flat bonded to the termination of an active fibre using the hydroxide-catalysis bonding can maximise

the optical damage threshold of the bond and minimise the feedback in a fibre due to the Fresnel reflection from the bond. They measured the optical damage threshold and feedback of one-hundred high-quality fused silica samples (6 *mm x* 6 *mm x* 20 *mm*) bonded using different concentrations of sodium trisilicate solution ($Na_2Si_3O_7$), different solution volumes and different curing temperatures. It was found that the best bonded samples were obtained using a sodium trisilicate solution diluted to 16.7% by volume with a total applied solution volume of 0.10 $\mu l mm^{-2}$, and curing them at a temperature between 90 $^{\circ}C$ and 120 $^{\circ}C$ for eight hours. They measured optical damage thresholds at bond greater than 70 Jcm^{-2} using a pulsed light of duration 25 *ns* at a wavelength 1064 *nm*. The Fresnel reflection from all of the bonded samples was measured at normal angle of incidence and it was found to be less than 7.08×10^{-4}. No scattering was observed from these bonds [48].

1.6 Summary

In the previous sections, five bonding techniques were investigated: optical contact bonding (section 1.1), diffusion bonding (section 1.2), epoxy bonding (section 1.3), glass frit bonding (section 1.4) and hydroxide-catalysis bonding (section 1.5).

The main properties with pros and cons of these jointing techniques are summarised in Table 1.1. It compares the joining techniques discussed in this chapter in terms of the performance of bonding processes (such as the ease of process, use of any materials and adjustability) and performance of bonds (mechanical strength, transparency, thin thickness and tolerance to thermal shocks).

		Optical contact	Diffusion	Epoxy	Glass frit	Hydroxide catalysis
Performance of bonding technique	Easiness of process	−	−	+	○	+
	Use of any materials	+	+	+	+	○
	Adjustability	−	−	+	−	+
Performance of bond	Mechanical strength	○	+	−	○	○
	Transparency	+	+	−	−	+
	Thin thickness	+	+	−	−	+
	Tolerance to thermal shocks	−	○	○	○	+

Table 1.1 Comparison of jointing techniques and their properties. + = excellent, ○ = fair, − = poor.

Chapter 2

Method to determine the optical reflectivity of hydroxide-catalysis bonds

In this chapter, a setup for studying the optical reflectivity of hydroxide-catalysis bonds is described and a possible non-destructive technique for determining the refractive index and thickness of a hydroxide-catalysis bond from the optical reflectivity measurements is investigated.

More specifically, a setup for measuring the reflectance of incident light of a laser from the interface between two isotropic or anisotropic substrates, jointed using a hydroxide solution, was planned, made and improved to make it more sensitive. Two polarisations (perpendicular and parallel to the plane of incidence of a sample) and two colours (green and red) of the incident light of a laser were considered.

The reflection of two orthogonal linearly polarised components of the incident light of the laser on the front face of a sample can be seen in Figure 2.1.

When the laser beam is incident on the surface of the sample at a non-normal angle of incidence, the polarisation of the laser can be decomposed into two orthogonal components in the plane of incidence. The linearly polarised components are perpendicular and parallel to the plane of incidence of the sample which is a plane that contains both the incident and reflected laser beams and is normal to the sample surface.

If the refractive index of air and substrate are known together with the wavelength of the laser light and its angle of incidence, then the most likely values for refractive index and thickness of bond can be extracted from reflectivity measurements collected by the optical setup. This is achieved using Bayesian likelihood comparison between these experimental data and those obtained by a mathematical model which describes the reflection of a bond layer between two substrates taking into account thin film interference.

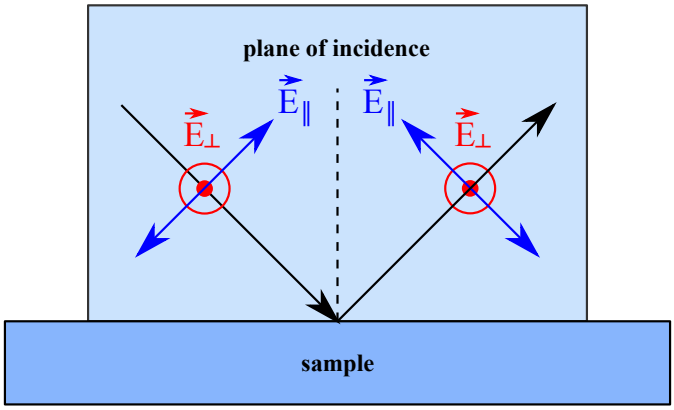

Fig. 2.1 Schematic diagram of the reflection of the two polarisation components: they are perpendicular ($\perp$) and parallel ($\parallel$) to the plane of incidence of the sample, respectively.

The first section is dedicated to the description of this optical setup which allows the intensity of the light reflected from a bonded interface to be measured (2.1.3). The first setup made (2.1.1) has undergone several changes which made it more sensitive (2.1.2). The two important steps of the fabrication of this assembly are also reported: measurements of the linearity of the two photodiodes used (2.1.4) and the reduction of the laser beam width (2.1.5). The linearity measurements allow the optical reflectances of a sample to be estimated, whereas the diameter measurements are to reduce the interference from the front and the back of the sample.

In the second section, the theoretical model of reflectances developed for isotropic (2.2.1) and anisotropic material (2.2.2) is described.

In the third section, after explaining the limits of an analytical approach in solving the reflectance equations (2.3.1), the Bayesian likelihood analysis (2.3.2) necessary to compare the experimental and theoretical data is described. The code written in Matlab (2.3.3) which allows this comparison to be evaluated and gives the refractive index and thickness of the bond as output is also explained.

Next, the procedure for producing the bonded samples which were used in this thesis (2.4) is presented.

Finally, the study for obtaining the flatness map of the interface between the two substrates which are bonded each other is also reported (2.5).

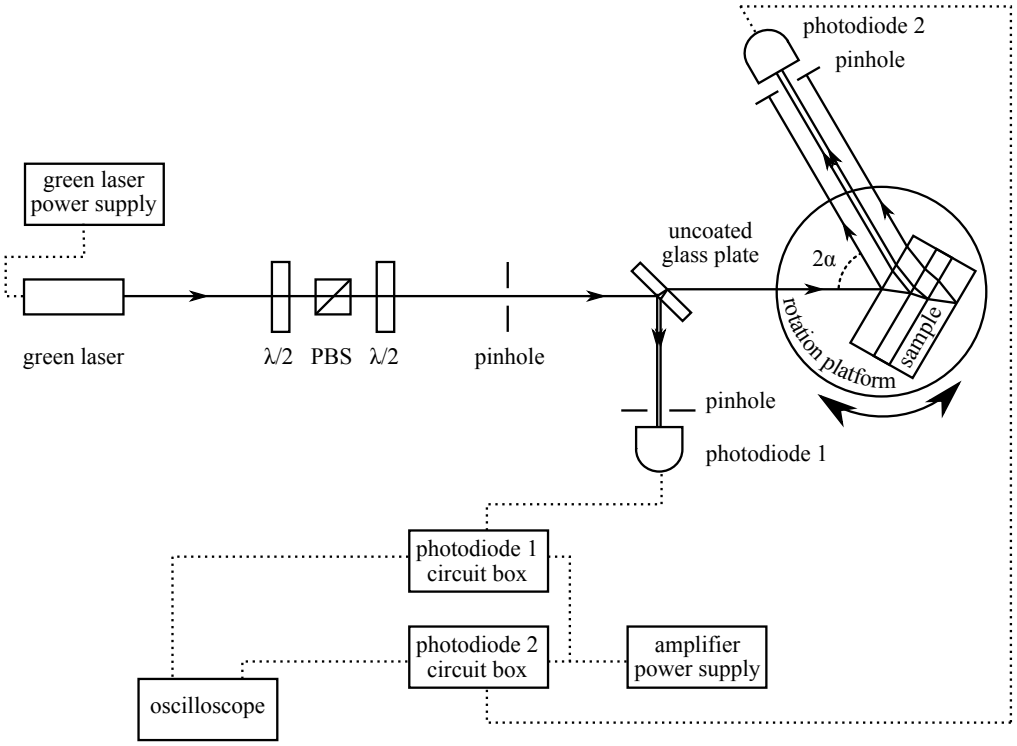

Fig. 2.2 Schematic diagram of the first setup used to measure the optical reflectivity of interfaces between two substrates bonded each other using the hydroxide-catalysis bonding.

2.1 Optical setup

In this section, the first assembly built for collecting the reflectivity measurements (2.1.1) and its upgraded and more sensitive version (2.1.2) are described. The main equations used to calculate the optical reflectances from data collected by two photodetectors are reported (2.1.3). The linearity of these photodetectors is verified (2.1.4), and the technique to reduce the laser beam width is also explained (2.1.5).

2.1.1 Initial and less sensitive assembly

The first optical assembly made to measure the optical reflectivity from a hydroxide-catalysis bond is shown in Figure 2.2 and its components are introduced below.

Laser. A green laser diode module ($\lambda = 532\ nm$) is connected to its power supply. The maximum output power is less than 1 mW and the $1/e^2$ diameter is 0.9 mm with a divergence of $\sim 0.2\ mrad$. The light does not have a pure polarisation.

Half-wave plates and polarising beamsplitter cube. The first half-wave plate $\lambda/2$ together with a polarising beamsplitter cube PBS linearly polarise the laser light and fix the orientation of the polarisation of the laser light. The second half-wave plate allows the selection of the perpendicular ($\perp$) and parallel ($\parallel$) polarisation of the light incident on the sample (see subsection 'Selection of the incident light polarisation' below for details). The two half-wave plates (Thorlabs WPH10M-532) have a diameter of 2.54 *cm*, and the polarising beamsplitter cube (Thorlabs PBS101) is $10.0 \times 10.0 \times 10.0$ *mm* and covers the wavelength range $420 - 680$ *nm*. This polarising beamsplitter cube has parallel polarisation transmission efficiency $T_{\parallel} > 90.0\%$ and perpendicular polarisation reflection efficiency $R_{\perp} > 99.5\%$, with ratio of maximum to minimum transmission (extinction ratio) of a linearly polarised input $T_{\parallel} : T_{\perp} > 1000 : 1$.

Uncoated glass plate. An uncoated glass plate ($7.6 \times 2.6 \times 0.1$ *cm*) allows a small fraction of the light incident on a bonded sample to be sent to photodiode 1.

Bonded sample and rotation platform. The sample to be studied is placed on a rotation platform (Thorlabs PR01/M) from which the light can be reflected at a range of angles of incidence α.

Pinholes. The pinholes (4 *mm* diameter) aid with alignment and minimise stray light. Also, as the laser beam incident on the sample produces three reflected spots due to the light reflected at its front, bonded and back surfaces, the use of a pinhole in front of photodiode 2 allows the beam spot off the bond to be separated from the other reflected beams.

Photodiodes. Photodiode 1 (Vishay TEMD5510FX01) has a sensitive area of 2.75×2.75 *mm* and its sensitivity curve as a function of wavelength is shown in Figure 2.3 (left). This is especially tuned for green light, whereas it has about 70% less sensitivity for red light. This photodiode monitors any fluctuation in intensity of the probe beam allowing the effect of these to be removed from the resulting analysis and the intensity of the incident beam to be measured (see subsection 2.1.4 for details). Photodiode 2 (Centronic OSD5-5T) has a sensitive area of $\varnothing$ 2.52 *mm* and its sensitivity curve as a function of wavelength is shown in Figure 2.3 (right). The spectral response of this photodiode to green and red light is about the same. This photodiode and its corresponding pinhole are rotated together around the sample on a square gridded breadboard to measure the intensity of the reflected beam, making sure the beam is at normal angle of incidence to the photodiode surface and, as much as

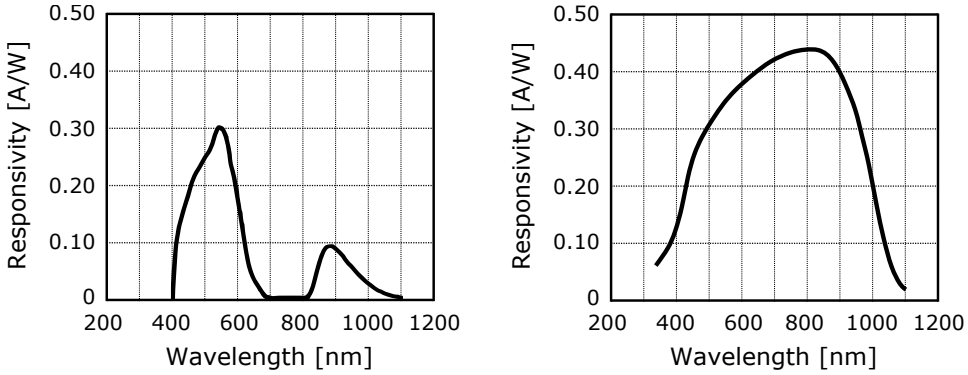

Fig. 2.3 (left) Responsivity of photodiode 1 as a function of wavelength (source: TEMD5510FX01 data sheet downloaded from http://www.vishay.com/ppg?81293). The wavelength of the peak sensitivity is of 540 *nm*. (right) Typical spectral response as a function of wavelength for photodiode 2 (source: Detector Series 5T data sheet downloaded from http://www.centronic.co.uk/products/1/general-purpose).

possible, at constant distance from the sample at all angles measured (though this was not critical due to the low beam divergence).

The two photodiodes are connected to their photodiode circuit boxes (see Appendix B), where using an internal operational amplifier the currents of the photodiodes are converted to voltages which are measured with an oscilloscope (Tektronix TDS2002).

The photodiode circuit boxes have three possible sensitivity levels (1 $mV/\mu A$, 10 $mV/\mu A$ and 100 $mV/\mu A$).

The proportional factor between two different sensitivity levels of photodiodes is determined by the ratio of the two corresponding precision resistors (see Appendix B).

The proportional factor between 10 $mV/\mu A$ and 100 $mV/\mu A$ for the photodiode 2 is $F_{100/10,initial,green} = 10$ with an error of 0.014.

The first use of this setup was to study the reflectivity of sample $\text{Silica1}_{\text{Na2SiO3(1:6)}}$ (see section 3.1). The results obtained have allowed not only the reliability and validity of the optical setup to be verified (and consequently the theoretical model too), but also its limitations to be identified.

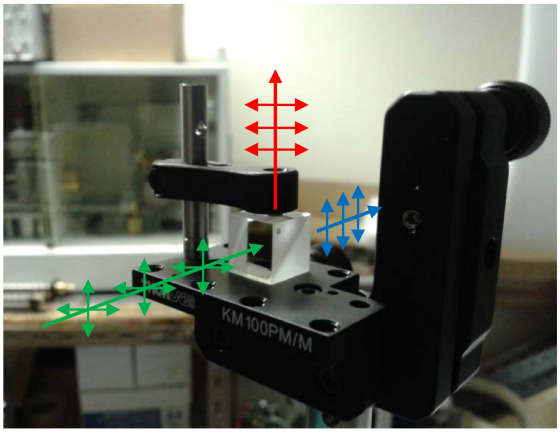

Fig. 2.4 A polarising beamsplitter cube separates the perpendicular and parallel polarisation components of a randomly polarised beam (green) by reflecting the perpendicular component (red) and allowing the parallel component to pass through the cube (blue).

Selection of the incident light polarisation

The green laser light is partially polarised and the orientation of polarisation is not known. For determining bond refractive index and thickness from bond reflectivity measurements, the reflectivity of the bond has to be measured with linearly polarised light where the electric field is perpendicular or parallel to the plane of incidence of the sample. This is made possible by the combination of two half-wave plates and a polarising beamsplitter cube.

The first half-wave plate decomposes the laser beam into two perpendicular components with a 180° phase difference between them. The component of the polarisation oriented along the fast axis is advanced by 180° relative to the component along the slow axis (both of which are perpendicular to each other and to the direction of propagation of the wave).

As the polarising beamsplitter cube Thorlabs PBS101 reflects the perpendicular polarised light ($R_{\perp} > 99.5\%$) and transmits the parallel polarised light ($T_{\parallel} > 90.0\%$) with extinction ratio $T_{\parallel} : T_{\perp} > 1000 : 1$ (Figure 2.4), the first half-wave plate is rotated such that the orientation of the dominant polarisation of the laser light is parallel to the plane of incidence of the polarising beamsplitter. To obtain this, the first half-wave plate is rotated such that maximum power comes through the beamsplitter and this was determined by putting one of the photodiodes in front and measuring the power. This allows the laser light to be maximally transmitted through the cube, reducing its power losses.

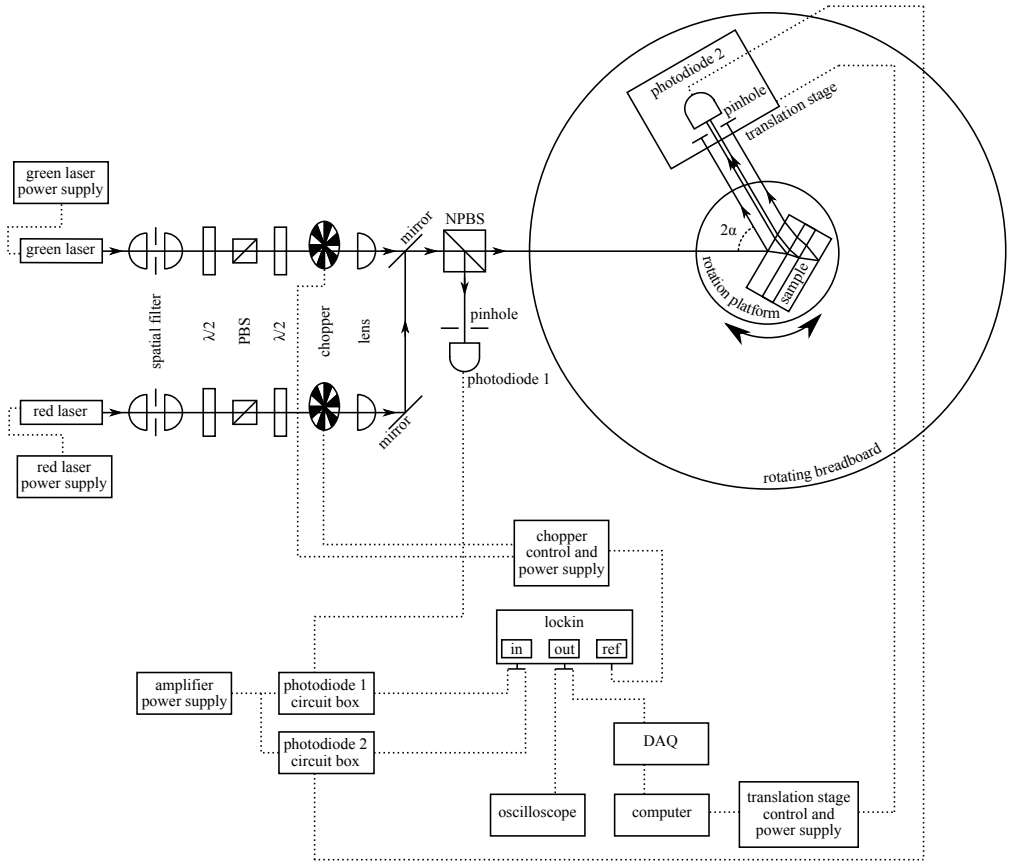

Fig. 2.5 Schematic diagram of the upgraded setup used to measure the optical reflectivity of hydroxide-catalysis bonds of samples.

Another half-wave plate is then used to change the orientation of the polarisation of the laser light such that the electrical field is either perpendicular or parallel to the plane of incidence of sample.

2.1.2 Upgraded and more sensitive assembly

As will be shown in section 3.1, the initial setup had limitations to the sensitivity of the reflectivity measurements which did not allow sufficient data to be taken. Typically the minimum reflectance level that could be measured using the initial setup was $\sim 10^{-5}$.

To improve the sensitivity, modifications to the setup were made and new components were added which are described below (Figure 2.5).

Laser. Power fluctuations from the green laser diode module used in the initial setup increased over time and began to limit the measurement sensitivity.
For this reason, it was substituted with a new collimated laser diode module (Thorlabs CPS532-C2). This green laser module ($\lambda = 532$ *nm*) is a Class 2 with a minimum and maximum optical output power of 0.8 *mW* and 1.0 *mW* respectively. It produces an output beam that has a round beam shape of diameter 3.5 *mm* measured at a distance of 50.8 *mm* from the front of the housing and a maximum beam divergence of 0.5 *mrad*.
To reduce the uncertainty in particular on the estimation of bond thickness found using the maximum-likelihood analysis (see section 3.1), measurements were carried out using not only green, but also red light. This colour was chosen because it was as far away from green as possible so that the measurements could be considered independent while considering the limited number of options available with circular beams.
The red collimated laser diode module (Thorlabs CPS180) has a wavelength of $\lambda =$ 635 *nm* and falls within Class 3R with the typical optical output power of 1.0 *mW*. It produces an output beam that has a round beam shape of diameter 4.0 *mm* measured at a distance of 50.8 *mm* from the front of the housing with a maximum beam divergence of 0.3 *mrad*.
Both laser modules are connected to their corresponding power supplies.

Spatial filter. A spatial filter was mounted in front of each laser to reduce the diameter of the beam and make it Gaussian. It is composed of a focusing plano-convex lens ($f =$ 100 *mm*), a pinhole ($d = 75$ μm) and a collimating plano-convex lens ($f = 30$ *mm*).
The ratio between the exit and entrance beam diameters is related to the ratio of the focal length of collimating lens to that of the focusing lens: in the spatial filter the diameter of the beam from the laser is reduced by a factor 0.3 (see subsection 2.1.5 for details).

Half-wave plates and polarising beamsplitter cube. Two half-wave plates $\lambda/2$ (Thorlabs WPH10M-532 and WPH10M-633 for the green and red laser, respectively) and the polarising beamsplitter cube PBS (Thorlabs PBS101), as above-mentioned, allow the polarisation of the light incident on the sample to be set to perpendicular or parallel to the plane of incidence of the sample.

Optical chopper and lock-in amplifier. An optical chopper is used in the phase-sensitive detection of the signal intensity by a lock-in amplifier, improving noise levels on photodiode read-out. Any unwanted background signal (e.g. ambient light) can be rejected and thus lower intensities of the reflected light can be detected.

The chopper (Thorlabs MC2000) is composed of an optical head with a 10-slot blade and a controller. The chopper wheel frequency is locked to 429 Hz in order to avoid noise frequencies (like the mains frequency and its positive integer multiples and laboratory interferences) in the range from 20 Hz to 1 kHz specified for this 10-slot blade, and its signal is sent to the reference channel of the lock-in amplifier.
The lock-in amplifier (Stanford Research Systems SR830) has two input channels, one for the signal from photodiode 1 or photodiode 2, and the other for the reference signal from the chopper. It provides a DC voltage which is proportional to the signal amplitude and does not depend on the phase difference between the signal and reference.

Lens. Another plano-convex lens is used to reduce the diameter of the beam further so that the front, bond and back spots can be better separated from each other ($f = 200\ mm$ and $f = 250\ mm$ for green and red laser). These are at a distance of 39.1 cm and 49.5 cm from the sample for green and red laser, respectively (see subsection 2.1.5 for details).

Mirrors. Two silver mirrors (Thorlabs PF05-03-P01) are added when the red arm is used and removed when the green laser is on. They have an average reflectance greater than 97.5% for 450 $nm - 2\ \mu m$.

Non-polarising beamsplitter cube. The uncoated glass plate of the initial setup was substituted with a non-polarising beamsplitter cube NPBS (Thorlabs BS025) for maintaining the incident light's polarisation state. It is a N-BK7 $25.4 \times 25.4 \times 25.4\ mm$ cube and has a wavelength range $400 - 700\ nm$. It has a split ratio of 10:90 (R:T), that is, the cube reflects 10% of the incident light to photodiode 1 and transmits 90% to the bonded sample. The corresponding split ratio tolerance is $|T_\perp - T_\parallel| < 15\%$ and $|R_\perp - R_\parallel| < 15\%$ over entire wavelength range.

Bonded sample and rotation platform. The sample is placed on the rotation platform (Thorlabs PR01/M) of the initial setup which allows the reflected light to be measured at different angles of incidence α.

Translation stage. Photodiode 2 and its pinhole are placed on a translation stage (Thorlabs LNR50K1/M): for each angle of incidence it is possible to scan the Gaussian profile of the bond spot. This allows the maximum intensity of the bond spot to be measured with precision. The device is connected to its power supply and can be controlled using the Thorlabs APT (Advanced Positioning Technology) software installed on a computer.

Rotating breadboard. The translation stage with photodiode 2 and its pinhole sits on a rotating breadboard (Thorlabs RBB450A/M) which is rotated with 2α to measure the reflected beam at a constant distance to the sample and at right angles.

Pinholes. Two pinholes (Thorlabs ID12/M) are in front of two photodetectors to minimise stray light and allow beams reflected from the sample to be separated so that only the light from the bond can be detected by photodiode 2. These pinholes have a diameter of ~ 3.2 *mm* and are distant from their corresponding photodiodes ~ 7.5 *mm* (photodiode 1) and ~ 4.5 *cm* (photodiode 2).

Photodiodes. These are the same as those used in the initial setup.
To reduce the effective surface area of the photodiode and thus minimise the cross-talk of front-back and bond reflection, a rectangular slit of ~ 1 *mm* wide is placed directly in front of each photodetector.
The photodiodes are connected to their circuit boxes (see Appendix B), where the internal operational amplifier is supplied from a power supply. The signal from these circuit boxes is passed to a lock-in amplifier and then is sent to either an oscilloscope (Tektronix TDS2002) or a computer. For photodiode 1, the signal is shown on an oscilloscope because the entire profile of the beam does not have to be measured. For photodiode 2, the signal from the lock-in is sent to a computer through a DAQ device (National Instrument USB-6218). Here, the data is recorded using the LabVIEW software allowing the entire profile of bond spot to be saved.
The proportional factor between the sensitivity levels 10 $mV/\mu A$ and 100 $mV/\mu A$ for photodiode 2 in green and red light mode is always determined by their corresponding precision resistors (see Appendix B): $F_{100/10,upgraded,green} = F_{100/10,upgraded,red} = 10$ with an error of 0.014.

After these changes, reflectivities at extremely low levels (down to 10^{-7}) could be measured, as will be shown in Chapter 3, 4 and 5.

2.1.3 Measure of the bond reflectance

The power of the incident and reflected laser beam directed to the bond layer of a bonded sample was measured by photodiode 1 and photodiode 2, respectively, for a range of angles of incidence α. These measurements were carried out for the perpendicular ($\perp$) and parallel ($\parallel$) polarisations of the laser beam.

From the ratio between the reflected V_{output} and incident V_{input} powers (measured in Volts using the photodiodes with a current to voltage amplifier circuit, see Appendix B), the reflectances for perpendicular and parallel polarised light, $R_{\perp}$ and $R_{\parallel}$ respectively, could be determined:

$$R_{\perp} = V_{\text{output},\perp}/V_{\text{input},\perp} \tag{2.1}$$

$$R_{\parallel} = V_{\text{output},\parallel}/V_{\text{input},\parallel} \tag{2.2}$$

The error in the reflectance was calculated by the formula of propagation of uncertainty as follows:

$$\sigma(R_{\text{i}}) = |R_{\text{i}}|\sqrt{\left(\sigma(V_{\text{input,i}})/V_{\text{input,i}}\right)^2 + \left(\sigma(V_{\text{output,i}})/V_{\text{output,i}}\right)^2} \tag{2.3}$$

where the subscript i stands for the polarisation of the incident beam and the correlation coefficient between V_{input} and V_{output} is considered equal to zero for both perpendicular and parallel polarisation. Measurements on both photodiodes were always taken simultaneously to cancel out any errors caused by fluctuations of laser power in the reflectance.

Actually, the power of the light incident on photodiode 1 was not the power of the light incident on the sample, but they could be approximated to be directly proportional each other provided that the linearity of the two photodetectors was verified (see next section 2.1.4):

$$V_{\text{input,i}} = k_{\text{i}} V_{\text{photodiode1,i}} \tag{2.4}$$

where k is the conversion factor to be determined for both polarisations i ($\perp$ and $\parallel$) of the laser beam. The corresponding error was calculated using the following formula of propagation of uncertainty:

$$\sigma(V_{\text{input,i}}) = |V_{\text{input,i}}|\sqrt{\left(\sigma(k_{\text{i}})/k_{\text{i}}\right)^2 + \left(\sigma(V_{\text{photodiode1,i}})/V_{\text{photodiode1,i}}\right)^2} \tag{2.5}$$

Photodiode 2 was used for measuring the intensity of the reflected beam off the bond V_{output}. As the light reflected from the bonded interface was considerably weaker than that incident on the sample, the signal from the bonded interface at photodiode 2 was measured with a sensitivity of 100 $mV/\mu A$ in order to better detect this weak signal whereas the signal at photodiode 1 was measured with a sensitivity of 10 $mV/\mu A$. Consequently, V_{output} at polarisation i of the incident beam was defined as follows:

$$V_{\text{output,i}} = \frac{V_{\text{output,100,i}}}{F_{\text{100/10,i}}} \tag{2.6}$$

where $V_{\text{output,100}}$ was the signal collected from photodiode 2 at 100 $mV/\mu A$ and $F_{100/10}$ was the proportional factor between the sensitivity levels 10 $mV/\mu A$ and 100 $mV/\mu A$ of the photodiode 2. In this way, both V_{input} and V_{output} were expressed at the same sensitivity of 10 $mV/\mu A$. The error on V_{output} was calculated using the following formula of propagation of uncertainty:

$$\sigma(V_{\text{output,i}}) = |V_{\text{output,i}}| \sqrt{\left(\sigma(F_{100/10,\text{i}})/F_{100/10,\text{i}}\right)^2 + \left(\sigma(V_{\text{output,100,i}})/V_{\text{output,100,i}}\right)^2} \quad (2.7)$$

For more information on the values used to calculate these errors, see section 3.1.2.1.

2.1.4 Linearity of the two photodetectors

To obtain V_{input} from the measurements performed using photodiode 1 (equation 2.4), the linearity of the two photodetectors had to be verified.

For this aim, photodiode 2 was placed between the uncoated glass plate and the sample for the initial assembly in green light (Figure 2.2), and between the non-polarising beamsplitter cube and the sample for the upgraded assembly in green and red light (Figure 2.5).
The intensity of the laser was varied by means of absorptive filters at different optical densities OD ($T = 10^{-OD}$, where T is the light transmission of the filter) or some coloured windows. This was determined for a range of light power levels and on several different days.

The powers of the beams reflected or transmitted at the glass plate or beamsplitter cube were measured by photodiode 1 and photodiode 2, respectively, and were plotted in Figure 2.6 for the initial assembly in green light, in Figure 2.7 for the upgraded assembly in green light and Figure 2.8 for the upgraded assembly in red light. A regression analysis was also performed.

For the initial assembly in green light, the linearity of two photodetectors for $\perp$ polarisation was verified for a large range of light intensities, whereas that for $\parallel$ polarisation was limited by the sensitivity of photodiode 1. In the latter case the intensity of laser beam that entered photodiode 1 was really low because of the low coefficient of reflection of the uncoated glass plate which reduced this intensity.

For the upgraded assembly, the ratio of the parallel to perpendicular gradient for both green and red light is about 20 (Figure 2.7 and Figure 2.8). This value is due to the polarisation dependence of the split ratio of the non-polarising beamsplitter cube, which turned out to be stronger than the minimal dependence on the polarisation of the incident light assumed by Thorlabs. The ratio of the red to green gradient for both perpendicular and parallel

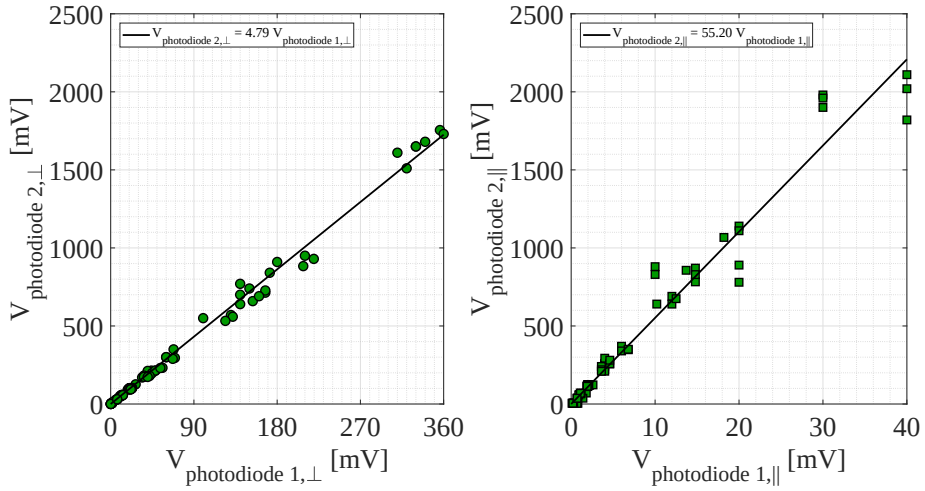

Fig. 2.6 Photodiode linearity measurements of the initial assembly in green light. The voltage produced by the laser light incident on the sample plotted as a function of the voltage of photodiode 1 for $\perp$ (left, green dots) and $\parallel$ (right, green squares) polarisation where the light power was varied using OD filters. In each plot the equation of the trend line is reported. The green dot and square symbols are the experimental data. The regression lines are shown in black. The individual points have a 1% error which is too small to be presented in the figure.

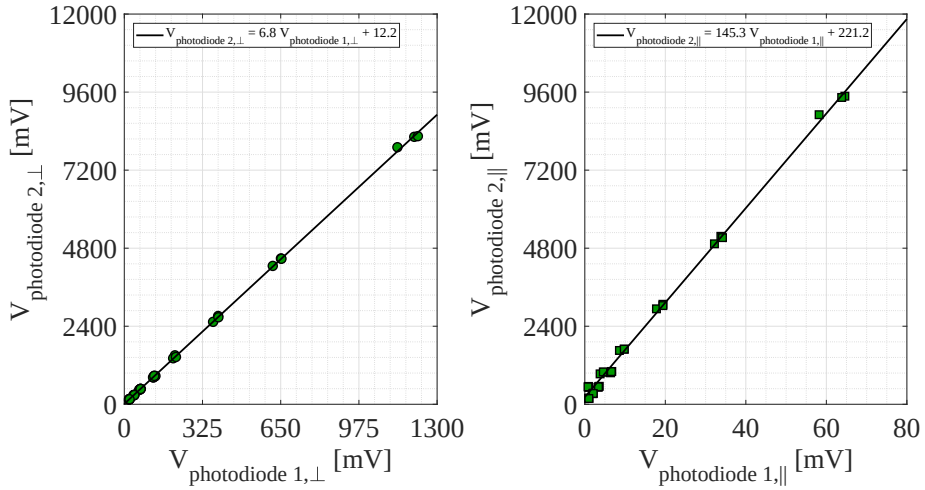

Fig. 2.7 Photodiode linearity measurements of the upgraded assembly in green light. The voltage produced by the laser light incident on the sample plotted as a function of the voltage of photodiode 1 for $\perp$ (left, green dots) and $\parallel$ (right, green squares) polarisation where the light power was varied using OD filters. In each plot the equation of the trend line is reported. The green dot and square symbols are the experimental data. The regression lines are shown in black. The individual points have a 1% error which is too small to be presented in the figure.

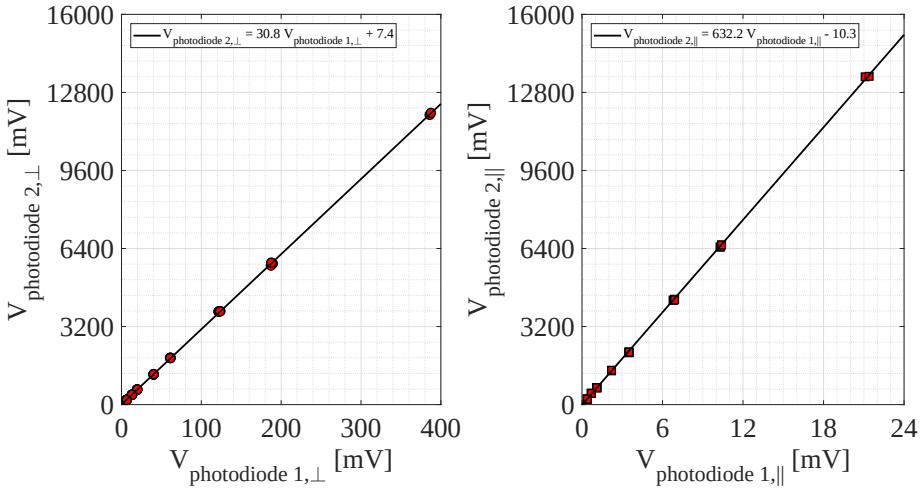

Fig. 2.8 Photodiode linearity measurements of the upgraded assembly in red light. The voltage produced by the laser light incident on the sample plotted as a function of the voltage of photodiode 1 for $\perp$ (left, red dots) and $\parallel$ (right, red squares) polarisation where the light power was varied using OD filters. In each plot the equation of the trend line is reported. The red dot and square symbols are the experimental data. The regression lines are shown in black. The individual points have a 1% error which is too small to be presented in the figure.

polarisation of light is about 5 (Figure 2.7 and Figure 2.8). This value is due mostly to the wavelength dependence of the responsivity of photodiode 1 (Figure 2.3): the ratio of red to green responsivity of photodiode 1 is about 20%, whereas that of photodiode 2 may be considered about 1 (equation 2.4).

2.1.5 Reduction of the beam diameter

To better separate the three beams reflected from front, bond and back surfaces of a bonded sample from each other, the laser beam width had to be reduced. This reduction in the upgraded setup was made in the following order: measurement of the diameter of the laser beam, construction of a spatial filter (to reduce the beam diameter and make it Gaussian), and introduction of a lens between the spatial filter and the sample (to reduce the diameter of the beam incident on the sample even further).

Beam width

The first step was the determination of the $1/e^2$ width of the laser beam, defined as the distance between the points where the intensity falls to $1/e^2 = 0.135$ times the maximum

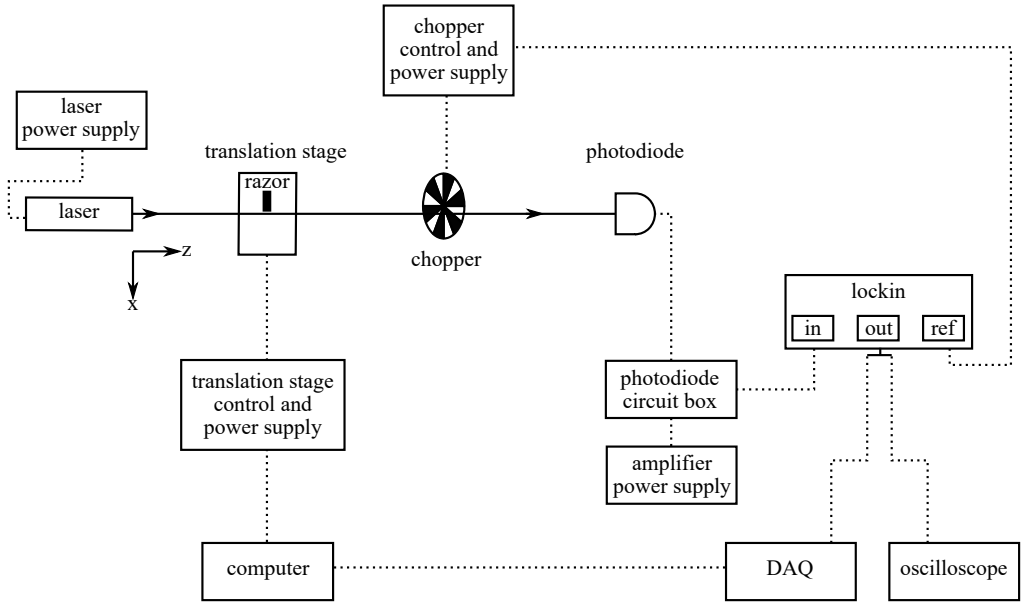

Fig. 2.9 Schematic diagram of the setup made to measure the beam width at different distances from the laser.

value [74].
This width was estimated using the knife edge technique assuming that the laser beam propagated with a Gaussian intensity profile in the z direction (Figure 2.9) [75].

The beam was progressively covered by a razor blade (placed at a distance z from the laser), which was translated through the beam in the x direction using a translation stage. For each position x of the razor, the power of the beam that was not blocked ($P_{\text{measured}}(x)$) was measured using a photodiode (Silonex SLSD-71N5) with the circuit box set at 1 $mV/\mu A$, of which the active area (9.67 $\times$ 9.67 mm sensitive area) was bigger than the spot size of the laser at that position. The sensitivity spectral range of this photodiode is $400-1100$ nm with maximum sensitivity wavelength of 930 nm. These measured powers were fitted using the following function which was determined in section C.1 of Appendix C [75]:

$$P_{\text{measured}}(x) = \frac{P_{\text{tot}}}{2}\left[1 - \text{erf}\left(\frac{\sqrt{2}(x-x_0)}{R_x}\right)\right] \tag{2.8}$$

where P_{tot} is the total power of the beam when fully exposed, x_0 is the position of the Gaussian beam centre relative to the razor origin position ($P_{\text{measured}}(x_0) = P_{\text{tot}}/2$), and R_x is the $1/e^2$ radius of the Gaussian beam in the x direction at z position. The error function erf(t) is

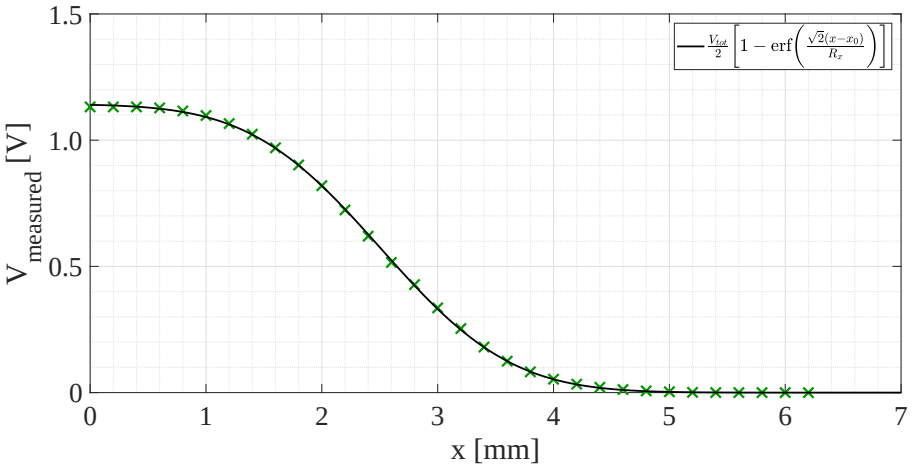

Fig. 2.10 The measured voltage of the green beam as a function of the position of the blade in the x direction where the razor was placed at $z = 23.5\ cm$ from the laser. The cross symbols are the experimental data. The black line indicates the fitting model.

defined as:

$$\text{erf(t)} = \frac{2}{\sqrt{\pi}} \int_0^t e^{-u^2}\, du \tag{2.9}$$

with erf(0) = 0, erf(∞) = 1 and erf(-t) = −erf(t).

Using a current to voltage converter (see Appendix B), the voltage reading (measured with an oscilloscope) is proportional to the current which the photodiode produces ($V = IR$). Since the light power is $P = IV$, the voltage reading is also proportional to the light power.

In Figure 2.10, the detected voltage V_{measured} as a function of x at a distance $z = 23.5\ cm$ is shown for the green laser: the curve starts at the total beam voltage (beam not covered by the blade) and decreases gradually to zero voltage (beam completely blocked).

The three parameters V_{tot}, x_0 and R_x obtained from the fit are reported in Table 2.1 for both the green and the red laser. These were obtained for three different positions z of the razor along the direction of propagation of the Gaussian beam.

Spatial filter

The next step was the assembly of a spatial filter (Thorlabs KT310/M), composed of two lenses and a pinhole, which reduced the width of a laser beam and made it a clean Gaussian beam (Figure 2.11).

The reduction of the beam diameter was achieved using two lenses, where the forward focal point of a focusing lens coincided with the rear focal point of a collimating lens [76].

laser	z (cm)	V_{tot} (V)	x_0 (mm)	R_x (mm)
green	23.5	$1.14^{+0.01}_{-0.01}$	$2.51^{+0.01}_{-0.01}$	$1.77^{+0.02}_{-0.02}$
	43.5	$1.14^{+0.01}_{-0.01}$	$2.94^{+0.01}_{-0.01}$	$1.81^{+0.02}_{-0.02}$
	83.5	$1.15^{+0.01}_{-0.01}$	$3.30^{+0.01}_{-0.01}$	$1.91^{+0.02}_{-0.02}$
red	12.9	$1.57^{+0.01}_{-0.01}$	$5.85^{+0.01}_{-0.01}$	$1.88^{+0.03}_{-0.03}$
	27.9	$1.57^{+0.01}_{-0.01}$	$6.08^{+0.01}_{-0.01}$	$1.88^{+0.03}_{-0.03}$
	50.4	$1.57^{+0.01}_{-0.01}$	$6.71^{+0.01}_{-0.01}$	$1.89^{+0.03}_{-0.03}$
	77.9	$1.57^{+0.01}_{-0.01}$	$6.38^{+0.01}_{-0.01}$	$1.88^{+0.03}_{-0.03}$

Table 2.1 Measurements of the total voltage V_{tot}, the centre x_0 and the $1/e^2$ radius along the x-axis R_x of the Gaussian beam as a function of the distance z from the green and red laser.

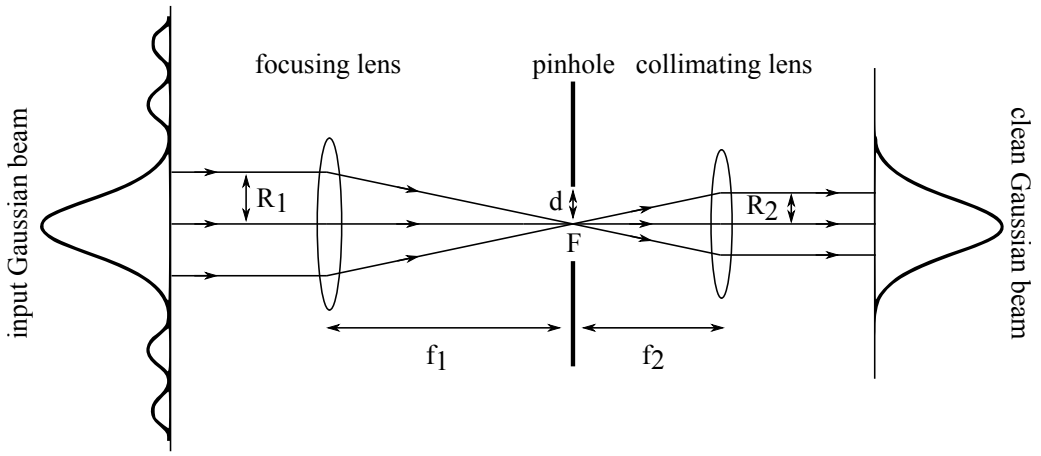

Fig. 2.11 Schematic diagram of a spatial filter used to reduce the diameter of a laser beam, making it Gaussian. The input and exit beams were assumed to be collimated. The focusing lens brings the focused beam through the centre of the pinhole.

The ratio between the exit and entrance beam radius is related to the ratio of the focal length of collimating lens and focusing lens by the following relation [76]:

$$\frac{f_2}{f_1} = \frac{R_2}{R_1} \tag{2.10}$$

where f_1 (f_2) and R_1 (R_2) are the focal length and the radius of the focusing (collimating) lens (Figure 2.11). The radius of the exit beam depends only on the radius of the input beam and the optical parameters of the lenses used.
To achieve a significant reduction in the beam radius, respecting at the same time the space limits on the optical bench, a focusing plano-convex lens of $f_1 = 100\ mm$ (Thorlabs LA1207-A-ML) and a collimating plano-convex lens of $f_2 = 30\ mm$ (Thorlabs LA1289-A-ML) were chosen for both lasers. This implied that the radius of the entrance beam would have been reduced by a factor $f_2/f_1 = 0.3$. These lenses work in the frequency range of $350 - 700\ nm$.

For space reasons, the focusing lens of the spatial filter was mounted at a distance of 14.4 *cm* (9.9 *cm*) relative to the green (red) laser. As the beam waist of the two lasers (minimum $1/e^2$ beam radius w_0) was not known, extrapolation of w_0 and the $1/e^2$ radius of the Gaussian beam $w(z)$ at the distances of the focusing lenses from the data reported in Table 2.1 was possible using the following formula [77] (λ is the wavelength of laser light):

$$w(z) = w_0 \sqrt{1 + \left(\frac{\lambda z}{\pi w_0^2} \right)^2} \tag{2.11}$$

The $1/e^2$ beam radii of 1.77 *mm* and 1.88 *mm* were obtained for the green laser at $z = 14.4\ cm$ and for the red laser at $z = 9.9\ cm$, respectively.

To clean up the beam making it Gaussian, a pinhole was placed at the focal point F (as shown in Figure 2.11). If the correct diameter is chosen, the pinhole can remove the unwanted multiple-order peaks of the intensity profile of the laser beam allowing only a very bright and uniform spot without rings to pass.
The beam width at this point had to be determined in order to select the correct diameter of this pinhole. When a collimated Gaussian beam propagates through a lens of focal length f, it is focused in the point F where the beam waist w can be approximated by the following equation [78, 79]:

$$w(F) \simeq \frac{\lambda f}{\pi R} \tag{2.12}$$

where R is the $1/e^2$ radius of the collimated beam.
As the focal length of the chosen focusing lens was $f = f_1 = 100\ mm$ for both lasers, and the

beam radius was $R = R_{1,\text{green}} = 1.77\ mm$ for the green laser ($\lambda = 532\ nm$) and $R = R_{1,\text{red}} = 1.88\ mm$ for the red laser ($\lambda = 635\ nm$), substituting these values in equation 2.12, the beam waist in point F was $w_{1,\text{green}}(F) = 9.6\ \mu m$ for the green laser and $w_{1,\text{red}}(F) = 10.8\ \mu m$ for the red laser. The radius of pinhole had to be greater than this value.
During the construction of the spatial filter, it was decided to test four pinholes of different size (diameter $d = 40\ \mu m$, $50\ \mu m$, $75\ \mu m$, $100\ \mu m$) to select one that would have eliminated the fringes of the Airy disc best. For both lasers, a pinhole of $d = 75\ \mu m$ (Thorlabs P75S) was selected.

Finally, the collimating lens for the green (red) laser was mounted to achieve good collimation of the exit beam at a distance of 110.6 *cm* (131.6 *cm*) from the sample.

After the construction of the spatial filter, the $1/e^2$ beam radius in the x direction was measured again using the knife edge technique. Figure 2.9 can be taken as a reference, but the reader has to consider that a spatial filter is added between the laser and the translation stage now. The measurements were performed using the photodiode 2 with the circuit box set at 1 $mV/\mu A$ whose signal was sent to the computer through the DAQ device. For the green laser, a $1/e^2$ radius of $0.37^{+0.01}_{-0.01}\ mm$ was found at a distance $z = 132.0\ cm$ from the laser (6.7 *cm* from the sample placed after the blade).

Additional lens

Since a beam with a given beam waist can be transformed into another beam of desired waist by means of addition of one or more lenses, another lens was added to reduce the beam diameter at the sample even further. By using mode matching of Gaussian beams, the position relative to the sample and the focal length of this lens could be determined [77].

To make this possible, all parameters of the collimating lens had to be known. For this reason, the problem was divided in two steps, first focusing the attention on the collimating lens and then on the additional lens (Figure 2.12).

Before passing through the collimating lens of focal length f_2, the Gaussian beam has its beam waist w_1 at a distance l_1. When the Gaussian beam passes through this lens, it produces another beam waist w_2 at distance l_{21} (Figure 2.12). If the two beam waists w_1 and w_2 and the focal length f_2 of the collimating lens are known, the distances l_1 and l_{21} can be calculated using the following matching formulae [77]:

$$l_1 = f_2 + \frac{w_1}{w_2}\sqrt{f_2^2 - f_*^2} \tag{2.13}$$

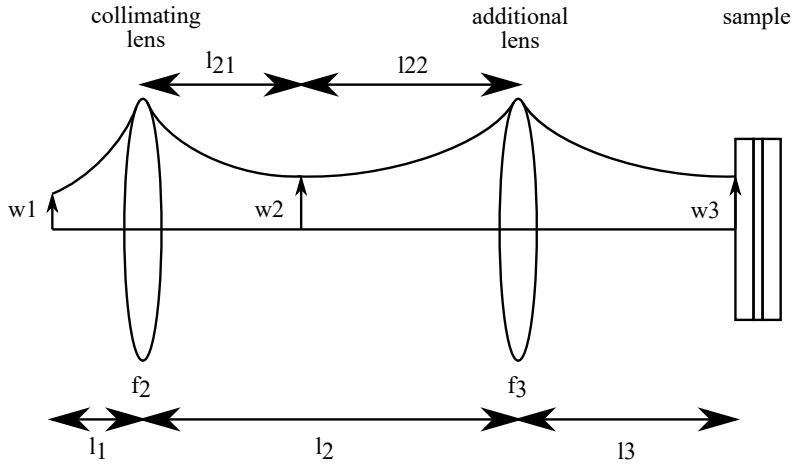

Fig. 2.12 Schematic diagram of the mode matching of a Gaussian beam which passes through a collimating and additional lens before arriving at the sample.

$$l_{21} = f_2 + \frac{w_2}{w_1}\sqrt{f_2^2 - f_*^2} \tag{2.14}$$

where f_2 has to be greater than the characteristic length $f_* = \pi w_1 w_2/\lambda$ defined by the waists of the two matched beams.
The corresponding values for green ($\lambda = 532\ nm$) and red ($\lambda = 635\ nm$) laser are reported in Table 2.2.

laser	$w_1(\mu m)$	$w_2(\mu m)$	$f_2(mm)$	$f_*(mm)$	$l_1(cm)$	$l_{21}(cm)$
green	10	100	30	5.9	3.3	32.4
red	10	100	30	4.9	3.3	32.6

Table 2.2 The beam waists w_1 and w_2 and their corresponding distances l_1 and l_2 relative to the collimating lens with focal length $f_2 > f_*$ for both lasers.

Here $w_1 = 10\mu m$ is a rounded number of the values found at the positions of the pinhole (see the previous step), whereas $w_2 = 100\mu m$ is the final beam waist desired.

Taking the additional lens into consideration, in addition to the data reported in Table 2.2, if the beam waist w_3 and $l_2 + l_3$ are known, the distances l_{22}, l_3 and l_2, and the focal length f_3 of this lens can be calculated by the following equations [77] (Figure 2.12):

$$l_{22} = f_3 + \frac{w_2}{w_3}\sqrt{f_3^2 - f_{**}^2} \tag{2.15}$$

$$l_3 = f_3 + \frac{w_3}{w_2}\sqrt{f_3^2 - f_{**}^2} \tag{2.16}$$

$$l_2 = l_{21} + l_{22} \tag{2.17}$$

$$f_3 = \begin{cases} \dfrac{-2\left[(l_2+l_3)-l_{21}\right] + \left(\frac{w_2}{w_3}+\frac{w_3}{w_2}\right)\sqrt{\left[\left(\frac{w_2}{w_3}+\frac{w_3}{w_2}\right)^2-4\right]f_{**}^2+\left[(l_2+l_3)-l_{21}\right]^2}}{\left(\frac{w_2}{w_3}+\frac{w_3}{w_2}\right)^2-4} & \text{if } w_2 \neq w_3, \\ \dfrac{4f_{**}^2+\left[(l_2+l_3)-l_{21}\right]^2}{4\left[(l_2+l_3)-l_{21}\right]} & \text{if } w_2 = w_3. \end{cases} \tag{2.18}$$

and again the focal length of the additional lens f_3 has to be greater than the characteristic length $f_{**} = \pi w_2 w_3/\lambda$ defined by the two matched beams. The demonstration of equation 2.18 is reported in section C.2 of Appendix C.
The beam waist $w_3 = 100\ \mu m$ was the final value that was desired at the front surface of sample, whereas the value of the distance $l_2 + l_3$ depended on the space in the setup which had to allow other optical components (half-waves plates, beamsplitters, chopper and mirrors) to be inserted.
The corresponding values for the green ($\lambda = 532\ nm$) and the red ($\lambda = 635\ nm$) laser are reported in Table 2.3.

laser	$w_3(\mu m)$	$l_2 + l_3\ (cm)$	$f_3(mm)$	$f_{**}(mm)$	$l_{22}(cm)$	$l_2(cm)$	$l_3(cm)$
green	100	110.6	200	59.1	39.1	71.5	39.1
red	100	131.6	250	49.5	49.5	82.1	49.5

Table 2.3 The beam waist w_3 and the distances $l_2 + l_3$, l_{22}, l_2 and l_3 are reported together with the focal length $f_3 > f_{**}$ of the additional lens for both lasers.

Plano-convex lenses of focal length 200 *mm* (Thorlabs LA1708-A-ML) and 250 *mm* (Thorlabs LA1461-A-ML) were used as additional lenses for the green and red laser, respectively. Both lenses work in the frequency range of $350 - 700\ nm$ and are at a distance of 99.6 *cm* and 105.6 *cm* from the green and the red laser (39.1 *cm* and 49.5 *cm* from the sample, respectively).

Taking Figure 2.5 into consideration, the translational stage with the razor was placed between the non-polarising beamsplitter cube NPBS and the sample. The measurements

were collected by photodiode 2 with the circuit box set at 1 $mV/\mu A$ and sent to the computer through the DAQ device. For the green laser, a $1/e^2$ radius of $0.25^{+0.01}_{-0.01}$ mm at a distance $z = 132.0$ cm from the laser (6.7 cm from the sample placed after the blade) was found, whereas for the red laser a $1/e^2$ radius of $0.25^{+0.01}_{-0.01}$ mm at a distance $z = 148.4$ cm from the laser (6.7 cm from the sample placed after the blade). Their corresponding theoretical $1/e^2$ radii obtained using equation 2.11 at $|z| = 6.7$ cm from the beam waist $w_0 = w_3$ are 0.15 mm (67% error) and 0.17 mm (47% error) for green and red laser, respectively.

2.2 Optical model

In order to obtain the refractive index and thickness of a hydroxide-catalysis bond from the measurements of reflectance, the experimental data has to be compared with the values obtained from a theoretical model. In subsection 2.2.1 the theoretical optical model for an isotropic material (such as the fused silica) is described. In subsection 2.2.2 the theoretical optical model for an anisotropic material with the optic axis perpendicular to the bonding surface (such as the sapphire) is reported.

2.2.1 Isotropic material

This theoretical model is based on the arrangement shown in Figure 2.13 and assumes air, fused silica substrates and bond material are isotropic and non-absorbing media. The effects of thin film interference are included as the bond layer can have a thickness that makes this relevant [80, 81].

Two fused silica discs are bonded together using a hydroxide-catalysis solution (see subsection 2.4.1 for details). The bond material is sandwiched between much thicker layers of fused silica and their interfaces are very flat ($< 1/5$ of the wavelength of the light). Three different media are therefore involved: medium 0 is air with refractive index n_0, medium 1 is fused silica with refractive index n_1 and thickness d_1, and medium 2 is the bond material which is assumed to have refractive index n_2 and thickness d_2.

The fused silica is illuminated by laser light of wavelength λ at a given angle of incidence α. From the Snell's law of refraction [81]:

$$n_0 \sin\alpha = n_1 \sin\beta = n_2 \sin\gamma \tag{2.19}$$

where the angles β and γ can be derived from α.

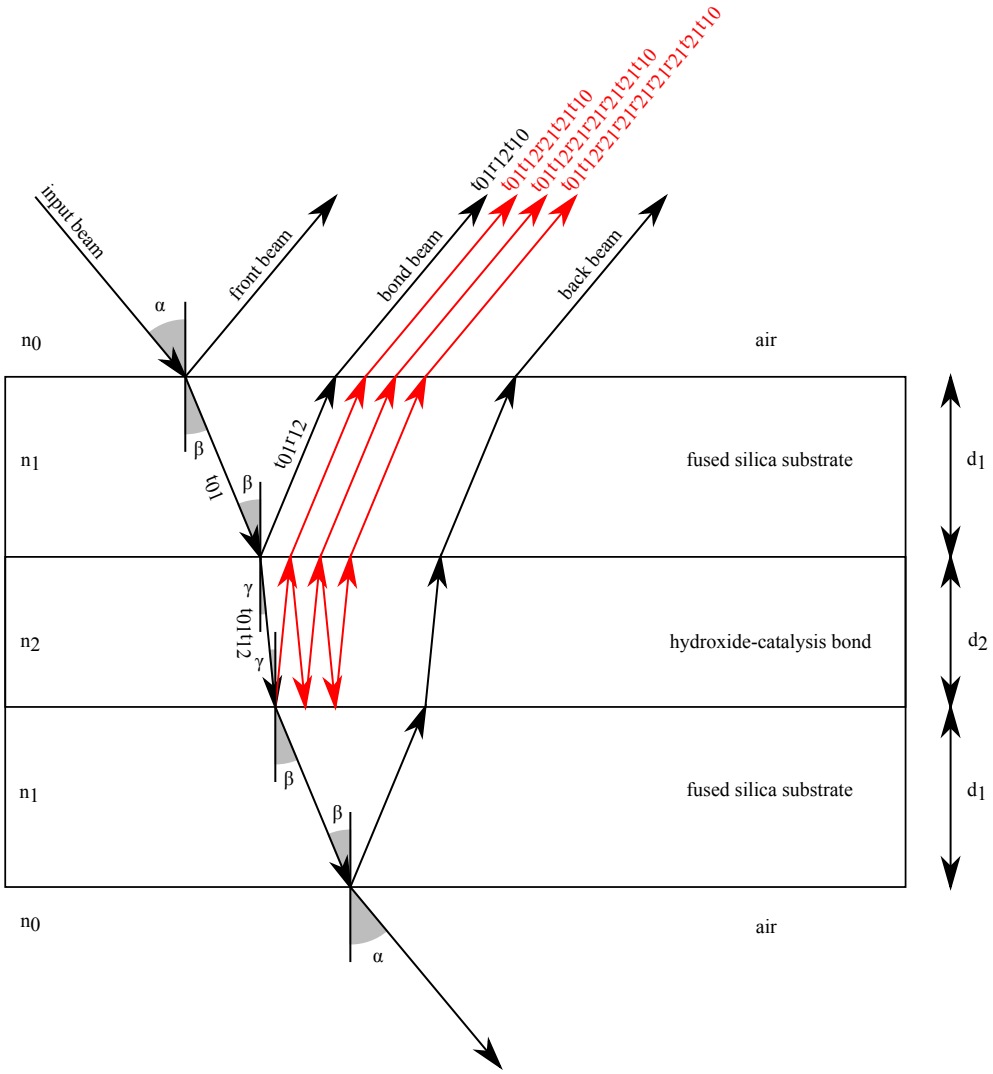

Fig. 2.13 Schematic diagram of a bonded sample (not to scale). Two discs of fused silica are joined by hydroxide-catalysis bonding.

When a light beam reaches the boundary between two media of different refractive index, a portion of the wave reflects off the boundary and a portion is transmitted through the boundary. The transmitted portion of the wave enters the fused silica medium and continues travelling through it until it reaches the bond layer (a thin film), of which the thickness is comparable to or smaller than the laser wavelength. Here, the beam bounces back and forth in the layer following a zigzag path. Thus, there are two sets of beams which emerge from the film layer: one which is reflected off the top of the film and the others which are reflected off the bottom of the film. The bond beam is obtained by summing the multiply-reflected elements.

The reflection and transmission coefficients, r_{lm} and t_{lm}, for each boundary between media l and m (in order of the propagation direction of the ray) of different refractive index are also shown in Figure 2.13. For example, r_{01} is the fraction of the amplitude of the incident light reflected at the interface between the medium with refractive index n_0 and that with refractive index n_1 [80, 81].

The reflection coefficient of a bond is defined as the ratio of the amplitude of the reflected electric field to the amplitude of the incident electric field [80, 81]:

$$
\begin{aligned}
r_{\text{bond}} &= \frac{E_{\text{bond}}}{E_{\text{input}}} \\
&= t_{01} r_{12} t_{10}\, e^{-i2\delta_1} + t_{01} t_{12} r_{21} t_{21} t_{10}\, e^{-i2\delta_1}\, e^{-i2\delta_2} \\
&\quad + t_{01} t_{12} r_{21} r_{21} t_{21} t_{10}\, e^{-i2\delta_1}\, e^{-i4\delta_2} \\
&\quad + t_{01} t_{12} r_{21} r_{21} r_{21} t_{21} t_{10}\, e^{-i2\delta_1}\, e^{-i6\delta_2} + \ldots \\
&= t_{01} r_{12} t_{10}\, e^{-i2\delta_1} - t_{01} t_{12} r_{12} t_{21} t_{10}\, e^{-i2\delta_1}\, e^{-i2\delta_2} \\
&\quad - t_{01} t_{12} r_{12} r_{12} t_{21} t_{10}\, e^{-i2\delta_1}\, e^{-i4\delta_2} \\
&\quad - t_{01} t_{12} r_{12} r_{12} r_{12} t_{21} t_{10}\, e^{-i2\delta_1}\, e^{-i6\delta_2} + \ldots \\
&= t_{01} r_{12} t_{10}\, e^{-i2\delta_1} - t_{01} t_{12} r_{12} t_{21} t_{10}\, e^{-i2\delta_1}\, e^{-i2\delta_2} \left[\sum_{n=0}^{+\infty} r_{12}^{2n}\, e^{-i2n\delta_2} \right] \\
&= t_{01} r_{12} t_{10}\, e^{-i2\delta_1} - t_{01} t_{12} r_{12} t_{21} t_{10}\, e^{-i2\delta_1}\, e^{-i2\delta_2} \sum_{n=0}^{+\infty} \left[r_{12}^{2}\, e^{-i2\delta_2} \right]^n \\
&= t_{01} r_{12} t_{10}\, e^{-i2\delta_1} - t_{01} t_{12} r_{12} t_{21} t_{10}\, e^{-i2\delta_1}\, e^{-i2\delta_2} \frac{1}{1 - r_{12}^2\, e^{-i2\delta_2}} \\
&= \left(1 - r_{01}^2\right) r_{12}\, e^{-i2\delta_1} - \frac{\left(1 - r_{01}^2\right)\left(1 - r_{12}^2\right) r_{12}\, e^{-i2\delta_1}\, e^{-i2\delta_2}}{1 - r_{12}^2\, e^{-i2\delta_2}} \\
&= \frac{\left(1 - r_{01}^2\right)\left(1 - r_{12}^2\, e^{-i2\delta_2}\right) r_{12}\, e^{-i2\delta_1} - \left(1 - r_{01}^2\right)\left(1 - r_{12}^2\right) r_{12}\, e^{-i2\delta_1}\, e^{-i2\delta_2}}{1 - r_{12}^2\, e^{-i2\delta_2}} \\
&= \frac{\left(1 - r_{01}^2\right) r_{12}\, e^{-i2\delta_1} \left[1 - e^{-i2\delta_2}\right]}{1 - r_{12}^2\, e^{-i2\delta_2}}
\end{aligned}
\tag{2.20}
$$

where:

- $r_{lm} = -r_{ml}$ and $t_{lm} t_{ml} = 1 - r_{lm}^2$ (assuming lossless dielectric media),
- $\sum_{k=0}^{+\infty} x^k = 1/(1-x)$ if $|x| < 1$ (geometric series),
- $\delta_1 = (2\pi/\lambda) n_1 d_1 \cos\beta$ and $\delta_2 = (2\pi/\lambda) n_2 d_2 \cos\gamma$ (change in phase of the beam on traversing the fused silica substrate and the bond layer, respectively).

This result is valid for both the polarisations of light, perpendicular and parallel to the plane of incidence of the substrate, which contains the normal to its surface and both the incident and reflected laser beams.

The reflectance of the bond R_{bond} is defined as the ratio of the powers W of the reflected and incident beams, which are proportional to the square of the electric field amplitude E, and is given by [80, 81]:

$$\begin{aligned}
R_{\text{bond}} &= \frac{W_{\text{bond}}}{W_{\text{input}}} = \left|\frac{E_{\text{bond}}}{E_{\text{input}}}\right|^2 = |r_{\text{bond}}|^2 \\
&= \frac{\left(1-r_{01}^2\right) r_{12}\, e^{-i2\delta_1}\left[1-e^{-i2\delta_2}\right]}{1-r_{12}^2\, e^{-i2\delta_2}} \frac{\left(1-r_{01}^2\right) r_{12}\, e^{i2\delta_1}\left[1-e^{i2\delta_2}\right]}{1-r_{12}^2\, e^{i2\delta_2}} \\
&= \frac{\left(1-r_{01}^2\right)^2 r_{12}^2\left(1-\left(e^{i2\delta_2}+e^{-i2\delta_2}\right)+1\right)}{1-r_{12}^2\, e^{i2\delta_2}-r_{12}^2\, e^{-i2\delta_2}+r_{12}^4} \\
&= \frac{\left(1-r_{01}^2\right)^2 r_{12}^2\left(2-2\cos(2\delta_2)\right)}{1-2r_{12}^2\cos(2\delta_2)+r_{12}^4} \\
&= \frac{2\left(1-r_{01}^2\right)^2 r_{12}^2\left(1-\cos(2\delta_2)\right)}{1-2r_{12}^2\cos(2\delta_2)+r_{12}^4}
\end{aligned} \tag{2.21}$$

where $|z|^2 = z\bar{z}$ ($\bar{z}$ is the complex conjugate of z) and $\cos\theta = \left(e^{i\theta}+e^{-i\theta}\right)/2$.

Rewriting the previous result in terms of perpendicular ($\perp$) and parallel ($\parallel$) polarisation components of the incident light, the reflectances of a hydroxide-catalysis bond are:

$$R_{\text{bond},\perp} = \frac{2\left(1-r_{01,\perp}^2\right)^2 r_{12,\perp}^2\left(1-\cos(2\delta_2)\right)}{1-2r_{12,\perp}^2\cos(2\delta_2)+r_{12,\perp}^4} \tag{2.22}$$

$$R_{\text{bond},\parallel} = \frac{2\left(1-r_{01,\parallel}^2\right)^2 r_{12,\parallel}^2\left(1-\cos(2\delta_2)\right)}{1-2r_{12,\parallel}^2\cos(2\delta_2)+r_{12,\parallel}^4} \tag{2.23}$$

where the reflection coefficients are expressed by Fresnel equations using Figure 2.13 as reference [80, 81]:

$$r_{01,\perp} = \frac{\cos\alpha - \sqrt{\left(\frac{n_1}{n_0}\right)^2 - \sin^2\alpha}}{\cos\alpha + \sqrt{\left(\frac{n_1}{n_0}\right)^2 - \sin^2\alpha}} \tag{2.24}$$

$$r_{01,\parallel} = \frac{\left(\frac{n_1}{n_0}\right)^2\cos\alpha - \sqrt{\left(\frac{n_1}{n_0}\right)^2 - \sin^2\alpha}}{\left(\frac{n_1}{n_0}\right)^2\cos\alpha + \sqrt{\left(\frac{n_1}{n_0}\right)^2 - \sin^2\alpha}} \tag{2.25}$$

$$r_{12,\perp} = \frac{\cos\beta - \sqrt{\left(\frac{n_2}{n_1}\right)^2 - \sin^2\beta}}{\cos\beta + \sqrt{\left(\frac{n_2}{n_1}\right)^2 - \sin^2\beta}} \tag{2.26}$$

$$r_{12,\parallel} = \frac{\left(\frac{n_2}{n_1}\right)^2 \cos\beta - \sqrt{\left(\frac{n_2}{n_1}\right)^2 - \sin^2\beta}}{\left(\frac{n_2}{n_1}\right)^2 \cos\beta + \sqrt{\left(\frac{n_2}{n_1}\right)^2 - \sin^2\beta}} \tag{2.27}$$

and the change in phase of the beam on traversing the film is [80]:

$$\begin{aligned}\delta_2 &= \frac{2\pi}{\lambda} n_2 d_2 \cos\gamma = \frac{2\pi}{\lambda} n_2 d_2 \cos\left(\arcsin\left(\frac{n_0}{n_2}\sin\alpha\right)\right) \\ &= \frac{2\pi}{\lambda} n_2 d_2 \sqrt{1 - \left(\frac{n_0}{n_2}\sin\alpha\right)^2}\end{aligned} \tag{2.28}$$

with $\beta = \arcsin\big((n_0/n_1)\sin\alpha\big)$, $\gamma = \arcsin\big((n_0/n_2)\sin\alpha\big)$, $\cos(\arcsin x) = \sqrt{1-x^2}$.

Equations 2.22 and 2.23 are functions of the angle of incidence (α), the wavelength of the light source used (λ), the refractive indices of the three media (n_0, n_1, n_2) and the thickness of the bond layer (d_2).

The angle of incidence is varied during the measurements (independent variable), the refractive indices of the air and the fused silica substrate are known, as well as the wavelength of the laser ($\lambda_{\text{green}} = 532\ nm$, $\lambda_{\text{red}} = 635\ nm$).
The refractive index of the air n_0 was approximated by 1, whereas the refractive index of fused silica was $n_{1,\text{green}} = 1.4607$ for the green laser and $n_{1,\text{red}} = 1.4570$ for the red laser (https://refractiveindex.info/?shelf=main&book=SiO2&page=Malitson) [82].
As the refractive index and thickness of the bond are not known, it is necessary to define a method to find them (see section 2.3).

2.2.2 Anisotropic material (optic axis perpendicular to bonding surface)

Sapphire is a variety of the mineral corundum which is a crystalline form of aluminium oxide (Al_2O_3). Corundum belongs to the trigonal crystal system for which the structural elementary cell is both rhombohedral and hexagonal [83].

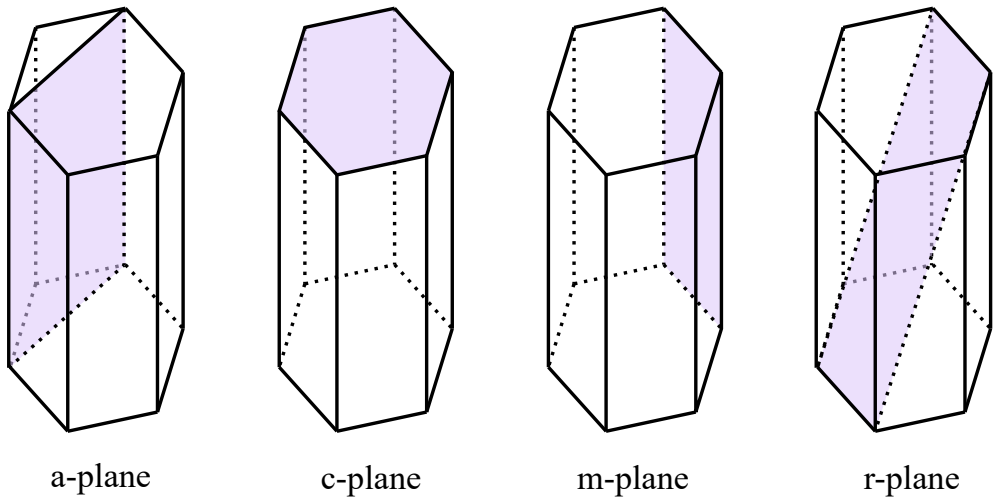

Fig. 2.14 Hexagonal cell of the trigonal crystal system showing four of the crystal planes highlighted in lilac.

Four main crystallographic planes of sapphire are illustrated in Figure 2.14: a-plane $(11\bar{2}0)$, c-plane (0001), m-plane $(1\bar{1}00)$ and r-plane $(1\bar{1}02)$ [83].

Sapphire is a uniaxial optically negative crystal and exhibits birefringence [83].
Birefringence (or double refraction) occurs when a light beam incident on a birefringent medium is split into two refracted beams, besides the reflected one. The beam which propagates with the same phase velocity (or refractive index) in every direction through the crystal is referred to as the ordinary beam, whereas the extraordinary beam travels with the phase velocity (or refractive index) which depends on the direction of propagation relative to the optic axis within the crystal [84].
The term uniaxial indicates that the crystal has one optic axis, along which ordinary and extraordinary rays coincide, travel with the same phase velocity and have the same refractive index. Along the optic axis, a beam does not exhibit birefringence. In c-plane sapphire, the c-crystallographic axis (perpendicular to the c-plane) is the optic axis of the crystal. For any other angle of incidence with respect to the optic axis, the ordinary beam is polarised perpendicular to the plane formed by the incident beam and the optic axis, whereas the polarisation of the extraordinary beam is parallel to this plane. Therefore, they will be mutually orthogonally polarised [84].
Also, sapphire is an optically negative crystal, which means the refractive index of the ordinary beam is greater than that of the extraordinary beam, which is equivalent to saying

that the ordinary beam is slower than the extraordinary beam. For sapphire, the difference between the refractive indices is about 0.008 in the visible region of the spectrum [83, 84].

In this thesis, the reflectivity of bonded sapphire samples with c-crystallographic plane was measured. Therefore, the theoretical model described in this chapter is only valid for this case, where the c-crystallographic axis, perpendicular to the c-plane, and the optic axis of the crystal coincide.

A vectorial approach described by Simon [85–87] is used for this and it is based on reflection and transmission of a wave when it passes from an isotropic to uniaxial birefringent medium, and vice versa (the bond medium is assumed to be isotropic). Using coordinate transformations and applying boundary conditions at the interface, the electromagnetic field vectors of the reflected and refracted waves are written in terms of those of the incident wave. The reflection and transmission coefficients depend not only on the polarisation of the incident wave, the incidence angle and the refractive indices of the involved media, but also on the direction of the optic axis of the uniaxial birefringent medium and the position of the incidence plane [85–88].

Below, three coordinate systems used in this approach, the description of waves in a uniaxial birefringent medium and the corresponding theoretical model of reflectances are introduced. The three cases that a wave is exposed to during its travel through a bonded sample are taken in consideration and are described in detail in section C.3 of Appendix C:

- case 1: an incident wave passes from an isotropic to uniaxial birefringent medium;
- case 2: an ordinary wave passes from a uniaxial birefringent to isotropic medium;
- case 3: an extraordinary wave passes from a uniaxial birefringent to isotropic medium.

For the samples discussed in this thesis (Figure 2.15), case 1 describes the passage of a wave from air to sapphire, whereas case 2 and case 3 refer to the interface between the sapphire and the bond layer, where the bond is considered to be isotropic.

Coordinate systems

When a wave travels in an isotropic medium, its polarisation can be decomposed in components perpendicular and parallel to the plane of incidence. In a uniaxial birefringent medium these components are perpendicular and parallel to the optic axis of the medium. Therefore, the components of the electromagnetic field vectors of a wave in an anisotropic medium are written following the principal axes of the medium, and they cannot be applied to the solution of the boundary conditions because these are written in the discontinuity surface system.

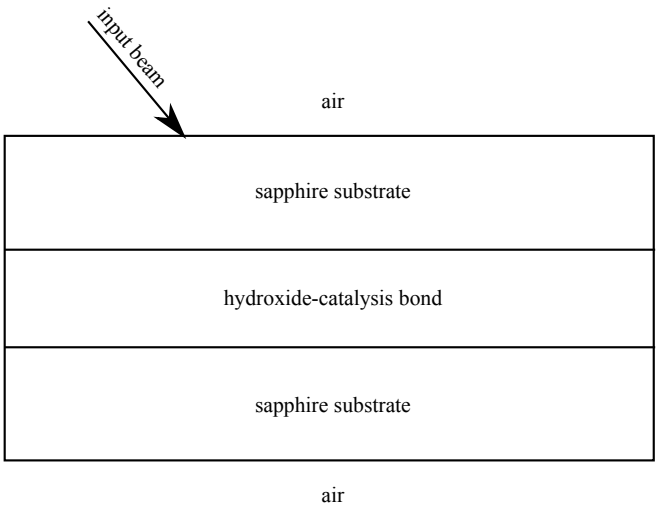

Fig. 2.15 Schematic diagram of a bonded sample (not to scale). Two discs of sapphire are joined by hydroxide-catalysis bonding.

To determine the reflection and transmission coefficients at an interface formed by an isotropic and a uniaxial birefringent medium or vice versa, three coordinate systems have to be considered [85–87]:

- the principal axis system ($\check{z}_1$, $\check{z}_2$, $\check{z}_3$), where $\check{z}_3$ is the optic axis of the uniaxial birefringent medium contained in the ($\check{x}$, $\check{z}$) plane and ϑ angle between the optic axis and interface;

- the discontinuity surface system ($\check{x}$, $\check{y}$, $\check{z}$), where $\check{x}$ is perpendicular to the surface which separates two media (the unit vector normal to the interface $\check{n} = \check{x}$), and $\check{y}$ and $\check{z}_2$ may be taken to coincide without loss of generality;

- the incidence plane system ($\check{x}'$, $\check{y}'$, $\check{z}'$) for describing the polarisation of the incident beam which is perpendicular or parallel to this plane, where δ is the angle between the incidence plane and the ($\check{x}$, $\check{z}$) plane.

In Figure 2.16, the three coordinate systems are shown in the case where the incidence plane is perpendicular to the z-axis ($\delta = +\,90^\circ$) and the optic axis is perpendicular to the discontinuity surface ($\vartheta = \pm\,90^\circ$) [85–87].

Here, the incidence plane is determined by the unit vector normal to the incident wavefront and the unit vector normal to the interface: all unit vectors normal to the incident, reflected and refracted wavefronts are contained in this plane [89].

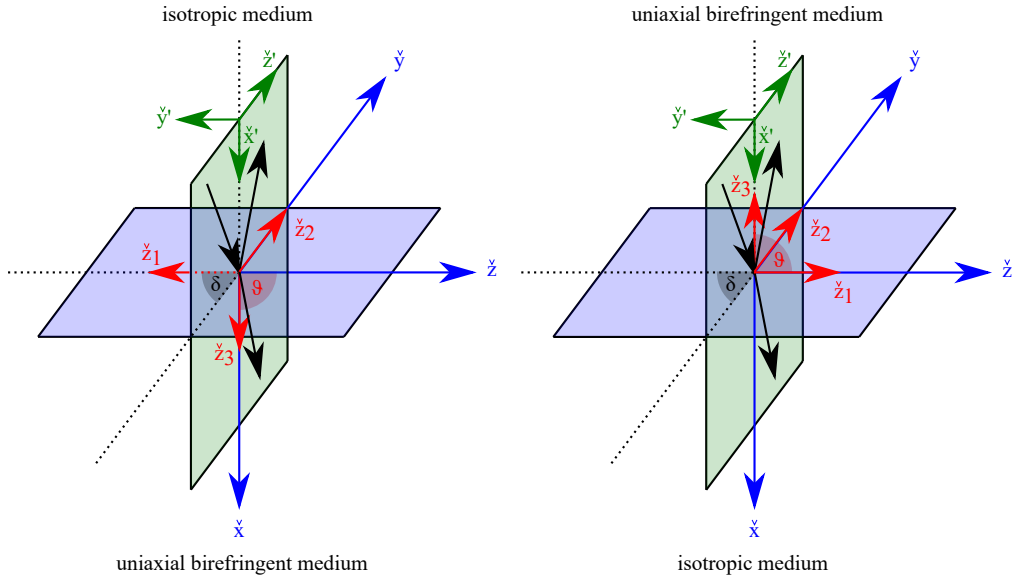

Fig. 2.16 Schematic diagram of the three coordinate systems for the isotropic-uniaxial birefringent (left) and the uniaxial birefringent-isotropic interface (right) for $\delta = +90°$ and $\vartheta = \pm 90°$. The optic axis of the uniaxial birefringent medium is $\check{z}_3$. The principal axis system is shown in red, the discontinuity surface system in blue and the incidence plane system in green. The incident, reflected and refracted beams are shown in black.

The components of a generic vector $\vec{\Omega}$ in these systems are related through the following equations [85–87]:

$$\begin{bmatrix} (\vec{\Omega}\cdot\check{x}) \\ (\vec{\Omega}\cdot\check{y}) \\ (\vec{\Omega}\cdot\check{z}) \end{bmatrix} = \begin{bmatrix} \sqrt{1-(\check{n}\cdot\check{z}_3)^2} & 0 & (\check{n}\cdot\check{z}_3) \\ 0 & 1 & 0 \\ -(\check{n}\cdot\check{z}_3) & 0 & \sqrt{1-(\check{n}\cdot\check{z}_3)^2} \end{bmatrix} \begin{bmatrix} (\vec{\Omega}\cdot\check{z}_1) \\ (\vec{\Omega}\cdot\check{z}_2) \\ (\vec{\Omega}\cdot\check{z}_3) \end{bmatrix} \tag{2.29}$$

$$\begin{bmatrix} (\vec{\Omega}\cdot\check{x}') \\ (\vec{\Omega}\cdot\check{y}') \\ (\vec{\Omega}\cdot\check{z}') \end{bmatrix} = \begin{bmatrix} 1 & 0 & 0 \\ 0 & \cos\delta & -\sin\delta \\ 0 & \sin\delta & \cos\delta \end{bmatrix} \begin{bmatrix} (\vec{\Omega}\cdot\check{x}) \\ (\vec{\Omega}\cdot\check{y}) \\ (\vec{\Omega}\cdot\check{z}) \end{bmatrix} \tag{2.30}$$

with $\check{n}$ the unit vector normal to the discontinuity surface.

Ordinary and extraordinary waves in uniaxial birefringent medium

If the medium is neither magnetic nor absorbing and plane wave solutions are postulated, the field amplitudes of a wave can be described by the following expressions, obtained from the Maxwell's equations [85, 87, 89]:

$$\begin{aligned} \check{\mathscr{N}}\times\vec{\mathscr{H}} &= -u\vec{\mathscr{D}} \\ \check{\mathscr{N}}\times\vec{\mathscr{E}} &= \mu_0 u\vec{\mathscr{H}} \\ \check{\mathscr{N}}\cdot\vec{\mathscr{D}} &= 0 \\ \check{\mathscr{N}}\cdot\vec{\mathscr{H}} &= 0 \end{aligned} \tag{2.31}$$

where $\check{\mathscr{N}}$ is the unit vector normal to the wavefront, $\vec{\mathscr{D}}$ is the electric displacement field, $\vec{\mathscr{E}}$ is the electric field, $\vec{\mathscr{H}}$ is the magnetic field, μ_0 is the magnetic induction constant of the vacuum and u is the phase velocity of the wave.

The most important difference between a wave propagating in an isotropic medium and one in uniaxial birefringent medium is the different relationship between the electric displacement $\vec{\mathscr{D}}$ and the electric field $\vec{\mathscr{E}}$ [85, 87].
In an isotropic medium, these vectors are parallel and related by the dielectric constant ε_i as follows [85, 87].

$$\vec{\mathscr{D}} = \varepsilon_i\vec{\mathscr{E}} = \frac{1}{\mu_0 u_i^2}\vec{\mathscr{E}} \tag{2.32}$$

where $u_i = c/n_i$ is the phase velocity of the wavefront and c the speed of wave in vacuum.
In a uniaxial birefringent medium, the electric displacement and the electric field vectors of the ordinary and extraordinary wavefront are not orientated in the same direction and

are related through the dielectric constant tensor. In the principal axis system this tensor is diagonal and in the case of uniaxial birefringent media two of its elements are the same: $\vec{\varepsilon} = (\varepsilon_o, \varepsilon_o, \varepsilon_e)$, with ε_o and ε_e the principal dielectric constants. The relationship between the electric displacement and the electric field vectors is defined as follows [85, 87, 89]:

$$\begin{aligned}
(\vec{\mathscr{D}} \cdot \check{z}_1) &= \varepsilon_o (\vec{\mathscr{E}} \cdot \check{z}_1) = \frac{1}{\mu_0 u_o^2} (\vec{\mathscr{E}} \cdot \check{z}_1) \\
(\vec{\mathscr{D}} \cdot \check{z}_2) &= \varepsilon_o (\vec{\mathscr{E}} \cdot \check{z}_2) = \frac{1}{\mu_0 u_o^2} (\vec{\mathscr{E}} \cdot \check{z}_2) \\
(\vec{\mathscr{D}} \cdot \check{z}_3) &= \varepsilon_e (\vec{\mathscr{E}} \cdot \check{z}_3) = \frac{1}{\mu_0 u_e^2} (\vec{\mathscr{E}} \cdot \check{z}_3)
\end{aligned} \tag{2.33}$$

where $u_o = c/n_o$ and $u_e = c/n_e$ are the principal phase velocity of the ordinary and extraordinary wavefronts, respectively.

In the principal axis system, the components of the electric displacement vector of an ordinary wave $\vec{D}_o$ are [85, 87, 89].

$$\begin{aligned}
(\vec{D}_o \cdot \check{z}_1) &= -\frac{(\check{N}_o \cdot \check{z}_2)}{(\check{N}_o \cdot \check{z}_1)} (\vec{D}_o \cdot \check{z}_2) \\
(\vec{D}_o \cdot \check{z}_3) &= 0
\end{aligned} \tag{2.34}$$

where ordinary wave $\vec{D}_o$ travels in the direction of the unit vector normal to the wavefront $\check{N}_o$ with principal phase velocity u_o and refractive index n_o constant for any direction in the medium. Therefore, the ordinary wave is linearly polarised with $\vec{D}_o$ and $\vec{E}_o$ which are perpendicular to the plane defined by the optic axis $\check{z}_3$ and $\check{N}_o$.
Also, Snell's law is valid and the refractive index of the ordinary wave is the principal refractive index n_o [89].

In the case of an extraordinary wave propagating in the direction of the unit vector normal to the wavefront $\check{N}_e$ with phase velocity u, the principal components of the electric displacement vector of an extraordinary wavefront $\vec{D}_e$ are [85, 87, 89]:

$$\begin{aligned}
(\vec{D}_e \cdot \check{z}_1) &= \frac{(\check{N}_e \cdot \check{z}_1)}{(\check{N}_e \cdot \check{z}_2)} (\vec{D}_e \cdot \check{z}_2) \\
(\vec{D}_e \cdot \check{z}_3) &= \frac{(\check{N}_e \cdot \check{z}_3)^2 - 1}{(\check{N}_e \cdot \check{z}_2)(\check{N}_e \cdot \check{z}_3)} (\vec{D}_e \cdot \check{z}_2)
\end{aligned} \tag{2.35}$$

The phase velocity u and the refractive index n of the extraordinary wave are defined as follows [85, 87, 89].

$$u = \frac{c}{n} = \sqrt{u_e^2 + (u_o^2 - u_e^2)(\check{N}_e \cdot \check{z}_3)^2} \tag{2.36}$$

$$n = \frac{n_o n_e}{\sqrt{n_o^2 + (n_e^2 - n_o^2)(\check{N}_e \cdot \check{z}_3)^2}} \tag{2.37}$$

Both of these variables depend on the propagation direction of the wavefront $\check{N}_e$ and on the direction of the optic axis $\check{z}_3$.

The optic axis of uniaxial birefringent medium is the direction in which the wave is not subjected to birefringence, which means the phase velocities of the ordinary and extraordinary waves are equal. This happens when $\check{N}_e$ is equal to $\check{z}_3$ ($u = u_o$), so the optic axis coincides with the principal axis $\check{z}_3$ [89].

The polarisation of an extraordinary wave is perpendicular to the ordinary one, where $\vec{D}_e$ is coplanar with $\vec{E}_e$ and $\check{N}_e$. In fact, $\vec{D}_e$ is parallel to the plane defined by $\check{N}_e$ and $\check{z}_3$, perpendicular to $\check{N}_e$ and is not parallel to $\vec{E}_e$.

It follows also that the extraordinary wave satisfies Snell's law only if its refractive index is n [89].

Theoretical model

The theoretical model used to study the reflectivity from a bond between two sapphire substrates with the optic axis perpendicular to the bonding surface assumes air and bond material as isotropic and non-absorbing media, and sapphire as a uniaxial optically negative crystal. The reflectance of the bond layer defined for the perpendicular ($\perp$) and parallel ($\parallel$) polarisations of the incident light is given from equation 2.21:

$$R_{\text{bond},\perp} = \frac{2\left(1 - r_{\perp\perp}^2\right)^2 r_{oo}^2 \left(1 - \cos(2\delta_2)\right)}{1 - 2r_{oo}^2 \cos(2\delta_2) + r_{oo}^4} \tag{2.38}$$

$$R_{\text{bond},\parallel} = \frac{2\left(1 - r_{\parallel\parallel}^2\right)^2 r_{ee}^2 \left(1 - \cos(2\delta_2)\right)}{1 - 2r_{ee}^2 \cos(2\delta_2) + r_{ee}^4} \tag{2.39}$$

where

$$r_{\perp\perp} = \frac{\cos\alpha - \sqrt{\left(\frac{n_{1o}}{n_0}\right)^2 - \sin^2\alpha}}{\cos\alpha + \sqrt{\left(\frac{n_{1o}}{n_0}\right)^2 - \sin^2\alpha}} \tag{2.40}$$

$$r_{oo} = \frac{\cos\beta' - \sqrt{\left(\frac{n_2}{n_{1o}}\right)^2 - \sin^2\beta'}}{\cos\beta' + \sqrt{\left(\frac{n_2}{n_{1o}}\right)^2 - \sin^2\beta'}} \tag{2.41}$$

$$r_{\parallel\parallel} = \frac{\left(\frac{n_{1o}n_{1e}}{n_0^2}\right)\cos\alpha - \sqrt{\left(\frac{n_{1e}}{n_0}\right)^2 - \sin^2\alpha}}{\left(\frac{n_{1o}n_{1e}}{n_0^2}\right)\cos\alpha + \sqrt{\left(\frac{n_{1e}}{n_0}\right)^2 - \sin^2\alpha}} \tag{2.42}$$

$$r_{ee} = \frac{\left(\frac{n_2}{n_{1o}}\right)^2\cos\beta'' - \sqrt{\left(\frac{n_2}{n''}\right)^2 - \sin^2\beta''}}{\left(\frac{n_2}{n_{1o}}\right)^2\cos\beta'' + \sqrt{\left(\frac{n_2}{n''}\right)^2 - \sin^2\beta''}} \tag{2.43}$$

$$n'' = \frac{n_{1o}n_{1e}}{\sqrt{n_{1o}^2 + (n_{1e}^2 - n_{1o}^2)\cos^2\beta''}} \tag{2.44}$$

$$\beta' = \arcsin\left(\frac{n_0}{n_{1o}}\sin\alpha\right) \tag{2.45}$$

$$\beta'' = \arcsin\left(\frac{n_{1e}n_0\sin\alpha}{\sqrt{n_{1o}^2n_{1e}^2 + (n_{1e}^2 - n_{1o}^2)n_0^2\sin^2\alpha}}\right) \tag{2.46}$$

and δ_2 is given by equation 2.28 (Figure 2.17).

The refractive index of air n_0 was approximated by 1, whereas the ordinary and extraordinary refractive indices of sapphire were $n_{1\text{o,green}} = 1.7717$ and $n_{1\text{e,green}} = 1.7636$ for the green laser, $n_{1\text{o,red}} = 1.7658$ and $n_{1\text{e,red}} = 1.7578$ for the red laser. The source for the ordinary refractive indices is https://refractiveindex.info/?shelf=main&book=Al2O3&page=Malitson-o, for the extraordinary https://refractiveindex.info/?shelf=main&book=Al2O3&page=Malitson-e [90, 91].

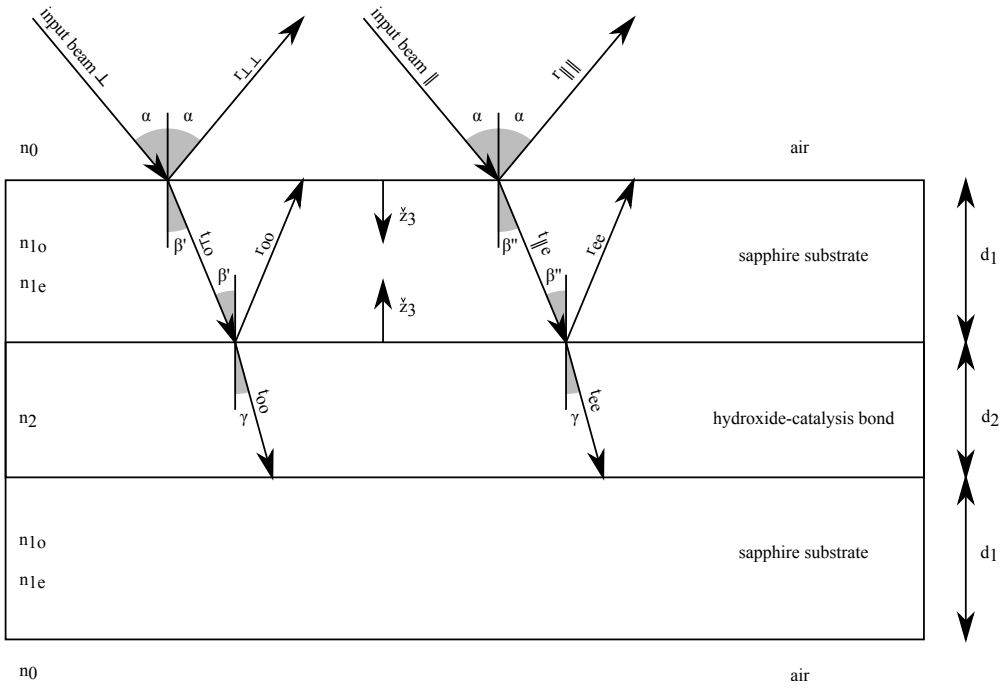

Fig. 2.17 Schematic diagram of a bonded sample (not to scale). Two discs of sapphire are joined by hydroxide-catalysis bonding. The reflection and transmission coefficient are also shown.

2.3 Analysis method

2.3.1 Analytical method

The theoretical reflectances, expressed by equations 2.22 and 2.23 for isotropic material or 2.38 and 2.39 for uniaxial birefringent substrate, constitute a system of two equations with two unknowns (bond refractive index n_2 and thickness d_2) for fixed value of angle of incidence.

Using the method of substitution, one of the two equations is solved for n_2 yielding a quintic equation for n_2. Substituting the value of n_2 into the other equation, the value of the remaining variable d_2 can be found by solving a trigonometric equation in cosine. As the range in which d_2 falls into is very broad (anywhere between 0.0 *nm* and 8000.0 *nm*, see Chapter 3 for details), the trigonometric equation gives more than one solution for d_2. Also, it is a deterministic method and does not take into account measurement errors.

This makes the analytical method unsuitable for determining the refractive index and thickness of a bond for one fixed angle of incidence. For this reason, a Bayesian approach has been preferred which allows the most probable values of n_2 and d_2 to be estimated for a given set of data with a suitable approximation of the errors.

2.3.2 Bayesian analysis

Differently from the analytical approach which showed its limits in solving the reflectance equations in an unequivocal way (2.3.1), the Bayesian likelihood analysis allows the refractive index and thickness of a bond to be determined. This was done through the comparison of the data collected by the optical setup and that simulated by the theoretical model (2.2). The calculations are facilitated by the use of some scripts and functions written in Matlab (2.3.3).

The first step for any Bayesian analysis is to write down Bayes' theorem [92]:

$$p(H|D,I) = \frac{p(H|I)p(D|H,I)}{p(D|I)} \tag{2.47}$$

where H, D and I are propositions which represent, respectively, the truth of a hypothesis of interest, the data and the prior information. $p(H|D,I)$ is the posterior probability density function (PDF) of H, $p(H|I)$ is the prior probability density function of H, $p(D|H,I)$ is the likelihood function of H, and $p(D|I)$ is the normalisation factor which ensures that $\int_{\Delta H} p(H|D,I)\,dH = 1$, where ΔH is the range of integration corresponding to the continuous hypothesis space of interest.

The Bayesian probability theory allows the inference of the unknown parameters of a theoretical model M from experimental data and prior information [92].
The theoretical model of reflectances has two unknown parameters, the refractive index n_2 and thickness d_2 of the hydroxide-catalysis bond layer. The corresponding joint posterior probability density function of n_2 and d_2, given data D and prior information I, can be written as follows [92]:

$$p(n_2,d_2|D,M,I) = \frac{p(n_2,d_2|M,I)p(D|M,n_2,d_2,I)}{p(D|M,I)} \propto p(D|M,n_2,d_2,I) \tag{2.48}$$

It is proportional to the likelihood function $p(D|M,n_2,d_2,I)$ if the prior probability density function $p(n_2,d_2|M,I)$ is constant within the study area and zero outside. Also, $p(D|M,I)$ is a normalisation constant and, thus, irrelevant in parameter estimation.

If a Gaussian distribution of probability is assumed for the likelihood function, the joint posterior probability density function is given by [92, 93]:

$$p(n_2,d_2|D,M,I) = C\exp\left[-\frac{1}{2}\left(\chi^2_{\perp}+\chi^2_{\parallel}-\chi^2_{min}\right)\right] \tag{2.49}$$

where C is a constant of proportionality which can be calculated using the fact that the double integral of $p(n_2,d_2|D,M,I)$ must be one, $\iint p(n_2,d_2|D,M,I)\,dn_2dd_2 = 1$ (more details in Appendix D), and χ^2_k is an indicator of the agreement between the theoretical and measured values of the reflectances:

$$\chi^2_k = \sum_{i=1}^{n} \frac{\left(R^{th}_{k,i} - R^{exp}_{k,i}\right)^2}{(\sigma R^{exp}_{k,i})^2} \tag{2.50}$$

with $k = (\perp, \parallel)$, the theoretical reflectance R^{th}_k expressed by equations 2.22 and 2.23 for isotropic material or 2.38 and 2.39 for uniaxial birefringent substrate, the measured reflectance R^{exp}_k and its statistical error σR^{exp}_k, and the minimum value χ^2_{min} of the quantity $(\chi^2_{\perp}+\chi^2_{\parallel})$.

For a grid of n_2 and d_2 possible combinations, the theoretical reflectances are calculated and then compared to the experimental reflectances (for a specific curing time) obtained by means of the optical setup taking into account measurement errors. The comparison is made using the chi-squared method, that is, minimising the sum of the squares of the residuals weighted by the variance. The residual is the difference between an observed value and the corresponding theoretical value provided by a model. The total residual value is calculated for each model with a specific n_2 and d_2 combination. It is postulated that the most likely combination for n_2 and d_2 is that for which the residual is the smallest.

If n_2, d_2 and $p(n_2, d_2|D, M, I)$ are plotted on the x-axis, y-axis and z-axis respectively, a three-dimensional bell curve is obtained. To estimate the two unknown parameters, the joint posterior probability density function is intersected by three planes at constant z so that three confidence levels at 1σ, 2σ and 3σ, which contain 68.3%, 95.5% and 99.7% of probability content respectively, are obtained. These contour ellipses specify the credible regions for the two parameters (more details in Appendix D) [92].

2.3.3 Matlab program

Some scripts were written using Matlab to carry out the Bayesian analysis described in the previous subsection.

In the first part of these scripts, the most probable values of the refractive index and thickness of a hydroxide-catalysis bond are obtained from the corresponding confidence levels of probability, by minimising the sum of the squares of the difference between measured and calculated reflectances weighted by the variance.
In the second part, the theoretical reflectances are calculated using these values of bond refractive index and thickness estimated statistically and then are plotted as a function of the angles of incidence together with the measured reflectances. This allowed the two trends, obtained from theory and measurements, to be compared.

Appendix D contains the full MATLAB codes used to carry out the analysis for fused silica and sapphire samples together with their description. The code reported refers only to one wavelength of the laser light (green in this case), however equivalent code was used for the measurements made using red laser light.

2.4 Bonding procedure

The procedure used for making hydroxide-catalysis bonds of the samples analysed in this thesis can be summarised by the following steps [94, 95]:

- measuring the flatness of the surfaces of substrates to be bonded,
- cleaning the substrates (particularly their bonding surfaces),
- preparing the bonding solution,
- bonding the two substrates using hydroxide-catalysis solution,
- and curing the bond.

These steps are described in more detail below.

Measurement of flatness

As seen in section 1.5.1, an important factor in forming a hydroxide-catalysis bond between substrates to be bonded is the figure mismatch of their surfaces [3, 4].

To obtain a good bond, it is recommended to have samples characterised by a peak-to-valley flatness of $\lambda/10$ or better, where $\lambda = 633\ nm$ [94, 95].

To assess this, the flatness of all samples studied in this thesis was measured before bonding using a ZYGO® GPI XP/D laser interferometer. The maps obtained not only allowed the selection of the best surfaces to be bonded, but also could be combined to determine the total flatness of the two surfaces that were bonded together (see subsection 2.5 for details).

Cleaning of substrates

Another important factor in forming a hydroxide-catalysis bond is the cleanliness of the bonding surfaces. Any contamination on these surfaces can inhibit the hydroxide-catalysis process or increase their figure mismatch (see section 1.5.1) [94, 95].

The cleaning procedure, carried out in a clean room environment, starts with the substrates being rinsed with de-ionised water and then rubbed with cerium oxide paste using a wet clean room wipe (Anticon® Gold StandardWeight™, 495353-903) for about a minute. This makes the surfaces hydrophilic.
After rinsing with de-ionised water, the samples have to be rubbed with bicarbonate of soda paste using a new wet clean room wipe for about a minute. This removes the remains of the cerium oxide paste. This is repeated.
Finally, the samples are rinsed with de-ionised water and then methanol at $\geq 99.9\%$ (Sigma-Aldrich®, 34885-1L-R) which removes the water from the surface [94, 95].

Before bonding, the cleaned surfaces have to be inspected using a high intensity light source to see if they are free from residues of cerium oxide and bicarbonate of soda paste, particles or films. If not, the cleaning procedure has to be repeated again. If only a single small contaminant is present, the surface can be cleaned using a clean room wipe soaked with $\geq 99.9\%$ methanol to remove it. The substrates are then covered with a clean room wipe until they will be bonded [94, 95].

Preparation of bonding solution

The bonding solutions used to make the bonds studied in this thesis, which were prepared in a clean room environment at room temperature, are described below:

- Sodium silicate solution diluted with de-ionised water.
  Two samples were bonded by diluting 2 *ml* of sodium silicate solution (Sigma-Aldrich®, 338443) with 12 *ml* of de-ionised water at a volumetric ratio of 1 : 6 into a 15 *ml* centrifuge tube (CORNING™, 430790). Two pairs of samples were also made by diluting 2 *ml* (1 *ml*) of sodium silicate solution with 6 *ml* (10 *ml*) of de-ionised water at a volumetric ratio of 1 : 3 (1 : 10). The ratio of 1 : 6 was chosen as it was used to bond the ears to the sides of the intermediate and test masses of quasi-monolithic fused silica mirror suspensions in the advanced LIGO detectors [18–21] (see subsection 1.5.3), whereas the ratios of 1 : 3 and 1 : 10 were chosen in an attempt to create a large enough difference in concentration compared to the 1 : 6 sodium silicate solution to allow the investigation of the comparative effects of concentration on bond reflectivity. Sodium silicate solution was composed of $\sim$ 10.6% sodium oxide (Na_2O), $\sim$ 26.5% silicon dioxide (SiO_2) and $\sim$ 62.9% water (H_2O). After shaking the centrifuge tube for about a minute to ensure that two liquids are mixed, the bonding solution was transferred into three 1.5 *ml* centrifuge tubes.

- Potassium hydroxide solution (0.1 *N*).
  Potassium hydroxide solution (Sigma-Aldrich®, 319325-500ML) KOH was used without diluting it with de-ionised water. It was composed of 0.1 *N* solution in water and was transferred into three 1.5 *ml* centrifuge tubes without shaking. This solution was chosen as it was used to bond fused silica substrates for the Gravity Probe B mission [4, 14, 16, 19] (see subsection 'Gravity Probe B' in section 1.5.3).

These bonding solutions were chosen to allow the comparison of the results reported in this thesis, such as reflectivity, refractive index and thickness of a hydroxide-catalysis bond between fused silica and sapphire samples, with studies of bond properties performed until now [14, 19, 27, 48, 51–53, 96].

The three 1.5 ml centrifuge tubes were centrifuged for about a minute at 6200 *rpm* (TOMY Capsulefuge, PMC-060) to bring larger particles to the bottom. The solution contained in two of three centrifuge tubes was then transferred to the outer shell of a medical filter (Whatman® UniPrep™, 0.2 μm pore size by ion), paying attention to leave a bit of solution in the centrifuge tubes because it contained the larger particles. Once the

solution was filtered to remove any remaining smaller particles, it was ready to be used for bonding [94, 95].

Bonding

Bonding was carried out in a clean room flow cabinet to minimise the risk of contamination of the bonding surfaces. Before final inspection and subsequent bonding, the clean surfaces were wiped with methanol. Also, the tip of the pipette had to take the bonding solution from near the solution-air interface without touching the medical filter, and had to be changed for each bond [94, 95].

The amount of bonding solution per square cm of area taken by the pipette was 0.8 $\mu l/cm^2$ (as used in aLIGO [97, 98]).
For the fused silica samples analysed in this thesis, which had a diameter of 5.0 cm, the bonding area of the disc was 19.6 cm^2 and, therefore, the amount of solution used was 15.70 μl. The same amount was used for the sapphire samples (see section 2.4.1).

The solution was dispensed onto the first clean bonding surface and then the bonding surface of the second substrate was placed on top of the first. This might float on the layer of bonding solution for a settling time defined by the concentration of hydroxide ions and silicate material in the bonding solution or the temperature at which bonding occurred (see section 1.5.2). During this time, it is possible to correct alignment between two samples without damaging the bond. Jigs for alignment could be useful in cases where precision alignment is required [3, 4, 27, 28, 94, 95].

If the bonding surfaces are sufficiently flat, clean and hydrophilic, the bonding solution will spread between the two surfaces in contact and the chemical reactions described in section 1.5.1 will begin. Any bubbles should move towards the edges, otherwise weights to aid the migration of bubbles out the bond can be used [94, 95].

Curing

The bonded substrates can be cured at room temperature and only a few hours after the start of the jointing process the bond has sufficient strength to allow the bonded sample to be touched [4, 64].

It is also possible to accelerate the curing of the bond by means of a heat treatment [4, 27, 96, 99]. In this thesis, two fused silica samples, after one hour from bonding, were placed inside an oven (CARBOLITE®, 3216) for eight hours at 100 $°C$ and thereafter at room temperature. This curing temperature was chosen considering the results reported by

Kim [96] and Green [99] (both used 100 $°C$ for their measurements), whereas the baking time was chosen because it should be sufficient for the reactions to reach completion quickly (see section 3.4 for details).

2.4.1 Samples

For this thesis, twelve samples were bonded by the author and their reflectivity analysed. Fused silica and sapphire samples were bonded using either sodium silicate solution with de-ionised water at different volumetric ratios or potassium hydroxide solution KOH (0.1 N). They are listed in Table 2.4.
For the fused silica samples, uncoated discs were bought from Edmund Optics Inc. (stock no. 47-836) with a diameter and thickness of $50.0^{+0.0}_{-0.2}$ mm and $5.0^{+0.1}_{-0.1}$ mm, respectively.
For the sapphire samples, the discs were bought from Melles Griot Inc. (SCD2028-02A) with a diameter and thickness of $50.80^{+0.03}_{-0.03}$ mm and $6.35^{+0.03}_{-0.03}$ mm, respectively. Also, the optic axis of these samples was directed along the c-axis, perpendicular to its bonding surface.

Name of sample	Material of disc	Bonding solution	Pipetting volume	Heat treatment
$\text{Silica1}_{\text{Na2SiO3(1:6)}}$	fused silica	2 *ml* of Na_2SiO_3 with 12 *ml* of DI H_2O (1:6)	15.70 μl	no
$\text{Silica2}_{\text{Na2SiO3(1:6)}}$	fused silica	2 *ml* of Na_2SiO_3 with 12 *ml* of DI H_2O (1:6)	15.70 μl	no
$\text{Silica1}_{\text{KOH(0.1N)}}$	fused silica	KOH (0.1 *N*)	15.70 μl	no
$\text{Silica2}_{\text{KOH(0.1N)}}$	fused silica	KOH (0.1 *N*)	15.70 μl	no
$\text{Silica1}_{\text{Na2SiO3(1:3)}}$	fused silica	2 *ml* of Na_2SiO_3 with 6 *ml* of DI H_2O (1:3)	15.70 μl	no
$\text{Silica2}_{\text{Na2SiO3(1:3)}}$	fused silica	2 *ml* of Na_2SiO_3 with 6 *ml* of DI H_2O (1:3)	15.70 μl	no
$\text{Silica1}_{\text{Na2SiO3(1:10)}}$	fused silica	1 *ml* of Na_2SiO_3 with 10 *ml* of DI H_2O (1:10)	15.70 μl	no
$\text{Silica2}_{\text{Na2SiO3(1:10)}}$	fused silica	1 *ml* of Na_2SiO_3 with 10 *ml* of DI H_2O (1:10)	15.70 μl	no
$\text{Silica}_{\text{Na2SiO3(1:6),T}}$	fused silica	2 *ml* of Na_2SiO_3 with 12 *ml* of DI H_2O (1:6)	15.70 μl	100 $^\circ C$ for 8 hours
$\text{Silica}_{\text{KOH(0.1N),T}}$	fused silica	KOH (0.1 *N*)	15.70 μl	100 $^\circ C$ for 8 hours
$\text{Sapphire}_{\text{Na2SiO3(1:6)}}$	sapphire (c-axis)	2 *ml* of Na_2SiO_3 with 12 *ml* of DI H_2O (1:6)	15.70 μl	no
$\text{Sapphire}_{\text{KOH(0.1N)}}$	sapphire (c-axis)	KOH (0.1 *N*)	15.70 μl	no

Table 2.4 Fused silica and sapphire samples made with different hydroxide-bonding solutions and cured at room temperature or at 100 $^\circ C$ for eight hours.

2.5 Flatness study

As introduced in section 2.4, one of the first steps of the bonding procedure is measuring the flatness of the surfaces of substrates to be bonded. The maps of the samples analysed in this thesis were obtained using a ZYGO® GPI XP/D laser interferometer. Then, these maps were combined with each other to determine the total flatness of the two surfaces that had to be bonded together.

Some scripts were written using Matlab to obtain the total flatness maps of all samples listed in Table 2.4. The surface maps obtained from these scripts will be shown in Chapter 3, 4 and 5, and their results will be compared with those estimated from the Bayesian analysis and SEM imaging measurements.

First, the surface maps obtained using the ZYGO® were processed to rescale the surface height data into nanometres and zoom in on the valid area of the map, excluding non-valid elements and correcting for some possible tilt. Preparing surface maps was carried out by the SimTools package, a collection of Matlab files for optical simulations used in gravitational wave field (available for download from http://www.gwoptics.org/simtools/, SimTools version 0.7).

Then, one of two surface maps was flipped and tilted with respect to the other surface map. The tilt angles were determined by the condition that the two maps had three points of contact with the centre of the sample inside the triangle formed by these three points. As a first approximation, this assured the stability of the system and positive total flatness maps (negative values of total flatness meant that a disc penetrated another disc during bonding and this is not physically possible).

As an example, Appendix E contains the MATLAB full code used to carry out the analysis for sample $\text{Silica2}_{\text{Na2SiO3(1:3)}}$.

Chapter 3

Measurements on fused silica samples bonded with sodium silicate

In this chapter the values of bond reflectivity, refractive index and thickness are reported for fused silica samples bonded with sodium silicate solution at different concentrations with de-ionised water, precisely at volumetric ratios of 1 : 6 (section 3.1, $\text{Silica1}_{\text{Na2SiO3(1:6)}}$ and $\text{Silica2}_{\text{Na2SiO3(1:6)}}$), 1 : 3 (section 3.2, $\text{Silica1}_{\text{Na2SiO3(1:3)}}$ and $\text{Silica2}_{\text{Na2SiO3(1:3)}}$), 1 : 10 (section 3.3, $\text{Silica1}_{\text{Na2SiO3(1:10)}}$ and $\text{Silica2}_{\text{Na2SiO3(1:10)}}$) of solution to water. For each concentration, two samples were prepared in order to compare and confirm the results obtained from this study. All these six samples were left to cure in air at room temperature after bonding. One sample (section 3.4, $\text{Silica}_{\text{Na2SiO3(1:6),T}}$) was bonded using 1 : 6 sodium silicate solution and cured at elevated temperature (100 $^{\circ}C$) for 8 hours and thereafter at room temperature. This allowed the influence of temperature on the reflectivity, refractive index and thickness of a bond to be studied. See section 2.4 for details about bonding solutions and samples used in this chapter.

The initial setup was used to measure reflectivities in green laser light only and at different positions on the front surface of sample $\text{Silica1}_{\text{Na2SiO3(1:6)}}$. From these initial measurements it was clear that a better sensitivity was required and that analysing the bonds in different colours of light could be useful to constrain the values for the bond refractive index and thickness better. Therefore, the reflectances of $\text{Silica1}_{\text{Na2SiO3(1:6)}}$ and all other samples analysed in this chapter were collected using the upgraded setup in two colours of laser light (green and red).

From the measured reflectances, the values of bond refractive index and thickness were obtained using the Bayesian likelihood analysis (discussed in detail in Chapter 2).

All bonds were measured as a function of curing time (the amount of time passed since the first bond was made) in order to understand how their optical properties vary with time.

All measurements were performed in the dark to better see the weak light spots due to the reflected beams off the sample and to reduce the unwanted light sources.

3.1 Sodium silicate 1:6 solution

The first measurements were performed on bonds made nominally identical using sodium silicate solution at a volumetric ratio of 1 : 6 with de-ionised water.

This ratio was chosen as it was used to bond the ears to the sides of the intermediate and test masses of quasi-monolithic fused silica mirror suspensions in the advanced LIGO detectors, keeping the thermal noise as low as possible [18–21] (see subsection 1.5.3).

3.1.1 Silica1$_{Na2SiO3(1:6)}$ and Silica2$_{Na2SiO3(1:6)}$

Samples Silica1$_{Na2SiO3(1:6)}$ and Silica2$_{Na2SiO3(1:6)}$ were made by bonding two fused silica discs with 15.70 μl of solution composed of 2 *ml* of sodium silicate solution with 12 *ml* of de-ionised water (a volumetric ratio of 1 : 6). These samples were then left to cure in air at room temperature for some days before measuring the reflectivity of their bonds.

Silica1$_{Na2SiO3(1:6)}$ is the only sample for which the bond reflectivity was measured using both optical assemblies described in Chapter 2, whereas only the upgraded setup was used for studying Silica2$_{Na2SiO3(1:6)}$ (Figure 2.2 and Figure 2.5).

3.1.2 Reflectivity measurements

As described in Chapter 2, photodiode 2 was placed on a translation stage, which was moved by increments of 0.1 *mm*, to scan the entire Gaussian profile of the bond spot for each angle of incidence. In the top of Figure 3.1 the reflectance for perpendicular polarisation of laser light plotted as a function of the position of photodiode 2 for the central position on the front surface of Silica2$_{Na2SiO3(1:6)}$ is shown as an example.

As the laser beam incident on the sample produces three reflected spots due to the light reflected at its front, bonded and back surfaces, the background due to the front and back reflected beams may affect the reflectivity of the bond. For this reason, this background has to be estimated and subtracted from the values of the bond reflectivity. The contribution of the background to the bond reflectance is assumed to be particularly significant when the bond reflectivity is very low (ratio between the reflectivity of peak and background less than

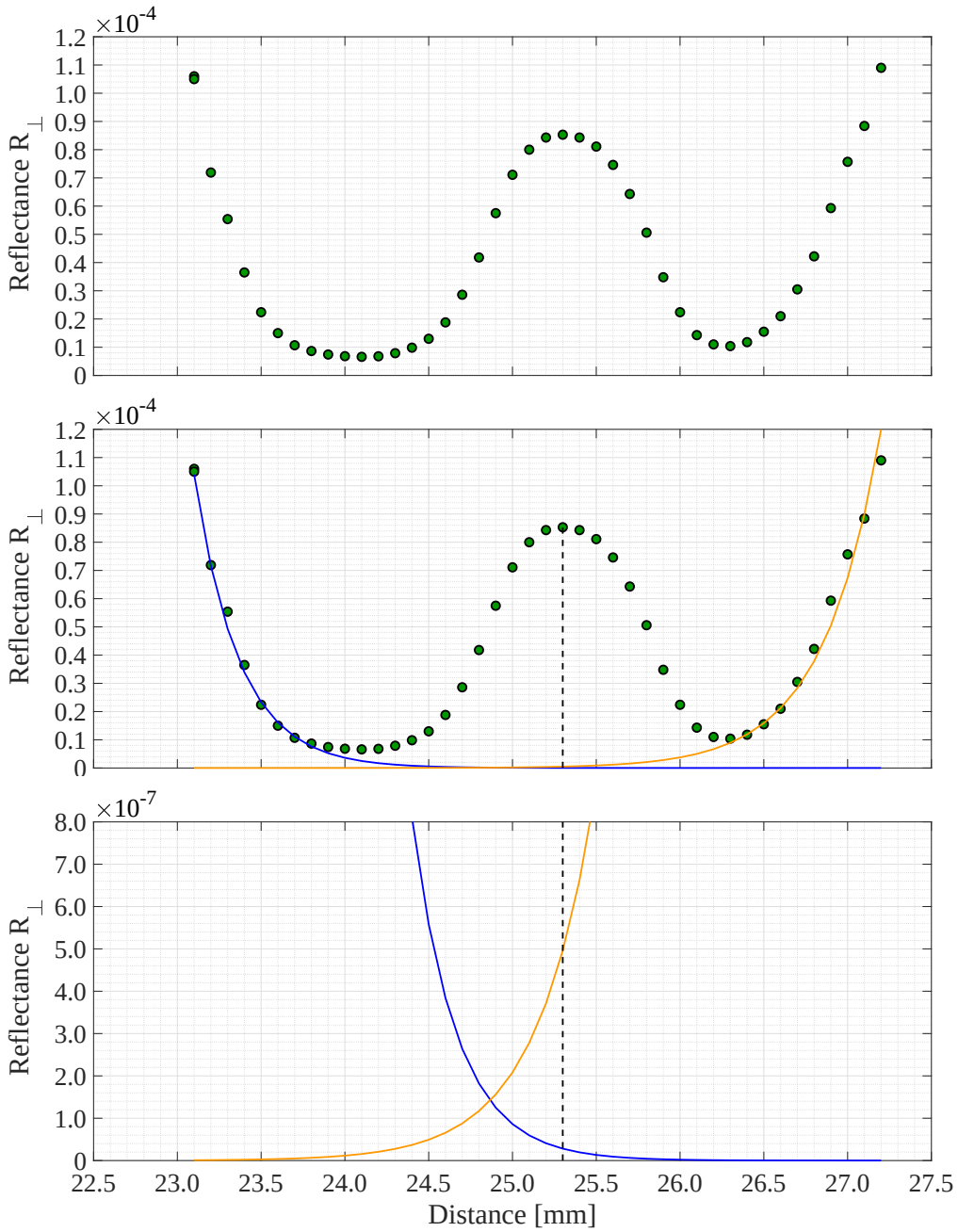

Fig. 3.1 (top) Measured reflectance for ⊥ polarisation plotted as a function of the position of photodiode 2 (green dots). This measurement was performed in the central position on the front surface of Silica2$_{\text{Na2SiO3(1:6)}}$ using the upgraded setup in green mode at 104 days after bonding for the angle of incidence 35°. (middle) Two exponential trendlines are used to fit the tails of the back (blue line) and front (orange line) spot profile. The vertical dashed line passes through the peak of the bond spot profile. (bottom) Zoom in of the two points of intersection where the two exponential trendlines cross with the vertical dashed line: the background under the peak is given by the sum of the values of these two points which has to be subtracted from the peak reflectivity.

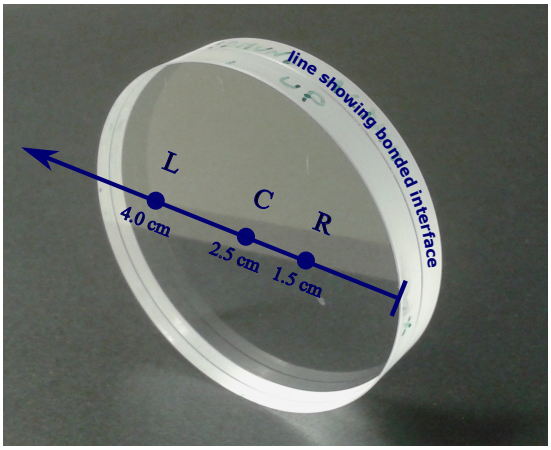

Fig. 3.2 Photograph of the pair of fused silica discs of Silica1$_{Na2SiO3(1:6)}$ with the three measurement locations shown. These are referred to as *L*, *C* and *R* to indicate, respectively, the points on the left, at centre and on the right compared to the front surface of the sample.

100) and at low or high angles of incidence where the three reflected spots are close each other.

As the goal was to measure the bond reflectivity at its peak, the approach used in this thesis for estimating the background was to fit two exponential trendlines to the tails of the Gaussian profiles of the front and back spots (the middle of Figure 3.1) and sum the values that these two fits had under the peak (the bottom of Figure 3.1). The background was measured and subtracted from the peak reflectivity of all the samples studied in this thesis.

The reflectances of Silica1$_{Na2SiO3(1:6)}$ were measured for three different positions on its front surface (locations *L*, *C* and *R*) at a number of different time intervals after bonding. In this way the effect of curing time on the refractive index and thickness of the bond could be studied, as well as the spatial homogeneity of these properties (Figure 3.2).

The bond reflectivity of Silica2$_{Na2SiO3(1:6)}$ was measured only in the central position of its front surface.

Plots of measured reflectivity for perpendicular ($\perp$) and parallel ($\parallel$) polarisations (equations 2.1 and 2.2) and all three positions as a function of angle of incidence α are shown in Figure 3.3 (position *L*), Figure 3.4 (position *C*) and Figure 3.5 (position *R*) for Silica1$_{Na2SiO3(1:6)}$. Figure 3.6 (green laser) and Figure 3.7 (red laser) show these results for Silica2$_{Na2SiO3(1:6)}$.

For Silica1$_{Na2SiO3(1:6)}$, it is observed that the values of bond reflectances are all less than 1% for both polarisations and the three locations on its surface.

Initially the reflectance values fluctuate. During this phase, the reflectivity values do not

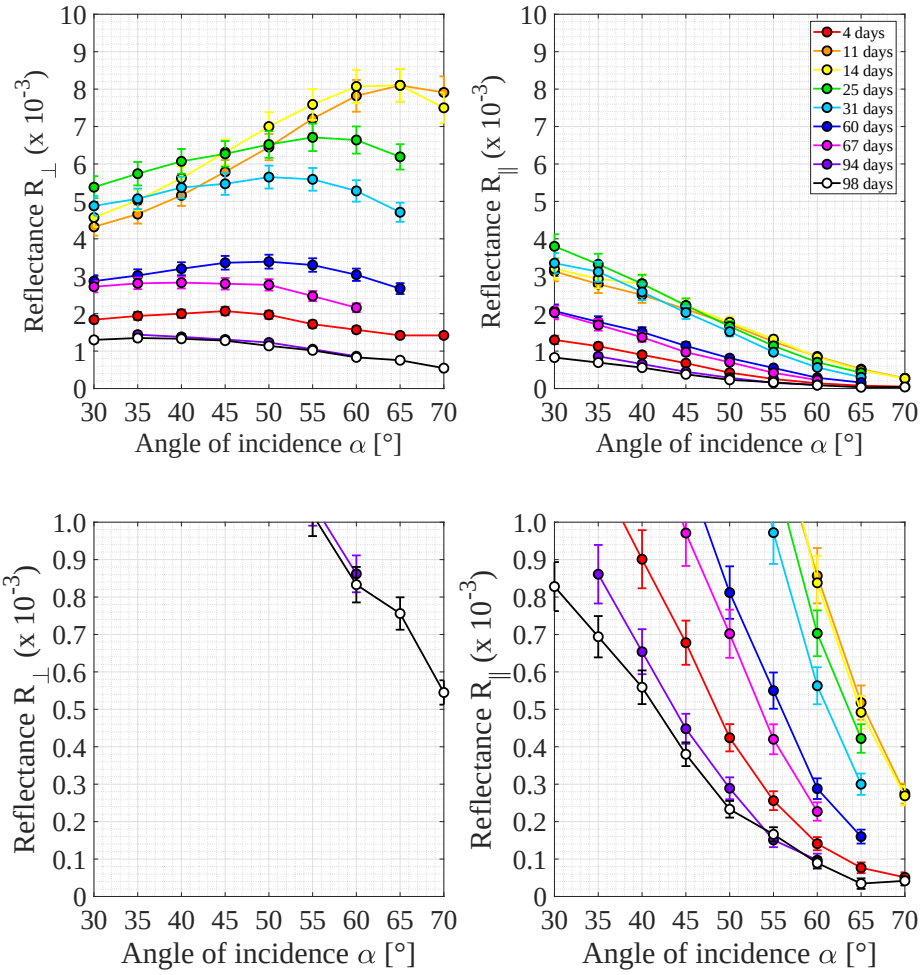

Fig. 3.3 (top) Measured reflectances for $\perp$ (left) and $\parallel$ (right) polarisation plotted as a function of the angle of incidence α for position L on the front surface of Silica1$_{\text{Na2SiO3(1:6)}}$. (bottom) Zooms in of the measured reflectances are also shown to allow the reader to see the lower reflectances. In the legend, the curing time is reported. All measurements were taken using the initial setup in green mode.

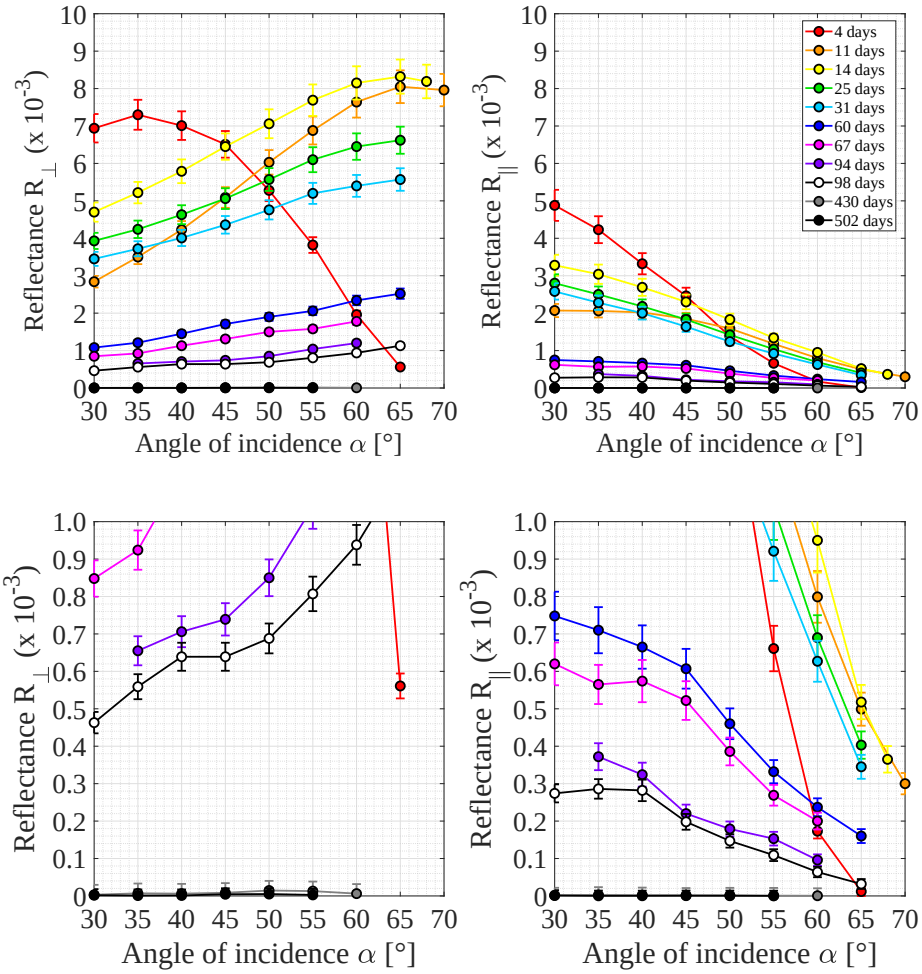

Fig. 3.4 (top) Measured reflectances for $\perp$ (left) and $\parallel$ (right) polarisation plotted as a function of the angle of incidence α for position C on the front surface of Silica1$_{\text{Na2SiO3(1:6)}}$. (bottom) Zooms in of the measured reflectances are also shown to allow the reader to see the lower reflectances. In the legend, the curing time is reported. The measurements from the 4th to 98th day were taken using the initial setup in green mode, the measurements performed on the 430th and 502nd day were collected using the upgraded setup in green and red mode, respectively.

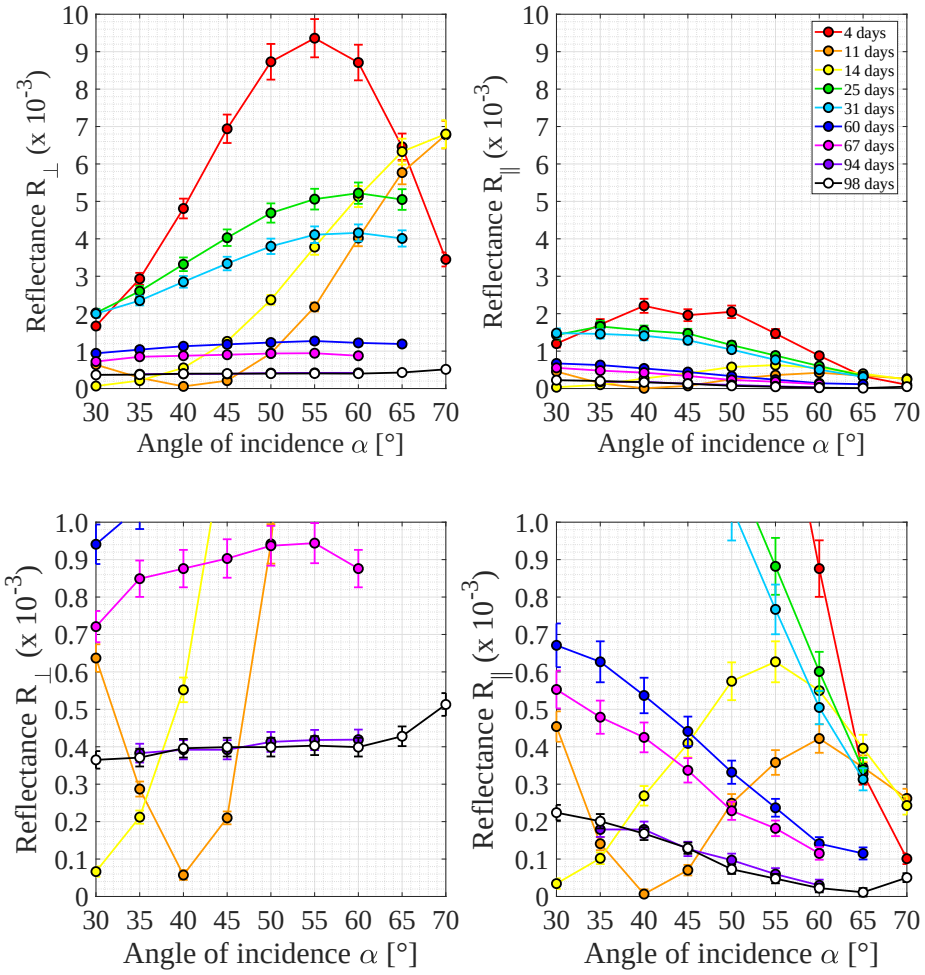

Fig. 3.5 (top) Measured reflectances for $\perp$ (left) and $\parallel$ (right) polarisation plotted as a function of the angle of incidence α for position R on the front surface of Silica1$_{\mathrm{Na2SiO3(1:6)}}$. (bottom) Zooms in of the measured reflectances are also shown to allow the reader to see the lower reflectances. In the legend, the curing time is reported. All measurements were taken using the initial setup in green mode.

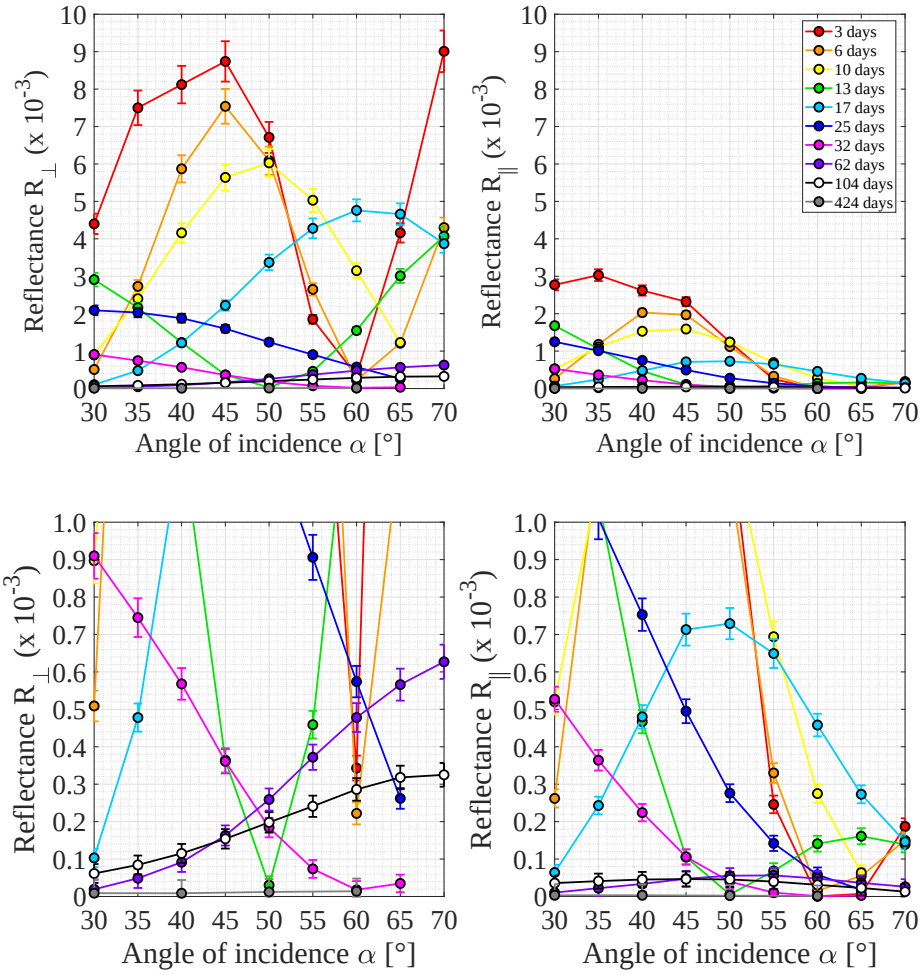

Fig. 3.6 (top) Measured reflectances for $\perp$ (left) and $\parallel$ (right) polarisation plotted as a function of the angle of incidence α for the central position on the front surface of Silica2$_{\text{Na2SiO3(1:6)}}$. (bottom) Zooms in of the measured reflectances are also shown to allow the reader to see the lower reflectances. In the legend, the curing time is reported. All measurements were taken using the upgraded setup in green mode.

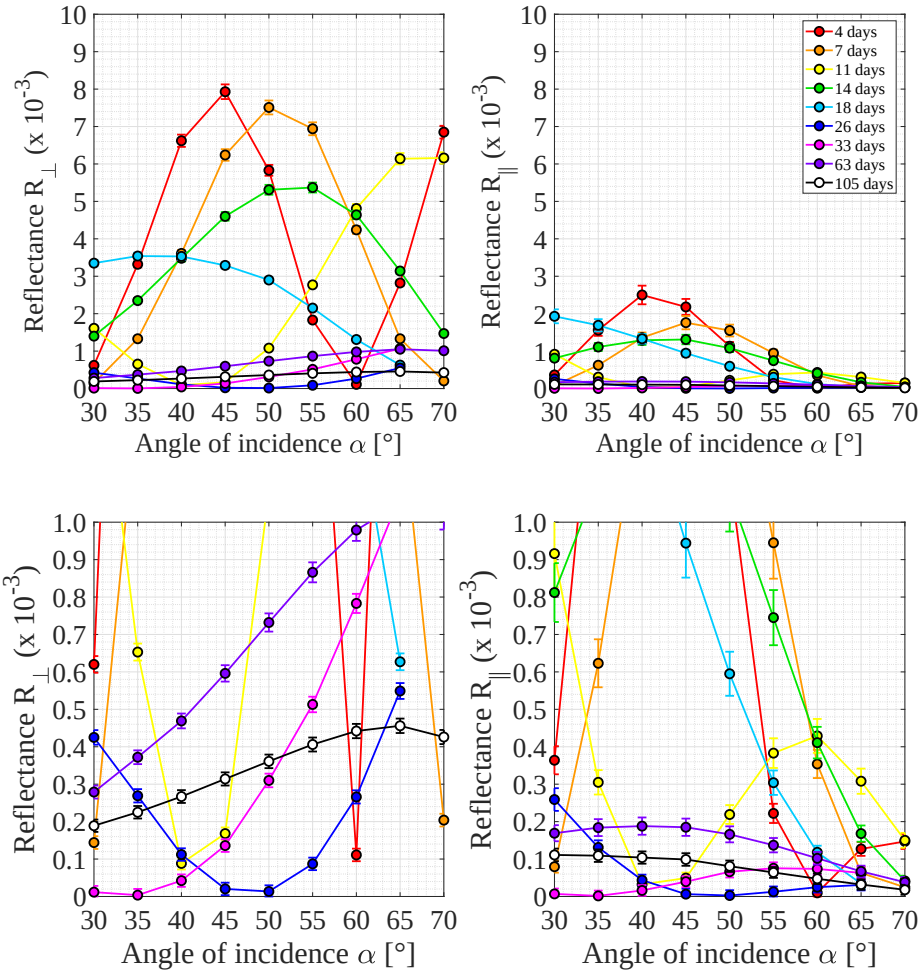

Fig. 3.7 (top) Measured reflectances for $\perp$ (left) and $\parallel$ (right) polarisation plotted as a function of the angle of incidence α for the central position on the front surface of $\text{Silica2}_{\text{Na2SiO3(1:6)}}$. (bottom) Zooms in of the measured reflectances are also shown to allow the reader to see the lower reflectances. In the legend, the curing time is reported. All measurements were taken using the upgraded setup in red mode.

follow a well-defined trend over the curing time. For the data taken at the positions marked *L* and *R* on the sample, this 'adjustment' phase lasts up to the 14$^{\text{th}}$ day, whereas for position *C*, this is observed up to the 11$^{\text{th}}$ day (red, orange and yellow data points in Figure 3.3, Figure 3.4 and Figure 3.5). After this period, the reflectivity steadily starts to drop as curing time increases. This implies that the centre settled before the areas near edges.
After about three months, the reflectivity values are less than 0.1% for all locations and angles of incidence and, after more than a year, they are less than 0.01% for the *C* position using the upgraded setup (grey and black data points in Figure 3.4).
The different magnitude of reflectivity found between the three positions *L*, *C* and *R* may be influenced by the surface profile of the bonded interfaces. As will be possible to see in the following pages, the bonding surfaces of discs are not uniformly flat (Figure 3.16) and the bond thickness may vary not only with the curing time but also with location (Figure 3.14).

For $\text{Silica2}_{\text{Na2SiO3(1:6)}}$, the reflectivity for the *C* position on the front face is also less than 1% for both polarisations and colours of laser light: it decreases as curing time increases like $\text{Silica1}_{\text{Na2SiO3(1:6)}}$. For the green light, another measurement was performed after more than a year and the reflectivities are less than 0.01% in agreement with $\text{Silica1}_{\text{Na2SiO3(1:6)}}$.

3.1.2.1 Estimation of errors

The principal source of error for the angle of incidence α was a random error introduced during initial alignment of the setup for each measurement day, equal to $\pm 0.2^{\circ}$, which systematically appeared at each angle of incidence.

The error in the measured reflectances (calculated separately for both polarisations $\text{i} = (\perp, \parallel)$ of the laser beam) was determined by equation 2.3 (see section 2.1.3):

$$\sigma(R_{\text{i}}) = |R_{\text{i}}| \sqrt{\left(\sigma(V_{\text{input,i}})/V_{\text{input,i}}\right)^2 + \left(\sigma(V_{\text{output,i}})/V_{\text{output,i}}\right)^2} \tag{2.3}$$

For the initial assembly in green light, $\sigma(V_{\text{input}})$ was not calculated using equation 2.5, but it was obtained from the deviation from the linearity between voltages measured for both detectors for different light powers shown in Figure 2.6, from which the conversion factor could be also estimated:

- $k_{\perp,initial,green} \pm \sigma(k_{\perp,initial,green}) = 4.79 \pm 0.03$;
- $k_{\parallel,initial,green} \pm \sigma(k_{\parallel,initial,green}) = 55.20 \pm 1.01$;
- $\sigma(V_{\text{input},\perp,initial,green}) = 37.99\ mV$;

- $\sigma(V_{\text{input},\parallel,initial,green}) = 107.86\ mV$.

The error $\sigma(V_{\text{output}})$ was calculated using equation 2.7 and the following values:

- $F_{100/10,\perp \text{ and } \parallel,\text{initial,green}} \pm \sigma(F_{100/10,\perp \text{ and } \parallel,\text{initial,green}}) = 10.12 \pm 0.49$;
- $\sigma(V_{\text{output,100},\perp \text{ and } \parallel,\text{initial,green}}) = 0.20\ mV$

The proportional factor between 10 $mV/\mu A$ and 100 $mV/\mu A$ $F_{100/10}$ for photodiode 2 was determined by measuring a large range of light powers (using filters) at both 10 $mV/\mu A$ and 100 $mV/\mu A$ instead of using the ratio between the two corresponding precision resistors (10 with an error of 0.014, see section 2.1.1). The difference between these two values was due to the error when a measurement is made with an oscilloscope: the precision with which a reading is made from the screen of an oscilloscope is associated with the linewidth of the trace which is noisier at low signals. The statistical random variation of $V_{\text{output,100}}$ was caused both by noise of the circuitry and power fluctuations of the laser and was determined by monitoring bond reflection power at an angle of incidence of 45° at both polarisations. Both values were independent of polarisation of the laser light.

For the upgraded assembly, $\sigma(V_{\text{input}})$ was calculated using equation 2.5, where:

- $k_{\perp,upgraded,green} \pm \sigma(k_{\perp,upgraded,green}) = 6.5 \pm 0.4$;
- $k_{\parallel,upgraded,green} \pm \sigma(k_{\parallel,upgraded,green}) = 144.5 \pm 5.8$;
- $k_{\perp,upgraded,red} \pm \sigma(k_{\perp,upgraded,red}) = 29.1 \pm 0.7$;
- $k_{\parallel,upgraded,red} \pm \sigma(k_{\parallel,upgraded,red}) = 614.4 \pm 17.1$;
- $\sigma(V_{\text{photodiode1},\perp \text{ and } \parallel,\text{upgraded,green and red}}) = 2.2\ mV$.

The conversion factor k was measured with the method explained in section 2.1.4, without varying the intensity of the laser by filters. For each polarisation and colour of the laser light, its value was determined by the average of all the conversion factors measured at all their curing times (more than three months) during the reflectivity measurements of three random fused silica samples ($\text{Silica2}_{\text{Na2SiO3(1:6)}}$, $\text{Silica1}_{\text{Na2SiO3(1:10)}}$ and $\text{Silica2}_{\text{Na2SiO3(1:10)}}$). Its corresponding uncertainty was given by the absolute error between the average and the most extreme values of the conversion factor measured for the three samples. As $V_{\text{photodiode1}}$ was the signal from the lock-in read using an oscilloscope, its error was given by the square root of the sum of the squares of the error on the output of lock-in amplifier equal to 2.0 mV and the error in reading values with the oscilloscope equal to 1.0 mV for both the polarisations

of the laser beam equalling 2.2 mV.
The error $\sigma(V_{\text{output}})$ was calculated using equation 2.7 with the following values:

- $F_{100/10,\perp \text{ and } \parallel,\text{upgraded,green and red}} \pm \sigma(F_{100/10,\perp \text{ and } \parallel,\text{upgraded,green and red}}) = 10.000 \pm 0.014$;
- $\sigma(V_{\text{output,100},\perp \text{ and } \parallel,\text{upgraded,green and red}}) = 2.0\ mV$

where $F_{100/10}$ is the proportional factor between 10 $mV/\mu A$ and 100 $mV/\mu A$ for photodiode 2 (see section 2.1.2), and the error on $V_{\text{output,100}}$ was given by the error on the output of the lock-in only, because the data was recorded using the LabVIEW software and not the oscilloscope. These values were independent of polarisation of the laser light.

This error analysis was used for all the samples studied in this thesis.

3.1.3 Analysis result: reflectivity

In Figure 3.8 and Figure 3.9, the peak reflectivity of the bond for both polarisations of the laser light is plotted as a function of curing time for $\text{Silica1}_{\text{Na2SiO3(1:6)}}$ and $\text{Silica2}_{\text{Na2SiO3(1:6)}}$, respectively: as said previously, after an initial fluctuation of the reflectance values, these decrease as curing time increases.

Note that for both one can fit an exponential curve through the data. This is particularly obvious for the perpendicular polarisation. There is some discrepancy between when the curves for both samples starts levelling off. For $\text{Silica1}_{\text{Na2SiO3(1:6)}}$ this occurs after about 75 days, whereas the maximum reflectance of $\text{Silica2}_{\text{Na2SiO3(1:6)}}$ levels off more quickly after about 30 days.

In Figure 3.10, the tensile strength of bonds made between fused silica substrates, using 1 : 6 sodium silicate solution and cured at room temperature, is plotted as a function of curing time. An exponential fit is also plotted, suggesting the strength decreases with time, plateauing after about 50 days.

From the comparison of these figures, it may be concluded that there is a correlation between the optical reflectivity and strength of a bond both of which decrease as a function of curing time.

3.1.4 Analysis result: refractive index and thickness

To estimate the bond refractive index and thickness of $\text{Silica1}_{\text{Na2SiO3(1:6)}}$ and $\text{Silica2}_{\text{Na2SiO3(1:6)}}$, a script written in Matlab and based on Bayesian analysis (see section 2.3.2 and Appendix D) was used. In this script the following values were considered:

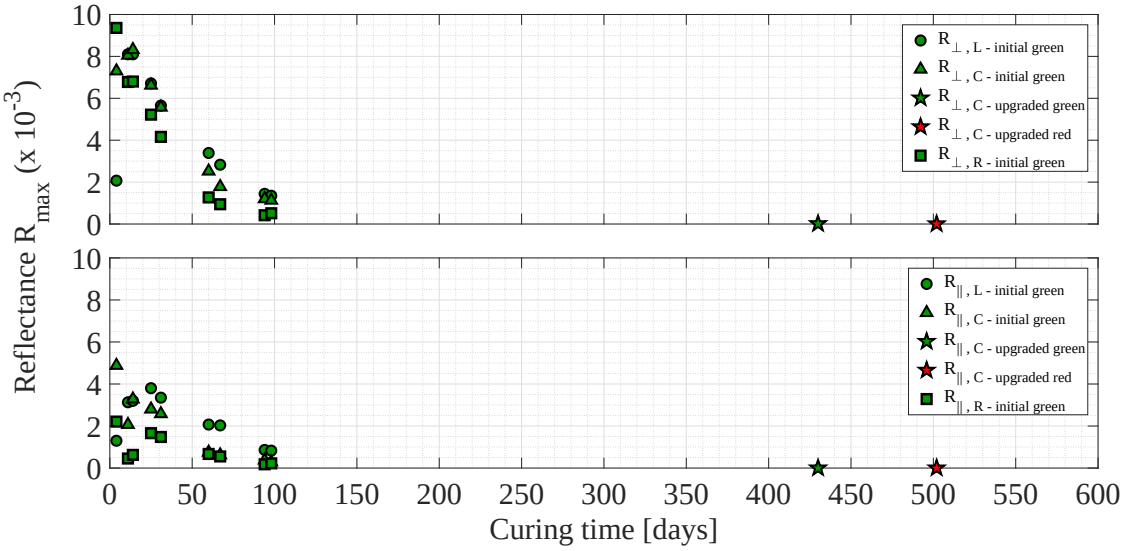

Fig. 3.8 Maximum value of measured reflectances for $\perp$ (top) and $\parallel$ (bottom) polarisation plotted as a function of the curing time for the three positions *L*, *C* and *R* on the front surface of Silica1$_{Na2SiO3(1:6)}$ and for green and red laser light. Measurements were taken using both the initial (only green laser light) and upgraded (green and red laser light) assembly.

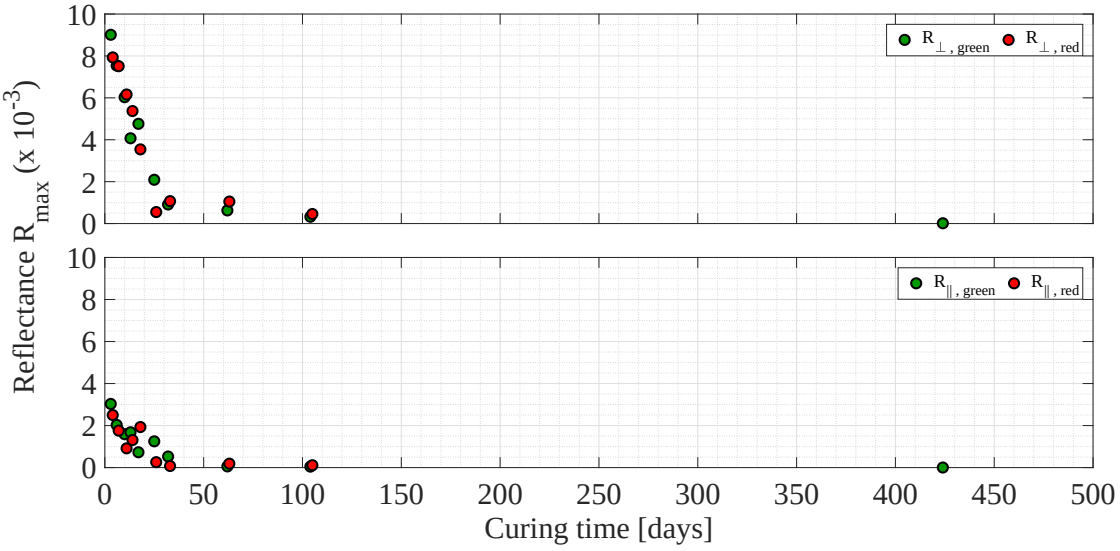

Fig. 3.9 Maximum value of measured reflectances for $\perp$ (top) and $\parallel$ (bottom) polarisation plotted as a function of the curing time for the central position on the front surface of Silica2$_{Na2SiO3(1:6)}$ and for green and red laser light. Measurements were taken using the upgraded assembly.

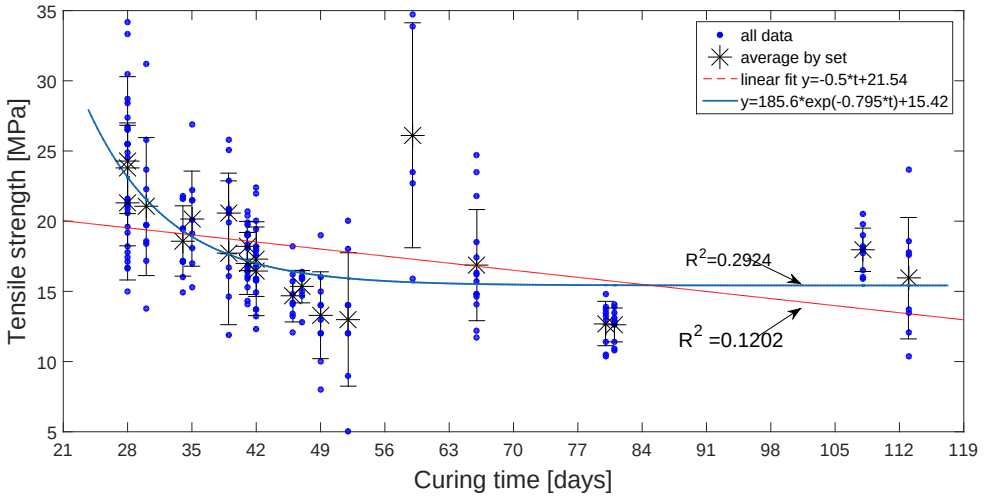

Fig. 3.10 Combined curing time tensile strength results (from 4-point bend tests) of hydroxide-catalysis bonded fused silica made using very similar procedures as used for the samples in this section (using 1 : 6 sodium silicate solution and curing at room temperature). Sets were made between 2009-2014 by a number of people. An exponential fit has been made showing the strength levels of after about 50 days of curing. Courtesy of Dr. M. Phelps [100].

- the fused silica disc had refractive index $n_{1,\text{green}} = 1.4607$ for green light and $n_{1,\text{red}} = 1.4570$ for red light [82], and thickness $d_1 = 0.5\ cm$;

- the grid of values for the bond layer (n_2 and d_2) was set, where the bond refractive index n_2 varied between 1.3000 and 1.4800 with step 0.0001, and the bond thickness d_2 between 0.0 nm and 8000.0 nm with step 0.5.

The grid of values for the bond refractive index was set because the refractive index was expected to be not less than water and not more than fused silica.
As discussed in Chapter 2, the amount of bonding solution used was 15.70 $\mu l = 15.70 \times 10^{-9}\ m^3$. As all fused silica samples analysed in this chapter had a diameter of 5.00 cm, the bonding area of the disc was $1.96 \times 10^{-3}\ m^2$. This meant that the starting thickness of the amount of fluid was expected to be around $(15.70 \times 10^{-9}\ m^3)/(1.96 \times 10^{-3}\ m^2) = 8010\ nm$. Even though the bond refractive index and thickness were not known with this accuracy, a finer step mapped the three contours of probability better, while having a good trade-off with calculation efficiency.
These values were used for all the other fused silica samples analysed in this thesis.

Figure 3.11 and Figure 3.12 show two examples of the results obtained from the Matlab script for sample $\text{Silica2}_{\text{Na2SiO3(1:6)}}$ in green mode after 25 days and red mode after 63 days,

respectively: at the top of each figure the three confidence levels of probability obtained from the Bayesian analysis (see subsection 2.3.2) at one specific curing time, and at the bottom the comparison between experimental data and theoretical model (see subsection 2.2.1) for both polarisations of the incident light, where the theoretical model uses the most likely n_2 and d_2 obtained from the confidence levels of probability.

$\mathbf{Silica1_{Na2SiO3(1:6)}}$

In Figure 3.13, Figure 3.14 and Figure 3.15, the bond refractive index (n_2) and thickness (d_2) values, obtained from a Bayesian likelihood analysis of each reflectivity measurement run separately for green and red light, are plotted as a function of the curing time for the three positions on the front surface of $\mathrm{Silica1_{Na2SiO3(1:6)}}$ (see Figure 3.2).
In these plots, the error bars are not Gaussian but represent the 3σ confidence limits of each solution (the blue confidence level in Figure 3.11 and Figure 3.12). These confidence levels, and consequently these errors bars, are not necessarily symmetrical due to the fact that the Bayesian analysis determines the discrepancy between the experimental data and the theoretical reflectivity model and this may not be symmetrical. This is true for all error bars shown in plots of the bond refractive index or thickness as a function of curing time from here on.

For some data sets, multiple solutions were found, which are presented in order from the highest to the lowest joint posterior probability density function by the black, blue and yellow marker edge colour in Figure 3.13, Figure 3.14 and Figure 3.15. This is due to the fact that the cosine function in equations 2.22 and 2.23 can have more than one solution, which can survive as a result of limits to the sensitivity of the setup. This has a larger effect on the bond thickness than on the refractive index as the solutions found for refractive index generally overlap, whereas the solutions found for bond thickness can be very different. This was found to be an issue once the reflectivity levels dipped below 10^{-4} (perpendicular component) and 10^{-5} (parallel component) for the initial setup as it was at the limit of its capabilities.

Figure 3.13 shows an increasing trend of the refractive index for all three measurement locations starting at around n_2 equalling 1.35 at 4 days of curing and steadily increasing to 1.46 at 430 days of curing for position *C* in green mode.
These results are in agreement with logical expectations: as the byproduct of the chemical reaction in hydroxide-catalysis bonding, namely water, migrates out of the bond (through evaporation or absorption into the bulk material), the silicate will become denser and more like fused silica.
For the *R* position, the values of n_2 at 94 and 98 days of curing are characterised by greater

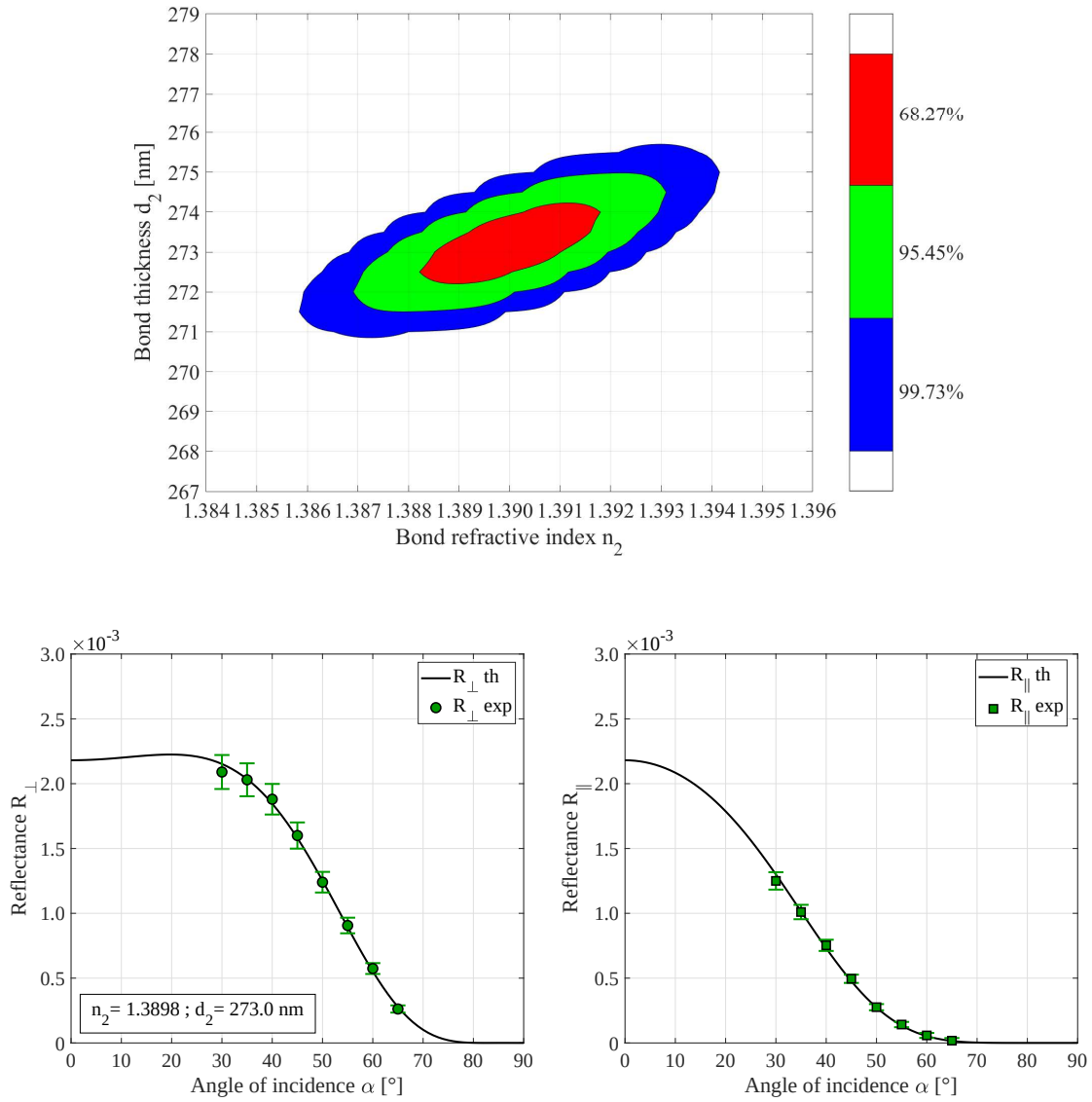

Fig. 3.11 (top) Three confidence levels of 68.3%, 95.5% and 99.7% probability. (bottom) Measured data with their corresponding error bars and theoretical curves. The green dots and squares represent the reflectances measured for perpendicular and parallel polarisation, respectively. The black solid lines are the theoretical perpendicular and parallel reflectances obtained using the most likely values of bond refractive index and thickness of the Bayesian analysis ($n_2 = 1.3898$ and $d_2 = 273.0$). These measurements were taken at 25 days after bonding for $\text{Silica2}_{\text{Na2SiO3(1:6)}}$ in green light.

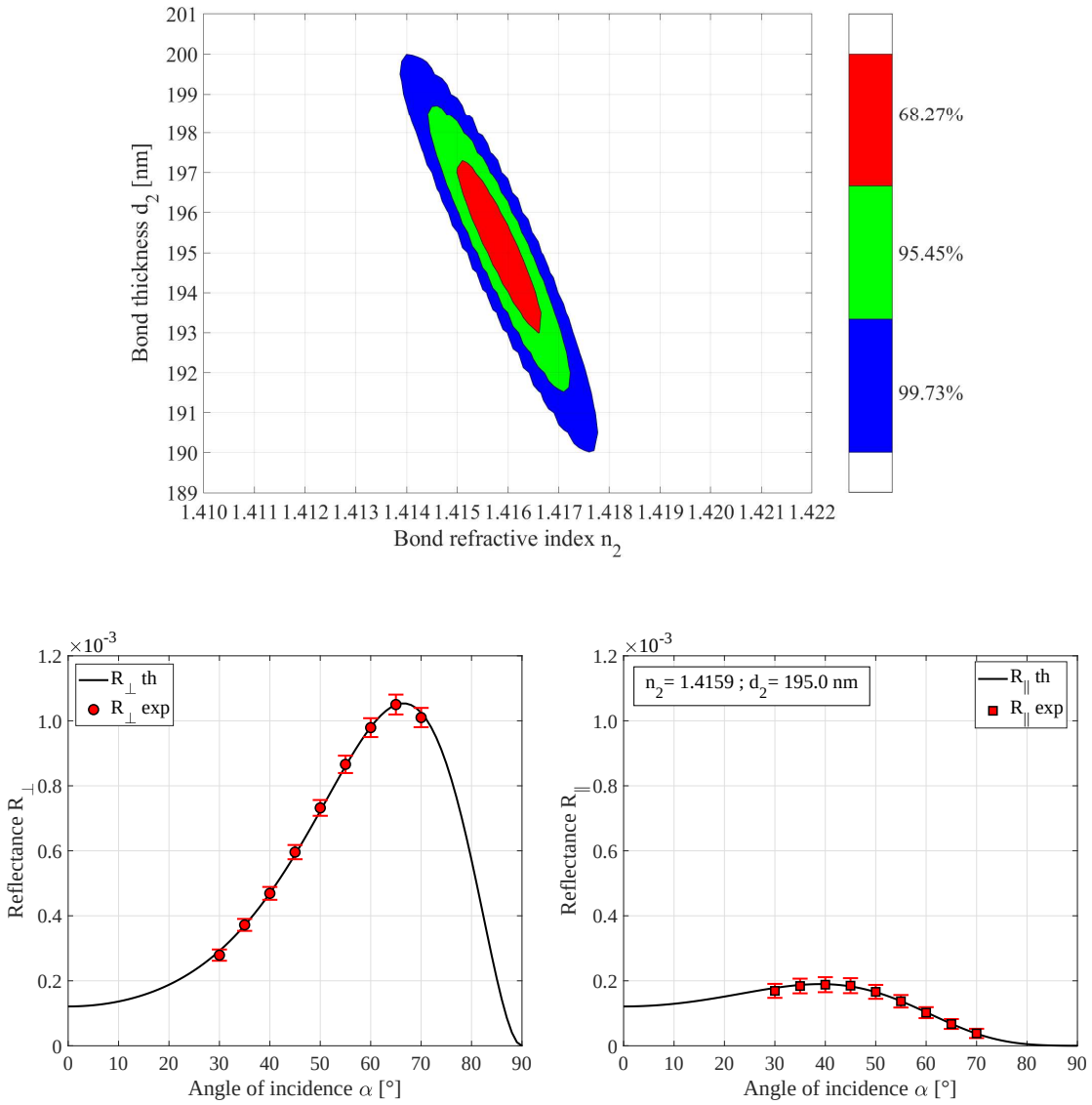

Fig. 3.12 (top) Three confidence levels of 68.3%, 95.5% and 99.7% probability. (bottom) Measured data with their corresponding error bars and theoretical curves. The red dots and squares represent the reflectances measured for perpendicular and parallel polarisation, respectively. The black solid lines are the theoretical perpendicular and parallel reflectances obtained using the most likely values of bond refractive index and thickness of the Bayesian analysis ($n_2 = 1.4159$ and $d_2 = 195.0$). These measurements were taken at 63 days after bonding for $\text{Silica2}_{\text{Na2SiO3(1:6)}}$ in red light.

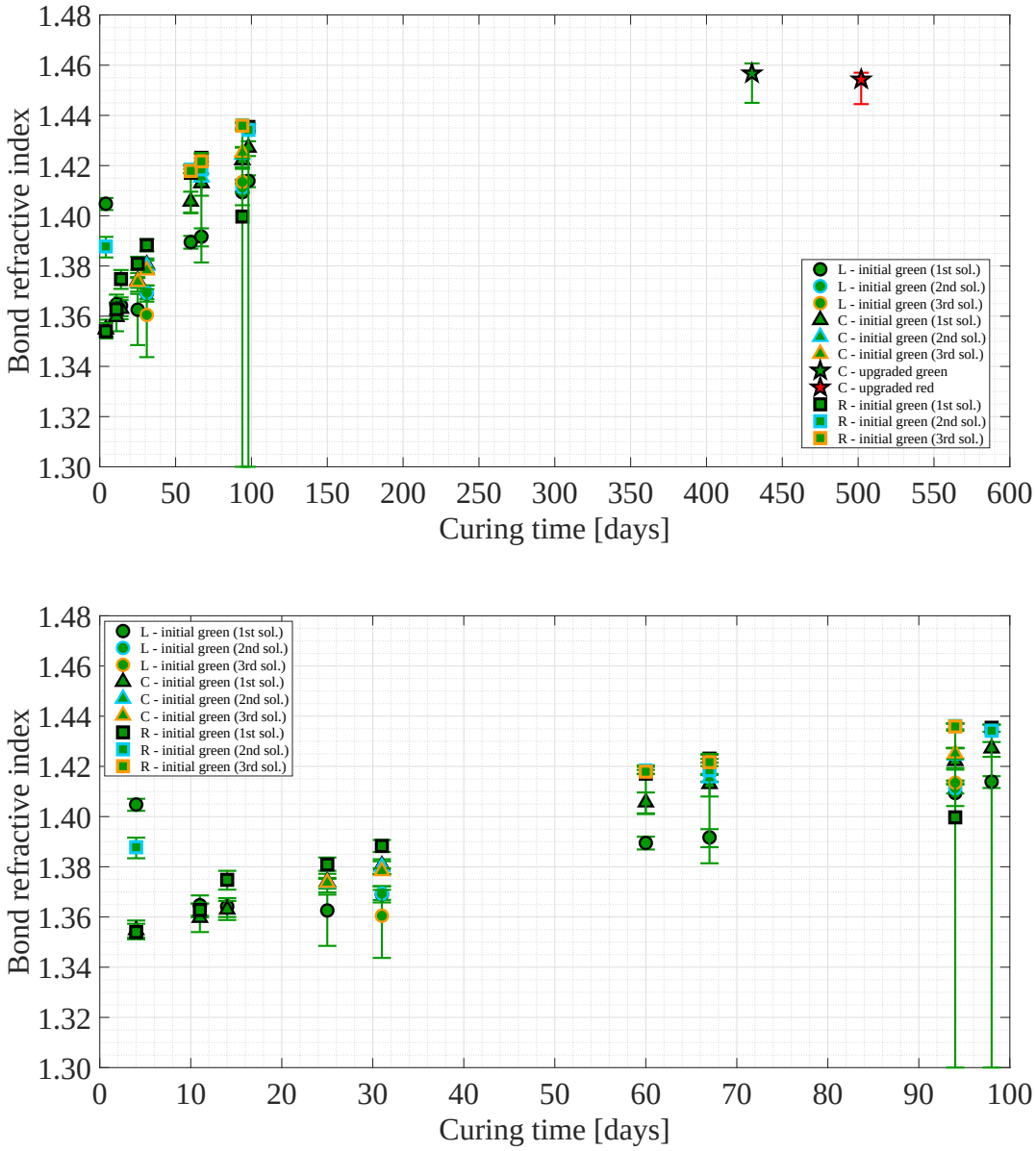

Fig. 3.13 Refractive index of the bond of Silica1$_{\mathrm{Na2SiO3(1:6)}}$ as a function of the curing time for the three positions *L*, *C* and *R*. In the top panel, the measurements were collected using the initial and upgraded setup in green mode and the upgrade setup in red mode, whereas in the bottom panel the zoom in of the data in the first 100 days of the curing time is reported. Some data sets have multiple solutions, which are presented in order from the highest to the lowest joint posterior probability density function by the black, blue and yellow marker edge colour.

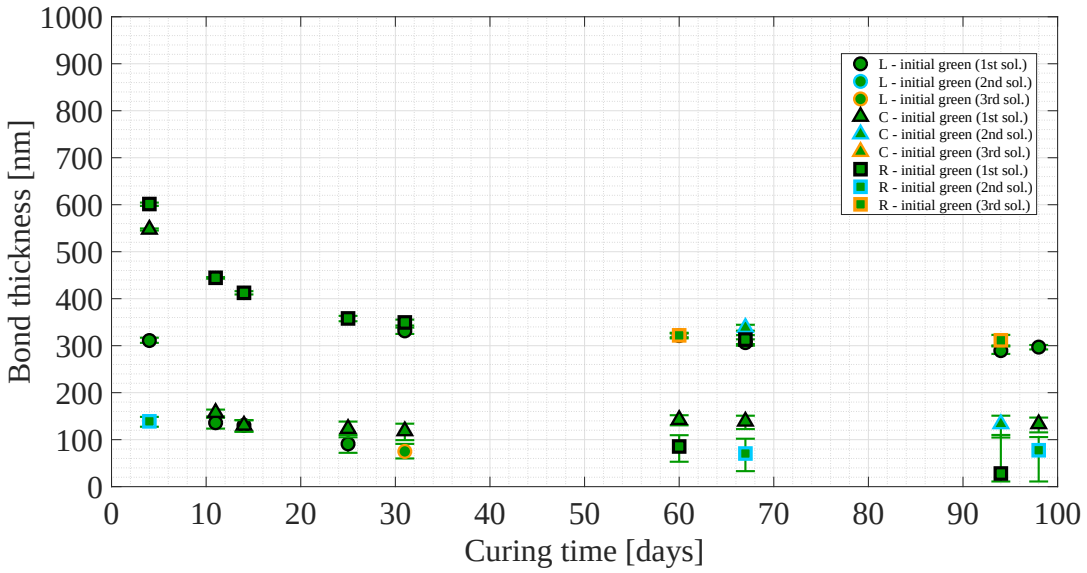

Fig. 3.14 Thickness of the bond of Silica1$_{Na2SiO3(1:6)}$ as a function of the curing time for the three positions *L*, *C* and *R*. The measurements were collected using the initial and upgraded setup in green mode and the upgrade setup in red mode. The thicknesses at 430 and 502 days (green and red upgraded data sets, respectively) were not reported, because they were not measurable because of the relatively large uncertainty on these measurements due to the extremely low reflectance of the bond. Some data sets have multiple solutions, which are presented in order from the highest to the lowest joint posterior probability density function by the black, blue and yellow marker edge colour.

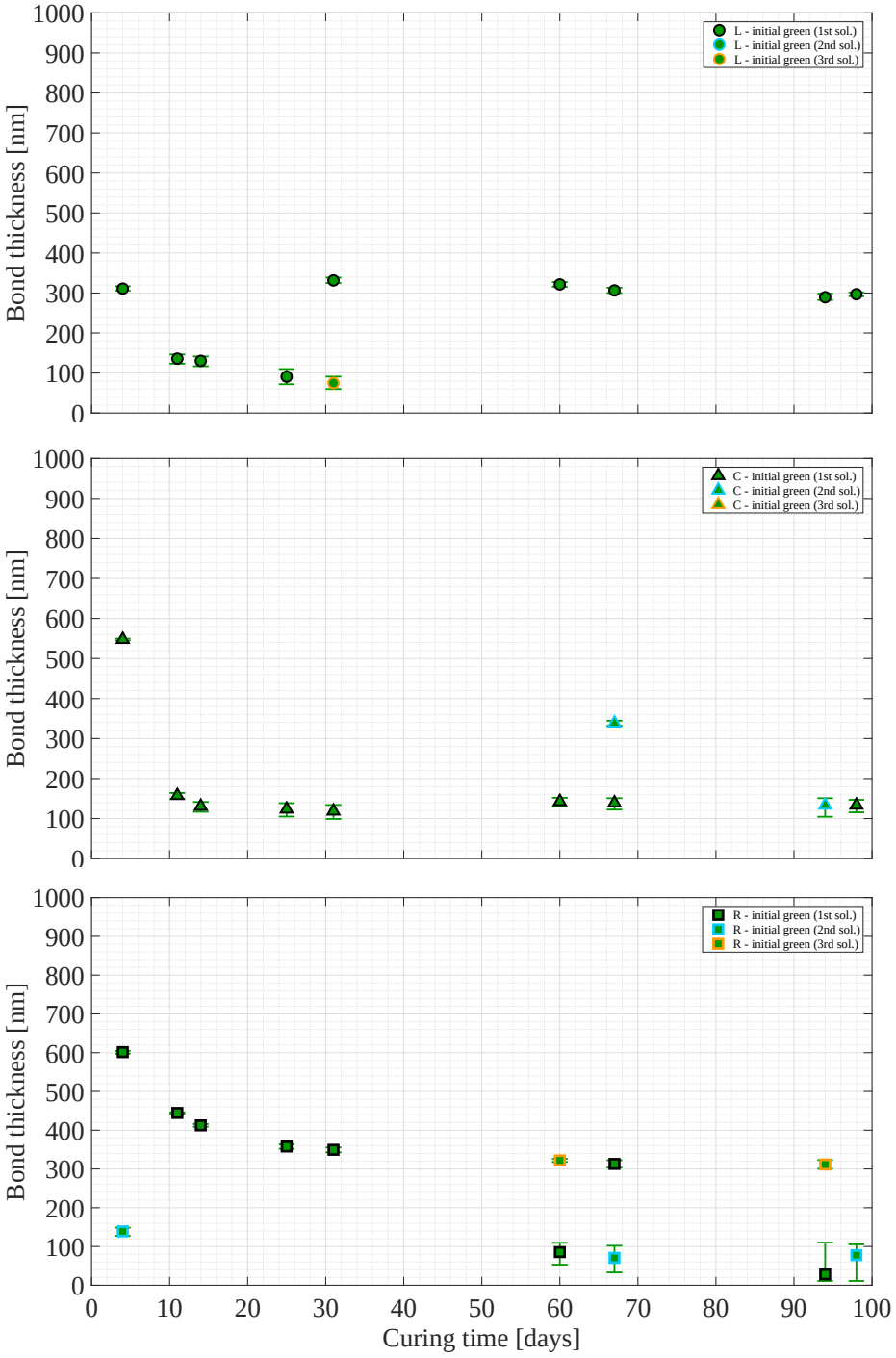

Fig. 3.15 Bond thickness measurements (Figure 3.14) collected using the initial setup in green mode for Silica1$_{\mathrm{Na2SiO3(1:6)}}$ in the first 100 days of the curing time for the three positions *L* (top), *C* (middle) and *R* (bottom). Some data sets have multiple solutions, which are presented in order from the highest to the lowest joint posterior probability density function by the black, blue and yellow marker edge colour.

error bars. These values are less accurate than the other measurements due to the reflectance levels approaching the initial setup sensitivity.

In Figure 3.14 and Figure 3.15 the bond thickness is shown as a function of the curing time for the three positions *L*, *C* and *R*.

The thicknesses at 430 and 502 days (green and red upgraded data sets, respectively) were not shown as these could not be calculated because of the relatively large uncertainty that characterised these measurements. This uncertainty was relatively large due to the extremely low reflectance of the bond, which affects the bond thickness measurements more than the bond refractive index measurements. This is probably due to the fact that, as said above, the solutions found for refractive index generally overlap, but those for bond thickness can be multiple because of the cosine function.

Bond thicknesses greater than 4500 *nm* (obtained after 25 days from bonding) were not shown in Figure 3.14 and Figure 3.15 as they are physically highly unlikely. It is thought that these appear due to an aliasing issue. The Nyquist rule says that the sampling frequency should be at least twice the highest frequency in the sample [101]. For a bond thickness of about 4500 *nm*, the number of oscillations in the reflectance is eight in 90° range, which equals a frequency of 0.1/degree, whereas the reflectivity data was sampled at a frequency of one measurement every 5° (0.2/degree). As the number of oscillations in the reflectance goes up relatively linearly with bond thickness, this means that aliasing could occur for bond thicknesses over 4500 *nm*. For this reason, the angle of incidence step size of 5° makes it possible to find solutions above 4500 *nm* due to aliasing.

Figure 3.14 shows that the thickness of the bond in three different positions does not have as well-defined a trend particularly because the data points with the highest joint posterior probability density function in some cases swap between two apparent trend lines. However, it is possible to infer that bond thickness decreases rapidly in the first four weeks and then settles on a constant value, different for each position. One can postulate that this can be influenced by the surface figure mismatch of the two bonding surfaces.

This is in agreement with the dehydration phase of hydroxide-catalysis bonding: the water, created during the polymerisation, migrates or evaporates in time until a strong and durable bond is formed.

The ambiguity of the thickness could be solved by improving the sensitivity of the reflectivity setup further and taking reflectivity measurements at multiple optical wavelengths. This led to the construction of the upgraded setup.

From Figure 3.14 and Figure 3.15, the Bayesian analysis suggests that the bond thickness at

98 days after bonding ranges between 297^{+4}_{-5} *nm* in position *L*, 134^{+14}_{-18} *nm* in position *C* and 78^{+28}_{-67} *nm* in position *R* (see Table 3.1).

The flatness of the bonding surfaces of the two discs that make $\text{Silica1}_{\text{Na2SiO3(1:6)}}$ was measured using a ZYGO® GPI XP/D laser interferometer: it was found that the bonding surfaces had a flatness of about 123 *nm* and 155 *nm* peak-to-valley respectively. Since the orientation of the two discs that were bonded was noted, it was possible to combine their maps and thus give the relative separation between the bonding surfaces of two discs assuming physical contact in just three locations (see section 2.5 and Appendix E for details). The flatness maps of these two discs are shown in the first row of Figure 3.16. These were obtained using the functions of the Simtools package (see Appendix E) which zoomed in on a valid area and removed various offsets from the ZYGO® maps. The map of the relative separation between two bonding surfaces of bonded discs is shown in the second row of Figure 3.16: letters *L*, *C* and *R* indicate the locations at which later the reflectances were measured (see Figure 3.2). The analysis of relative separation map shows bond thickness ranging from 84^{+3}_{-3} *nm* and 83^{+3}_{-3} *nm* in positions *L* and *C* respectively, to 101^{+5}_{-5} *nm* in position *R* (Table 3.1).

After completing the reflectivity measurements, the destructive method of the SEM imaging was used to determine the thickness of this bond, so that it could be compared with the results obtained from the Bayesian analysis and flatness maps. The bond thicknesses of three slices of $\text{Silica1}_{\text{Na2SiO3(1:6)}}$ were taken and the results of these measurements were shown in Figure 3.17: x and y were the coordinates of the thickness measurement d within the sample. All three slices showed a consistent increase in bond thickness for increasing x-location. As the reflectances of $\text{Silica1}_{\text{Na2SiO3(1:6)}}$ were measured for three different positions on the front surface (see Figure 3.2), the locations *L*, *C* and *R* correspond to $x = 10$ *mm*, $x = 25$ *mm* and $x = 35$ *mm*, respectively. The average bond thicknesses found for these locations after 978 days from bonding were: $d(L) = (44 \pm 9)$ *nm*, $d(C) = (34 \pm 10)$ *nm* and $d(R) = (82 \pm 24)$ *nm* (Table 3.1).

Comparing the bond thickness values obtained via studies of bond reflectivity, relative surface figures of the surfaces to be bonded and destructive SEM measurements (taken a considerable period after initial bond formation) suggests that the relative surface figures of the surfaces to be bonded do not necessarily define accurately the final thickness of the hydroxide-catalysis bonds and that the bonds may continue to evolve over periods longer than 100 days. This latter conclusion is consistent with visual changes in the appearance of bonds formed between fused silica samples and with the mechanical loss of those hydroxide-catalysis bonds [102].

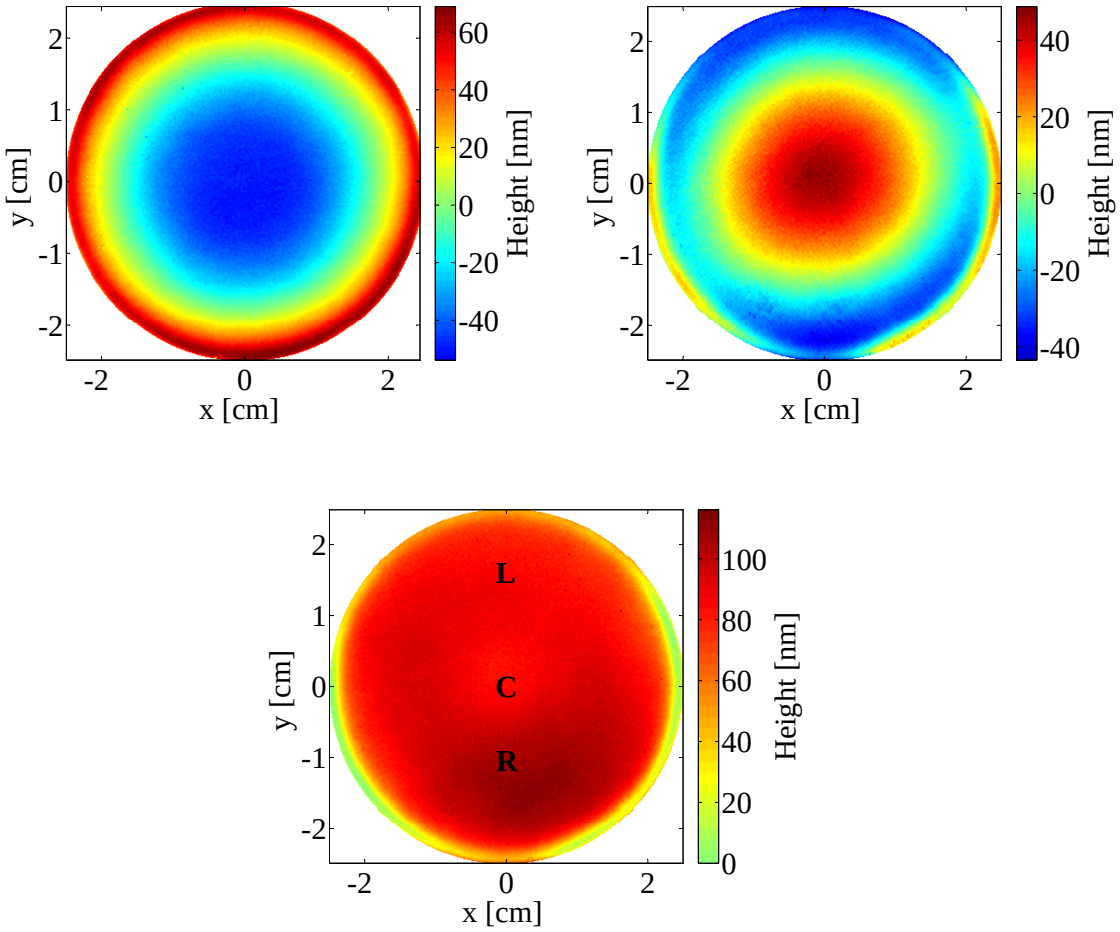

Fig. 3.16 (first row) Flatness maps of the bonding surfaces of the two discs which make Silica1$_{Na2SiO3(1:6)}$. These were obtained using the functions of the Simtools package (see Appendix E) which zoomed in on a valid area and remove various offsets from the ZYGO® maps. (second row) Relative separation between two bonding surfaces of discs bonded by hydroxide-catalysis bonding. This map was obtained using the Matlab code reported in Appendix E.

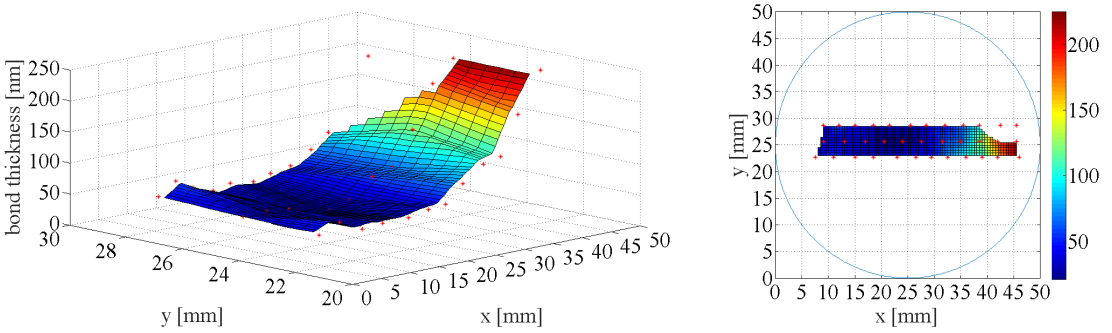

Fig. 3.17 Surface plots of the bond thicknesses measured across three slices of Silica1$_{\text{Na2SiO3(1:6)}}$, where x and y were the coordinates of the thickness measurement within the sample. The surface plots were made by linearly interpolating between measurements.

Silica2$_{\text{Na2SiO3(1:6)}}$

In the top of Figure 3.18 and Figure 3.19, the bond refractive index and thickness values are plotted as a function of the curing time for the central position on the front surface of Silica2$_{\text{Na2SiO3(1:6)}}$ and for both the colours of the laser light.

Also for this sample multiple solutions were found for the bond refractive index and thickness, but the ambiguity could be solved by comparing the results obtained using the green laser light with those of the red laser light. For each two consecutive days (the measurements in red mode were always taken one day after those in green mode), the green and red data, of which the Bayesian values had similar probability volumes, was averaged and the results are shown in the bottom of Figure 3.18 and Figure 3.19.

Differently from the results obtained for Silica1$_{\text{Na2SiO3(1:6)}}$, a clear and well-defined trend for the refractive index and thickness is shown for Silica2$_{\text{Na2SiO3(1:6)}}$. The values of bond refractive index increase when the curing time increases, whereas the bond thickness decreases. The bond average refractive index is about 1.35 at 3/4 days of curing and close to 1.46 at 424 days after curing, just like the case for Silica1$_{\text{Na2SiO3(1:6)}}$ (Figure 3.18), and the bond average thickness obtained by the Bayesian analysis is 173^{+11}_{-18} *nm* at 104/105 days of curing (Figure 3.19 and Table 3.1). The thickness at 424 days is hard to determine due to the extremely low reflectance of the bond because of the close match of the refractive index of the bond to the refractive index of fused silica.

The bonding surfaces of the two discs that form Silica2$_{\text{Na2SiO3(1:6)}}$ had a flatness of about 133 *nm* and 147 *nm* peak-to-valley respectively, which was measured using the ZYGO®. The flatness maps are shown in the first row of Figure 3.20 for the two discs. Combining these

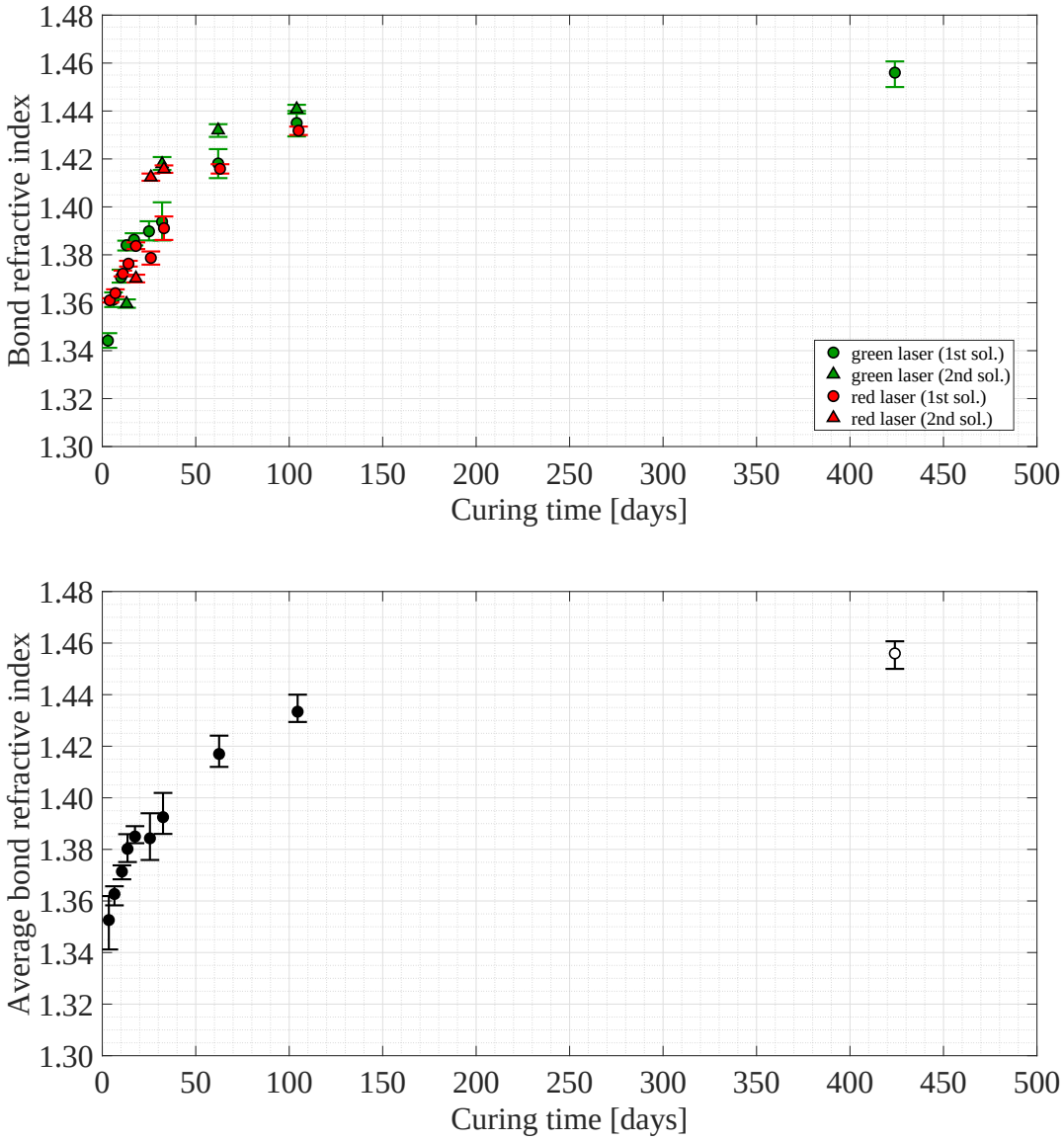

Fig. 3.18 (top) Refractive index of the bond in Silica2$_{Na2SiO3(1:6)}$ as a function of the curing time for the central position. These values were determined from measurements collected using the upgraded setup in green (green dots and triangles) and red (red dots and triangles) mode. Some data sets have multiple solutions, which are presented in order from the highest to the lowest joint posterior probability density function by dots and triangles. (bottom) Average of the green and red refractive indices of which the Bayesian values have similar probability volumes. This average was calculated for each two consecutive days (the difference between green and red curing time is always one day). For all filled data points both green and red were averaged. For the green data set at 424 days no average could be calculated because of the absence of the corresponding value in red (unfilled data point). The error bars represent the spread of the data that was averaged.

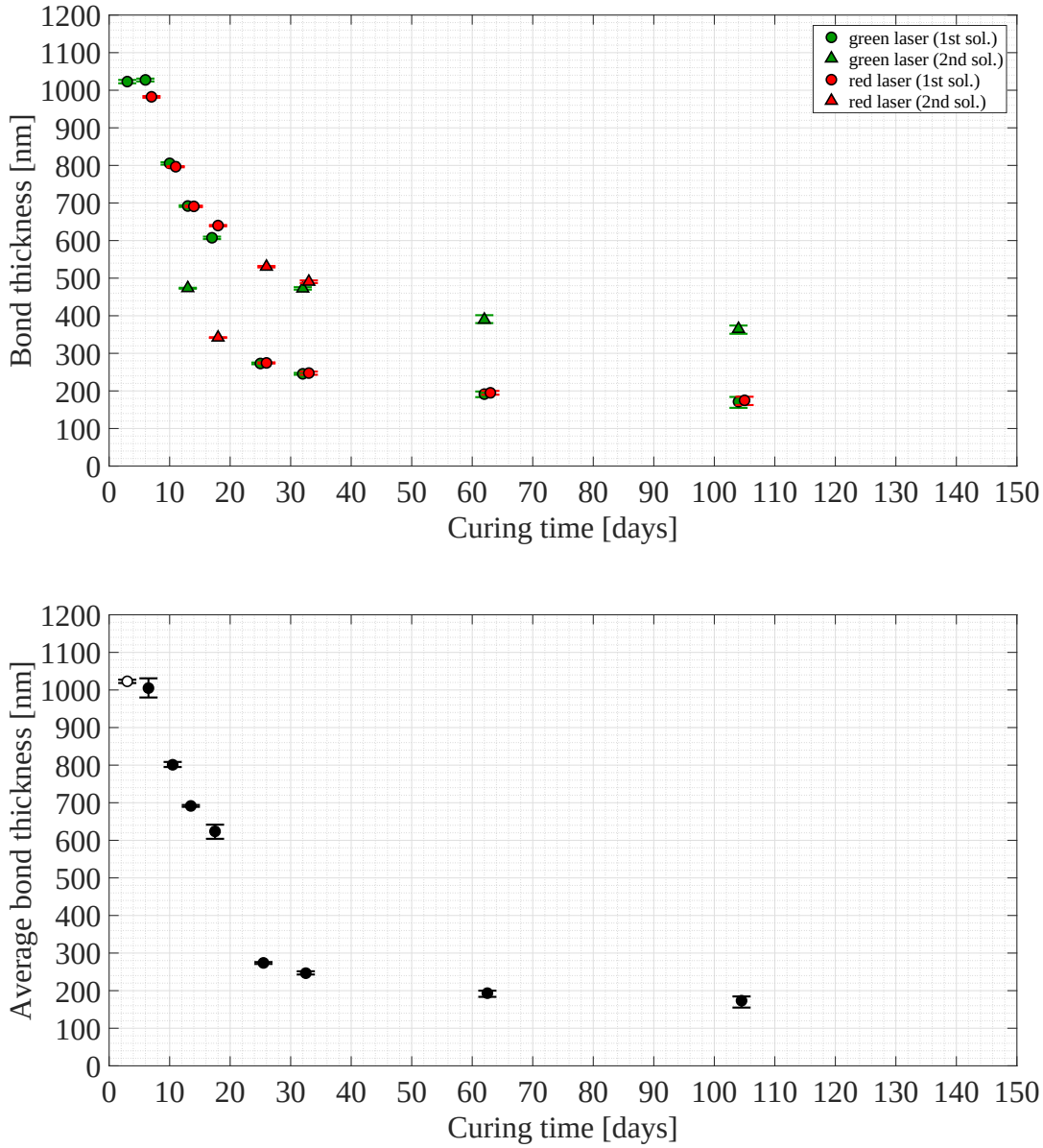

Fig. 3.19 (top) Thickness of the bond in Silica2$_{Na2SiO3(1:6)}$ as a function of the curing time for the central position. These values were determined from measurements collected using the upgraded setup in green (green dots and triangles) and red (red dots and triangles) mode. Some data sets have multiple solutions, which are presented in order from the highest to the lowest joint posterior probability density function by dots and triangles. The thickness at 424 days (green data set) was not reported, because it was not measurable because of the relatively large uncertainty on this measurement due to the extremely low reflectance of the bond. (bottom) Average of the green and red thicknesses of which the Bayesian values have similar probability volumes. This average was calculated for each two consecutive days (the difference between green and red curing time is always one day). For all filled data points both green and red were averaged. For the green data set at 3 days no average could be calculated because of the absence of the corresponding value in red (unfilled data point). The error bars represent the spread of the data that was averaged.

maps, the relative separation between two bonding surfaces was obtained and it is shown in the second row of Figure 3.20: the relative separation map gives a value of 63^{+15}_{-15} *nm* for the bond thickness in the central position (Table 3.1).

No SEM measurements were taken on this sample.

Again, as seen for $\text{Silica1}_{\text{Na2SiO3(1:6)}}$, it can be seen that the relative surface figures do not accurately define the resulting bond thickness.

3.1.5 Analysis result: discussion

Reflectivity data has been used to estimate the magnitude and time-dependence of the refractive indices and thicknesses of hydroxide-catalysis bonds formed between fused silica substrates jointed using 15.70 μl of solution composed of 2 *ml* of sodium silicate solution with 12 *ml* of de-ionised water (a volumetric ratio of 1 : 6).
Two nominally identical bonds were studied: for one bond measurements were made at three points in a line on the sample, for the other at one point only. The values obtained for them were then compared.

The refractive indices obtained for both bonds showed very consistent asymptotically increasing trends in magnitude and in behaviour as a function of curing time, with initial refractive index values a few days after bonding of around 1.35, rising steadily for the first 100 days (around 1.41 after two months) and eventually reaching a value of about 1.46 after one year from bonding. The average rate of increase is approximately the same for both $\text{Silica1}_{\text{Na2SiO3(1:6)}}$ and $\text{Silica2}_{\text{Na2SiO3(1:6)}}$. This is consistent with the expected chemical evolution of the bond changing from a predominantly aqueous sodium silicate solution to a silica-like network.

The bond thickness values obtained in all cases showed a steadily decreasing trend as a function of curing time, plateauing after about 50 days: the bond thickness settles more quickly than the refractive index. Table 3.1 in section 3.5 gives an overview of the bond thicknesses obtained using the Bayesian, flatness and SEM methods. Even if the bond thicknesses obtained for the central position of these two samples are very close (134^{+14}_{-18} *nm* for $\text{Silica1}_{\text{Na2SiO3(1:6)}}$ and 173^{+11}_{-18} *nm* for $\text{Silica2}_{\text{Na2SiO3(1:6)}}$), the results of the Bayesian analysis differ from those measured using the flatness maps or the SEM imaging.
For $\text{Silica1}_{\text{Na2SiO3(1:6)}}$, the bond thickness obtained from the Bayesian analysis of reflectivity ranges from 11 *nm* to 301 *nm* (values at about 100 days). The relative separation maps obtained from the measured figures of the samples taken before bonding suggest thicknesses from 80 *nm* to 106 *nm*, whereas the SEM measurements give considerably thinner values

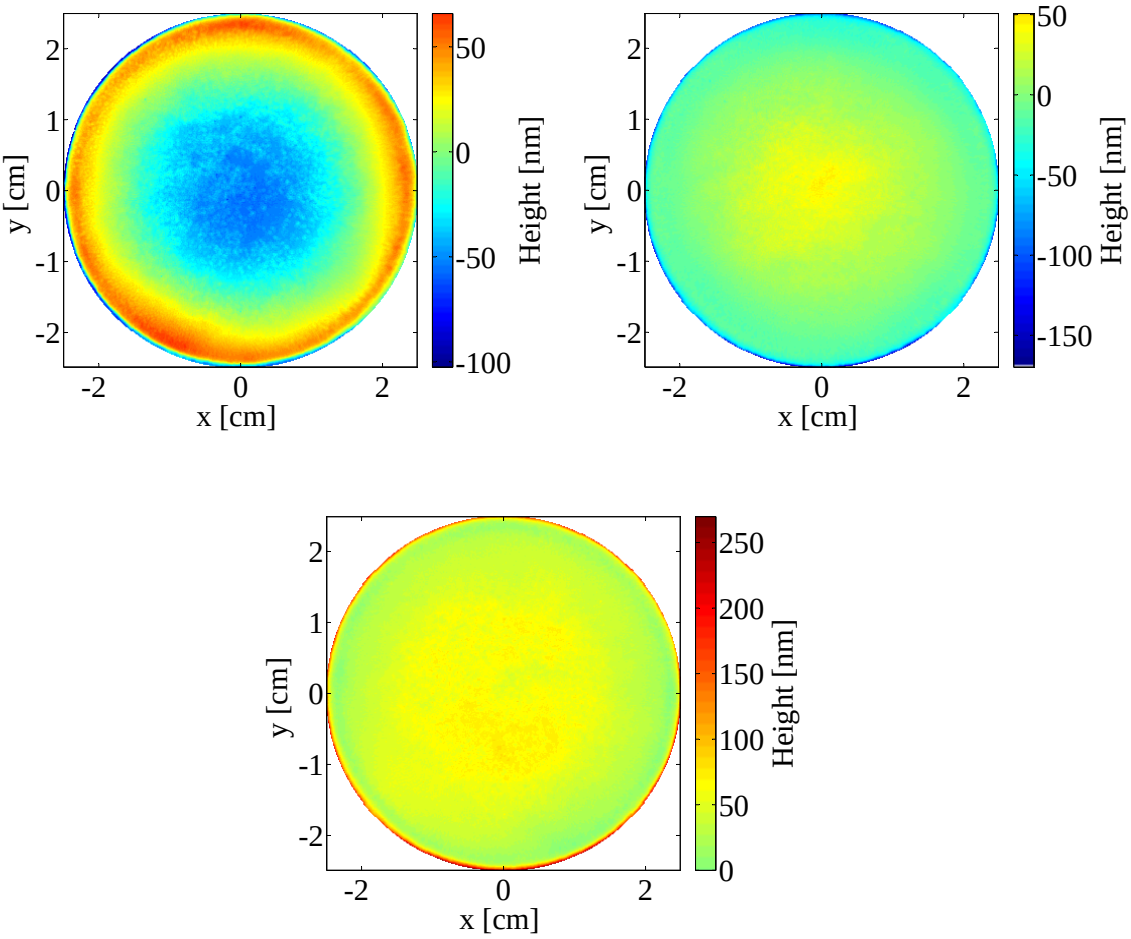

Fig. 3.20 (first row) Flatness maps of the bonding surfaces of the two discs which make Silica2$_{Na2SiO3(1:6)}$. These were obtained using the functions of the Simtools package (see Appendix E) which zoomed in on a valid area and remove various offsets from the ZYGO® maps. (second row) Relative separation between two bonding surfaces of discs bonded by hydroxide-catalysis bonding. This map was obtained using the Matlab code reported in Appendix E.

ranging from 24 *nm* to 106 *nm* (values after two years). Only for the *R* position there is agreement between all three methods of determining the bond thickness. For the *L* and *C* position the Bayesian bond thicknesses are higher than using the flatness map method which in turn is higher than the values determined using the SEM method. Importantly, it should be noted that the SEM images were taken more than a year after the last reflectance measurement was taken, suggesting that the bonds continued to evolve and reduce in thickness over this time. This is in line with research on mechanical loss which is lower three years after bonding than one year after bonding [102]. As the values were still reducing after 100 days, it is not unfeasible that the thickness discrepancy between SEM images and reflectance measurements can be explained by reduction of thickness over time.
For $\text{Silica2}_{\text{Na2SiO3(1:6)}}$, the bond thickness calculated for the central position using the flatness maps is close to that calculated for the central position of $\text{Silica1}_{\text{Na2SiO3(1:6)}}$ (from 48 *nm* to 78 *nm*). In both cases these are less than their corresponding Bayesian value (from 155 *nm* to 184 *nm*). No SEM measurements were taken for $\text{Silica2}_{\text{Na2SiO3(1:6)}}$.
These results may suggest that the optical thickness of a bond is not necessarily constrained by the separation between the bonding surfaces of two discs bonded each other. Also, the bond formation and curing may still cause changes.

Comparing the bond strength shown in Figure 3.10 with the thickness behaviour of the bonds for the two samples shown in Figure 3.14 and Figure 3.19, a correlation between the strength and thickness of a bond may be seen: the bond strengths become weaker when bond thicknesses become thinner. This needs further investigation.

3.2 Sodium silicate 1:3 solution

In this section the bonds are formed between four fused silica substrates, jointed to create two nominally identical bonded substrate pairs using a bonding solution made with sodium silicate solution at a volumetric ratio of 1 : 3 with de-ionised water.

3.2.1 $\text{Silica1}_{\text{Na2SiO3(1:3)}}$ and $\text{Silica2}_{\text{Na2SiO3(1:3)}}$

The bonding solution for the fused silica samples $\text{Silica1}_{\text{Na2SiO3(1:3)}}$ and $\text{Silica2}_{\text{Na2SiO3(1:3)}}$ was made by diluting 2 ml of sodium silicate solution with 6 ml of de-ionised water (a volumetric ratio of 1 : 3). As for the samples $\text{Silica1}_{\text{Na2SiO3(1:6)}}$ and $\text{Silica2}_{\text{Na2SiO3(1:6)}}$, 15.70 μl of solution was pipetted onto one of the discs and then the other disc was placed on

top. The samples were left to cure in air at room temperature for two days before measuring the reflectivity of their bonds using the upgraded setup in green and red light (Figure 2.5).

3.2.2 Reflectivity measurements

The reflectances of these two samples were measured for the central position on their front surface at four different time intervals, respectively a few days, about one, two and three months after bonding. In this way the effect of curing time on the refractive index and thickness of the bond could be studied.

Plots of the measured reflectivity for perpendicular ($\perp$) and parallel ($\parallel$) polarisations (equations 2.1 and 2.2) as a function of the angle of incidence α are shown in Figure 3.21 ($\text{Silica1}_{\text{Na2SiO3(1:3)}}$ in green mode), Figure 3.22 ($\text{Silica1}_{\text{Na2SiO3(1:3)}}$ in red mode), Figure 3.23 ($\text{Silica2}_{\text{Na2SiO3(1:3)}}$ in green mode) and Figure 3.24 ($\text{Silica2}_{\text{Na2SiO3(1:3)}}$ in red mode).

For both polarisations and colours of laser light, the values of bond reflectances are less than 1% and they decrease as curing time increases. Like for the 1 : 6 sodium silicate bonds the reflectance is less than 0.1% after 3 months.

3.2.3 Analysis result: reflectivity

The peak reflectivity of the bond for both polarisations is plotted as a function of curing time for $\text{Silica1}_{\text{Na2SiO3(1:3)}}$ and $\text{Silica2}_{\text{Na2SiO3(1:3)}}$ in Figure 3.25. The reflectance values of these samples are similar to within 30% and decrease as curing time increases at a rate which is very similar to the 1 : 6 sodium silicate bonds discussed in section 3.1.

3.2.4 Analysis result: refractive index and thickness

$\text{Silica1}_{\text{Na2SiO3(1:3)}}$

Figure 3.26 shows one example of the results obtained from the Matlab script for sample $\text{Silica1}_{\text{Na2SiO3(1:3)}}$ in red mode after 57 days.

In the top of Figure 3.27 and Figure 3.28, the green and red bond refractive index and thickness values are plotted as a function of the curing time for the central position on the front surface of $\text{Silica1}_{\text{Na2SiO3(1:3)}}$. In the bottom of Figure 3.27 and Figure 3.28, the time average of the green and red bond refractive indices and thicknesses, of which the Bayesian values had similar probability volumes, are also shown.

These plots show a clear increasing trend over curing time for the bond average refractive index, whereas a decreasing one for the bond thickness. The bond average refractive index

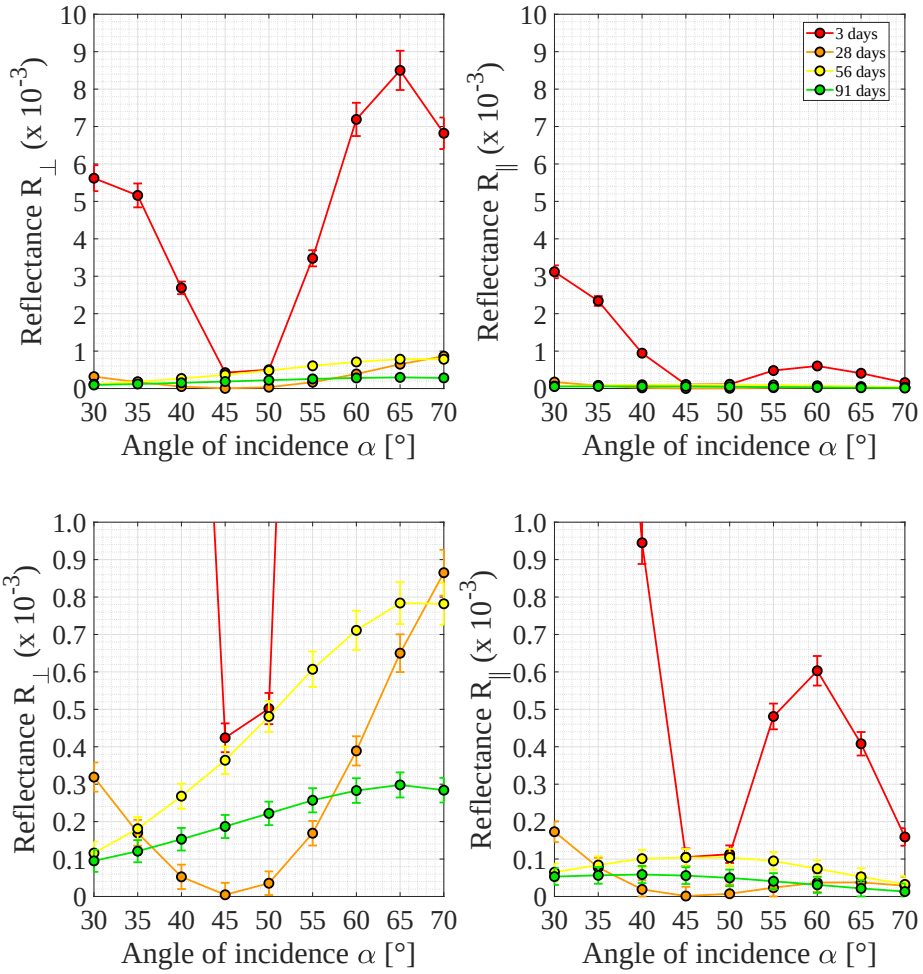

Fig. 3.21 (top) Measured reflectances for $\perp$ (left) and $\parallel$ (right) polarisation plotted as a function of the angle of incidence α for the central position on the front surface of $\text{Silica1}_{\text{Na2SiO3(1:3)}}$. (bottom) Zooms in of the measured reflectances are also shown to allow the reader to see the lower reflectances. In the legend, the curing time is reported. All measurements were taken using the upgraded setup in green mode.

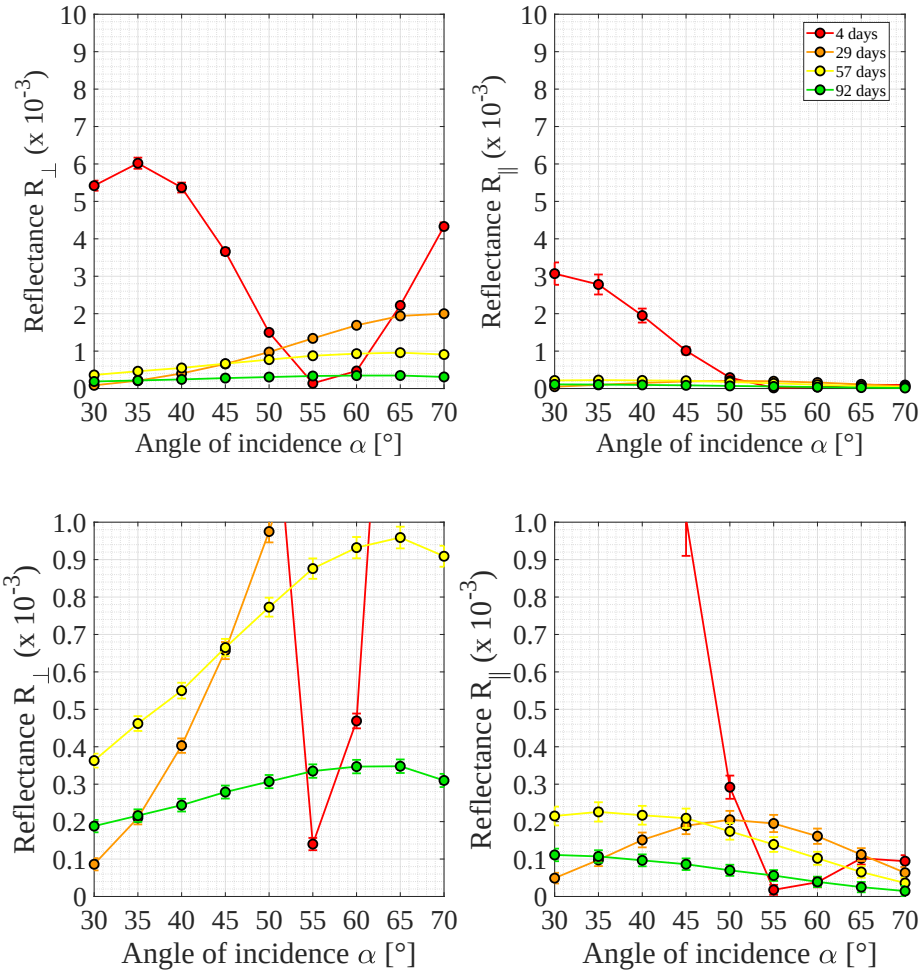

Fig. 3.22 (top) Measured reflectances for $\perp$ (left) and $\parallel$ (right) polarisation plotted as a function of the angle of incidence α for the central position on the front surface of $\text{Silica1}_{\text{Na2SiO3(1:3)}}$. (bottom) Zooms in of the measured reflectances are also shown to allow the reader to see the lower reflectances. In the legend, the curing time is reported. All measurements were taken using the upgraded setup in red mode.

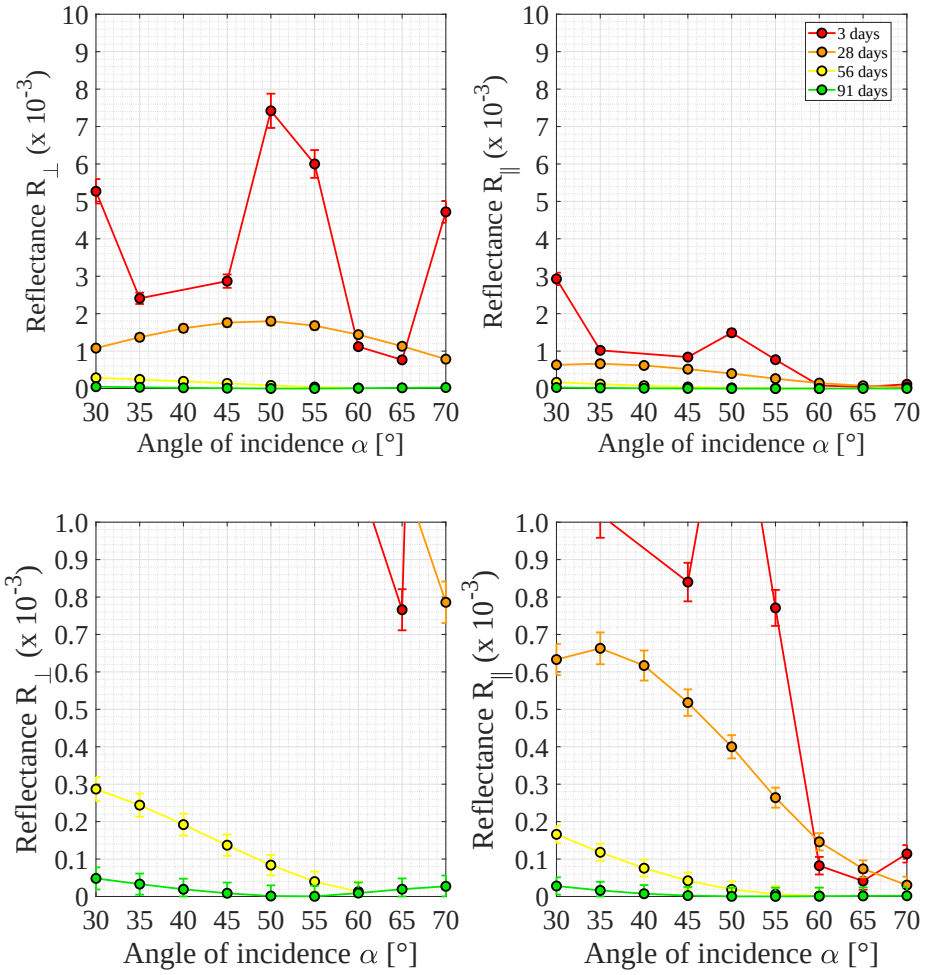

Fig. 3.23 (top) Measured reflectances for $\perp$ (left) and $\parallel$ (right) polarisation plotted as a function of the angle of incidence α for the central position on the front surface of $\text{Silica2}_{\text{Na2SiO3(1:3)}}$. (bottom) Zooms in of the measured reflectances are also shown to allow the reader to see the lower reflectances. In the legend, the curing time is reported. All measurements were taken using the upgraded setup in green mode.

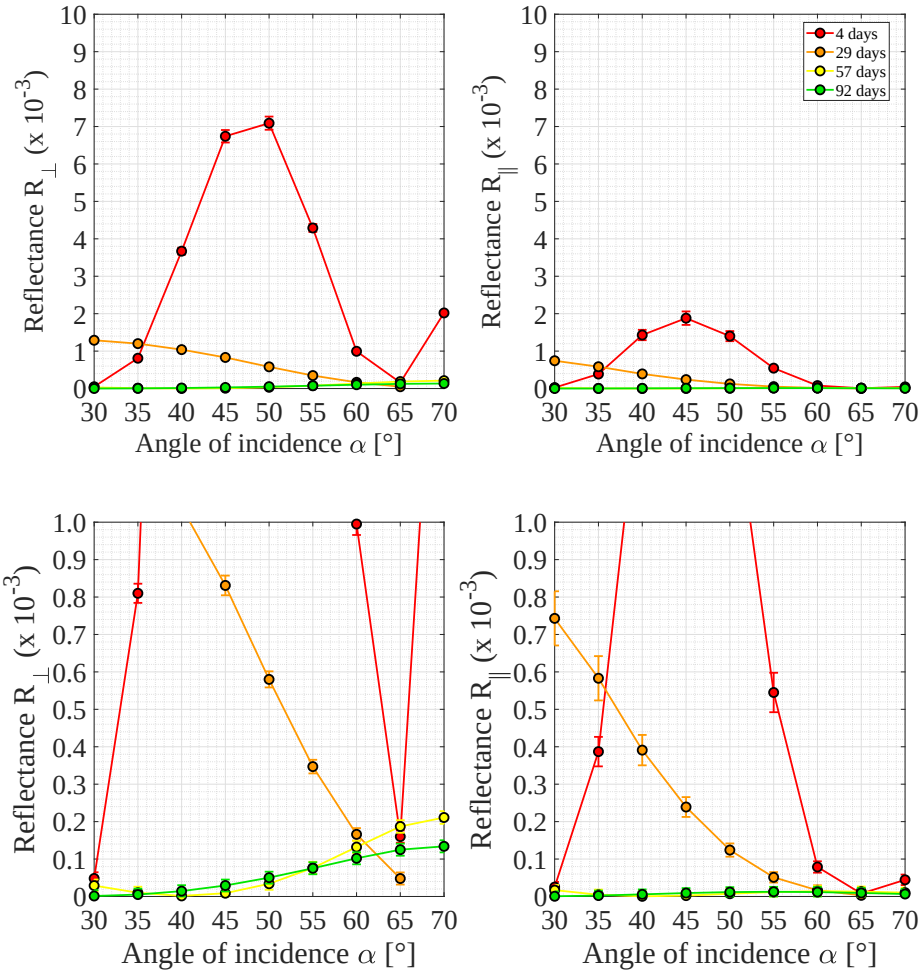

Fig. 3.24 (top) Measured reflectances for $\perp$ (left) and $\parallel$ (right) polarisation plotted as a function of the angle of incidence α for the central position on the front surface of $\text{Silica2}_{\text{Na2SiO3(1:3)}}$. (bottom) Zooms in of the measured reflectances are also shown to allow the reader to see the lower reflectances. In the legend, the curing time is reported. All measurements were taken using the upgraded setup in red mode.

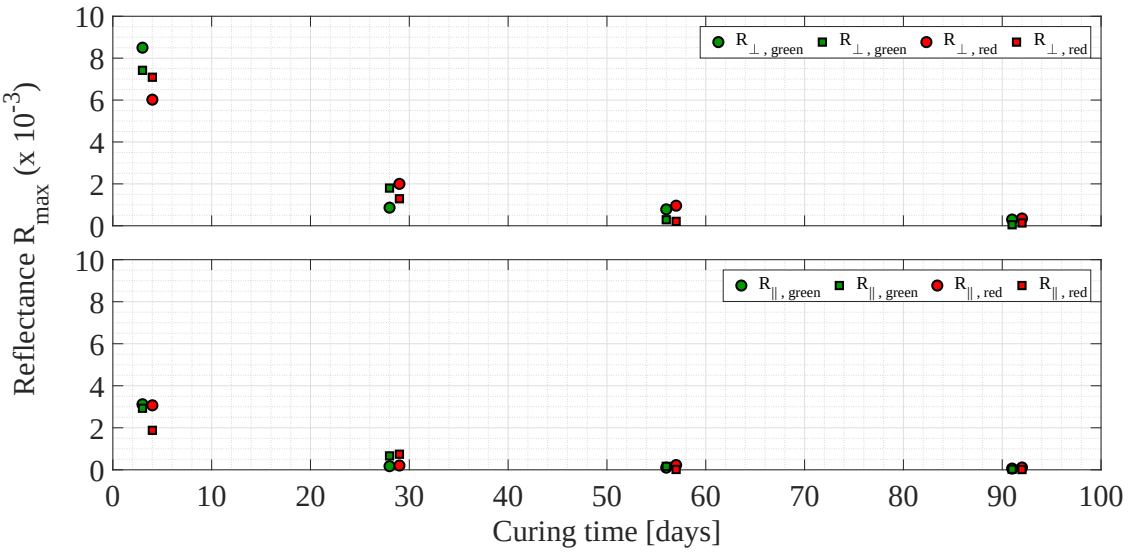

Fig. 3.25 Maximum value of measured reflectances for $\perp$ (top) and $\parallel$ (bottom) polarisation plotted as a function of the curing time for the central position on the front surface of $\text{Silica1}_{\text{Na2SiO3(1:3)}}$ (dot markers) and $\text{Silica2}_{\text{Na2SiO3(1:3)}}$ (square markers) and for green and red laser light. Measurements were taken using the upgraded assembly.

is about 1.36 after 3/4 days from bonding and close to 1.44 after three months, and the bond average thickness obtained by the Bayesian analysis is 155^{+19}_{-26} *nm* after three months (Table 3.1).

The flatness of the two bonding surfaces of $\text{Silica1}_{\text{Na2SiO3(1:3)}}$ was measured using the ZYGO® and was about 74 *nm* and 125 *nm* peak-to-valley respectively: the flatness maps are shown in the first row of Figure 3.29 for the two discs. Combining these maps, the relative separation between two bonding surfaces was obtained and it is shown in the second row of Figure 3.29. The relative separation map gives a value of 80^{+4}_{-4} *nm* for the bond thickness in the central position (Table 3.1).

For the SEM imaging, four slices were cut for $\text{Silica1}_{\text{Na2SiO3(1:3)}}$ and the results of these measurements are shown in Figure 3.30: the average bond thickness found for this sample in the centre location was (110 ± 15) *nm* after 288 days from bonding (Table 3.1).

There is not an agreement between the results obtained using these three methods. The SEM value is smaller than the Bayesian one and this may again suggest that the bond thickness may continue to decrease over time. The relative separation value is the smallest one and this implies that it does not necessarily define the final thickness of a bond.

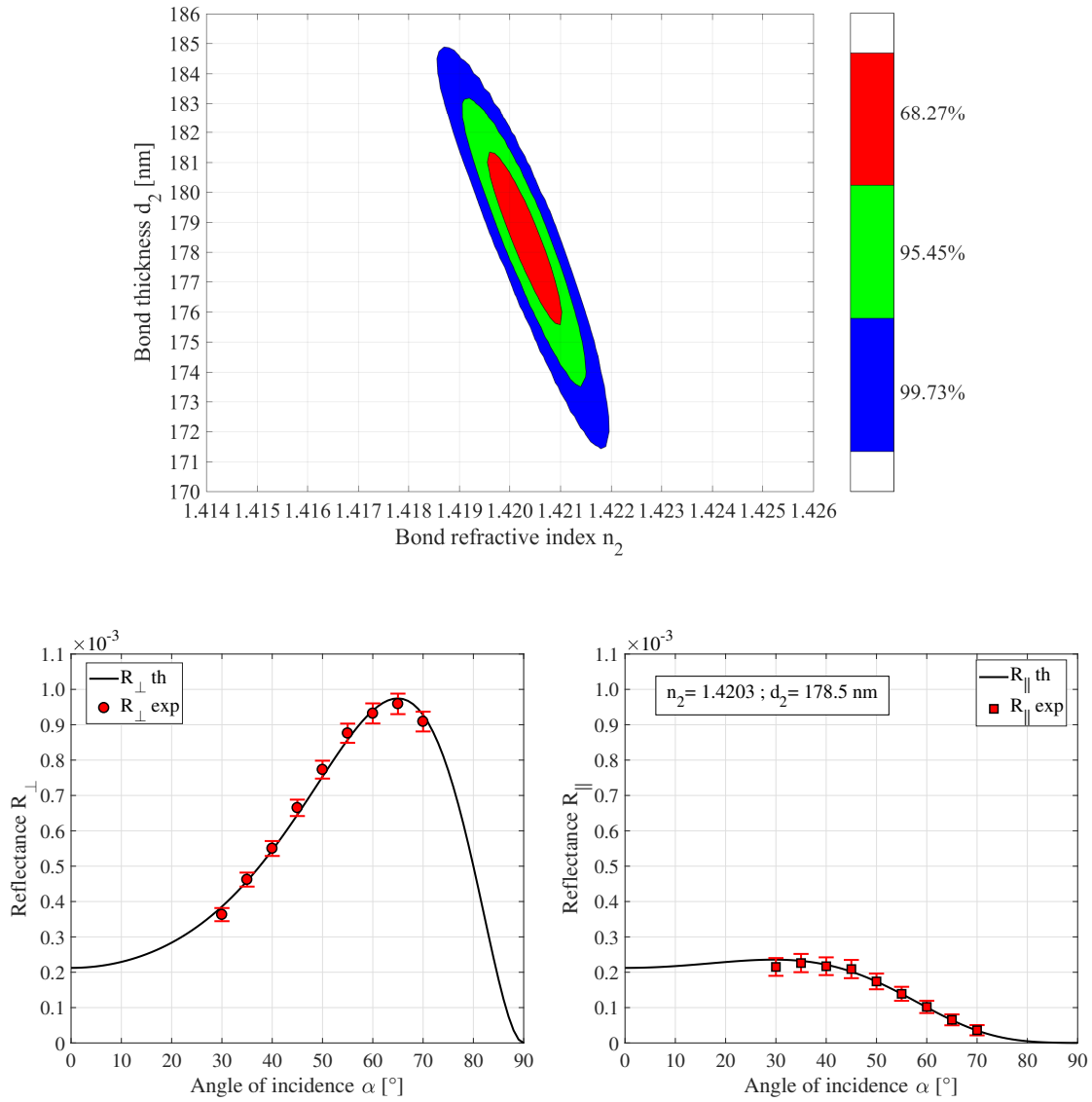

Fig. 3.26 (top) Three confidence levels of 68.3%, 95.5% and 99.7% probability. (bottom) Measured data with their corresponding error bars and theoretical curves. The red dots and squares represent the reflectances measured for perpendicular and parallel polarisation, respectively. The black solid lines are the theoretical perpendicular and parallel reflectances obtained using the most likely values of bond refractive index and thickness of the Bayesian analysis ($n_2 = 1.4203$ and $d_2 = 178.5$). These measurements were taken at 57 days after bonding for $\text{Silica1}_{\text{Na2SiO3(1:3)}}$ in red light.

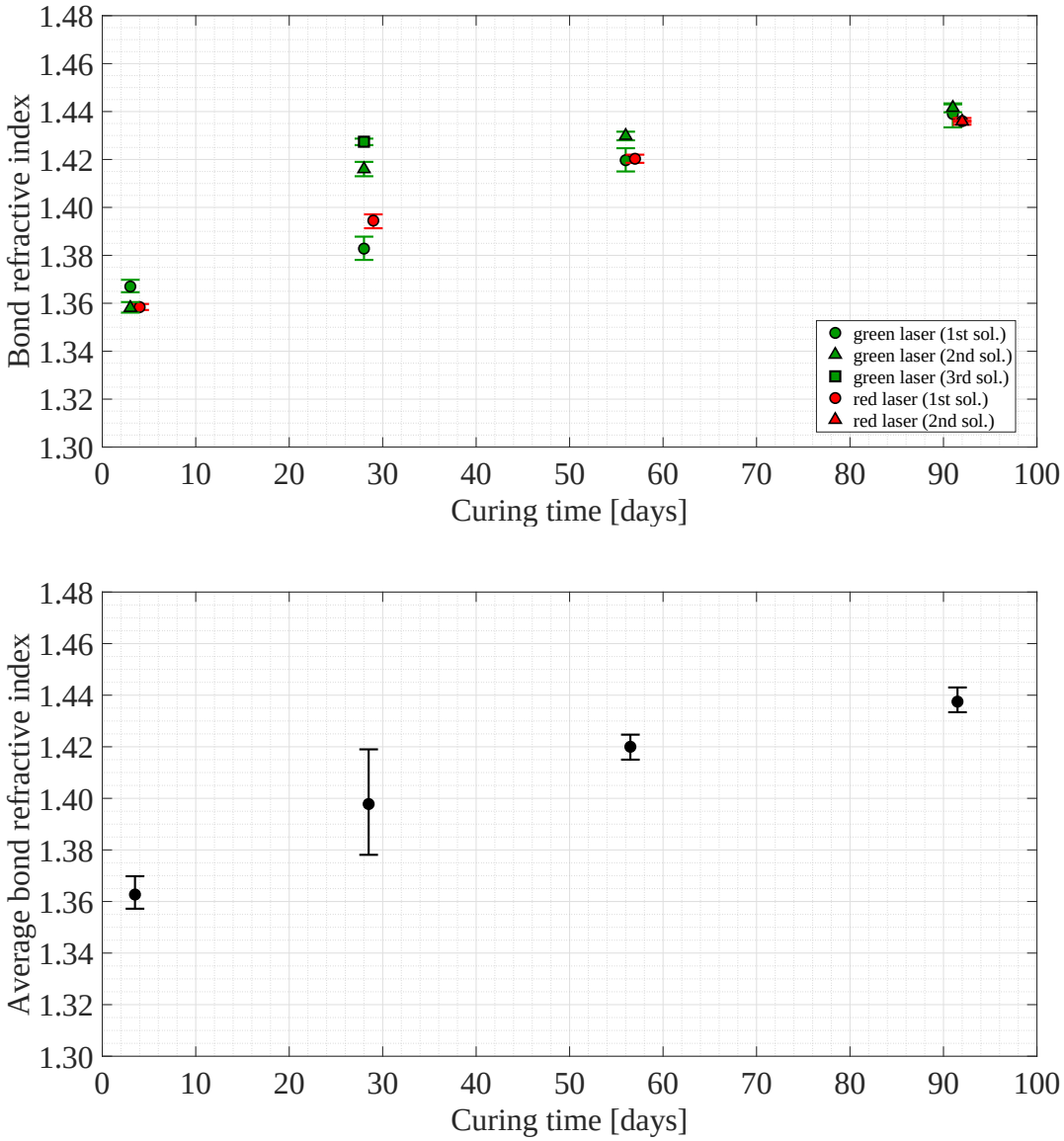

Fig. 3.27 (top) Refractive index of the bond as a function of the curing time for the central position on the front surface of Silica1$_{\mathrm{Na2SiO3(1:3)}}$. These values were determined from measurements collected using the upgraded setup in green (green dots, triangles and squares) and red (red dots and triangles) mode. Some data sets have multiple solutions, which are presented in order from the highest to the lowest joint posterior probability density function by dots, triangles and squares. (bottom) Average of the green and red refractive indices of which the Bayesian values have similar probability volumes. This average was calculated for each two consecutive days (the difference between green and red curing time is always one day). The error bars represent the spread of the data that was averaged.

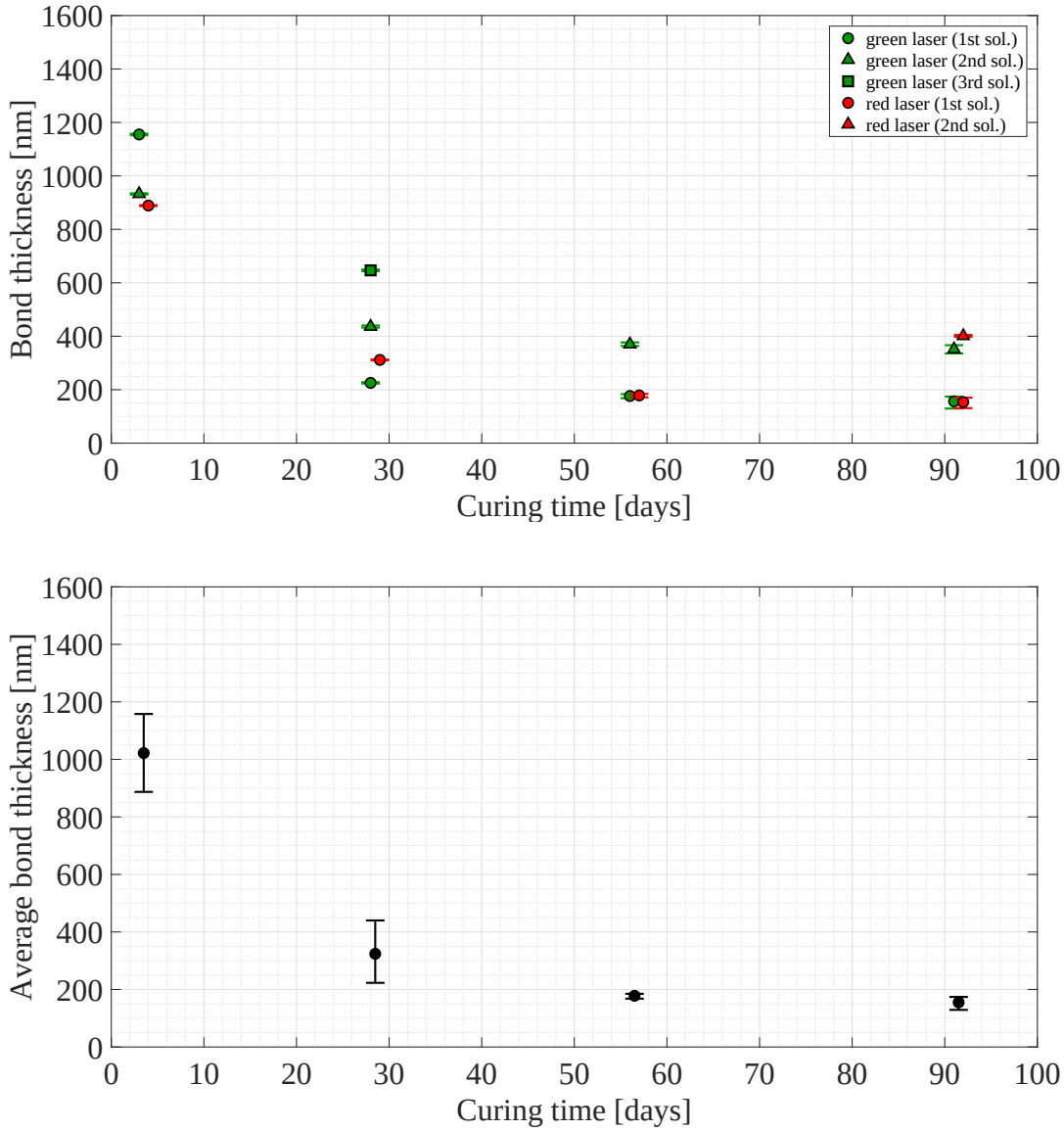

Fig. 3.28 (top) Thickness of the bond as a function of the curing time for the central position on the front surface of Silica1$_{Na2SiO3(1:3)}$. These values were determined from measurements collected using the upgraded setup in green (green dots, triangles and squares) and red (red dots and triangles) mode. Some data sets have multiple solutions, which are presented in order from the highest to the lowest joint posterior probability density function by dots, triangles and squares. (bottom) Average of the green and red thicknesses of which the Bayesian values have similar probability volumes. This average was calculated for each two consecutive days (the difference between green and red curing time is always one day). The error bars represent the spread of the data that was averaged.

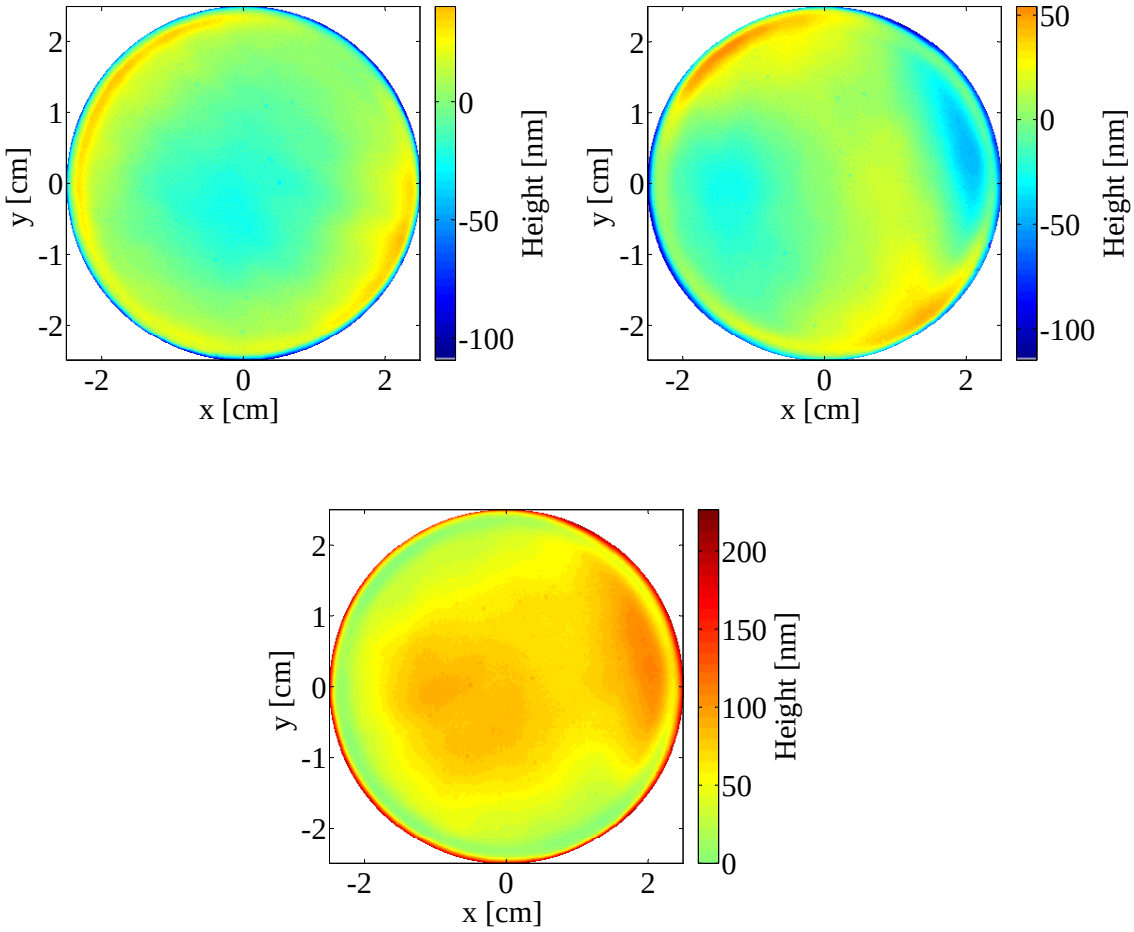

Fig. 3.29 (first row) Flatness maps of the bonding surfaces of the two discs which make $\text{Silica1}_{\text{Na2SiO3(1:3)}}$. These were obtained using the functions of the Simtools package (see Appendix E) which zoomed in on a valid area and remove various offsets from the ZYGO® maps. (second row) Relative separation between two bonding surfaces of discs bonded by hydroxide-catalysis bonding. This map was obtained using the Matlab code reported in Appendix E.

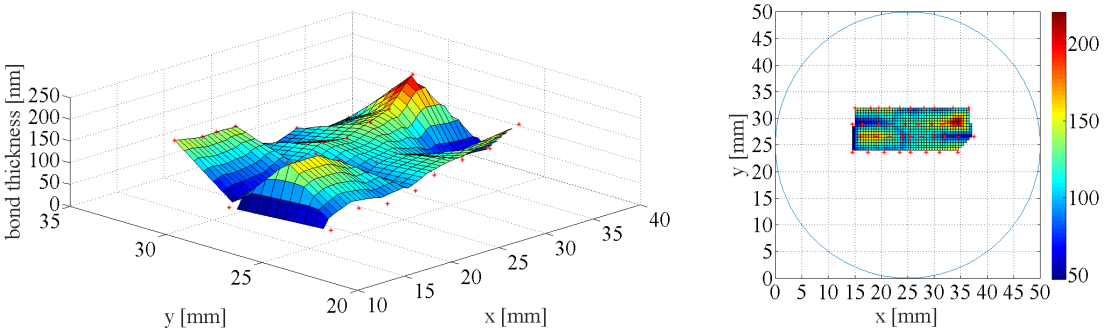

Fig. 3.30 Surface plots of the bond thicknesses measured across four slices of $\text{Silica1}_{\text{Na2SiO3(1:3)}}$, where x and y were the coordinates of the thickness measurement within the sample. The surface plots were made by linearly interpolating between measurements.

$\text{Silica2}_{\text{Na2SiO3(1:3)}}$

Figure 3.31 shows one example of the results obtained from the Matlab script for sample $\text{Silica2}_{\text{Na2SiO3(1:3)}}$ in green mode after 3 days.

In the top and bottom of Figure 3.32 and Figure 3.33, the green and red bond refractive indices and thicknesses are plotted and then averaged (only the data of which the Bayesian values had similar probability volumes) as a function of the curing time for the central position on the front surface of $\text{Silica2}_{\text{Na2SiO3(1:3)}}$.

Like $\text{Silica1}_{\text{Na2SiO3(1:3)}}$, the bond average refractive index is 1.36 at 3/4 curing days and close to 1.44 after three months, whereas the bond average thickness obtained by the Bayesian analysis is 473^{+271}_{-267} *nm* after three months (Table 3.1).

The bonding surfaces of the two discs of $\text{Silica2}_{\text{Na2SiO3(1:3)}}$ had a flatness of about 94 *nm* and 88 *nm* peak-to-valley respectively, which was measured using the ZYGO®. The flatness maps shown in the first row of Figure 3.34 were obtained for the two discs. Combining these maps, the relative separation between the two bonding surfaces was obtained and it is shown in the second row of Figure 3.34: the relative separation map gives a value of 95^{+3}_{-3} *nm* for the bond thickness in central position (Table 3.1).

No SEM imaging were taken for this sample.

The relative separation and Bayesian thicknesses are significantly different. Again, this confirms that either the relative separation between two bonding surfaces of discs may not be the final bond thickness or the bond thickness continues to decrease after three months.

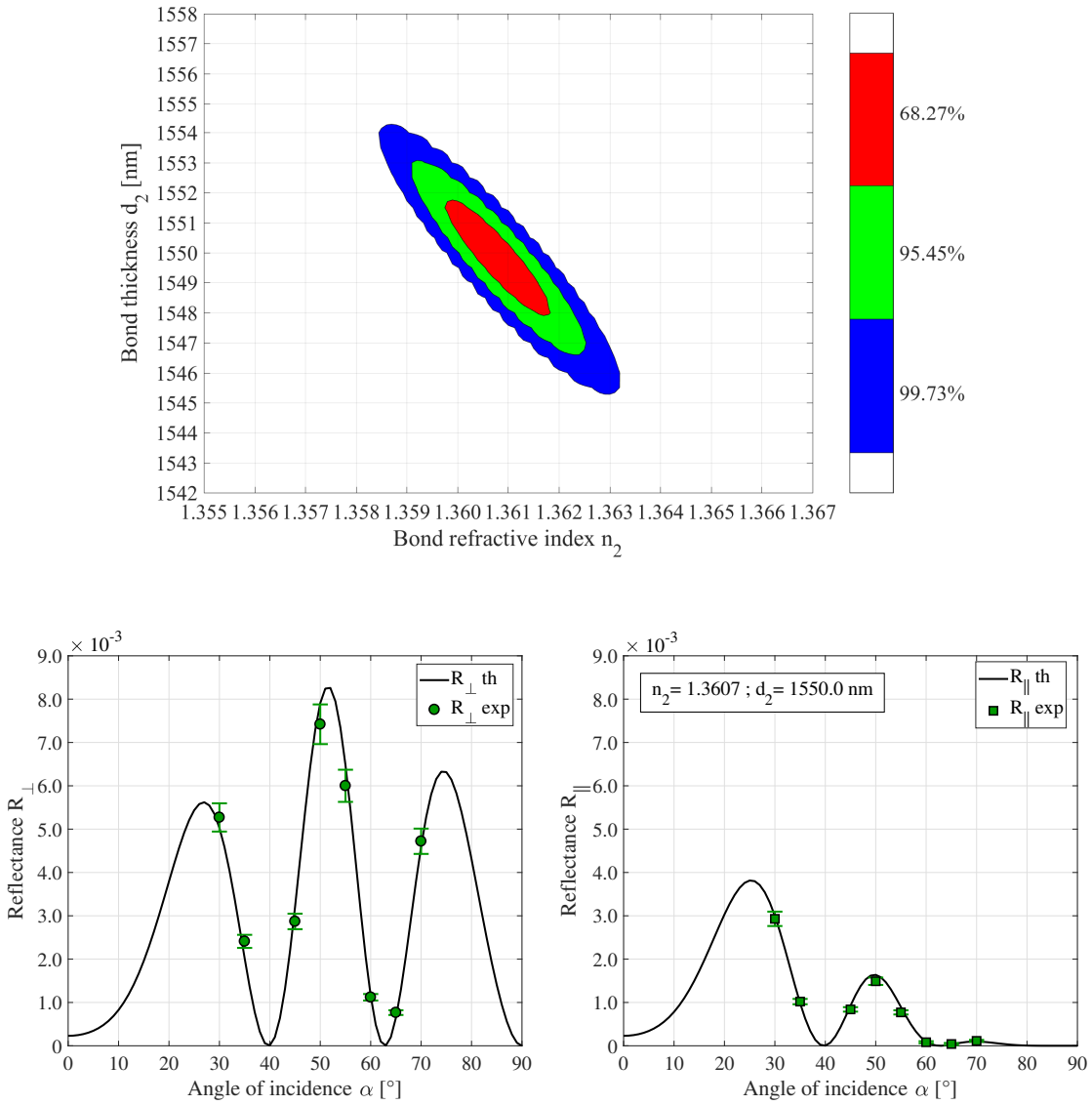

Fig. 3.31 (top) Three confidence levels of 68.3%, 95.5% and 99.7% probability. (bottom) Measured data with their corresponding error bars and theoretical curves. The green dots and squares represent the reflectances measured for perpendicular and parallel polarisation, respectively. The black solid lines are the theoretical perpendicular and parallel reflectances obtained using the most likely values of bond refractive index and thickness of the Bayesian analysis ($n_2 = 1.3607$ and $d_2 = 1550.0$). These measurements were taken at 3 days after bonding for $\text{Silica2}_{\text{Na2SiO3(1:3)}}$ in green light.

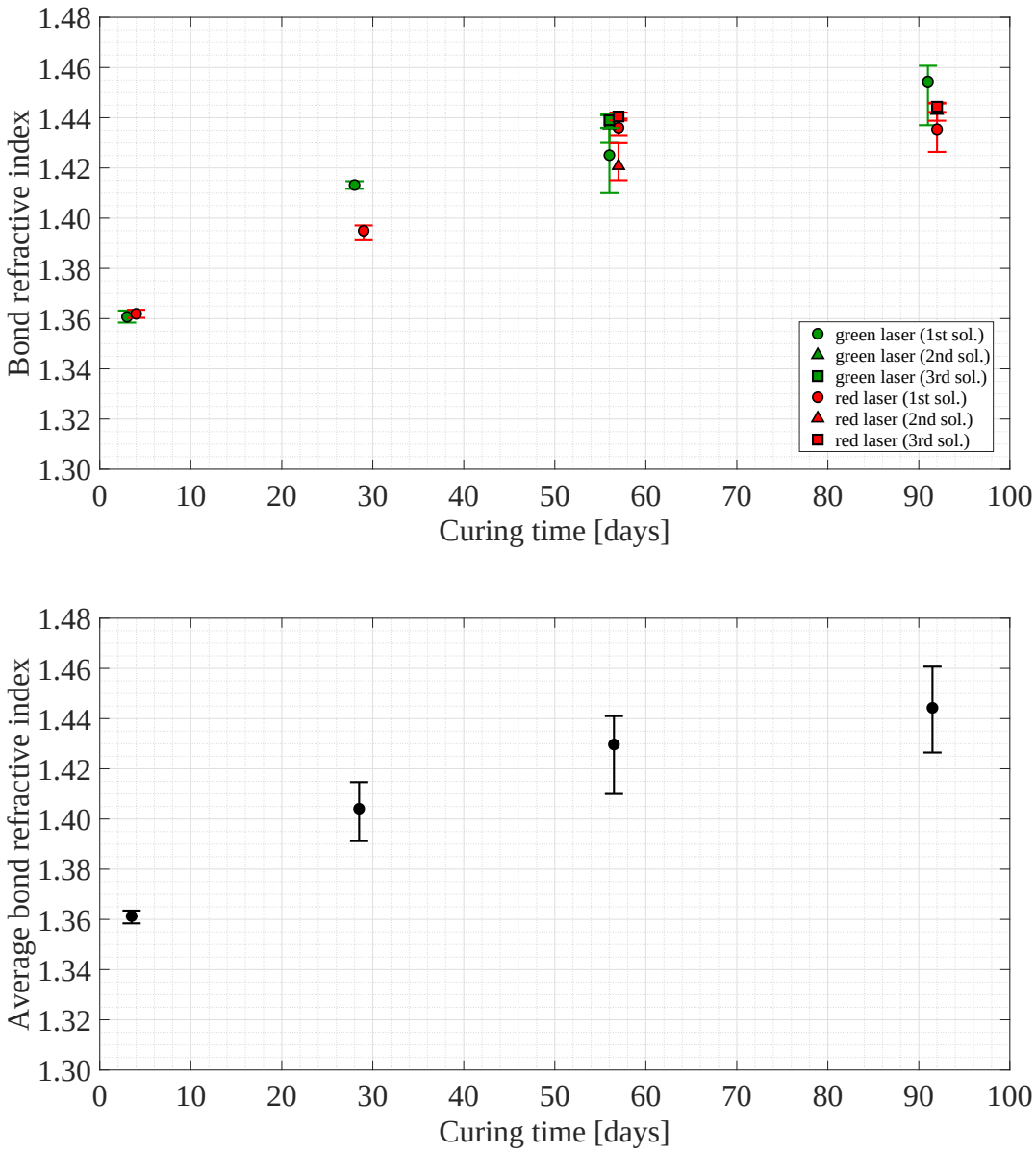

Fig. 3.32 (top) Refractive index of the bond as a function of the curing time for the central position on the front surface of Silica2$_{Na2SiO3(1:3)}$. These values were determined from measurements collected using the upgraded setup in green (green dots, triangles and squares) and red (red dots, triangles and squares) mode. Some data sets have multiple solutions, which are presented in order from the highest to the lowest joint posterior probability density function by dots, triangles and squares. (bottom) Average of the green and red refractive indices of which the Bayesian values have similar probability volumes. This average was calculated for each two consecutive days (the difference between green and red curing time is always one day). The error bars represent the spread of the data that was averaged.

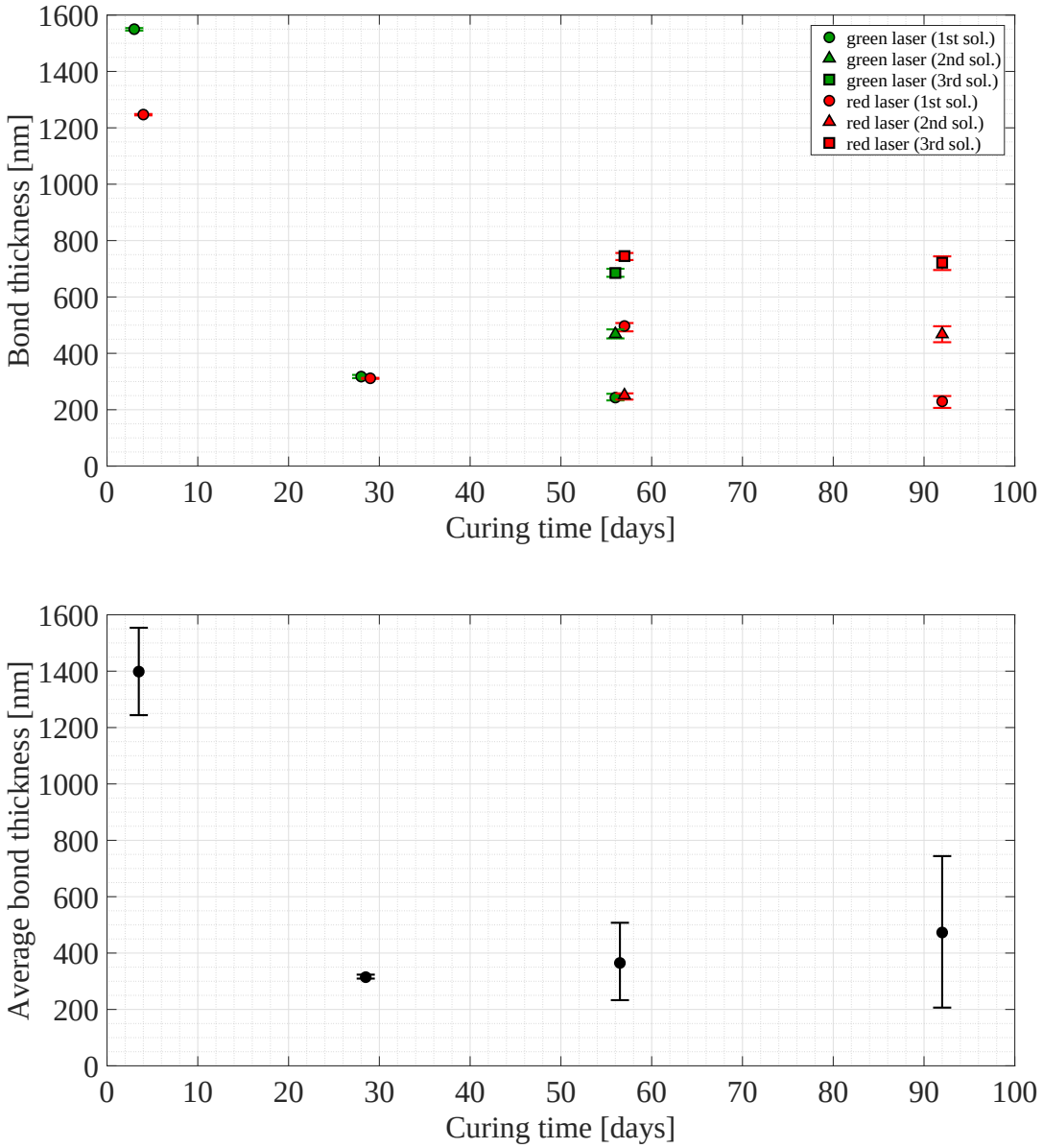

Fig. 3.33 (top) Thickness of the bond as a function of the curing time for the central position on the front surface of Silica2$_{Na2SiO3(1:3)}$. These values were determined from measurements collected using the upgraded setup in green (green dots, triangles and squares) and red (red dots, triangles and squares) mode. Some data sets have multiple solutions, which are presented in order from the highest to the lowest joint posterior probability density function by dots, triangles and squares. The thickness at 91 days (green data set) was not reported, because it was not measurable because of the relatively large uncertainty on this measurement due to the extremely low reflectance of the bond. (bottom) Average of the green and red thicknesses of which the Bayesian values have similar probability volumes. This average was calculated for each two consecutive days (the difference between green and red curing time is always one day). For the red data sets at 92 days the average of the three red refractive indices (similar probability volumes) was considered because of the absence of the corresponding value in green. The error bars represent the spread of the data that was averaged.

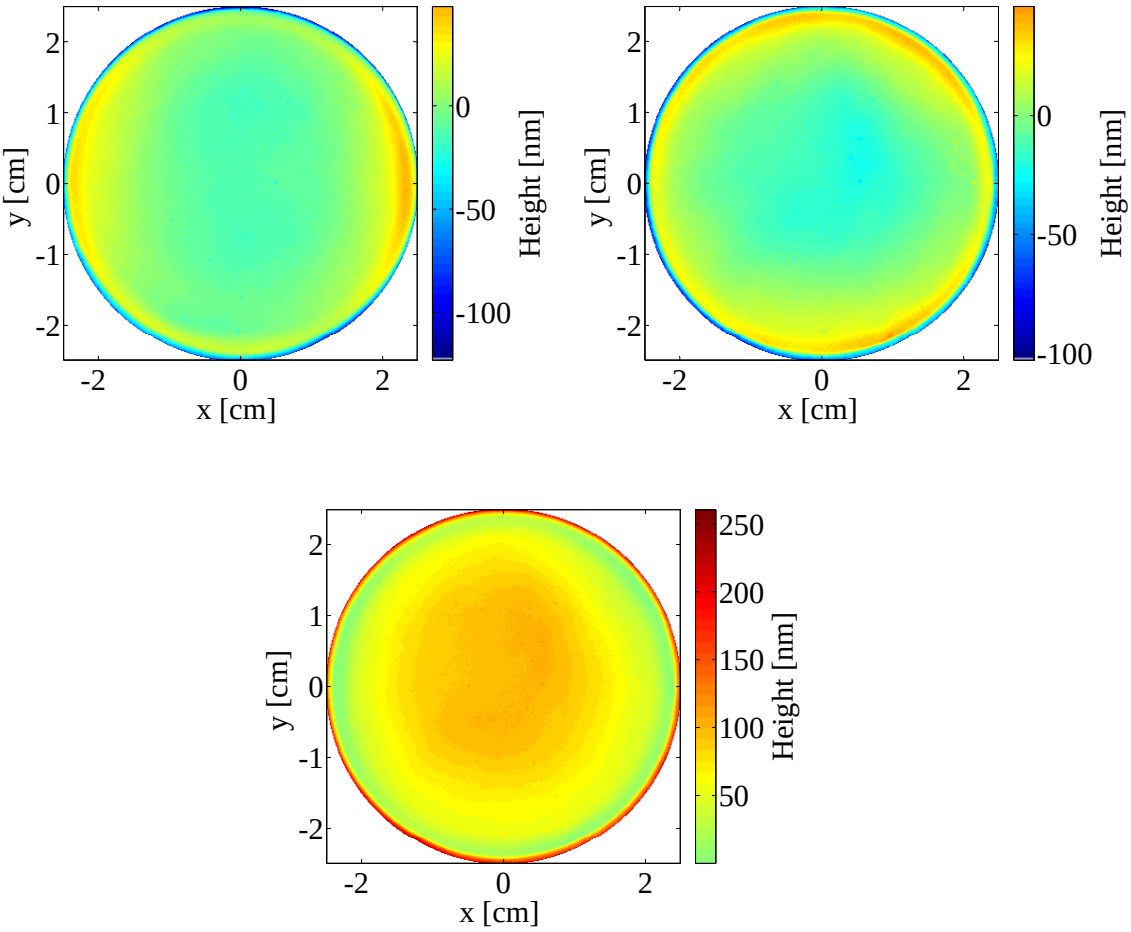

Fig. 3.34 (first row) Flatness maps of the bonding surfaces of the two discs which make Silica2$_{Na2SiO3(1:3)}$. These were obtained using the functions of the Simtools package (see Appendix E) which zoomed in on a valid area and remove various offsets from the ZYGO® maps. (second row) Relative separation between two bonding surfaces of discs bonded by hydroxide-catalysis bonding. This map was obtained using the Matlab code reported in Appendix E.

3.2.5 Analysis result: discussion

Both $\text{Silica1}_{\text{Na2SiO3(1:3)}}$ and $\text{Silica2}_{\text{Na2SiO3(1:3)}}$ show the same asymptotically increasing trend of the bond refractive index as a function of curing time, and both have a value of about 1.44 after about three months from curing. The rate of increase is very similar to that of the 1 : 6 sodium silicate bonds shown in section 3.1.

In Table 3.1 (section 3.5) the bond thicknesses obtained using the Bayesian, flatness and SEM methods are shown. The bond thickness solutions obtained by the Bayesian analysis for these two samples decrease as curing time increases and then settle after roughly 30 days on a more or less constant value, different for the both two cases (about 155^{+19}_{-26} *nm* for $\text{Silica1}_{\text{Na2SiO3(1:3)}}$ and 473^{+271}_{-267} *nm* for $\text{Silica2}_{\text{Na2SiO3(1:3)}}$). Both these values are higher than those obtained using the flatness maps, suggesting that either the optical thickness of the bond is not necessarily constrained by the flatness of two bonded discs or it could decrease further over time. Only the Bayesian bond thickness of $\text{Silica1}_{\text{Na2SiO3(1:3)}}$ is very close to the value measured by the scanning electron microscopy (110^{+15}_{-15} *nm* , see Table 3.1).

3.3 Sodium silicate 1:10 solution

In this section the properties of bonds between fused silica substrates, jointed to create two nominally identical bonded sample sets using a bonding solution made with sodium silicate solution at a volumetric ratio of 1 : 10 with de-ionised water, are described.

3.3.1 $\text{Silica1}_{\text{Na2SiO3(1:10)}}$ and $\text{Silica2}_{\text{Na2SiO3(1:10)}}$

Samples $\text{Silica1}_{\text{Na2SiO3(1:10)}}$ and $\text{Silica2}_{\text{Na2SiO3(1:10)}}$ were jointed using 15.70 μl of solution obtained by diluting 1 ml of sodium silicate solution with 10 ml of de-ionised water (a volumetric ratio of 1 : 10). These samples were left to cure in air at room temperature for two days before measuring the reflectivity of their bonds by means of the upgraded setup with both colours of laser light (Figure 2.5).

3.3.2 Reflectivity measurements

The reflectances of $\text{Silica1}_{\text{Na2SiO3(1:10)}}$ and $\text{Silica2}_{\text{Na2SiO3(1:10)}}$ were measured for the central position on their front surface at the same time intervals as $\text{Silica1}_{\text{Na2SiO3(1:3)}}$ and $\text{Silica2}_{\text{Na2SiO3(1:3)}}$ (a few days and about one, two and three months after bonding). The ef-

fect of curing time on the bond refractive index and thickness could be studied and compared with the previous cases.

Plots of the measured reflectivity for perpendicular ($\perp$) and parallel ($\parallel$) polarisations (equations 2.1 and 2.2) as a function of angle of incidence α are shown in Figure 3.35 ($\text{Silica1}_{\text{Na2SiO3(1:10)}}$ in green mode), Figure 3.36 ($\text{Silica1}_{\text{Na2SiO3(1:10)}}$ in red mode), Figure 3.37 ($\text{Silica2}_{\text{Na2SiO3(1:10)}}$ in green mode) and Figure 3.38 ($\text{Silica2}_{\text{Na2SiO3(1:10)}}$ in red mode).

As the previous samples, also in this case the values of bond reflectances are all less than 1% and they decrease as curing time increases for both polarisations and colours of laser light, reaching values of reflectance less than 0.1% after three months.

3.3.3 Analysis result: reflectivity

The bond peak reflectivity for $\text{Silica1}_{\text{Na2SiO3(1:10)}}$ and $\text{Silica2}_{\text{Na2SiO3(1:10)}}$ is plotted as a function of curing time for both polarisations in Figure 3.39. Also in this case, the reflectance values decrease as curing time increases. This decrease appears to be more gradual than for the 1 : 3 and 1 : 6 sodium silicate bonds as the maximum reflectance especially at 30 and 60 days is twice as high.

3.3.4 Analysis result: refractive index and thickness

$\text{Silica1}_{\text{Na2SiO3(1:10)}}$

Figure 3.40 shows one example of the results obtained from the Matlab script for sample $\text{Silica1}_{\text{Na2SiO3(1:10)}}$ in green mode after 28 days.

The bond refractive index and thickness values are plotted as a function of the curing time for the central position on the front surface of $\text{Silica1}_{\text{Na2SiO3(1:10)}}$ and for both the two colours of the laser light in the top of Figure 3.41 and Figure 3.42.

The values of the green and red bond refractive index and thickness were also time averaged and are shown in the bottom of Figure 3.41 and Figure 3.42: the average was calculated using the Bayesian values that had similar probability volumes. At 3/4 days after bonding, the bond average refractive index is about 1.36 and close to 1.43 after three months. The bond average thickness obtained by the Bayesian analysis is 51^{+62}_{-43} *nm* after three months (Table 3.1). The measurements are affected by relatively large and asymmetric error bars which result from the 3σ confidence limits of each solution. The bond thickness is very low, which gets the model in a region where a small change in reflectivity measured causes a

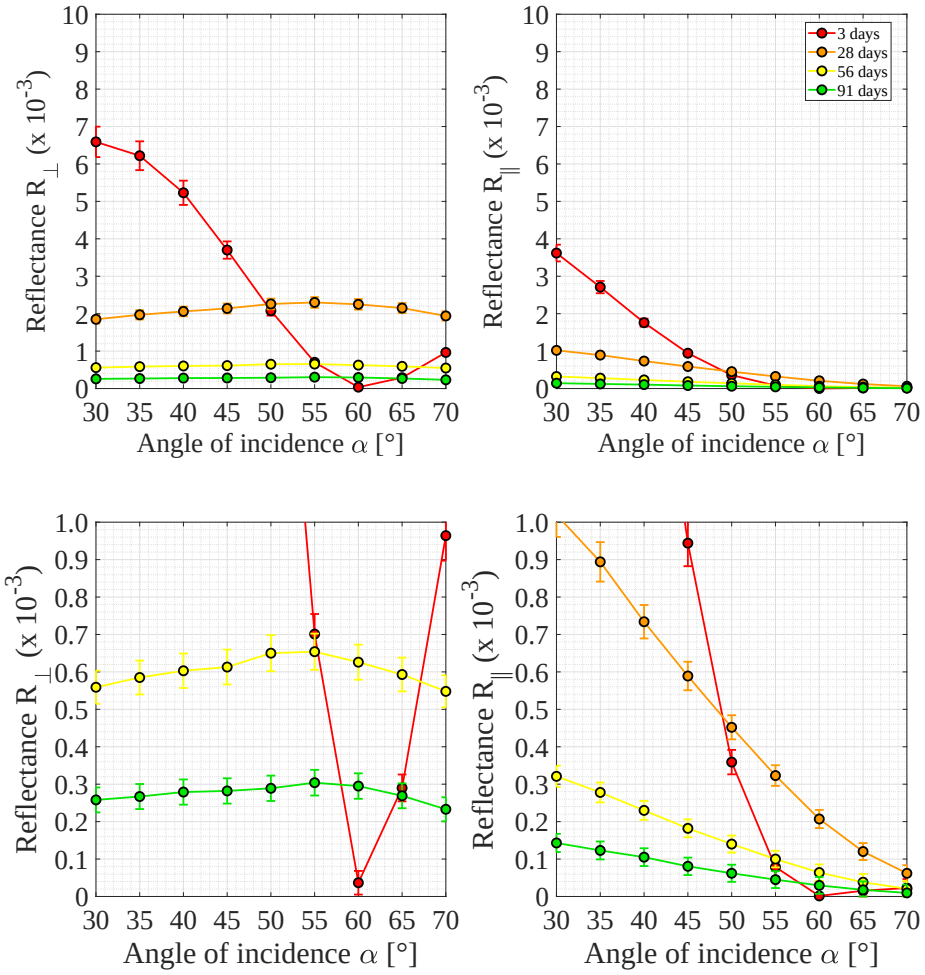

Fig. 3.35 (top) Measured reflectances for $\perp$ (left) and $\parallel$ (right) polarisation plotted as a function of the angle of incidence α for the central position on the front surface of $\text{Silica1}_{\text{Na2SiO3(1:10)}}$. (bottom) Zooms in of the measured reflectances are also shown to allow the reader to see the lower reflectances. In the legend, the curing time is reported. All measurements were taken using the upgraded setup in green mode.

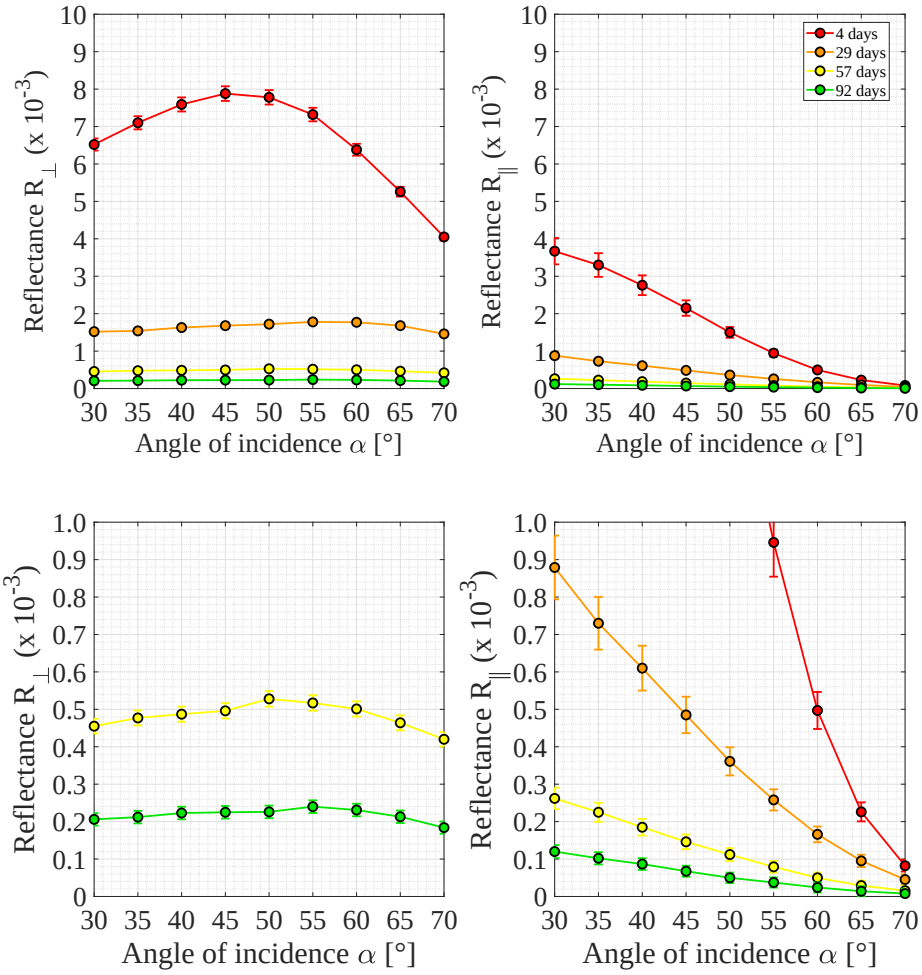

Fig. 3.36 (top) Measured reflectances for $\perp$ (left) and $\parallel$ (right) polarisation plotted as a function of the angle of incidence α for the central position on the front surface of $\text{Silica1}_{\text{Na2SiO3(1:10)}}$. (bottom) Zooms in of the measured reflectances are also shown to allow the reader to see the lower reflectances. In the legend, the curing time is reported. All measurements were taken using the upgraded setup in red mode.

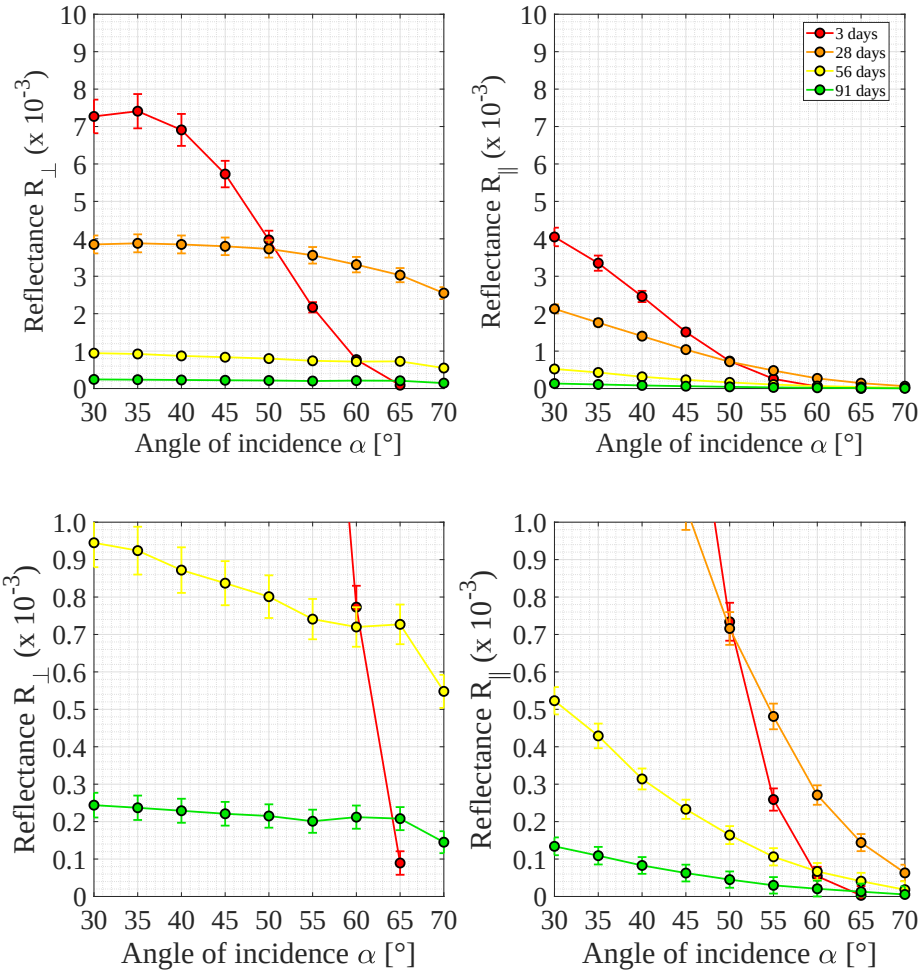

Fig. 3.37 (top) Measured reflectances for $\perp$ (left) and $\parallel$ (right) polarisation plotted as a function of the angle of incidence α for the central position on the front surface of $\text{Silica2}_{\text{Na2SiO3(1:10)}}$. (bottom) Zooms in of the measured reflectances are also shown to allow the reader to see the lower reflectances. In the legend, the curing time is reported. All measurements were taken using the upgraded setup in green mode.

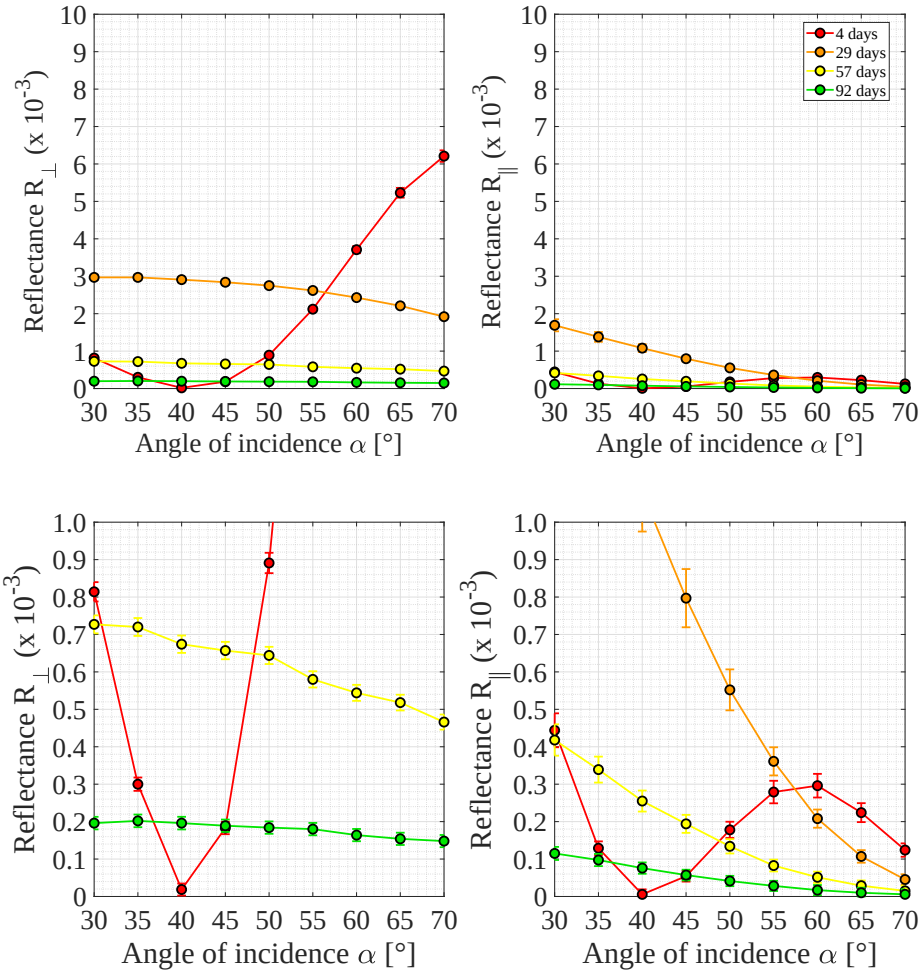

Fig. 3.38 (top) Measured reflectances for $\perp$ (left) and $\parallel$ (right) polarisation plotted as a function of the angle of incidence α for the central position on the front surface of $\text{Silica2}_{\text{Na2SiO3(1:10)}}$. (bottom) Zooms in of the measured reflectances are also shown to allow the reader to see the lower reflectances. In the legend, the curing time is reported. All measurements were taken using the upgraded setup in red mode.

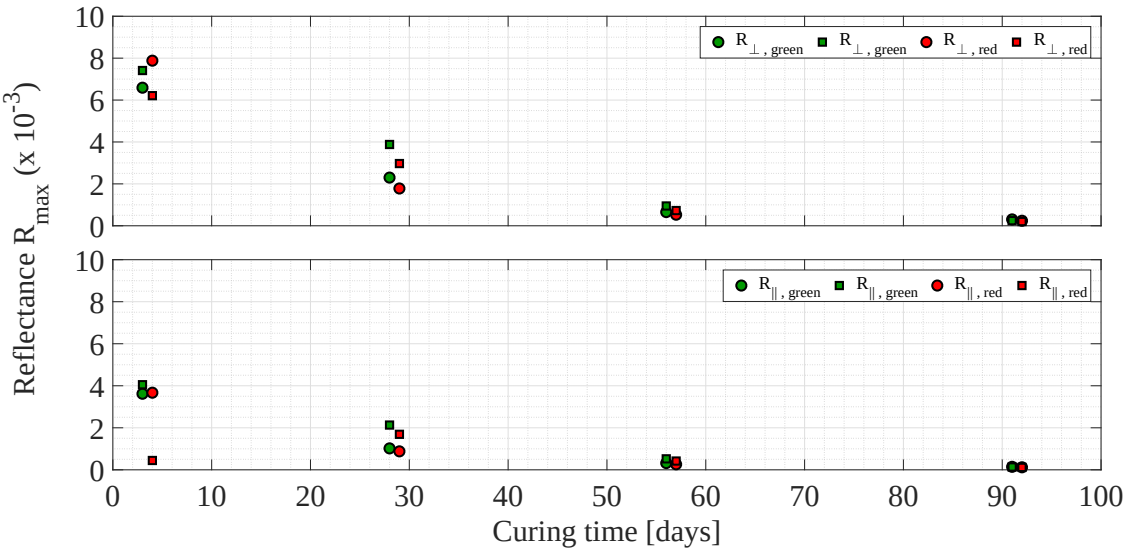

Fig. 3.39 Maximum value of measured reflectances for $\perp$ (top) and $\parallel$ (bottom) polarisation plotted as a function of the curing time for the central position on the front surface of $\text{Silica1}_{\text{Na2SiO3(1:10)}}$ (dot markers) and $\text{Silica2}_{\text{Na2SiO3(1:10)}}$ (square markers) and for green and red laser light. Measurements were taken using the upgraded assembly.

small change in bond thickness, but a large change in refractive index. The asymmetric shape of the confidence levels is given by the discrepancy between the experimental data and the theoretical reflectivity model.

The bonding surfaces of the two discs of $\text{Silica1}_{\text{Na2SiO3(1:10)}}$ had a flatness of about 102 *nm* and 99 *nm* peak-to-valley respectively. These measurements were taken using the ZYGO®. The flatness maps shown in the first row of Figure 3.43 were obtained for the two discs. Combining these maps, the relative separation between the two bonding surfaces was obtained and it is shown in the second row of Figure 3.43: the relative separation map gives a value of 97^{+4}_{-4} *nm* for the bond thickness in the central position (Table 3.1).

For the SEM imaging, four slices were cut for $\text{Silica1}_{\text{Na2SiO3(1:10)}}$ and the results of all measurements taken were plotted as surface plots using linear interpolation in Figure 3.44: the average bond thickness measured in the centre of this sample was (47 ± 9) *nm* after 304 days from bonding (Table 3.1).

There is an excellent agreement between the SEM and reflectivity measurements. Though the flatness maps results are within the error of the reflectance measurements, the SEM and flatness results deviate.

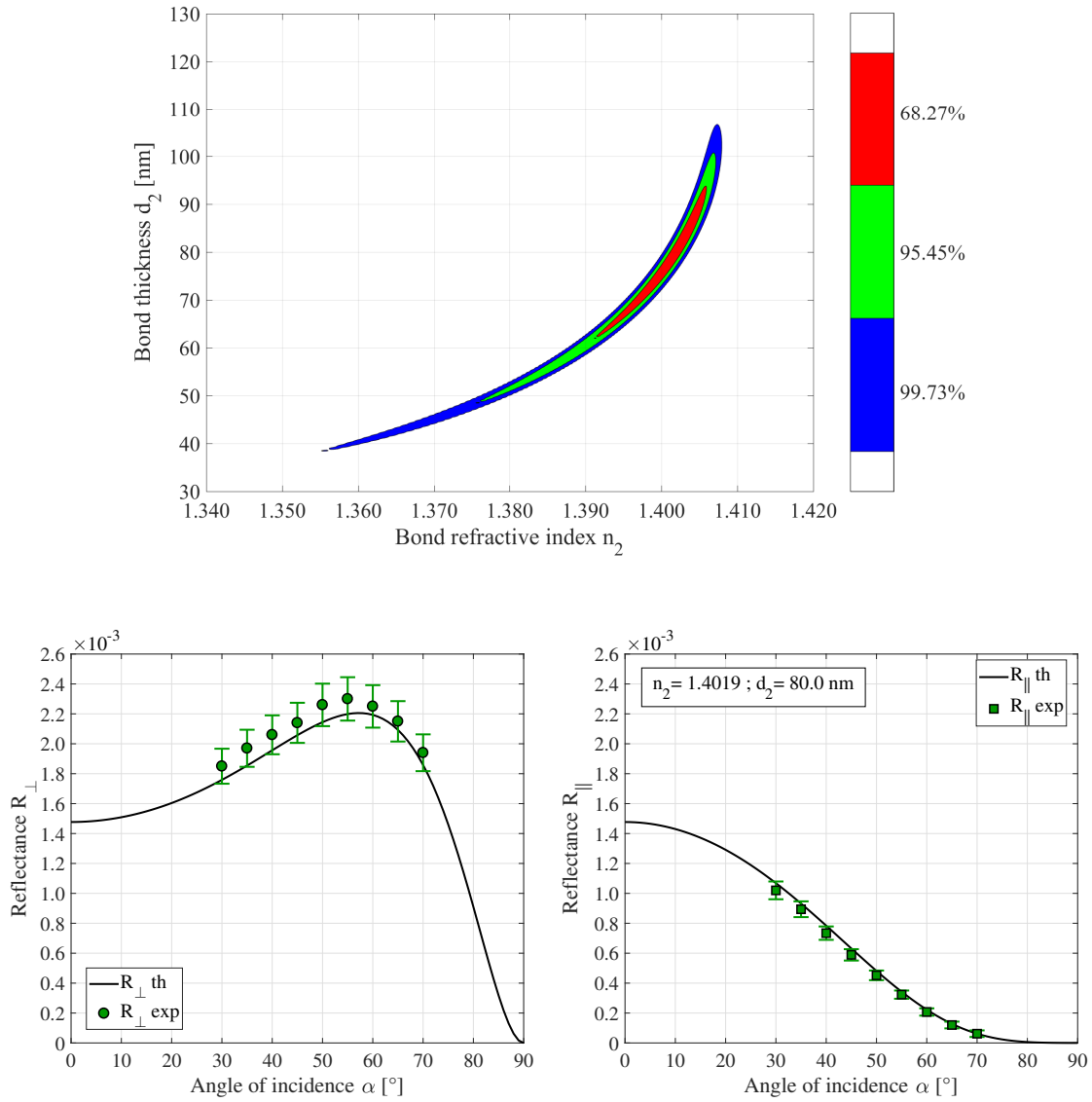

Fig. 3.40 (top) Three confidence levels of 68.3%, 95.5% and 99.7% probability. (bottom) Measured data with their corresponding error bars and theoretical curves. The green dots and squares represent the reflectances measured for perpendicular and parallel polarisation, respectively. The black solid lines are the theoretical perpendicular and parallel reflectances obtained using the most likely values of bond refractive index and thickness of the Bayesian analysis ($n_2 = 1.4019$ and $d_2 = 80.0$). These measurements were taken at 28 days after bonding for $\text{Silica1}_{\text{Na2SiO3(1:10)}}$ in green light.

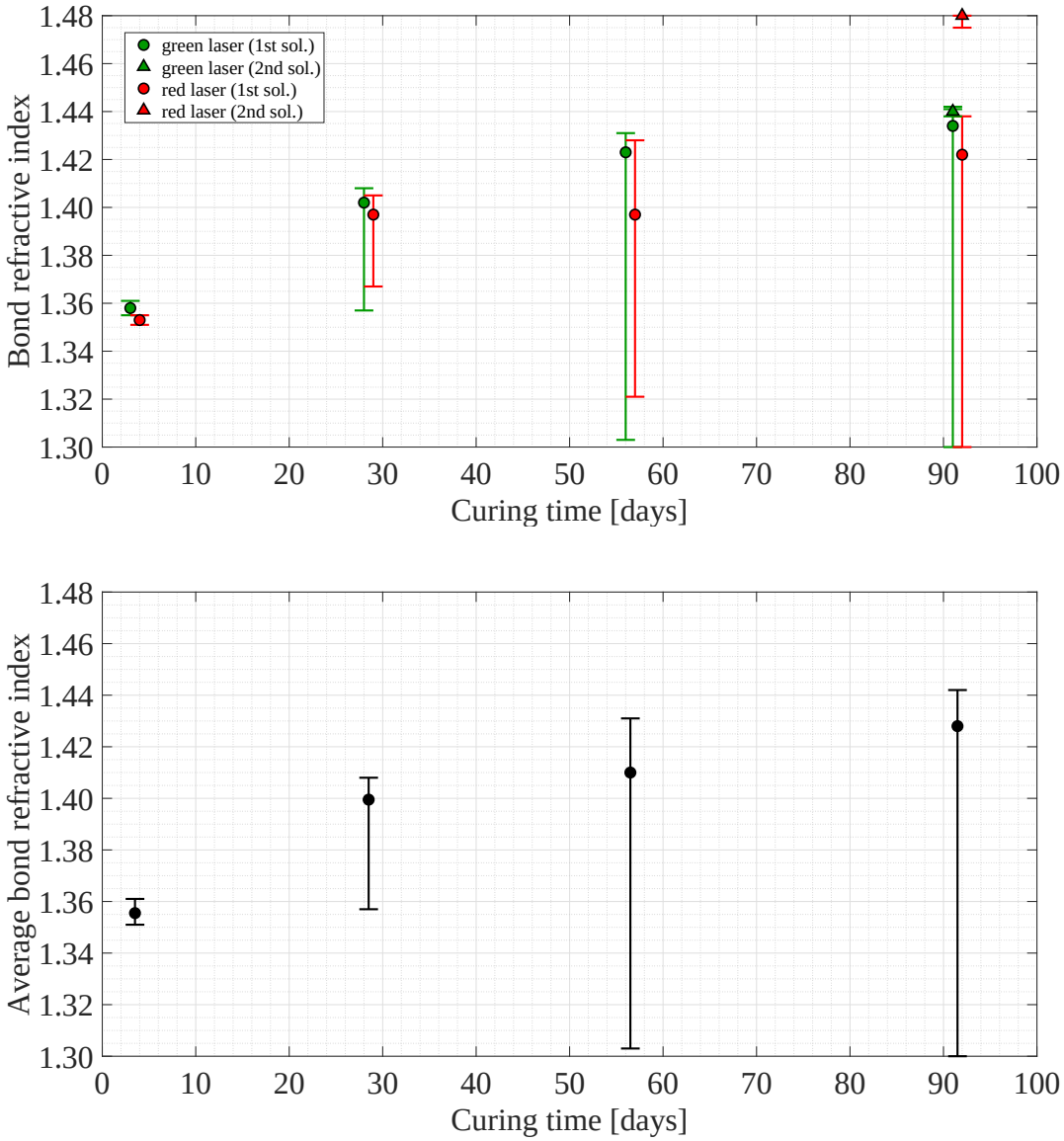

Fig. 3.41 (top) Refractive index of the bond as a function of the curing time for the central position on the front surface of Silica1$_{\mathrm{Na2SiO3(1:10)}}$. These values were determined from measurements collected using the upgraded setup in green (green dots and triangles) and red (red dots and triangles) mode. Some data sets have multiple solutions, which are presented in order from the highest to the lowest joint posterior probability density function by dots and triangles. (bottom) Average of the green and red refractive indices of which the Bayesian values have similar probability volumes. This average was calculated for each two consecutive days (the difference between green and red curing time is always one day). The error bars represent the spread of the data that was averaged.

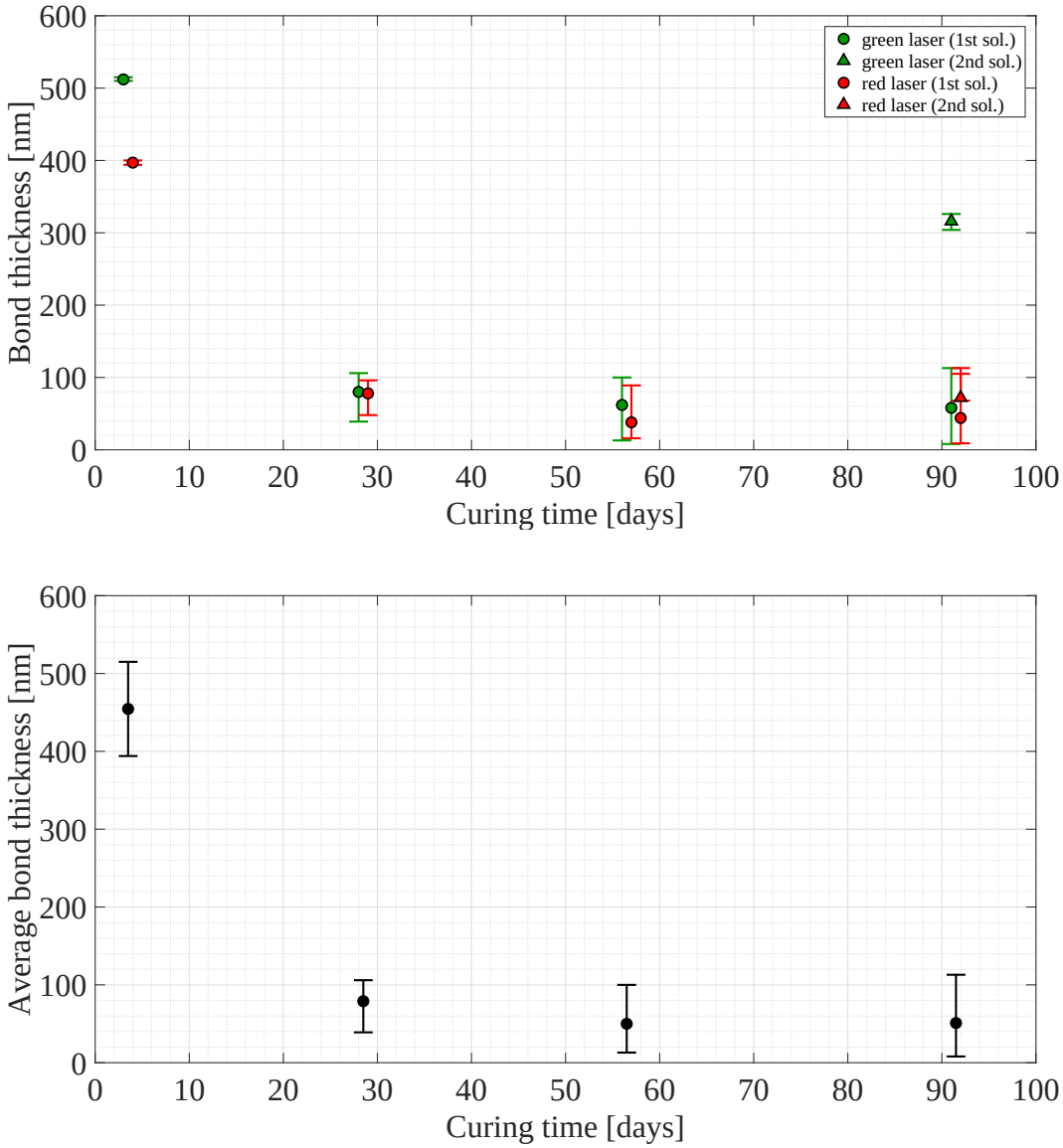

Fig. 3.42 (top) Thickness of the bond as a function of the curing time for the central position on the front surface of Silica1$_{Na2SiO3(1:10)}$. These values were determined from measurements collected using the upgraded setup in green (green dots and triangles) and red (red dots and triangles) mode. Some data sets have multiple solutions, which are presented in order from the highest to the lowest joint posterior probability density function by dots and triangles. (bottom) Average of the green and red thicknesses of which the Bayesian values have similar probability volumes. This average was calculated for each two consecutive days (the difference between green and red curing time is always one day). The error bars represent the spread of the data that was averaged.

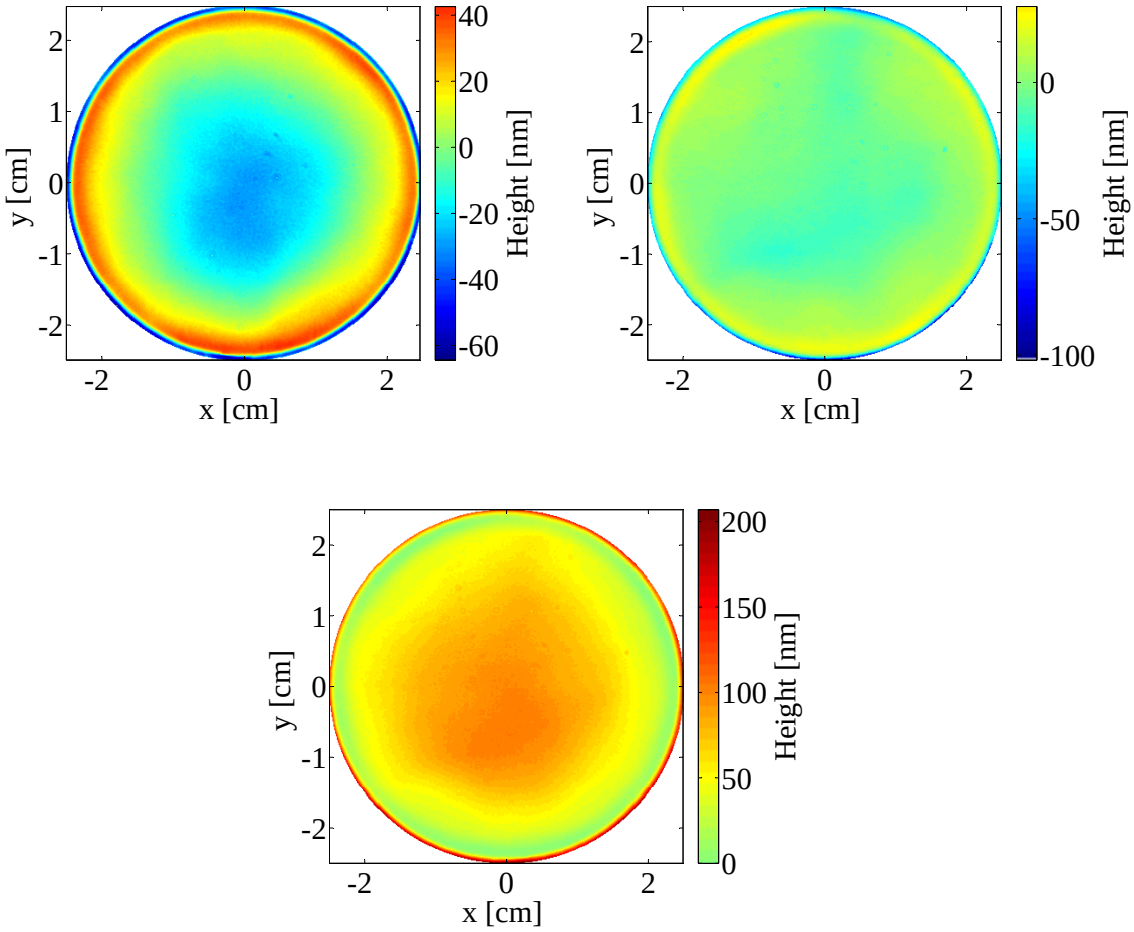

Fig. 3.43 (first row) Flatness maps of the bonding surfaces of the two discs which make $\text{Silica1}_{\text{Na2SiO3(1:10)}}$. These were obtained using the functions of the Simtools package (see Appendix E) which zoomed in on a valid area and remove various offsets from the ZYGO® maps. (second row) Relative separation between two bonding surfaces of discs bonded by hydroxide-catalysis bonding. This map was obtained using the Matlab code reported in Appendix E.

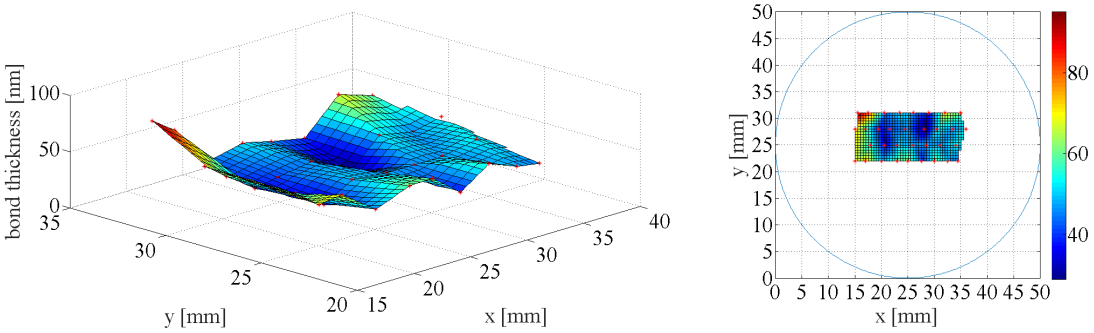

Fig. 3.44 Surface plots of the bond thicknesses measured across four slices of $\text{Silica1}_{\text{Na2SiO3(1:10)}}$, where x and y were the coordinates of the thickness measurement within the sample. The surface plots were made by linearly interpolating between measurements.

$\text{Silica2}_{\text{Na2SiO3(1:10)}}$

Figure 3.45 shows one example of the results obtained from the Matlab script for sample $\text{Silica2}_{\text{Na2SiO3(1:10)}}$ in red mode after 4 days.

In the top of Figure 3.46 and Figure 3.47, the green and red bond refractive index and thickness values are plotted as a function of the curing time for the central position on the front surface of $\text{Silica2}_{\text{Na2SiO3(1:10)}}$. In the bottom of Figure 3.46 and Figure 3.47, their time averages are also plotted over curing time: only the data of which the Bayesian values had similar probability volumes was used to calculate these averages.

In the first days after bonding (3/4 days), the bond average refractive index is about 1.36 and close to 1.38 after three months which is much smaller than that obtained for $\text{Silica1}_{\text{Na2SiO3(1:10)}}$. The bond average thickness obtained by the Bayesian analysis is 17^{+74}_{-10} *nm* after three months (Table 3.1). Both the bond refractive index and thickness values are affected by relatively large and asymmetric error bars. These are determined by the 3σ confidence limits of each solution. The fact that the bond thickness is almost certainly extremely low causes the large error bars on its values and on those of the refractive index. The latter changes a lot for small changes in bond thickness in the model. The asymmetric shape of the confidence levels is due to the discrepancy between the experimental data and the theoretical reflectivity model.

Using the ZYGO®, it was found that the bonding surfaces of the two discs of sample $\text{Silica2}_{\text{Na2SiO3(1:10)}}$ had a flatness of about 145 *nm* and 122 *nm* peak-to-valley respectively. The flatness maps shown in the first row of Figure 3.48 were obtained for the two discs. Combining these maps, the relative separation between two bonding surfaces was obtained

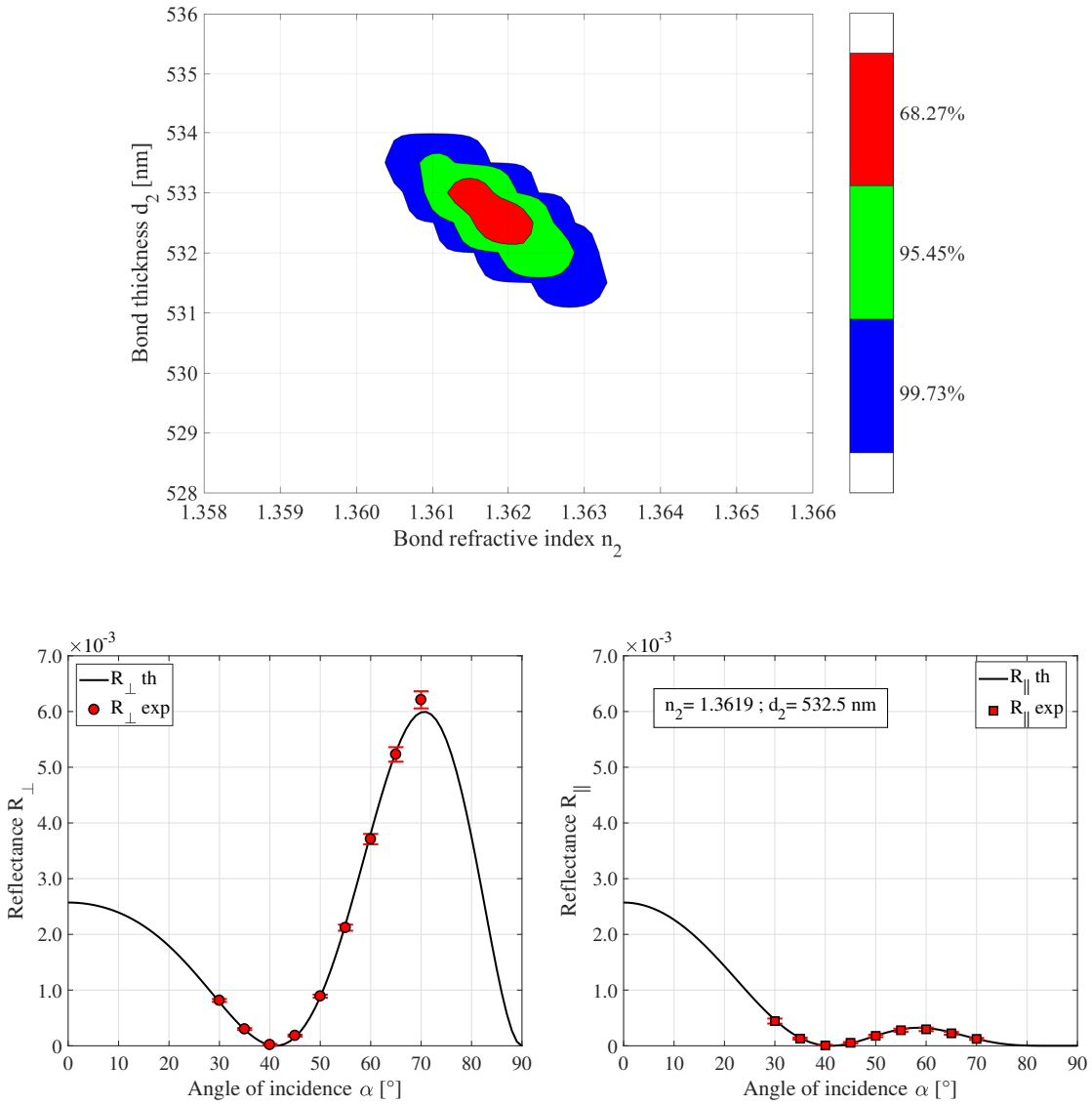

Fig. 3.45 (top) Three confidence levels of 68.3%, 95.5% and 99.7% probability. (bottom) Measured data with their corresponding error bars and theoretical curves. The red dots and squares represent the reflectances measured for perpendicular and parallel polarisation, respectively. The black solid lines are the theoretical perpendicular and parallel reflectances obtained using the most likely values of bond refractive index and thickness of the Bayesian analysis ($n_2 = 1.3619$ and $d_2 = 532.5$). These measurements were taken at 4 days after bonding for $\text{Silica2}_{\text{Na2SiO3(1:10)}}$ in red light.

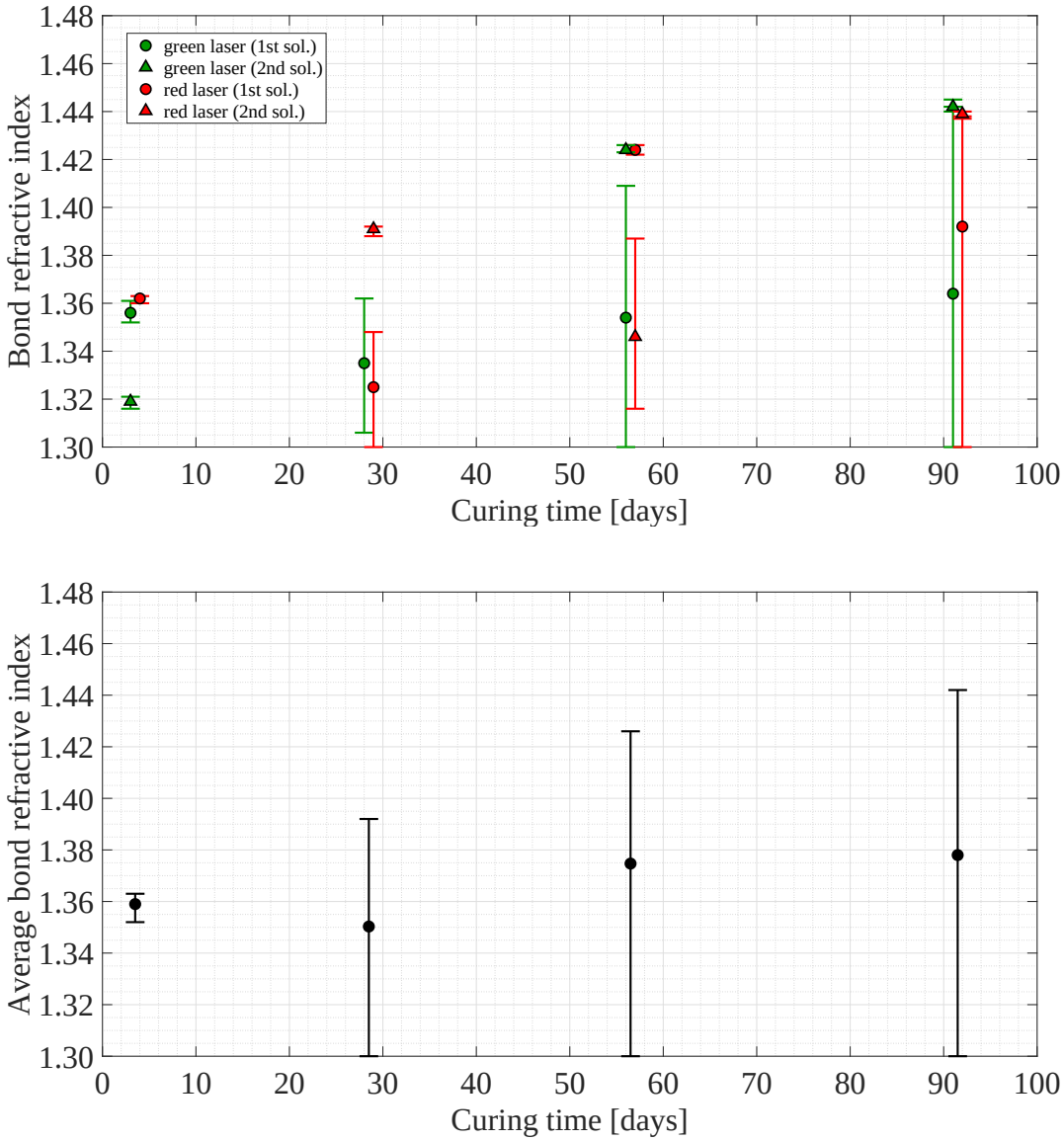

Fig. 3.46 (top) Refractive index of the bond as a function of the curing time for the central position on the front surface of Silica2$_{\mathrm{Na2SiO3(1:10)}}$. These values were determined from measurements collected using the upgraded setup in green (green dots and triangles) and red (red dots and triangles) mode. Some data sets have multiple solutions, which are presented in order from the highest to the lowest joint posterior probability density function by dots and triangles. (bottom) Average of the green and red refractive indices of which the Bayesian values have similar probability volumes. This average was calculated for each two consecutive days (the difference between green and red curing time is always one day). The error bars represent the spread of the data that was averaged.

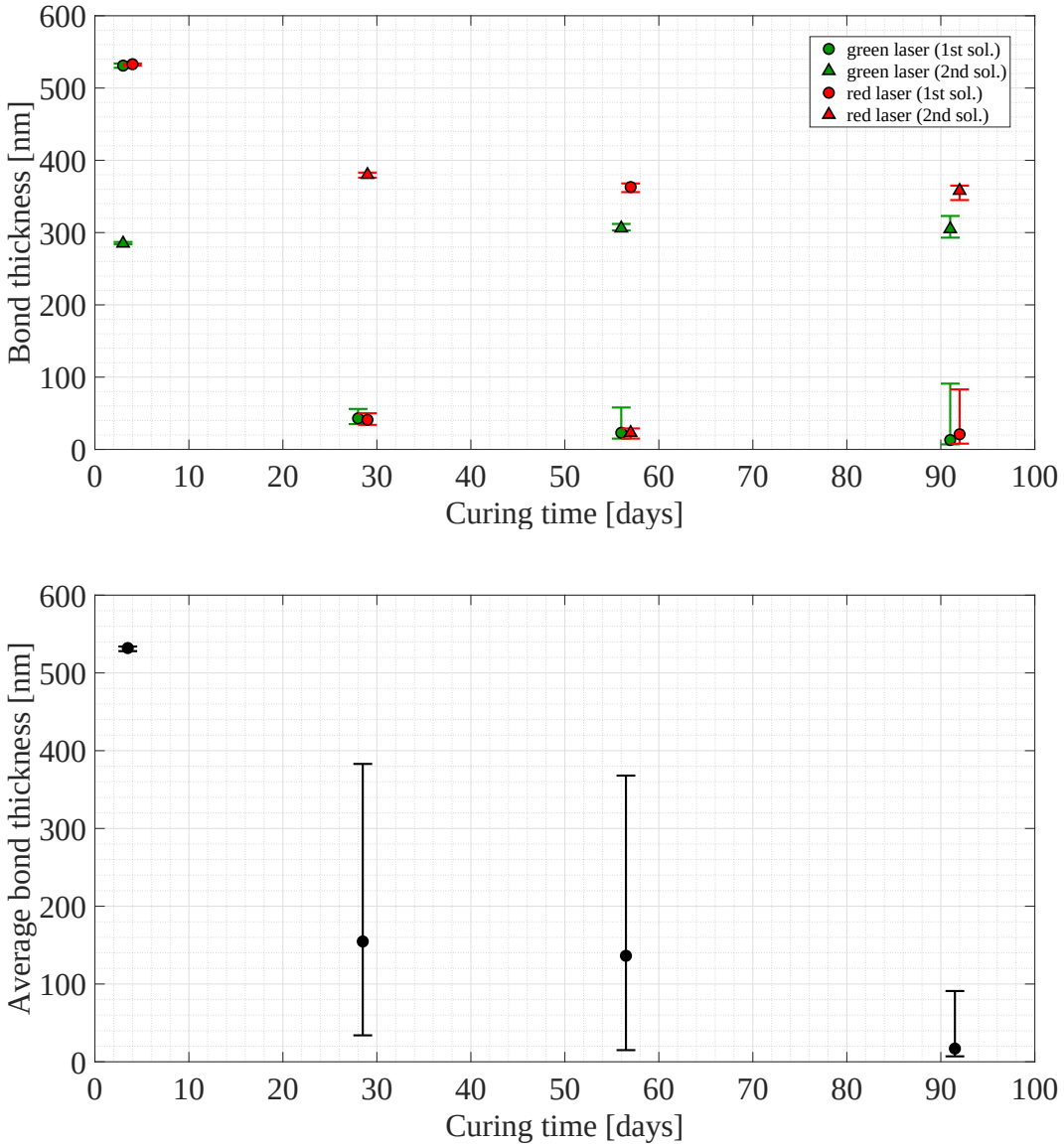

Fig. 3.47 (top) Thickness of the bond as a function of the curing time for the central position on the front surface of Silica2$_{Na2SiO3(1:10)}$. These values were determined from measurements collected using the upgraded setup in green (green dots and triangles) and red (red dots and triangles) mode. Some data sets have multiple solutions, which are presented in order from the highest to the lowest joint posterior probability density function by dots and triangles. (bottom) Average of the green and red thicknesses of which the Bayesian values have similar probability volumes. This average was calculated for each two consecutive days (the difference between green and red curing time is always one day). The error bars represent the spread of the data that was averaged.

and it is shown in the second row of Figure 3.48: the relative separation map gives a value of 63^{+3}_{-3} *nm* for the bond thickness in central position (Table 3.1).

The bond thicknesses of three slices of $\text{Silica2}_{\text{Na2SiO3(1:10)}}$ measured by SEM imaging were shown in Figure 3.49: the average bond thickness found for the centre of this sample was of (70 ± 16) *nm* after 239 days from bonding (Table 3.1).

Interestingly for this sample the thickness results using the SEM method, the flatness map and reflectance measurements agree within error (Table 3.1).

3.3.5 Analysis result: discussion

After three months of curing, the bond average refractive index reaches the value of 1.43 for $\text{Silica1}_{\text{Na2SiO3(1:10)}}$ and 1.38 for $\text{Silica2}_{\text{Na2SiO3(1:10)}}$, in agreement within their error bars. Their Bayesian bond average thicknesses are less than about 110 *nm*, in agreement with the results obtained from the SEM imaging and the flatness maps. The bond thicknesses obtained using the Bayesian, flatness and SEM methods are summarised in Table 3.1 (section 3.5).

Measurements suggest that the maximum bond reflectivity goes down more slowly and the bond refractive index goes up more slowly than the 1 : 3 and 1 : 6 sodium silicate bonds. This suggests that a more dilute solution (1 : 10) appears to slow down the evolution of the refractive index of the bonds. The thickness settles after 30 days, which is also approximately the same as for the other concentrations. It does appear that the bonds using the more dilute solution are thinner. Thinner bond thicknesses may be due to the fact that the evaporation and/or absorption in the fused silica substrate of water is more active for those bonding solutions predominantly based on water and lower in sodium silicate than for those with an abundant amount of sodium silicate.

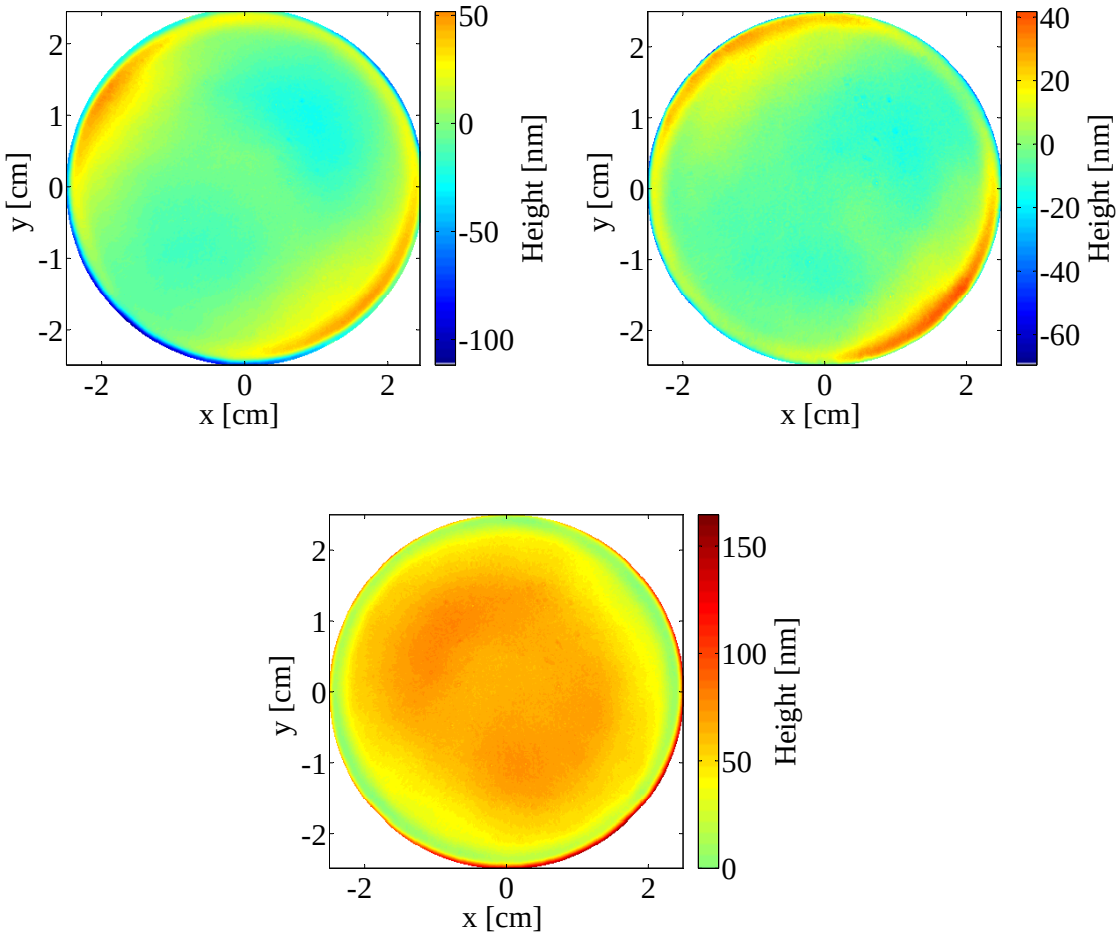

Fig. 3.48 (first row) Flatness maps of the bonding surfaces of the two discs which make $Silica2_{Na2SiO3(1:10)}$. These were obtained using the functions of the Simtools package (see Appendix E) which zoomed in on a valid area and remove various offsets from the ZYGO® maps. (second row) Relative separation between two bonding surfaces of discs bonded by hydroxide-catalysis bonding. This map was obtained using the Matlab code reported in Appendix E.

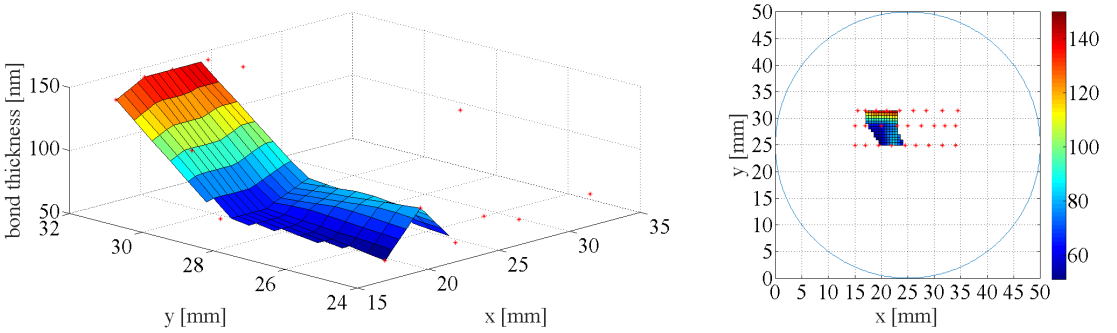

Fig. 3.49 Surface plots of the bond thicknesses measured across three slices of $\text{Silica2}_{\text{Na2SiO3(1:10)}}$, where x and y were the coordinates of the thickness measurement within the sample. The surface plots were made by linearly interpolating between measurements.

3.4 Sodium silicate bond cured at elevated temperature

Once the surfaces of two substrates are bonded together, they can be cured at room temperature. As this may be a long time for some applications, a reduction of the curing time is desired. During the curing process, water migrates or evaporates out of the bond: a heat treatment can accelerate this dehydration step and, consequently, the curing time for maximum strength can be significantly reduced, provided that the bond and substrates are not compromised (see subsection 1.5.2 for details) [4, 27, 96, 99].

Two samples were studied for this purpose: $\text{Silica}_{\text{Na2SiO3(1:6),T}}$ was made using sodium silicate solution at a volumetric ratio of 1 : 6 with de-ionised water and its data is reported in this section, and $\text{Silica}_{\text{KOH(0.1N),T}}$ was made using potassium hydroxide solution (0.1 N solution in water) without diluting it with de-ionised water and it is discussed in Chapter 4 (see subsection 4.2.1).

After bonding, these samples were left to cure in air at room temperature for one hour and then were placed inside an oven (Carbolite®, 3216) at 100 $^{\circ}C$ for eight hours. The controller of this oven allowed a program to be set which was split up into two segments, an increasing ramp and a dwell. Starting from room temperature, the oven was heated up at a speed of 3 $^{\circ}C/min$. Once it reached the temperature of 100 $^{\circ}C$, the oven kept this temperature for eight hours. After this time, the oven was turned off and the samples left inside the oven (without opening its door) to cool slowly. The reflectivity of their bonds was measured the following day using the upgraded assembly in green and red laser light.

This curing method was chosen on the basis of results published by Kim [96] and Green [99].
Kim studied the influence of curing time on shear strength for glass-glass bonds produced using sodium silicate solution to de-ionised water. Kim found that the bond strength increased both with extended curing times and with elevated curing temperatures. The bond strength of the samples cured only at room temperature increased with curing time and its maximum was achieved after four weeks. The same shear strength was obtained for a curing time of 24 hours at room temperature followed by one hour at 100 $^{\circ}C$ [96].
Green studied the breaking stresses of Zerodur^{TM} samples bonded using hydroxide solutions (like KOH and NaOH) and silicate solutions. These samples were baked to accelerate the curing process and study its behaviour when different times or temperatures of baking were used. Green used different temperatures for fixed time of baking (temperature as potential substitute for time) and different times of baking for fixed temperature (time as potential substitute for elevated temperature). Precisely, the Zerodur^{TM} samples bonded with hydroxide solutions were baked at 100 $^{\circ}C$ for 24 hours, 200 $^{\circ}C$ for 24 hours and 100 $^{\circ}C$ for seven days, whereas those ones bonded using silicate solution were baked at 100 $^{\circ}C$ for 48 hours and for seven days. Green found that a heat treatment shortened the time needed for the bond to reach full strength and increased the bond strength compared to that of the bonds cured at room temperature [99].
To accelerate the curing of a bond by increasing the reaction rate, the author decided to bake the samples at the same temperature that was chosen by Kim and Green equalling 100 $^{\circ}C$ (the higher the temperature, the faster reaction rate is). Eight hours of baking should be a sufficient time for the reactions to go to completion.

3.4.1 Silica$_{Na2SiO3(1:6),T}$

Sample Silica$_{Na2SiO3(1:6),T}$ was made by bonding two fused silica discs with 15.70 μl of solution composed of 2 ml of sodium silicate solution with 12 ml of de-ionised water (a volumetric ratio of 1 : 6).

3.4.2 Reflectivity measurements

The reflectivity of this sample was measured for the central position on its front surface at three different curing times, respectively, the following day, about one and two months after bonding. Thanks to these measurements, the effect of curing time on the refractive index and thickness of the bond could be studied.

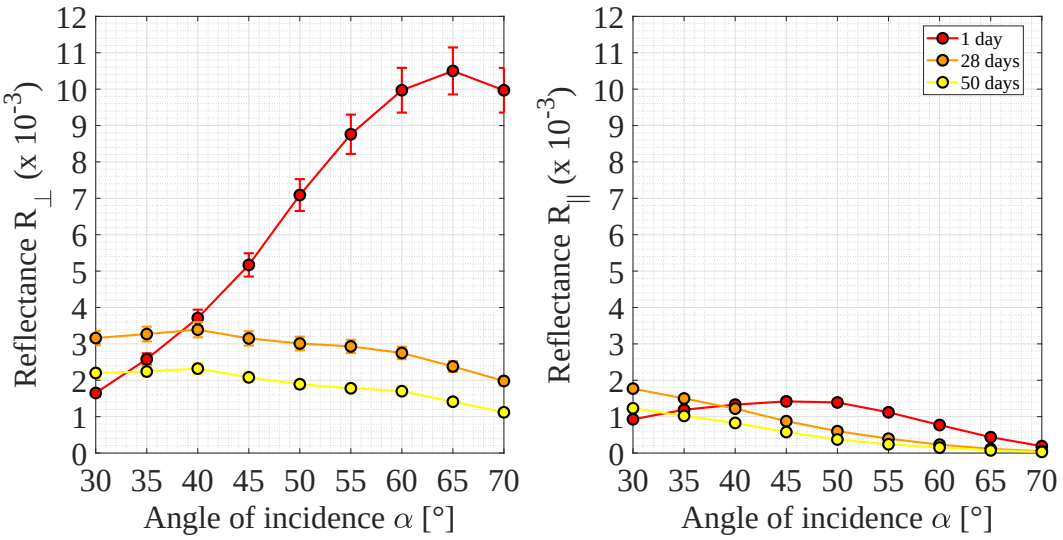

Fig. 3.50 Measured reflectances for $\perp$ (left) and $\parallel$ (right) polarisation plotted as a function of the angle of incidence α for the central position on the front surface of $\text{Silica}_{\text{Na2SiO3(1:6),T}}$. In the legend, the curing time is reported. All measurements were taken using the upgraded setup in green mode.

Plots of measured reflectivity for perpendicular ($\perp$) and parallel ($\parallel$) polarisations (equations 2.1 and 2.2) as a function of angle of incidence α are shown in Figure 3.50 ($\text{Silica}_{\text{Na2SiO3(1:6),T}}$ in green mode) and Figure 3.51 ($\text{Silica}_{\text{Na2SiO3(1:6),T}}$ in red mode).

For both polarisations and colours of laser light, the values of bond reflectances are all less than 1% and they decrease as the curing time increases.

3.4.3 Analysis result: reflectivity

In Figure 3.52, the peak reflectivity of the bond for both polarisations and laser light colours is plotted as a function of curing time for $\text{Silica}_{\text{Na2SiO3(1:6),T}}$. The reflectance values decrease as curing time increases. It should be noted that this drop is significantly less than that of the room temperature cured sample $\text{Silica2}_{\text{Na2SiO3(1:6)}}$. Where that dropped to about 0.1% (0.02%) after about two months, for the sample cured at elevated temperature the reflectance is still about 0.2% (0.1%) for perpendicular (parallel) polarisation of light.

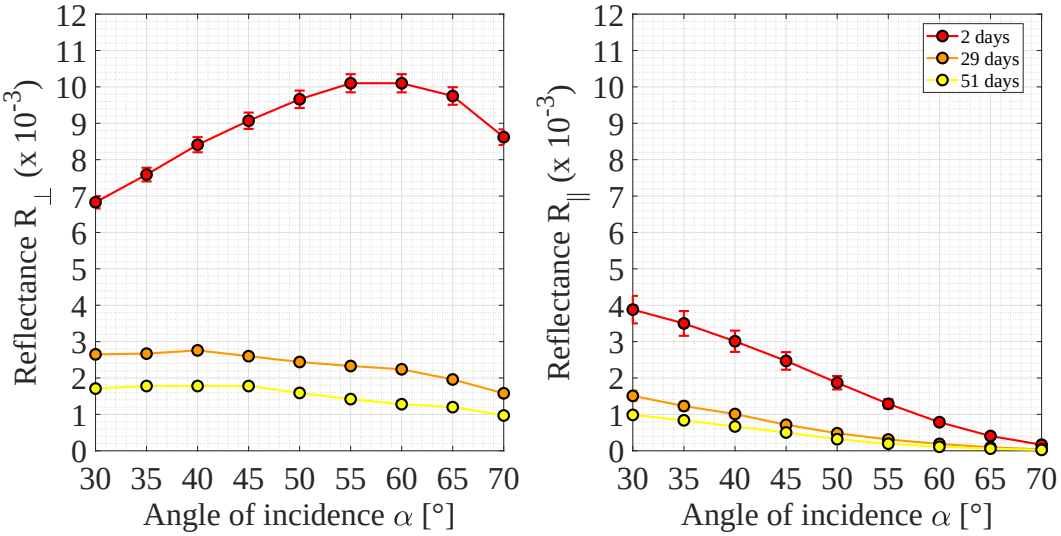

Fig. 3.51 Measured reflectances for ⊥ (left) and ∥ (right) polarisation plotted as a function of the angle of incidence α for the central position on the front surface of $\text{Silica}_{\text{Na2SiO3(1:6),T}}$. In the legend, the curing time is reported. All measurements were taken using the upgraded setup in red mode.

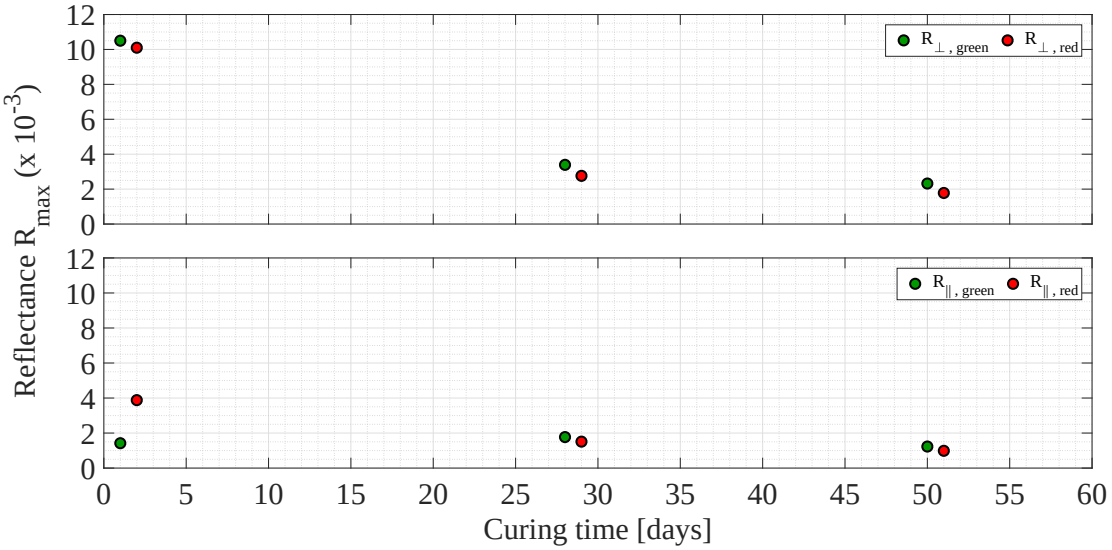

Fig. 3.52 Maximum value of measured reflectances for ⊥ (top) and ∥ (bottom) polarisation plotted as a function of the curing time for the central position on the front surface of $\text{Silica}_{\text{Na2SiO3(1:6),T}}$ and for green and red laser light. Measurements were taken using the upgraded assembly.

3.4.4 Analysis result: refractive index and thickness

Figure 3.53 and Figure 3.54, and Figure 3.55 show three examples of the results obtained from the Matlab script for sample $\text{Silica}_{\text{Na2SiO3(1:6),T}}$ in green mode after 1 day (first and second solution), and in red mode after 2 days, respectively. The measurements in Figure 3.53 and Figure 3.54 were taken in the early phase of curing (precisely the next day after bonding) and for this reason the values may change over the time it takes to move from one angle of incidence to another one. This effect may be particularly significant at low or high angles of incidence where the three reflected spots are close each other.

In the top of Figure 3.56 and Figure 3.57, the bond refractive index and thickness for $\text{Silica}_{\text{Na2SiO3(1:6),T}}$ are plotted as a function of the curing time for both green and red laser light.

In the bottom of these figures the time averages of the green and red bond refractive indices and thicknesses, of which the Bayesian values had similar probability volumes, are shown. The bond average refractive index is 1.34 and close to 1.40 (which is 0.01 to 0.02 lower than the room temperature cured samples) at 1/2 and 50/51 days after bonding, respectively. The bond average thickness obtained by the Bayesian analysis is 337^{+34}_{-37} *nm* after 50/51 days (Table 3.1).

The bonding surfaces of the two discs of $\text{Silica}_{\text{Na2SiO3(1:6),T}}$ had a flatness of about 70 *nm* and 106 *nm* peak-to-valley respectively, which was measured using the ZYGO®. The flatness maps shown in the first row of Figure 3.58 were obtained for the two discs. Combining these maps, the relative separation between two bonding surfaces was obtained and it is shown in the second row of Figure 3.58: the relative separation map gives a value of 128^{+4}_{-4} *nm* for the bond thickness in central position (Table 3.1).

For the SEM imaging, four slices were cut from sample $\text{Silica}_{\text{Na2SiO3(1:6),T}}$ and the results of these measurements were shown in Figure 3.59: SEM measurements of the centre of the sample gave an average of (35 ± 11) *nm* after 237 days from bonding (Table 3.1).

For this sample, the bond thickness results obtained using these three methods gave different values, with as usual the SEM measurements giving the smallest value for the bond thickness.

3.4.5 Analysis result: discussion

In contrast to results found for the other samples studied, the bond thickness of sample $\text{Silica}_{\text{Na2SiO3(1:6),T}}$ does not decrease rapidly in the first days after bonding, but it seems to increase and approach a constant value over time. Also, the bond thickness values from the

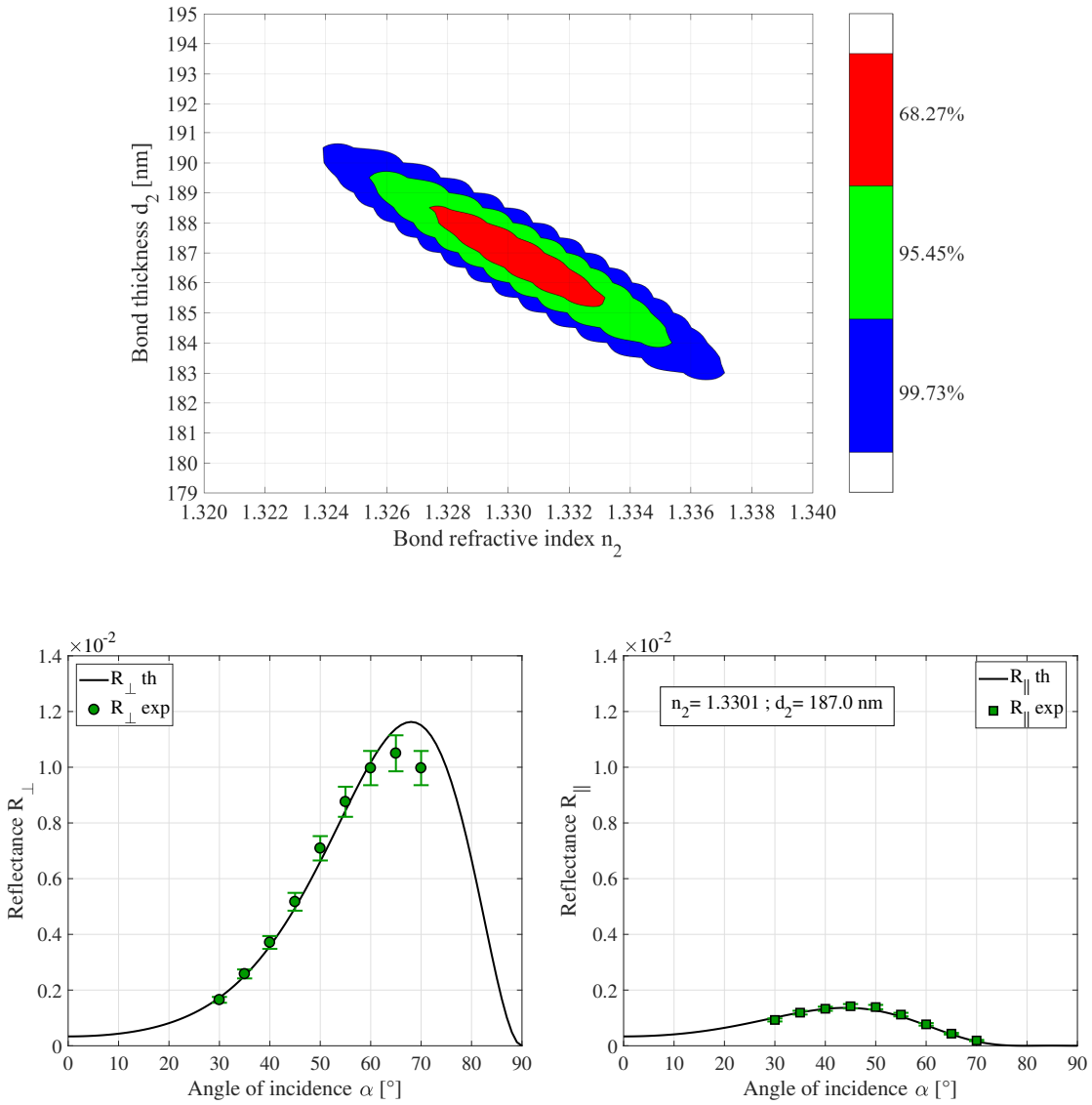

Fig. 3.53 (top) Three confidence levels of 68.3%, 95.5% and 99.7% probability. (bottom) Measured data with their corresponding error bars and theoretical curves. The green dots and squares represent the reflectances measured for perpendicular and parallel polarisation, respectively. The black solid lines are the theoretical perpendicular and parallel reflectances obtained using the first solution of bond refractive index and thickness of the Bayesian analysis ($n_2 = 1.3301$ and $d_2 = 187.0$). These measurements were taken at 1 day after bonding for $\text{Silica}_{\text{Na2SiO3(1:6),T}}$ in green light.

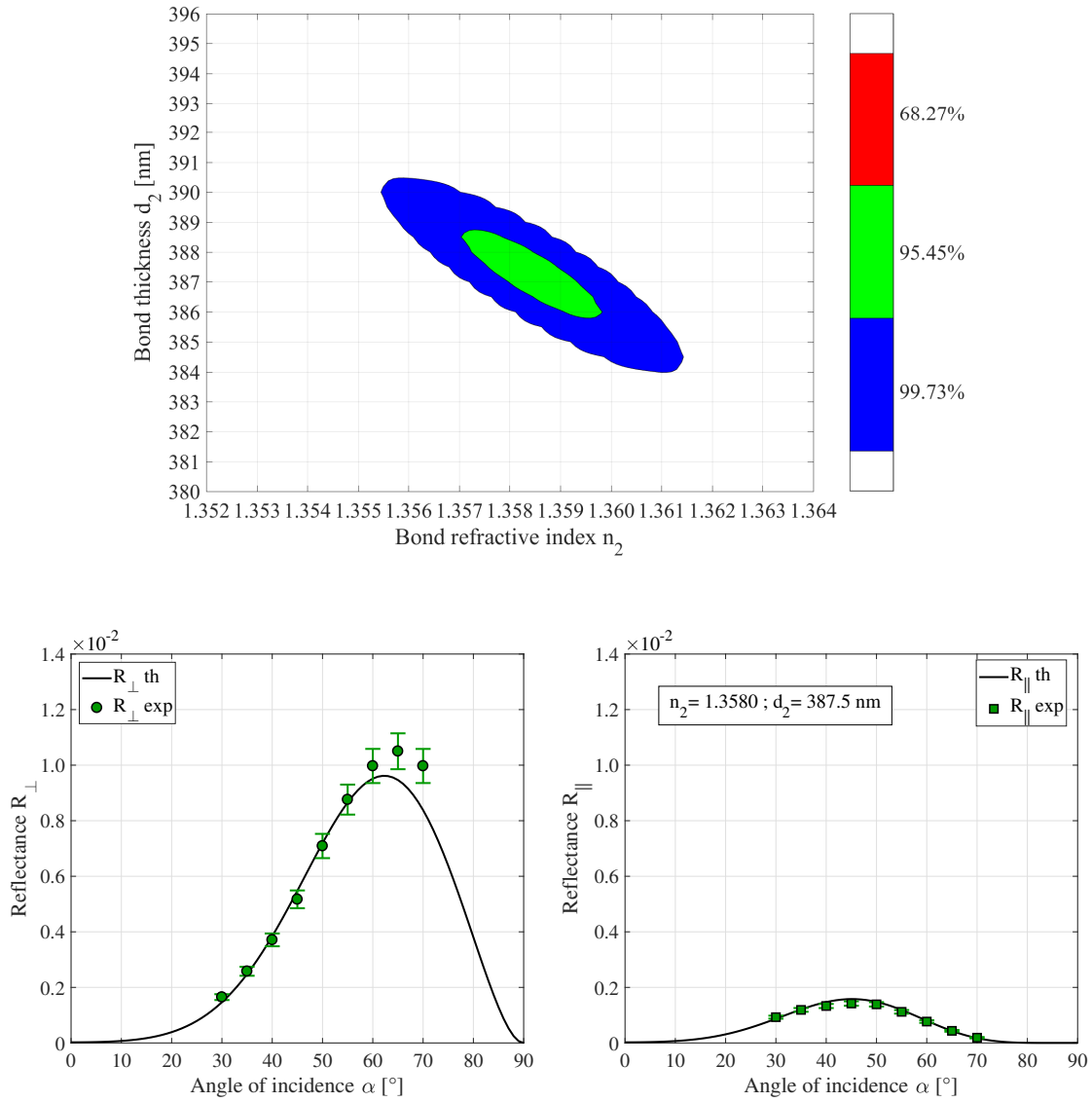

Fig. 3.54 (top) Three confidence levels of 68.3%, 95.5% and 99.7% probability. (bottom) Measured data with their corresponding error bars and theoretical curves. The green dots and squares represent the reflectances measured for perpendicular and parallel polarisation, respectively. The black solid lines are the theoretical perpendicular and parallel reflectances obtained using the second solution of bond refractive index and thickness of the Bayesian analysis ($n_2 = 1.3580$ and $d_2 = 387.5$). These measurements were taken at 1 day after bonding for $\text{Silica}_{\text{Na2SiO3(1:6),T}}$ in green light.

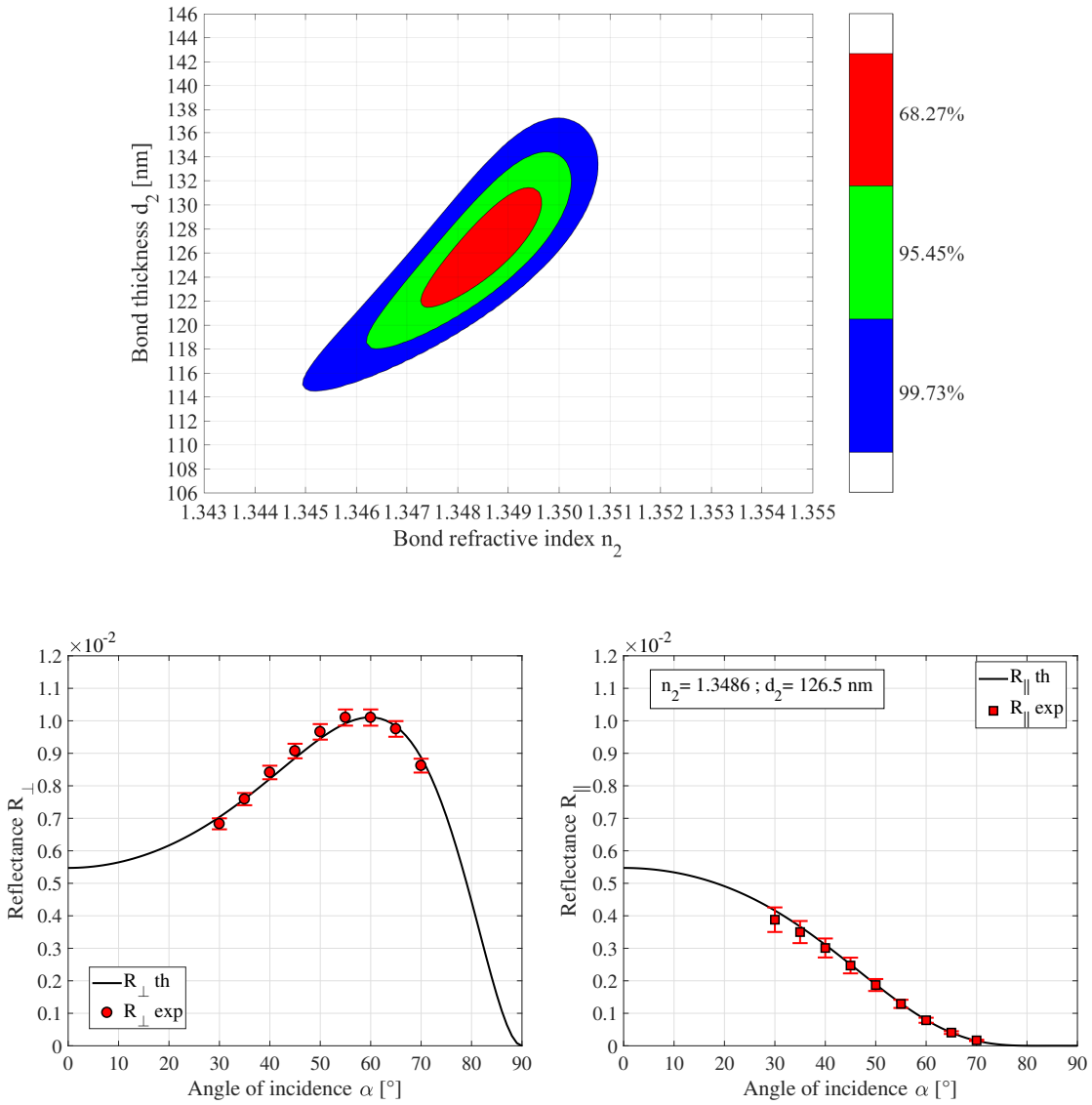

Fig. 3.55 (top) Three confidence levels of 68.3%, 95.5% and 99.7% probability. (bottom) Measured data with their corresponding error bars and theoretical curves. The red dots and squares represent the reflectances measured for perpendicular and parallel polarisation, respectively. The black solid lines are the theoretical perpendicular and parallel reflectances obtained using the most likely values of bond refractive index and thickness of the Bayesian analysis ($n_2 = 1.3486$ and $d_2 = 126.5$). These measurements were taken at 2 days after bonding for $\text{Silica}_{\text{Na2SiO3(1:6),T}}$ in red light.

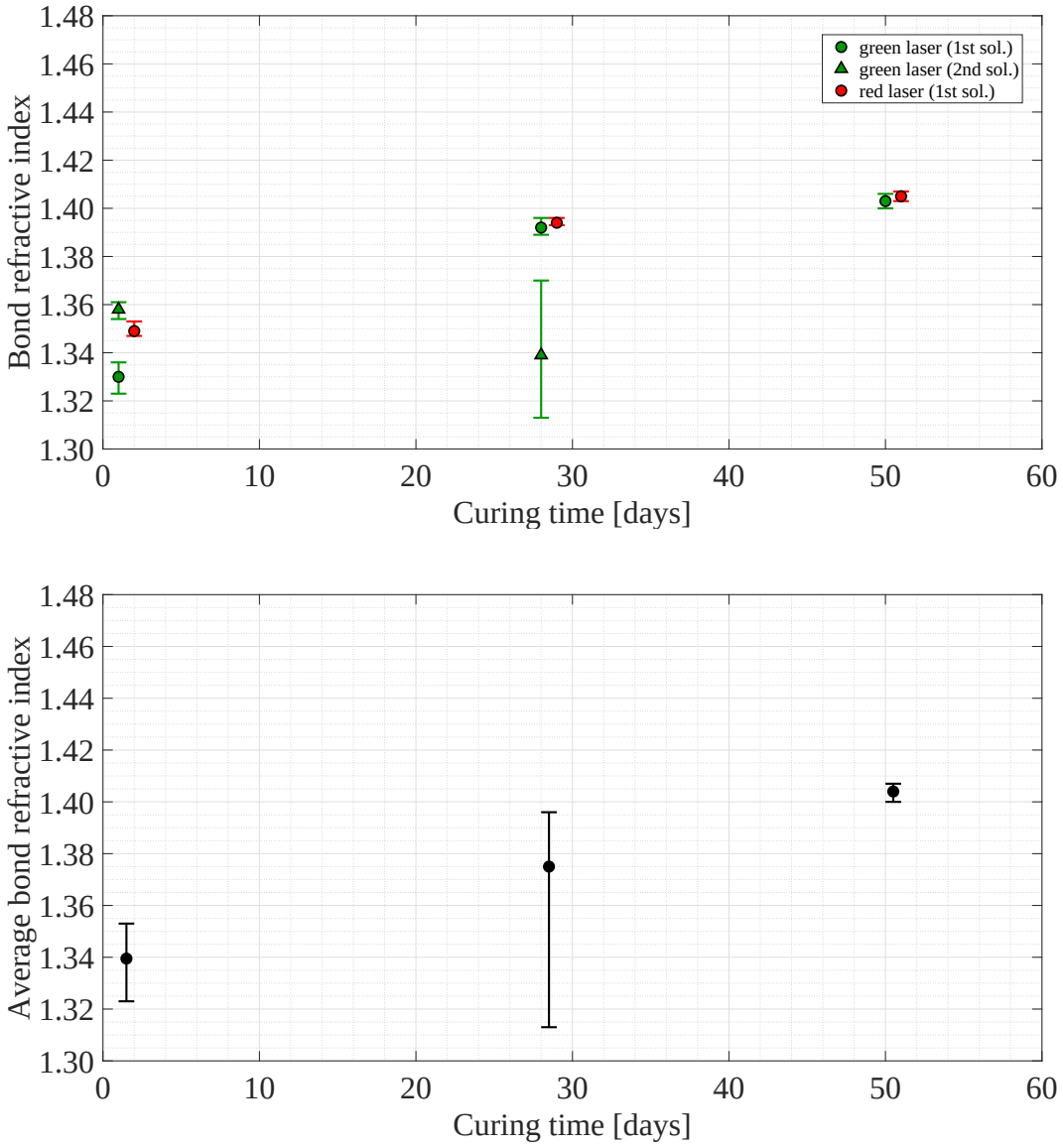

Fig. 3.56 (top) Refractive index of the bond as a function of the curing time for the central position on the front surface of $\text{Silica}_{\text{Na2SiO3(1:6),T}}$. These values were determined from measurements collected using the upgraded setup in green (green dots and triangles) and red (red dots) mode. Some data sets have multiple solutions, which are presented in order from the highest to the lowest joint posterior probability density function by dots and triangles. (bottom) Average of the green and red refractive indices of which the Bayesian values have similar probability volumes. This average was calculated for each two consecutive days (the difference between green and red curing time is always one day). The error bars represent the spread of the data that was averaged.

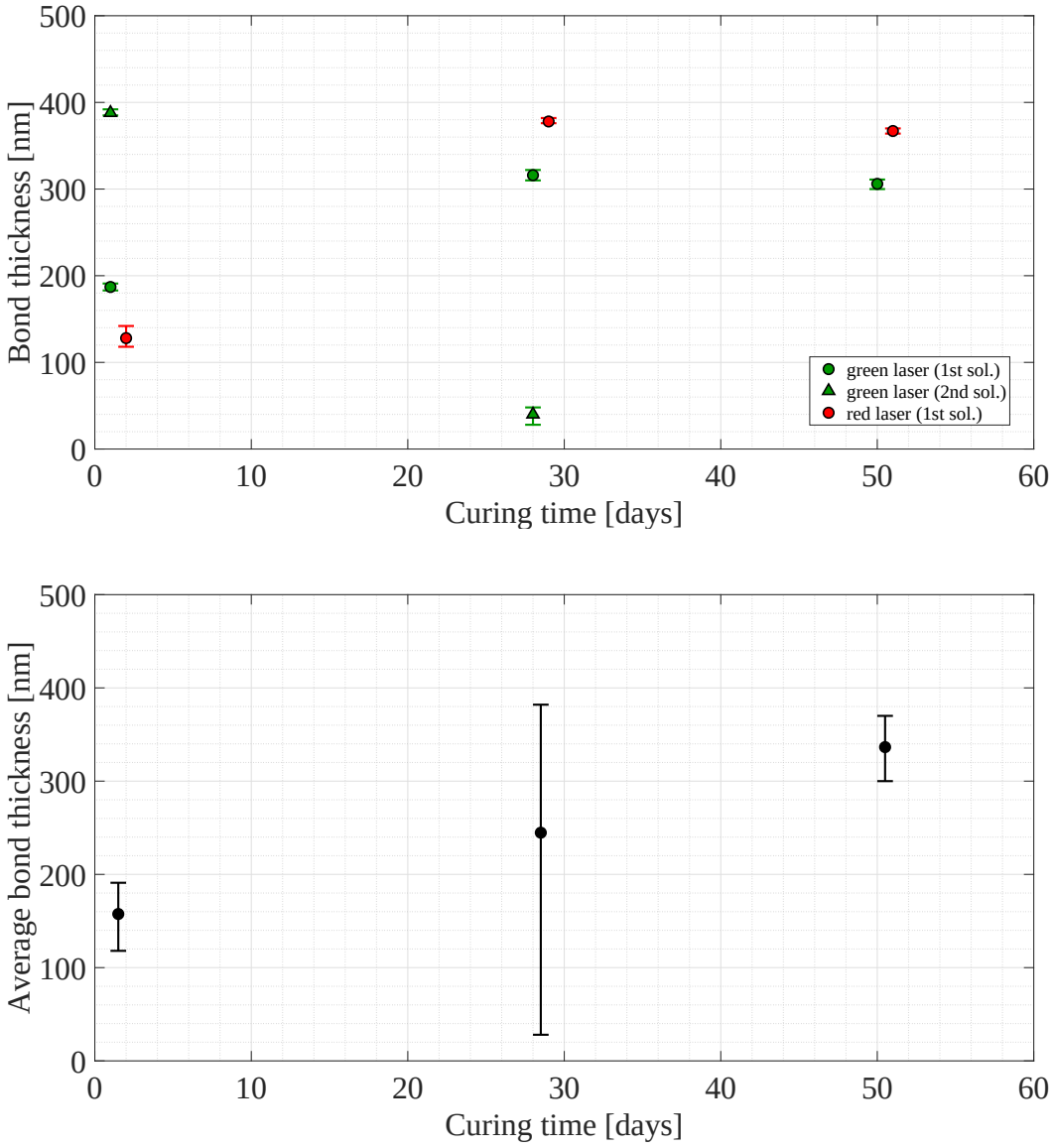

Fig. 3.57 (top) Thickness of the bond as a function of the curing time for the central position on the front surface of $\text{Silica}_{\text{Na2SiO3(1:6),T}}$. These values were determined from measurements collected using the upgraded setup in green (green dots and triangles) and red (red dots) mode. Some data sets have multiple solutions, which are presented in order from the highest to the lowest joint posterior probability density function by dots and triangles. (bottom) Average of the green and red thicknesses of which the Bayesian values have similar probability volumes. This average was calculated for each two consecutive days (the difference between green and red curing time is always one day). The error bars represent the spread of the data that was averaged.

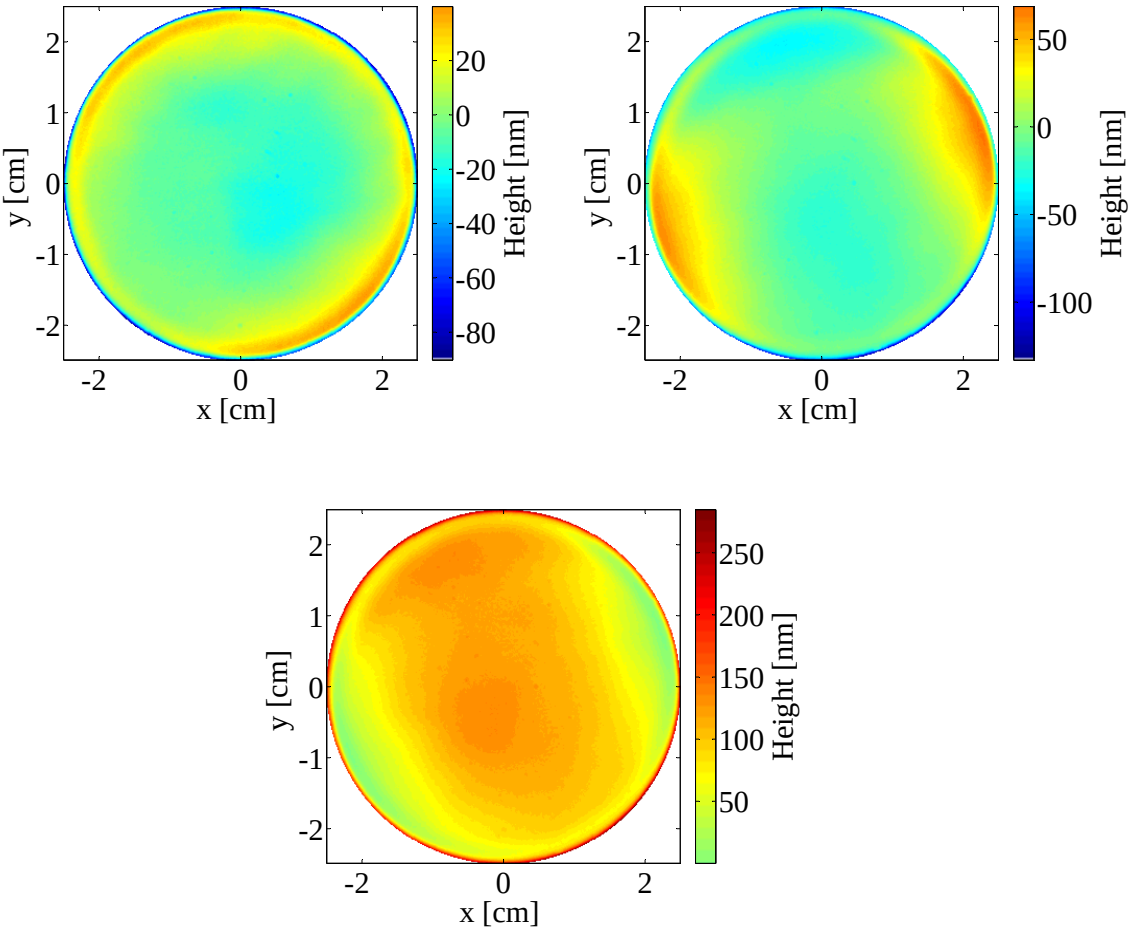

Fig. 3.58 (first row) Flatness maps of the bonding surfaces of the two discs which make $\text{Silica}_{\text{Na2SiO3(1:6),T}}$. These were obtained using the functions of the Simtools package (see Appendix E) which zoomed in on a valid area and remove various offsets from the ZYGO® maps. (second row) Relative separation between two bonding surfaces of discs bonded by hydroxide-catalysis bonding. This map was obtained using the Matlab code reported in Appendix E.

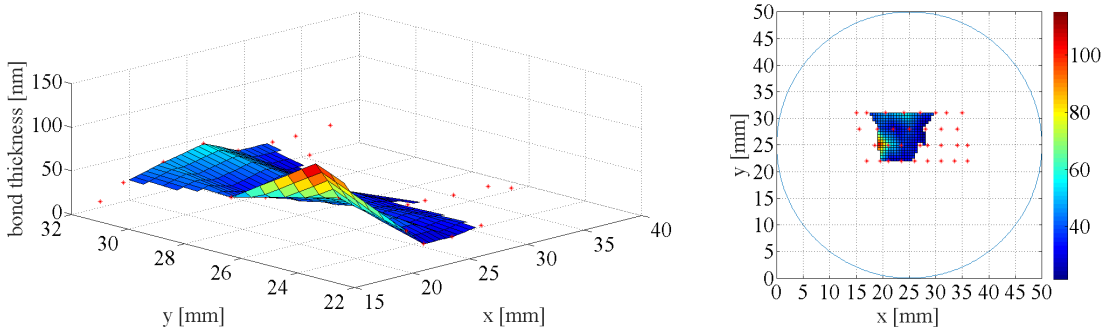

Fig. 3.59 Surface plots of the bond thicknesses measured across four slices of $\text{Silica}_{\text{Na2SiO3(1:6),T}}$, where x and y were the coordinates of the thickness measurement within the sample. The surface plots were made by linearly interpolating between measurements.

Bayesian analysis are much greater than those measured using the flatness maps or the SEM imaging (Table 3.1). These results suggest that this specific elevated temperature cure may have interrupted normal curing chemistry and impacted the evolution of the bond properties.

The use of elevated temperature has previously been shown in the literature to increase the bond strength [96, 99, 102]. There may be a correlation between the strength and thickness of a bond, where both increase as the curing temperature increases. This suggests further investigation would be necessary if elevated curing temperatures were to be used in creating bonds intended for use in optical applications.

3.5 Summary

The measurements of reflectivity, together with the theoretical model and Matlab script based on the Bayesian analysis, have allowed information to be gained not only on the intensity of the light that is reflected from a bonded interface, but also on the refractive index and thickness of hydroxide-catalysis bonds.

In this chapter the reflectances from the bonded interfaces between pairs of fused silica discs, jointed using sodium silicate solution at three different concentrations (1 : 6, 1 : 3 and 1 : 10) and cured at room or elevated temperatures, were investigated. For the curing at room temperature, two samples were bonded and made nominally identical for each concentration, whereas only one sample was bonded for the curing at elevated temperature.

The levels of reflectivity found here were very low decreasing to less than 1×10^{-3}. This was in agreement with the value obtained by Sinha [48]: he measured reflections

from a hydroxide-catalysis bond at normal incidence between fused silica parts to be less than 7.08×10^{-4}.

Even though some variation in values was found, the time evolution of the bond peak reflectivity of all the samples studied in this chapter broadly fit an exponential curve through the data. The changes of reflectivity with time are closely related to the variations of the refractive index and thickness of the bond that occur as the bonding solution gradually cures: this suggests that as the bond refractive index approaches that of the fused silica, the bond reflectivity becomes low.

For all the samples studied in this chapter, the bond refractive index trend as a function of the time had a clear behaviour: as the curing time increased, the bond refractive index increased. This was in agreement with logical expectations of hydroxide-catalysis bonding. The refractive index was shown to be greater than the refractive index of water 1.30 (a lower limit based on the composition of the bonding solution) and approached with time the refractive index of fused silica (1.4607 for green light and 1.4570 for red light [82]). The refractive index of the bonding solution (at the time of bonding) was measured to be 1.34 ± 0.01 (using minimum deviation refractometry [103]), which is just below the value found for the first days of curing for all the samples cured at room temperature (about 1.36), and in agreement with the starting value of $\text{Silica}_{\text{Na2SiO3(1:6),T}}$ cured at elevated temperature. The rate of increase of the refractive index of these samples is very similar (though that of the 1 : 10 solution samples is slightly lower) and this may suggest that, within the parameters considered here, the concentration of the solution or the temperature used for curing do not significantly influence the evolution of the refractive index of the bonds.

The optical bond thickness was shown to decrease rapidly in the first four weeks, to then approach a constant value. $\text{Silica}_{\text{Na2SiO3(1:6),T}}$ was the only case where the bond thickness did not decrease rapidly in the first days after bonding but increased as a function of the curing time. This may suggest that the elevated temperature used for curing affected the chemistry of the hydroxide-catalysis solution. A summary of results of the bond thickness obtained from flatness maps, Bayesian analysis and SEM imagining for the samples studied in this chapter is shown in Table 3.1. In general, the Bayesian bond thickness values found differed significantly from those of the flatness maps or SEM imaging. As the SEM images were taken more than a year after the last reflectance measurements, the thickness discrepancy between SEM images and reflectance measurements (where the SEM results gave overall lower thickness than the reflectance results) may be explained by reduction of thickness over time. The bonds may continue to reduce in thickness over periods longer than 100 days and their final thicknesses may not coincide necessarily with the relative separation between two

bonding surfaces of substrates. Another factor could be the result of preferential etching of the bond material by the alkali polishing compound used in sample preparation, which could result in an apparently thinner bond layer. The variation of concentration appeared to have an impact on the values of the bond thickness cured at room temperature. The samples made using 1 : 3 solution seemed to have a thickness greater than the 1 : 6 solution samples, which were in turn thicker than the 1 : 10 solution samples. This may suggest that a solution predominantly based on water and lower in sodium silicate (like 1 : 10 solution) gives the smallest thickness for a bond.

Name of sample	Location	Flatness maps	Optical reflectivity		SEM imaging	
		d (nm)	d (nm)	t_c (days)	d (nm)	t_c (days)
$\text{Silica1}_{\text{Na2SiO3(1:6)}}$	L	84^{+3}_{-3}	297^{+4}_{-5}	98	44^{+9}_{-9}	978
	C	83^{+3}_{-3}	134^{+14}_{-18}	98	34^{+10}_{-10}	978
	R	101^{+5}_{-5}	78^{+28}_{-67}	98	82^{+24}_{-24}	978
$\text{Silica2}_{\text{Na2SiO3(1:6)}}$	C	63^{+15}_{-15}	173^{+11}_{-18}	104.5	-	-
$\text{Silica1}_{\text{Na2SiO3(1:3)}}$	C	80^{+4}_{-4}	155^{+19}_{-26}	91.5	110^{+15}_{-15}	288
$\text{Silica2}_{\text{Na2SiO3(1:3)}}$	C	95^{+3}_{-3}	473^{+271}_{-267}	92	-	-
$\text{Silica1}_{\text{Na2SiO3(1:10)}}$	C	97^{+4}_{-4}	51^{+62}_{-43}	91.5	47^{+9}_{-9}	304
$\text{Silica2}_{\text{Na2SiO3(1:10)}}$	C	63^{+3}_{-3}	17^{+74}_{-10}	91.5	70^{+16}_{-16}	239
$\text{Silica}_{\text{Na2SiO3(1:6),T}}$	C	128^{+4}_{-4}	337^{+34}_{-37}	50.5	35^{+11}_{-11}	237

Table 3.1 Summary of bond thicknesses d obtained using three different methods: the relative separation map (third column), the Bayesian analysis of reflectivity measurements (fourth column), and SEM imaging (fifth column). In the Bayesian analysis column, for $\text{Silica1}_{\text{Na2SiO3(1:6)}}$ the thicknesses obtained using the initial setup in green mode were considered, whereas for the other samples the average of the green and red thicknesses was reported. Location on the front surface of sample (L, C and R) and curing time (t_c) expressed in days were also reported.

The effects of the heat treatment on the bond reflectivity of $\text{Silica}_{\text{Na2SiO3(1:6),T}}$ were reported for a bond made using sodium silicate solution at a volumetric ratio of 1 : 6 with de-ionised water. An accelerated curing approach was proposed to understand if the bond

refractive index and thickness responded in an accelerated way as well. One hour after bonding the sample was heated up to 100 $^{\circ}C$ and held there for 8 hours and then allowed to cool. This elevated curing did not apparently harm the visual bond quality, but could have changed the chemistry of the hydroxide-catalysis bonding. The initial bond reflectivity values found were similar to those of $\text{Silica1}_{\text{Na2SiO3(1:6)}}$ and $\text{Silica2}_{\text{Na2SiO3(1:6)}}$ (which had not been heat treated), but the reflectivity reduced more slowly, which is consistent with a slower increase of bond refractive index. The trend of decreasing bond thickness with curing time observed for non-heat-treated sample however was absent for the heat-treated sample, although the refractive index for the heat-treated bond did show some increase with curing time.

For $\text{Silica1}_{\text{Na2SiO3(1:6)}}$ and $\text{Silica2}_{\text{Na2SiO3(1:6)}}$ it was possible to compare the bond tensile strength with the bond thickness. Both decrease as a function of curing time with similar time constant and this suggests that there may be a correlation between the optical reflectivity and strength of a bond. Phelps [100] proposed that the decrease in strength was due to the reduction of water in the bond. It is possible that the water is mainly absorbed by the silica and that some may evaporate from the edge of the bond.

For sample $\text{Silica}_{\text{Na2SiO3(1:6),T}}$, the results suggest that a heat treatment may cause an increase of thickness of the bond over curing time. If a correlation between the tensile strength and thickness of a bond holds, this may suggest that the heat treatment also results in an increase of the strength of bond. This is in broad agreement with the results obtained by Haughian et al. [102], though it should be noted that the heat treatment used was different from that used in this thesis (48 hours at 150 $^{\circ}C$ after four weeks of curing at room temperature against 8 hours at 100 $^{\circ}C$ shortly after bonding). Haughian et al. found that heat treatment bonds at 150 $^{\circ}C$ for 48 hours increased the bond strength significantly, while it seems counterintuitive that heating can increase bond thickness, since simplistically the thickness would be determined by the number of SiO_2 molecules in bonding solution. It is however possible that heating changes the chemistry leading to water molecules being firmly bound in the resulting solgel.

Chapter 4

Measurements on fused silica samples bonded with potassium hydroxide

The study of the properties of hydroxide-catalysis bonds between two fused silica discs was focused not only on sodium silicate solution at different concentrations with de-ionised water at room or elevated temperatures, but also on potassium hydroxide solution. Investigating different chemical bonding solutions allows an understanding of how the properties of hydroxide-catalysis bond vary and, consequently, can be tailored to various utilisations of interest.

In the first part of this chapter, the properties of KOH bonds cured in air at room temperature after bonding were investigated and two samples were made for this purpose (see section 4.1).
In the second part, the properties of one KOH bond cured at elevated temperatures (at 100 $^{\circ}C$ for 8 hours) were studied (see section 4.2).

The bond reflectivity of these samples was measured and the results were analysed for different curing times after bonding using the upgraded setup in green and red laser light (Figure 2.5). For details of the bonding solutions and samples used, see section 2.4.

4.1 KOH bonds cured at room temperature

Together with sodium silicate solution, potassium hydroxide is another hydroxide solution commonly used for bonding [3, 4, 19].

It was chosen as the jointing technique for the Gravity Probe B mission (see subsection 'Gravity Probe B' in section 1.5.3 for details), where the bonds between fused silica substrates were made using potassium hydroxide at a molecular ratio of 1 : 500 with de-ionised water [4,

14, 16, 19]. Also, potassium hydroxide solution was used to bond different materials (like fused silica, sapphire and silicon) to each other in order to study the properties of bonds, like mechanical strength and thickness (see subsection 1.5.2 for details) [19].

Studying the optical properties of bonds (such as the reflectivity) obtained using potassium hydroxide solution gives a more complete picture of the situation and a better understanding of the hydroxide-catalysis bonds.

In this section the properties of two bonds cured at room temperature are reported.

4.1.1 Silica1$_{\mathbf{KOH(0.1N)}}$ and Silica2$_{\mathbf{KOH(0.1N)}}$

Samples Silica1$_{\mathrm{KOH(0.1N)}}$ and Silica2$_{\mathrm{KOH(0.1N)}}$ were made nominally identical bonding two fused silica discs with 15.70 μl of potassium hydroxide solution KOH. It was composed of 0.1 N solution in water (molecular ratio of 1 : 500) and was used without diluting it with de-ionised water. These samples were then left to cure in air at room temperature for some days before measuring the reflectivity of their bonds.

4.1.2 Reflectivity measurements

The bond reflectivity of Silica1$_{\mathrm{KOH(0.1N)}}$ and Silica2$_{\mathrm{KOH(0.1N)}}$ was measured for the central position on their front surface at three different times after bonding.

Plots of measured reflectivity for perpendicular ($\perp$) and parallel ($\parallel$) polarisations (equations 2.1 and 2.2) as a function of angle of incidence α are shown in Figure 4.1 (Silica1$_{\mathrm{KOH(0.1N)}}$ in green mode), Figure 4.2 (Silica1$_{\mathrm{KOH(0.1N)}}$ in red mode), Figure 4.3 (Silica2$_{\mathrm{KOH(0.1N)}}$ in green mode) and Figure 4.4 (Silica2$_{\mathrm{KOH(0.1N)}}$ in red mode).
In Figure 4.1, Figure 4.2 and Figure 4.3, the reflectances for the parallel polarisation at about one month after bonding were not measured.
It was not always possible to detect the profile of the beam reflected off the bond layer between the two profiles of the front and back beams. This was because the reflectance of the bond spot was lower than level of reflectivity defined by the tails of the front and back profiles. For these cases, measurements of the minimum reflectance of the tails between the front and back spots were reported. In Figure 4.1, Figure 4.2, Figure 4.3 and Figure 4.4, the values of the reflectance peaks for the bond spot are indicated by the dots, whereas the downward-pointing triangles are used for the values at the lowest point of the tails of the reflectance between the front and back spots.

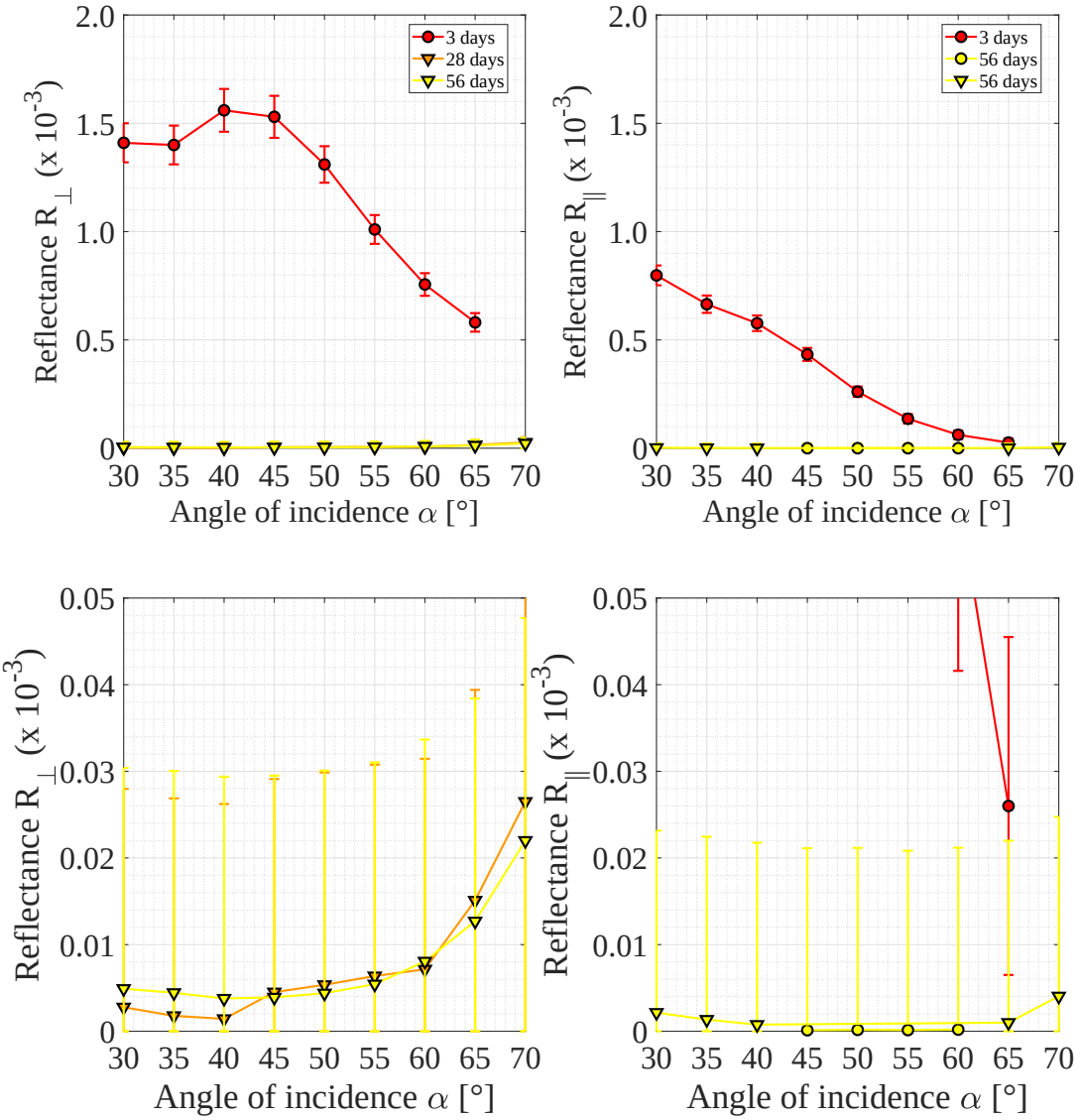

Fig. 4.1 Measured reflectances for $\perp$ (top left) and $\parallel$ (top right) polarisation plotted as a function of the angle of incidence α for the central position on the front surface of $\text{Silica1}_{\text{KOH(0.1N)}}$. Zooms in of the measured reflectances for $\perp$ (bottom left) and $\parallel$ (bottom right) polarisation are also shown to allow the reader to see the lower reflectances. In the legend, the curing time is reported: the dots indicate that the reflectance was measured at the peak of the bond profile, the downward-pointing triangles show the values of the minimum reflectance of the tails between the front and back profile (the reflectance of the bond is lower than the value of this threshold). All measurements were taken using the upgraded setup in green mode.

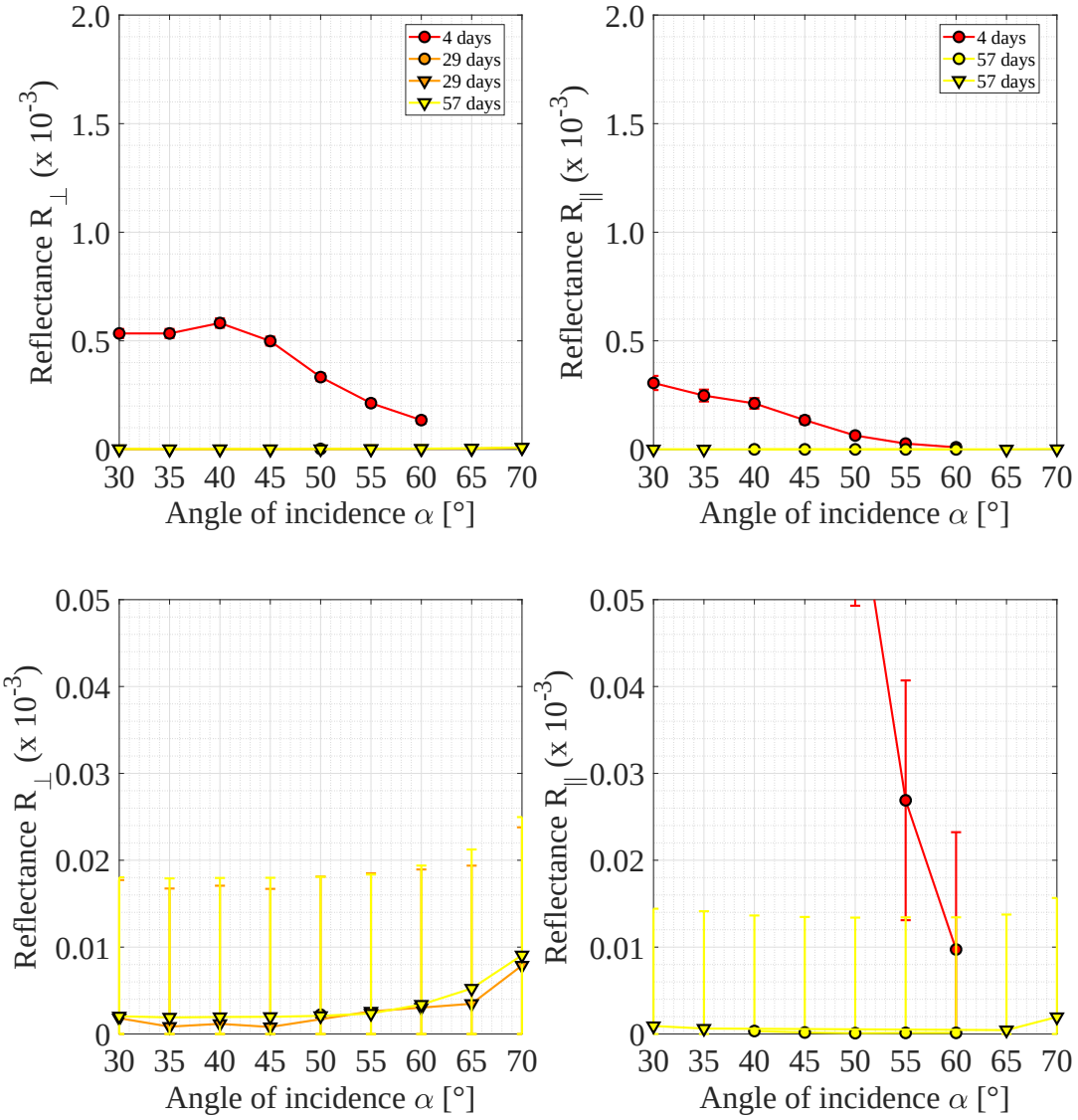

Fig. 4.2 Measured reflectances for $\perp$ (top left) and $\parallel$ (top right) polarisation plotted as a function of the angle of incidence α for the central position on the front surface of $\text{Silica1}_{\text{KOH(0.1N)}}$. Zooms in of the measured reflectances for $\perp$ (bottom left) and $\parallel$ (bottom right) polarisation are also shown to allow the reader to see the lower reflectances. In the legend, the curing time is reported: the dots indicate that the reflectance was measured at the peak of the bond profile, the downward-pointing triangles show the values of the minimum reflectance of the tails between the front and back profile (the reflectance of the bond is lower than the value of this threshold). All measurements were taken using the upgraded setup in red mode.

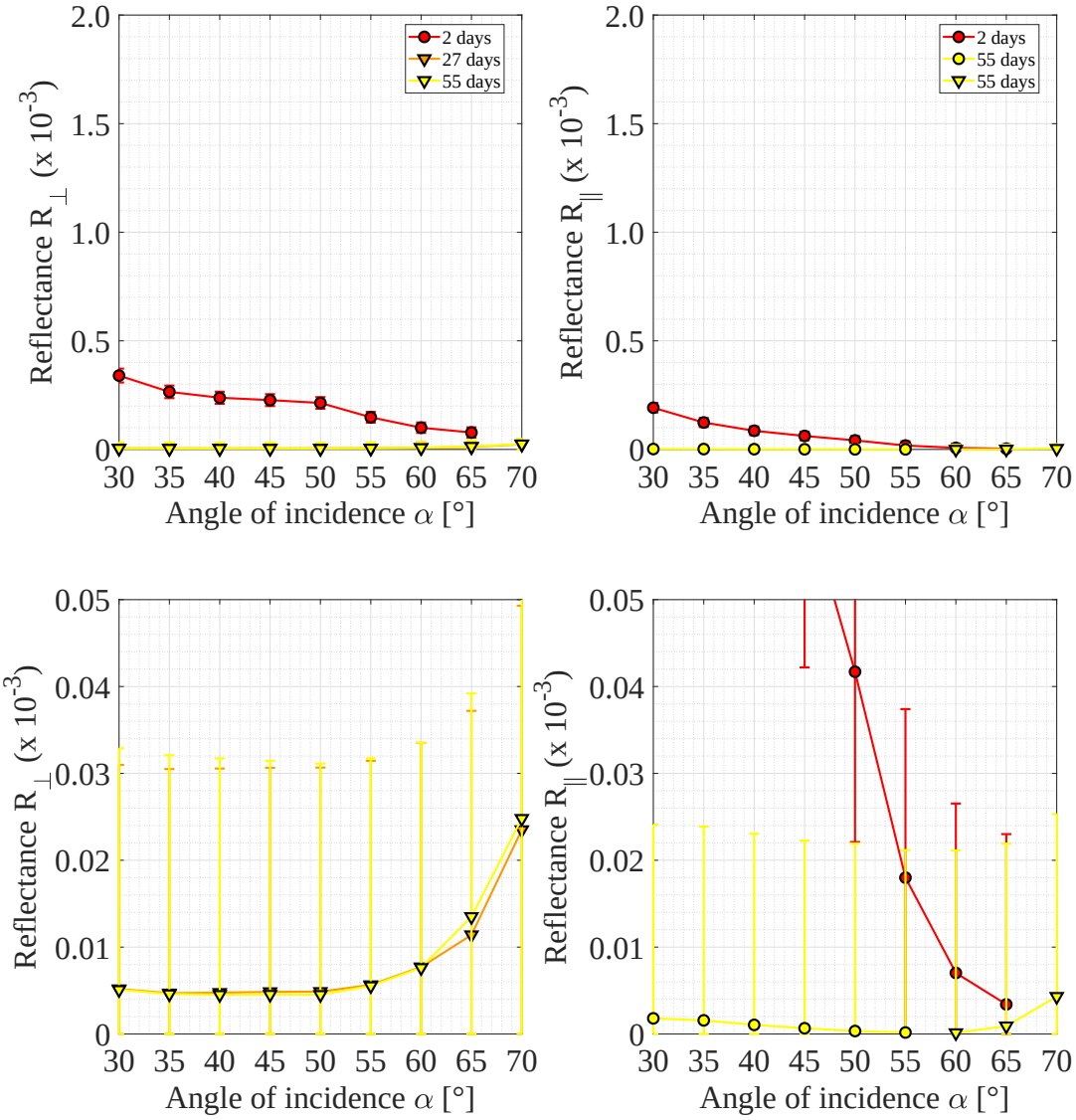

Fig. 4.3 Measured reflectances for $\perp$ (top left) and $\parallel$ (top right) polarisation plotted as a function of the angle of incidence α for the central position on the front surface of $\text{Silica2}_{\text{KOH(0.1N)}}$. Zooms in of the measured reflectances for $\perp$ (bottom left) and $\parallel$ (bottom right) polarisation are also shown to allow the reader to see the lower reflectances. In the legend, the curing time is reported: the dots indicate that the reflectance was measured at the peak of the bond profile, the downward-pointing triangles show the values of the minimum reflectance of the tails between the front and back profile (the reflectance of the bond is lower than the value of this threshold). All measurements were taken using the upgraded setup in green mode.

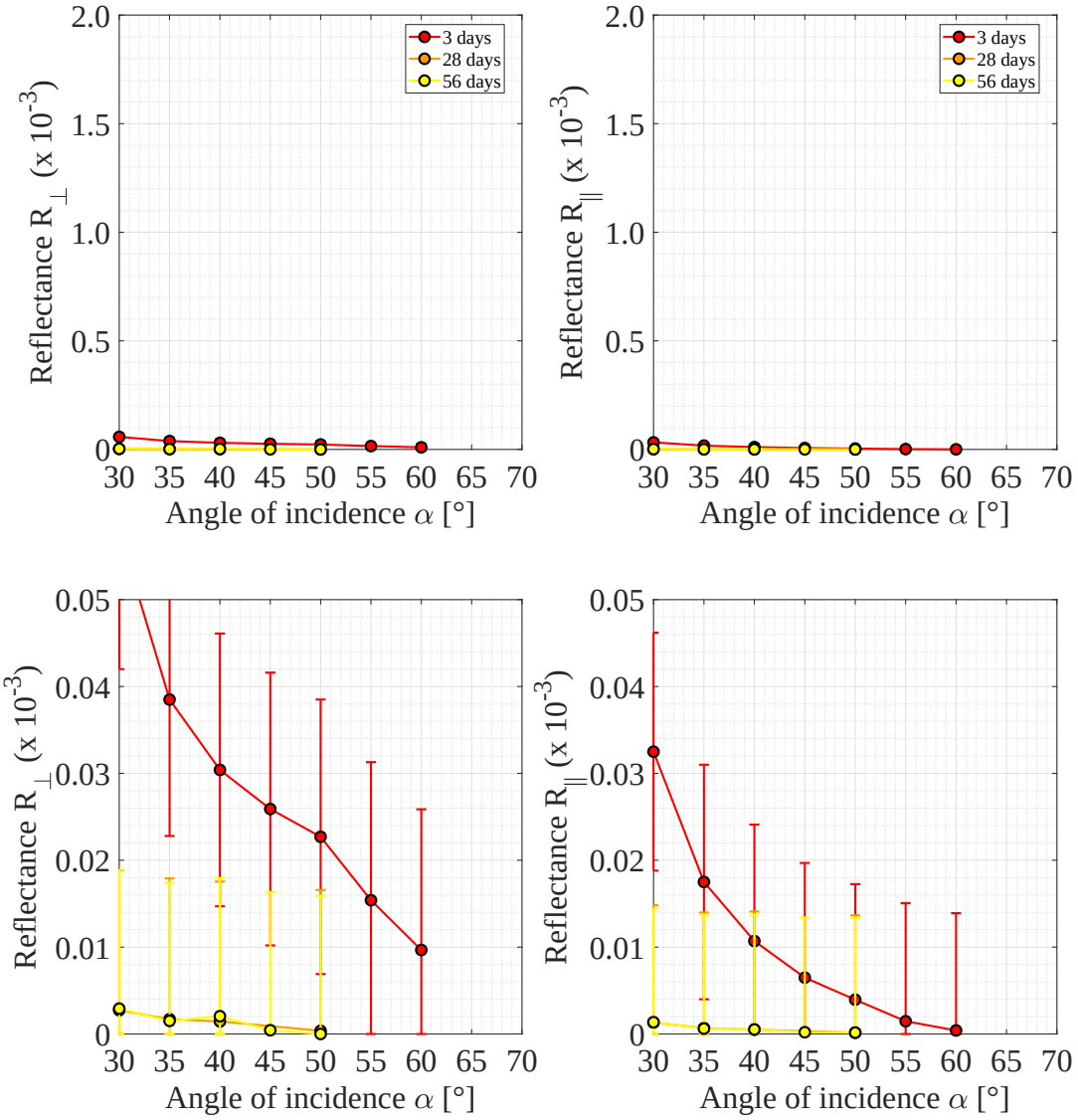

Fig. 4.4 Measured reflectances for $\perp$ (top left) and $\parallel$ (top right) polarisation plotted as a function of the angle of incidence α for the central position on the front surface of $\text{Silica2}_{\text{KOH(0.1N)}}$. Zooms in of the measured reflectances for $\perp$ (bottom left) and $\parallel$ (bottom right) polarisation are also shown to allow the reader to see the lower reflectances. In the legend, the curing time is reported: the dots indicate that the reflectance was measured at the peak of the bond profile, the downward-pointing triangles show the values of the minimum reflectance of the tails between the front and back profile (the reflectance of the bond is lower than the value of this threshold). All measurements were taken using the upgraded setup in red mode.

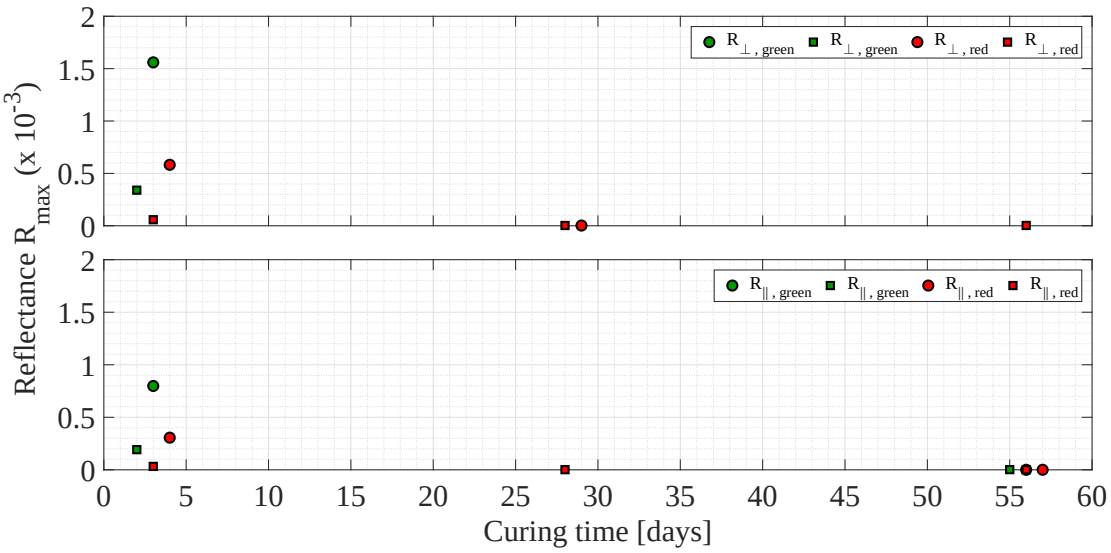

Fig. 4.5 Maximum value of measured reflectances for $\perp$ (top) and $\parallel$ (bottom) polarisation plotted as a function of the curing time for the central position on the front surface of $\text{Silica1}_{\text{KOH(0.1N)}}$ (dot markers) and $\text{Silica2}_{\text{KOH(0.1N)}}$ (square markers) and for green and red laser light. Measurements were taken using the upgraded assembly.

As shown in these figures, after about one month from bonding, the reflectances were below about 0.01×10^{-3}. This could be due to extremely well matching refractive index to the fused silica.

4.1.3 Analysis result: reflectivity

In Figure 4.5, the peak reflectivity of the bond is plotted for both polarisations as a function of curing time for $\text{Silica1}_{\text{KOH(0.1N)}}$ and $\text{Silica2}_{\text{KOH(0.1N)}}$: the reflectance values decrease as curing time increases. In the first days after bonding, the maximum reflectivity of $\text{Silica1}_{\text{KOH(0.1N)}}$ is a factor 5 (green laser light) or 10 (red laser light) greater than that of $\text{Silica2}_{\text{KOH(0.1N)}}$. This difference in reflectivity is related to the starting values of the bond refractive index and thickness which may fluctuate significantly in the first days after bonding.

4.1.4 Analysis result: refractive index and thickness

Figure 4.6 and Figure 4.7 show two examples of the results obtained from the Matlab script for sample $\text{Silica1}_{\text{KOH(0.1N)}}$ in green mode after 3 days and red mode after 4 days, respectively. In both the reflectance plots for perpendicular polarisation of Figure 4.6 and Figure 4.7, a

jump around 40° and 45° can be observed: it is not clear what caused it. It may be due to a not accurate measurement of the reflectance because of the low bond reflectivity or an 'adjustment' that may happen in the first few days after bonding.

In the top of Figure 4.8 and Figure 4.9, the bond refractive index and thickness values are plotted as a function of the curing time for the central position on the front surface of $\text{Silica1}_{\text{KOH(0.1N)}}$ and for both the colours of the laser light. In the bottom of these figures, the time average of the green and red bond refractive indices and thicknesses, of which the Bayesian values had similar probability volumes, are also shown.
In the top and bottom of Figure 4.10, the bond green and red refractive indices and their averages (only between the Bayesian values that had similar probability volumes) are plotted as a function of the curing time for the central position on the front surface of $\text{Silica2}_{\text{KOH(0.1N)}}$. In Figure 4.11, the bond thickness of this sample is plotted as a function of the curing time.

Since the bond reflectivity was very low (less than 0.01×10^{-3} at about a month after bonding), it was not possible to collect sufficient data at each curing time for both polarisations and laser light. This determined a significant uncertainty on the values of bond refractive index and, especially, on those of bond thickness obtained from the Bayesian analysis. As it was not possible to see any bond spot in the measurements of a few data sets, the noise floor value (the background due to the front and back reflected beams) was used as a limit to the bond peak reflectivity with appropriate errors in the Bayesian analysis.

The values of bond average refractive index increase as the curing time increases, starting from 1.42 ($\text{Silica1}_{\text{KOH(0.1N)}}$) or 1.44 ($\text{Silica2}_{\text{KOH(0.1N)}}$) in the first curing days and approaching that of the fused silica 1.46 after about two months from bonding. The starting values of the bond refractive index for these two samples are higher than those obtained for the fused silica samples bonded using the sodium silicate solution (about 1.36). This explains the extremely low reflectance of the bond measured. It was possible to measure the bond thickness only for the first curing days due to the low bond reflectance that appears to affect the thickness measurements more than the reflectivity ones. The bond thickness is 441^{+158}_{-158} *nm* at 3/4 days of curing for $\text{Silica1}_{\text{KOH(0.1N)}}$ and 266^{+15}_{-11} *nm* at 2 days of curing for $\text{Silica2}_{\text{KOH(0.1N)}}$ (see Table 4.1).

The flatness of the bonding surfaces of these two samples was measured using the ZYGO®. The flatness was about 160 *nm* and 348 *nm* peak-to-valley for $\text{Silica1}_{\text{KOH(0.1N)}}$, and about 174 *nm* and 243 *nm* peak-to-valley for $\text{Silica2}_{\text{KOH(0.1N)}}$: the flatness maps of the two discs that form $\text{Silica1}_{\text{KOH(0.1N)}}$ and $\text{Silica2}_{\text{KOH(0.1N)}}$ are shown in the first row of Figure 4.12 and Figure 4.13 respectively. Combining these maps, the relative separation between two bonding surfaces of each sample was determined and it is shown in the second row of

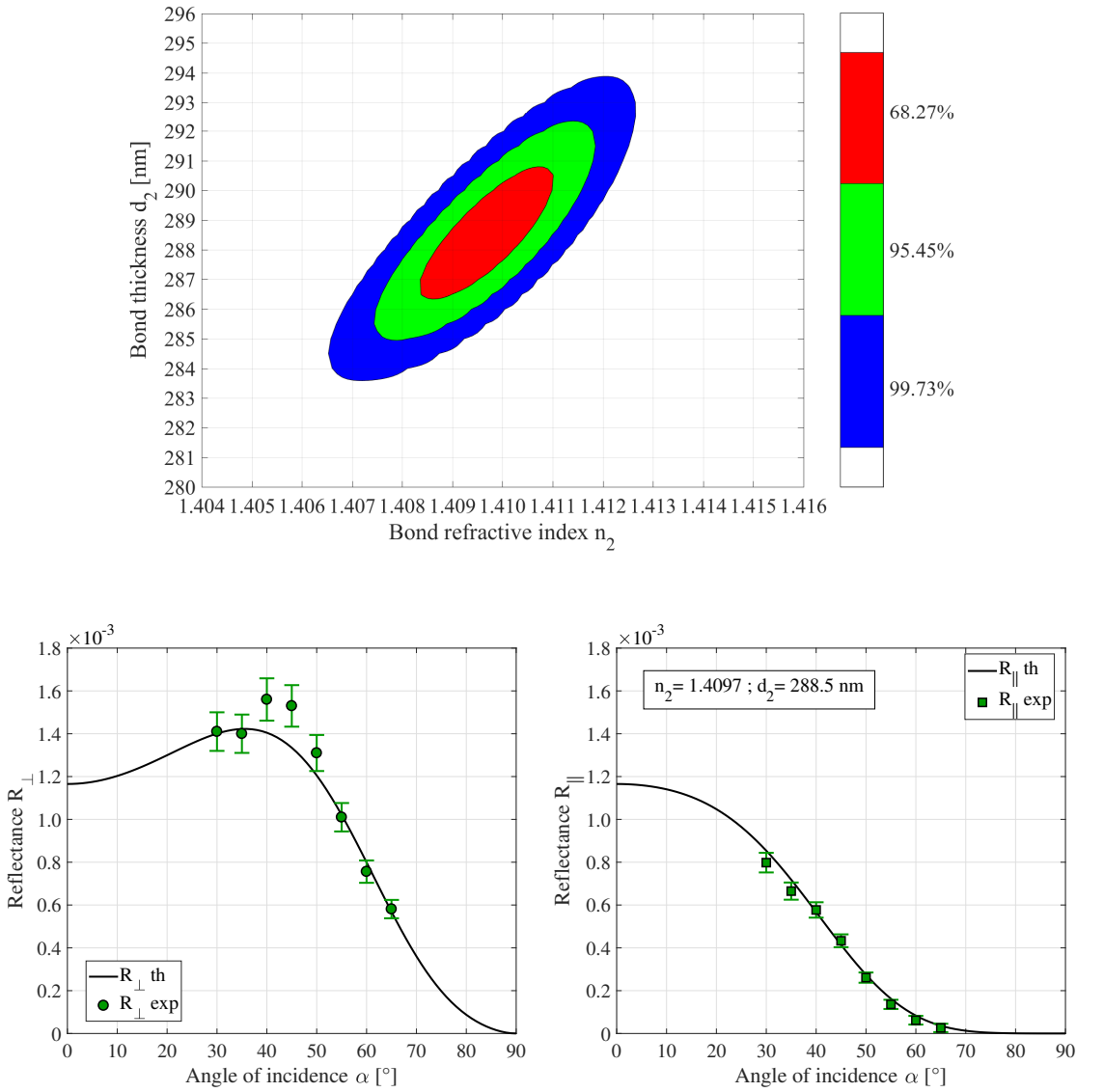

Fig. 4.6 (top) Three confidence levels of 68.3%, 95.5% and 99.7% probability. (bottom) Measured data with their corresponding error bars and theoretical curves. The green dots and squares represent the reflectances measured for perpendicular and parallel polarisation, respectively. The black solid lines are the theoretical perpendicular and parallel reflectances obtained using the most likely values of bond refractive index and thickness of the Bayesian analysis ($n_2 = 1.4097$ and $d_2 = 288.5$). These measurements were taken at 3 days after bonding for $\text{Silica1}_{\text{KOH(0.1N)}}$ in green light.

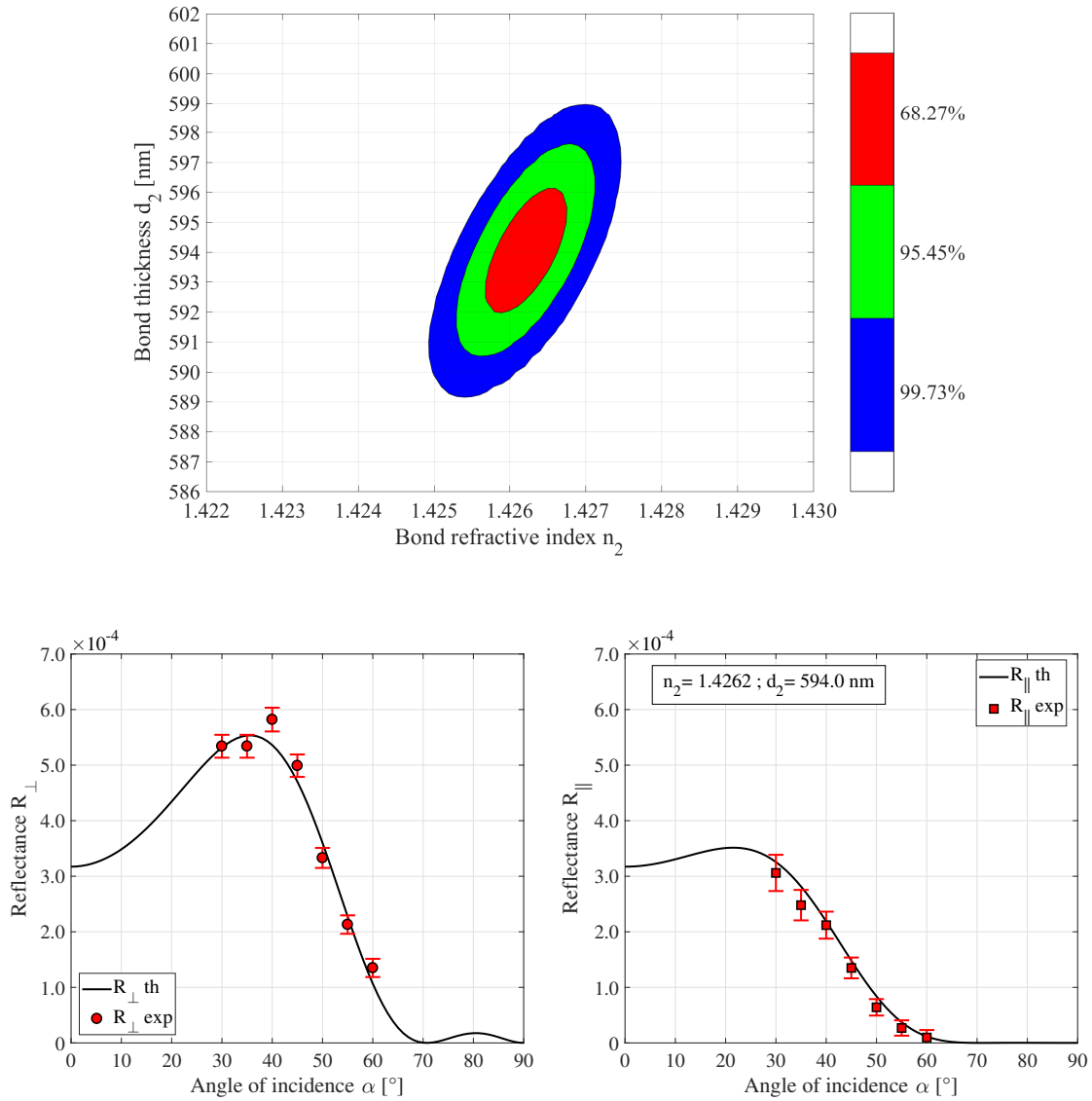

Fig. 4.7 (top) Three confidence levels of 68.3%, 95.5% and 99.7% probability. (bottom) Measured data with their corresponding error bars and theoretical curves. The red dots and squares represent the reflectances measured for perpendicular and parallel polarisation, respectively. The black solid lines are the theoretical perpendicular and parallel reflectances obtained using the most likely values of bond refractive index and thickness of the Bayesian analysis ($n_2 = 1.4262$ and $d_2 = 594.0$). These measurements were taken at 4 days after bonding for $\text{Silica1}_{\text{KOH(0.1N)}}$ in red light.

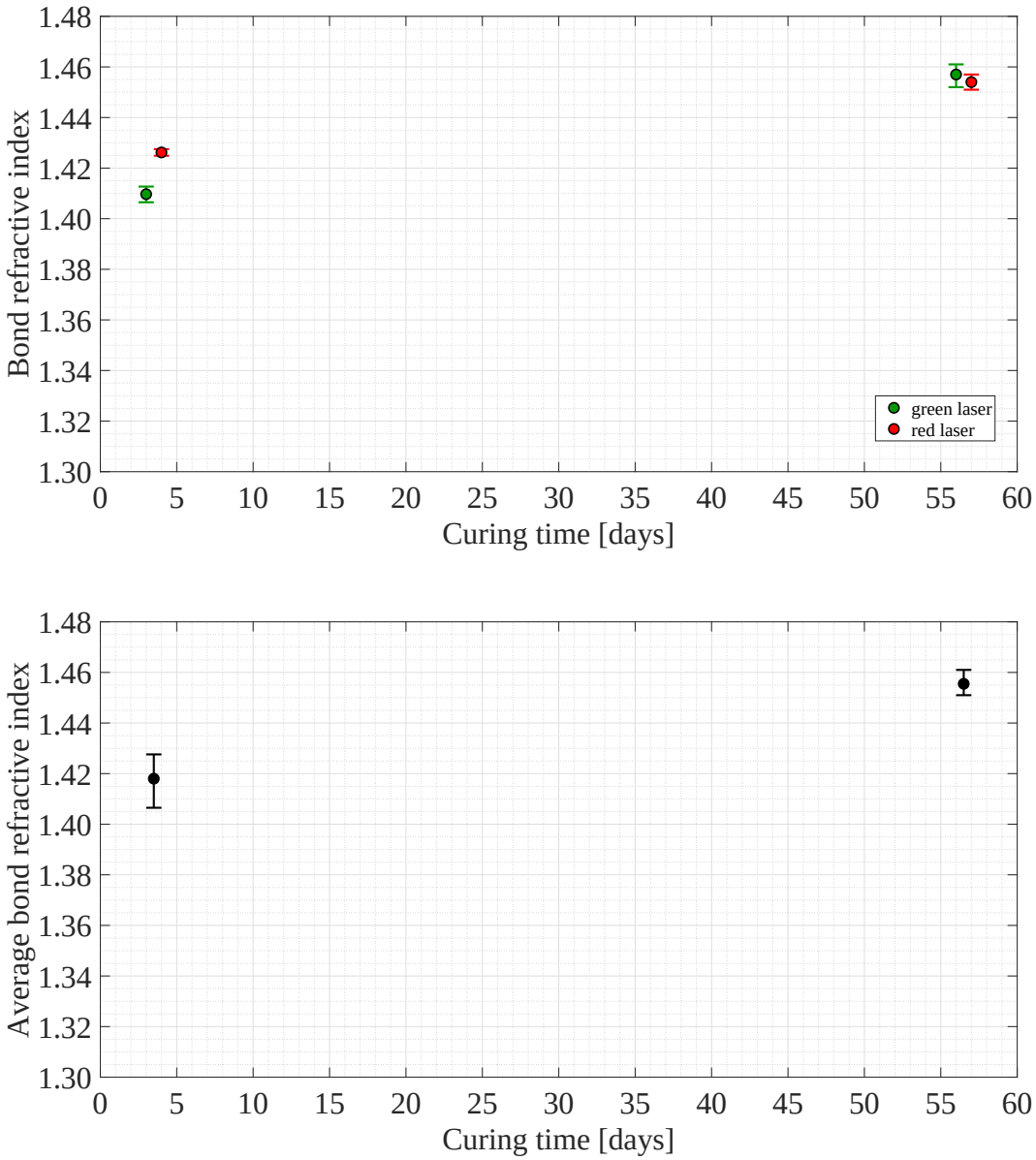

Fig. 4.8 (top) Refractive index of the bond as a function of the curing time for the central position on the front surface of Silica1$_{\mathrm{KOH(0.1N)}}$. These values were determined from measurements collected using the upgraded setup in green (green dots) and red (red dots) mode. (bottom) Average of the green and red refractive indices, which was calculated for each two consecutive days (the difference between green and red curing time is always one day). The error bars represent the spread of the data that was averaged.

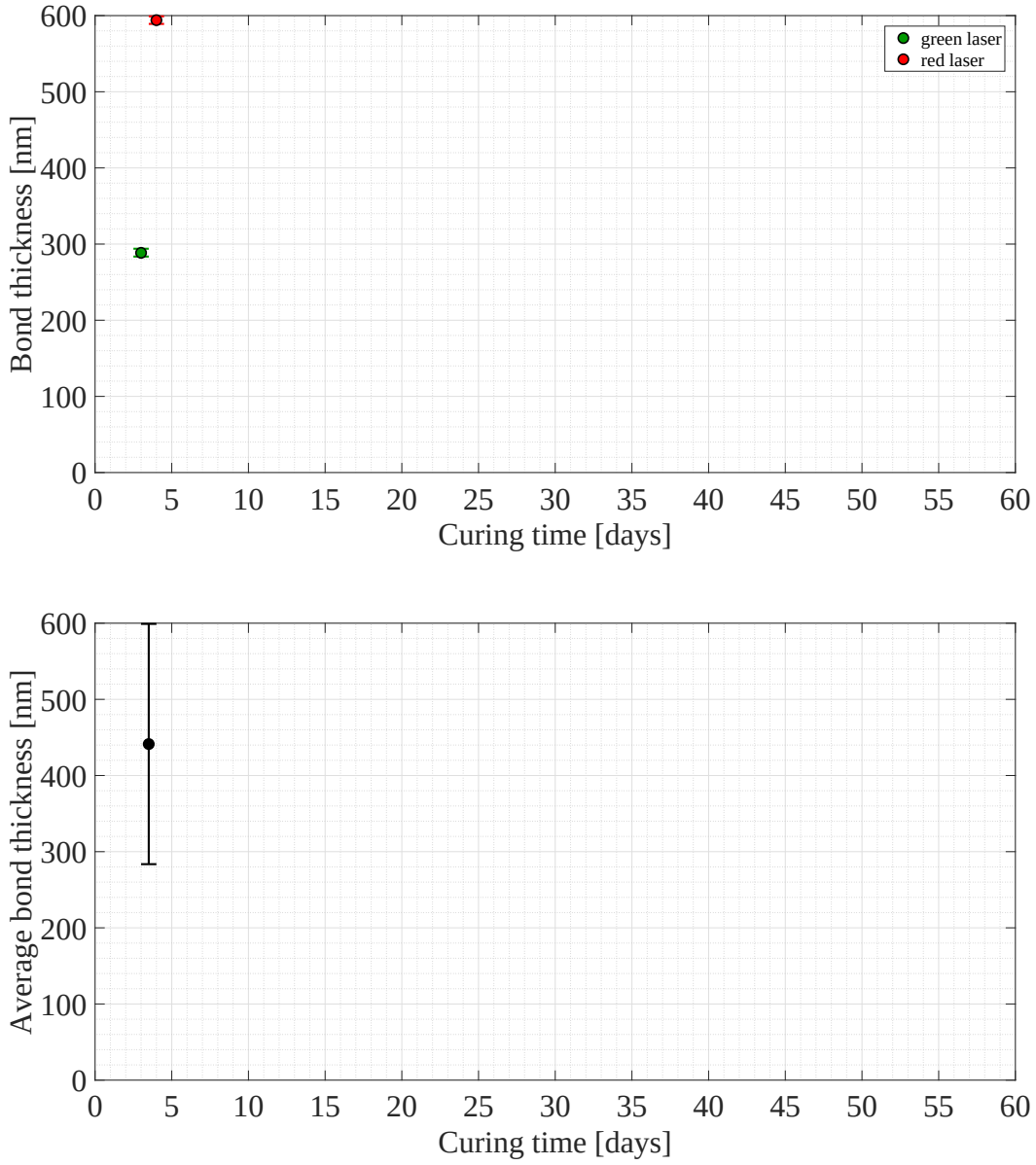

Fig. 4.9 (top) Thickness of the bond as a function of the curing time for the central position on the front surface of Silica1$_{\mathrm{KOH(0.1N)}}$. These values were determined from measurements collected using the upgraded setup in green (green dots) and red (red dots) mode. The thicknesses at 56 and 57 days (green and red data sets) were not reported, because they were not measurable because of the relatively large uncertainty on this measurement due to the extremely low reflectance of the bond. (bottom) Average of the green and red refractive indices, which was calculated for each two consecutive days (the difference between green and red curing time is always one day). The error bars represent the spread of the data that was averaged.

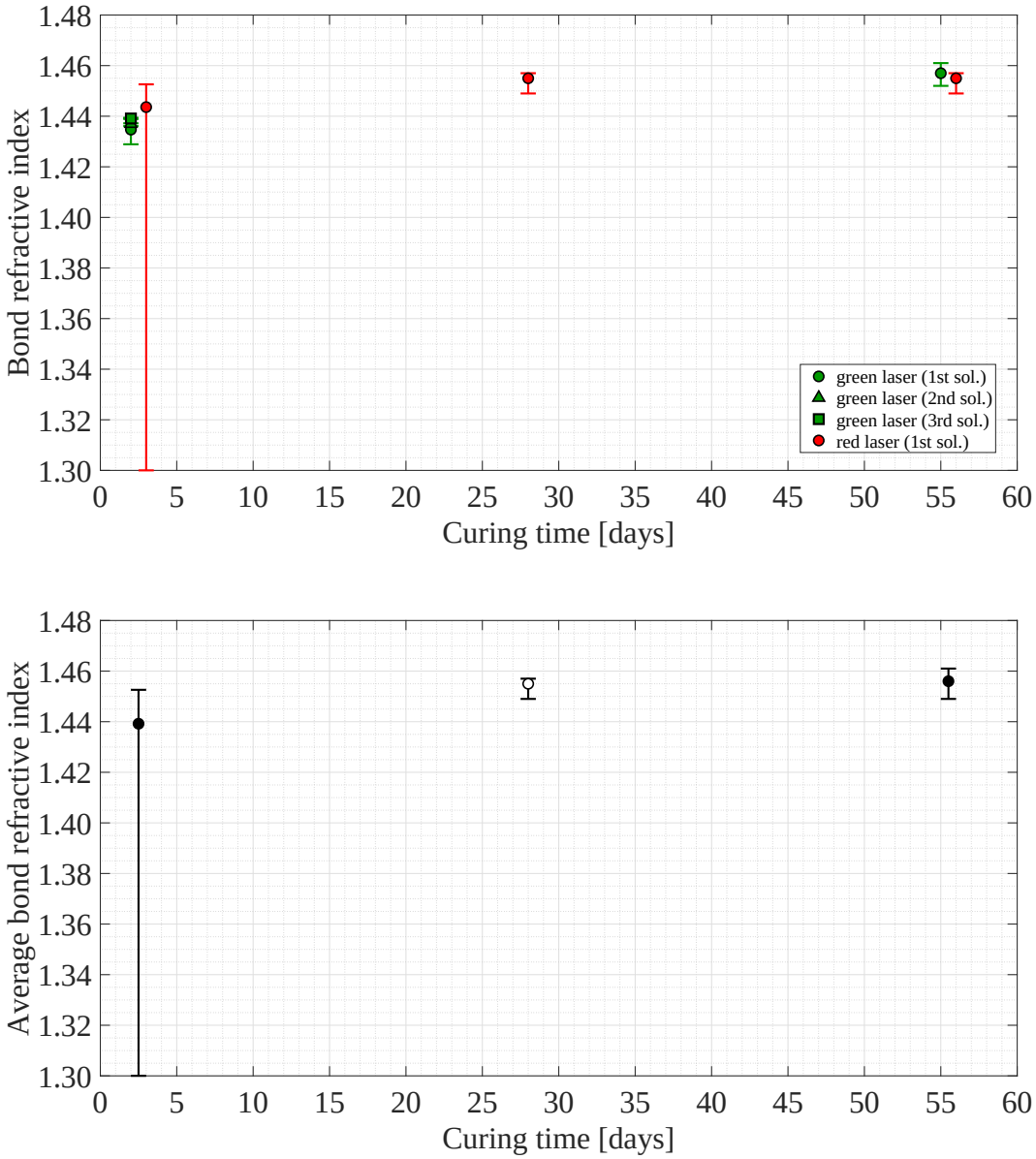

Fig. 4.10 (top) Refractive index of the bond as a function of the curing time for the central position on the front surface of Silica2$_{\mathrm{KOH(0.1N)}}$. These values were determined from measurements collected using the upgraded setup in green (green dots, triangles and squares) and red (red dots) mode. Some data sets have multiple solutions, which are presented in order from the highest to the lowest joint posterior probability density function by dots, triangles and squares. (bottom) Average of the green and red refractive indices of which the Bayesian values have similar probability volumes. This average was calculated for each two consecutive days (the difference between green and red curing time is always one day). For all filled data points both green and red were averaged. For the red data set at 28 days no average could be calculated because of the absence of the corresponding value in green (unfilled data point). The error bars represent the spread of the data that was averaged.

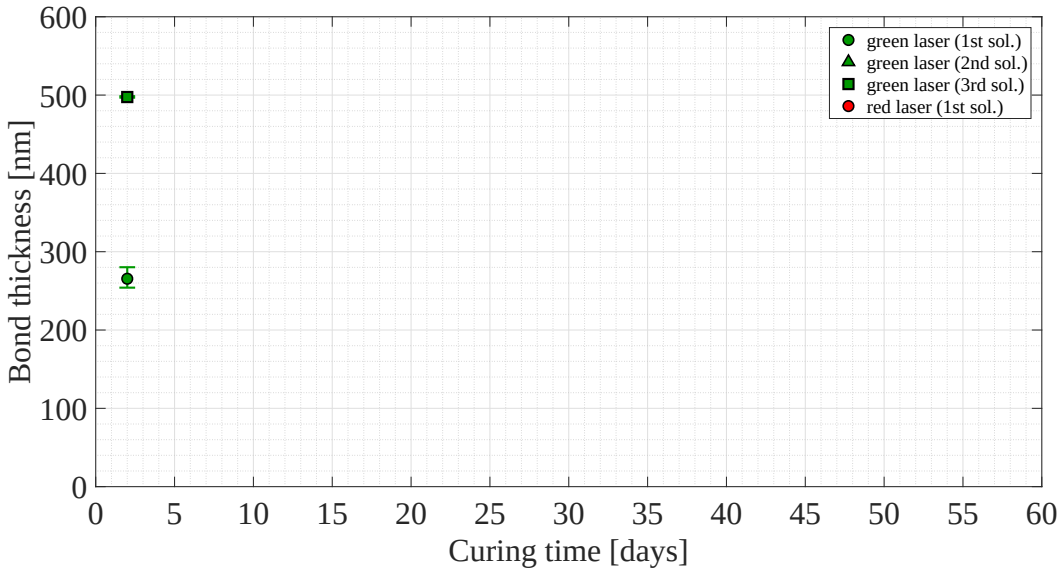

Fig. 4.11 Thickness of the bond as a function of the curing time for the central position on the front surface of $\text{Silica2}_{\text{KOH(0.1N)}}$. These values were determined from measurements collected using the upgraded setup in green (green dots, triangles and squares) and red (red dots) mode. Some data sets have multiple solutions, which are presented in order from the highest to the lowest joint posterior probability density function by dots, triangles and squares. The thicknesses at 55 days (green data set) and at 3, 28, 56 days (red data sets) were not reported, because they were not measurable because of the relatively large uncertainty on this measurement due to the extremely low reflectance of the bond.

Figure 4.12 for $\text{Silica1}_{\text{KOH(0.1N)}}$ and Figure 4.13 for $\text{Silica2}_{\text{KOH(0.1N)}}$: the relative separation maps give a value of 8^{+4}_{-4} *nm* for the bond thickness in central position of $\text{Silica1}_{\text{KOH(0.1N)}}$, 320^{+6}_{-6} *nm* for that of $\text{Silica2}_{\text{KOH(0.1N)}}$ (Table 4.1).

In Figure 4.14 the bond thicknesses measured by SEM imaging for three slices of $\text{Silica1}_{\text{KOH(0.1N)}}$ were shown. The reflectances of $\text{Silica1}_{\text{KOH(0.1N)}}$ were measured in central position of its front surface: for this location, the SEM analysis gave an average thickness of (41 ± 12) *nm* after 430 days from bonding (Table 4.1). No SEM measurements were taken for $\text{Silica2}_{\text{KOH(0.1N)}}$.

For $\text{Silica1}_{\text{KOH(0.1N)}}$, it should again be noted that for the bond thickness values obtained via Bayesian and SEM imaging methods (Table 4.1), the former was measured at 3/4 days of curing, while the latter was taken at a considerable period after the initial bond formation. Also, these values differ from those obtained from the relative separation method and this may suggest that the relative surface figures may not define the final bond thickness and that the bonds may continue to evolve over periods longer than 430 days.
Also for $\text{Silica2}_{\text{KOH(0.1N)}}$, the Bayesian and flatness map results differ (Table 4.1). Again, this suggests that relative surface figures may not determine the final thickness of a bond.

4.1.5 Analysis result: discussion

The bond reflectances of two nominally identical fused silica samples ($\text{Silica1}_{\text{KOH(0.1N)}}$ and $\text{Silica2}_{\text{KOH(0.1N)}}$), bonded using potassium hydroxide solution and cured at room temperature, were studied. It was found that the bond reflectances are less than those measured for the fused silica samples bonded using the sodium silicate solution: the reflectances are below about 0.01×10^{-3} after one month from bonding.

From this it can be deduced that there is a relatively high value of refractive index for the bonds between these samples soon after bonding (1.42 for $\text{Silica1}_{\text{KOH(0.1N)}}$ and 1.44 for $\text{Silica2}_{\text{KOH(0.1N)}}$). These values are higher than those estimated for the fused silica samples bonded using the sodium silicate solution (equal to about 1.36), discussed in Chapter 3. Also, the refractive index of these potassium hydroxide bonds approaches that of fused silica (1.46) after about two months, in contrast to the sodium silicate bonds which need more than three months (more than one year for sodium silicate 1 : 6 bonds). This may suggest that potassium hydroxide solution influences the evolution of the bond refractive index which reaches the value of the fused silica much more quickly than the sodium silicate solution counterparts. This may be due to the fact that KOH ions etch the fused silica substrate more efficiently than SiO_2 ions, increasing the content of silica in the bonding solution.

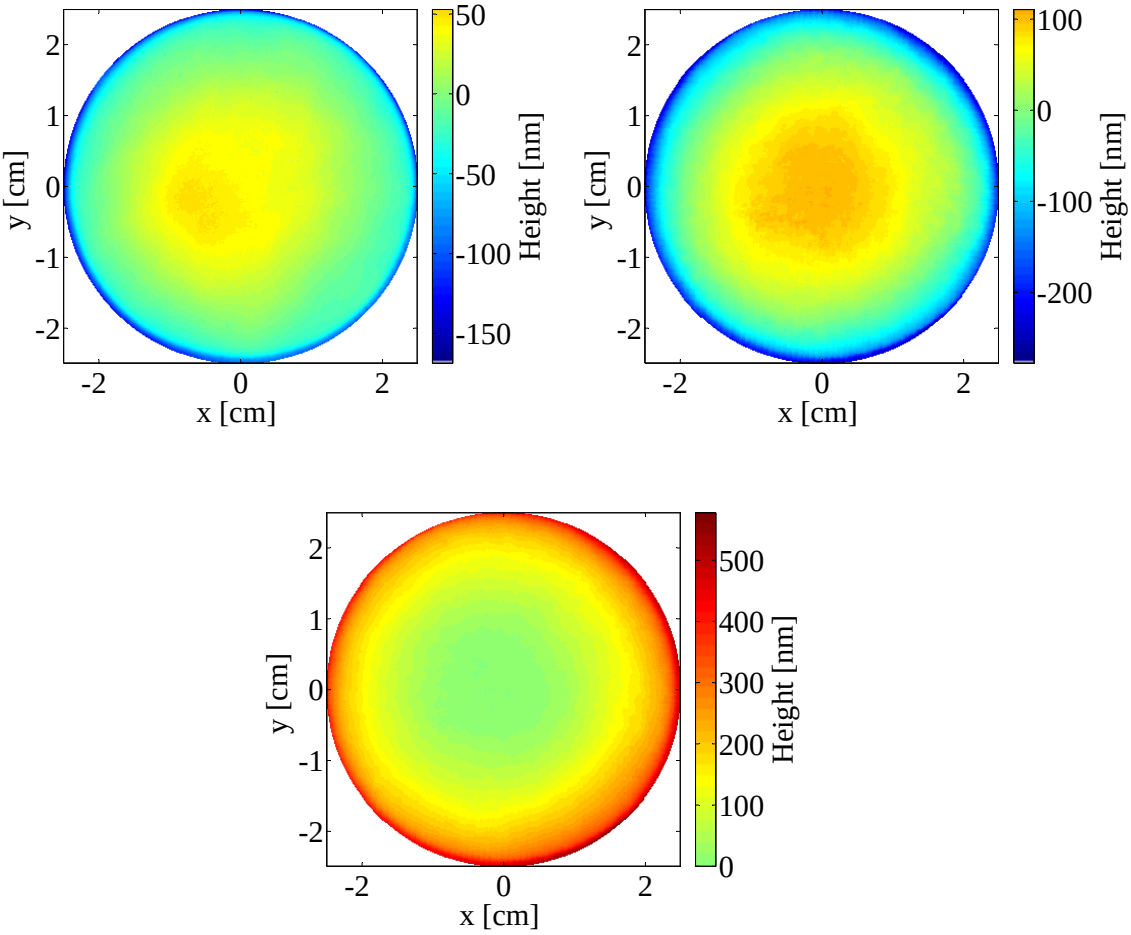

Fig. 4.12 (first row) Flatness maps of the bonding surfaces of the two discs which make Silica1$_{\mathrm{KOH(0.1N)}}$. These were obtained using the functions of the Simtools package (see Appendix E) which zoomed in on a valid area and remove various offsets from the ZYGO® maps. (second row) Relative separation between two bonding surfaces of discs bonded by hydroxide-catalysis bonding. This map was obtained using the Matlab code reported in Appendix E.

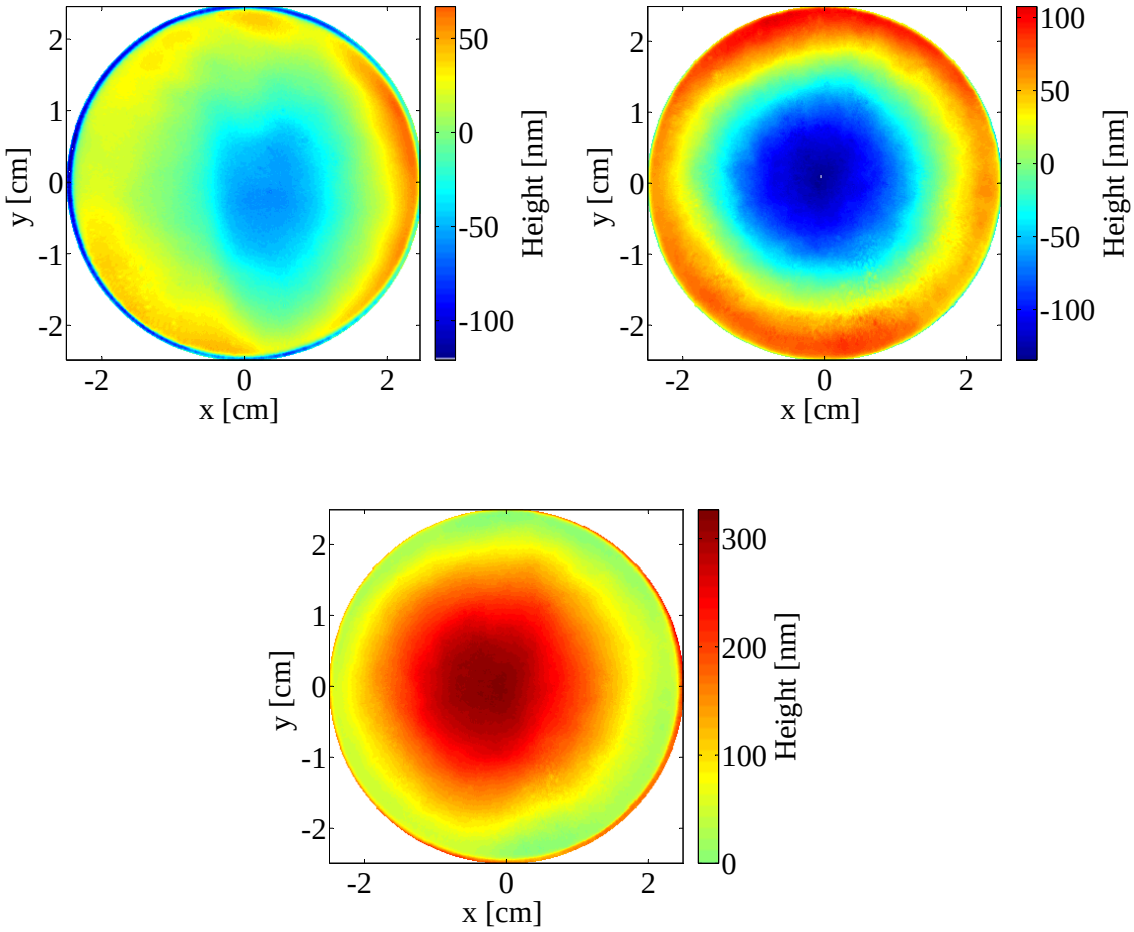

Fig. 4.13 (first row) Flatness maps of the bonding surfaces of the two discs which make $Silica2_{KOH(0.1N)}$. These were obtained using the functions of the Simtools package (see Appendix E) which zoomed in on a valid area and remove various offsets from the ZYGO® maps. (second row) Relative separation between two bonding surfaces of discs bonded by hydroxide-catalysis bonding. This map was obtained using the Matlab code reported in Appendix E.

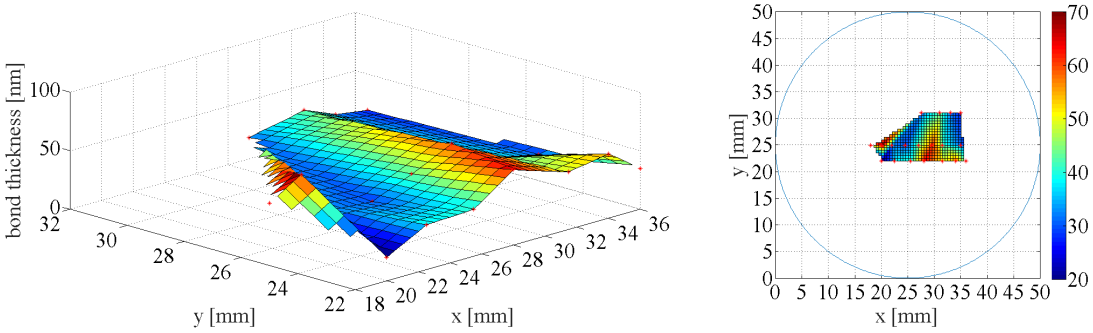

Fig. 4.14 Surface plots of the bond thicknesses measured across three slices of $\text{Silica1}_{\text{KOH(0.1N)}}$, where x and y were the coordinates of the thickness measurement within the sample. The surface plots were made by linearly interpolating between measurements.

It is not possible to make statements about how the bond thickness evolves as a function of curing time, because of the low reflectivity of the KOH bonds which seems to affect estimation of thickness more than refractive index. Table 4.1 (section 4.3) gives an overview of the bond thicknesses obtained using the Bayesian, flatness and SEM methods. Bond thicknesses, obtained by the Bayesian analysis, were obtained only for the first curing days after bonding: 441^{+158}_{-158} *nm* at 3/4 days of curing for $\text{Silica1}_{\text{KOH(0.1N)}}$ and 266^{+15}_{-11} *nm* at 2 days of curing for $\text{Silica2}_{\text{KOH(0.1N)}}$. As the Bayesian values were measured in the early days after bonding and the SEM measurements were taken after more than one year from bonding, these results cannot be directly compared: the bond thickness could decrease over that period. Also, as said for the sodium silicate samples, the relative surface figures may not necessarily define the final thickness of a bond.

4.2 KOH bond cured at elevated temperature

Once the surfaces of two substrates are bonded together, they can also be cured at elevated temperature: this may reduce the curing time of a hydroxide-catalysis bond. According to the curing method studied in this thesis, a bonded sample is left to cure in air at room temperature for one hour after bonding, and then it is placed inside an oven at 100 $^{\circ}C$ for eight hours. See section 3.4 for details about this curing method.

Two samples were cured at these elevated temperatures: one was made using sodium silicate solution ($\text{Silica}_{\text{Na2SiO3(1:6),T}}$) and it is discussed in subsection 3.4.1, the other was

made using potassium hydroxide solution ($\text{Silica}_{\text{KOH(0.1N),T}}$) and it is reported in this section (see subsection 4.2.1).

4.2.1 $\text{Silica}_{\text{KOH(0.1N),T}}$

Sample $\text{Silica}_{\text{KOH(0.1N),T}}$ was made by bonding two fused silica discs with 15.70 μl of potassium hydroxide solution KOH. It was composed of 0.1 N solution in water and was used without further diluting it with de-ionised water.

4.2.2 Reflectivity measurements

The reflectivity of $\text{Silica}_{\text{KOH(0.1N),T}}$ was measured for the central position on its front surface at four different curing times (the following day, about one, two and five months after bonding) to monitor the changes of bond refractive index and thickness over time.

Plots of measured perpendicular ($\perp$) and parallel ($\parallel$) reflectances (equations 2.1 and 2.2) as a function of angle of incidence α are shown in Figure 4.15 ($\text{Silica}_{\text{KOH(0.1N),T}}$ in green mode) and Figure 4.16 ($\text{Silica}_{\text{KOH(0.1N),T}}$ in red mode).

For both polarisations and colours of laser light, the values of bond reflectances are all less than 1% and they decrease as curing time increases. They are less than 0.1% after 50 days and less than 0.01% after 150 days. These values are one order of magnitude greater than the corresponding reflectances measured for the KOH bonds cured at room temperature, and similar to those of the fused silica samples bonded using the sodium silicate solution. This suggests that an elevated temperature used for curing may modify the chemical reactions between potassium hydroxide solution and fused silica substrate material at room temperature.

4.2.3 Analysis result: reflectivity

In Figure 4.17, the peak reflectivity of the bond for both polarisations is plotted to illustrate this as a function of curing time for $\text{Silica}_{\text{KOH(0.1N),T}}$: the reflectance values decrease as curing time increases. The trend shows starting levels of reflectance that are very similar to the samples bonded using sodium silicate shown in Chapter 3. The reflectance levels drop more quickly though.

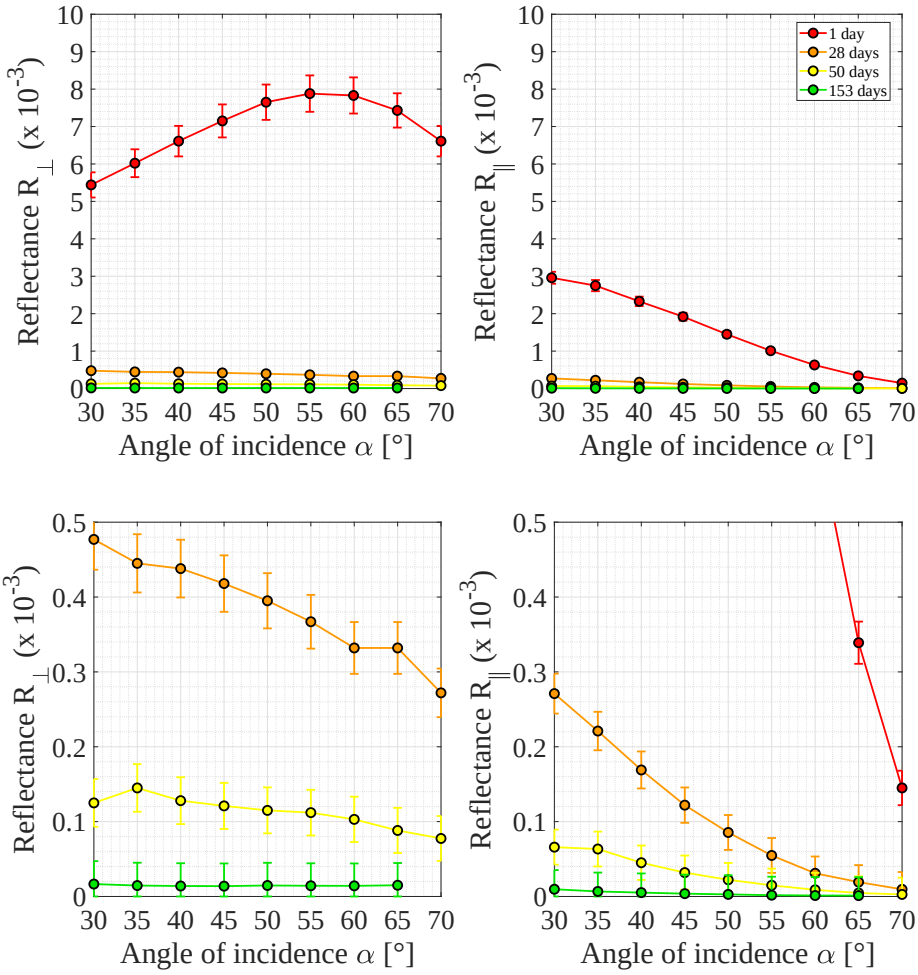

Fig. 4.15 (top) Measured reflectances for $\perp$ (left) and $\parallel$ (right) polarisation plotted as a function of the angle of incidence α for the central position on the front surface of $\text{Silica}_{\text{KOH(0.1N),T}}$. (bottom) Zooms in of the measured reflectances are also shown to allow the reader to see the lower reflectances. In the legend, the curing time is reported. All measurements were taken using the upgraded setup in green mode.

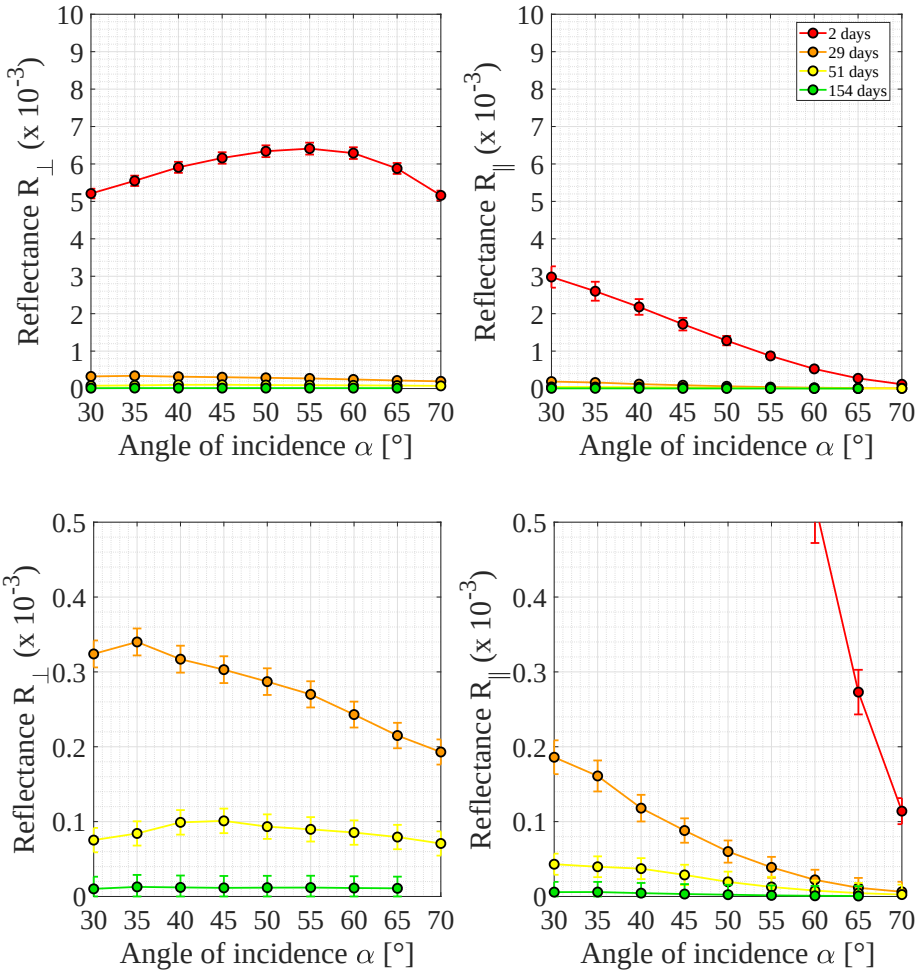

Fig. 4.16 (top) Measured reflectances for $\perp$ (left) and $\parallel$ (right) polarisation plotted as a function of the angle of incidence α for the central position on the front surface of $\text{Silica}_{\text{KOH(0.1N),T}}$. (bottom) Zooms in of the measured reflectances are also shown to allow the reader to see the lower reflectances. In the legend, the curing time is reported. All measurements were taken using the upgraded setup in red mode.

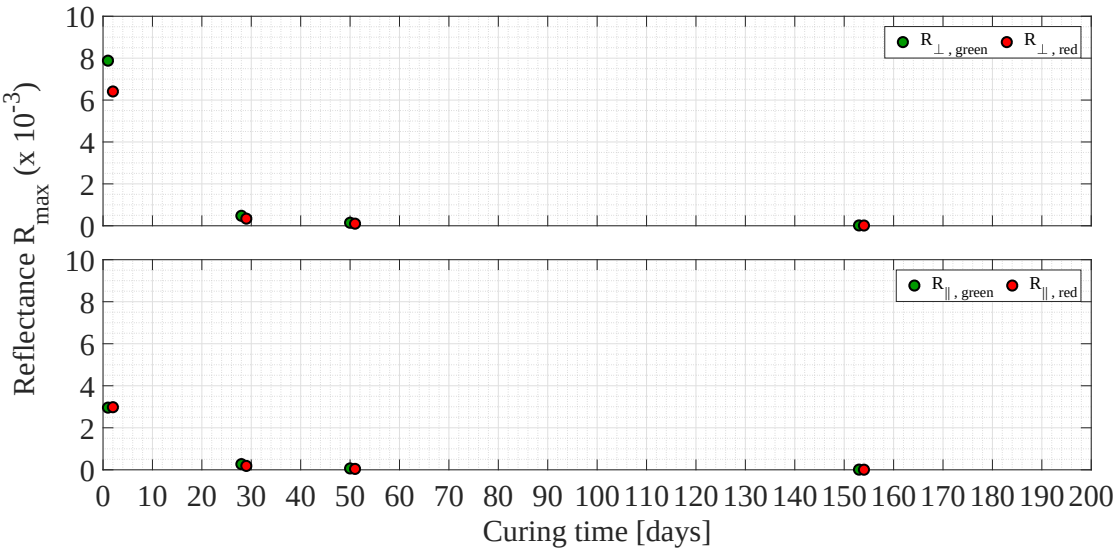

Fig. 4.17 Maximum value of measured reflectances for $\perp$ (top) and $\parallel$ (bottom) polarisation plotted as a function of the curing time for the central position on the front surface of $Silica_{KOH(0.1N),T}$ and for green and red laser light. Measurements were taken using the upgraded assembly.

4.2.4 Analysis result: refractive index and thickness

Figure 4.18 and Figure 4.19 show two examples of the results obtained from the Matlab script for sample $Silica_{KOH(0.1N),T}$ in green mode after 1 day and red mode after 2 days, respectively.

In the top of Figure 4.20 and Figure 4.21, the bond refractive index and thickness for $Silica_{KOH(0.1N),T}$ are plotted as a function of the curing time for both colours of laser light. For each two consecutive days, the green and red data, of which the Bayesian values had similar probability volumes, was averaged and the results are shown in the bottom of Figure 4.20 and Figure 4.21.

The bond average refractive index is 1.36 and close to 1.45 at 1/2 and 153/154 days after bonding, respectively. Comparing these results with those obtained for the KOH bonds cured at room temperature (1.42 for $Silica1_{KOH(0.1N)}$ and 1.44 for $Silica2_{KOH(0.1N)}$ in the first days after bonding, and 1.46 after about two months), it seems that the heat treatment slows down the curing of a bond.

Like its sodium silicate solution counterpart (sample $Silica_{Na2SiO3(1:6),T}$) discussed in Chapter 3, the bond thickness of $Silica_{KOH(0.1N),T}$ seems to increase or settle on a constant value over time. This confirms that an heat treatment may interrupt the chemistry of the

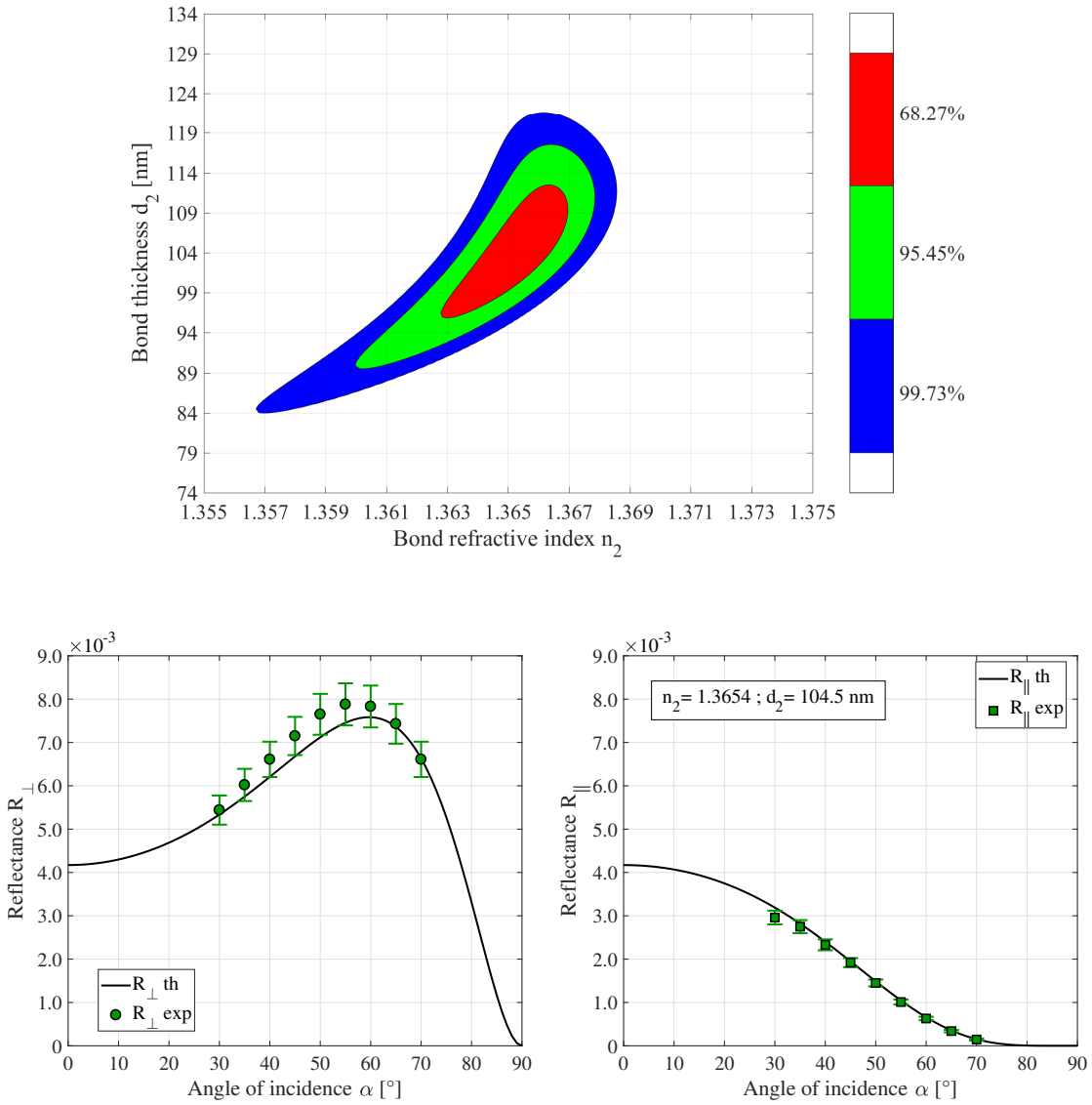

Fig. 4.18 (top) Three confidence levels of 68.3%, 95.5% and 99.7% probability. (bottom) Measured data with their corresponding error bars and theoretical curves. The green dots and squares represent the reflectances measured for perpendicular and parallel polarisation, respectively. The black solid lines are the theoretical perpendicular and parallel reflectances obtained using the most likely values of bond refractive index and thickness of the Bayesian analysis ($n_2 = 1.3654$ and $d_2 = 104.5$). These measurements were taken at 1 day after bonding for $\text{Silica}_{\text{KOH(0.1N),T}}$ in green light.

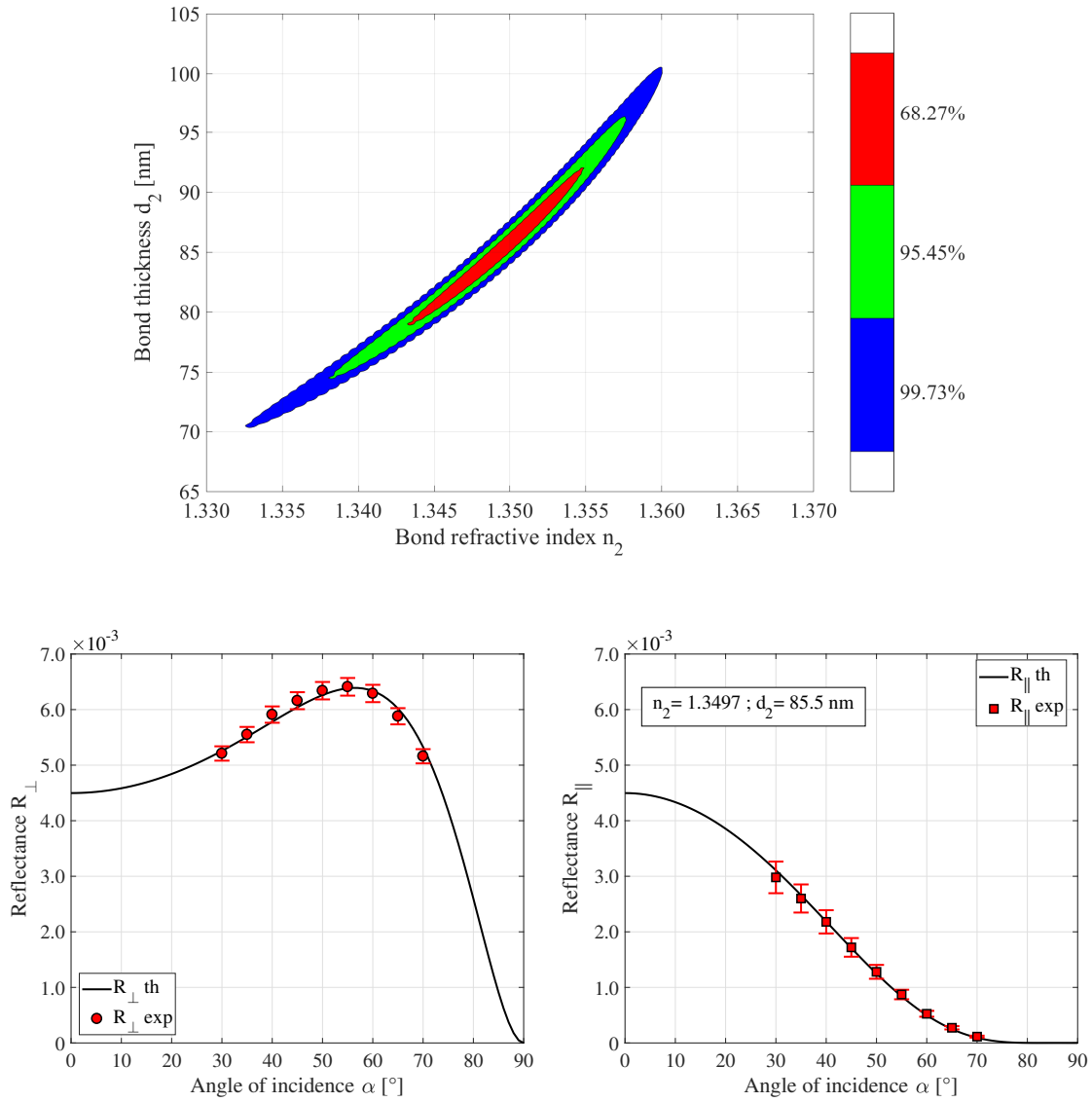

Fig. 4.19 (top) Three confidence levels of 68.3%, 95.5% and 99.7% probability. (bottom) Measured data with their corresponding error bars and theoretical curves. The red dots and squares represent the reflectances measured for perpendicular and parallel polarisation, respectively. The black solid lines are the theoretical perpendicular and parallel reflectances obtained using the most likely values of bond refractive index and thickness of the Bayesian analysis ($n_2 = 1.3497$ and $d_2 = 85.5$). These measurements were taken at 2 days after bonding for $\text{Silica}_{\text{KOH(0.1N),T}}$ in red light.

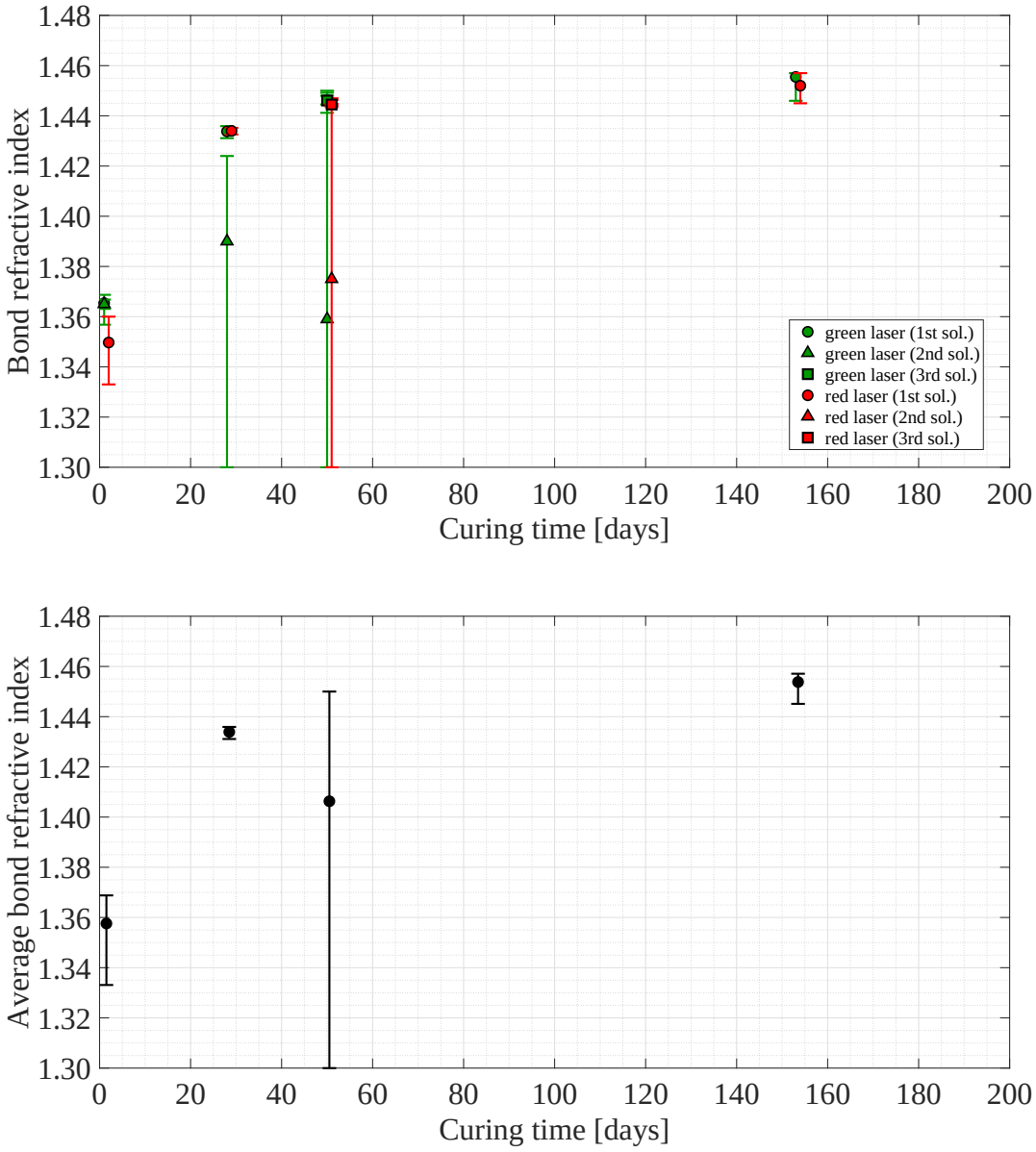

Fig. 4.20 (top) Refractive index of the bond as a function of the curing time for the central position on the front surface of $\text{Silica}_{\text{KOH(0.1N),T}}$. These values were determined from measurements collected using the upgraded setup in green (green dots, triangles and squares) and red (red dots and triangles) mode. Some data sets have multiple solutions, which are presented in order from the highest to the lowest joint posterior probability density function by dots, triangles and squares. (bottom) Average of the green and red refractive indices of which the Bayesian values have similar probability volumes. This average was calculated for each two consecutive days (the difference between green and red curing time is always one day). The error bars represent the spread of the data that was averaged.

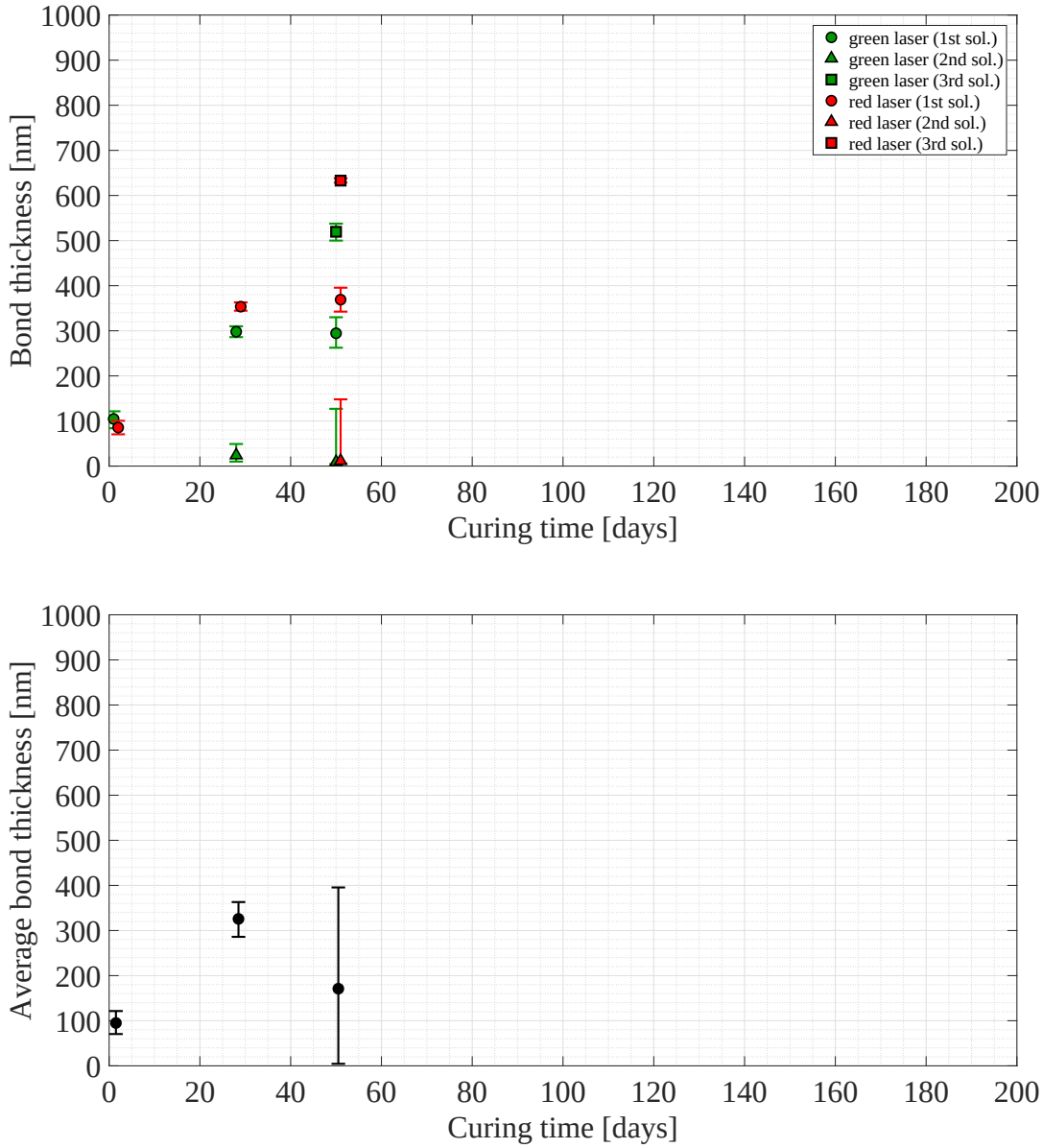

Fig. 4.21 (top) Thickness of the bond as a function of the curing time for the central position on the front surface of $\text{Silica}_{\text{KOH(0.1N),T}}$. These values were determined from measurements collected using the upgraded setup in green (green dots, triangles and squares) and red (red dots and triangles) mode. Some data sets have multiple solutions, which are presented in order from the highest to the lowest joint posterior probability density function by dots, triangles and squares. The thicknesses at 153 and 154 days (green and red data sets) were not reported, because they were not measurable because of the relatively huge uncertainty on this measurement due to the extremely low reflectance of the bond. (bottom) Average of the green and red thicknesses of which the Bayesian values have similar probability volumes. This average was calculated for each two consecutive days (the difference between green and red curing time is always one day). The error bars represent the spread of the data that was averaged.

hydroxide-catalysis bonding. The bond average thickness obtained by the Bayesian analysis is 171^{+225}_{-167} *nm* after 50/51 days (Table 4.1).

The bonding surfaces of the two discs of $\text{Silica}_{\text{KOH(0.1N),T}}$ had a flatness of about 86 *nm* and 83 *nm* peak-to-valley respectively, which was measured using the ZYGO®: the flatness maps shown in the first row of Figure 4.22 were obtained for the two discs. Combining these maps, the relative separation between two bonding surfaces was obtained and it is shown in the second row of Figure 4.22: the relative separation map gives a value of 105^{+4}_{-4} *nm* for the bond thickness in central position (Table 4.1).

No SEM measurements were made of this sample.

For this sample, the thickness results obtained using the reflectance measurements and the flatness maps agree within error.

4.2.5 Analysis result: discussion

The bond reflectances are less than 1% in the first days after bonding, reaching the value of less than 0.1% after 50 days and less than 0.01% after 150 days. These values are similar to those measured for fused silica samples bonded using the sodium silicate solution and are higher than those measured for fused silica samples bonded using potassium hydroxide solution but cured at room temperature.

$\text{Silica}_{\text{KOH(0.1N),T}}$ shows an increasing trend of the bond refractive index as a function of curing time for both colours of light, from 1.36 (1/2 days) to 1.45 (153/154 days). This trend is comparable to that of the room temperature cured sodium silicate bonds though the refractive index starting at the same value goes up more quickly to close to that of fused silica: this corresponds to the faster drop in the reflectance observed. However the rate of increase seems to be slower than that of potassium hydroxide samples cured at room temperature (1.42 for $\text{Silica1}_{\text{KOH(0.1N)}}$ and 1.44 for $\text{Silica2}_{\text{KOH(0.1N)}}$ in the first days after bonding, and 1.46 after about two months).

The bond thickness of $\text{Silica}_{\text{KOH(0.1N),T}}$ seems to increase as a function of curing time, as was seen for $\text{Silica}_{\text{Na2SiO3(1:6),T}}$ (sodium silicate sample cured using the same heat treatment), from 95^{+27}_{-25} *nm* (1/2 days) to 171^{+225}_{-167} *nm* (153/154 days). The starting bond thickness of $\text{Silica}_{\text{KOH(0.1N),T}}$ is smaller than the corresponding values of $\text{Silica1}_{\text{KOH(0.1N)}}$ (441^{+158}_{-158} *nm*) and $\text{Silica2}_{\text{KOH(0.1N)}}$ (266^{+15}_{-11} *nm*). In Table 4.1 (section 4.3) the bond thicknesses obtained using the Bayesian and flatness methods are shown.

The values of the bond reflectivity, refractive index and thickness of $\text{Silica}_{\text{KOH(0.1N),T}}$ suggest that an elevated temperature to cure a hydroxide-catalysis bond may modify the

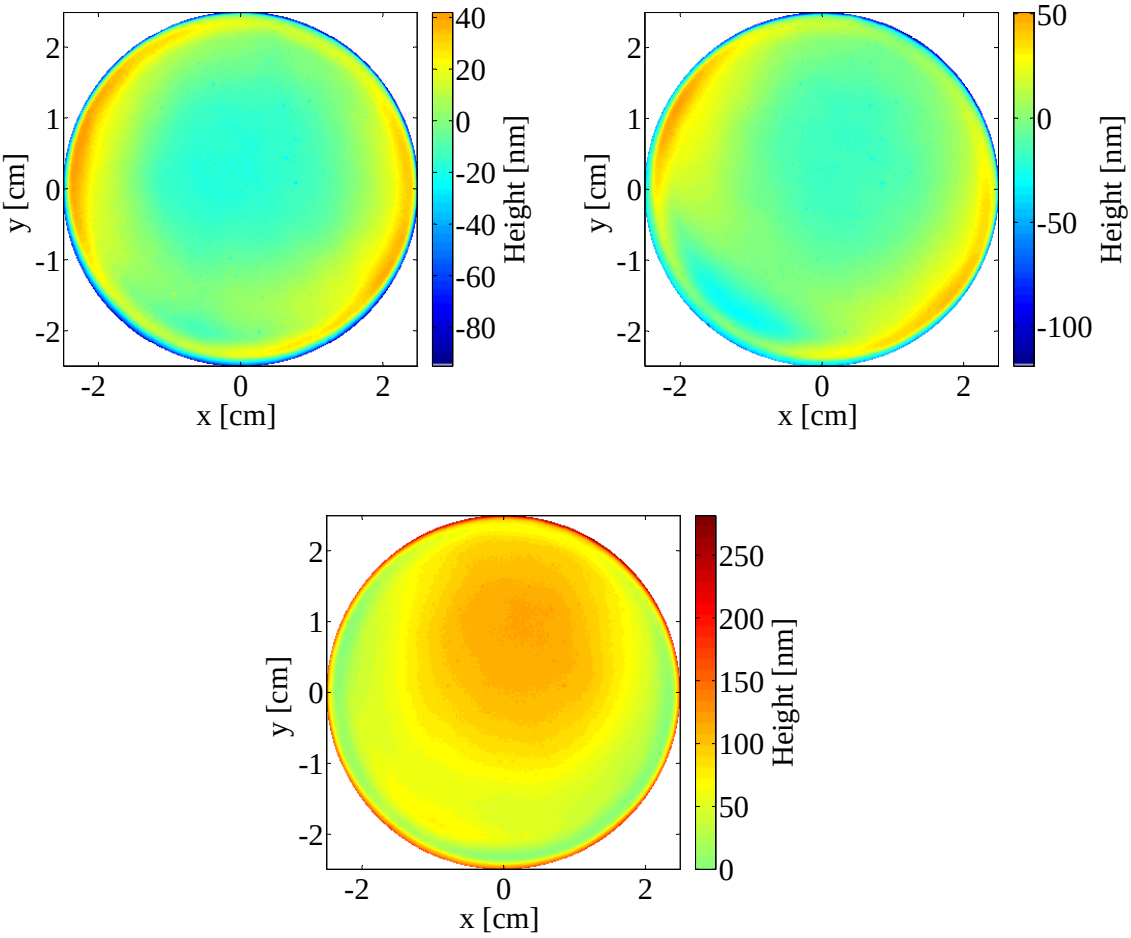

Fig. 4.22 (first row) Flatness maps of the bonding surfaces of the two discs which make $\text{Silica}_{\text{KOH(0.1N),T}}$. These were obtained using the functions of the Simtools package (see Appendix E) which zoomed in on a valid area and remove various offsets from the ZYGO® maps. (second row) Relative separation between two bonding surfaces of discs bonded by hydroxide-catalysis bonding. This map was obtained using the Matlab code reported in Appendix E.

chemistry of the hydroxide-catalysis bonding between potassium hydroxide solution and fused silica substrate material. It seems that the heat treatment used in this thesis slows down the bond refractive index from reaching that of fused silica or increases the value of the bond thickness. This should be investigated further.

4.3 Summary

In this chapter the reflectivities of the bonds between two fused silica discs bonded using potassium hydroxide solution (0.1 N solution in water) were measured. Two samples ($\text{Silica1}_{\text{KOH(0.1N)}}$ and $\text{Silica2}_{\text{KOH(0.1N)}}$) were bonded and made nominally identical for the curing at room temperature, whereas only one sample ($\text{Silica}_{\text{KOH(0.1N),T}}$) was bonded for the curing at elevate temperature (100 $^{\circ}C$ for 8 hours).

The bond reflectances found for $\text{Silica1}_{\text{KOH(0.1N)}}$ and $\text{Silica2}_{\text{KOH(0.1N)}}$ are lower than those of $\text{Silica}_{\text{KOH(0.1N),T}}$ for both polarisations and colour of laser light: they are below 0.01×10^{-3} after one month from bonding for the room temperature cured samples, whereas the elevated temperature cured sample reaches this level of reflectivity only after 150 curing days. These different levels of reflectivity were due to the variations of the refractive index and thickness that a bond may suffer during the curing period: the low reflectivity could be explained by the matching of the refractive index of solution to that of fused silica. The reflectivity of $\text{Silica}_{\text{KOH(0.1N),T}}$ is similar to that measured for the sodium silicate solution counterparts.

For all the three samples, the bond refractive index increases as a function of the curing time, but the rate of increase of $\text{Silica1}_{\text{KOH(0.1N)}}$ and $\text{Silica2}_{\text{KOH(0.1N)}}$ seems to be faster than that of $\text{Silica}_{\text{KOH(0.1N),T}}$. For the two room temperature cured samples, the bond refractive index varies from 1.42 ($\text{Silica1}_{\text{KOH(0.1N)}}$) or 1.44 ($\text{Silica2}_{\text{KOH(0.1N)}}$) in the first days after bonding to 1.46 after about two months, whereas for the elevated temperature cured sample it increases from 1.36 (1/2 days) to 1.45 (153/154 days). This seems to suggest that the heat treatment used in this thesis influences the evolution of the refractive index of the bonds, making it reach the value of the fused silica more slowly than the other samples. The fact that the bond refractive index approaches that of the fused silica quickly explains why the reflectivity of $\text{Silica1}_{\text{KOH(0.1N)}}$ and $\text{Silica2}_{\text{KOH(0.1N)}}$ is so low after one month from bonding. Also, the values obtained for $\text{Silica1}_{\text{KOH(0.1N)}}$ and $\text{Silica2}_{\text{KOH(0.1N)}}$ are higher and go up more quickly than those estimated for the sodium silicate samples discussed in Chapter 3 of which the trend is more comparable to that of $\text{Silica}_{\text{KOH(0.1N),T}}$. The trend of $\text{Silica}_{\text{KOH(0.1N),T}}$ is the same as that of sodium silicate bonds, but with a more rapid increase of the refractive index

toward the refractive index of fused silica. The refractive index of the potassium hydroxide solution was calculated to be about 1.33 (an approximate value of the refractive index of the bonding solution can be calculated if the refractive index of mixed liquids is supposed to be proportional to the volumes of each liquid used), which is below the value found for the first days of curing for all the samples cured at room and elevated temperature.
It might seem counterintuitive that the refractive index of the KOH bonds goes up much faster than sodium silicate bonds between fused silica substrates as the number of hydroxide ions OH^- in the sodium silicate solution should be much higher than in 0.1 *N* KOH solution. However, it is thought that the sodium silicate solution keeps the pH at a more or less constant value due to the buffering effect of the silicate in the solution [104] (the pH between the different concentrations used does not vary much). As the hydroxide ions in the sodium silica solution etch the fused silica substrate, the number of these hydroxide ions does not reduce because of the buffering effect and the pH is slow to drop below 11 (section 1.5.1). This delays further gelling or siloxane chain formation. Potassium hydroxide solution is not a buffered solution (as it does not contain silicates) and it etches fused silica substrate more efficiently than sodium silicate solution, enriching the bond with silicates. Consequently, the pH of hydroxide ions OH^- in this solution can fall below 11 fast during the etching process, causing gelling much more quickly. This may be what causes a refractive index of the KOH bond to be much higher more quickly than that for sodium silicate bonds.

For $\text{Silica1}_{\text{KOH(0.1N)}}$ and $\text{Silica2}_{\text{KOH(0.1N)}}$, it was not possible to collect sufficient data to measure the changes of the bond thickness as a function of curing, because of the very low bond reflectances. Like the samples discussed in Chapter 3, the low levels of reflectivity seem to affect the thickness measurements more than the reflectivity ones. For $\text{Silica}_{\text{KOH(0.1N),T}}$, the bond thickness increased as a function of the curing time, like $\text{Silica}_{\text{Na2SiO3(1:6),T}}$. A summary of results of the bond thickness obtained from flatness maps, Bayesian analysis and SEM imagining for the samples studied in this chapter is shown in Table 4.1.
As noted for other samples, the SEM images for $\text{Silica1}_{\text{KOH(0.1N)}}$ were taken more than a year after the bond reflectivity measurements and, for this reason, it is not easy to simply compare the bond thicknesses found. Except for $\text{Silica}_{\text{KOH(0.1N),T}}$, the bond thickness values obtained from the Bayesian analysis and those from the flatness maps differ: the thickness of a bond does not have to coincide with the the relative separation between two bonding surfaces of substrates necessarily.

The results obtained for the bond reflectivity, refractive index and thickness of these three samples seem to suggest that the KOH ions etch the surface effectively at room temperature, making the bond refractive index approach that of fused silica substrate within a short time

Name of sample	Location	Flatness maps	Optical reflectivity		SEM imaging	
		d (nm)	d (nm)	t_c (days)	d (nm)	t_c (days)
$\text{Silica1}_{\text{KOH(0.1N)}}$	C	8^{+4}_{-4}	441^{+158}_{-158}	3.5	41^{+12}_{-12}	430
$\text{Silica2}_{\text{KOH(0.1N)}}$	C	320^{+6}_{-6}	266^{+15}_{-11}	2	-	-
$\text{Silica}_{\text{KOH(0.1N),T}}$	C	105^{+4}_{-4}	171^{+225}_{-167}	50.5	-	-

Table 4.1 Summary of bond thicknesses d obtained using three different methods: the relative separation map (third column), the Bayesian analysis of reflectivity measurements (fourth column), and SEM imaging (fifth column). In the Bayesian analysis column, for $\text{Silica2}_{\text{KOH(0.1N)}}$ the thickness obtained from the highest joint posterior probability density function was considered, whereas for the other samples the average of the green and red thicknesses was reported. Location on the front surface of sample (C) and curing time (t_c) expressed in days were also reported.

and, as a consequence, making the bond reflectivity decrease to very low values. But the heat treatment used in this thesis, even if it does not damage the visual bond quality, seems to alter the chemistry of the hydroxide-catalysis bonding, slowing down the rate of increase for the bond refractive index (compared to that of potassium hydroxide samples cured at room temperature) and determining an increase of the bond thickness over time. This may give interesting insight in the chemistry involved and this needs further investigation.

Also, it would be recommended conducting strength tests on samples cured at elevated temperatures (like $\text{Silica}_{\text{Na2SiO3(1:6),T}}$ and $\text{Silica}_{\text{KOH(0.1N),T}}$) to verify the possible correlation between curing temperature, tensile strength and thickness of a hydroxide-catalysis bond. If it is confirmed that a heat treatment increases the bond strength (as obtained by Haughian et al. [102]) and the bond thickness (the upper value is less than 400 *nm* for $\text{Silica}_{\text{Na2SiO3(1:6),T}}$ and $\text{Silica}_{\text{KOH(0.1N),T}}$), this may be an important property of the hydroxide-catalysis bonding. Heat-treated samples may be recommended for those applications which require that the bonds between various optical components reach high mechanical strength quickly and do not necessarily have to meet strict requirements for thickness to obtain high precision alignment and high positional stability.

Chapter 5

Measurements on sapphire samples

The ultimate goal of research described here is to evaluate and tailor optical and physical properties of hydroxide-catalysis bonds, such as bond refractive index and thickness, for optimum use in optical applications. Substrate materials of interest in the commercial optics industry can be, for example, fused silica and phosphate glass (isotropic in material properties), and sapphire (anisotropic material). Sapphire is also one of the materials taken into consideration for the fabrication of quasi-monolithic mirror suspensions operating at cryogenic temperatures to reduce thermal noise for the next generation of gravitational wave detectors (see subsection 1.5.3 and Appendix A for details) [105]. Investigating the mechanical properties of test masses and suspensions made with sapphire using hydroxide-catalysis bonding at cryogenic temperatures is currently an active area of research.

In this chapter, the properties of hydroxide-catalysis bonds between sapphire substrates bonded using sodium silicate solution (section 5.1) and potassium hydroxide solution (section 5.2) are reported. Samples were analysed for different curing times after bonding using the upgraded setup in green and red laser light (Figure 2.5). Their physical characteristics are described in subsection 2.4.1.

5.1 Bond with sodium silicate 1:6 solution

Sodium silica solution was chosen to make the comparison of results obtained using the same bonding solution, but different substrate materials, in this case fused silica (discussed in Chapter 3) and sapphire. This allowed a better understanding of how the reflectivity, refractive index and thickness of a bond might vary because of the different chemical interaction between bonding solution and material.

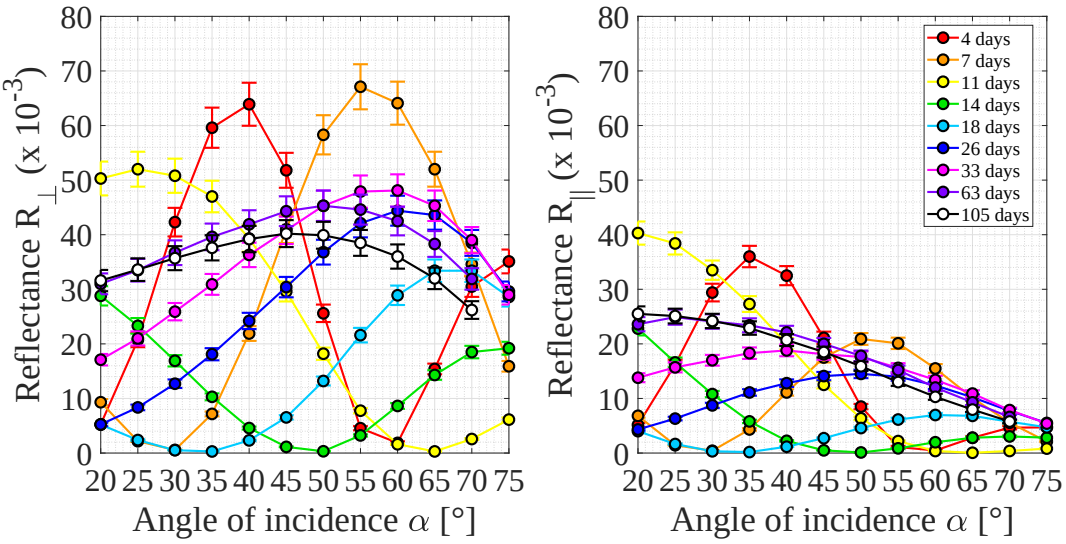

Fig. 5.1 Measured reflectances for $\perp$ (left) and $\parallel$ (right) polarisation plotted as a function of the angle of incidence α for the central position on the front surface of $\text{Sapphire}_{\text{Na2SiO3(1:6)}}$. In the legend, the curing time is reported. All measurements were taken using the upgraded setup in green mode.

5.1.1 $\text{Sapphire}_{\text{Na2SiO3(1:6)}}$

Sample $\text{Sapphire}_{\text{Na2SiO3(1:6)}}$ was made by bonding together sapphire substrates with c-crystallographic planes oriented parallel to the surfaces being bonded. The amount of sodium silicate solution diluted with de-ionised water (volumetric ratio of 1 : 6) used was 15.70 μl. This sample was left to cure in air at room temperature for four days before measuring the reflectivity of its bond.

5.1.2 Reflectivity measurements

The reflectances of this sample were measured for the central position on its front surface at different time intervals after bonding.

Plots of the measured reflectivities for perpendicular ($\perp$) and parallel ($\parallel$) polarisations (equations 2.1 and 2.2) as a function of the angle of incidence α are shown in Figure 5.1 ($\text{Sapphire}_{\text{Na2SiO3(1:6)}}$ in green mode) and Figure 5.2 ($\text{Sapphire}_{\text{Na2SiO3(1:6)}}$ in red mode). The calculation of the error bars for the measured angles of incidence and reflectances is explained in subsection 3.1.2.1: the values used are the same as those reported for fused silica case. This error analysis was used for both sapphire samples analysed in this thesis.

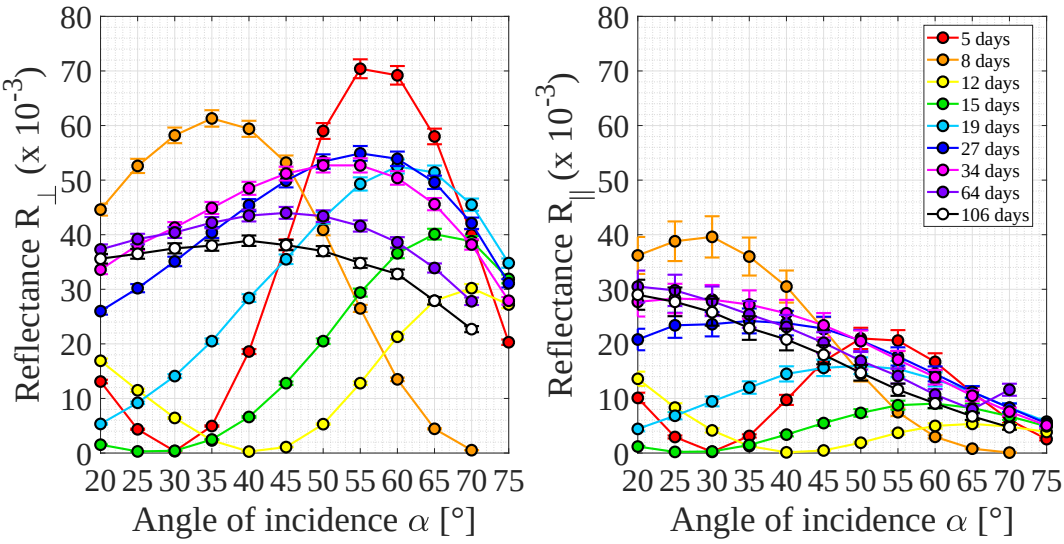

Fig. 5.2 Measured reflectances for $\perp$ (left) and $\parallel$ (right) polarisation plotted as a function of the angle of incidence α for the central position on the front surface of $\text{Sapphire}_{\text{Na2SiO3(1:6)}}$. In the legend, the curing time is reported. All measurements were taken using the upgraded setup in red mode.

For both polarisations and colours of laser light, the values of bond reflectances are all less than 10%, one order of magnitude greater than the corresponding reflectances measured for fused silica samples (see section 3.1). This is due to the difference in refractive index between substrate material and hydroxide-catalysis layer: the bigger the difference between the refractive index of sapphire and that of bond is, the bigger the reflectance of bond is. Also, differently from the fused silica samples, the reflectivity values do not follow a well-defined trend over the curing time. In the first two weeks the reflectivity seemed to drop as curing time increases, then the reflectivity increased and after one month it decreased again. Because of the insufficient time, it was not possible to collect more data. Measuring reflectivity of this bond at a long time interval after bonding could be useful to understand if this trend was only an 'adjustment' phase which lasted up to a month and after this period the reflectivity started to drop in a similar manner to that seen for the silica samples.

5.1.3 Analysis result: reflectivity

The peak reflectivity of the bond for both polarisations and colours of laser light as a function of curing time for $\text{Sapphire}_{\text{Na2SiO3(1:6)}}$ is plotted in Figure 5.3. After the initial fluctuation mentioned above, the values of the bond reflectivity decrease slowly as the cure proceeds. A

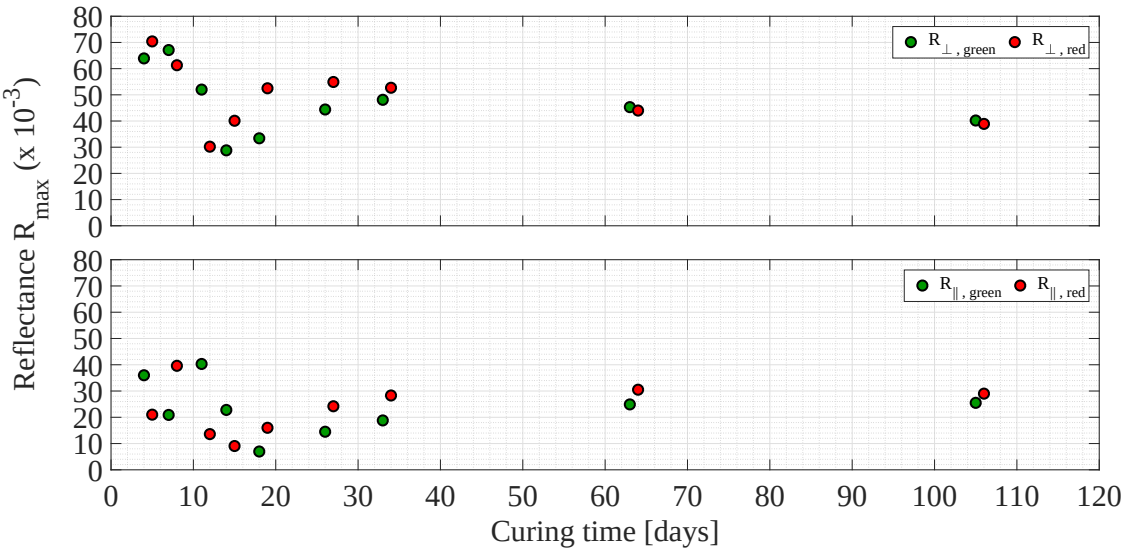

Fig. 5.3 Maximum value of measured reflectances for $\perp$ (top) and $\parallel$ (bottom) polarisation plotted as a function of the curing time for the central position on the front surface of $\text{Sapphire}_{\text{Na2SiO3(1:6)}}$ and for green and red laser light. Measurements were taken using the upgraded assembly.

discrepancy between the green and red maximum reflectances can be seen, where the red values are generally greater than the green ones. This is most likely due to a systematic error in the reflectance measurements (see 'Discussion' in section 5.1.5 for more details).

In Figure 5.4, the tensile strength of bonds made between sapphire substrates (optic axis directed along the c-axis), using 1 : 6 sodium silicate solution and cured at room temperature, is plotted as a function of curing time. An exponential fit is plotted as well showing the strength is higher in the first five weeks and then decreases in the following weeks. Differently from $\text{Silica1}_{\text{Na2SiO3(1:6)}}$ in Chapter 3, no strong correlation between the optical reflectivity and strength of a bond, both of which decrease as a function of curing time, can be seen from the comparison of Figure 5.4 and Figure 5.3.

5.1.4 Analysis result: refractive index and thickness

In the analysis of data for obtaining the bond refractive index and thickness, the script written in Matlab (see section 2.3.2 and Appendix D) was run using the following values:

- the refractive index of the air n_0 was approximated by 1, whereas the ordinary and extraordinary refractive indices of sapphire were $n_{1\text{o,green}} = 1.7717$ and $n_{1\text{e,green}} =$

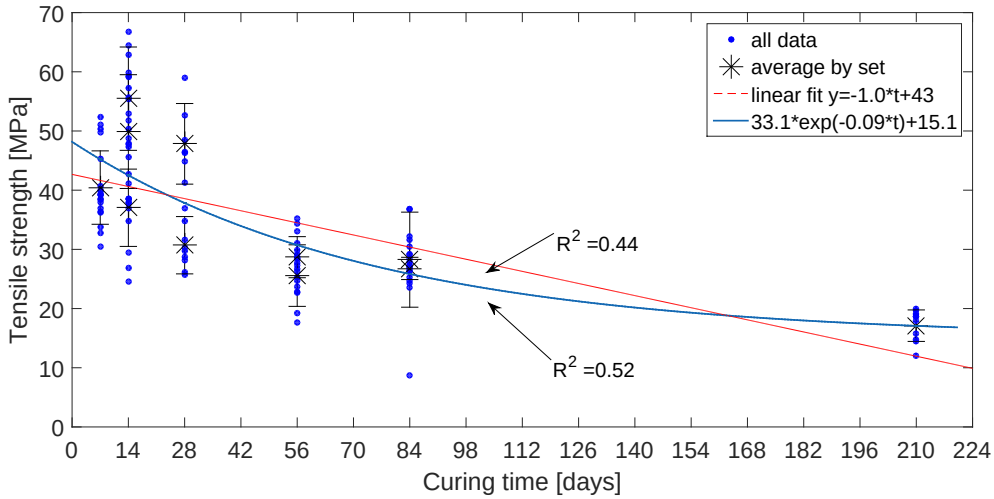

Fig. 5.4 Combined curing time tensile strength results (from 4-point bend tests) of hydroxide-catalysis bonded sapphire made using very similar procedures as used for the sample in this section (using 1 : 6 sodium silicate solution and curing at room temperature). Sets were made between 2014-2017 by a number of people. An exponential fit has been made showing the strength levels of after about 30 weeks of curing. Courtesy of Dr. M. Phelps [100].

1.7636 for the green laser, $n_{1o,red} = 1.7658$ and $n_{1e,red} = 1.7578$ for the red laser [90, 91];

- the grid of values for the bond layer (n_2 and d_2) was set, where the bond refractive index n_2 varied between 1.3000 and 1.7800 with step 0.0001, and the bond thickness d_2 between 0.0 nm and 8000.0 nm with step 0.5.

The range of values for n_2 is given by the condition that it cannot be less than the refractive index of water nor can it be more than the refractive index of sapphire.
As the amount of bonding solution used was 15.70 $\mu l = 15.70 \times 10^{-9}\ m^3$ and the bonding area of the disc was $2.03 \times 10^{-3}\ m^2$ (the diameter of these samples was 5.08 cm), the starting thickness of the amount of fluid was expected to be around $(15.70 \times 10^{-9}\ m^3)/(2.03 \times 10^{-3}\ m^2) = 7734\ nm$.

Figure 5.5 and Figure 5.6 show two examples of the results obtained from the Matlab script for sample $\text{Sapphire}_{\text{Na2SiO3(1:6)}}$ in green mode after 11 days and red mode after 106 days, respectively.

In Figure 5.7 and Figure 5.8, the bond refractive index (n_2) and thickness (d_2) values for $\text{Sapphire}_{\text{Na2SiO3(1:6)}}$ are plotted as a function of the curing time for both green and red laser light, respectively.

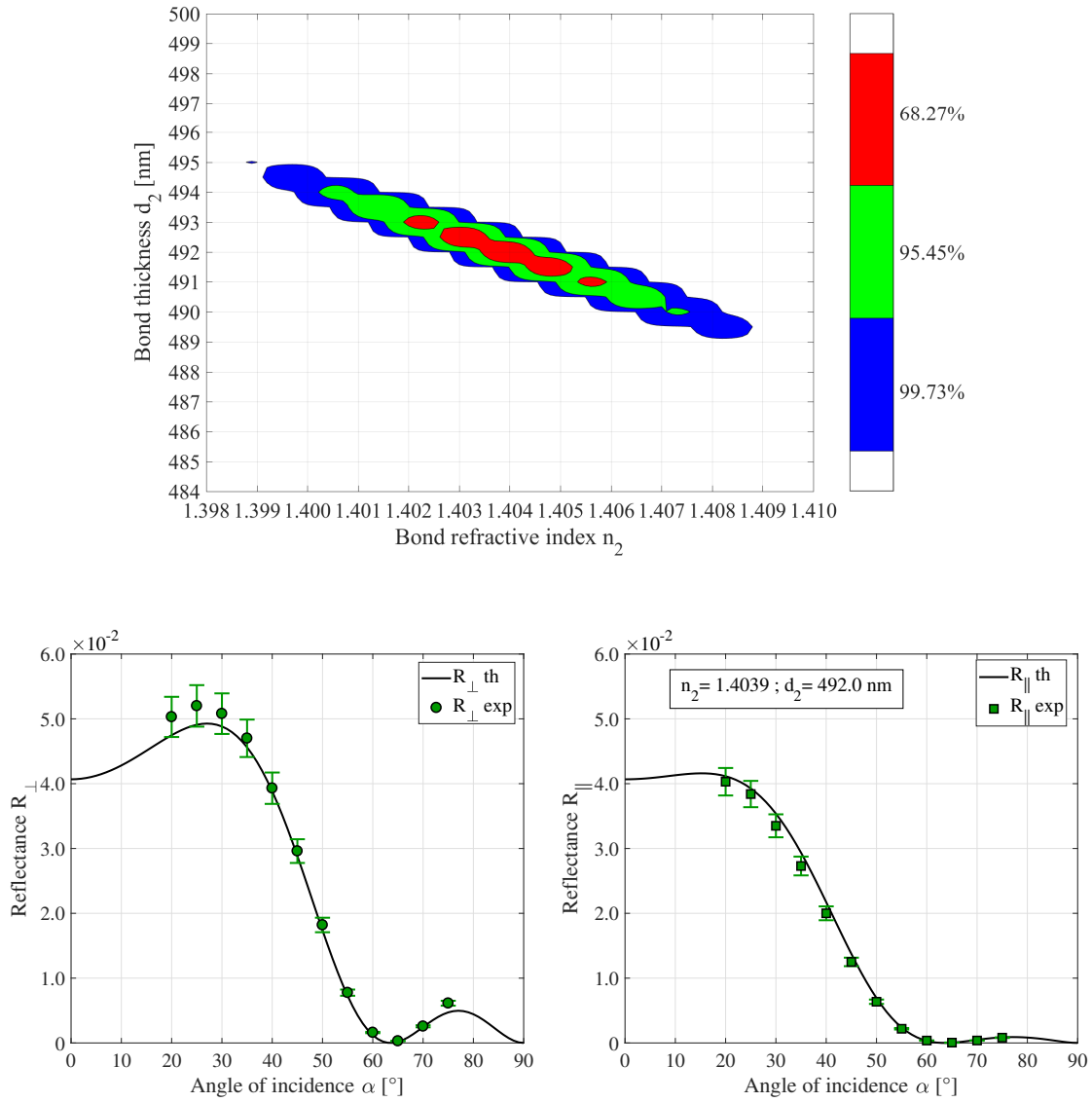

Fig. 5.5 (top) Three confidence levels of 68.3%, 95.5% and 99.7% probability. (bottom) Measured data with their corresponding error bars and theoretical curves. The green dots and squares represent the reflectances measured for perpendicular and parallel polarisation, respectively. The black solid lines are the theoretical perpendicular and parallel reflectances obtained using the most likely values of bond refractive index and thickness of the Bayesian analysis ($n_2 = 1.4039$ and $d_2 = 492.0$). These measurements were taken at 11 days after bonding for $\text{Sapphire}_{\text{Na2SiO3(1:6)}}$ in green light.

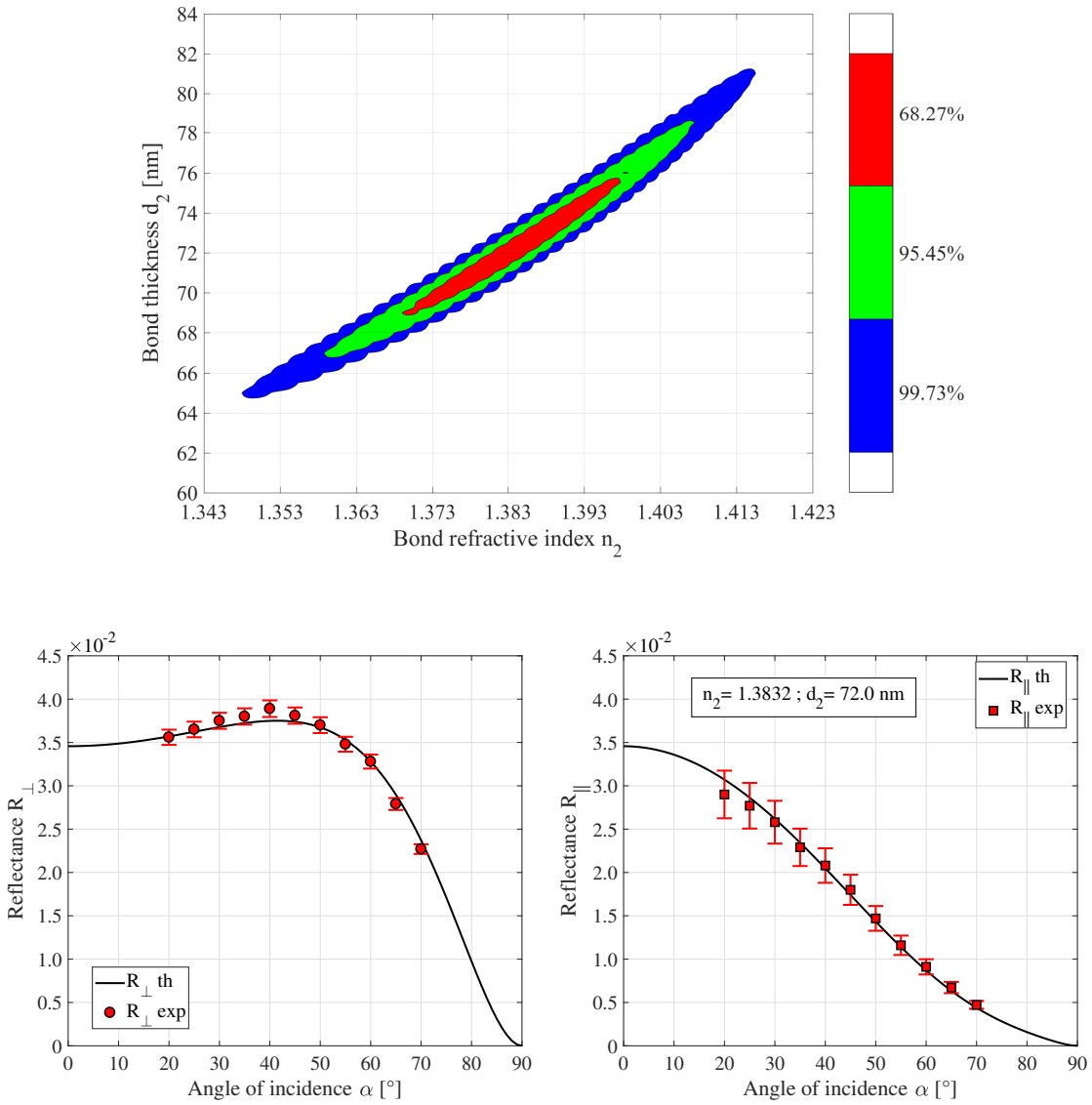

Fig. 5.6 (top) Three confidence levels of 68.3%, 95.5% and 99.7% probability. (bottom) Measured data with their corresponding error bars and theoretical curves. The red dots and squares represent the reflectances measured for perpendicular and parallel polarisation, respectively. The black solid lines are the theoretical perpendicular and parallel reflectances obtained using the most likely values of bond refractive index and thickness of the Bayesian analysis ($n_2 = 1.3832$ and $d_2 = 72.0$). These measurements were taken at 106 days after bonding for $\text{Sapphire}_{\text{Na2SiO3(1:6)}}$ in red light.

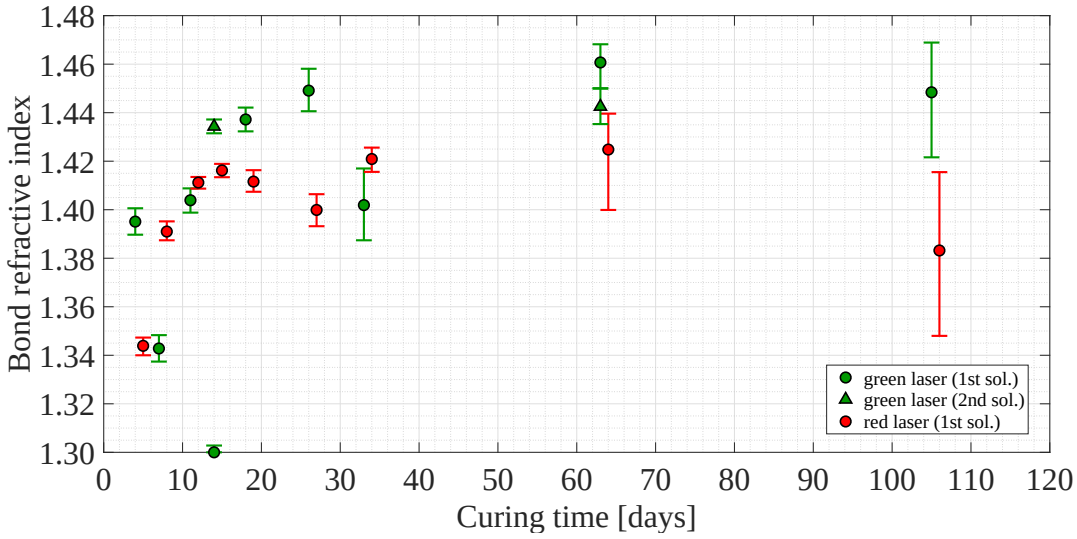

Fig. 5.7 Refractive index of the bond as a function of the curing time for the central position on the front surface of Sapphire$_{Na2SiO3(1:6)}$. These values were determined from measurements collected using the upgraded setup in green (green dots and triangles) and red (red dots) mode. Some data sets have multiple solutions, which are presented in order from the highest to the lowest joint posterior probability density function by dots and triangles.

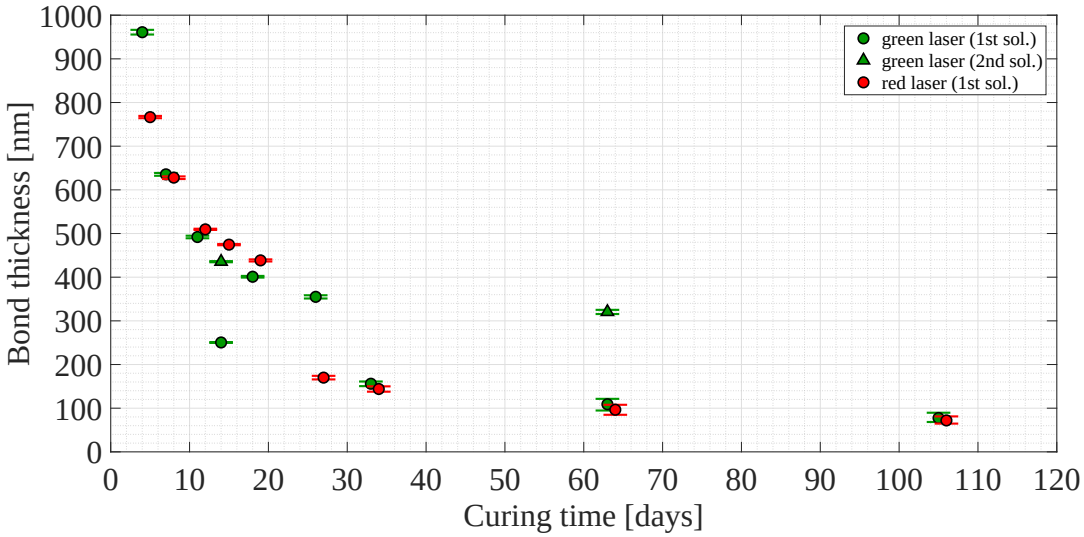

Fig. 5.8 Thickness of the bond as a function of the curing time for the central position on the front surface of Sapphire$_{Na2SiO3(1:6)}$. These values were determined from measurements collected using the upgraded setup in green (green dots and triangles) and red (red dots) mode. Some data sets have multiple solutions, which are presented in order from the highest to the lowest joint posterior probability density function by dots and triangles.

As for the peak reflectances shown in Figure 5.3, Figure 5.7 shows a discrepancy between the refractive indices found for green and red, where red has generally lower refractive index values than green. The average value of the difference between green and red refractive indices is about 0.04. For all silica samples no such discrepancy in bond refractive index was ever observed. This is most likely due to a systematic error in the reflectance measurements (see 'Discussion' in section 5.1.5 for details). Though the green and red bond refractive indices do not match up, it is possible to infer that bond refractive index increases rapidly in the first four weeks and then settles on a more or less constant value, which is different for each colour of the laser light. The green bond refractive index starts from about 1.40 (4 days) to about 1.45 (105 days), whereas the red bond refractive index varies from about 1.34 (5 days) to about 1.38 (106 days).

Figure 5.8 shows that the thickness of the bond decreases over time reaching the value 78^{+12}_{-9} *nm* for the green light and 72^{+9}_{-7} *nm* for the red one after more than three months, in agreement within their errors (Table 5.1). These bond thicknesses are smaller with respect to those found for 1 : 6 sodium silicate bonded fused silica samples ($\text{Silica1}_{\text{Na2SiO3(1:6)}}$ and $\text{Silica2}_{\text{Na2SiO3(1:6)}}$, see Chapter 3). From the comparison of Figure 5.8 and Figure 5.4 (as opposed to the reflectance), a correlation between the bond strength and bond thickness, both of which decrease as a function of curing time, can be seen.

In both plots, a jump around one month after bonding can be observed: this reflects the trend seen in Figure 5.3. This behaviour is not seen for any of the fused silica samples. It is not clear what caused it. Measurements on more samples should reveal if this is a repeatable feature.

The bonding surfaces of the two discs of $\text{Sapphire}_{\text{Na2SiO3(1:6)}}$ had a flatness of about 91 *nm* and 77 *nm* peak-to-valley respectively, which was measured using the ZYGO®: the flatness maps shown in the first row of Figure 5.9 were obtained for the two discs. Combining these maps, the relative separation between two bonding surfaces was obtained and it is shown in the second row of Figure 5.9: the relative separation map gives a value of 26^{+2}_{-2} *nm* for the bond thickness in central position (Table 5.1). The Bayesian bond thicknesses are greater than that calculated using the flatness maps.

No SEM measurements were taken on this sample.

As was discussed for the other samples studied in Chapter 3 and Chapter 4, the thicknesses obtained using the Bayesian analysis do not have to be necessarily in agreement with those obtained from the flatness maps. The bond thickness may continue to decrease with time reaching a smaller value and, also, the relative separation between two bonding surfaces is not necessarily the final thickness of a hydroxide-catalysis bond.

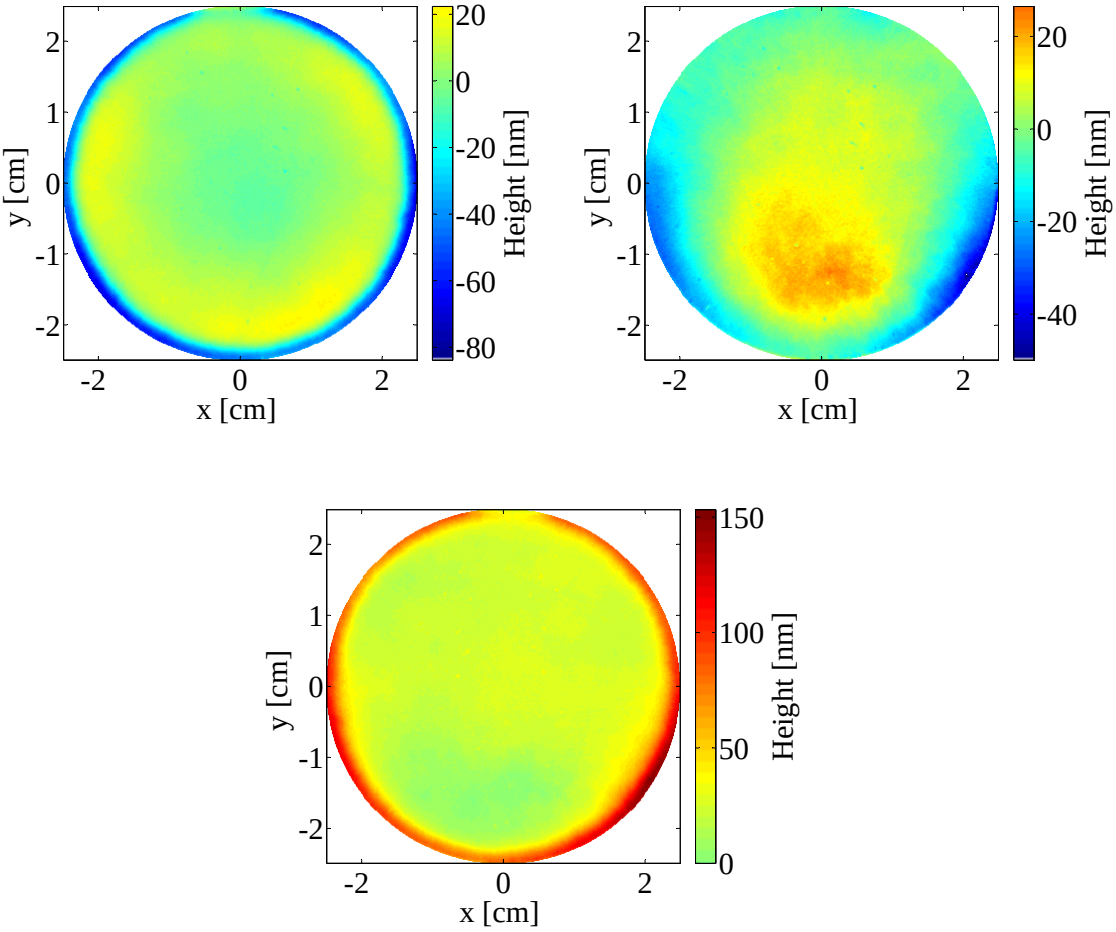

Fig. 5.9 (first row) Flatness maps of the bonding surfaces of the two discs which make $\text{Sapphire}_{\text{Na2SiO3(1:6)}}$. These were obtained using the functions of the Simtools package (see Appendix E) which zoomed in on a valid area and remove various offsets from the ZYGO® maps. (second row) Relative separation between two bonding surfaces of discs bonded by hydroxide-catalysis bonding. This map was obtained using the Matlab code reported in Appendix E.

5.1.5 Analysis result: discussion

The bond reflectances of $\text{Sapphire}_{\text{Na2SiO3(1:6)}}$ are less than 10%. This is one order of magnitude greater than those measured for the fused silica samples bonded using 1 : 6 sodium silica solution ($\text{Silica1}_{\text{Na2SiO3(1:6)}}$ and $\text{Silica2}_{\text{Na2SiO3(1:6)}}$, in Chapter 3). This is due to the larger difference between the refractive index of the sapphire substrate material and the bonding solution with respect to that between the fused silica substrate and the bonding solution. Also, it seems that there is no strong correlation between the optical reflectivity and strength of a bond as it was found for $\text{Silica1}_{\text{Na2SiO3(1:6)}}$ and $\text{Silica2}_{\text{Na2SiO3(1:6)}}$: the reduction in the strength of the sapphire is slower than for fused silica.

Both the bond maximum reflectivity and refractive index measurements for sample $\text{Sapphire}_{\text{Na2SiO3(1:6)}}$ show some discrepancy between the green and red results, which does not seem to be present in the bond thickness measurements. This may be due to a systematic error in calculating the bond optical reflectances. Also, it is possible that other physical processes, dependent on the wavelength of the incident light, take place in sapphire material, in addition to the birefringence. Hypotheses that may explain the nature of this discrepancy are considered below.

The first one may be the Rayleigh scattering of the light in the substrate material. The Rayleigh scattering losses are caused by the interaction of laser light with inhomogeneities/defects in the propagation medium or in the interface between crystalline and bonding material, or with surface roughness [74, 106, 107]. It is known that crystalline materials (like sapphire) generally have more scattering than amorphous materials (like fused silica) as most crystalline materials have flaws in their crystal lattice which can cause this. Rayleigh scattering occurs when the size of defect/roughness is smaller than one-tenth of the wavelength of the radiation. The intensity of the scattered light is inversely proportional to the fourth power of the wavelength: shorter wavelengths are scattered more than longer wavelengths of the incident light. This means that as the wavelength increases, the loss caused by Rayleigh scattering decreases: in this case, green light ($\lambda = 532\ nm$) is scattered about two times more than red light ($\lambda = 635\ nm$) [74, 106]. This means that in making reflectance measurements there is an overall underestimation of the actual reflectance from the bond and that the reflectance of the bond green is underestimated more than for red. This translates in different answers for the refractive index for green and red, where the green refractive index is higher, which is indeed what one can see. This suggests that the red refractive index, and in general the red data, is more correct than the green ones.

Ju et al. have shown that the optical scattering intensity in sapphire sample is a function of the angle between the incident light polarisation direction and the crystal optical axis

(c-axis orientation in this paper) [107]. The sapphire sample used by Ju et al. had the c-axis perpendicular to the cylindrical axis and the a-axis along the cylindrical axis, and the incident light was perpendicular to the c-axis [107]. Even if the method of measurement was different from that used for the two sapphire samples studied in this chapter (the optic axis was directed along the c-axis, perpendicular to the bonding surface, and the incident beam formed an angle with this), the angular dependence of the scattering from sapphire on the directions between the optical axis of the crystal, the polarisation of the laser beam and the observation angle should be observed in these samples as well. A similar study should be done on these samples in order to measure, if present, the scattering intensities and their angular dependence on the c-axis. If this was found to be the case, then the theoretical model described in section 2.2.2 would have to be modified to take into consideration these losses. However, as Rayleigh scattering in sapphire has been measured to be 13 ppm/cm at wavelengths of 633 *nm* and 1064 *nm* [108], whereas in fused silica it is only 0.7 ppm/cm at 1064 *nm* wavelength [109], this seems unlikely to be responsible for the discrepancy in the results here, because its contribution is negligible compared to the values of bond reflectances measured for $\text{Sapphire}_{\text{Na2SiO3(1:6)}}$.

The second hypothesis taken into account was the optical absorption of the intensity of the laser light inside the sapphire substrate. Alexandrovski et al. measured optical absorption coefficients for different sapphire crystals at 532 *nm* and 1064 *nm* wavelength [110]: optical absorption coefficients ranged from 1150 ppm/cm to 1910 ppm/cm for 532 *nm*, and from 46 ppm/cm to 211 ppm/cm for 1064 *nm*. For wavelength of 1064 *nm*, the optical absorptions measured by Alexandrovski et al. at room temperature were in agreement with those obtained by Tomaru at al. [111] at cryogenic temperatures: the optical absorption coefficients of two mono-crystalline sapphire samples (cylinder axis parallel to the c-axis) cooled to 5 *K* ranged from 88 ppm/cm to 90 ppm/cm (± 10 ppm/cm) at 1064 *nm*. Comparing these results with those reported for Rayleigh scattering, optical absorption in sapphire material at 1064 *nm* is about ten times bigger than scattering at the same wavelength. Even if optical absorption in green wavelength (532 *nm*) is bigger, this contribution was still negligible with respect to the values of bond reflectances measured for $\text{Sapphire}_{\text{Na2SiO3(1:6)}}$.

The last hypothesis considered was the effect that a systematic error in the estimation of the optical reflectances could have on the values of the refractive index of a bond. As said in Chapter 2, a rectangular slit (~ 1 *mm* wide) was placed in front of photodetector 2 which was used for measuring both the conversion factor k (that is V_{input}) and the intensity of the reflected beam off the bond (that is V_{output}). See section 2.1.3 for details. If the size of the laser beam at the two positions of photodiode 2 is not the same, the reflectivity

measurements can be under/over-estimated. Indeed, due to this effect, the measurement of the intensity of the reflected green light at the photodiode was approximately 25% lower than the value suggested by the calibration. For the red light, this effect was considerably smaller, approximately 2%.

An approximated estimation of the significance of this effect is given by considering the simple case of normal incidence of light (angle of incidence α is zero, see Figure 2.13 and Figure 2.17). Under this condition, both equations 2.22 and 2.23 for fused silica material, and equations 2.38 and 2.39 for sapphire material can be simplified in the following way:

$$R_{\text{bond}} = \mathscr{C}(n_1 - n_2)^2 \tag{5.1}$$

where $\mathscr{C}$ is a constant, n_1 is the refractive index of the fused silica for the isotropic case ($n_{1,\text{green}} = 1.4607$ for green light and $n_{1,\text{red}} = 1.4570$ for red light [82]) and it is the ordinary refractive index of the sapphire for the anisotropic case ($n_{1\text{o,green}} = 1.7717$ for the green laser and $n_{1\text{o,red}} = 1.7658$ for the red laser [90, 91]), n_2 is the refractive index of the bonding solution. The corresponding reflection coefficients (equations 2.24, 2.25, 2.26, 2.27, 2.40, 2.41, 2.42 and 2.43) reduce to:

$$r_{lm} = \left| \frac{n_l - n_m}{n_l + n_m} \right| \tag{5.2}$$

where n_l and n_m are the refractive indices of the two media l and m (in order of the propagation direction of the ray) that define the interface where reflection happens. This means that for normal incidence the reflection coefficients coincide with those that would be obtained for an interface formed by two isotropic media l and m of refractive indices n_l and n_m [80]. If R_{bond} changes by some amount ΔR_{bond}, from equation 5.1 one obtains:

$$\frac{\Delta R_{\text{bond}}}{R_{\text{bond}}} = -\frac{2}{(n_1 - n_2)} \Delta n_2 \tag{5.3}$$

and consequently:

$$\Delta n_2 = -\frac{1}{2}(n_1 - n_2) \frac{\Delta R_{\text{bond}}}{R_{\text{bond}}} \tag{5.4}$$

$\Delta R_{\text{bond}}/R_{\text{bond}}$ was measured to be about 25% for the green laser light and 2% for the red one. These results suggest that the bond reflectivities measured using green laser light are underestimated and that they should be increased by about 25%, whereas the error on R_{bond} for the red laser light can effectively be neglected. As a consequence, Δn_2 is negligible for the red values of the bond refractive index obtained for both fused silica and sapphire samples, but it represents a systematic error for the green values of the bond refractive index.

As the quantity $(n_1 - n_2)$ is smaller for fused silica samples ($n_{1,\text{green}} = 1.4607$ [82]) than for sapphire samples ($n_{1\text{o,green}} = 1.7717$ [90, 91]), Δn_2 is negligible for the former and is around -0.04 for the latter. This means that the values of refractive index for sapphire samples studied using the red laser are correct, whereas those in green are overestimated and the quantity Δn_2 should be subtracted from the green refractive index measurements. For $\text{Sapphire}_{\text{Na2SiO3(1:6)}}$, the value of Δn_2 equalling 0.04 is in agreement with the average value of the difference between the green and red refractive indices of approximately 0.04. This appears to be the most likely hypothesis to explain the discrepancy in bond refractive index between the green and red data for sapphire samples. This appears to affect the thickness measurements less than the refractive indices.

If one considers the results obtained using the red light to be closer to the correct values than those obtained using green light, this suggests that the refractive index of the 1 : 6 sodium silicate bond is not higher than 1.38 after three months. This result is lower than the values for bonds between silica, which reach a refractive index equalling 1.43 ($\text{Silica1}_{\text{Na2SiO3(1:6)}}$ and $\text{Silica2}_{\text{Na2SiO3(1:6)}}$ in Chapter 3). This agrees with expectations that little aluminium oxide is introduced into the bond, which suggests that the bond material should be mostly silicates. This discounts the proposed reactions stated in section 1.5.1 and suggests the silicates in the solution merely attach to the sapphire.

Table 5.1 in section 5.3 shows the bond thicknesses obtained using the Bayesian and flatness methods. The bond thickness obtained by the Bayesian analysis decreases as curing time increases and then settles on a constant value (78^{+12}_{-9} *nm* for the green light and 72^{+9}_{-7} *nm* for the red light), which is greater than the value measured by the flatness map (26^{+2}_{-2} *nm*). As said for the other samples, this suggests that the optical bond thickness is not necessarily determined by the conformity of the substrates bonded together. Also, this value is smaller than that of the corresponding fused silica samples, 134^{+14}_{-18} *nm* for $\text{Silica1}_{\text{Na2SiO3(1:6)}}$ (98 days) and 173^{+11}_{-18} *nm* for $\text{Silica2}_{\text{Na2SiO3(1:6)}}$ (104.5 days) for their central positions (see Table 3.1). This suggests again that the sapphire is not etched and does not facilitate bulking out the bond with polymer chains which means the bond thickness is determined by the silicates in the solution only.

5.2 Bond with KOH solution

Potassium hydroxide solution was chosen for the same reasons as discussed above for sodium silica solution: the comparison of results obtained using the same bonding solution, but different substrate materials (fused silica in Chapter 4 and sapphire) allowed the understanding of

how the properties of a hydroxide-catalysis bond (like the optical reflectivity, refractive index and thickness) might change because of the different chemical reaction between bonding solution and substrate material.

5.2.1 Sapphire$_{\mathbf{KOH(0.1N)}}$

Sample Sapphire$_{\mathrm{KOH(0.1N)}}$ was made by bonding two sapphire discs with c-crystallographic planes parallel to the bonding surfaces and using 15.70 μl of potassium hydroxide solution KOH which was composed of 0.1 N solution in water and was used without diluting it with de-ionised water. This sample was then left to cure in air at room temperature for some days before measuring the reflectivity of their bonds.

Some difficulties were encountered on attempting to bond these sapphire discs using potassium hydroxide solution. Two more samples were prepared before Sapphire$_{\mathrm{KOH(0.1N)}}$, but both of them started to debond a few days after bonding. Sapphire$_{\mathrm{KOH(0.1N)}}$ was better but also showed a strong debonding after about two weeks. However, reflectivity measurements were attempted using this sample. In Figure 5.10, some photos of sample Sapphire$_{\mathrm{KOH(0.1N)}}$ are shown, where it is possible to see some phases of its debonding. The other two samples were easily debonded fully by rinsing under water a week after bonding. It should be noted that it is somewhat unexpected that these samples did not bond well as at Glasgow University sapphire samples were bonded using potassium hydroxide solution successfully [52], though Dari et al. [51] reported difficulties. The reasons could be twofold: the surface finish of the sapphire could have played a part or the pH of the solution could have influenced the success of the bond. These should be investigated further.

5.2.2 Reflectivity measurements

The reflectance of this sample was measured for the central position on its front surface at three different time intervals after bonding (approximately two weeks, one and two months after bonding).

Plots of measured reflectivity for perpendicular and parallel polarisations (equations 2.1 and 2.2) as a function of the angle of incidence α are shown in Figure 5.11 (Sapphire$_{\mathrm{KOH(0.1N)}}$ in green mode) and Figure 5.12 (Sapphire$_{\mathrm{KOH(0.1N)}}$ in red mode).

Like Sapphire$_{\mathrm{Na2SiO3(1:6)}}$, bond reflectances are all less than 10% for both polarisations and colours of laser light and greater than the corresponding reflectances measured for fused silica samples (see section 4.1). This is in all cases expected as being due to the difference between the refractive index of sapphire and the refractive index of the bond layer: the bond

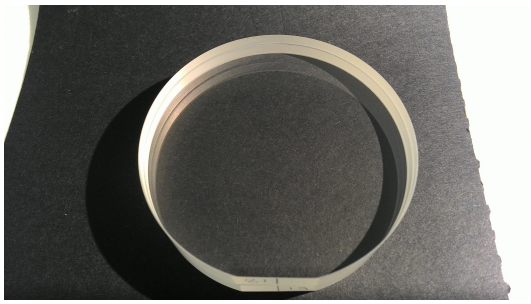

(a) Day of bonding

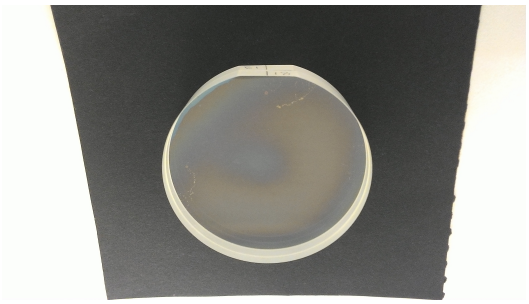

(b) 1 day after bonding

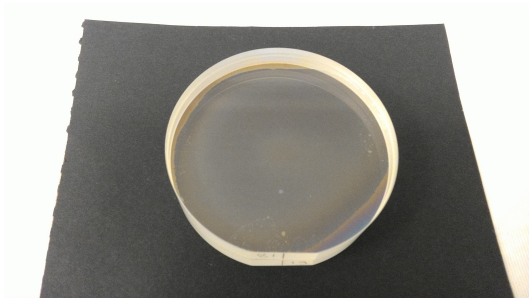

(c) 6 days after bonding

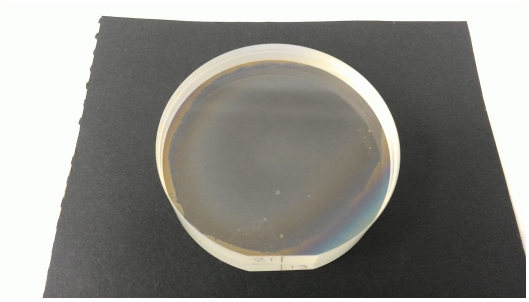

(d) 14 days after bonding

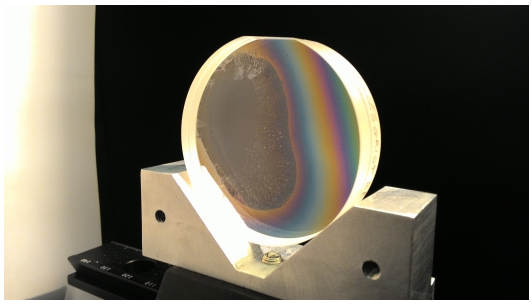

(e) 22 days after bonding

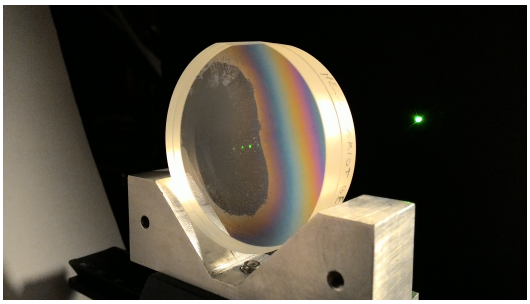

(f) 35 days after bonding

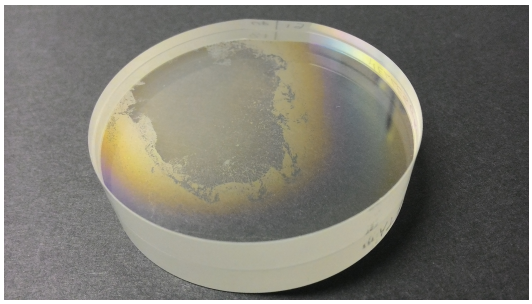

(g) 56 days after bonding

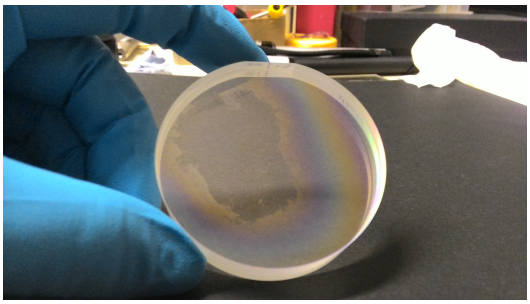

(h) 80 days after bonding

Fig. 5.10 Photographs of sample $\text{Sapphire}_{\text{KOH(0.1N)}}$ taken at different time intervals after bonding. The bond between two sapphire discs seemed successful in the day of bonding, but a light debonding already came into view the day after bonding. After about two weeks, debonding started to affect all the surface of sample.

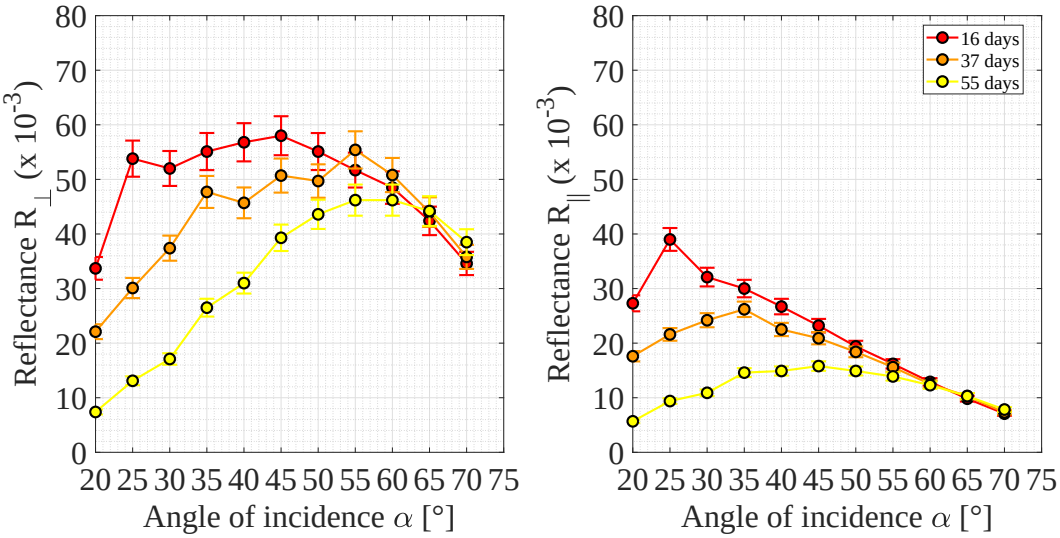

Fig. 5.11 Measured reflectances for $\perp$ (left) and $\parallel$ (right) polarisation plotted as a function of the angle of incidence α for the central position on the front surface of $\text{Sapphire}_{\text{KOH(0.1N)}}$. In the legend, the curing time is reported. All measurements were taken using the upgraded setup in green mode.

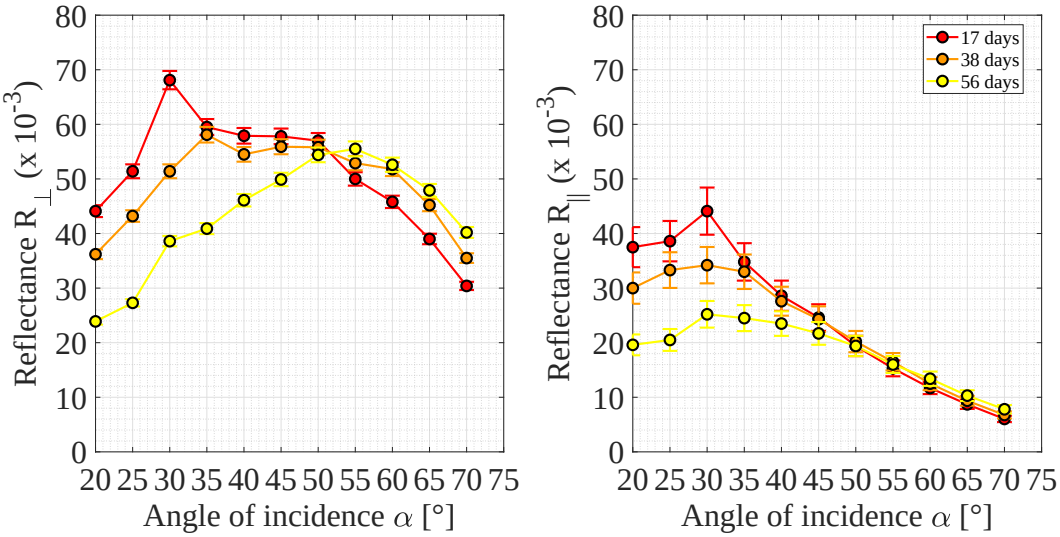

Fig. 5.12 Measured reflectances for $\perp$ (left) and $\parallel$ (right) polarisation plotted as a function of the angle of incidence α for the central position on the front surface of $\text{Sapphire}_{\text{KOH(0.1N)}}$. In the legend, the curing time is reported. All measurements were taken using the upgraded setup in red mode.

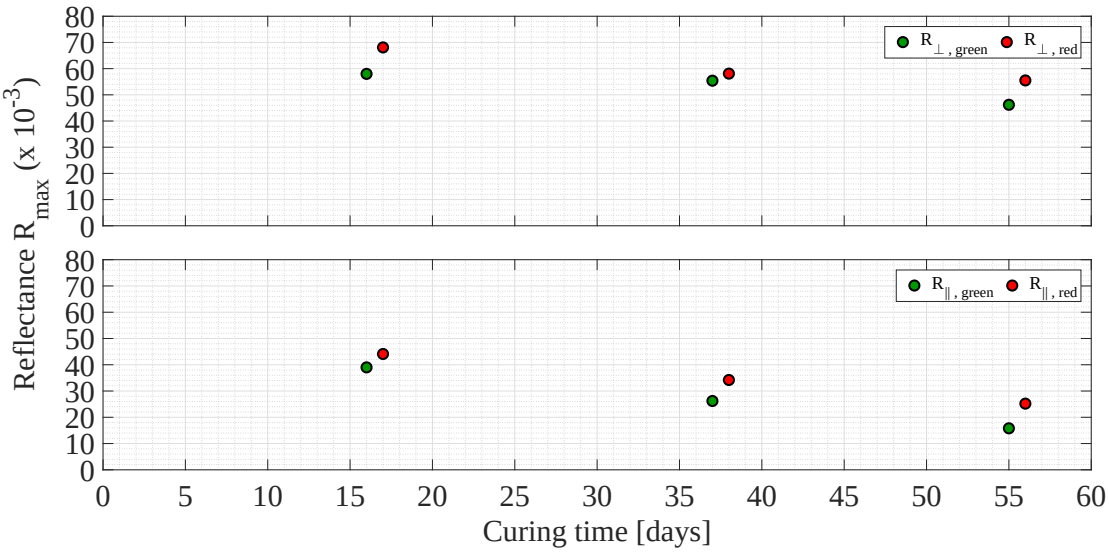

Fig. 5.13 Maximum value of measured reflectances for $\perp$ (top) and $\parallel$ (bottom) polarisation plotted as a function of the curing time for the central position on the front surface of $\text{Sapphire}_{\text{KOH(0.1N)}}$ and for green and red laser light. Measurements were taken using the upgraded assembly.

reflectance of $\text{Sapphire}_{\text{KOH(0.1N)}}$ is higher, because the difference in refractive index between sapphire and bond is bigger than that between fused silica and bond ($n_{1,\text{green}} = 1.4607$ and $n_{1,\text{red}} = 1.4570$ for fused silica [82], $n_{1\text{o,green}} = 1.7717$, $n_{1\text{e,green}} = 1.7636$, $n_{1\text{o,red}} = 1.7658$ and $n_{1\text{e,red}} = 1.7578$ for sapphire [90, 91]). Because of debonding, it was not possible to collect more data to confirm this decreasing trend over time.

5.2.3 Analysis result: reflectivity

To illustrate the overall time evolution of bond reflectance for $\text{Sapphire}_{\text{KOH(0.1N)}}$, in Figure 5.13 the peak reflectivities of the bond for both polarisations and colours of laser light are plotted as a function of curing time: the reflectance values decrease as curing time increases slowly. The reflectance levels have a less reduction in reflectance than the sapphire sample bonded with sodium silicate, but reflectance levels are very comparable. Like $\text{Sapphire}_{\text{Na2SiO3(1:6)}}$, a discrepancy between green and red data is shown, where the red values are again greater than the green ones. As explained in section 5.1.5, this is most likely due to a systematic underestimation of the reflectivity of the bond as measured using green light of about 25%.

5.2.4 Analysis result: refractive index and thickness

Figure 5.14 and Figure 5.15 show two examples of the results obtained from the Matlab script for sample $\text{Sapphire}_{\text{KOH(0.1N)}}$ in green mode after 37 days and red mode after 56 days, respectively.

The bond refractive index and thickness values for $\text{Sapphire}_{\text{KOH(0.1N)}}$ as a function of the curing time for both green and red laser light are plotted in Figure 5.16 and Figure 5.17.

In both Figure 5.16 and Figure 5.17, a discrepancy in bond refractive index and thickness between green and red data is shown. The average difference in bond refractive index equalling about 0.05 may be due to the underestimation (about 25%) of the values of the green bond reflectance that, in turn, determines an overestimation (about 0.04) of the values of the green bond refractive index. This means that the most likely trend for the bond refractive index is the red one (see section 5.1.5). The difference (more or less constant after 20 days) in bond thickness equalling 60 *nm* may be due to the debonding which affects this sample.

Figure 5.16 shows an increasing trend of the bond refractive index as curing time increases for both colours of the laser light, where it reaches the value about 1.44 (55 days) and 1.41 (56 days) for the green and red laser, respectively. If $\Delta n_2 = 0.04$ (section 5.1.5) is subtracted from the green values of the bond refractive index, these are in good agreement with the red values, confirming that the correct trend is the red one. The rate of increase for the bond refractive index of $\text{Sapphire}_{\text{KOH(0.1N)}}$ is similar to that of its 1 : 6 sodium silicate solution counterpart ($\text{Sapphire}_{\text{Na2SiO3(1:6)}}$), but the values of the bond refractive index for $\text{Sapphire}_{\text{KOH(0.1N)}}$ are slightly smaller than those for $\text{Sapphire}_{\text{Na2SiO3(1:6)}}$. Also, the bond refractive indices of $\text{Sapphire}_{\text{KOH(0.1N)}}$ are smaller than those of the KOH bonded fused silica samples ($\text{Silica1}_{\text{KOH(0.1N)}}$ and $\text{Silica2}_{\text{KOH(0.1N)}}$, see Chapter 4).

In Figure 5.17 the bond thickness seems to settle on a constant value with time: 351^{+4}_{-4} *nm* (55 days) for the green light and 409^{+3}_{-4} *nm* (56 days) for the red laser (Table 5.1). These values are much bigger than those obtained for $\text{Sapphire}_{\text{Na2SiO3(1:6)}}$ (less than 90 nm).

The bonding surfaces of the two discs of $\text{Sapphire}_{\text{KOH(0.1N)}}$ had a flatness of about 58 *nm* and 51 *nm* peak-to-valley respectively. These measurements were taken using the ZYGO®. The flatness maps shown in the first row of Figure 5.18 were obtained for the two discs. Combining these maps, the relative separation between two bonding surfaces was obtained and it is shown in the second row of Figure 5.18: the relative separation map gives a value of 7^{+4}_{-4} *nm* for the bond thickness in central position (Table 5.1).

No SEM measurements were taken for this sample.

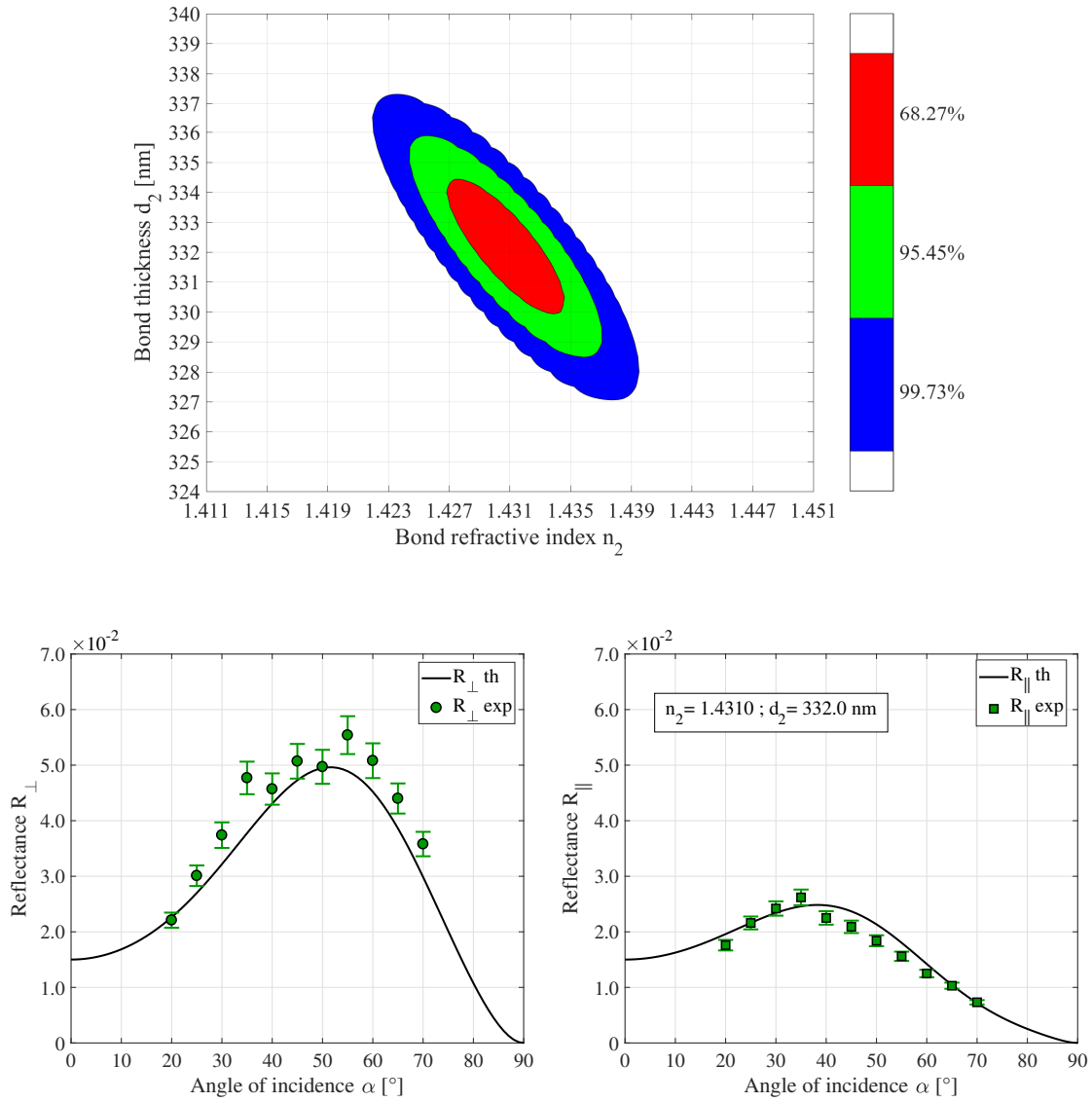

Fig. 5.14 (top) Three confidence levels of 68.3%, 95.5% and 99.7% probability. (bottom) Measured data with their corresponding error bars and theoretical curves. The green dots and squares represent the reflectances measured for perpendicular and parallel polarisation, respectively. The black solid lines are the theoretical perpendicular and parallel reflectances obtained using the most likely values of bond refractive index and thickness of the Bayesian analysis ($n_2 = 1.4310$ and $d_2 = 332.0$). These measurements were taken at 37 days after bonding for $\text{Sapphire}_{\text{KOH(0.1N)}}$ in green light.

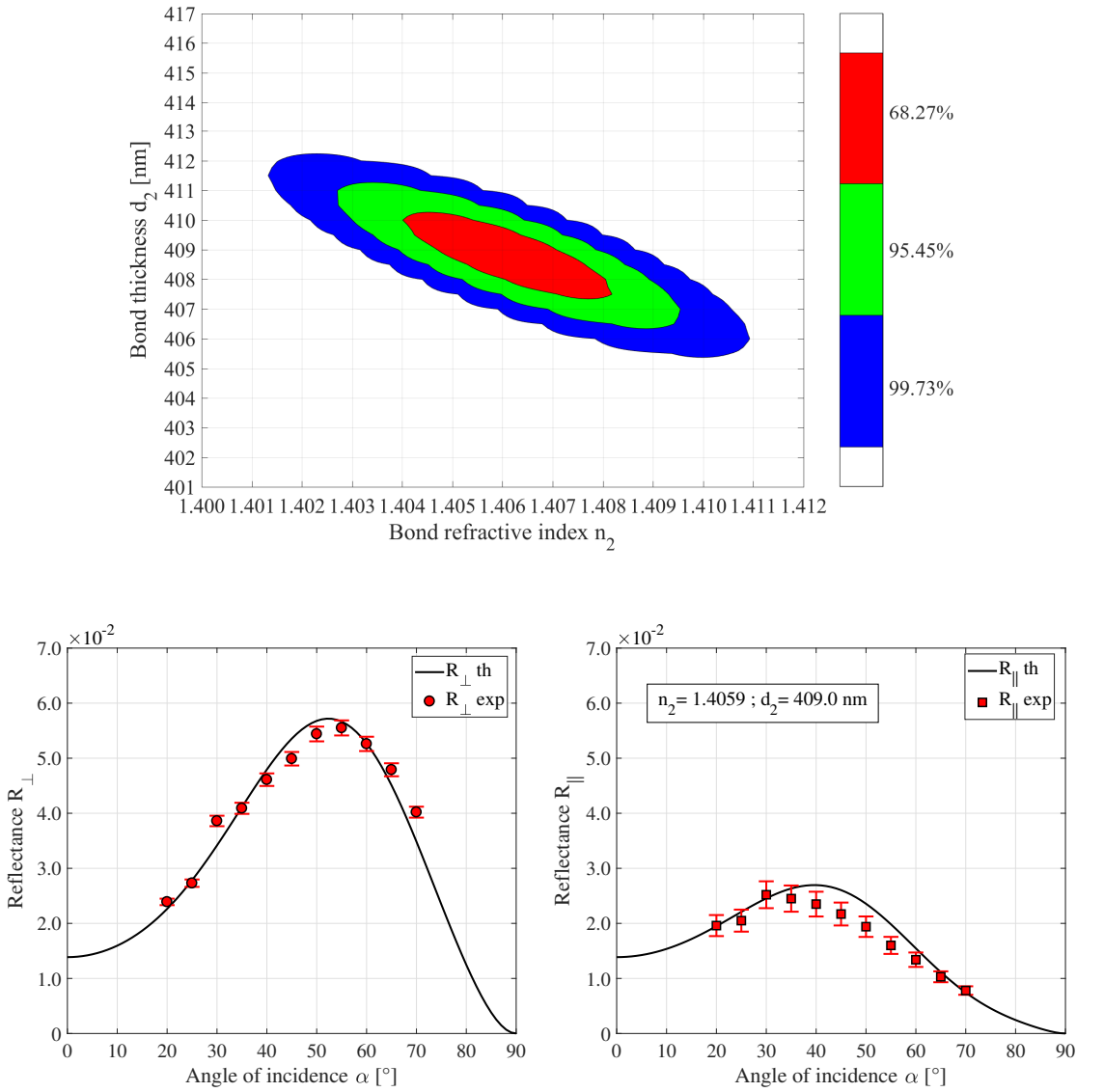

Fig. 5.15 (top) Three confidence levels of 68.3%, 95.5% and 99.7% probability. (bottom) Measured data with their corresponding error bars and theoretical curves. The red dots and squares represent the reflectances measured for perpendicular and parallel polarisation, respectively. The black solid lines are the theoretical perpendicular and parallel reflectances obtained using the most likely values of bond refractive index and thickness of the Bayesian analysis ($n_2 = 1.4059$ and $d_2 = 409.0$). These measurements were taken at 56 days after bonding for $\text{Sapphire}_{\text{KOH(0.1N)}}$ in red light.

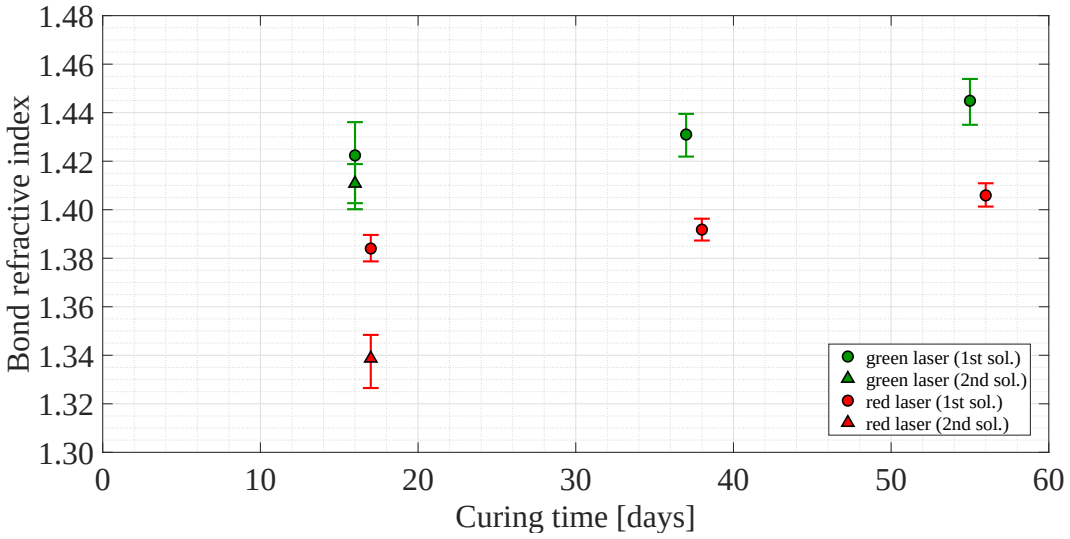

Fig. 5.16 Refractive index of the bond as a function of the curing time for the central position on the front surface of $\text{Sapphire}_{\text{KOH(0.1N)}}$. These values were determined from measurements collected using the upgraded setup in green (green dots and triangles) and red (red dots and triangles) mode. Some data sets have multiple solutions, which are presented in order from the highest to the lowest joint posterior probability density function by dots and triangles.

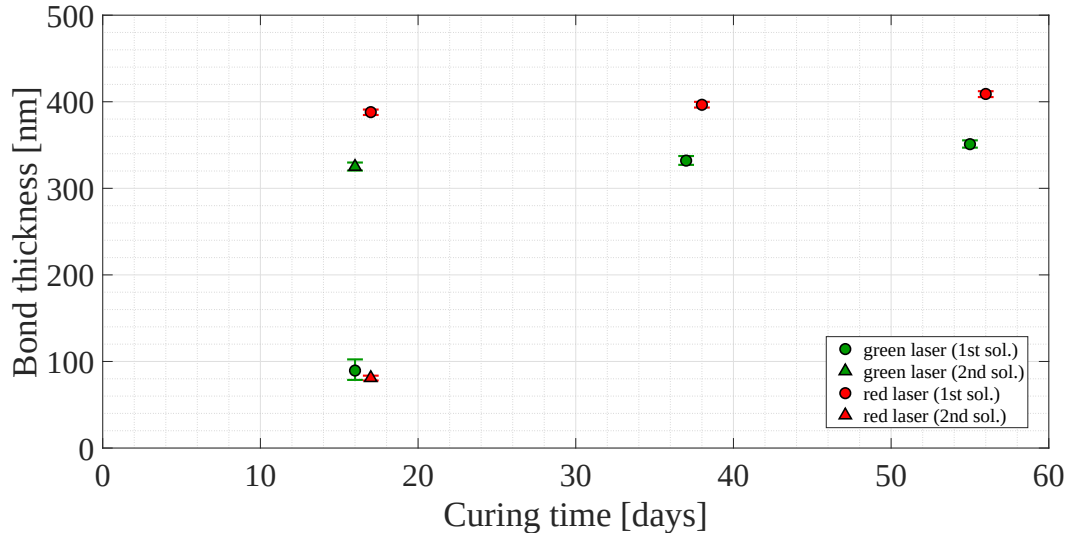

Fig. 5.17 Thickness of the bond as a function of the curing time for the central position on the front surface of $\text{Sapphire}_{\text{KOH(0.1N)}}$. These values were determined from measurements collected using the upgraded setup in green (green dots and triangles) and red (red dots and triangles) mode. Some data sets have multiple solutions, which are presented in order from the highest to the lowest joint posterior probability density function by dots and triangles.

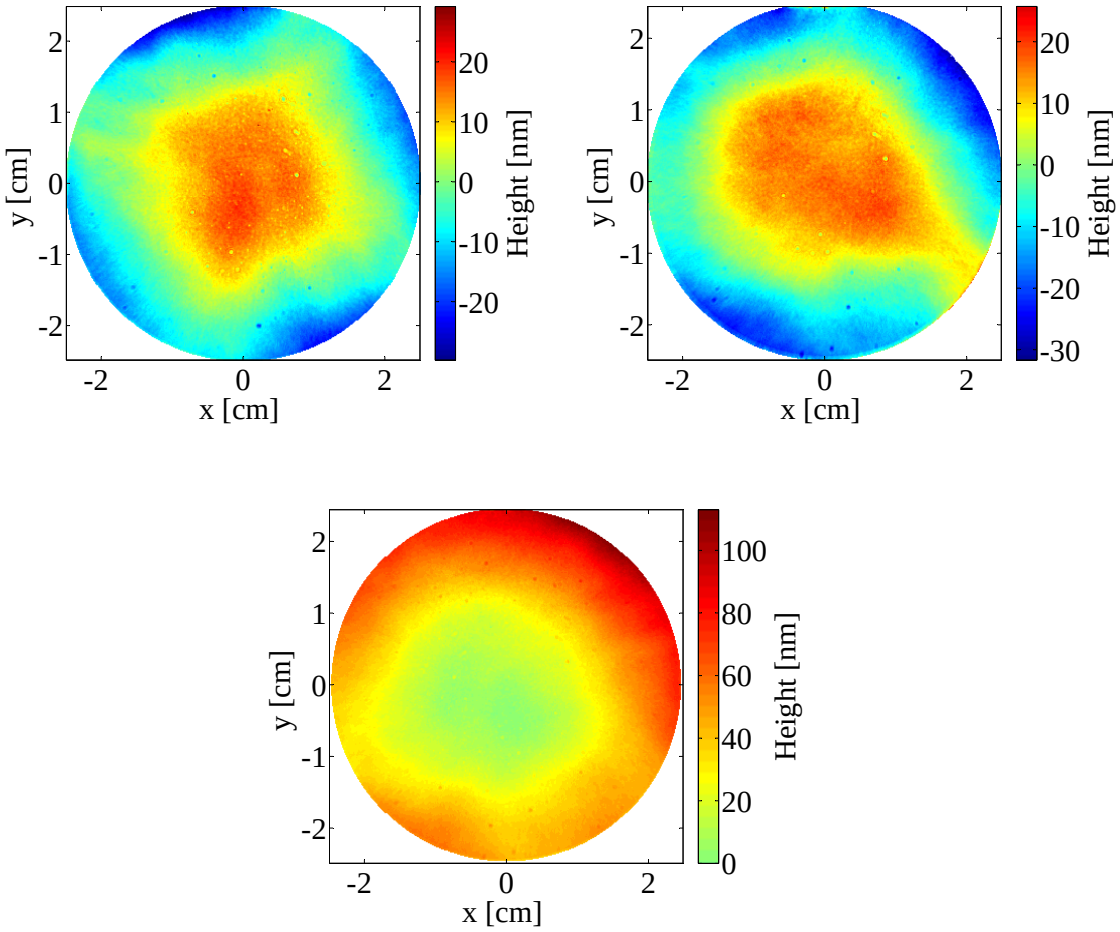

Fig. 5.18 (first row) Flatness maps of the bonding surfaces of the two discs which make $\text{Sapphire}_{\text{KOH(0.1N)}}$. These were obtained using the functions of the Simtools package (see Appendix E) which zoomed in on a valid area and remove various offsets from the ZYGO® maps. (second row) Relative separation between two bonding surfaces of discs bonded by hydroxide-catalysis bonding. This map was obtained using the Matlab code reported in Appendix E.

Because of the debonding which affects the measurements of bond thickness of this sample, the values calculated using the Bayesian analysis are clearly much bigger than those obtained from the flatness maps.

5.2.5 Analysis result: discussion

Like $\text{Sapphire}_{\text{Na2SiO3(1:6)}}$, the bond reflectances of $\text{Sapphire}_{\text{KOH(0.1N)}}$ are less than 10% and are about two orders of magnitude higher than the reflectances measured for the two KOH bonded fused silica samples studied in Chapter 4 ($\text{Silica1}_{\text{KOH(0.1N)}}$ and $\text{Silica2}_{\text{KOH(0.1N)}}$). Also for sample $\text{Sapphire}_{\text{KOH(0.1N)}}$ there is a disagreement between green and red measurements. The green bond maximum reflectivities are lower than those measured using the red laser light. This is most likely due to the fact that the green bond reflectivity was underestimated by about 25% (section 5.1.5).

As a consequence, the values of the green bond refractive index are likely to have been overestimated by about 0.04 with respect to the red ones (section 5.1.5), which are considered to be the most likely values of refractive index for $\text{Sapphire}_{\text{KOH(0.1N)}}$. After about two months, the value of the red refractive index is approximately 1.41, slightly lower than the red refractive index of $\text{Sapphire}_{\text{Na2SiO3(1:6)}}$ (about 1.42) and lower than that of KOH bonded fused silica samples (about 1.45 for $\text{Silica1}_{\text{KOH(0.1N)}}$ and 1.46 for $\text{Silica2}_{\text{KOH(0.1N)}}$, see Chapter 4). This suggests that little aluminium oxide is introduced into the bond. The bond material is mostly composed of potassium hydroxide in water and this means that the refractive index of this solution is about 1.33 (an approximate value of the refractive index of the bonding solution can be obtained by the refractive index of mixed liquids assuming that the resultant index is proportional to the volumes of each liquid used). As the bond cures, water evaporates (it cannot diffuse into the sapphire) and, consequently, the refractive index of bond approaches the value of potassium hydroxide solution (about 1.41). This seems to be in agreement with the Bayesian results obtained.

In contrast to the other samples cured at room temperature, where the bond thickness decreases as a function of curing time, the values of the bond thickness obtained by the Bayesian analysis settle on a constant value with green lower than red: 351^{+4}_{-4} *nm* (55 days) for green light and 409^{+3}_{-4} *nm* (56 days) for red laser. This may be due mainly to the debonding which affects this sample (Table 5.1 in section 5.3).

5.3 Summary

In this chapter the properties of two hydroxide-catalysis bonds made using materials different from fused silica substrates, such as sapphire, were reported.
$\text{Sapphire}_{\text{Na2SiO3(1:6)}}$ was the sapphire sample bonded using sodium silicate solution diluted with de-ionised water at 1 : 6.
Sample $\text{Sapphire}_{\text{KOH(0.1N)}}$ was bonded with potassium hydroxide solution at 0.1 N. Some problems were identified during curing this sample: surfaces of two sapphire discs (c-plane) tended to debond a few days after bonding. $\text{Sapphire}_{\text{KOH(0.1N)}}$ was the only sample which had a debonding slower than the other two samples bonded under the same conditions. The reflectivity of this bonded sample was measured, noting that debonding could influence these measurements, particularly the value of bond thickness. Because of this, it was not possible to collect sufficient data to determine the exact trend of bond refractive index and thickness over time.

The bond perpendicular and parallel reflectivities of these two samples were measured for both colours of laser light at different time intervals after bonding. They appear to drop slowly as curing time increases and are much higher (and less than 10%) than those of the fused silica samples bonded using the same solution. This can be explained by the refractive index mismatch between sapphire and the silicate solution: the bigger difference between these two refractive indices explains why the reflectivity for sapphire samples is higher than that measured for fused silica samples. Also, no strong correlation between the bond optical reflectivity and strength of a bond was found, both of which decrease as a function of curing time.

For both sapphire samples, the values of bond reflectance, refractive index and thickness are significantly different for green and red laser light. The reason for this discrepancy may be due to systematic errors introduced in the measurement of the bond optical reflectances. The cause of these systematic errors was not entirely clear and the author considered some hypotheses to explain the nature of this discrepancy, like scattering and absorption of the light in the substrate material. Both reduce the overall reflectance and are dependent on wavelength of the laser light. However, these contributions were negligible compared to the values of bond reflectances measured for these sapphire samples. The most likely explanation for this was that a systematic error in the measurement was affecting the refractive index values found. It was found that the green bond reflectances were underestimated and had to be increased by about 25%. This suggested that the green bond refractive indices were overestimated and that the refractive index of the bond between sapphire discs was closer

to that of the values for the red data. The variation in the red bond optical reflectances was negligible (2%), and for this reason the red results were taken as reference values. The quantity 0.04 (section 5.1.5) that should be subtracted from the green refractive indices is in broad agreement with the average difference between the red and green refractive indices for both the two samples. The variation in the optical reflectivity did not seem to affect the thickness measurements significantly. It should be noted that, for $\text{Sapphire}_{\text{KOH(0.1N)}}$, another important effect that has to be considered is debonding, above all for the bond thickness measurements.

The refractive index of the bond of sample $\text{Sapphire}_{\text{Na2SiO3(1:6)}}$ obtained using red light was found to be not higher than 1.38 after three months. This value is much lower than that measured for the bonds between fused silica substrates like $\text{Silica1}_{\text{Na2SiO3(1:6)}}$ and $\text{Silica2}_{\text{Na2SiO3(1:6)}}$ (about 1.43, see Chapter 3).
For sample $\text{Sapphire}_{\text{KOH(0.1N)}}$ the bond refractive index found using red light was 1.41 after approximately two months, and again this is lower than that of KOH bonded fused silica samples (about 1.45 for $\text{Silica1}_{\text{KOH(0.1N)}}$ and about 1.46 for $\text{Silica2}_{\text{KOH(0.1N)}}$, see Chapter 4). This suggests that little aluminium oxide goes into the hydroxide-catalysis bond, which might have increased the value of the bond refractive index, and that the refractive index approaches that of dry KOH.

A summary of results of the bond thickness obtained from flatness maps and Bayesian analysis (no SEM measurements were made) for the two samples studied in this chapter is shown in Table 5.1.
For $\text{Sapphire}_{\text{Na2SiO3(1:6)}}$, the bond thickness decreased as the curing time increased and then settled on a constant value that was larger than the relative separation estimated from the flatness maps, but lower than equivalent fused silica samples ($\text{Silica1}_{\text{Na2SiO3(1:6)}}$ and $\text{Silica2}_{\text{Na2SiO3(1:6)}}$).
For $\text{Sapphire}_{\text{KOH(0.1N)}}$, the bond thickness settled on a constant but high value at several hundred nanometres and this may be due to the debonding that characterised this sample.

Name of sample	Location	Flatness maps	Optical reflectivity			SEM imaging	
		d (nm)	d (nm)	laser light	t_c (days)	d (nm)	t_c (days)
$\text{Sapphire}_{\text{Na2SiO3(1:6)}}$	C	26^{+2}_{-2}	78^{+12}_{-9}	green	105	-	-
			72^{+9}_{-7}	red	106		
$\text{Sapphire}_{\text{KOH(0.1N)}}$	C	7^{+4}_{-4}	351^{+4}_{-4}	green	55	-	-
			409^{+3}_{-4}	red	56		

Table 5.1 Summary of bond thicknesses d obtained using two different methods: the relative separation map (third column) and the Bayesian analysis of reflectivity measurements (fourth column). No SEM measurements were made of these samples (fifth column). For the Bayesian thickness, the correct solution is taken to be the one for which the green and red results have the closest overlap. Location on the front surface of sample (C), colour of laser light (green and red) and curing time (t_c) expressed in days were also reported.

Chapter 6

Conclusions and plans for future work

Thanks to its reliability and versatility, hydroxide-catalysis bonding is the jointing technique of choice for the fabrication and assembly of optical-mechanical components with high performance in a wide range of possible applications. As described in Chapter 1, it has been used in the NASA satellite mission Gravity Probe B, in the ESA LISA Pathfinder mission and in ground-based gravitational wave detectors such as GEO600 and advanced LIGO.

The purpose of this thesis is to provide the basis for a new way to study the properties of a hydroxide-catalysis bond. A non-destructive technique was developed to extract the information on the bond refractive index and thickness from reflectivity measurements without damaging sample and bond. This study was the first step towards enhancing the understanding of these bonds and the parameters which influence them for fused silica and sapphire substrates bonded using this technique.

In section 6.1 the most important results obtained in the previous chapters are ordered by bonding solution ('Sodium silicate 1 : 6 solution', 'Different concentrations of sodium silicate solution' and 'Potassium hydroxide solution') and summarised to bring out the key conclusions ('Key findings'). In section 6.2 a summary of the limitations found during this work is reported. Future investigations and improvements (assembly and analysis) are also suggested.

6.1 Summary and conclusions

Sodium silicate 1:6 solution

Three fused silica samples ($\text{Silica1}_{\text{Na2SiO3(1:6)}}$ and $\text{Silica2}_{\text{Na2SiO3(1:6)}}$, which were bonded nominally identical, and $\text{Silica}_{\text{Na2SiO3(1:6),T}}$) and one sapphire sample ($\text{Sapphire}_{\text{Na2SiO3(1:6)}}$)

were bonded using 2 *ml* of sodium silicate solution with 12 *ml* of de-ionised water (a volumetric ratio of 1 : 6). $\text{Silica1}_{\text{Na2SiO3(1:6)}}$, $\text{Silica2}_{\text{Na2SiO3(1:6)}}$ and $\text{Sapphire}_{\text{Na2SiO3(1:6)}}$ were cured at room temperature, whereas $\text{Silica}_{\text{Na2SiO3(1:6),T}}$ was exposed to high temperatures (100 $^{\circ}C$ for eight hours) in the early stages of curing.

Both reflectances measured in perpendicular and parallel polarisation of sapphire sample (less than 10%) are one order of magnitude higher than those of the fused silica samples cured at room and elevated temperature (less than 1%). This is due to the difference in refractive index between the bond layer and sample material: the bigger this difference is, the bigger the reflectance of bond is. Sapphire has a higher refractive index than fused silica and the refractive index for the bond for both substrate materials remains lower than that of fused silica. The bond peak reflectances of fused silica samples start to drop as curing time increases: they seem to follow an exponential trend where they decrease rapidly in the first days after bonding and approach a constant value over time. On the contrary, the bond peak reflectivities of sapphire sample decrease more slowly as the cure proceeds. For fused silica samples, as the refractive index of the bonding solution increases and approaches that of fused silica with time, the difference in refractive index between the bond layer and sample material becomes smaller and smaller and, consequently, the bond reflectivity decreases. This is still holds for sapphire samples but, since the refractive index of the bonding solution does not reach that of sapphire material but remains below that of fused silica, this difference stays relatively constant over time.

An approximate value of the refractive index of this bonding solution is given by the refractive index of mixed liquids assuming that the resultant index is proportional to the volumes of each liquid used. It was found that the refractive index of this bonding solution is approximately 1.34 and it is in agreement with the value of the refractive index of the bonding solution at the time of bonding that was found to be 1.34 ± 0.01 using minimum deviation refractometry [103]. The bond refractive index of all the four 1 : 6 sodium silicate bonded samples increases as a function of curing time, starting at a value which was just a little bit higher than the refractive index of the bonding solution and approaching the refractive index of fused silica more or less quickly. This is in agreement with logical expectations: during the etching process (see subsection 1.5.1), the number of silicates coming from fused silica substrate and/or bonding solution increases and this causes an increase of the refractive index of the bonding solution. As the values of the bond refractive index of sapphire sample are lower than those of the fused silica samples, this suggests that little or no aluminium oxides are introduced into the bonding solution which is mostly composed of silicates coming only from the bonding solution. This means that the sample material may influence significantly

the final value of the refractive index of a bond and/or the time it takes to get there. Finally, the increasing trend of the refractive index is approximately the same for the fused silica samples cured at room and high temperature: this suggests that the curing temperature used in this thesis does not influence the final value of the refractive index of a 1 : 6 sodium silicate bond between fused silica discs.

Except for $\text{Silica}_{\text{Na2SiO3(1:6),T}}$, the bond thickness shows a decreasing trend over the curing time reaching a constant value (generally being of the order of a few hundred nanometres for the fused silica samples or less for the sapphire sample) after about a month after bonding (Table 6.1 and Table 6.3). This is still in agreement with logical expectations: the water, created during the polymerisation process (see subsection 1.5.1), is absorbed by the substrate material (this is possible for fused silica not for sapphire) and may evaporate from the edge of the bond over time. This makes the bond thinner in time where the final thickness is determined by the number of silicates present in the bond.

For the samples cured at room temperature, the bond thicknesses of the sapphire sample are a bit lower than those of the fused silica samples. This again seems to suggest that the content of silicate in a hydroxide-catalysis bond is an important factor that influences not only the values of the refractive index but also those of the bond thicknesses: the bigger the number of silicates in the solution is, the thicker the bond layer is. SEM images were also taken of some fused silica samples which suggested generally thinner bonds. Though these were made at much longer curing times and this could explain the discrepancy, one cannot discount the possibility that the etching action has a broader influence on optical thickness than can be seen in SEM images.

In contrast to results found for the samples cured at room temperature, the bond thickness of $\text{Silica}_{\text{Na2SiO3(1:6),T}}$ cured at high temperature (100 $^{\circ}C$ for eight hours) increases slightly as the cure proceeds. The thickness of a hydroxide-catalysis bond should be determined by the number of silicate molecules present in bonding solution: it takes into account both the silicates produced by water molecules and hydroxide ions during the etching process as well as silicates already present. These results suggest that this specific elevated temperature cure may have interrupted normal curing chemistry and impacted the evolution of the bond properties. If the correlation between the bond tensile strength and thickness holds, heat treatment might increase not only the thickness but also the strength of bond [96, 99, 102]. This should be investigated.

Indeed, interesting is the correlation found between the bond optical reflectivity and thickness of $\text{Silica1}_{\text{Na2SiO3(1:6)}}$ and $\text{Silica2}_{\text{Na2SiO3(1:6)}}$ and tensile strength of a bond made using very similar procedures as those used for this sample [100]. These decrease as curing

time increases with similar time constant and this may suggest that at decreasing values of the bond thickness correspond decreasing tensile strengths and optical reflectivities. A similar result is obtained for $\text{Sapphire}_{\text{Na2SiO3(1:6)}}$, even if no correlation between the bond optical reflectivity and strength of a bond was found: it seems that the bond tensile strength is correlated to the thickness of a bond.

Different concentrations of sodium silicate solution

Six fused silica samples were bonded at room temperature using three different volumetric ratios between sodium silicate solution and de-ionised water (each couple of samples was made nominally identical): 1 : 3 ($\text{Silica1}_{\text{Na2SiO3(1:3)}}$ and $\text{Silica2}_{\text{Na2SiO3(1:3)}}$), 1 : 6 ($\text{Silica1}_{\text{Na2SiO3(1:6)}}$ and $\text{Silica2}_{\text{Na2SiO3(1:6)}}$), 1 : 10 ($\text{Silica1}_{\text{Na2SiO3(1:10)}}$ and $\text{Silica2}_{\text{Na2SiO3(1:10)}}$). The reason why these ratios were chosen is to create a large enough difference between each other so that their influence over the values of bond reflectance, refractive index and thickness can be studied.

The values of the optical reflectances of these samples are less than 1% and decrease as curing time increases, reaching values less than 0.1% after three months. No significant difference in bond reflectances is observed when different concentrations of sodium silicate and water are used, though this decrease seems to be more gradual for the 1 : 10 solution (the maximum bond reflectance at 30 and 60 days is about twice as high) than for the 1 : 3 and 1 : 6 solution. This is in agreement with the fact that a solution poor in sodium silicate has a refractive index closer to that of water and this means that the difference in refractive index between the bonding solution and sample material is bigger for the 1 : 10 solution than for the 1 : 3 solution.

Bond refractive indices of these samples increase as a function of curing time, starting from a value (about 1.36) a bit greater than the refractive index of water and approaching, more or less quickly, the refractive index of fused silica 1.46 (upper limit for which the optical reflectivity is zero). The rate of increase of the refractive index of these samples is very similar though samples made using the 1 : 3 solution seem to reach the refractive index of fused silica a bit earlier than those bonded using the 1 : 10 solution. This may be due to less water present in the 1 : 3 solution: a solution richer in sodium silicate reduces the difference between refractive indices of bond and sample material faster than a solution poor in sodium silicate. However, this suggests that the concentrations of the solution used in this thesis do not influence the final value of the bond refractive index significantly.

The bond thickness of these samples decreases over the curing time and reaches a constant value after about a month after bonding (Table 6.1). This value is higher in the 1 : 3 bonded samples (greater than a hundred nanometres) and lower in the 1 : 10 bonded samples (less than a hundred nanometres) with respect to that of the 1 : 6 bonded samples (around a hundred nanometres). This suggests that a higher presence of sodium silicate in the bonding solution increases the thickness of the bond layer.

Potassium hydroxide solution

Three fused silica samples ($\text{Silica1}_{\text{KOH(0.1N)}}$ and $\text{Silica2}_{\text{KOH(0.1N)}}$, which are made nominally identical, and $\text{Silica}_{\text{KOH(0.1N),T}}$) and one sapphire sample ($\text{Sapphire}_{\text{KOH(0.1N)}}$) were bonded using potassium hydroxide solution KOH without diluting it with de-ionised water (0.1 N). $\text{Silica1}_{\text{KOH(0.1N)}}$, $\text{Silica2}_{\text{KOH(0.1N)}}$ and $\text{Sapphire}_{\text{KOH(0.1N)}}$ were cured at room temperature, whereas $\text{Silica}_{\text{KOH(0.1N),T}}$ was exposed to 100 $^{\circ}C$ for 8 hours in the early stages of curing.

The bond reflectances of $\text{Sapphire}_{\text{KOH(0.1N)}}$ (less than 10%) are about two orders of magnitude higher than the reflectances of $\text{Silica1}_{\text{KOH(0.1N)}}$ and $\text{Silica2}_{\text{KOH(0.1N)}}$ (less than 0.1%) and about one order of magnitude higher than the reflectances of $\text{Silica}_{\text{KOH(0.1N),T}}$ (less than 1%). As said previously, this is due to the fact that the difference between the refractive index of bond and sapphire is bigger than that between bond and fused silica. For this reason, the reflectances of $\text{Sapphire}_{\text{KOH(0.1N)}}$ decrease over time more slowly than its fused silica counterparts.

The bond reflectance of $\text{Silica}_{\text{KOH(0.1N),T}}$ cured at high temperature is one order of magnitude higher than that $\text{Silica1}_{\text{KOH(0.1N)}}$ and $\text{Silica2}_{\text{KOH(0.1N)}}$ cured at room temperature. This seems to suggest that the chemical reactions between potassium hydroxide solution and fused silica substrate cured at room temperature are different from those between potassium hydroxide solution and fused silica substrate cured at 100 $^{\circ}C$ for 8 hours. The low reflectance of $\text{Silica1}_{\text{KOH(0.1N)}}$ and $\text{Silica2}_{\text{KOH(0.1N)}}$ may be due to an increase of silicates in their bonds soon after bonding that makes their bond refractive indices approach that of fused silica quickly.

In fact, already in the first curing days, the values of the bond refractive index of $\text{Silica1}_{\text{KOH(0.1N)}}$ and $\text{Silica2}_{\text{KOH(0.1N)}}$ are the highest with respect to those estimated for all the samples studied in this thesis. The bond refractive index starts from 1.42 for $\text{Silica1}_{\text{KOH(0.1N)}}$ and 1.44 for $\text{Silica2}_{\text{KOH(0.1N)}}$ in the first curing days and approaches that of the fused silica 1.46 after about two months from bonding. This suggests that hydroxide ions in the potassium hydroxide solution etch the fused silica substrate more efficiently than the hydroxide ions in

the sodium silicate solution. This causes an increase of the content of silicates in the bonding solution and, consequently, a reduction of the difference in refractive index between bond and fused silica.
Also for $\text{Silica}_{\text{KOH(0.1N),T}}$ the refractive index seems to approach that of fused silica quickly, but the rate of increase is slower than that of $\text{Silica1}_{\text{KOH(0.1N)}}$ and $\text{Silica2}_{\text{KOH(0.1N)}}$ (from 1.36 at 1/2 days to 1.45 at 153/154 days). This suggests that the heat treatment chosen for this thesis slows down the bond refractive index from reaching that of fused silica.
The values of the bond refractive index of $\text{Sapphire}_{\text{KOH(0.1N)}}$ are smaller than those of $\text{Silica1}_{\text{KOH(0.1N)}}$ and $\text{Silica2}_{\text{KOH(0.1N)}}$. After about two months, the refractive index of $\text{Sapphire}_{\text{KOH(0.1N)}}$ is about 1.41 against 1.46 for $\text{Silica1}_{\text{KOH(0.1N)}}$ and $\text{Silica2}_{\text{KOH(0.1N)}}$. This suggests that hydroxide ions in potassium hydroxide solution do not etch the sapphire substrate so efficiently as they do for the fused silica substrate. Therefore, there are neither silicates in potassium hydroxide solution nor enough aluminium oxides which go into the hydroxide-catalysis bond because of etching that may increase the value of the bond refractive index. This also is evident in the fact these samples did not bond well. The potassium hydroxide bonding solution (see Chapter 2) is composed of potassium hydroxide ($n_{\text{KOH}} \sim 1.41$) in water ($n_{\text{H}_2\text{O}} \sim 1.33$) and its refractive index is about 1.33 (refractive index of mixed liquids [112]). As water evaporates (no diffusion into the sapphire is possible) during the curing, the refractive index of bond approaches that of potassium hydroxide solution (about 1.41), in agreement with the Bayesian results obtained.

Because of the low bond reflectances of $\text{Silica1}_{\text{KOH(0.1N)}}$ and $\text{Silica2}_{\text{KOH(0.1N)}}$ (bond thickness only for the first curing days) and the debonding of $\text{Sapphire}_{\text{KOH(0.1N)}}$ (the bond thickness seems to settle on a constant value over time), no statements about how the bond thickness evolves as a function of curing time can be made (Table 6.2 and Table 6.3).
Like sample $\text{Silica}_{\text{Na2SiO3(1:6),T}}$, the bond thickness of $\text{Silica}_{\text{KOH(0.1N),T}}$ seems to increase over time. This confirms that an heat treatment may interrupt the chemistry of the hydroxide-catalysis and may cause an increase of thickness of the bond over curing time.

Key findings

The results reported in this thesis are the first step in understanding how the reflectivity, refractive index and thickness of a hydroxide-catalysis bond may vary when different bonding solutions (sodium silicate solution at a volumetric ratio of 1 : 3, 1 : 6 and 1 : 10 with de-ionised water or potassium hydroxide solution), substrate materials (fused silica or sapphire) and curing temperatures (room temperature or 100 $^{\circ}C$ for eight hours) are used.

These results may be very useful for all those applications requiring low bond reflectivity, namely, transparent bond layer of which refractive index can approach that of substrates to be bonded in a short time. A low reflectivity minimises the stray and spurious reflections which are undesirable effects as they may introduce noise or reduce the efficiency of the optical device.
As an example, for the high power fibre laser industry the key results are that the bond reflectivity is less than 0.1% in bonding silica-silica substrates, and parameters of the bonding solution can be varied quite a lot without actually causing any real variation on the end result optically [48].
For sapphire more research is needed maybe to include anti-reflective coatings, because unexpectedly the bond refractive index does not match the sapphire (not enough etching of aluminates) and therefore the reflectance in directly bonding sapphire-sapphire substrates maybe be too high.
Considering the results obtained in this thesis, for fused silica substrates the best bonding solution to reduce its own reflectivity is potassium hydroxide solution cured at room temperature (this will be followed by potassium hydroxide solution cured at 100 $^{\circ}C$ for eight hours and then sodium silicate $1:6$ solution cured at either room or elevated temperature), whereas for sapphire substrates the best bonding solution is sodium silicate at $1:6$ concentration with de-ionised water.

These results may also be very important for the applications that need thin thickness for their bonds. A thin bond can minimise the tilt of bonded components and obtain high precision alignment and high positional stability (important requirement for LISA Pathfinder and eLISA space missions) or to keep thermal noise as low as possible in those systems that are sensitive to mechanical dissipation (such as in the gravitational wave detectors like Advanced LIGO). For example, in Advanced LIGO the calculated thermal noise at 100 Hz from the bonds between the ears and the sides of a single Advanced LIGO test mass which are 61 nm thick is approximately $5.4 \times 10^{-22} m/\sqrt{Hz}$ [53], whereas in LISA Pathfinder thin bonds were particularly useful for the construction of the interferometer optical bench where the optical components had to be precision aligned within 10 μrad [57].
For substrates cured at elevated temperatures (like 100 $^{\circ}C$ for eight hours) more studies are necessary because the bond thickness may increase as a function of curing time: it is important to understand how it evolves over time and to estimate the highest value that it can have.
Taking into account the results reported in this thesis, a thinner bond layer (less than a

hundred nanometres) can be obtained if sapphire substrates, more dilute solutions and curing at room temperature are preferred.

6.2 Plans for continuing and future work

These first results confirm that the optical method presented in this thesis for determining the reflectivity, refractive index and thickness of a hydroxide-catalysis bond is highly promising. Its strength lies in the non-destructive approach which allows the determination of these optical properties without damaging samples. In applications like, for example, the mirror suspensions of interferometric gravitational wave detectors, this may allow for in situ non-destructive measurements of the bond thickness which would aid the calculation of the thermal noise introduced by the bonds.

This work highlighted some limitations in the measurements and laid the groundwork for the future study and development of this optical method.

One issue encountered was obtaining different results for the bond reflectance, refractive index and thickness for the sapphire samples from the Bayesian analysis when different colours of laser light were used. Even though the trend was often the same, the values found using the green light deviated from the results obtained using the red laser. A possible explanation for this is that the sizes of the green beams at the two positions of photodiode 2 (those used for calibration and measurement of the beams) were not identical, leading to a systematic error in the intensity of the reflected light. For the simple case of normal incidence of green light (this effect was negligible for red laser light), an underestimation of the bond green reflectivity equalling 25% determines an overestimation of the bond green refractive index equalling 0.04 which should be subtracted from these values. For both sapphire samples, this is a systematic error that has to be taken into account in the measurements when the green laser is used, whereas the red values of the refractive index can be considered to be more accurate. Also, this appears to affect the thickness measurements less than the refractive index ones. Future measurements should ensure that the beam sizes are the same for the calibration and measurement beams hitting the photodiodes for all colours of light to remove this effect.

A second issue to resolve for future studies is understanding what determines the thickness of a hydroxide-catalysis bond. This is a fundamental step, because the thickness of a bond influences the behaviour of the system it is used in, such as thermal noise and possibly strength.

Three different methods (optical reflectances, flatness maps and scanning electron mi-

croscopy) were used for estimating the value of the bond thickness of some samples studied in this thesis, and generally each of them gave different results. For the sake of convenience, the results of the bond thickness obtained from flatness maps, Bayesian analysis and SEM imagining and presented in Chapter 3 (Table 6.1), Chapter 4 (Table 6.2) and Chapter 5 (Table 6.3) are reported again below.

Name of sample	Location	Flatness maps	Optical reflectivity		SEM imaging	
		d (nm)	d (nm)	t_c (days)	d (nm)	t_c (days)
$\text{Silica1}_{\text{Na2SiO3(1:6)}}$	L	84^{+3}_{-3}	297^{+4}_{-5}	98	44^{+9}_{-9}	978
	C	83^{+3}_{-3}	134^{+14}_{-18}	98	34^{+10}_{-10}	978
	R	101^{+5}_{-5}	78^{+28}_{-67}	98	82^{+24}_{-24}	978
$\text{Silica2}_{\text{Na2SiO3(1:6)}}$	C	63^{+15}_{-15}	173^{+11}_{-18}	104.5	-	-
$\text{Silica1}_{\text{Na2SiO3(1:3)}}$	C	80^{+4}_{-4}	155^{+19}_{-26}	91.5	110^{+15}_{-15}	288
$\text{Silica2}_{\text{Na2SiO3(1:3)}}$	C	95^{+3}_{-3}	473^{+271}_{-267}	92	-	-
$\text{Silica1}_{\text{Na2SiO3(1:10)}}$	C	97^{+4}_{-4}	51^{+62}_{-43}	91.5	47^{+9}_{-9}	304
$\text{Silica2}_{\text{Na2SiO3(1:10)}}$	C	63^{+3}_{-3}	17^{+74}_{-10}	91.5	70^{+16}_{-16}	239
$\text{Silica}_{\text{Na2SiO3(1:6),T}}$	C	128^{+4}_{-4}	337^{+34}_{-37}	50.5	35^{+11}_{-11}	237

Table 6.1 Summary of the values of the thicknesses d for sodium silicate bonds between fused silica samples. These were obtained using the relative separation map (third column), the Bayesian analysis of reflectivity measurements (fourth column), and SEM imaging (fifth column). In the Bayesian analysis column, for $\text{Silica1}_{\text{Na2SiO3(1:6)}}$ the thicknesses obtained using the initial setup in green mode were considered, whereas for the other samples the average of the green and red thicknesses was reported. Location on the front surface of sample (L, C and R) and curing time (t_c) expressed in days were reported.

It is interesting to note that the values of bond thickness obtained with the SEM technique are generally smaller than those estimated using relative surface maps and Bayesian analysis of optical reflectances. There are several possible factors which may contribute to this observation.

The first one takes the curing time dependence of a bond thickness in consideration. The thickness of a bond could have changed over time such that the lower bond thickness found

Name of sample	Location	Flatness maps	Optical reflectivity		SEM imaging	
		d (nm)	d (nm)	t_c (days)	d (nm)	t_c (days)
$\text{Silica1}_{\text{KOH(0.1N)}}$	C	8^{+4}_{-4}	441^{+158}_{-158}	3.5	41^{+12}_{-12}	430
$\text{Silica2}_{\text{KOH(0.1N)}}$	C	320^{+6}_{-6}	266^{+15}_{-11}	2	-	-
$\text{Silica}_{\text{KOH(0.1N),T}}$	C	105^{+4}_{-4}	171^{+225}_{-167}	50.5	-	-

Table 6.2 Summary of the values of the thicknesses d for potassium hydroxide bonds between fused silica samples. These were obtained using the relative separation map (third column), the Bayesian analysis of reflectivity measurements (fourth column), and SEM imaging (fifth column). In the Bayesian analysis column, for $\text{Silica2}_{\text{KOH(0.1N)}}$ the thickness obtained from the highest joint posterior probability density function was considered, whereas for the other samples the average of the green and red thicknesses was reported. Location on the front surface of sample (C) and curing time (t_c) expressed in days were reported.

Name of sample	Location	Flatness maps	Optical reflectivity			SEM imaging	
		d (nm)	d (nm)	laser light	t_c (days)	d (nm)	t_c (days)
$\text{Sapphire}_{\text{Na2SiO3(1:6)}}$	C	26^{+2}_{-2}	78^{+12}_{-9}	green	105	-	-
			72^{+9}_{-7}	red	106		
$\text{Sapphire}_{\text{KOH(0.1N)}}$	C	7^{+4}_{-4}	351^{+4}_{-4}	green	55	-	-
			409^{+3}_{-4}	red	56		

Table 6.3 Summary of the values of the thicknesses d for sodium silicate and potassium hydroxide bonds between sapphire samples. These were obtained using the relative separation map (third column) and the Bayesian analysis of reflectivity measurements (fourth column). No SEM measurements were made of these samples (fifth column). For the Bayesian thickness, the correct solution is taken to be the one for which the green and red results have the closest overlap. Location on the front surface of sample (C), colour of laser light (green and red) and curing time (t_c) expressed in days were reported.

during the SEM imaging was due to continued curing and thinning of the bond at room temperature. This could be relevant in the studies here as 5 to 29 months have passed between optical reflectivity and SEM measurements.
A second consideration is that the bond thickness could have altered during the preparation of sample for the SEM imaging. Alkali polishing compounds were used for polishing the samples and these could have etched the bond material making it apparently thinner.
The third consideration is that the bond material is not homogeneous. Potentially the bond structure was most different from the silica substrates in a narrower area than where the chemical etching and polymer formation has actually made more minor changes to the structure. Possibly the optical reflection acted over a broader width than what could be seen using scanning electron microscopy. This might mean that the three methods might consider the boundaries of a bond differently, and this might explain why the values of bond thickness obtained from these three methods did not match each other.
Finally, the separation between the surfaces to be bonded given by the flatness maps does not necessarily give the final thickness that a hydroxide-catalysis bond has to reach over time. As seen previously, there are some factors, like the presence of silicate component or curing temperature, which can alter the properties of a bond.
However, further studies, which take other different techniques into account for measuring the thickness of a hydroxide-catalysis bond (like electron diffraction techniques), will need to be undertaken in order to have a better understanding of the matter. Also, the Matlab code which determines the relative separation maps of bonded samples might be updated improving the determination of the points of contact between two bonding surfaces and the angles of rotation to overlap the two discs, whereas the models written for describing the optical reflectances could need to be improved including, for example, loss mechanisms.

A few possible ways in which theoretical model of the optical reflectances might not fully capture the physical processes involved include the fact that:

- it was supposed that the laser beam beats a small part of the bond of which refractive index and thickness remain constant during the data collection, but this might not be true: SEM imaging demonstrated that bond thickness can vary as much as 30% in just a few *mm*;

- in the early phase of curing (in particular in the first few days after bonding) values of the bond refractive index and thickness may change over the time it takes to move from one angle of incidence to another one.

Future work could include work to update the theoretical model taking into account, if necessary, the significant physical effects mentioned above.

Finally, a new upgrade of the optical assembly should be also considered to improve the sensitivity of the reflectivity measurements with the minimum less than 10^{-7}. For example, a further reduction of the laser beam diameter could be obtained by inserting other plano-convex lenses along the laser path or by recalculating the focal length of the additional lens used in this thesis and its position relative to the photodiode 2 instead of the sample (see subsection 2.1.5).

Appendix A

Thermal noise

As described in subsection 'Advanced LIGO detectors' in section 1.5.3, the current interferometers measure the variation of the distance between two pairs of test masses to detect the passage of a gravitational wave. These test masses have to be free from noise sources, since every noise manifests itself as a change of the position of the mirrors and the movement of these test masses caused by a noise source can simulate that induced by the passage of a gravitational wave [21].

Of the many noise sources, the thermal noise limits the sensitivity of a ground-based gravitational wave detector in the frequency band between about 10 and 100 Hz [21, 113, 114]. Thermal noise is explained in more detail in this appendix as background information for the reader.

In section A.1, the fluctuation-dissipation theorem is introduced: this is an important tool in calculating the thermal noise from different sources of dissipation (from the mechanical losses) which affect a gravitational wave detector.

In section A.2, the most important sources of thermal noise in a gravitational wave detector are described. Their definition allows the thermal noise to be lowered, by designing new suspensions, choosing low mechanical loss materials and cooling the optics, which increase the detector sensitivity.

A.1 Introduction

Thermal noise is the statistical motion of the atoms in the test masses, their coatings and suspensions of a gravitational wave detector driven by thermal energy. It results in a displacement noise in the measured position of the test mass faces which are sensed by the laser beam. The most important contributions to the thermal noise [94, 95] are:

Brownian noise. It is due to the random motion of the atoms which results in energy dissipation within the material. If the internal friction in a material is reduced by choosing, for example, low mechanical loss materials to construct the test masses and suspensions, then this noise is also reduced and the sensitivity of detector increases [115, 116].

Thermo-elastic noise. It is caused by statistical temperature fluctuations of a system which make the material expand or contract [117].

Thermo-refractive noise. It is determined by fluctuations in refractive index of a system, caused by statistical fluctuations in temperature, which result in phase fluctuations of the transmitted or reflected laser light [118].

Thermo-elastic and thermo-refractive noise are referred to as thermo-optic noise [119].

A.1.1 Brownian motion

Brown is considered to be the first person to have reported the Brownian motion, having observed the random motion of grains of dust and pollen floating in water. Brown stated that such a motion was due to the grains which were moving under their own power [113, 120].

Einstein understood not only that the motion of the grains was due to the stochastic collisions of the water molecules with the grains themselves, but also that as a consequence of these impacts, grains dissipated their kinetic energy while they moved through the water. He demonstrated that the mean-square displacement of a grain was [113, 115, 116]:

$$\overline{x^2_{\text{therm}}} = k_B T \frac{1}{3\pi a \eta} \tau \tag{A.1}$$

where k_B is the Boltzmann's constant, T and η the temperature and viscosity of the fluid in which the grain floats, a the radius of a spherical grain, and τ the duration of the observation. Einstein, for the first time, related the phenomenon of fluctuation (such as the random displacement of a grain) to the process of dissipation (such as the energy loss due to the viscosity of the water) [113].

A.1.2 Fluctuation-dissipation theorem

The relationship between the excitation of a system (namely the fluctuation), and the frictional mechanisms by which the excitation is damped (namely the dissipation), is established by

the fluctuation-dissipation theorem, formulated by Callen, which is applied to linear systems in thermodynamic equilibrium [113, 121, 122].

The fluctuation-dissipation theorem relates the power spectral density of the fluctuating force on a system $S_f(f)$ to the real and dissipative component of the impedance of the system $\mathbb{R}[Z(f)]$ as follows [113]:

$$S_f(f) = 4k_B T \mathbb{R}[Z(f)] \tag{A.2}$$

where $Z(f) = F(f)/v(f)$ is defined as the ratio between the amplitude of the force $F(f)$ which moves the system with a velocity of amplitude $v(f)$.

This theorem can be also written in terms of the power spectral density of the fluctuating motion of the system $S_x(f)$ which is related to the real component of the admittance of the system $\mathbb{R}[Y(f)]$ [113]:

$$S_x(f) = \frac{k_B T}{\pi^2 f^2} \mathbb{R}[Y(f)] \tag{A.3}$$

where $Y(f) = Z^{-1}(f) = v(f)/F(f)$.

The biggest advantage of this theorem is that it is sufficient to determine the macroscopic mechanical impedance as a function of frequency to estimate the thermal noise spectrum of a system. In fact, it is not necessary to write detailed microscopic models of any dissipation to describe the fluctuation associated with it, but it is important to include their effects in one expression for the impedance [113].

The Fluctuation-Dissipation theorem is therefore an important tool to predict thermal noise from dissipation in a gravitational wave detector. [113].

A.2 Thermal noise in gravitational wave detectors

As said, thermal noise limits the sensitivity of current ground-based gravitational wave detectors in the frequency band between about 10 and 100 Hz [21, 113, 114].

The most important sources of thermal noise in detectors come from the thermal energy of the suspensions, test masses and their optical coatings, which result in displacements of the test mass faces [21, 114].

Below, these thermal noises are explained together with the contribution of the welding and hydroxide-catalysis bonds.

A.2.1 Suspension thermal noise

The test masses of a gravitational wave detector are suspended by multi-stage pendulums to minimise the seismic noise, and are attached to the penultimate masses through fused silica fibres to reduce the suspension thermal noise [21].

The sources that contribute to the suspension thermal noise are (Figure A.1) [94, 95]:

Pendulum modes. The off-resonance thermal noise associated with the pendulum modes of a suspended mass can modify the front face of this mass and, consequently, vary the distance between the test masses in an interferometer. Most of the energy of the pendulum is stored as gravitational potential energy in the Earth's lossless gravitational field, and only the energy which is stored in the suspension fibres can be dissipated. This means that the pendulum loss is lower than that of the material used for the suspension fibre. The length of suspension fibres can also be increased such that the frequency of the pendulum mode can be lowered and lies below the detection frequency band of the gravitational wave interferometer.

Violin modes. The suspension fibres are subject to resonant modes called violin modes, which lie within the detection band of the gravitational wave interferometer. For low loss suspensions, thermal noise peaks from the violin modes are narrow and centred at the resonant frequencies of the violin modes. They can be filtered from the signal causing only a small reduction of the bandwidth of the detector.

Vertical, torsional and tilt modes of the pendulum. If the laser beam is incident exactly into centre of a test mass and these modes do not couple to the horizontal motion, then they should not give rise to noise and, consequently, should not change the distance between the test masses of the detector. However, due to design tolerances there is some noise associated with these modes.

A.2.2 Coating and substrate thermal noise

Dielectric multilayer coatings are applied to the front faces of the test masses of a gravitational wave detector to make them highly reflective to the incident light laser [114].

The coatings are composed of alternating layers of two dielectric materials with different refractive indices. A combination of the large number of pairs of layers and the large difference in the refractive indices of the materials chosen is responsible for the high (or low) reflectivity of the coatings [114].

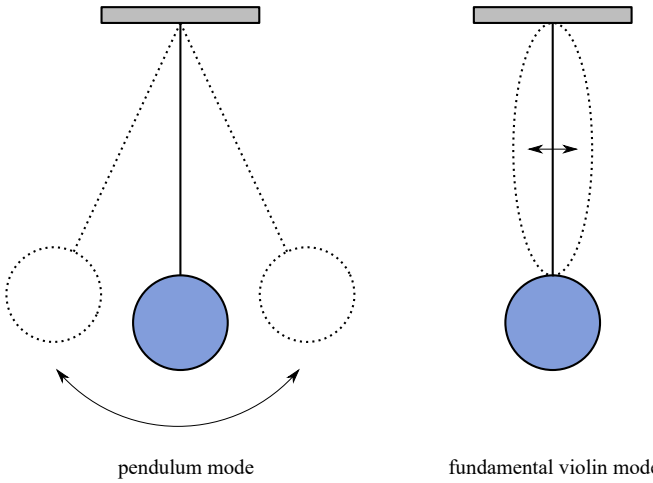

Fig. A.1 (left) Schematic illustration of the fundamental violin mode and (right) the pendulum mode of a suspended test mass.

In the advanced LIGO and Virgo detectors, the coatings applied to the fused silica test masses are formed from dielectric multilayer of silica and tantala (SiO_2 / Ta_2O_5), where the tantala is doped with titania. The tantala coating is doped with titania because it reduces the coating dissipation significantly with respect to an undoped tantala layer [21, 114, 123].

In a coated mirror, the contributions to the thermal noise come not only from reflective coatings, but also from mirror substrate material. Since the thermal noise associated with mirror coatings is higher than that of the substrate, the coating thermal noise is currently the dominant source of thermal noise in gravitational wave detectors [114]. The mechanical loss angle of these coatings is approximately 2×10^{-4} [124], whereas that of the fused silica substrate that is approximately 1×10^{-9} [125].

Currently, research has been investigating new techniques and configurations to reduce the thermal noise of the coatings. These include doping the coatings with different materials, heat treatment, thickness optimisation and testing new coating materials [114].

A.2.3 Weld thermal noise

As discussed in subsection ‘Advanced LIGO detectors’ in section 1.5.3, the fused silica masses of the quasi-monolithic mirror suspensions are attached to each other through ears and fibres to keep the thermal noise as low as possible. The fused silica ears are bonded to the sides of the masses using sodium silicate solution, and the fused silica fibres are welded to the two horns of ears using a carbon dioxide CO_2 laser (Figure 1.10).

The small region where the material is heated with the laser to fuse the fibres to the ears is subjected to thermal stresses which are due to the melting and solidifying process. For this reason, the weld can be considered as an additional source of thermal noise [126].

When a welded fibre is excited and vibrates in a resonant mode, a fraction of the energy associated with the mode is stored (and thus dissipated) in the welded region [126].

The thermal noise from welded interfaces can depend on the geometry and quality of the weld, and it can be reduced by increasing the length of a fibre [126].

Modelling of fibres of the quasi-monolithic mirror suspensions, like those of the Advanced LIGO detectors, showed that the thermal noise associated with welding did not provide a significant contribution to the total thermal noise [126].

A.2.4 Bond thermal noise

The method of attaching the suspension fibres to the test masses has to have very low loss and avoid thermal stresses [127].

In advanced LIGO, hydroxide-catalysis bonding is used to join the ears, where the suspension fibres are welded, onto the sides of the test masses. Because of the proximity of these bonds to the surface of the test mass, hydroxide-catalysis bonding could be another source of thermal noise that is necessary to consider [94, 95].

The properties of hydroxide-catalysis bonds between various materials were investigated finding that their contribution to the thermal noise was very small. This is more due to the low thickness (of order 100 nm) than it is due to loss, because the bond material is actually quite lossy (of order 0.1 at room temperature). Also, hydroxide-catalysis bonding demonstrated to be not only a low thermal noise but also high strength jointing technique for fused silica, sapphire and silicon suspensions [54, 64, 128].

For the next generation of gravitational wave detectors, quasi-monolithic mirror suspensions operating at cryogenic temperatures to reduce thermal noise further are being considered [65, 66, 129]. At these temperatures, fused silica is no longer a good material for the mirrors and the suspension fibres [130], because it exhibits a broad dissipation peak centred around 40 K [94, 95]. Also due to its low thermal conductivity, it is not possible to have efficient extraction of the heat deposited by the laser on the interferometric mirrors [105]. Thus different materials, such as sapphire and silicon, are being investigated as possible candidates for test masses and suspensions material in future detectors [105].

There are pros and cons to the use of each material, for example, silicon has a higher thermal conductivity than sapphire [131] allowing for more efficient heat extraction, but

sapphire, unlike silicon, is optically transparent at 1064 *nm*, the laser wavelength currently used to illuminate gravitational wave interferometers [131]. Investigating if the suspensions made with other materials are possible using hydroxide-catalysis bonding at cryogenic temperatures is currently an active area of research.

Appendix B

Current to voltage converter circuit

In this appendix the current to voltage converter circuit used to measure the voltage produced by the laser light incident on and reflected off a hydroxide-catalysis bond is reported.

In section B.1, the schematic of the current to voltage converter circuit used by the author is shown and a short description of its main components is presented. In section B.2 the description of how this circuit works and the relationship between the current produced by the photodiode when illuminated and the voltage measured, for example, with an oscilloscope are also reported.

B.1 Introduction

Photodiodes are semiconductor diodes that produce a current when illuminated: the photocurrent generated is proportional to the absorbed intensity of incoming light [132].

A current to voltage converter is a circuit which amplifies and converts this photocurrent to a proportional electrical voltage using an operational amplifier [133].

Figure B.1 shows a simplified schematic of the current to voltage converter circuit used in this thesis, where its four main components are described briefly below.

Operational amplifier

In Figure B.1, the operational amplifier (OP AMP) is represented as a right-pointing triangle with five terminals: two inputs labelled $-$ (inverting input) and $+$ (non-inverting input), one output (V_{out}), and two terminals for powering the operational amplifier ($V+$ and $V-$).

It is a device which amplifies the difference between the signals on its two inputs and sends it out as output. Since the input signals have to have a phase difference of 180° to

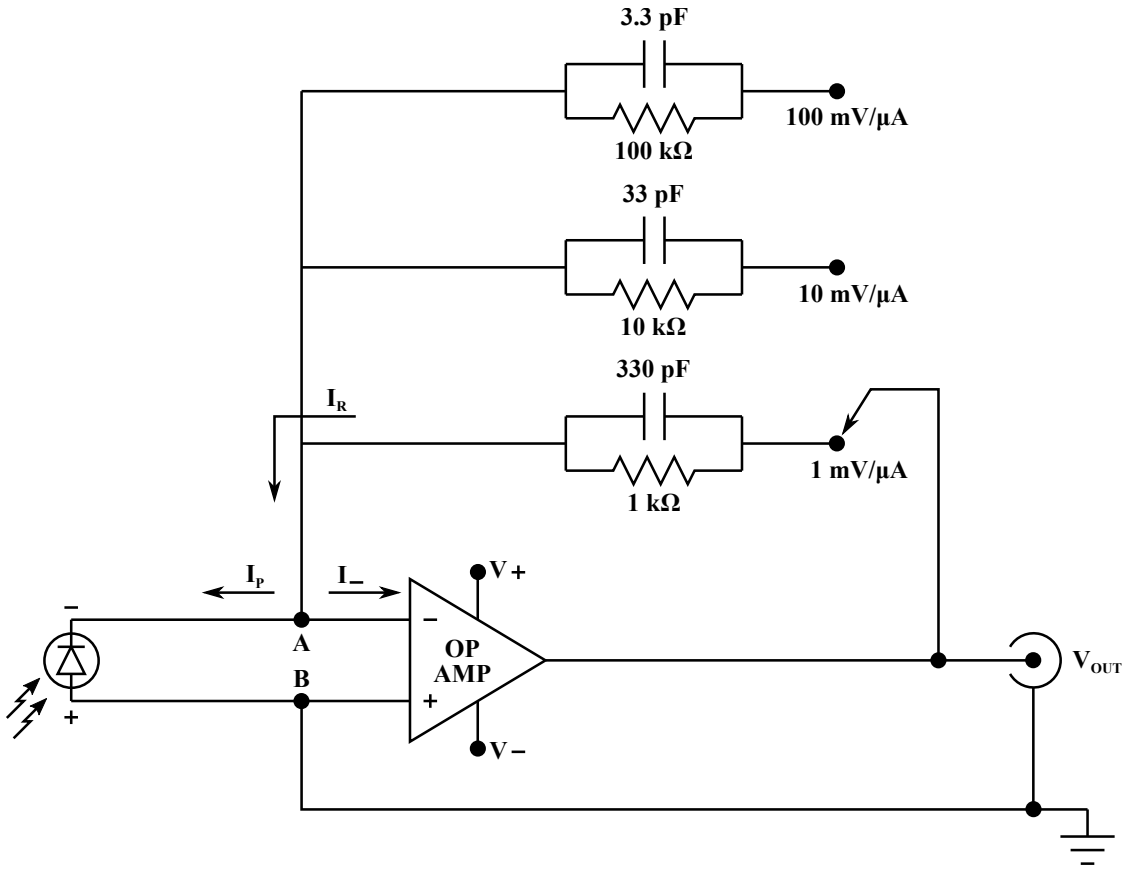

Fig. B.1 Schematic illustration of the current to voltage converter used by the author in this thesis.

get this difference, one input inverts the signal on it (inverting input) and the other does not change the phase of its signal (non inverting input).

Precision Monolithics Inc. PMI 0P77 GP was the operational amplifier used in this thesis. It was connected to a $\pm 12\ V$ power supply.

Photodiode

Two photodiodes were used in the initial and upgraded assembly (Figure 2.2 and 2.5): photodiode 1 (Vishay TEMD5510FX01) and photodiode 2 (Centronic OSD5-5T).

In Figure B.1, the photodiode is represented with a triangle pressed up against a line and two arrows which point towards the triangle and indicate the incoming light. It has two terminals, one positive called anode $(+)$ and one negative called cathode $(-)$.

A photodiode can be used in either photovoltaic or photoconductive mode: in photovoltaic mode the photodiode is unbiased and no external voltage is applied to it; in photoconductive mode an external reverse bias voltage is applied to the photodiode (a negative voltage is connected to anode and a positive voltage to cathode). Photodiodes used in this thesis are in photovoltaic mode: the anode is connected to ground and the cathode to the inverting input of the operational amplifier where $V_{\mathrm{A}} = V_{\mathrm{B}} = 0$ (see section B.2).

Resistor

Three precision resistors with resistance of 1, 10 and 100 $k\Omega$ and tolerance of $\pm 0.1\%$ (TE Connectivity H81K0BYA, H810KBYA and H8100KBYA) are used in this circuit.

These resistors are connected between the output terminal and the inverting input terminal of the operational amplifier. This connection allows a fraction of the output signal to feed back into the input signal and forces the differential input voltage towards zero. This effect is known as negative feedback. See section B.2 for details.

Capacitor

To filter out or roll off the high frequency noise in the output, a capacitor can be added in parallel with the resistor. This forms a low pass filter which allows low frequency signals until the 3 dB cut-off frequency to pass through and blocks high frequency signals.

The 3 dB cut-off frequency is the frequency at which the output voltage has dropped by 0.707 or $-3\ dB$ of the maximum output voltage and it is given by:

$$f_{3\text{dB}} = \frac{1}{2\pi RC} \tag{B.1}$$

Three capacitors with capacitance C of 330, 33 and 3.3 pF are used in parallel respectively with three precision resistors of resistance R equal to 1, 10 and 100 $k\Omega$: the 3 dB cut-off frequency $f_{3\text{dB}}$ is $4.8 \times 10^5 Hz$.

The impedance of R and C in parallel is:

$$Z = \frac{1}{\sqrt{(1/R)^2 + (\omega C)^2}} \tag{B.2}$$

where $\omega = 2\pi f$ is the angular frequency. At low frequencies the impedance is determined by R.

B.2 Description of circuit

Horowitz and Hill provided two golden rules in their book 'The Art of Electronics' to analyse the behaviour of an operational amplifier [133].

The first golden rule is the result of the negative feedback. It says that an operational amplifier adjusts the output such that the voltage of the inverting input equals that of the non-inverting input (the voltage difference between the inputs is zero). Since the non-inverting input (node B) is grounded (0 V), the inverting input (node A) is also at 0 V even if it is not connected to ground: $V_\text{A} = V_\text{B} = 0$. The node A is called virtual ground because it is at ground potential without being connected to ground. As a result, since one end of R is at 0 V, the potential difference across the resistor is:

$$V_\text{out} - V_\text{A} = V_\text{out} = RI_\text{R} \tag{B.3}$$

When a photodiode is exposed to light, the total current of the photodiode I is given by the current of diode for the case of no light absorption (first term) and by the photocurrent produced when light is absorbed (I_P) [132]:

$$I = I_0 \left[\exp\left(\frac{eV}{\beta k_B T} \right) - 1 \right] - I_\text{P} \tag{B.4}$$

where I_0 is the dark current (present even with no light incident on the detector), e is the magnitude of electron charge equal to $1.6 \times 10^{-19}\ C$, V is the voltage across the photodiode, β is a diode ideality factor, k_B is the Boltzmann's constant ($1.38 \times 10^{-23}\ J/K$), T is the absolute temperature (in Kelvin). Being $V_A = V_B = 0$, the voltage across the photodiode is $0\ V$ and the only current in the circuit is the photocurrent I_P produced by the absorption of the incident light.

By the second golden rule (no current flows into the inputs of an operational amplifier) and Kirchhoff's junction rule (the algebraic sum of the currents into any junction is zero), the current to the inverting input I_- is equal to zero, and the current produced by the photodiode I_P and that across the feedback resistor I_R are equal:

$$I_R - I_P - I_- = 0 \quad \Longrightarrow \quad I_R = I_P \tag{B.5}$$

From equations B.3 and B.5, the positive output voltage V_{out} can be written as follows:

$$V_{out} = RI_R = RI_P \tag{B.6}$$

and it is simply given by the feedback resistor R multiplied by photodiode current I_P.

The value of R sets the value of the conversion factor. If the resistance is $1\ k\Omega$ and the output voltage is $+1\ mV$, then the current in R is $1\ \mu A$ and the conversion factor is $1\ mV/\mu A$. In Figure B.1, three resistors of resistance 1, 10 and 100 $k\Omega$ are used and, consequently, three possible sensitivity levels ($1\ mV/\mu A$, $10\ mV/\mu A$ and $100\ mV/\mu A$) can be chosen: the proportional factor between two different sensitivity levels of photodiodes is determined by the ratio of the two corresponding precision resistors.

The total voltage noise in V_{out} is mainly due to the noise of the circuit and shot noise, where the noise of the circuit is composed of photodiode, operational amplifier and precision resistor. Both these contributions are of the order of nV in $1\ Hz$.

Appendix C

Demonstration of some equations

In this appendix some of the equations given in this thesis are demonstrated step by step.

C.1 Equation 2.8

In subsection 2.1.5, equation 2.8 was used to fit the power of the beam measured as a function of the position of the knife edge which was translated through the beam (knife edge technique). Assuming that the laser beam propagated with a Gaussian intensity profile, the $1/e^2$ radius of the Gaussian beam could be estimated.

The main steps involved in obtaining equation 2.8 are reported in this section. The procedure follows the guide "Gaussian Beams and the Knife-Edge Measurement" available at http://massey.dur.ac.uk/resources/lab_resources.html.
The Gaussian intensity profile of a beam which propagates in the z direction (Figure 2.9) is:

$$I(x,y) = I_0 \exp\left(-\frac{2x^2}{R_x^2}\right) \exp\left(-\frac{2y^2}{R_y^2}\right)$$

where R_x and R_y are the $1/e^2$ radii of the Gaussian beam in the x and y directions and I_0 is the peak intensity.
The total power of the beam when fully exposed is obtained by integration of the beam intensity:

$$P_{\text{tot}} = I_0 \int_{-\infty}^{+\infty} \exp\left(-\frac{2x^2}{R_x^2}\right) dx \int_{-\infty}^{+\infty} \exp\left(-\frac{2y^2}{R_y^2}\right) dy = \frac{\pi}{2} I_0 R_x R_y$$

To solve these Gaussian integrals, see the point 4 of subsection "Some properties of definite integrals" reported at the end of this section.
If the beam is progressively covered by a razor blade, which is translated through the beam in the x direction (Figure 2.9), the transmitted power of the beam $P_{\text{measured}}(x)$ is given by the covered power subtracted from the total power of the beam:

$$\begin{aligned}
P_{\text{measured}}(x) &= P_{\text{tot}} - I_0 \int_{-\infty}^{x} \exp\left(-\frac{2x^2}{R_x^2}\right) dx \int_{-\infty}^{+\infty} \exp\left(-\frac{2y^2}{R_y^2}\right) dy \\
&= P_{\text{tot}} - \sqrt{\frac{\pi}{2}} I_0 R_y \int_{-\infty}^{x} \exp\left(-\frac{2x^2}{R_x^2}\right) dx \\
&= P_{\text{tot}} - \sqrt{\frac{\pi}{2}} I_0 R_y \left[\int_{-\infty}^{0} \exp\left(-\frac{2x^2}{R_x^2}\right) dx + \int_{0}^{x} \exp\left(-\frac{2x^2}{R_x^2}\right) dx\right] \\
&= P_{\text{tot}} - \sqrt{\frac{\pi}{2}} I_0 R_y \left[\sqrt{\frac{\pi}{8}} R_x + \int_{0}^{x} \exp\left(-\frac{2x^2}{R_x^2}\right) dx\right] \\
&= P_{\text{tot}} - \frac{\pi}{4} I_0 R_x R_y - \sqrt{\frac{\pi}{2}} I_0 R_y \int_{0}^{x} \exp\left(-\frac{2x^2}{R_x^2}\right) dx \\
&= P_{\text{tot}} - \frac{P_{\text{tot}}}{2} - \sqrt{\frac{\pi}{2}} I_0 R_y \int_{0}^{x} \exp\left(-\frac{2x^2}{R_x^2}\right) dx \\
&= \frac{P_{\text{tot}}}{2} - \sqrt{\frac{\pi}{2}} I_0 R_y \int_{0}^{x} \exp\left(-\frac{2x^2}{R_x^2}\right) dx \\
&= \frac{P_{\text{tot}}}{2} - \sqrt{\frac{\pi}{2}} I_0 R_y \int_{0}^{(\sqrt{2}/R_x)x} \exp(-u^2) \frac{R_x}{\sqrt{2}} du \\
&= \frac{P_{\text{tot}}}{2} - \frac{\pi}{4} I_0 R_x R_y \frac{2}{\sqrt{\pi}} \int_{0}^{(\sqrt{2}/R_x)x} \exp(-u^2)\, du
\end{aligned}$$

where $u = (\sqrt{2}/R_x)x$ and $dx = (R_x/\sqrt{2})du$. In these steps the points 1, 3 and 4 of subsection "Some properties of definite integrals" (see below) are used.
Defining the error function erf(t) as follows:

$$\text{erf(t)} = \frac{2}{\sqrt{\pi}} \int_0^t e^{-u^2}\, du \tag{2.9}$$

with erf(0) = 0, erf(∞) = 1 and erf(-t) = −erf(t), equation 2.8 is found:

$$P_{\text{measured}}(x) = \frac{P_{\text{tot}}}{2}\left[1 - \text{erf}\left(\frac{\sqrt{2}(x-x_0)}{R_x}\right)\right] \tag{2.8}$$

where x_0 is the position of the Gaussian beam centre relative to the razor origin position ($P_{\text{measured}}(x_0) = P_{\text{tot}}/2$).

Some properties of definite integrals

The following is a list of some properties of definite integrals. Some Gaussian integral is also reported [134].

1. Additivity of integration on intervals.

   $$\int_a^b f(x)\,dx = \int_a^c f(x)\,dx + \int_c^b f(x)\,dx$$

   where c is an element of $[a,b]$. From this, the following relations are obtained:

   $$\int_a^c f(x)\,dx = \int_a^b f(x)\,dx - \int_c^b f(x)\,dx$$

   and:

   $$\int_{-\infty}^0 f(x)\,dx = \int_{-\infty}^{+\infty} f(x)\,dx - \int_0^{+\infty} f(x)\,dx$$

2. Even function ($f(-x) = f(x)$).

   $$\int_{-a}^a f(x)\,dx = 2\int_0^a f(x)\,dx$$

3. Change of variable.

   $$\int_a^b f(x)\,dx = \int_\alpha^\beta f[g(t)]g'(t)\,dt$$

   where:
   $x = g(t)$

$dx = g'(t)dt$
$t = g^{-1}(x)$
$\alpha = g^{-1}(a)$
$\beta = g^{-1}(b)$.

4. Gaussian integral.
   It is the integral of an arbitrary Gaussian function e^{-ax^2} over the entire real line and it is defined by:

$$\int_{-\infty}^{+\infty} e^{-ax^2}\,dx = \sqrt{\frac{\pi}{a}} \quad \text{for } a > 0$$

As the function e^{-ax^2} for $a > 0$ is even, considering the points 1 and 2 expressed above, the following relationships are found:

$$\int_{0}^{+\infty} e^{-ax^2}\,dx = \frac{1}{2}\sqrt{\frac{\pi}{a}} \quad \text{for } a > 0$$

and

$$\int_{-\infty}^{0} e^{-ax^2}\,dx = \int_{-\infty}^{+\infty} e^{-ax^2}\,dx - \int_{0}^{+\infty} e^{-ax^2}\,dx = \frac{1}{2}\sqrt{\frac{\pi}{a}} \quad \text{for } a > 0.$$

C.2 Equation 2.18

As described in subsection 2.1.5, an additional lens was introduced between the spatial filter and the sample in the upgraded setup (Figure 2.5) to reduce the diameter of the beam incident on the sample further.

In this section the relationship of the focal length of this additional lens f_3 is derived as a function of the values of beam waists before and after passing through the lens w_2 and w_3 (equation 2.18 and Figure 2.12).

The starting condition is that $l_2 + l_3$ is known and its value is k.
In this thesis, k was measured using a retractable flexible rule and it depended on the space in the setup which had to allow other optical components (half-waves plates, beamsplitters, chopper and mirrors) to be inserted. It was found to be 110.6 *cm* or 131.6 *cm* depending on

the laser light used (Table 2.3).
Taking Figure 2.12 into consideration, the following lines can be written:

$$l_2 + l_3 = k$$

$$l_{21} + l_{22} + l_3 = k$$

$$l_{22} + l_3 = k - l_{21}$$

$$l_{22} + l_3 = a$$

Using equations 2.15 and 2.16, the last relationship is written as follow:

$$f_3 + \frac{w_2}{w_3}\sqrt{f_3^2 - f_{**}^2} + f_3 + \frac{w_3}{w_2}\sqrt{f_3^2 - f_{**}^2} = a$$

$$2f_3 + \left(\frac{w_2}{w_3} + \frac{w_3}{w_2}\right)\sqrt{f_3^2 - f_{**}^2} = a$$

$$2f_3 + b\sqrt{f_3^2 - f_{**}^2} = a$$

$$\sqrt{f_3^2 - f_{**}^2} = \frac{a - 2f_3}{b}$$

$$f_3^2 - f_{**}^2 = \frac{a^2 - 4af_3 + 4f_3^2}{b^2}$$

$$b^2 f_3^2 - 4f_3^2 + 4af_3 - b^2 f_{**}^2 - a^2 = 0$$

$$\left(b^2 - 4\right)f_3^2 + 4af_3 + \left(-b^2 f_{**}^2 - a^2\right) = 0$$

$$cf_3^2 + df_3 + e = 0$$

where:

$$\begin{cases} a = k - l_{21} = (l_2 + l_3) - l_{21} \\ b = \left(\frac{w_2}{w_3} + \frac{w_3}{w_2}\right) \\ c = b^2 - 4 = \left(\frac{w_2}{w_3} + \frac{w_3}{w_2}\right)^2 - 4 = \left(\frac{w_2^2 + w_3^2}{w_2 w_3}\right)^2 - 4 = \left(\frac{w_2^2 - w_3^2}{w_2 w_3}\right)^2 \\ d = 4a = 4\left[(l_2 + l_3) - l_{21}\right] \\ e = -b^2 f_{**}^2 - a^2 = -\left(\frac{w_2}{w_3} + \frac{w_3}{w_2}\right)^2 f_{**}^2 - \left[(l_2 + l_3) - l_{21}\right]^2 \end{cases} \tag{C.1}$$

Depending on the value of the coefficient c (if it is equal to zero or not), the quadratic equation obtained can be solved as follow:

$$c f_3^2 + d f_3 + e = 0 \Rightarrow \begin{cases} f_3 = \frac{-d + \sqrt{d^2 - 4ce}}{2c} & \text{if } c \neq 0 \text{ or } w_2 \neq w_3, \\ f_3 = -\frac{e}{d} & \text{if } c = 0 \text{ or } w_2 = w_3. \end{cases} \tag{C.2}$$

Substituting the relationships C.1 into equations C.2, equations 2.18 are found:

$$f_3 = \begin{cases} \dfrac{-2\left[(l_2+l_3)-l_{21}\right] + \left(\frac{w_2}{w_3}+\frac{w_3}{w_2}\right)\sqrt{\left[\left(\frac{w_2}{w_3}+\frac{w_3}{w_2}\right)^2 - 4\right] f_{**}^2 + \left[(l_2+l_3)-l_{21}\right]^2}}{\left(\frac{w_2}{w_3}+\frac{w_3}{w_2}\right)^2 - 4} & \text{if } w_2 \neq w_3, \\ \dfrac{4f_{**}^2 + \left[(l_2+l_3)-l_{21}\right]^2}{4\left[(l_2+l_3)-l_{21}\right]} & \text{if } w_2 = w_3. \end{cases} \tag{2.18}$$

C.3 Theoretical model for anisotropic material with optic axis perpendicular to bonding surface

As introduced in subsection 2.2.2, a vectorial approach described by Simon [85–87] is used for determining the reflectivity of bonded sapphire samples with c-crystallographic plane. Below, the three cases that a wave is exposed to during its travel through a bonded sample are described and the main relationships are obtained:

- case 1: an incident wave passes from an isotropic to uniaxial birefringent medium;
- case 2: an ordinary wave passes from a uniaxial birefringent to isotropic medium;
- case 3: an extraordinary wave passes from a uniaxial birefringent to isotropic medium.

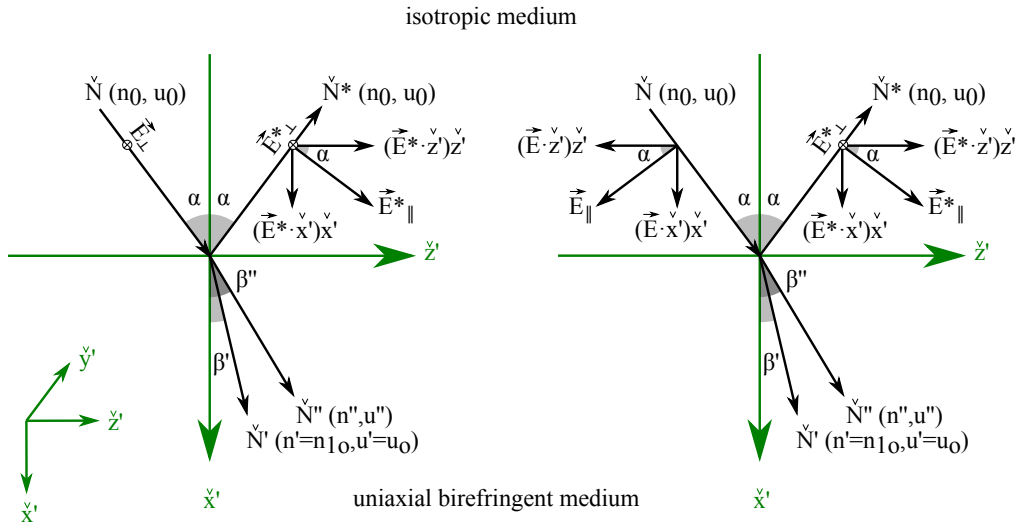

Fig. C.1 Schematic diagram of the incidence plane with the unit vector normal to the incident ($\check{N}$), reflected ($\check{N}^*$), ordinary refracted ($\check{N}'$) and extraordinary refracted ($\check{N}''$) wavefront. The electric field vectors for a polarisation perpendicular (left) and parallel (right) to the incidence plane of the incident beam are shown.

Case 1: isotropic to uniaxial birefringent interface

A wave is incident from an isotropic medium, characterised by refractive index n_0, and propagates in a uniaxial birefringent medium whose principal refractive indices are n_{1o} and n_{1e}. This incident wave produces one reflected and two refracted waves at the interface [87, 89].

If an incident wave polarised perpendicular or parallel to the incidence plane is postulated, the polarisation of the reflected wave does not necessarily coincide with that of the incident wave. The same goes for the polarisation of the two refracted waves, which depends only on the propagation direction and the orientation of the optic axis, and not on the polarisation of the incident wave [87, 89].

Here, the incidence plane is perpendicular to the z-axis ($\delta = +\,90°$), the optic axis is perpendicular to the discontinuity surface ($\vartheta = -\,90°$) and, consequently, the ordinary and extraordinary waves are perpendicular and parallel to the incidence plane (see 'Ordinary and extraordinary waves in a uniaxial birefringent medium' in subsection 2.2.2 and the left hand side of Figure 2.16).

In Figure C.1, the two cases in which the incident wave has the electric field vector $\vec{E}$ perpendicular (left) or parallel (right) to the incidence plane are shown [87].

The electric field vector of the reflected wave $\vec{E}^*$ will have in general components both perpendicular and parallel to that plane. The incident and reflected beams propagate in an isotropic medium, travelling in the $\check{N}$ and $\check{N}^*$ direction, respectively, with equal phase velocity $u_0 = c/n_0$ [87].

The ordinary and extraordinary refracted beams propagate in a uniaxial birefringent medium: the former in the $\check{N}'$ direction with principal phase velocity u_o, the latter in $\check{N}''$ with u'' obtained from equation 2.36 [87]:

$$u'' = \frac{c}{n''} = \sqrt{u_e^2 + (u_o^2 - u_e^2)\cos^2\beta''} \tag{C.3}$$

where $u_o = c/n_{1o}$ and $u_e = c/n_{1e}$. It depends on the propagation direction of the wavefront $\check{N}''$ and on the direction of the optic axis $\check{z}_3$ (parallel to the x-axis) which form the angle β''. From this equation, the refractive index for the extraordinary wave n'' can be written as follows (equation 2.37) [87]:

$$n'' = \frac{n_{1o}n_{1e}}{\sqrt{n_{1o}^2 + (n_{1e}^2 - n_{1o}^2)\cos^2\beta''}} \tag{2.44}$$

Also, the unit vector normal to the incident ($\check{N}$), ordinary refracted ($\check{N}'$) and extraordinary refracted ($\check{N}''$) wavefront are related to each other by the following Snell's laws [87, 89]:

$$n_0 \sin\alpha = n_{1o} \sin\beta' \tag{C.4}$$

$$n_0 \sin\alpha = n'' \sin\beta'' \tag{C.5}$$

From these relationships, the angles β' and β'' are expressed as follows:

$$\beta' = \arcsin\left(\frac{n_0}{n_{1o}}\sin\alpha\right) \tag{2.45}$$

$$\beta'' = \arcsin\left(\frac{n_{1e}n_0\sin\alpha}{\sqrt{n_{1o}^2 n_{1e}^2 + (n_{1e}^2 - n_{1o}^2)n_0^2\sin^2\alpha}}\right) \tag{2.46}$$

From Figure C.1, the electric field vectors of the incident, reflected and refracted waves can be determined for perpendicular and parallel polarisations. Consequently, the corresponding reflection r (transmission t) coefficients can be calculated as the quotient of the magnitudes of the reflected (refracted) and incident electric fields. A subscript will be inserted

after each reflection and transmission coefficient, where the first element will stand for the polarisation of the incident beam, whereas the second one for describing the state of reflected or refracted beam [87].

If the polarisation of the incident wave is perpendicular to the incidence plane, the incident, reflected and refracted waves are expressed in the incidence plane system as [87]:

$$\begin{aligned}
\text{incident wave}: &\begin{cases} \vec{E}_{\perp} = (\vec{E}\cdot\check{y'})\check{y'} \\ \vec{E}_{\parallel} = 0 \end{cases} \\
\text{reflected wave}: &\begin{cases} \vec{E}^{*}_{\perp} = (\vec{E}^{*}\cdot\check{y'})\check{y'} \\ \vec{E}^{*}_{\parallel} = (\vec{E}^{*}\cdot\check{x'})\check{x'} + (\vec{E}^{*}\cdot\check{z'})\check{z'} \end{cases} \\
\text{refracted wave}: &\begin{cases} \vec{E}' = (\vec{E}'\cdot\check{y'})\check{y'} \\ \vec{E}'' = (\vec{E}''\cdot\check{x'})\check{x'} - (\vec{E}''\cdot\check{z'})\check{z'} \end{cases}
\end{aligned} \tag{C.6}$$

where $\vec{E}'$ and $\vec{E}''$ are the electric field vectors of the ordinary and extraordinary wave, and the corresponding reflection and transmission coefficients are (Figure C.1) [87]:

$$r_{\perp\perp} = +\frac{|\vec{E}^{*}_{\perp}|}{|\vec{E}_{\perp}|} = +\frac{|(\vec{E}^{*}\cdot\check{y'})\check{y'}|}{|(\vec{E}\cdot\check{y'})\check{y'}|} \tag{C.7}$$

$$r_{\perp\parallel} = +\frac{|\vec{E}^{*}_{\parallel}|}{|\vec{E}_{\perp}|} = +\frac{|(\vec{E}^{*}\cdot\check{x'})\check{x'} + (\vec{E}^{*}\cdot\check{z'})\check{z'}|}{|(\vec{E}\cdot\check{y'})\check{y'}|} \tag{C.8}$$

$$t_{\perp o} = +\frac{|\vec{E}'|}{|\vec{E}_{\perp}|} = +\frac{|(\vec{E}'\cdot\check{y'})\check{y'}|}{|(\vec{E}\cdot\check{y'})\check{y'}|} \tag{C.9}$$

$$t_{\perp e} = -\frac{|\vec{E}''|}{|\vec{E}_{\perp}|} = -\frac{|(\vec{E}''\cdot\check{x'})\check{x'} - (\vec{E}''\cdot\check{z'})\check{z'}|}{|(\vec{E}\cdot\check{y'})\check{y'}|} \tag{C.10}$$

If the polarisation of the incident wave is parallel to the incidence plane, the incident, reflected and refracted waves are expressed in the incidence plane system as [87]:

$$\begin{aligned}
\text{incident wave}: &\begin{cases} \vec{E}_{\perp} = 0 \\ \vec{E}_{\parallel} = (\vec{E}\cdot\check{x'})\check{x'} - (\vec{E}\cdot\check{z'})\check{z'} \end{cases} \\
\text{reflected wave}: &\begin{cases} \vec{E}^{*}_{\perp} = (\vec{E}^{*}\cdot\check{y'})\check{y'} \\ \vec{E}^{*}_{\parallel} = (\vec{E}^{*}\cdot\check{x'})\check{x'} + (\vec{E}^{*}\cdot\check{z'})\check{z'} \end{cases} \\
\text{refracted wave}: &\begin{cases} \vec{E}' = (\vec{E}'\cdot\check{y'})\check{y'} \\ \vec{E}'' = (\vec{E}''\cdot\check{x'})\check{x'} - (\vec{E}''\cdot\check{z'})\check{z'} \end{cases}
\end{aligned} \tag{C.11}$$

and the reflection and transmission coefficients are (Figure C.1) [87]:

$$r_{\parallel\perp} = -\frac{|\vec{E}^{*}_{\perp}|}{|\vec{E}_{\parallel}|} = -\frac{|(\vec{E}^{*}\cdot\check{y'})\check{y'}|}{|(\vec{E}\cdot\check{x'})\check{x'} - (\vec{E}\cdot\check{z'})\check{z'}|} \tag{C.12}$$

$$r_{\parallel\parallel} = -\frac{|\vec{E}^{*}_{\parallel}|}{|\vec{E}_{\parallel}|} = -\frac{|(\vec{E}^{*}\cdot\check{x'})\check{x'} + (\vec{E}^{*}\cdot\check{z'})\check{z'}|}{|(\vec{E}\cdot\check{x'})\check{x'} - (\vec{E}\cdot\check{z'})\check{z'}|} \tag{C.13}$$

$$t_{\parallel o} = -\frac{|\vec{E}'|}{|\vec{E}_{\parallel}|} = -\frac{|(\vec{E}'\cdot\check{y'})\check{y'}|}{|(\vec{E}\cdot\check{x'})\check{x'} - (\vec{E}\cdot\check{z'})\check{z'}|} \tag{C.14}$$

$$t_{\parallel e} = +\frac{|\vec{E}''|}{|\vec{E}_{\parallel}|} = +\frac{|(\vec{E}''\cdot\check{x'})\check{x'} - (\vec{E}''\cdot\check{z'})\check{z'}|}{|(\vec{E}\cdot\check{x'})\check{x'} - (\vec{E}\cdot\check{z'})\check{z'}|} \tag{C.15}$$

Knowing the expressions for the reflection and transmission coefficients in the incidence plane system, these can then be expressed in the discontinuity surface system, using equation 2.30.

The following step is, therefore, to express the electric field vector $\vec{\mathscr{E}}$ through its corresponding electric displacement vector $\vec{\mathscr{D}}$ in the discontinuity surface system [87]. From equation 2.32 and Maxwell's equation $(\check{\mathscr{N}}\cdot\vec{\mathscr{D}}) = 0$ (see equations 2.31), the components of the electric field in the discontinuity surface system for the incident and reflected waves

which propagate in the isotropic medium are [87]:

$$\begin{cases} (\vec{E}\cdot\check{x}) = -\mu_0 u_0^2 \left[\frac{(\vec{N}\cdot\check{y})}{(\vec{N}\cdot\check{x})}(\vec{D}\cdot\check{y}) + \frac{(\vec{N}\cdot\check{z})}{(\vec{N}\cdot\check{x})}(\vec{D}\cdot\check{z}) \right] \\ (\vec{E}\cdot\check{y}) = \mu_0 u_0^2 (\vec{D}\cdot\check{y}) \\ (\vec{E}\cdot\check{z}) = \mu_0 u_0^2 (\vec{D}\cdot\check{z}) \end{cases} \tag{C.16}$$

and

$$\begin{cases} (\vec{E}^*\cdot\check{x}) = \mu_0 u_0^2 \left[\frac{(\vec{N}^*\cdot\check{y})}{(\vec{N}^*\cdot\check{x})}(\vec{D}^*\cdot\check{y}) + \frac{(\vec{N}^*\cdot\check{z})}{(\vec{N}^*\cdot\check{x})}(\vec{D}^*\cdot\check{z}) \right] \\ (\vec{E}^*\cdot\check{y}) = \mu_0 u_0^2 (\vec{D}^*\cdot\check{y}) \\ (\vec{E}^*\cdot\check{z}) = \mu_0 u_0^2 (\vec{D}^*\cdot\check{z}) \end{cases} \tag{C.17}$$

From equations 2.33, 2.34, 2.35 and 2.29, the components of the electric field in the discontinuity surface system for the ordinary and extraordinary refracted waves in the uniaxial birefringent medium can be written as follows [87]:

$$\vec{E}' = \mu_0 u_o^2 \left[\frac{((\check{n}\cdot\check{z}_3)^2 - 1)(\check{N}'\cdot\check{y})}{(\check{N}'\cdot\check{n}) - (\check{n}\cdot\check{z}_3)(\check{N}'\cdot\check{z}_3)}\check{x} + \check{y} + \frac{\sqrt{1-(\check{n}\cdot\check{z}_3)^2}(\check{n}\cdot\check{z}_3)(\check{N}'\cdot\check{y})}{(\check{N}'\cdot\check{n}) - (\check{n}\cdot\check{z}_3)(\check{N}'\cdot\check{z}_3)}\check{z} \right] (\vec{D}'\cdot\check{y}) \tag{C.18}$$

and

$$\begin{aligned} \vec{E}'' = \mu_0 \Bigg[& \frac{u_o^2(\check{N}''\cdot\check{n})(\check{N}''\cdot\check{z}_3) - u''^2(\check{n}\cdot\check{z}_3)}{(\check{N}''\cdot\check{y})(\check{N}''\cdot\check{z}_3)}\check{x} + u_o^2\check{y} \\ & + \frac{u_e^2[(\check{N}''\cdot\check{z}_3)^2 - 1] - u_o^2(\check{n}\cdot\check{z}_3)(\check{N}''\cdot\check{n})(\check{N}''\cdot\check{z}_3) + u''^2(\check{n}\cdot\check{z}_3)^2}{\sqrt{1-(\check{n}\cdot\check{z}_3)^2}(\check{N}''\cdot\check{y})(\check{N}''\cdot\check{z}_3)}\check{z} \Bigg] (\vec{D}''\cdot\check{y}) \end{aligned} \tag{C.19}$$

Finally, at the interface between the isotropic and uniaxial birefringent media the electromagnetic waves are subject to the boundary conditions. These require the matching of the tangential components of the electric field $\vec{\mathscr{E}}$ and magnetic field $\vec{\mathscr{H}}$, and that of the normal components of electric displacement field $\vec{\mathscr{D}}$, and are written in the discontinuity surface coordinate system as follows [87]:

$$\begin{aligned} (\vec{D}\cdot\check{x}) + (\vec{D}^*\cdot\check{x}) &= (\vec{D}'\cdot\check{x}) + (\vec{D}''\cdot\check{x}) \\ (\vec{E}\cdot\check{y}) + (\vec{E}^*\cdot\check{y}) &= (\vec{E}'\cdot\check{y}) + (\vec{E}''\cdot\check{y}) \\ (\vec{E}\cdot\check{z}) + (\vec{E}^*\cdot\check{z}) &= (\vec{E}'\cdot\check{z}) + (\vec{E}''\cdot\check{z}) \\ (\vec{H}\cdot\check{y}) + (\vec{H}^*\cdot\check{y}) &= (\vec{H}'\cdot\check{y}) + (\vec{H}''\cdot\check{y}) \end{aligned} \tag{C.20}$$

From these relationships, the electric displacement vector of the reflected, ordinary and extraordinary refracted waves can be expressed as a function of that of the incident wave [87]:

$$\begin{aligned}
(\vec{D}^* \cdot \check{y}) &= \frac{u_o^2}{u_0^2}\left[\frac{C_2(B_2-B_1)-C_1(A_2-A_1)}{A_1B_2-A_2B_1}\right]-(\vec{D}\cdot\check{y}) \\
(\vec{D}^* \cdot \check{z}) &= \frac{1}{u_0^2}\left[\frac{D_1(C_2B_2-C_1A_2)+D_2(C_1A_1-C_2B_1)}{A_1B_2-A_2B_1}\right]-(\vec{D}\cdot\check{z}) \\
(\vec{D}' \cdot \check{y}) &= \frac{C_2B_2-C_1A_2}{A_1B_2-A_2B_1} \\
(\vec{D}'' \cdot \check{y}) &= \frac{C_1A_1-C_2B_1}{A_1B_2-A_2B_1}
\end{aligned} \tag{C.21}$$

where

$$\begin{aligned}
A_1 &= u_o^2(\check{N}\cdot\check{y})(\check{N}\cdot\check{z})+[1-(\check{N}\cdot\check{y})^2]D_1+\frac{u_0u_o\sqrt{1-(\check{n}\cdot\check{z}_3)^2}(\check{N}\cdot\check{x})(\check{N}'\cdot\check{z}_3)(\check{N}'\cdot\check{y})}{(\check{N}'\cdot\check{n})-(\check{n}\cdot\check{z}_3)(\check{N}'\cdot\check{z}_3)} \\
A_2 &= u_o^2(\check{N}\cdot\check{y})(\check{N}\cdot\check{z})+[1-(\check{N}\cdot\check{y})^2]D_2-\frac{u_0u''(\check{N}\cdot\check{x})[(\check{N}''\cdot\check{n})-(\check{n}\cdot\check{z}_3)(\check{N}''\cdot\check{z}_3)]}{\sqrt{1-(\check{n}\cdot\check{z}_3)^2}(\check{N}''\cdot\check{z}_3)(\check{N}''\cdot\check{y})} \\
B_1 &= -u_o^2\frac{(\check{N}\cdot\check{y})}{(\check{N}\cdot\check{x})}-\frac{(\check{N}\cdot\check{z})}{(\check{N}\cdot\check{x})}D_1+\frac{u_0^2[(\check{n}\cdot\check{z}_3)^2-1](\check{N}'\cdot\check{y})}{(\check{N}'\cdot\check{n})-(\check{n}\cdot\check{z}_3)(\check{N}'\cdot\check{z}_3)} \\
B_2 &= -u_o^2\frac{(\check{N}\cdot\check{y})}{(\check{N}\cdot\check{x})}-\frac{(\check{N}\cdot\check{z})}{(\check{N}\cdot\check{x})}D_2+\frac{u_0^2[(\check{N}''\cdot\check{n})(\check{N}''\cdot\check{z}_3)-(\check{n}\cdot\check{z}_3)]}{(\check{N}''\cdot\check{y})(\check{N}''\cdot\check{z}_3)} \\
C_1 &= -2u_0^2\left[\frac{(\check{N}\cdot\check{y})}{(\check{N}\cdot\check{x})}(\vec{D}\cdot\check{y})+\frac{(\check{N}\cdot\check{z})}{(\check{N}\cdot\check{x})}(\vec{D}\cdot\check{z})\right] \\
C_2 &= 2u_0^2\left[(\check{N}\cdot\check{y})(\check{N}\cdot\check{z})(\vec{D}\cdot\check{y})+[1-(\check{N}\cdot\check{y})^2](\vec{D}\cdot\check{z})\right] \\
D_1 &= \frac{u_o^2\sqrt{1-(\check{n}\cdot\check{z}_3)^2}(\check{n}\cdot\check{z}_3)(\check{N}'\cdot\check{y})}{(\check{N}'\cdot\check{n})-(\check{n}\cdot\check{z}_3)(\check{N}'\cdot\check{z}_3)} \\
D_2 &= \frac{u_e^2[(\check{N}''\cdot\check{z}_3)^2-1]-u_o^2(\check{n}\cdot\check{z}_3)(\check{N}''\cdot\check{n})(\check{N}''\cdot\check{z}_3)+u''^2(\check{n}\cdot\check{z}_3)^2}{\sqrt{1-(\check{n}\cdot\check{z}_3)^2}(\check{N}''\cdot\check{y})(\check{N}''\cdot\check{z}_3)}
\end{aligned} \tag{C.22}$$

When the incidence plane is perpendicular to the z-axis ($\delta = +\,90°$) and the optic axis is perpendicular to the discontinuity surface ($\vartheta = -\,90°$), like samples Melles Griot described in Chapter 5, the z components of all the normals to the wavefront vanish ($(\vec{N}\cdot\check{z}) = (\vec{N}^*\cdot\check{z}) = (\vec{N}'\cdot\check{z}) = (\vec{N}''\cdot\check{z}) = 0$) and $(\check{z}_3\cdot\check{n})$ is equal to one (Figure 2.16, left). Thanks to these conditions, the expressions for the reflection and transmission coefficients for both polarisations at an isotropic-uniaxial birefringent interface can be simplified considerably. It is found that $r_{\perp\parallel} = r_{\parallel\perp} = 0$ and $t_{\perp e} = t_{\parallel o} = 0$, and the other coefficients of reflection are

given by [87]:

$$r_{\perp\perp} = \frac{\cos\alpha - \sqrt{\left(\frac{n_{1o}}{n_0}\right)^2 - \sin^2\alpha}}{\cos\alpha + \sqrt{\left(\frac{n_{1o}}{n_0}\right)^2 - \sin^2\alpha}} \tag{2.40}$$

$$r_{\parallel\parallel} = \frac{\left(\frac{n_{1o}n_{1e}}{n_0^2}\right)\cos\alpha - \sqrt{\left(\frac{n_{1e}}{n_0}\right)^2 - \sin^2\alpha}}{\left(\frac{n_{1o}n_{1e}}{n_0^2}\right)\cos\alpha + \sqrt{\left(\frac{n_{1e}}{n_0}\right)^2 - \sin^2\alpha}} \tag{2.42}$$

Summarising: when the incident wave has a polarisation perpendicular (parallel) to the incidence plane, only the ordinary (extraordinary) refracted wave exists, therefore the polarisation of both the reflected and ordinary (extraordinary) refracted wave is perpendicular (parallel) to this plane.

Case 2: uniaxial birefringent to isotropic interface when the incident wave is ordinary

When an ordinary wave passes from a uniaxial birefringent to an isotropic medium, it produces two reflected waves (ordinary and extraordinary) and a single refracted wave [85, 88, 89].

As in the previous case, the incidence plane is perpendicular to the z-axis ($\delta = +90°$), the optic axis is perpendicular to the discontinuity surface ($\vartheta = +90°$) and the ordinary and extraordinary waves are perpendicular and parallel to the incidence plane (see again 'Ordinary and extraordinary waves in a uniaxial birefringent medium' in subsection 2.2.2 and the right hand side of Figure 2.16).

Figure C.2 shows the case in which the incident wave propagating through the uniaxial birefringent medium is ordinary and travels in the $\check{N}'$ direction with phase velocity $u_o = c/n_{1o}$. The ordinary and extraordinary reflected beams propagate in the $\check{N}'_o$ and $\check{N}'_e$ direction, respectively, with different phase velocities $u_o = c/n_{1o}$ and $u'_e = c/n'_e = \left[u_e^2 + (u_o^2 - u_e^2)(\check{N}'_e \cdot \check{z}_3)^2\right]$ with $u_e = c/n_{1e}$ (see equation 2.36).
The refracted beam propagates in an isotropic medium, travelling in the $\check{N}'''$ direction with phase velocity $u_2 = c/n_2$ [85].
The unit vector normal to the incident, ordinary and extraordinary reflected and refracted wavefronts are related each other by the following relationships [85, 89]:

$$n_0 \sin\alpha = n_{1o} \sin\beta' = n_2 \sin\gamma \tag{C.23}$$

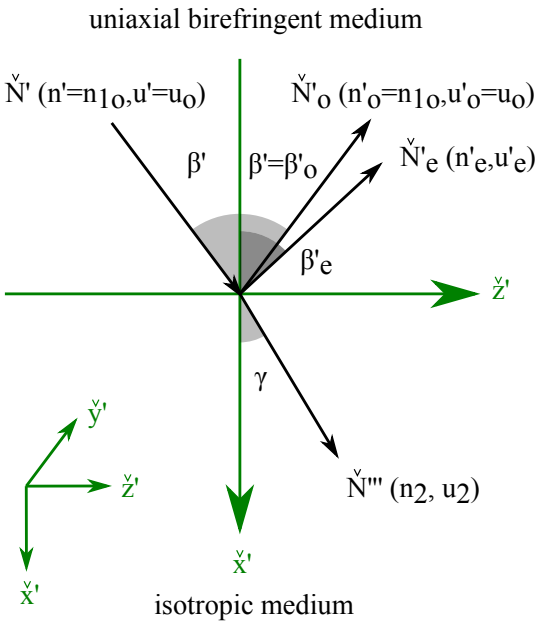

Fig. C.2 Schematic diagram of the incidence plane with the unit vector normal to the ordinary incident ($\check{N}'$), ordinary reflected ($\check{N}'_o$), extraordinary reflected ($\check{N}'_e$) and refracted ($\check{N}'''$) wavefront.

$$\begin{aligned} \beta'_o &= \beta' \\ \beta'_e &\neq \beta' \end{aligned} \tag{C.24}$$

Only for the ordinary incident and reflected wave, the reflection angle coincides with the incident one.

Even if the polarisation of the refracted wave is not known, the electric field vectors of the incident, ordinary and extraordinary reflected, and refracted wave are expressed as follows [85]:

$$\begin{aligned} \text{incident wave}: & \left\{ \vec{E}' = (\vec{E}' \cdot \check{y}')\check{y}' \right. \\ \text{reflected wave}: & \begin{cases} \vec{E}'_o = (\vec{E}'_o \cdot \check{y}')\check{y}' \\ \vec{E}'_e = (\vec{E}'_e \cdot \check{x}')\check{x}' + (\vec{E}'_e \cdot \check{z}')\check{z}' \end{cases} \\ \text{refracted wave}: & \left\{ \vec{E}''' = (\vec{E}''' \cdot \check{x}')\check{x}' + (\vec{E}''' \cdot \check{y}')\check{y}' + (\vec{E}''' \cdot \check{z}')\check{z}' \right. \end{aligned} \tag{C.25}$$

and the reflection and transmission coefficients are (Figure C.2) [85]:

$$r_{oo} = +\frac{|\vec{E}'_o|}{|\vec{E}'|} = +\frac{|(\vec{E}'_o \cdot \check{y}')\check{y}'|}{|(\vec{E}' \cdot \check{y}')\check{y}'|} \tag{C.26}$$

$$r_{oe} = +\frac{|\vec{E}'_e|}{|\vec{E}'|} = +\frac{|(\vec{E}'_e \cdot \check{x}')\check{x}' + (\vec{E}'_e \cdot \check{z}')\check{z}'|}{|(\vec{E}' \cdot \check{y}')\check{y}'|} \tag{C.27}$$

$$t_{ox} = \frac{|\vec{E}'''|}{|\vec{E}'|} = \frac{|(\vec{E}''' \cdot \check{x}')\check{x}' + (\vec{E}''' \cdot \check{y}')\check{y}' + (\vec{E}''' \cdot \check{z}')\check{z}'|}{|(\vec{E}' \cdot \check{y}')\check{y}'|} \tag{C.28}$$

where the index x in the subscript of the transmission coefficient stands for the unknown state of the refracted beam.

The expressions for the reflection and transmission coefficients in the incidence plane system are then written in the discontinuity surface system, using equation 2.30. The next step is to express the electric field vector $\vec{\mathscr{E}}$ through its corresponding electric displacement vector $\vec{\mathscr{D}}$ in the discontinuity surface system [85].
From equations 2.33, 2.34, 2.35 and 2.29, the components of the electric field in the discontinuity surface system for the ordinary incident, ordinary and extraordinary reflected waves in the uniaxial birefringent medium can be written as follows [85]:

$$\begin{cases} (\vec{E}' \cdot \check{x}) = \frac{-\mu_0 u_o^2 \sqrt{1-(\check{n}\cdot\check{z}_3)^2}\left[\check{N}'\cdot(\check{z}_3\times\check{n})\right]}{(\check{N}'\cdot\check{n})-(\check{n}\cdot\check{z}_3)(\check{N}'\cdot\check{z}_3)}(\vec{D}'\cdot\check{y}) \\ (\vec{E}' \cdot \check{y}) = \mu_0 u_o^2 (\vec{D}' \cdot \check{y}) \\ (\vec{E}' \cdot \check{z}) = \frac{\mu_0 u_o^2 (\check{n}\cdot\check{z}_3)\left[\check{N}'\cdot(\check{z}_3\times\check{n})\right]}{(\check{N}'\cdot\check{n})-(\check{n}\cdot\check{z}_3)(\check{N}'\cdot\check{z}_3)}(\vec{D}'\cdot\check{y}) \end{cases} \tag{C.29}$$

$$\begin{cases} (\vec{E}'_o \cdot \check{x}) = \frac{-\mu_0 u_o^2 \sqrt{1-(\check{n}\cdot\check{z}_3)^2}\left[\check{N}'_o\cdot(\check{z}_3\times\check{n})\right]}{(\check{N}'_o\cdot\check{n})-(\check{n}\cdot\check{z}_3)(\check{N}'_o\cdot\check{z}_3)}(\vec{D}'_o\cdot\check{y}) \\ (\vec{E}'_o \cdot \check{y}) = \mu_0 u_o^2 (\vec{D}'_o \cdot \check{y}) \\ (\vec{E}'_o \cdot \check{z}) = \frac{\mu_0 u_o^2 (\check{n}\cdot\check{z}_3)\left[\check{N}'_o\cdot(\check{z}_3\times\check{n})\right]}{(\check{N}'_o\cdot\check{n})-(\check{n}\cdot\check{z}_3)(\check{N}'_o\cdot\check{z}_3)}(\vec{D}'_o\cdot\check{y}) \end{cases} \tag{C.30}$$

$$\begin{cases} (\vec{E}'_e \cdot \check{x}) = \frac{\mu_0 \sqrt{1-(\check{n}\cdot\check{z}_3)^2}\left[u_o^2(\check{N}'_e\cdot\check{n})(\check{N}'_e\cdot\check{z}_3)-u_e'^2(\check{n}\cdot\check{z}_3)\right]}{\left[\check{N}'_e\cdot(\check{z}_3\times\check{n})\right](\check{N}'_e\cdot\check{z}_3)}(\vec{D}'_e\cdot\check{y}) \\ (\vec{E}'_e \cdot \check{y}) = \mu_0 u_o^2 (\vec{D}'_e \cdot \check{y}) \\ (\vec{E}'_e \cdot \check{z}) = \frac{-\mu_0\left[u_o^2\left((\check{n}\cdot\check{z}_3)(\check{N}'_e\cdot\check{z}_3)(\check{N}'_e\cdot\check{n})-(\check{N}'_e\cdot\check{z}_3)^2\right)+u_e'^2\left(1-(\check{n}\cdot\check{z}_3)^2\right)\right]}{\left[\check{N}'_e\cdot(\check{z}_3\times\check{n})\right](\check{N}'_e\cdot\check{z}_3)}(\vec{D}'_e\cdot\check{y}) \end{cases} \tag{C.31}$$

Finally, the following relationships are found using the boundary conditions at the uniaxial birefringent-isotropic interface for the electric field $\vec{\mathscr{E}}$ and the magnetic field $\vec{\mathscr{H}}$, written in the discontinuity surface coordinate system [85]:

$$\begin{aligned}
(\vec{E}''' \cdot \check{y}) &= (\vec{E}' \cdot \check{y}) + (\vec{E}'_o \cdot \check{y}) + (\vec{E}'_e \cdot \check{y}) \\
(\vec{E}''' \cdot \check{z}) &= (\vec{E}' \cdot \check{z}) + (\vec{E}'_o \cdot \check{z}) + (\vec{E}'_e \cdot \check{z}) \\
(\vec{H}''' \cdot \check{y}) &= (\vec{H}' \cdot \check{y}) + (\vec{H}'_o \cdot \check{y}) + (\vec{H}'_e \cdot \check{y}) \\
(\vec{H}''' \cdot \check{z}) &= (\vec{H}' \cdot \check{z}) + (\vec{H}'_o \cdot \check{z}) + (\vec{H}'_e \cdot \check{z})
\end{aligned} \tag{C.32}$$

and from this, the electric displacement vector of the ordinary and extraordinary reflected waves can be expressed as a function of that of the incident wave. The electric field of the refracted wave can be written as a function of those of the incident and reflected waves [85]:

$$\begin{aligned}
(\vec{D}'_o \cdot \check{y}) &= \frac{E_3F_1 - E_1F_3}{E_2F_3 - E_3F_2}(\vec{D}' \cdot \check{y}) \\
(\vec{D}'_e \cdot \check{y}) &= \frac{E_1F_2 - E_2F_1}{E_2F_3 - E_3F_2}(\vec{D}' \cdot \check{y}) \\
(\vec{E}''' \cdot \check{y}) &= \mu_0^2 u_2^2 \left[G_1(\vec{D}' \cdot \check{y}) + G_2(\vec{D}'_o \cdot \check{y}) + G_3(\vec{D}'_e \cdot \check{y}) \right] \\
(\vec{E}''' \cdot \check{z}) &= -\mu_0^2 u_2^2 \left[H_1(\vec{D}' \cdot \check{y}) + H_2(\vec{D}'_o \cdot \check{y}) + H_3(\vec{D}'_e \cdot \check{y}) \right]
\end{aligned} \tag{C.33}$$

where

$$
\begin{aligned}
E_1 &= \frac{\left[(\check{N}''' \cdot \check{x})^2 + (\check{N}''' \cdot \check{z})^2\right]}{u_2(\check{N}''' \cdot \check{x})} \frac{u_o^2(\check{n} \cdot \check{z}_3)\left[\check{N}' \cdot (\check{z}_3 \times \check{n})\right]}{(\check{N}' \cdot \check{n}) - (\check{n} \cdot \check{z}_3)(\check{N}' \cdot \check{z}_3)} + \frac{u_o^2(\check{N}''' \cdot \check{y})(\check{N}''' \cdot \check{z})}{u_2(\check{N}''' \cdot \check{x})} \\
&\quad - \frac{u_o(\check{N}' \cdot \check{z}_3)\left[\check{N}' \cdot (\check{z}_3 \times \check{n})\right]}{(\check{N}' \cdot \check{n}) - (\check{n} \cdot \check{z}_3)(\check{N}' \cdot \check{z}_3)} \\
E_2 &= \frac{\left[(\check{N}''' \cdot \check{x})^2 + (\check{N}''' \cdot \check{z})^2\right]}{u_2(\check{N}''' \cdot \check{x})} \frac{u_o^2(\check{n} \cdot \check{z}_3)\left[\check{N}_o' \cdot (\check{z}_3 \times \check{n})\right]}{(\check{N}_o' \cdot \check{n}) - (\check{n} \cdot \check{z}_3)(\check{N}_o' \cdot \check{z}_3)} + \frac{u_o^2(\check{N}''' \cdot \check{y})(\check{N}''' \cdot \check{z})}{u_2(\check{N}''' \cdot \check{x})} \\
&\quad - \frac{u_o(\check{N}_o' \cdot \check{z}_3)\left[\check{N}_o' \cdot (\check{z}_3 \times \check{n})\right]}{(\check{N}_o' \cdot \check{n}) - (\check{n} \cdot \check{z}_3)(\check{N}_o' \cdot \check{z}_3)} \\
E_3 &= -\frac{\left[(\check{N}''' \cdot \check{x})^2 + (\check{N}''' \cdot \check{z})^2\right]}{u_2(\check{N}''' \cdot \check{x})} \frac{\left[u_o^2\left((\check{n} \cdot \check{z}_3)(\check{N}_e' \cdot \check{z}_3)(\check{N}_e' \cdot \check{n}) - (\check{N}_e' \cdot \check{z}_3)^2\right) + u_e'^2\left(1 - (\check{n} \cdot \check{z}_3)^2\right)\right]}{\left[\check{N}_e' \cdot (\check{z}_3 \times \check{n})\right](\check{N}_e' \cdot \check{z}_3)} \\
&\quad + \frac{u_o^2(\check{N}''' \cdot \check{y})(\check{N}''' \cdot \check{z})}{u_2(\check{N}''' \cdot \check{x})} + \frac{u_e'\left[(\check{N}_e' \cdot \check{n}) - (\check{n} \cdot \check{z}_3)(\check{N}_e' \cdot \check{z}_3)\right]}{(\check{N}_e' \cdot \check{z}_3)\left[\check{N}_e' \cdot (\check{z}_3 \times \check{n})\right]} \\
F_1 &= \frac{(\check{N}''' \cdot \check{y})(\check{N}''' \cdot \check{z})}{u_2(\check{N}''' \cdot \check{x})} \frac{u_o^2(\check{n} \cdot \check{z}_3)\left[\check{N}' \cdot (\check{z}_3 \times \check{n})\right]}{(\check{N}' \cdot \check{n}) - (\check{n} \cdot \check{z}_3)(\check{N}' \cdot \check{z}_3)} + \frac{u_o^2\left[(\check{N}''' \cdot \check{x})^2 + (\check{N}''' \cdot \check{y})^2\right]}{u_2(\check{N}''' \cdot \check{x})} \\
&\quad - \frac{u_o\left[(\check{N}' \cdot \check{z}_3)(\check{N}' \cdot \check{n})(\check{n} \cdot \check{z}_3) - (\check{N}' \cdot \check{z}_3)^2 + \left(1 - (\check{n} \cdot \check{z}_3)^2\right)\right]}{(\check{N}' \cdot \check{n}) - (\check{n} \cdot \check{z}_3)(\check{N}' \cdot \check{z}_3)} \\
F_2 &= \frac{(\check{N}''' \cdot \check{y})(\check{N}''' \cdot \check{z})}{u_2(\check{N}''' \cdot \check{x})} \frac{u_o^2(\check{n} \cdot \check{z}_3)\left[\check{N}_o' \cdot (\check{z}_3 \times \check{n})\right]}{(\check{N}_o' \cdot \check{n}) - (\check{n} \cdot \check{z}_3)(\check{N}_o' \cdot \check{z}_3)} + \frac{u_o^2\left[(\check{N}''' \cdot \check{x})^2 + (\check{N}''' \cdot \check{y})^2\right]}{u_2(\check{N}''' \cdot \check{x})} \\
&\quad - \frac{u_o\left[(\check{N}_o' \cdot \check{z}_3)(\check{N}_o' \cdot \check{n})(\check{n} \cdot \check{z}_3) - (\check{N}_o' \cdot \check{z}_3)^2 + \left(1 - (\check{n} \cdot \check{z}_3)^2\right)\right]}{(\check{N}_o' \cdot \check{n}) - (\check{n} \cdot \check{z}_3)(\check{N}_o' \cdot \check{z}_3)} \\
F_3 &= -\frac{(\check{N}''' \cdot \check{y})(\check{N}''' \cdot \check{z})}{u_2(\check{N}''' \cdot \check{x})} \frac{\left[u_o^2\left((\check{n} \cdot \check{z}_3)(\check{N}_e' \cdot \check{z}_3)(\check{N}_e' \cdot \check{n}) - (\check{N}_e' \cdot \check{z}_3)^2\right) + u_e'^2\left(1 - (\check{n} \cdot \check{z}_3)^2\right)\right]}{\left[\check{N}_e' \cdot (\check{z}_3 \times \check{n})\right](\check{N}_e' \cdot \check{z}_3)} \\
&\quad + \frac{u_o^2\left[(\check{N}''' \cdot \check{x})^2 + (\check{N}''' \cdot \check{y})^2\right]}{u_2(\check{N}''' \cdot \check{x})} - \frac{u_e'(\check{n} \cdot \check{z}_3)}{(\check{N}_e' \cdot \check{z}_3)}
\end{aligned}
\tag{C.34}
$$

and

$$
\begin{aligned}
G_1 &= -\frac{(\check{N}'''\cdot\check{y})(\check{N}'''\cdot\check{z})}{\mu_0 u_2(\check{N}'''\cdot\check{x})}\frac{u_o(\check{N}'\cdot\check{z}_3)\left[\check{N}'\cdot(\check{z}_3\times\check{n})\right]}{(\check{N}'\cdot\check{n})-(\check{n}\cdot\check{z}_3)(\check{N}'\cdot\check{z}_3)} \\
&\quad+\frac{\left[(\check{N}'''\cdot\check{x})^2+(\check{N}'''\cdot\check{z})^2\right]}{\mu_0 u_2(\check{N}'''\cdot\check{x})}\frac{u_o\left[(\check{N}'\cdot\check{z}_3)(\check{N}'\cdot\check{n})(\check{n}\cdot\check{z}_3)-(\check{N}'\cdot\check{z}_3)^2+\left(1-(\check{n}\cdot\check{z}_3)^2\right)\right]}{(\check{N}'\cdot\check{n})-(\check{n}\cdot\check{z}_3)(\check{N}'\cdot\check{z}_3)} \\
G_2 &= -\frac{(\check{N}'''\cdot\check{y})(\check{N}'''\cdot\check{z})}{\mu_0 u_2(\check{N}'''\cdot\check{x})}\frac{u_o(\check{N}'_o\cdot\check{z}_3)\left[\check{N}'_o\cdot(\check{z}_3\times\check{n})\right]}{(\check{N}'_o\cdot\check{n})-(\check{n}\cdot\check{z}_3)(\check{N}'_o\cdot\check{z}_3)} \\
&\quad+\frac{\left[(\check{N}'''\cdot\check{x})^2+(\check{N}'''\cdot\check{z})^2\right]}{\mu_0 u_2(\check{N}'''\cdot\check{x})}\frac{u_o\left[(\check{N}'_o\cdot\check{z}_3)(\check{N}'_o\cdot\check{n})(\check{n}\cdot\check{z}_3)-(\check{N}'_o\cdot\check{z}_3)^2+\left(1-(\check{n}\cdot\check{z}_3)^2\right)\right]}{(\check{N}'_o\cdot\check{n})-(\check{n}\cdot\check{z}_3)(\check{N}'_o\cdot\check{z}_3)} \\
G_3 &= \frac{(\check{N}'''\cdot\check{y})(\check{N}'''\cdot\check{z})}{\mu_0 u_2(\check{N}'''\cdot\check{x})}\frac{u'_e\left[(\check{N}'_e\cdot\check{n})-(\check{n}\cdot\check{z}_3)(\check{N}'_e\cdot\check{z}_3)\right]}{(\check{N}'_e\cdot\check{z}_3)\left[\check{N}'_e\cdot(\check{z}_3\times\check{n})\right]} \\
&\quad+\frac{\left[(\check{N}'''\cdot\check{x})^2+(\check{N}'''\cdot\check{z})^2\right]}{\mu_0 u_2(\check{N}'''\cdot\check{x})}\frac{u'_e(\check{n}\cdot\check{z}_3)}{(\check{N}'_e\cdot\check{z}_3)} \\
H_1 &= -\frac{\left[(\check{N}'''\cdot\check{x})^2+(\check{N}'''\cdot\check{y})^2\right]}{\mu_0 u_2(\check{N}'''\cdot\check{x})}\frac{u_o(\check{N}'\cdot\check{z}_3)\left[\check{N}'\cdot(\check{z}_3\times\check{n})\right]}{(\check{N}'\cdot\check{n})-(\check{n}\cdot\check{z}_3)(\check{N}'\cdot\check{z}_3)} \\
&\quad+\frac{(\check{N}'''\cdot\check{y})(\check{N}'''\cdot\check{z})}{\mu_0 u_2(\check{N}'''\cdot\check{x})}\frac{u_o\left[(\check{N}'\cdot\check{z}_3)(\check{N}'\cdot\check{n})(\check{n}\cdot\check{z}_3)-(\check{N}'\cdot\check{z}_3)^2+\left(1-(\check{n}\cdot\check{z}_3)^2\right)\right]}{(\check{N}'\cdot\check{n})-(\check{n}\cdot\check{z}_3)(\check{N}'\cdot\check{z}_3)} \\
H_2 &= -\frac{\left[(\check{N}'''\cdot\check{x})^2+(\check{N}'''\cdot\check{y})^2\right]}{\mu_0 u_2(\check{N}'''\cdot\check{x})}\frac{u_o(\check{N}'_o\cdot\check{z}_3)\left[\check{N}'_o\cdot(\check{z}_3\times\check{n})\right]}{(\check{N}'_o\cdot\check{n})-(\check{n}\cdot\check{z}_3)(\check{N}'_o\cdot\check{z}_3)} \\
&\quad+\frac{(\check{N}'''\cdot\check{y})(\check{N}'''\cdot\check{z})}{\mu_0 u_2(\check{N}'''\cdot\check{x})}\frac{u_o\left[(\check{N}'_o\cdot\check{z}_3)(\check{N}'_o\cdot\check{n})(\check{n}\cdot\check{z}_3)-(\check{N}'_o\cdot\check{z}_3)^2+\left(1-(\check{n}\cdot\check{z}_3)^2\right)\right]}{(\check{N}'_o\cdot\check{n})-(\check{n}\cdot\check{z}_3)(\check{N}'_o\cdot\check{z}_3)} \\
H_3 &= \frac{\left[(\check{N}'''\cdot\check{x})^2+(\check{N}'''\cdot\check{y})^2\right]}{\mu_0 u_2(\check{N}'''\cdot\check{x})}\frac{u'_e\left[(\check{N}'_e\cdot\check{n})-(\check{n}\cdot\check{z}_3)(\check{N}'_e\cdot\check{z}_3)\right]}{(\check{N}'_e\cdot\check{z}_3)\left[\check{N}'_e\cdot(\check{z}_3\times\check{n})\right]} \\
&\quad+\frac{(\check{N}'''\cdot\check{y})(\check{N}'''\cdot\check{z})}{\mu_0 u_2(\check{N}'''\cdot\check{x})}\frac{u'_e(\check{n}\cdot\check{z}_3)}{(\check{N}'_e\cdot\check{z}_3)}
\end{aligned}
\tag{C.35}
$$

When the incidence plane is perpendicular to the z-axis ($\delta = +\,90^\circ$) and the optic axis is perpendicular to the discontinuity surface ($\vartheta = +\,90^\circ$), the expressions for the reflection and transmission coefficients at a uniaxial birefringent-isotropic interface when the incident beam is ordinary can again be simplified considerably (Figure 2.16, right). The coefficients

of reflection are defined as follows:

$$r_{oo} = \frac{\cos\beta' - \sqrt{\left(\frac{n_2}{n_{1o}}\right)^2 - \sin^2\beta'}}{\cos\beta' + \sqrt{\left(\frac{n_2}{n_{1o}}\right)^2 - \sin^2\beta'}} \tag{2.41}$$

$$r_{oe} = 0 \tag{C.36}$$

where angle β' is expressed by equations 2.45 or C.23.

Summarising, it was found that an ordinary incident beam reflects and refracts in beams whose polarisation is perpendicular to the plane of incidence.

Case 3: uniaxial birefringent to isotropic interface when the incident wave is extraordinary

When an extraordinary wave is incident on the interface between a uniaxial birefringent and an isotropic medium, it gives rise to an ordinary and extraordinary reflected waves besides the refracted wave [86, 88, 89].

Still, the incidence plane is perpendicular to the z-axis ($\delta = +\,90^\circ$), the optic axis is perpendicular to the discontinuity surface ($\vartheta = +\,90^\circ$), and the ordinary and extraordinary waves are perpendicular and parallel to the incidence plane (see again 'Ordinary and extraordinary waves in a uniaxial birefringent medium' in subsection 2.2.2 and the right hand side of Figure 2.16).

In Figure C.3, the extraordinary incident wave propagates through the uniaxial birefringent medium in the $\check{N}''$ direction with phase velocity $u'' = c/n''$ (see equation C.3).
The ordinary and extraordinary reflected beams propagate in the $\check{N}_o''$ and $\check{N}_e''$ direction, respectively, with phase velocities $u_o = c/n_{1o}$ and $u_e'' = c/n_e'' = \left[u_e^2 + (u_o^2 - u_e^2)(\check{N}_e'' \cdot \check{z}_3)^2\right]$ (see equation 2.36).
The refracted beam propagates in the $\check{N}'''$ direction in an isotropic medium with phase velocity $u_2 = c/n_2$ [86].
The unit vector normal to the incident, ordinary and extraordinary reflected and refracted wavefront are related each other by the following relationships [86, 89]:

$$n_0 \sin\alpha = n'' \sin\beta'' = n_2 \sin\gamma \tag{C.37}$$

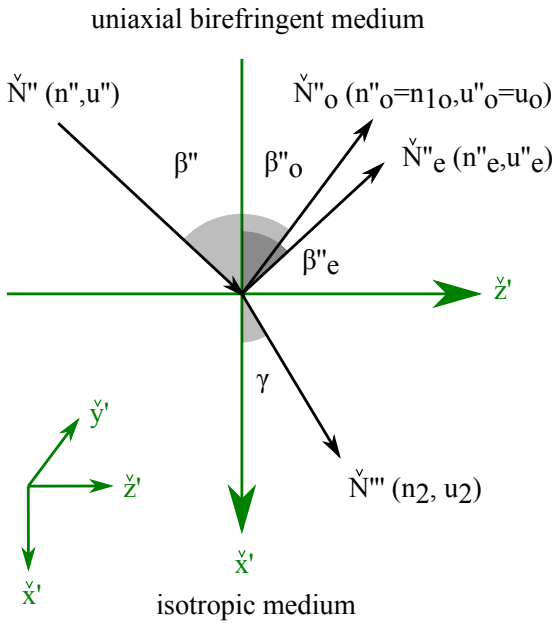

Fig. C.3 Schematic diagram of the incidence plane with the unit vector normal to the extraordinary incident ($\breve{N}''$), ordinary reflected ($\breve{N}''_o$), extraordinary reflected ($\breve{N}''_e$) and refracted ($\breve{N}'''$) wavefront.

$$\begin{aligned} \beta'' &\neq \beta''_o \\ \beta'' &\neq \beta''_e \end{aligned} \tag{C.38}$$

with n'' expressed by equation 2.44. For the reflected waves, neither of the two reflection angles coincides with the incident one, but when $\delta = +90^\circ$ and $\vartheta = +90^\circ$, it is found that $\beta'' = \beta''_e$ and, consequently, $n'' = n''_e$ [88].

The electric field vectors of the incident, ordinary and extraordinary reflected, and refracted wave can be written as follows [86]:

$$\begin{aligned} \text{incident wave}: & \left\{ \vec{E}'' = (\vec{E}'' \cdot \breve{x}')\breve{x}' - (\vec{E}'' \cdot \breve{z}')\breve{z}' \right. \\ \text{reflected wave}: & \begin{cases} \vec{E}''_o = (\vec{E}''_o \cdot \breve{y}')\breve{y}' \\ \vec{E}''_e = (\vec{E}''_e \cdot \breve{x}')\breve{x}' + (\vec{E}''_e \cdot \breve{z}')\breve{z}' \end{cases} \\ \text{refracted wave}: & \left\{ \vec{E}''' = (\vec{E}''' \cdot \breve{x}')\breve{x}' + (\vec{E}''' \cdot \breve{y}')\breve{y}' + (\vec{E}''' \cdot \breve{z}')\breve{z}' \right. \end{aligned} \tag{C.39}$$

and the reflection and transmission coefficients are (Figure C.3) [86]:

$$r_{eo} = -\frac{|\vec{E}''_o|}{|\vec{E}''|} = -\frac{|(\vec{E}''_o \cdot \check{y}')\check{y}'|}{|(\vec{E}'' \cdot \check{x}')\check{x}' - (\vec{E}'' \cdot \check{z}')\check{z}'|} \tag{C.40}$$

$$r_{ee} = -\frac{|\vec{E}''_e|}{|\vec{E}''|} = -\frac{|(\vec{E}''_e \cdot \check{x}')\check{x}' + (\vec{E}''_e \cdot \check{z}')\check{z}'|}{|(\vec{E}'' \cdot \check{x}')\check{x}' - (\vec{E}'' \cdot \check{z}')\check{z}'|} \tag{C.41}$$

$$t_{ex} = \frac{|\vec{E}'''|}{|\vec{E}''|} = \frac{|(\vec{E}''' \cdot \check{x}')\check{x}' + (\vec{E}''' \cdot \check{y}')\check{y}' + (\vec{E}''' \cdot \check{z}')\check{z}'|}{|(\vec{E}'' \cdot \check{x}')\check{x}' - (\vec{E}'' \cdot \check{z}')\check{z}'|} \tag{C.42}$$

where the index x in the subscript of the transmission coefficient means that the polarisation of the refracted beam is unknown.

The next step is to write these reflection and transmission coefficients and the electric field vector $\vec{\mathscr{E}}$ as a function of the electric displacement vector $\vec{\mathscr{D}}$ in the discontinuity surface system [86].

From equations 2.33, 2.34, 2.35 and 2.29, the components of the electric field in the discontinuity surface system for the extraordinary incident, ordinary and extraordinary reflected waves in the uniaxial birefringent medium can be written as follows [86]:

$$\begin{cases} (\vec{E}'' \cdot \check{x}) = \frac{\mu_0 \sqrt{1-(\check{n}\cdot\check{z}_3)^2}\left[u_o^2(\check{N}''\cdot\check{n})(\check{N}''\cdot\check{z}_3) - u''^2(\check{n}\cdot\check{z}_3)\right]}{\left[\check{N}''\cdot(\check{z}_3\times\check{n})\right](\check{N}''\cdot\check{z}_3)}(\vec{D}''\cdot\check{y}) \\ (\vec{E}'' \cdot \check{y}) = \mu_0 u_o^2(\vec{D}''\cdot\check{y}) \\ (\vec{E}'' \cdot \check{z}) = \frac{-\mu_0\left[u_o^2\left((\check{n}\cdot\check{z}_3)(\check{N}''\cdot\check{z}_3)(\check{N}''\cdot\check{n}) - (\check{N}''\cdot\check{z}_3)^2\right) + u''^2\left(1-(\check{n}\cdot\check{z}_3)^2\right)\right]}{\left[\check{N}''\cdot(\check{z}_3\times\check{n})\right](\check{N}''\cdot\check{z}_3)}(\vec{D}''\cdot\check{y}) \end{cases} \tag{C.43}$$

$$\begin{cases} (\vec{E}''_o \cdot \check{x}) = \frac{-\mu_0 u_o^2\sqrt{1-(\check{n}\cdot\check{z}_3)^2}\left[\check{N}''_o\cdot(\check{z}_3\times\check{n})\right]}{(\check{N}''_o\cdot\check{n}) - (\check{n}\cdot\check{z}_3)(\check{N}''_o\cdot\check{z}_3)}(\vec{D}''_o\cdot\check{y}) \\ (\vec{E}''_o \cdot \check{y}) = \mu_0 u_o^2(\vec{D}''_o\cdot\check{y}) \\ (\vec{E}''_o \cdot \check{z}) = \frac{\mu_0 u_o^2(\check{n}\cdot\check{z}_3)\left[\check{N}''_o\cdot(\check{z}_3\times\check{n})\right]}{(\check{N}''_o\cdot\check{n}) - (\check{n}\cdot\check{z}_3)(\check{N}''_o\cdot\check{z}_3)}(\vec{D}''_o\cdot\check{y}) \end{cases} \tag{C.44}$$

$$\begin{cases} (\vec{E}''_e \cdot \check{x}) = \frac{\mu_0 \sqrt{1-(\check{n}\cdot\check{z}_3)^2}\left[u_o^2(\check{N}''_e\cdot\check{n})(\check{N}''_e\cdot\check{z}_3) - u''^2_e(\check{n}\cdot\check{z}_3)\right]}{\left[\check{N}''_e\cdot(\check{z}_3\times\check{n})\right](\check{N}''_e\cdot\check{z}_3)}(\vec{D}''_e\cdot\check{y}) \\ (\vec{E}''_e \cdot \check{y}) = \mu_0 u_o^2(\vec{D}''_e\cdot\check{y}) \\ (\vec{E}''_e \cdot \check{z}) = \frac{-\mu_0\left[u_o^2\left((\check{n}\cdot\check{z}_3)(\check{N}''_e\cdot\check{z}_3)(\check{N}''_e\cdot\check{n}) - (\check{N}''_e\cdot\check{z}_3)^2\right) + u''^2_e\left(1-(\check{n}\cdot\check{z}_3)^2\right)\right]}{\left[\check{N}''_e\cdot(\check{z}_3\times\check{n})\right](\check{N}''_e\cdot\check{z}_3)}(\vec{D}''_e\cdot\check{y}) \end{cases} \tag{C.45}$$

The boundary conditions associated with the uniaxial birefringent-isotropic interface for the electric field $\vec{\mathscr{E}}$ and the magnetic field $\vec{\mathscr{H}}$ in the discontinuity surface coordinate system are [86]:

$$\begin{aligned}
(\vec{E}''' \cdot \check{y}) &= (\vec{E}'' \cdot \check{y}) + (\vec{E}''_o \cdot \check{y}) + (\vec{E}''_e \cdot \check{y}) \\
(\vec{E}''' \cdot \check{z}) &= (\vec{E}'' \cdot \check{z}) + (\vec{E}''_o \cdot \check{z}) + (\vec{E}''_e \cdot \check{z}) \\
(\vec{H}''' \cdot \check{y}) &= (\vec{H}'' \cdot \check{y}) + (\vec{H}''_o \cdot \check{y}) + (\vec{H}''_e \cdot \check{y}) \\
(\vec{H}''' \cdot \check{z}) &= (\vec{H}'' \cdot \check{z}) + (\vec{H}''_o \cdot \check{z}) + (\vec{H}''_e \cdot \check{z})
\end{aligned} \tag{C.46}$$

and from this, the electric displacement vector of the ordinary and extraordinary reflected waves can be expressed as a function of that of the incident wave, whereas the electric field of the refracted wave can be defined as a function of those of the incident and reflected waves [86]:

$$\begin{aligned}
(\vec{D}''_o \cdot \check{y}) &= \frac{I_3 J_1 - I_1 J_3}{I_2 J_3 - I_3 J_2} (\vec{D}'' \cdot \check{y}) \\
(\vec{D}''_e \cdot \check{y}) &= \frac{I_1 J_2 - I_2 J_1}{I_2 J_3 - I_3 J_2} (\vec{D}'' \cdot \check{y}) \\
(\vec{E}''' \cdot \check{y}) &= \mu_0^2 u_2^2 \left[K_1 (\vec{D}'' \cdot \check{y}) + K_2 (\vec{D}''_o \cdot \check{y}) + K_3 (\vec{D}''_e \cdot \check{y}) \right] \\
(\vec{E}''' \cdot \check{z}) &= -\mu_0^2 u_2^2 \left[L_1 (\vec{D}'' \cdot \check{y}) + L_2 (\vec{D}''_o \cdot \check{y}) + L_3 (\vec{D}''_e \cdot \check{y}) \right]
\end{aligned} \tag{C.47}$$

where

$$
\begin{aligned}
I_1 &= -\frac{\left[(\check{N}'''\cdot\check{x})^2+(\check{N}'''\cdot\check{z})^2\right]}{u_2(\check{N}'''\cdot\check{x})}\frac{\left[u_o^2\left((\check{n}\cdot\check{z}_3)(\check{N}''\cdot\check{z}_3)(\check{N}''\cdot\check{n})-(\check{N}''\cdot\check{z}_3)^2\right)+u''^2\left(1-(\check{n}\cdot\check{z}_3)^2\right)\right]}{\left[\check{N}''\cdot(\check{z}_3\times\check{n})\right](\check{N}''\cdot\check{z}_3)}\\
&\quad+\frac{u_o^2(\check{N}'''\cdot\check{y})(\check{N}'''\cdot\check{z})}{u_2(\check{N}'''\cdot\check{x})}+\frac{u''\left[(\check{N}''\cdot\check{n})-(\check{n}\cdot\check{z}_3)(\check{N}''\cdot\check{z}_3)\right]}{(\check{N}''\cdot\check{z}_3)\left[\check{N}''\cdot(\check{z}_3\times\check{n})\right]}\\
I_2 &= \frac{\left[(\check{N}'''\cdot\check{x})^2+(\check{N}'''\cdot\check{z})^2\right]}{u_2(\check{N}'''\cdot\check{x})}\frac{u_o^2(\check{n}\cdot\check{z}_3)\left[\check{N}_o''\cdot(\check{z}_3\times\check{n})\right]}{(\check{N}_o''\cdot\check{n})-(\check{n}\cdot\check{z}_3)(\check{N}_o''\cdot\check{z}_3)}+\frac{u_o^2(\check{N}'''\cdot\check{y})(\check{N}'''\cdot\check{z})}{u_2(\check{N}'''\cdot\check{x})}\\
&\quad-\frac{u_o(\check{N}_o''\cdot\check{z}_3)\left[\check{N}_o''\cdot(\check{z}_3\times\check{n})\right]}{(\check{N}_o''\cdot\check{n})-(\check{n}\cdot\check{z}_3)(\check{N}_o''\cdot\check{z}_3)}\\
I_3 &= -\frac{\left[(\check{N}'''\cdot\check{x})^2+(\check{N}'''\cdot\check{z})^2\right]}{u_2(\check{N}'''\cdot\check{x})}\frac{\left[u_o^2\left((\check{n}\cdot\check{z}_3)(\check{N}_e''\cdot\check{z}_3)(\check{N}_e''\cdot\check{n})-(\check{N}_e''\cdot\check{z}_3)^2\right)+u_e''^2\left(1-(\check{n}\cdot\check{z}_3)^2\right)\right]}{\left[\check{N}_e''\cdot(\check{z}_3\times\check{n})\right](\check{N}_e''\cdot\check{z}_3)}\\
&\quad+\frac{u_o^2(\check{N}'''\cdot\check{y})(\check{N}'''\cdot\check{z})}{u_2(\check{N}'''\cdot\check{x})}+\frac{u_e''\left[(\check{N}_e''\cdot\check{n})-(\check{n}\cdot\check{z}_3)(\check{N}_e''\cdot\check{z}_3)\right]}{(\check{N}_e''\cdot\check{z}_3)\left[\check{N}_e''\cdot(\check{z}_3\times\check{n})\right]}\\
J_1 &= -\frac{(\check{N}'''\cdot\check{y})(\check{N}'''\cdot\check{z})}{u_2(\check{N}'''\cdot\check{x})}\frac{\left[u_o^2\left((\check{n}\cdot\check{z}_3)(\check{N}''\cdot\check{z}_3)(\check{N}''\cdot\check{n})-(\check{N}''\cdot\check{z}_3)^2\right)+u''^2\left(1-(\check{n}\cdot\check{z}_3)^2\right)\right]}{\left[\check{N}''\cdot(\check{z}_3\times\check{n})\right](\check{N}''\cdot\check{z}_3)}\\
&\quad+\frac{u_o^2\left[(\check{N}'''\cdot\check{x})^2+(\check{N}'''\cdot\check{y})^2\right]}{u_2(\check{N}'''\cdot\check{x})}-\frac{u''(\check{n}\cdot\check{z}_3)}{(\check{N}''\cdot\check{z}_3)}\\
J_2 &= \frac{(\check{N}'''\cdot\check{y})(\check{N}'''\cdot\check{z})}{u_2(\check{N}'''\cdot\check{x})}\frac{u_o^2(\check{n}\cdot\check{z}_3)\left[\check{N}_o''\cdot(\check{z}_3\times\check{n})\right]}{(\check{N}_o''\cdot\check{n})-(\check{n}\cdot\check{z}_3)(\check{N}_o''\cdot\check{z}_3)}+\frac{u_o^2\left[(\check{N}'''\cdot\check{x})^2+(\check{N}'''\cdot\check{y})^2\right]}{u_2(\check{N}'''\cdot\check{x})}\\
&\quad-\frac{u_o\left[(\check{N}_o''\cdot\check{z}_3)(\check{N}_o''\cdot\check{n})(\check{n}\cdot\check{z}_3)-(\check{N}_o''\cdot\check{z}_3)^2+\left(1-(\check{n}\cdot\check{z}_3)^2\right)\right]}{(\check{N}_o''\cdot\check{n})-(\check{n}\cdot\check{z}_3)(\check{N}_o''\cdot\check{z}_3)}\\
J_3 &= -\frac{(\check{N}'''\cdot\check{y})(\check{N}'''\cdot\check{z})}{u_2(\check{N}'''\cdot\check{x})}\frac{\left[u_o^2\left((\check{n}\cdot\check{z}_3)(\check{N}_e''\cdot\check{z}_3)(\check{N}_e''\cdot\check{n})-(\check{N}_e''\cdot\check{z}_3)^2\right)+u_e''^2\left(1-(\check{n}\cdot\check{z}_3)^2\right)\right]}{\left[\check{N}_e''\cdot(\check{z}_3\times\check{n})\right](\check{N}_e''\cdot\check{z}_3)}\\
&\quad+\frac{u_o^2\left[(\check{N}'''\cdot\check{x})^2+(\check{N}'''\cdot\check{y})^2\right]}{u_2(\check{N}'''\cdot\check{x})}-\frac{u_e''(\check{n}\cdot\check{z}_3)}{(\check{N}_e''\cdot\check{z}_3)}
\end{aligned}
\tag{C.48}
$$

and

$$
\begin{aligned}
K_1 &= \frac{(\check{N}'''\cdot\check{y})(\check{N}'''\cdot\check{z})}{\mu_0 u_2(\check{N}'''\cdot\check{x})}\,\frac{u''\left[(\check{N}''\cdot\check{n})-(\check{n}\cdot\check{z}_3)(\check{N}''\cdot\check{z}_3)\right]}{(\check{N}''\cdot\check{z}_3)\left[\check{N}''\cdot(\check{z}_3\times\check{n})\right]}\\
&\quad+\frac{\left[(\check{N}'''\cdot\check{x})^2+(\check{N}'''\cdot\check{z})^2\right]}{\mu_0 u_2(\check{N}'''\cdot\check{x})}\,\frac{u''(\check{n}\cdot\check{z}_3)}{(\check{N}''\cdot\check{z}_3)}\\
K_2 &= -\frac{(\check{N}'''\cdot\check{y})(\check{N}'''\cdot\check{z})}{\mu_0 u_2(\check{N}'''\cdot\check{x})}\,\frac{u_o(\check{N}_o''\cdot\check{z}_3)\left[\check{N}_o''\cdot(\check{z}_3\times\check{n})\right]}{(\check{N}_o''\cdot\check{n})-(\check{n}\cdot\check{z}_3)(\check{N}_o''\cdot\check{z}_3)}\\
&\quad+\frac{\left[(\check{N}'''\cdot\check{x})^2+(\check{N}'''\cdot\check{z})^2\right]}{\mu_0 u_2(\check{N}'''\cdot\check{x})}\,\frac{u_o\left[(\check{N}_o''\cdot\check{z}_3)(\check{N}_o''\cdot\check{n})(\check{n}\cdot\check{z}_3)-(\check{N}_o''\cdot\check{z}_3)^2+\left(1-(\check{n}\cdot\check{z}_3)^2\right)\right]}{(\check{N}_o''\cdot\check{n})-(\check{n}\cdot\check{z}_3)(\check{N}_o''\cdot\check{z}_3)}\\
K_3 &= \frac{(\check{N}'''\cdot\check{y})(\check{N}'''\cdot\check{z})}{\mu_0 u_2(\check{N}'''\cdot\check{x})}\,\frac{u_e''\left[(\check{N}_e''\cdot\check{n})-(\check{n}\cdot\check{z}_3)(\check{N}_e''\cdot\check{z}_3)\right]}{(\check{N}_e''\cdot\check{z}_3)\left[\check{N}_e''\cdot(\check{z}_3\times\check{n})\right]}\\
&\quad+\frac{\left[(\check{N}'''\cdot\check{x})^2+(\check{N}'''\cdot\check{z})^2\right]}{\mu_0 u_2(\check{N}'''\cdot\check{x})}\,\frac{u_e''(\check{n}\cdot\check{z}_3)}{(\check{N}_e''\cdot\check{z}_3)}\\
L_1 &= \frac{\left[(\check{N}'''\cdot\check{x})^2+(\check{N}'''\cdot\check{y})^2\right]}{\mu_0 u_2(\check{N}'''\cdot\check{x})}\,\frac{u''\left[(\check{N}''\cdot\check{n})-(\check{n}\cdot\check{z}_3)(\check{N}''\cdot\check{z}_3)\right]}{(\check{N}''\cdot\check{z}_3)\left[\check{N}''\cdot(\check{z}_3\times\check{n})\right]}\\
&\quad+\frac{(\check{N}'''\cdot\check{y})(\check{N}'''\cdot\check{z})}{\mu_0 u_2(\check{N}'''\cdot\check{x})}\,\frac{u''(\check{n}\cdot\check{z}_3)}{(\check{N}''\cdot\check{z}_3)}\\
L_2 &= -\frac{\left[(\check{N}'''\cdot\check{x})^2+(\check{N}'''\cdot\check{y})^2\right]}{\mu_0 u_2(\check{N}'''\cdot\check{x})}\,\frac{u_o(\check{N}_o''\cdot\check{z}_3)\left[\check{N}_o''\cdot(\check{z}_3\times\check{n})\right]}{(\check{N}_o''\cdot\check{n})-(\check{n}\cdot\check{z}_3)(\check{N}_o''\cdot\check{z}_3)}\\
&\quad+\frac{(\check{N}'''\cdot\check{y})(\check{N}'''\cdot\check{z})}{\mu_0 u_2(\check{N}'''\cdot\check{x})}\,\frac{u_o\left[(\check{N}_o''\cdot\check{z}_3)(\check{N}_o''\cdot\check{n})(\check{n}\cdot\check{z}_3)-(\check{N}_o''\cdot\check{z}_3)^2+\left(1-(\check{n}\cdot\check{z}_3)^2\right)\right]}{(\check{N}_o''\cdot\check{n})-(\check{n}\cdot\check{z}_3)(\check{N}_o''\cdot\check{z}_3)}\\
L_3 &= \frac{\left[(\check{N}'''\cdot\check{x})^2+(\check{N}'''\cdot\check{y})^2\right]}{\mu_0 u_2(\check{N}'''\cdot\check{x})}\,\frac{u_e''\left[(\check{N}_e''\cdot\check{n})-(\check{n}\cdot\check{z}_3)(\check{N}_e''\cdot\check{z}_3)\right]}{(\check{N}_e''\cdot\check{z}_3)\left[\check{N}_e''\cdot(\check{z}_3\times\check{n})\right]}\\
&\quad+\frac{(\check{N}'''\cdot\check{y})(\check{N}'''\cdot\check{z})}{\mu_0 u_2(\check{N}'''\cdot\check{x})}\,\frac{u_e''(\check{n}\cdot\check{z}_3)}{(\check{N}_e''\cdot\check{z}_3)}
\end{aligned}
\tag{C.49}
$$

As in the previous cases, when the incidence plane is perpendicular to the z-axis ($\delta = +90^\circ$) and the optic axis is perpendicular to the discontinuity surface ($\vartheta = +90^\circ$), the expressions for the reflection and transmission coefficients at a uniaxial birefringent-isotropic interface when the incident beam is extraordinary are simplified considerably (Figure 2.16, right). It is found that:

$$r_{eo} = 0 \tag{C.50}$$

$$r_{ee} = \frac{\left(\frac{n_2}{n_{1o}}\right)^2 \cos\beta'' - \sqrt{\left(\frac{n_2}{n''}\right)^2 - \sin^2\beta''}}{\left(\frac{n_2}{n_{1o}}\right)^2 \cos\beta'' + \sqrt{\left(\frac{n_2}{n''}\right)^2 - \sin^2\beta''}} \tag{2.43}$$

where angle β'' is given by equations 2.46 or C.37.

In other words, an extraordinary incident beam reflects and refracts in beams whose polarisation is parallel to the plane of incidence.

Appendix D

Matlab code for reflectivity analysis

In this appendix, two Matlab scripts written for the fused silica (section D.1) and sapphire (section D.2) substrates are reported. These were used to process all data presented in this thesis and obtain the most probable values of bond refractive index and thickness corresponding to a given data set (see subsection 2.3.2).

Both codes are divided in six parts:

- *parameters*
  The refractive indices of air (n_0), fused silica (n_1) and sapphire (n_{1o} and n_{1e}), the wavelength of the green or red laser light (λ) in nanometres, and the range of the values for the refractive index ($n_{2,min} : dn_2 : n_{2,max}$) and thickness ($d_{2,min} : dd_2 : d_{2,max}$) of the bond layer on which the script runs are set;

- *R_input.dat*
  The script imports *R_input.dat*, which contains the measured values of the angles of incidence, the bond reflectances of perpendicular and parallel polarisation and their corresponding errors in the following order: α, $\sigma(\alpha)$, $R_{\text{bond},\perp}$, $\sigma(R_{\text{bond},\perp})$, $R_{\text{bond},\parallel}$ and $\sigma(R_{\text{bond},\parallel})$;

- *R_output.dat*
  For each possible combination of n_2 and d_2, the theoretical reflectances $R_{\text{bond},\perp}$ and $R_{\text{bond},\parallel}$ (equations 2.22 and 2.23 for fused silica substrates, 2.38 and 2.39 for sapphire substrates), and their corresponding $\chi^2_\perp$ and $\chi^2_\parallel$ (equation 2.50) are calculated;

- *PDFz*
  For each combination of n_2 and d_2, the joint posterior probability density function (equation 2.49), which defines a probability surface in three dimensions, is calculated.

Probability is the volume under this surface and, consequently, the total volume under the joint posterior probability density function surface must be one as the total probability is one. The calculation of the constant of proportionality C in equation 2.49 follows from these premises:

$$\begin{aligned} \iint p(n_2,d_2|D,M,I)\,dn_2dd_2 &= C\iint \exp\Big(-(\chi_\perp^2+\chi_\parallel^2-\chi_{min}^2)/2\Big)\,dn_2dd_2 \\ 1 &= C\sum_i \Big[\exp\Big(-(\chi_\perp^2+\chi_\parallel^2-\chi_{min}^2)/2\Big)\Delta n_2\Delta d_2\Big]_i \end{aligned} \tag{D.1}$$

and so:

$$C = \left\{\sum_i \Big[\exp\Big(-(\chi_\perp^2+\chi_\parallel^2-\chi_{min}^2)/2\Big)\Delta n_2\Delta d_2\Big]_i\right\}^{-1} \tag{D.2}$$

where the i-th volume is given by the multiplication of the likelihood function (proportional to the height of the Gaussian probability distribution) and Δn_2 and Δd_2 (small and positive quantity), and the total volume is the total summation of these i-th volumes. From equation 2.49 and D.2, the joint posterior probability density function ($PDFz$ in Matlab script) is found:

$$p(n_2,d_2|D,M,I) = \frac{\exp\Big[-\frac{1}{2}(\chi_\perp^2+\chi_\parallel^2-\chi_{min}^2)\Big]}{\sum_i \Big[\exp\Big(-(\chi_\perp^2+\chi_\parallel^2-\chi_{min}^2)/2\Big)\Delta n_2\Delta d_2\Big]_i} \tag{D.3}$$

- *confidence levels*

  The script calculates and plots three contour ellipses which specify the credible regions for the two unknown parameters (n_2 and d_2). The possible values of n_2 and d_2 are plotted on the x-axis and y-axis, whereas the value of the joint posterior probability density function ($PDFz$ in Matlab script) for any pair of such values is plotted on the z-axis. The probability that n_2 and d_2 together fall in any region of their two dimensions is given by the volume under the joint posterior probability density function above that region.

  Precisely, these three contour ellipses are obtained by the intersection of three planes at constant z with the joint posterior probability density function. The method used to compute these planes is to sort the values of the volumes under the joint posterior probability density function for each pair of n_2 and d_2 in descending order and, starting with the largest value, add successively smaller ones until adding the next value would exceed or equal the value of 0.6827, 0.9545 and 0.9973, which represent the

percentage of values that lie within 1σ, 2σ and 3σ around the mean in a normal distribution, respectively. The corresponding values of the joint posterior probability density function are the values that determine the three planes at constant z.

- *Rs and Rp (th and exp) vs alpha*
  The value of the refractive index and thickness of the bond associated to the highest total normalised probability is determined and for these values the corresponding theoretical reflectances are calculated and then plotted as a function of the angles of incidence together with the measured reflectances for both polarisations.

Both codes use *contourfcmap* to create a filled contour plot with a colormap more precise than *contourf*, and *ploterr* to plot data with x and/or y error bars (available for download from http://www.mathworks.com/matlabcentral/fileexchange).

In two Matlab scripts reported in the next sections, s and p stand for perpendicular and parallel linearly polarised light.

D.1 Code for fused silica substrates

The code reported here refers to the green laser light ($\lambda = 532$ *nm* and $n_{1,\text{green}} = 1.4607$): for the red case, the wavelength has to be set to $\lambda = 635$ *nm* and the refractive index of fused silica to $n_{1,\text{red}} = 1.4570$ [82]. For details, see subsection 2.2.1.

```
clear all
clc
close all

addpath(genpath('contourfcmap'));   % https://uk.mathworks.↙
com/matlabcentral/fileexchange/29638-contourfcmap--filled-contour-plot-with-precise-↙
colormap?s_tid=srchtitle
addpath(genpath('ploterr'));        % http://www.mathworks.↙
com/matlabcentral/fileexchange/22216-ploterr



%%%%%%%%%%%%%%%%%%%%%%%%%%%%%%%%%%%%%%%%%%%%%%%%%%%%%%%%%%%%%%%%%%%%%%%%%%%%%%%
%%% parameters %%%%%%%%%%%%%%%%%%%%%%%%%%%%%%%%%%%%%%%%%%%%%%%%%%%%%%%%%%%%%%%%
%%%%%%%%%%%%%%%%%%%%%%%%%%%%%%%%%%%%%%%%%%%%%%%%%%%%%%%%%%%%%%%%%%%%%%%%%%%%%%%
n0 = 1;      % refractive index of air
n1 = 1.4607; % refractive index of fused silica (green light)
%n1 = 1.4570; % refractive index of fused silica (red light)

lambda = 532; % wavelength of green laser light in nm
%lambda = 635; % wavelength of red   laser light in nm

n2min  = 1.3000;
n2step = 0.0001;
n2max  = 1.4800;

d2min  = 0.0;
d2step = 0.5;
d2max  = 8000.0;

n2for=((n2max-n2min)/n2step)+1;
d2for=((d2max-d2min)/d2step)+1;
n2d2for=round(n2for*d2for);



%%%%%%%%%%%%%%%%%%%%%%%%%%%%%%%%%%%%%%%%%%%%%%%%%%%%%%%%%%%%%%%%%%%%%%%%%%%%%%%
%%% R_input.dat %%%%%%%%%%%%%%%%%%%%%%%%%%%%%%%%%%%%%%%%%%%%%%%%%%%%%%%%%%%%%%%
%%%%%%%%%%%%%%%%%%%%%%%%%%%%%%%%%%%%%%%%%%%%%%%%%%%%%%%%%%%%%%%%%%%%%%%%%%%%%%%
A = importdata('R_input.dat');

alpha_d=A(:,1);           % alpha in degree
alpha_r=A(:,1).*(pi/180); % alpha in radians
alphaerr_d=A(:,2);        % sigma(alpha) in degree
Rsmag=A(:,3);             % Rs
Rserr=A(:,4);             % sigma(Rs)
Rpmag=A(:,5);             % Rp
Rperr=A(:,6);             % sigma(Rp)

m=length(alpha_r);



%%%%%%%%%%%%%%%%%%%%%%%%%%%%%%%%%%%%%%%%%%%%%%%%%%%%%%%%%%%%%%%%%%%%%%%%%%%%%%%
%%% R_output.dat %%%%%%%%%%%%%%%%%%%%%%%%%%%%%%%%%%%%%%%%%%%%%%%%%%%%%%%%%%%%%%
%%%%%%%%%%%%%%%%%%%%%%%%%%%%%%%%%%%%%%%%%%%%%%%%%%%%%%%%%%%%%%%%%%%%%%%%%%%%%%%
j=1;
vect1=zeros(n2d2for,4);
```

```
for n2=n2min:n2step:n2max;

    for d2=d2min:d2step:d2max;


        %%% theoretical Rs and Rp %%%
        for ind=1:m;

            beta(ind)=asin((n0/n1)*(sin(alpha_r(ind))));
            gamma(ind)=asin((n0/n2)*(sin(alpha_r(ind))));
            delta2(ind)=(2*pi/lambda)*n2*d2*cos(gamma(ind));

            rs01(ind)=[(cos(alpha_r(ind)))-(sqrt(((n1/n0)^2)-((sin(alpha_r(ind)))↙
^2)))]/[(cos(alpha_r(ind)))+(sqrt(((n1/n0)^2)-((sin(alpha_r(ind)))^2)))];
            rs12(ind)=[(cos(beta(ind)))-(sqrt(((n2/n1)^2)-((sin(beta(ind)))^2)))]/↙
[(cos(beta(ind)))+(sqrt(((n2/n1)^2)-((sin(beta(ind)))^2)))];

            rp01(ind)=[(((n1/n0)^2)*cos(alpha_r(ind)))-(sqrt(((n1/n0)^2)-((sin(alpha_r↙
(ind)))^2)))]/[(((n1/n0)^2)*cos(alpha_r(ind)))+(sqrt(((n1/n0)^2)-((sin(alpha_r(ind)))↙
^2)))];
            rp12(ind)=[(((n2/n1)^2)*cos(beta(ind)))-(sqrt(((n2/n1)^2)-((sin(beta↙
(ind)))^2)))]/[(((n2/n1)^2)*cos(beta(ind)))+(sqrt(((n2/n1)^2)-((sin(beta(ind)))^2)))];

            Rsmagth(ind)=[2*((1-((rs01(ind))^2))^2)*((rs12(ind))^2)*(1-cos(2*(delta2↙
(ind))))]/[1-(2*((rs12(ind))^2)*(cos(2*(delta2(ind)))))+((rs12(ind))^4)];
            Rpmagth(ind)=[2*((1-((rp01(ind))^2))^2)*((rp12(ind))^2)*(1-cos(2*(delta2↙
(ind))))]/[1-(2*((rp12(ind))^2)*(cos(2*(delta2(ind)))))+((rp12(ind))^4)];

        end


        %%% X2 %%%
        chi2mins=2000;
        chitots=0;
        for ind=1:m;
            chi2s=(abs((Rsmag(ind)-Rsmagth(ind)))^2)/((Rserr(ind))^2);
            chitots=chitots+chi2s;
        end
        if  chitots < chi2mins
            chi2mins=chitots;
        end

        chi2minp=2000;
        chitotp=0;
        for ind=1:m;
            chi2p=(abs((Rpmag(ind)-Rpmagth(ind)))^2)/((Rperr(ind))^2);
            chitotp=chitotp+chi2p;
        end
        if  chitotp < chi2minp
            chi2minp=chitotp;
        end


        %%% output file %%%
        vect1(j,:)=[n2 , d2 , chi2mins , chi2minp];
        j=j+1;


    end
```

```
end

save('R_output.mat','vect1')



%%%%%%%%%%%%%%%%%%%%%%%%%%%%%%%%%%%%%%%%%%%%%%%%%%%%%%%%%%%%%%%%%%%%%%%%%%%%%%%
%%% PDFz %%%%%%%%%%%%%%%%%%%%%%%%%%%%%%%%%%%%%%%%%%%%%%%%%%%%%%%%%%%%%%%%%%%%%
%%%%%%%%%%%%%%%%%%%%%%%%%%%%%%%%%%%%%%%%%%%%%%%%%%%%%%%%%%%%%%%%%%%%%%%%%%%%%%%
addition=vect1(:,3)+vect1(:,4);
minimum=min(addition);
addminusmin=addition-minimum;
PDF=exp(-addminusmin/2);

PDFvolume=n2step*d2step*PDF;
sumPDFvolume=sum(PDFvolume);

PDFz=PDF/sumPDFvolume;                % probability density function (PDF)

PDFzCheck=n2step*d2step*PDFz;
sumPDFzCheck=sum(PDFzCheck);          % the probability must be 1

vect2=[vect1(:,1), vect1(:,2), PDFz]; % [n2;d2;PDFz]



%%%%%%%%%%%%%%%%%%%%%%%%%%%%%%%%%%%%%%%%%%%%%%%%%%%%%%%%%%%%%%%%%%%%%%%%%%%%%%%
%%% confidence levels %%%%%%%%%%%%%%%%%%%%%%%%%%%%%%%%%%%%%%%%%%%%%%%%%%%%%%%%%
%%%%%%%%%%%%%%%%%%%%%%%%%%%%%%%%%%%%%%%%%%%%%%%%%%%%%%%%%%%%%%%%%%%%%%%%%%%%%%%
n2=n2min:n2step:n2max;
d2=d2min:d2step:d2max;
n_col=length(n2);
d_row=length(d2);

X = reshape(vect2(:,1),d_row,n_col);
Y = reshape(vect2(:,2),d_row,n_col);
Z = reshape(vect2(:,3),d_row,n_col);

sortPDFz = sort(PDFz,'descend');
totPDFz(1) = n2step*d2step*sortPDFz(1);
for x = 2:length(sortPDFz)
    totPDFz(x) = totPDFz(x-1) + n2step*d2step*sortPDFz(x);
end

% contour containing 68.27% of probability content
for xx3 = 1:length(sortPDFz)
    if totPDFz(xx3) >= 0.6827;
       value3 = sortPDFz(xx3);
       break
    else
    end
end

% contour containing 95.45% of probability content
for xx2 = 1:length(sortPDFz)
    if totPDFz(xx2) >= 0.9545;
       value2 = sortPDFz(xx2);
       break
    else
    end
```

```
end

% contour containing 99.73% of probability content
for xx1 = 1:length(sortPDFz)
    if totPDFz(xx1) >= 0.9973;
       value1 = sortPDFz(xx1);
       break
    else
    end
end

value4= max(sortPDFz);
cont=[value1 value2 value3 value4];

figure
map=[0 0 1 ; 0 1 0 ; 1 0 0];
tick=[0.15 ; 0.50 ; 0.85];
labels = {'99.73%','95.45%','68.27%',''};
hh=contourfcmap(X,Y,Z,cont,↙
map,'cbarloc','eastoutside','method','calccontour','evencb', true);
set(hh.cbax,'YTick',tick,'YTickLabel',labels,'fontsize',20,'FontName','Times');
set(gca,'fontsize',20,'FontName','Times');
xlabel('Bond refractive index n_2','fontsize',20,'FontName','Times')
ylabel('Bond thickness d_2 [nm]','fontsize',20,'FontName','Times')
grid on
savefig('d2_vs_n2.fig')



%%%%%%%%%%%%%%%%%%%%%%%%%%%%%%%%%%%%%%%%%%%%%%%%%%%%%%%%%%%%%%%%%%%%%%%%%%%%%%%
%%% Rs and Rp (th and exp) vs alpha %%%%%%%%%%%%%%%%%%%%%%%%%%%%%%%%%%%%%%%%%%%
%%%%%%%%%%%%%%%%%%%%%%%%%%%%%%%%%%%%%%%%%%%%%%%%%%%%%%%%%%%%%%%%%%%%%%%%%%%%%%%

%%% n2 and d2 associated to the highest value of probability %%%
Zmax=max(max(Z));           % find the highest value of probability
[row,column]=find(Z==Zmax);
n2_mostprob=X(row,column);  % n2 associated to the highest value of probability
d2_mostprob=Y(row,column);  % d2 associated to the highest value of probability


%%% theoretical Rs and Rp with n2_mostprob and d2_mostprob %%%
alpha_d090=[0:1:90];
alpha_r090=alpha_d090.*(pi/180);
m090=length(alpha_r090);
for ind=1:m090;

beta_r090(ind)=asin((n0/n1)*(sin(alpha_r090(ind))));
gamma_mostprob(ind)=asin((n0/n2_mostprob)*(sin(alpha_r090(ind))));
delta2_mostprob(ind)=(2*pi/lambda)*n2_mostprob*d2_mostprob*cos(gamma_mostprob(ind));

rs01_mostprob(ind)=[(cos(alpha_r090(ind)))-(sqrt(((n1/n0)^2)-((sin(alpha_r090(ind)))↙
^2)))]/[(cos(alpha_r090(ind)))+(sqrt(((n1/n0)^2)-((sin(alpha_r090(ind)))^2)))];
rs12_mostprob(ind)=[(cos(beta_r090(ind)))-(sqrt(((n2_mostprob/n1)^2)-((sin(beta_r090↙
(ind)))^2)))]/[(cos(beta_r090(ind)))+(sqrt(((n2_mostprob/n1)^2)-((sin(beta_r090(ind)))↙
^2)))];

rp01_mostprob(ind)=[(((n1/n0)^2)*cos(alpha_r090(ind)))-(sqrt(((n1/n0)^2)-((sin↙
(alpha_r090(ind)))^2)))]/[(((n1/n0)^2)*cos(alpha_r090(ind)))+(sqrt(((n1/n0)^2)-((sin↙
(alpha_r090(ind)))^2)))];
rp12_mostprob(ind)=[(((n2_mostprob/n1)^2)*cos(beta_r090(ind)))-(sqrt(((n2_mostprob/n1)↙
```

```
^2)-((sin(beta_r090(ind)))^2)))]/[(((n2_mostprob/n1)^2)*cos(beta_r090(ind)))+(sqrt↙
(((n2_mostprob/n1)^2)-((sin(beta_r090(ind)))^2)))];

Rsmagth_mostprob(ind)=[2*((1-((rs01_mostprob(ind))^2))^2)*((rs12_mostprob(ind))^2)*(1-↙
cos(2*(delta2_mostprob(ind))))]/[1-(2*((rs12_mostprob(ind))^2)*(cos(2*(delta2_mostprob↙
(ind)))))+((rs12_mostprob(ind))^4)];
Rpmagth_mostprob(ind)=[2*((1-((rp01_mostprob(ind))^2))^2)*((rp12_mostprob(ind))^2)*(1-↙
cos(2*(delta2_mostprob(ind))))]/[1-(2*((rp12_mostprob(ind))^2)*(cos(2*(delta2_mostprob↙
(ind)))))+((rp12_mostprob(ind))^4)];

end


%%% plots %%%
figure

% plot of theoretical and experimental Rs vs alpha
  subplot(1,2,1)
  aa= plot(alpha_d090,Rsmagth_mostprob,'c','LineWidth',2);            % theoretical Rs
  hold on

  bb= ploterr(alpha_d,Rsmag,alphaerr_d,Rserr,'x');                    % experimental↙
Rs plus error
  set(bb(1),'MarkerEdgeColor',[0,0,1],'LineWidth',2,'markersize',15);
  set(bb(2),'Color',[0,0,1],'LineWidth',2);
  set(bb(3),'Color',[0,0,1],'LineWidth',2);

  set(gca,'fontsize',20,'FontName','Times');
  set(gca,'XLim',[0 90]);
  set(gca,'XTick',(0:10:90));
  set(gca,'YLim',[0 inf]);
  xlabel('Angle of incidence \alpha [°]','fontsize',20,'FontName','Times');
  ylabel('Reflectance R_{\perp}','fontsize',20,'FontName','Times');
  legendone= legend([aa bb(1)],'R_{\perp} th','R_{\perp} exp','Location','best');
  set(legendone,'FontSize',20);
  grid on

% plot of theoretical and experimental Rp vs alpha
  subplot(1,2,2)
  dd= plot(alpha_d090,Rpmagth_mostprob,'m','LineWidth',2);            % theoretical Rp
  hold on

  ee= ploterr(alpha_d,Rpmag,alphaerr_d,Rperr,'x');                    % experimental↙
Rp plus error
  set(ee(1),'MarkerEdgeColor',[1,0,0],'LineWidth',2,'markersize',15);
  set(ee(2),'Color',[1,0,0],'LineWidth',2);
  set(ee(3),'Color',[1,0,0],'LineWidth',2);

  set(gca,'fontsize',20,'FontName','Times');
  set(gca,'XLim',[0 90]);
  set(gca,'XTick',(0:10:90));
  set(gca,'YLim',[0 inf]);
  xlabel('Angle of incidence \alpha [°]','fontsize',20,'FontName','Times');
  ylabel('Reflectance R_{||}','fontsize',20,'FontName','Times');
  legendtwo= legend([dd ee(1)],'R_{||} th','R_{||} exp','Location','best');
  set(legendtwo,'FontSize',20);
  grid on

  str = ['n_2= ',num2str(n2_mostprob),' ; d_2= ',num2str(d2_mostprob),' nm'];
  annotation('textbox','LineWidth',1,'BackgroundColor','white','String',↙
```

```
str,'fontsize',↙
20,'FontName','Times','FitBoxToText','on','HorizontalAlignment','center','VerticalAlig↙
nment','middle');
  savefig('R_vs_alpha.fig')
```

D.2 Code for sapphire substrates

The code reported here refers to the green laser light. In this case, the wavelength of the laser light and the ordinary and extraordinary refractive indices of sapphire are $\lambda = 532$ *nm*, $n_{1o,green} = 1.7717$ and $n_{1e,green} = 1.7636$, respectively. For the red case, the corresponding values are $\lambda = 635$ *nm*, $n_{1o,red} = 1.7658$ and $n_{1e,red} = 1.7578$, respectively [90, 91]. For details, see subsection 2.2.2.

```
clear all
clc
close all

addpath(genpath('contourfcmap'));   % https://uk.mathworks.↙
com/matlabcentral/fileexchange/29638-contourfcmap--filled-contour-plot-with-precise-↙
colormap?s_tid=srchtitle
addpath(genpath('ploterr'));        % http://www.mathworks.↙
com/matlabcentral/fileexchange/22216-ploterr



%%%%%%%%%%%%%%%%%%%%%%%%%%%%%%%%%%%%%%%%%%%%%%%%%%%%%%%%%%%%%%%%%%%%%%%%%%%%%%%
%%% parameters %%%%%%%%%%%%%%%%%%%%%%%%%%%%%%%%%%%%%%%%%%%%%%%%%%%%%%%%%%%%%%%%
%%%%%%%%%%%%%%%%%%%%%%%%%%%%%%%%%%%%%%%%%%%%%%%%%%%%%%%%%%%%%%%%%%%%%%%%%%%%%%%
n0=1;          % refractive index of air
n1o=1.7717;    % ordinary      refractive index of sapphire (green light)
n1e=1.7636;    % extraordinary refractive index of sapphire (green light)
% n1o=1.7658;    % ordinary      refractive index of sapphire (red light)
% n1e=1.7578;    % extraordinary refractive index of sapphire (red light)


lambda = 532; % wavelength of green laser light in nm
%lambda = 635; % wavelength of red   laser light in nm

n2min  = 1.3000;
n2step = 0.0001;
n2max  = 1.7800;

d2min  = 0.0;
d2step = 0.5;
d2max  = 8000.0;

n2for=((n2max-n2min)/n2step)+1;
d2for=((d2max-d2min)/d2step)+1;
n2d2for=round(n2for*d2for);



%%%%%%%%%%%%%%%%%%%%%%%%%%%%%%%%%%%%%%%%%%%%%%%%%%%%%%%%%%%%%%%%%%%%%%%%%%%%%%%
%%% R_input.dat %%%%%%%%%%%%%%%%%%%%%%%%%%%%%%%%%%%%%%%%%%%%%%%%%%%%%%%%%%%%%%%
%%%%%%%%%%%%%%%%%%%%%%%%%%%%%%%%%%%%%%%%%%%%%%%%%%%%%%%%%%%%%%%%%%%%%%%%%%%%%%%
A = importdata('R_input.dat');

alpha_d=A(:,1);           % alpha in degree
alpha_r=A(:,1).*(pi/180); % alpha in radians
alphaerr_d=A(:,2);        % sigma(alpha) in degree
Rsmag=A(:,3);             % Rs
Rserr=A(:,4);             % sigma(Rs)
Rpmag=A(:,5);             % Rp
Rperr=A(:,6);             % sigma(Rp)

m=length(alpha_r);



%%%%%%%%%%%%%%%%%%%%%%%%%%%%%%%%%%%%%%%%%%%%%%%%%%%%%%%%%%%%%%%%%%%%%%%%%%%%%%%
%%% R_output.dat %%%%%%%%%%%%%%%%%%%%%%%%%%%%%%%%%%%%%%%%%%%%%%%%%%%%%%%%%%%%%%
%%%%%%%%%%%%%%%%%%%%%%%%%%%%%%%%%%%%%%%%%%%%%%%%%%%%%%%%%%%%%%%%%%%%%%%%%%%%%%%
```

```
j=1;
vect1=zeros(n2d2for,4);

for n2=n2min:n2step:n2max;

    for d2=d2min:d2step:d2max;


        %%% theoretical Rs and Rp %%%
        for ind=1:m;

            beta_first(ind)=asin((n0/n1o)*(sin(alpha_r(ind))));
            beta_second(ind)=asin((n1e*n0*(sin(alpha_r(ind))))/sqrt(((n1o*n1e)^2)+↙
(((n1e^2)-(n1o^2))*((n0*sin(alpha_r(ind)))^2))));
            gamma(ind)=asin((n0/n2)*(sin(alpha_r(ind))));
            n_second(ind)=(n1o*n1e)/sqrt((n1o^2)+(((n1e^2)-(n1o^2))*((cos(beta_second↙
(ind)))^2)));
            delta2(ind)=(2*pi/lambda)*n2*d2*cos(gamma(ind));

            rss(ind)=[cos(alpha_r(ind))-sqrt(((n1o/n0)^2)-((sin(alpha_r(ind)))^2))]/↙
[cos(alpha_r(ind))+sqrt(((n1o/n0)^2)-((sin(alpha_r(ind)))^2))];
            roo(ind)=[cos(beta_first(ind))-sqrt(((n2/n1o)^2)-((sin(beta_first(ind)))↙
^2))]/[cos(beta_first(ind))+sqrt(((n2/n1o)^2)-((sin(beta_first(ind)))^2))];

            rpp(ind)=[((n1o*n1e)/(n0^2))*cos(alpha_r(ind))-sqrt(((n1e/n0)^2)-((sin↙
(alpha_r(ind)))^2))]/[((n1o*n1e)/(n0^2))*cos(alpha_r(ind))+sqrt(((n1e/n0)^2)-((sin↙
(alpha_r(ind)))^2))];
            ree(ind)=[((n2/n1o)^2)*cos(beta_second(ind))-sqrt(((n2/n_second(ind))^2)-↙
((sin(beta_second(ind)))^2))]/[((n2/n1o)^2)*cos(beta_second(ind))+sqrt(((n2/n_second↙
(ind))^2)-((sin(beta_second(ind)))^2))];

            Rsmagth(ind)=[2*((1-((rss(ind))^2))^2)*((roo(ind))^2)*(1-cos(2*(delta2↙
(ind))))]/[1-(2*((roo(ind))^2)*(cos(2*(delta2(ind)))))+((roo(ind))^4)];
            Rpmagth(ind)=[2*((1-((rpp(ind))^2))^2)*((ree(ind))^2)*(1-cos(2*(delta2↙
(ind))))]/[1-(2*((ree(ind))^2)*(cos(2*(delta2(ind)))))+((ree(ind))^4)];

        end


        %%% X2 %%%
        chi2mins=2000;
        chitots=0;
        for ind=1:m;
         chi2s=(abs((Rsmag(ind)-Rsmagth(ind)))^2)/((Rserr(ind))^2);
         chitots=chitots+chi2s;
        end
        if chitots < chi2mins
         chi2mins=chitots;
        end

        chi2minp=2000;
        chitotp=0;
        for ind=1:m;
         chi2p=(abs((Rpmag(ind)-Rpmagth(ind)))^2)/((Rperr(ind))^2);
         chitotp=chitotp+chi2p;
        end
        if chitotp < chi2minp
         chi2minp=chitotp;
        end
```

```
        %%% output file %%%
        vect1(j,:)=[n2 , d2 , chi2mins , chi2minp];
        j=j+1;


    end

end

save('R_output.mat','vect1')



%%%%%%%%%%%%%%%%%%%%%%%%%%%%%%%%%%%%%%%%%%%%%%%%%%%%%%%%%%%%%%%%%%%%%%%%%%%%%%%
%%% PDFz %%%%%%%%%%%%%%%%%%%%%%%%%%%%%%%%%%%%%%%%%%%%%%%%%%%%%%%%%%%%%%%%%%%%%
%%%%%%%%%%%%%%%%%%%%%%%%%%%%%%%%%%%%%%%%%%%%%%%%%%%%%%%%%%%%%%%%%%%%%%%%%%%%%%%
addition=vect1(:,3)+vect1(:,4);
minimum=min(addition);
addminusmin=addition-minimum;
PDF=exp(-addminusmin/2);

PDFvolume=n2step*d2step*PDF;
sumPDFvolume=sum(PDFvolume);

PDFz=PDF/sumPDFvolume;                % probability density function (PDF)

PDFzCheck=n2step*d2step*PDFz;
sumPDFzCheck=sum(PDFzCheck);          % the probability must be 1

vect2=[vect1(:,1), vect1(:,2), PDFz]; % [n2;d2;PDFz]



%%%%%%%%%%%%%%%%%%%%%%%%%%%%%%%%%%%%%%%%%%%%%%%%%%%%%%%%%%%%%%%%%%%%%%%%%%%%%%%
%%% confidence levels %%%%%%%%%%%%%%%%%%%%%%%%%%%%%%%%%%%%%%%%%%%%%%%%%%%%%%%%%
%%%%%%%%%%%%%%%%%%%%%%%%%%%%%%%%%%%%%%%%%%%%%%%%%%%%%%%%%%%%%%%%%%%%%%%%%%%%%%%
n2=n2min:n2step:n2max;
d2=d2min:d2step:d2max;
n_col=length(n2);
d_row=length(d2);

X = reshape(vect2(:,1),d_row,n_col);
Y = reshape(vect2(:,2),d_row,n_col);
Z = reshape(vect2(:,3),d_row,n_col);

sortPDFz = sort(PDFz,'descend');
totPDFz(1) = n2step*d2step*sortPDFz(1);
for x = 2:length(sortPDFz)
    totPDFz(x) = totPDFz(x-1) + n2step*d2step*sortPDFz(x);
end

% contour containing 68.27% of probability content
for xx3 = 1:length(sortPDFz)
    if totPDFz(xx3) >= 0.6827;
       value3 = sortPDFz(xx3);
       break
    else
    end
end
```

```
% contour containing 95.45% of probability content
for xx2 = 1:length(sortPDFz)
    if totPDFz(xx2) >= 0.9545;
       value2 = sortPDFz(xx2);
       break
    else
    end
end

% contour containing 99.73% of probability content
for xx1 = 1:length(sortPDFz)
    if totPDFz(xx1) >= 0.9973;
       value1 = sortPDFz(xx1);
       break
    else
    end
end

value4= max(sortPDFz);
cont=[value1 value2 value3 value4];

figure
map=[0 0 1 ; 0 1 0 ; 1 0 0];
tick=[0.15 ; 0.50 ; 0.85];
labels = {'99.73%','95.45%','68.27%',''};
hh=contourfcmap(X,Y,Z,cont,↙
map,'cbarloc','eastoutside','method','calccontour','evencb', true);
set(hh.cbax,'YTick',tick,'YTickLabel',labels,'fontsize',20,'FontName','Times');
set(gca,'fontsize',20,'FontName','Times');
xlabel('Bond refractive index n_2','fontsize',20,'FontName','Times')
ylabel('Bond thickness d_2 [nm]','fontsize',20,'FontName','Times')
grid on
savefig('d2_vs_n2.fig')



%%%%%%%%%%%%%%%%%%%%%%%%%%%%%%%%%%%%%%%%%%%%%%%%%%%%%%%%%%%%%%%%%%%%%%%%%%%%%%%
%%% Rs and Rp (th and exp) vs alpha %%%%%%%%%%%%%%%%%%%%%%%%%%%%%%%%%%%%%%%%%%%
%%%%%%%%%%%%%%%%%%%%%%%%%%%%%%%%%%%%%%%%%%%%%%%%%%%%%%%%%%%%%%%%%%%%%%%%%%%%%%%

%%% n2 and d2 associated to the highest value of probability %%%
Zmax=max(max(Z));           % find the highest value of probability
[row,column]=find(Z==Zmax);
n2_mostprob=X(row,column);  % n2 associated to the highest value of probability
d2_mostprob=Y(row,column);  % d2 associated to the highest value of probability


%%% theoretical Rs and Rp with n2_mostprob and d2_mostprob %%%
alpha_d090=[0:1:90];
alpha_r090=alpha_d090.*(pi/180);
m090=length(alpha_r090);
for ind=1:m090;

beta_first090(ind)=asin((n0/n1o)*(sin(alpha_r090(ind))));
beta_second090(ind)=asin((n1e*n0*(sin(alpha_r090(ind))))/sqrt(((n1o*n1e)^2)+(((n1e^2)-↙
(n1o^2))*((n0*sin(alpha_r090(ind)))^2))));
gamma_mostprob(ind)=asin((n0/n2_mostprob)*(sin(alpha_r090(ind))));
n_second090(ind)=(n1o*n1e)/sqrt((n1o^2)+(((n1e^2)-(n1o^2))*((cos(beta_second090(ind)))↙
^2)));
```

```
delta2_mostprob(ind)=(2*pi/lambda)*n2_mostprob*d2_mostprob*cos(gamma_mostprob(ind));

rss_mostprob(ind)=[cos(alpha_r090(ind))-sqrt(((n1o/n0)^2)-((sin(alpha_r090(ind)))^2))]↙
/[cos(alpha_r090(ind))+sqrt(((n1o/n0)^2)-((sin(alpha_r090(ind)))^2))];
roo_mostprob(ind)=[cos(beta_first090(ind))-sqrt(((n2_mostprob/n1o)^2)-((sin↙
(beta_first090(ind)))^2))]/[cos(beta_first090(ind))+sqrt(((n2_mostprob/n1o)^2)-((sin↙
(beta_first090(ind)))^2))];

rpp_mostprob(ind)=[((n1o*n1e)/(n0^2))*cos(alpha_r090(ind))-sqrt(((n1e/n0)^2)-((sin↙
(alpha_r090(ind)))^2))]/[((n1o*n1e)/(n0^2))*cos(alpha_r090(ind))+sqrt(((n1e/n0)^2)-↙
((sin(alpha_r090(ind)))^2))];
ree_mostprob(ind)=[((n2_mostprob/n1o)^2)*cos(beta_second090(ind))-sqrt↙
(((n2_mostprob/n_second090(ind))^2)-((sin(beta_second090(ind)))^2))]/↙
[((n2_mostprob/n1o)^2)*cos(beta_second090(ind))+sqrt(((n2_mostprob/n_second090(ind))↙
^2)-((sin(beta_second090(ind)))^2))];

Rsmagth_mostprob(ind)=[2*((1-((rss_mostprob(ind))^2))^2)*((roo_mostprob(ind))^2)*(1-↙
cos(2*(delta2_mostprob(ind))))]/[1-(2*((roo_mostprob(ind))^2)*(cos(2*(delta2_mostprob↙
(ind))))+((roo_mostprob(ind))^4)];
Rpmagth_mostprob(ind)=[2*((1-((rpp_mostprob(ind))^2))^2)*((ree_mostprob(ind))^2)*(1-↙
cos(2*(delta2_mostprob(ind))))]/[1-(2*((ree_mostprob(ind))^2)*(cos(2*(delta2_mostprob↙
(ind))))+((ree_mostprob(ind))^4)];

end


%%% plots %%%
figure

% plot of theoretical and experimental Rs vs alpha
  subplot(1,2,1)
  aa= plot(alpha_d090,Rsmagth_mostprob,'c','LineWidth',2);            % theoretical Rs
  hold on

  bb= ploterr(alpha_d,Rsmag,alphaerr_d,Rserr,'x');                    % experimental↙
Rs plus error
  set(bb(1),'MarkerEdgeColor',[0,0,1],'LineWidth',2,'markersize',15);
  set(bb(2),'Color',[0,0,1],'LineWidth',2);
  set(bb(3),'Color',[0,0,1],'LineWidth',2);

  set(gca,'fontsize',20,'FontName','Times');
  set(gca,'XLim',[0 90]);
  set(gca,'XTick',(0:10:90));
  set(gca,'YLim',[0 inf]);
  xlabel('Angle of incidence \alpha [°]','fontsize',20,'FontName','Times');
  ylabel('Reflectance R_{\perp}','fontsize',20,'FontName','Times');
  legendone= legend([aa bb(1)],'R_{\perp} th','R_{\perp} exp','Location','best');
  set(legendone,'FontSize',20);
  grid on

% plot of theoretical and experimental Rp vs alpha
  subplot(1,2,2)
  dd= plot(alpha_d090,Rpmagth_mostprob,'m','LineWidth',2);            % theoretical Rp
  hold on

  ee= ploterr(alpha_d,Rpmag,alphaerr_d,Rperr,'x');                    % experimental↙
Rp plus error
  set(ee(1),'MarkerEdgeColor',[1,0,0],'LineWidth',2,'markersize',15);
  set(ee(2),'Color',[1,0,0],'LineWidth',2);
  set(ee(3),'Color',[1,0,0],'LineWidth',2);
```

```
  set(gca,'fontsize',20,'FontName','Times');
  set(gca,'XLim',[0 90]);
  set(gca,'XTick',(0:10:90));
  set(gca,'YLim',[0 inf]);
  xlabel('Angle of incidence \alpha [°]','fontsize',20,'FontName','Times');
  ylabel('Reflectance R_{||}','fontsize',20,'FontName','Times');
  legendtwo= legend([dd ee(1)],'R_{||} th','R_{||} exp','Location','best');
  set(legendtwo,'FontSize',20);
  grid on

  str = ['n_2= ',num2str(n2_mostprob),' ; d_2= ',num2str(d2_mostprob),' nm'];
  annotation('textbox','LineWidth',1,'BackgroundColor','white','String',↙
str,'fontsize',↙
20,'FontName','Times','FitBoxToText','on','HorizontalAlignment','center','VerticalAlig↙
nment','middle');
  savefig('R_vs_alpha.fig')
```

Appendix E

Matlab code for flatness maps

A Matlab script was written for determining the total flatness map of a bonded sample. The surface maps can provide additional insight into what parameters determine the value of the thickness of a bond together with the results obtained from the Bayesian analysis and scanning electron microscopy. An example of this code is reported in section E.1 and is referred to sample $\text{Silica2}_{\text{Na2SiO3(1:3)}}$.

In the first part, this code uses some Matlab files of the Simtools package (available for download from http://www.gwoptics.org/simtools/, SimTools version 0.7). This package was written for optical simulations and used in gravitational wave field.

The code can be divided in seven parts, which are described below:

- The function *FT_read_zygo_map(filename, filetype)* of the Simtools package reads a surface map obtained using a ZYGO® GPI XP/D laser interferometer. It reads in two different file formats, either .xyz (filetype = 1) or .asc (filetype = 2), and returns a map in the standard structure, rescaling the surface height data into nanometres.

- Each disc had a mark on its edge made using a diamond point lab pen. This mark was used as reference point for the flatness measurements and bonding. All maps obtained using ZYGO® were carried out positioning these marks in the same way and taking note of their position with respect to the sample. During bonding, the two discs were bonded so that the two marks were aligned with each other. However, sometimes a disc floated on bonding solution rotating its mark with respect to the mark of the other disc. To take into consideration this angular displacement, some maps have to be rotated around its centre point (function *imrotate(map,angle)*).

- The functions of the Simtools package handle the maps obtained using ZYGO®, zooming in on a valid area of the map and removing various offsets.

Function *FT_recenter_mirror_map(map)* centres the surface map as read by function *FT_read_zygo_map(filename, filetype)* by computing the centre of gravity.
Function *FT_remove_elements_outside_map(map)* finds the NaN (Not-a-Number) element closest to the centre of map and removes all the points outside this radial position. Also, it zooms in on the valid map data.
Function *FT_calibrate_map_diameter(map, diameter)* changes the x-step and y-step scaling factors in the map to correspond with a surface with a given diameter expressed in *m*.
Function *FT_remove_offset_from_mirror_map(map,r)* measures the average value of the surface heights of a map over an area of radius *r* and removes this offset from the data of map.
Function *FT_remove_piston_from_mirror_map(map,0,0)* fits a tilted plane to a surface map and removes it.
After having made the size of the two maps equal to each other, the surface maps of two discs to be bonded are plotted using function *FT_plot_mirror_map(map,r)*.

- During bonding, a disc of map(1) is placed on the top of the other disc of map(2). If the map(2) is taken as reference, then the map(1) has to be flipped and its values has to change sign so that overlapping of the two maps reflects the interface between the two bonded discs (function *fliplr(map)*).

- Subtracting map(2) from map(1) allows the determination of the greatest negative value of their difference. This value is then added to map(1). This condition defines not only the first point of contact of the two maps but also that no point of map(1) is inside map(2).

- Since the two maps are not perfectly flat, it is probable that the disc placed on the top is subject to a tilt. Therefore, the map(1) has to be tilted by two angles of rotation which are determined by the condition that the two maps have three points of contact and that the centre of the sample is inside the triangle formed by these three points.
  Once three points of contact are determined manually, the equations of the two planes passing through these three points and tangent to the two maps are calculated using Wolfram Mathematica software. Fixing the origin and axes of rotation, the angles of rotation are calculated by the condition of overlapping the two planes.
  The rotation of map(1) is carried out using the function *rotate_output*. This is based on the original function of Matlab *rotate*, which was modify so that the function could return its outputs.

- Subtracting the unmodified map of the disc taken as reference from the modified map of the disc placed on the top gives the total flatness map of the interface between the two bonded discs.

E.1 Code for determining the total flatness map

The code reported here refers to sample $\text{Silica2}_{\text{Na2SiO3(1:3)}}$. For details about this sample, see Table 2.4 in Chapter 2.

```
clear all
clc
close all

addpath(genpath('Simtools07'));

D=0.05;   % real diameter of the sample in m



%%%%%%%%%%%%%%%%%%%%%%%%%%%%%%%%%%%%%%%%%%%%%%%%%%%%%%%%%%%%%%%%%%%%%%%%%%%%
%%% Read a surface map in Zygo format %%%%%%%%%%%%%%%%%%%%%%%%%%%%%%%%%%%%%%
%%%%%%%%%%%%%%%%%%%%%%%%%%%%%%%%%%%%%%%%%%%%%%%%%%%%%%%%%%%%%%%%%%%%%%%%%%%%
% The function reads in two different file formats,
% either .xyz (1) or .asc (2).

filename1='3_down_a.asc';
filename2='4_down_b.asc';
filetype=2;

orig_map(1)=FT_read_zygo_map(filename1, filetype);
orig_map(2)=FT_read_zygo_map(filename2, filetype);



%%%%%%%%%%%%%%%%%%%%%%%%%%%%%%%%%%%%%%%%%%%%%%%%%%%%%%%%%%%%%%%%%%%%%%%%%%%%
%%% Rotate image around its center point %%%%%%%%%%%%%%%%%%%%%%%%%%%%%%%%%%%%
%%%%%%%%%%%%%%%%%%%%%%%%%%%%%%%%%%%%%%%%%%%%%%%%%%%%%%%%%%%%%%%%%%%%%%%%%%%%

angle=0;  % angle expressed in degrees

orig_map(2).data=imrotate(orig_map(2).data,angle);
orig_map(2).nan=imrotate(orig_map(2).nan,angle);
orig_map(2).notnan=imrotate(orig_map(2).notnan,angle);



%%%%%%%%%%%%%%%%%%%%%%%%%%%%%%%%%%%%%%%%%%%%%%%%%%%%%%%%%%%%%%%%%%%%%%%%%%%%
%%% Preparing surface maps by Simtools package  %%%%%%%%%%%%%%%%%%%%%%%%%%%%
%%%%%%%%%%%%%%%%%%%%%%%%%%%%%%%%%%%%%%%%%%%%%%%%%%%%%%%%%%%%%%%%%%%%%%%%%%%%

for ii=1:2;

    map=orig_map(ii);

    % Recenter a map by computing the center of gravity.
    map=FT_recenter_mirror_map(map);

    % Remove outer ring of NaN data from a map.
    map=FT_remove_elements_outside_map(map);

    % Calibrate the delta x and y values of a map.
    map=FT_calibrate_map_diameter(map,D);

    % Remove an offset from a map.
    map=FT_remove_offset_from_mirror_map(map,D/2);

    % Fit a tilted plane to a map and removes it.
    fin_map(ii)=FT_remove_piston_from_mirror_map(map,0,0);
```

```
end


[sx1,sy1]=size(fin_map(1).data);
[sx2,sy2]=size(fin_map(2).data);
    if sx1<sx2
       fin_map(2).data=fin_map(2).data(1:sx1,:);
       fin_map(2).notnan=fin_map(2).notnan(1:sx1,:);
    else
        fin_map(1).data=fin_map(1).data(1:sx2,:);
        fin_map(1).notnan=fin_map(1).notnan(1:sx2,:);
    end

    if sy1<sy2
       fin_map(2).data=fin_map(2).data(:,1:sy1);
       fin_map(2).notnan=fin_map(2).notnan(:,1:sy1);
    else
        fin_map(1).data=fin_map(1).data(:,1:sy2);
        fin_map(1).notnan=fin_map(1).notnan(:,1:sy2);
    end


% Plot a surface map.
fin_map(1).name='Flatness of surface_3';
fin_map(2).name='Flatness of surface_4';
FT_plot_mirror_map(fin_map(1),D/2)
FT_plot_mirror_map(fin_map(2),D/2)


%%%%%%%%%%%%%%%%%%%%%%%%%%%%%%%%%%%%%%%%%%%%%%%%%%%%%%%%%%%%%%%%%%%%%%%%%%%%%%%
%%% Flip matrix in left/right direction  %%%%%%%%%%%%%%%%%%%%%%%%%%%%%%%%%%%%%
%%%%%%%%%%%%%%%%%%%%%%%%%%%%%%%%%%%%%%%%%%%%%%%%%%%%%%%%%%%%%%%%%%%%%%%%%%%%%%%

fin_map(1).data=-1*fliplr(fin_map(1).data);

fin_map(1).name='Flatness of surface_3spec&neg';
FT_plot_mirror_map(fin_map(1),D/2)


%%%%%%%%%%%%%%%%%%%%%%%%%%%%%%%%%%%%%%%%%%%%%%%%%%%%%%%%%%%%%%%%%%%%%%%%%%%%%%%
%%% Step A  %%%%%%%%%%%%%%%%%%%%%%%%%%%%%%%%%%%%%%%%%%%%%%%%%%%%%%%%%%%%%%%%%
%%%%%%%%%%%%%%%%%%%%%%%%%%%%%%%%%%%%%%%%%%%%%%%%%%%%%%%%%%%%%%%%%%%%%%%%%%%%%%%
% Sum the greatest negative value of the difference
% between map(1) and map(2) to map(1).
fin_map(1).data=(fin_map(1).data)+70.7053;


%%%%%%%%%%%%%%%%%%%%%%%%%%%%%%%%%%%%%%%%%%%%%%%%%%%%%%%%%%%%%%%%%%%%%%%%%%%%%%%
%%% Step B  %%%%%%%%%%%%%%%%%%%%%%%%%%%%%%%%%%%%%%%%%%%%%%%%%%%%%%%%%%%%%%%%%
%%%%%%%%%%%%%%%%%%%%%%%%%%%%%%%%%%%%%%%%%%%%%%%%%%%%%%%%%%%%%%%%%%%%%%%%%%%%%%%
% Rotation of map(1)

figure
map=surf(fin_map(1).data);
```

```
RotationAngle = [0.96200107 -0.096];
RotationAxis = {[890.75 1247.05 0],[0.81 -0.58 0]};
RotationOrigin = [14 202 23.5618];
for iRot = 1:2
[newx,newy,newz]=rotate_output(map,RotationAxis{iRot},RotationAngle(iRot),↙
RotationOrigin);
end
xlabel('x'); ylabel('y'); zlabel('z');
close



%%%%%%%%%%%%%%%%%%%%%%%%%%%%%%%%%%%%%%%%%%%%%%%%%%%%%%%%%%%%%%%%%%%%%%%%%%%%
%%% Total flatness map %%%%%%%%%%%%%%%%%%%%%%%%%%%%%%%%%%%%%%%%%%%%%%%%%%%%%
%%%%%%%%%%%%%%%%%%%%%%%%%%%%%%%%%%%%%%%%%%%%%%%%%%%%%%%%%%%%%%%%%%%%%%%%%%%%

fin_map(3)=fin_map(2);
fin_map(3).data=newz;

diff_right=fin_map(3).data-fin_map(2).data;
fin_map(4)=fin_map(2);
fin_map(4).data=diff_right;

fin_map(4).name='Total Flatness';
FT_plot_mirror_map(fin_map(4),D/2)
```

References

[1] V. Mangano, A. A. van Veggel, R. Douglas, J. Faller, A. Grant, J. Hough, and S. Rowan. Determination of the refractive index and thickness of a hydroxide-catalysis bond between fused silica from reflectivity measurements. *Optics Express*, 25(4):3196–3213, 2017.

[2] V. Greco, F. Marchesini, and G. Molesini. Optical contact and van der Waals interactions: the role of the surface topography in determining the bonding strength of thick glass plates. *Journal of Optics A: Pure and Applied Optics*, 3(1):85–88, 2001.

[3] D.-H. Gwo. Ultra precision and reliable bonding method. *U.S. Patent*, (US 6284085 B1):1–18, 2001.

[4] D.-H. Gwo. Hydroxide-catalyzed bonding. *U.S. Patent*, (US 6548176 B1):1–40, 2003.

[5] N. F. Kazakov. *Diffusion Bonding of Materials*. Pergamon Press, 1985.

[6] A. A. Shirzadi. *Diffusion Bonding Aluminium Alloys and Composites: New Approaches and Modelling*. PhD thesis, University of Cambridge, 1997.

[7] D. Lu and C. P. Wong. *Materials for Advanced Packaging*. Springer, 2009.

[8] R. C. Benson, N. deHaas, P. G. Goodwin, and T. E. Phillips. Epoxy Adhesives in Microelectronic Hybrid Applications. *Johns Hopkins APL Technical Digest*, 13(3):400–406, 1992.

[9] B. Ellis. *Chemistry and Technology of Epoxy Resins*. Springer Science+Business Media B.V., 1993.

[10] R. D. Adams, J. Comyn, and W. C. Wake. *Structural Adhesive Joints in Engineering*. Springer Science & Business Media, 1997.

[11] R. Knechtel. Glass frit bonding: an universal technology for wafer level encapsulation and packaging. *Microsystem Technologies*, 12(1):63–68, 2005.

[12] R. Knechtel, M. Wiemer, and J. Frömel. Wafer level encapsulation of microsystems using glass frit bonding. *Microsystem Technologies*, 12(5):468–472, 2006.

[13] P. Ramm, J. J.-Q. Lu, and M. M. V. Taklo. *Handbook of Wafer Bonding*. Wiley-VCH, 2012.

[14] D.-H. Gwo. Ultra-precision bonding for cryogenic fused-silica optics. *SPIE Proceedings*, 3435:136–142, 1998.

[15] D.-H. Gwo. Two unique aspects of Gravity Probe-B star-tracking space telescope: (1) focal-plane roof-edge diffraction and (2) fused-quartz bonding for 2.5-Kelvin applications. *SPIE Proceedings*, 3356:892–903, 1998.

[16] D.-H. Gwo, S. Wang, K. A. Bower, D. E. Davidson, P. Ehrensberger, L. Huff, E. Romero, M. T. Sullivan, K. Triebes, and J. A. Lipa. The Gravity Probe-B star-tracking telescope. *Advances in Space Research*, 32(7):1401–1405, 2003.

[17] C. W. F. Everitt, D. B. DeBra, B. W. Parkinson, J. P. Turneaure, J. W. Conklin, M. I. Heifetz, G. M. Keiser, A. S. Silbergleit, T. Holmes, J. Kolodziejczak, M. Al-Meshari, J. C. Mester, B. Muhlfelder, V. Solomonik, K. Stahl, P. Worden, W. Bencze, S. Buchman, B. Clarke, A. Al-Jadaan, H. Al-Jibreen, J. Li, J. A. Lipa, J. M. Lockhart, B. Al-Suwaidan, M. Taber, and S. Wang. Gravity Probe B: Final Results of a Space Experiment to Test General Relativity. *Physical Review Letters*, 106(22):1–5, 2011.

[18] A. V. Cumming, A. S. Bell, L. Barsotti, M. A. Barton, G. Cagnoli, D. Cook, L. Cunningham, M. Evans, G. D. Hammond, G. M. Harry, A. Heptonstall, J. Hough, R. Jones, R. Kumar, R. Mittleman, N. A. Robertson, S. Rowan, B. Shapiro, K. A. Strain, K. Tokmakov, C. Torrie, and A. A. van Veggel. Design and development of the advanced LIGO monolithic fused silica suspension. *Classical and Quantum Gravity*, 29(3):1–18, 2012.

[19] A. A. van Veggel and C. J. Killow. Hydroxide catalysis bonding for astronomical instruments. *Advanced Optical Technologies*, 3(3):293–307, 2014.

[20] B. P. Abbott et al. (LIGO Scientific Collaboration and Virgo Collaboration). Observation of Gravitational Waves from a Binary Black Hole Merger. *Physical Review Letters*, 116(6):061102–1–061102–16, 2016.

[21] B. P. Abbott et al. (LIGO Scientific Collaboration and Virgo Collaboration). GW150914: The Advanced LIGO Detectors in the Era of First Discoveries. *Physical Review Letters*, 116(13):131103–1–131103–12, 2016.

[22] G. Heinzel, C. Braxmaier, M. Caldwell, K. Danzmann, F. Draaisma, A. García, J. Hough, O. Jennrich, U. Johann, C. Killow, K. Middleton, M. te Plate, D. Robertson, A. Rüdiger, R. Schilling, F. Steier, V. Wand, and H. Ward. Successful testing of the LISA Technology Package (LTP) interferometer engineering model. *Classical and Quantum Gravity*, 22(10):S149–S154, 2005.

[23] P. McNamara, S. Vitale, and K. Danzmann (on behalf of the LISA Pathfinder Science Working Team). LISA Pathfinder. *Classical and Quantum Gravity*, 25(11):1–8, 2008.

[24] M. Armano, H. Audley, G. Auger, J. Baird, P. Binetruy, M. Born, D. Bortoluzzi, N. Brandt, A. Bursi, M. Caleno, A. Cavalleri, A. Cesarini, M. Cruise, K. Danzmann, I. Diepholz, R. Dolesi, N. Dunbar, L. Ferraioli, V. Ferroni, E. Fitzsimons, M. Freschi, J. Gallegos, C. García Marirrodriga, R. Gerndt, L. I. Gesa, F. Gibert, D. Giardini, R. Giusteri, C. Grimani, I. Harrison, G. Heinzel, M. Hewitson, D. Hollington, M. Hueller, J. Huesler, H. Inchauspé, O. Jennrich, P. Jetzer, B. Johlander, N. Karnesis, B. Kaune, N. Korsakova, C. Killow, I. Lloro, R. Maarschalkerweerd, S. Madden, D. Mance, V. Martín, F. Martin-Porqueras, I. Mateos, P. McNamara, J. Mendes, L. Mendes, A. Moroni, M. Nofrarias, S. Paczkowski, M. Perreur-Lloyd, A. Petiteau,

P. Pivato, E. Plagnol, P. Prat, U. Ragnit, J. Ramos-Castro, J. Reiche, J. A. Romera Perez, D. Robertson, H. Rozemeijer, G. Russano, P. Sarra, A. Schleicher, J. Slutsky, C. F. Sopuerta, T. Sumner, D. Texier, J. Thorpe, C. Trenkel, H. B. Tu, D. Vetrugno, S. Vitale, G. Wanner, H. Ward, S. Waschke, P. Wass, D. Wealthy, S. Wen, W. Weber, A. Wittchen, C. Zanoni, T. Ziegler, and P. Zweifel. The LISA Pathfinder Mission. *Journal of Physics: Conference Series*, 610(1):1–18, 2015.

[25] M. Armano, H. Audley, G. Auger, J. T. Baird, M. Bassan, P. Binetruy, M. Born, D. Bortoluzzi, N. Brandt, M. Caleno, L. Carbone, A. Cavalleri, A. Cesarini, G. Ciani, G. Congedo, A. M. Cruise, K. Danzmann, M. de Deus Silva, R. De Rosa, M. Diaz-Aguiló, L. Di Fiore, I. Diepholz, G. Dixon, R. Dolesi, N. Dunbar, L. Ferraioli, V. Ferroni, W. Fichter, E. D. Fitzsimons, R. Flatscher, M. Freschi, A. F. García Marín, C. García Marirrodriga, R. Gerndt, L. Gesa, F. Gibert, D. Giardini, R. Giusteri, F. Guzmán, A. Grado, C. Grimani, A. Grynagier, J. Grzymisch, I. Harrison, G. Heinzel, M. Hewitson, D. Hollington, D. Hoyland, M. Hueller, H. Inchauspé, O. Jennrich, P. Jetzer, U. Johann, B. Johlander, N. Karnesis, B. Kaune, N. Korsakova, C. J. Killow, J. A. Lobo, I. Lloro, L. Liu, J. P. López-Zaragoza, R. Maarschalkerweerd, D. Mance, V. Martín, L. Martin-Polo, J. Martino, F. Martin-Porqueras, S. Madden, I. Mateos, P.W. McNamara, J. Mendes, L. Mendes, A. Monsky, D. Nicolodi, M. Nofrarias, S. Paczkowski, M. Perreur-Lloyd, A. Petiteau, P. Pivato, E. Plagnol, P. Prat, U. Ragnit, B. Raïs, J. Ramos-Castro, J. Reiche, D. I. Robertson, H. Rozemeijer, F. Rivas, G. Russano, J. Sanjuán, P. Sarra, A. Schleicher, D. Shaul, J. Slutsky, C. F. Sopuerta, R. Stanga, F. Steier, T. Sumner, D. Texier, J. I. Thorpe, C. Trenkel, M. Tröbs, H. B. Tu, D. Vetrugno, S. Vitale, V. Wand, G. Wanner, H. Ward, C. Warren, P. J. Wass, D. Wealthy, W. J. Weber, L. Wissel, A. Wittchen, A. Zambotti, C. Zanoni, T. Ziegler, and P. Zweifel. Sub-Femto-g Free Fall for Space-Based Gravitational Wave Observatories: LISA Pathfinder Results. *Physical Review Letters*, 116(23):231101–1–231101–10, 2016.

[26] A. Rudolph, I. Harrison, F. Renk, D. Firre, F. Delhaise, C. Garcia Marirrodriga, P. McNamara, B. Johlander, M. Caleno, J. Grzymisch, F. Cordero, D. Wealthy, and J. P. Olive. LISA Pathfinder Mission Operations Concept and Launch and Early Orbit Phase - In-Orbit Experience. *SpaceOps 2016 Conference*, pages 1–16, 2016.

[27] E. J. Elliffe, J. Bogenstahl, A. Deshpande, J. Hough, C. Killow, S. Reid, D. Robertson, S. Rowan, H. Ward, and G. Cagnoli. Hydroxide-catalysis bonding for stable optical systems for space. *Classical and Quantum Gravity*, 22(10):S257–S267, 2005.

[28] S. Reid, G. Cagnoli, E. Elliffe, J. Faller, J. Hough, I. Martin, and S. Rowan. Influence of temperature and hydroxide concentration on the settling time of hydroxy-catalysis bonds. *Physics Letters A*, 363(5–6):341–345, 2007.

[29] R. B Holt, H. I. Smith, M. S. Gussenhoven, and Device Development Corporation Waltham MA. *Research on Optical Contact Bonding*. Defense Technical Information Center, 1966.

[30] G. A. C. M. Spierings, J. Haisma, and T. M. Michelsen. Surface-related phenomena in the direct bonding of silicon and fused-silica wafer pairs. *Philips Journal of Research*, 49(1–2):47–63, 1995.

[31] F. S. Ligler and J. S. Kim. *The Microflow Cytometer*. Pan Stanford, 2010.

[32] H.-J. Butt, K. Graf, and M. Kappl. *Physics and Chemistry of Interfaces*. Wiley-VCH, 2003.

[33] H.-J. Butt and M. Kappl. *Surface and Interfacial Forces*. Wiley-VCH, 2010.

[34] H. D. Young, R. A. Freedman, and A. L. Ford. *University Physics with Modern Physics*. Addison-Wesley, 2012.

[35] A. P. Goutzoulis and D. R. Pape. *Design and Fabrication of Acousto-Optic Devices*. Marcel Dekker, 1994.

[36] J. Haisma, N. Hattu, J. T. C. M. (D.) Pulles, E. Steding, and J. C. G. Vervest. Direct bonding and beyond. *Applied Optics*, 46(27):6793–6803, 2007.

[37] J. Haisma and G. A. C. M. Spierings. Contact bonding, including direct-bonding in a historical and recent context of materials science and technology, physics and chemistry: Historical view in a broader scope and comparative outlook. *Materials Science and Engineering: R: Reports*, 37(1–2):1–60, 2002.

[38] O. M. Akselsen. Diffusion bonding of ceramics. *Journal of Materials Science*, 27(3):569–579, 1992.

[39] A. A. Shirzadi, H. Assadi, and E. R. Wallach. Interface evolution and bond strength when diffusion bonding materials with stable oxide films. *Surface and Interface Analysis*, 31(7):609–618, 2001.

[40] S. Jahn, S. Sändig, S. Dahms, and F. Gemse. Diffusion bonding systems. *Materialwissenschaft und Werkstofftechnik*, 45(9):807–814, 2014.

[41] D. R. Askeland, P. P. Fulay, and W. J. Wright. *The Science and Engineering of Materials*. Cengage Learning, 2010.

[42] B. Bhushan. *Springer Handbook of Nanotechnology*. Springer-Verlag Berlin Heidelberg, 2010.

[43] D. A. Dillard. *Advances in structural adhesive bonding*. Woodhead Publishing Limited, 2010.

[44] L. Tam and D. Lau. Moisture effect on the mechanical and interfacial properties of epoxy-bonded material system: An atomistic and experimental investigation. *Polymer*, 57:132–142, 2015.

[45] R. Cruz, J. A. da Cruz Ranita, J. Maçaira, F. Ribeiro, A. M. B. da Silva, J. M. Oliveira, M. H. F. V. Fernandes, H. A. Ribeiro, J. G. Mendes, and A. Mendes. Glass–Glass Laser-Assisted Glass Frit Bonding. *IEEE Transactions on Components, Packaging and Manufacturing Technology*, 2(12):1949–1956, 2012.

[46] K. Nötzold, C. Dresbach, J. Graf, and B. Böttge. Temperature dependent fracture toughness of glass frit bonding layers. *Microsystem Technologies*, 16(7):1243–1249, 2010.

[47] K. J. D. Mackenzie, I. W. M. Brown, P. Ranchod, and R. H. Meinhold. Silicate bonding of inorganic materials. *Journal of Materials Science*, 26(3):763–768, 1991.

[48] S. Sinha, K. E. Urbanek, A. Krzywicki, and R. L. Byer. Investigation of the suitability of silicate bonding for facet termination in active fiber devices. *Optics Express*, 15(20):13003–13022, 2007.

[49] E. J. Elliffe. *Aspects of Thermal Noise Modeling in Ground-based Gravitational Wave Detectors and Developments of Hydroxide Catalysis Bonding for Space-based Gravitational Wave Detectors and other Optical Applications*. PhD thesis, University of Glasgow, 2005.

[50] K. R. Williams, K. Gupta, and M. Wasilik. Etch Rates for Micromachining Processing - Part II. *Journal of Microelectromechanical Systems*, 12(6):761–778, 2003.

[51] A. Dari, F. Travasso, H. Vocca, and L. Gammaitoni. Breaking strength tests on silicon and sapphire bondings for gravitational wave detectors. *Classical and Quantum Gravity*, 27(4):1–10, 2010.

[52] R. Douglas, A. A. van Veggel, L. Cunningham, K. Haughian, J. Hough, and S. Rowan. Cryogenic and room temperature strength of sapphire jointed by hydroxide-catalysis bonding. *Classical and Quantum Gravity*, 31(4):1–10, 2014.

[53] L. Cunningham, P. G. Murray, A. Cumming, E. J. Elliffe, G. D. Hammond, K. Haughian, J. Hough, M. Hendry, R. Jones, I. W. Martin, S. Reid, S. Rowan, J. Scott, K. A. Strain, K. Tokmakov, C. Torrie, and A. A. van Veggel. Re-evaluation of the mechanical loss factor of hydroxide-catalysis bonds and its significance for the next generation of gravitational wave detectors. *Physics Letters A*, 374(39):3993–3998, 2010.

[54] P. H. Sneddon, S. Bull, G. Cagnoli, D. R. M. Crooks, E. J. Elliffe, J. E. Faller, M. M. Fejer, J. Hough, and S. Rowan. The intrinsic mechanical loss factor of hydroxy-catalysis bonds for use in the mirror suspensions of gravitational wave detectors. *Classical and Quantum Gravity*, 20(23):5025–5037, 2003.

[55] B. Willke, P. Aufmuth, C. Aulbert, S. Babak, R. Balasubramanian, B. W. Barr, S. Berukoff, S. Bose, G. Cagnoli, M. M. Casey, D. Churches, D. Clubley, C. N. Colacino, D. R. M. Crooks, C. Cutler, K. Danzmann, R. Davies, R. Dupuis, E. Elliffe, C. Fallnich, A. Freise, S. Goßler, A. Grant, H. Grote, G. Heinzel, A. Heptonstall, M. Heurs, M. Hewitson, J. Hough, O. Jennrich, K. Kawabe, K. Kötter, V. Leonhardt, H. Lück, M. Malec, P. W. McNamara, S. A. McIntosh, K. Mossavi, S. Mohanty, S. Mukherjee, S. Nagano, G. P. Newton, B. J. Owen, D. Palmer, M. A. Papa, M. V. Plissi, V. Quetschke, D. I. Robertson, N. A. Robertson, S. Rowan, A. Rüdiger, B. S. Sathyaprakash, R. Schilling, B. F. Schutz, R. Senior, A. M. Sintes, K. D. Skeldon, P. Sneddon, F. Stief, K. A. Strain, I. Taylor, C. I. Torrie, A. Vecchio, H. Ward, U. Weiland, H. Welling, P. Williams, W. Winkler, G. Woan, and I. Zawischa. The GEO 600 gravitational wave detector. *Classical and Quantum Gravity*, 19(7):1377–1387, 2002.

[56] J. Bogenstahl. *Interferometry for the space mission LISA Pathfinder*. PhD thesis, University of Glasgow, 2010.

[57] D. I. Robertson, E. D. Fitzsimons, C. J. Killow, M. Perreur-Lloyd, H. Ward, J. Bryant, A. M. Cruise, G. Dixon, D. Hoyland, D. Smith, and J. Bogenstahl. Construction and testing of the optical bench for LISA Pathfinder. *Classical and Quantum Gravity*, 30(8):1–13, 2013.

[58] A. Einstein. Die Grundlage der allgemeinen Relativitätstheorie. *Annalen der Physik*, 354(7):769–822, 1916.

[59] B. P. Abbott et al. (LIGO Scientific Collaboration and Virgo Collaboration). GW151226: Observation of Gravitational Waves from a 22-Solar-Mass Binary Black Hole Coalescence. *Physical Review Letters*, 116(24):241103–1–241103–14, 2016.

[60] B. P. Abbott et al. (LIGO Scientific and Virgo Collaboration). GW170104: Observation of a 50-Solar-Mass Binary Black Hole Coalescence at Redshift 0.2. *Physical Review Letters*, 118(22):221101–1–221101–17, 2017.

[61] LIGO Scientific Collaboration and Virgo Collaboration. GW170608: Observation of a 19 Solar-mass Binary Black Hole Coalescence. *The Astrophysical Journal Letters*, 851(2):1–11, 2017.

[62] B. P. Abbott et al. (LIGO Scientific Collaboration and Virgo Collaboration). GW170814: A Three-Detector Observation of Gravitational Waves from a Binary Black Hole Coalescence. *Physical Review Letters*, 119(14):141101–1–141101–16, 2017.

[63] B. P. Abbott et al. (LIGO Scientific Collaboration and Virgo Collaboration). GW170817: Observation of Gravitational Waves from a Binary Neutron Star Inspiral. *Physical Review Letters*, 119(16):161101–1–161101–18, 2017.

[64] S. Rowan, S. M. Twyford, J. Hough, D.-H. Gwo, and R. Route. Mechanical losses associated with the technique of hydroxide-catalysis bonding of fused silica. *Physics Letters A*, 246(6):471–478, 1998.

[65] K. Somiya (for the KAGRA Collaboration). Detector configuration of KAGRA - the Japanese cryogenic gravitational-wave detector. *Classical and Quantum Gravity*, 29(12):1–14, 2012.

[66] ET Science Team. Einstein gravitational wave Telescope conceptual design study. *European Gravitational Observatory*, ET-0106C-10(4), 2011.

[67] LIGO Scientific Collaboration. Instrument Science White Paper. *Technical Note*, (LIGO-T1400316-v4), 2015.

[68] N. L. Beveridge, A. A. van Veggel, M. Hendry, P. Murray, R. A. Montgomery, E. Jesse, J. Scott, R. B. Bezensek, L. Cunningham, J. Hough, R. Nawrodt, S. Reid, and S. Rowan. Low-temperature strength tests and SEM imaging of hydroxide catalysis bonds in silicon. *Classical and Quantum Gravity*, 28(8):1–15, 2011.

[69] M. Evans. Cosmic Explorer R&D. *LIGO Document*, G1800983-v1, 2018.

[70] P. E. MacKay, N. L. Beveridge, and T. Wood. Low weight mirror substrates. *SPIE Proceedings*, 8884:88841N–1–88841N–12, 2013.

[71] M. Strachan, R. Myers, K. Cooke, J. Hampshire, J. Hough, S. Rowan, M. van Veggel, K. Kirk, D. Hutson, E. Uzgur, and S.-S. Kim. Novel technologies for small deformable mirrors. *SPIE Proceedings*, 7736:773661–1–773661–6, 2010.

[72] M. Strachan, D. Montgomery, R. Myers, K. Cooke, J. Hampshire, M. Kroedel, J. Hough, S. Rowan, M. van Veggel, K. Kirk, E. Uzgur, S.-S. Kim, and M. Strangwood. Novel technologies for large deformable mirrors. *SPIE Proceedings*, 7736:773664–1–773664–6, 2010.

[73] M. Duchêne, A. A. van Veggel, F. Lemarquis, C. Grèzes-Besset, S. Rowan, J. Hough, and M. Lequime. Transfer process of multilayer optical coatings for patterned components. *Optics Communications*, 285(2):128–132, 2012.

[74] E. Hecht. *Optics*. Pearson, 2017.

[75] A. Foltynowicz. *Fiber-laser-based Noise-Immune Cavity-Enhanced Optical Heterodyne Molecular Spectrometry*. PhD thesis, Umeå University, 2009.

[76] H. H. Telle, Á. González Ureña, and R. J. Donovan. *Laser Chemistry: Spectroscopy, Dynamics and Applications*. Wiley, 2007.

[77] H. Kogelnik and T. Li. Laser Beams and Resonators. *Proceedings of the IEEE*, 54(10):1312–1329, 1966.

[78] F. L. Pedrotti and L. S. Pedrotti. *Introduction to Optics*. Prentice-Hall international, 1993.

[79] E. J. Galvez. Gaussian Beams. *Colgate University*, pages i–54, 2009.

[80] O. S. Heavens. *Optical Properties of Thin Solid Films*. Dover Publications, 1991.

[81] S. Guldin. *Inorganic Nanoarchitectures by Organic Self-Assembly*. Springer International Publishing, 2013.

[82] I. H. Malitson. Interspecimen Comparison of the Refractive Index of Fused Silica. *Journal of the Optical Society of America*, 55(10):1205–1209, 1965.

[83] E. R. Dobrovinskaya, L. A. Lytvynov, and V. Pishchik. *Sapphire: Material, Manufacturing, Applications*. Springer US, 2009.

[84] A. Weidlich and A. Wilkie. Realistic rendering of birefringency in uniaxial crystals. *ACM Transactions on Graphics*, 27(1):6:1–6:12, 2008.

[85] M. C. Simon and R. M. Echarri. Internal reflection in uniaxial crystals II: Coefficients of transmission and reflection for an ordinary incident wave. *Journal of Modern Optics*, 37(1):131–144, 1990.

[86] M. C. Simon and R. M. Echarri. Internal reflection in uniaxial crystals, III: transmission and reflection coefficients for an extraordinary incident wave. *Journal of Modern Optics*, 37(6):1139–1148, 1990.

[87] M. C. Simon and L. I. Perez. Reflection and transmission coefficients in uniaxial crystals. *Journal of Modern Optics*, 38(3):503–518, 1991.

[88] M. C. Simon and R. M. Echarri. Internal reflection in uniaxial crystals I. Geometrical description. *Journal of Modern Optics*, 37(1):121–129, 1990.

[89] M. C. Simon and K. V. Gottschalk. Waves and rays in uniaxial birefringent crystals. *Optik - International Journal for Light and Electron Optics*, 118(10):457–470, 2007.

[90] I. H. Malitson and M. J. Dodge. Refractive Index and Birefringence of Synthetic Sapphire. *Journal of the Optical Society of America*, 62(11):1405, 1972.

[91] M. J. Dodge. Refractive Index. *Handbook of Laser Science and Technology - Volume IV: Optical Materials, Part 2 - CRC Press, Boca Raton*, 1986.

[92] P. Gregory. *Bayesian Logical Data Analysis for the Physical Sciences*. Cambridge University Press, 2005.

[93] J. R. Taylor. *An Introduction to Error Analysis: The Study of Uncertainties in Physical Measurements*. University Science Books, 1997.

[94] K. A. Haughian. *Aspects of Materials Research for Advanced and Future Generations of Gravitational Wave Detectors*. PhD thesis, University of Glasgow, 2012.

[95] R. C. Douglas. *Aspects of hydroxide catalysis bonding of sapphire and silicon for use in future gravitational wave detectors*. PhD thesis, University of Glasgow, 2017.

[96] H. S. Kim and T. L. Schmitz. Shear strength evaluation of hydroxide catalysis bonds for glass–glass and glass–aluminum assemblies. *Precision Engineering*, 37(1):23–32, 2013.

[97] M. van Veggel, H. Armandula, N. Beveridge, W. Cunningham, R. Jones, G. Moreno, and M. Barton. Preparation of an end or input penultimate mass (ETM/ITM PM) (Hydroxide-Catalysis Bonding of ears and gluing prisms and magnet flags). *LIGO Laboratory / LIGO Scientific Collaboration*, (LIGO-E1000277-v13):1–30, 2013.

[98] M. van Veggel, H. Armandula, N. Beveridge, W. Cunningham, R. Jones, and G. Moreno. Preparation of an end or input test mass (ETM/ITM) (Hydroxide-Catalysis Bonding of ears). *LIGO Laboratory / LIGO Scientific Collaboration*, (LIGO-E1000278-v10):1–20, 2014.

[99] K. Green, J. Burke, and B. Oreb. Chemical bonding for precision optical assemblies. *Optical Engineering*, 50(2):023401–1–023401–12, 2011.

[100] M. H. Phelps. *Hydroxide Catalysis and Indium Bonding Research for the Design of Ground-Based Gravitational Wave Detectors*. PhD thesis, University of Glasgow, 2018.

[101] U. Grenander. *Probability and Statistics: The Harald Cramér Volume*. Wiley Publications in Statistics, 1959.

[102] K. Haughian, A. A. van Veggel, L. Cunningham, J. Hough, P. G. Murray, S. Reid, and S. Rowan. Effect of heat treatment and aging on the mechanical loss and strength of hydroxide catalysis bonds between fused silica samples. *Physical Review D*, 96(4):042003–1–042003–9, 2017.

[103] D. Tentori-Santa-Cruz and J. R. Lerma. Refractometry by minimum deviation: accuracy analysis. *Optical Engineering*, 29(2):160–168, 1990.

[104] G. Lagaly, W. Tufar, A. Minihan, and A. Lovell. *Silicates. Ullmann's Encyclopedia of Industrial Chemistry*. Wiley-VCH Verlag GmbH & Co. KGaA, 2000.

[105] R. Nawrodt, S. Rowan, J. Hough, M. Punturo, F. Ricci, and J-Y. Vinet. Challenges in thermal noise for 3rd generation of gravitational wave detectors. *General Relativity and Gravitation*, 43(2):593–622, 2011.

[106] J. C. Stover. *Optical Scattering: Measurement and Analysis*. SPIE Optical Engineering Press, 1995.

[107] L. Ju, X. Chen, Z. Yan, C. Zhao, and D. G. Blair. Scattering in sapphire test masses for gravitational wave detectors. *Journal of Optics A: Pure and Applied Optics*, 11(12):1–9, 2009.

[108] F. Benabid, M. Notcutt, L. Ju, and D. G. Blair. Rayleigh scattering in sapphire test mass for laser interferometric gravitational-wave detectors: I. Measurement of scattering attenuation coefficient. *Optics Communications*, 167(1–6):7–13, 1999.

[109] X. Chen, L. Ju, R. Flaminio, H. Lück, C. Zhao, and D. G. Blair. Rayleigh scattering in fused silica samples for gravitational wave detectors. *Optics Communications*, 284(19):4732–4737, 2011.

[110] A. Alexandrovski, M. Fejer, and R. Route. Optical absorption measurements in sapphire. *LIGO Document*, (LIGO-G000072-00-D), 2000.

[111] T. Tomaru, T. Uchiyama, D. Tatsumi, S. Miyoki, M. Ohashi, K. Kuroda, T. Suzuki, A. Yamamoto, and T. Shintomi. Cryogenic measurement of the optical absorption coefficient in sapphire crystals at 1.064 μm for the large-scale cryogenic gravitational wave telescope. *Physics Letters A*, 283(1-2):80–84, 2001.

[112] J. C. R. Reis, I. M. S. Lampreia, A. F. S. Santos, M. L. C. J. Moita, and G. Douhéret. Refractive Index of Liquid Mixtures: Theory and Experiment. *ChemPhysChem*, 11(17):3722–3733, 2010.

[113] P. R. Saulson. *Fundamentals of Interferometric Gravitational Wave Detectors*. World Scientific, 1994.

[114] G. Harry, T. P. Bodiya, and R. DeSalvo. *Optical Coatings and Thermal Noise in Precision Measurement*. Cambridge University Press, 2012.

[115] A. Einstein. Über die von der molekularkinetischen Theorie der Wärme geforderte Bewegung von in ruhenden Flüssigkeiten suspendierten Teilchen. *Annalen der Physik*, 322(8):549–560, 1905.

[116] A. Einstein. *Investigations on the Theory of Brownian Movement*. Dover Publications, 1956.

[117] V. B. Braginsky, M. L. Gorodetsky, and S. P. Vyatchanin. Thermodynamical fluctuations and photo-thermal shot noise in gravitational wave antennae. *Physics Letters A*, 264(1):1–10, 1999.

[118] V. B. Braginsky, M. L. Gorodetsky, and S. P. Vyatchanin. Thermo-refractive noise in gravitational wave antennae. *Physics Letters A*, 271(5–6):303–307, 2000.

[119] M. Evans, S. Ballmer, M. Fejer, P. Fritschel, G. Harry, and G. Ogin. Thermo-optic noise in coated mirrors for high-precision optical measurements. *Physical Review D*, 78(10), 2008.

[120] R. Brown. A brief Account of Microscopical Observations made in the Months of June, July, and August, 1827, on the Particles contained in the Pollen of Plants; and on the general Existence of active Molecules in Organic and Inorganic Bodies. *Philosophical Magazine Series 2*, 4(21):161–173, 1828.

[121] H. B. Callen and T. A. Welton. Irreversibility and Generalized Noise. *Physical Review*, 83(1):34–40, 1951.

[122] H. B. Callen and R. F. Greene. On a Theorem of Irreversible Thermodynamics. *Physical Review*, 86(5):702–710, 1952.

[123] G. M. Harry, M. R. Abernathy, A. E. Becerra-Toledo, H. Armandula, E. Black, K. Dooley, M. Eichenfield, C. Nwabugwu, A. Villar, D. R. M. Crooks, G. Cagnoli, J. Hough, C. R. How, I. MacLaren, P. Murray, S. Reid, S. Rowan, P. H. Sneddon, M. M. Fejer, R. Route, S. D. Penn, P. Ganau, J.-M. Mackowski, C. Michel, L. Pinard, and A. Remillieux. Titania-doped tantala/silica coatings for gravitational-wave detection. *Classical and Quantum Gravity*, 24(2):405–415, 2007.

[124] R. Flaminio, J. Franc, C. Michel, N. Morgado, L. Pinard, and B. Sassolas. A study of coating mechanical and optical losses in view of reducing mirror thermal noise in gravitational wave detectors. *Classical and Quantum Gravity*, 27(8):1–9, 2010.

[125] A. Ageev, B. Cabrera Palmer, A. De Felice, S. D. Penn, and P. R. Saulson. Very high quality factor measured in annealed fused silica. *Classical and Quantum Gravity*, 21(16):3887–3892, 2004.

[126] A. Heptonstall, M. Barton, C. Cantley, A. Cumming, G. Cagnoli, J. Hough, R. Jones, R. Kumar, I. Martin, S. Rowan, C. Torrie, and S. Zech. Investigation of mechanical dissipation in CO_2 laser-drawn fused silica fibres and welds. *Classical and Quantum Gravity*, 27(3):1–14, 2010.

[127] S. Rowan, S. M. Twyford, R. Hutchins, J. Kovalik, J. E. Logan, A. C. McLaren, N. A. Robertson, and J. Hough. Q factor measurements on prototype fused quartz pendulum suspensions for use in gravitational wave detectors. *Physics Letters A*, 233(4–6):303–308, 1997.

[128] A. A. van Veggel, J. Scott, D. A. Skinner, B. Bezensek, W. Cunningham, J. Hough, I. Martin, P. Murray, S. Reid, and S. Rowan. Strength testing and SEM imaging of hydroxide-catalysis bonds between silicon. *Classical and Quantum Gravity*, 26(17):1–13, 2009.

[129] B. P. Abbott et al. (LIGO Scientific Collaboration). Exploring the sensitivity of next generation gravitational wave detectors. *Classical and Quantum Gravity*, 34(4):1–18, 2017.

[130] A. Schroeter, R. Nawrodt, R. Schnabel, S. Reid, I. Martin, S. Rowan, C. Schwarz, T. Koettig, R. Neubert, M. Thürk, W. Vodel, A. Tünnermann, K. Danzmann, and P. Seidel. On the mechanical quality factors of cryogenic test masses from fused silica and crystalline quartz. *arXiv:0709.4359 [gr-qc]*, 2007.

[131] E. Gustafson, D. Shoemaker, K. Strain, and R. Weiss. LSC White Paper on Detector Research and Development. *LIGO T990080-00-D*, 1999.

[132] R. S. Quimby. *Photonics and Lasers: An Introduction*. John Wiley & Sons, 2006.

[133] P. Horowitz and W. Hill. *The Art of Electronics (Second Edition)*. Cambridge University Press, 1989.

[134] I. S. Gradshteyn and I. M. Ryzhik. *Table of Integrals, Series, and Products (Eighth Edition)*. Elsevier, 2014.